7 Chemical Physics of Colloid Systems and Interfaces

Peter A. Kralchevsky, Krassimir D. Danov, and Nikolai D. Denkov

CONTENTS

7.1 INTRODUCTION

A colloidal system represents a multiphase (heterogeneous) system, in which at least one of the phases exists in the form of very small particles: typically smaller than 1 μm but still much larger than the molecules. Such particles are related to phenomena like Brownian motion, diffusion, and osmosis. The terms microheterogeneous system and disperse system (dispersion) are more general because they include also bicontinuous systems (in which none of the phases is split into separate particles) and systems containing larger, non-Brownian, particles. The term dispersion is often used as a synonym of colloidal system.

Classification of the colloids with respect to the state of aggregation of the disperse and the continuous phases is shown in Table 7.1. Some examples are following.

1. Examples for gas-in-liquid dispersions are the foams or the boiling liquids. Gas-in-solid dispersions are the various porous media like filtration membranes, sorbents, catalysts and isolation materials.
2. Examples for liquid-in-gas dispersions are the mist, the clouds, and other aerosols. Liquid-in-liquid dispersions are the emulsions. At room temperature there are only four types of mutually immiscible liquids: water, hydrocarbon oils, fluorocarbon oils, and liquid metals (Hg and Ga). Many raw materials and products in food and petroleum industries exist in the form of oil-in-water (O/W) or water-in-oil (W/O) emulsions. The soil and some biological tissues can be considered as liquid-in-solid dispersions.
3. Smoke, dust, and some other aerosols are examples for solid-in-gas dispersions. The solid-in-liquid dispersions are termed as suspensions or sols. The pastes and some glues are highly concentrated suspensions. The gels represent bicontinuous structures of solid and liquid. Solid-in-solid dispersions are some metal alloys, many kinds of rocks, some colored glasses, etc.

Below we will consider mostly liquid dispersions, i.e., dispersions with liquid continuous phase like foams, emulsions, and suspensions. Sometimes these are called complex fluids.

In general, the area of the interface between the disperse and continuous phases is rather large. For instance, 1 cm^3 of dispersion with particles of radius 100 nm and volume fraction 30% contains interface of area about 10 m^2. This is the reason why the interfacial properties are of crucial importance for the properties and stability of colloids.

The stabilizing factors for dispersions are the repulsive surface forces, the particle thermal motion, the hydrodynamic resistance of the medium, and the high surface elasticity of fluid particles and films.

TABLE 7.1
Types of Disperse Systems

| Disperse Phase | Continuous Phase | | |
	Gas	Liquid	Solid
Gas	—	Gas in liquid	Gas in solid
Liquid	Liquid in gas	L_1 in L_2	Liquid in solid
Solid	Solid in gas	Solid in liquid	S_1 in S_2

On the contrary, the factors destabilizing dispersions are the attractive surface forces, the factors suppressing the repulsive surface forces, and the low surface elasticity, gravity and other external forces tending to separate the phases.

Sections 7.2 and 7.3 consider effects related to the surface tension of surfactant solution and capillarity. Section 7.4 presents a review on the surface forces due to the intermolecular interactions. Section 7.5 describes the hydrodynamic interparticle forces originating from the effects of bulk and surface viscosity and related to surfactant diffusion. Section 7.6 is devoted to the kinetics of coagulation in dispersions. Section 7.7 discusses foams containing oil drops and solid particulates in relation to the antifoaming mechanisms and the exhaustion of antifoams. Finally, Sections 7.8 and 7.9 address the electrokinetic and optical properties of dispersions.

7.2 SURFACE TENSION OF SURFACTANT SOLUTIONS

7.2.1 STATIC SURFACE TENSION

As a rule the fluid dispersions (emulsions, foams) are stabilized by adsorption layers of amphiphile molecules. These can be ionic [1,2] and nonionic [3] surfactants, lipids, proteins, etc. All of them have the property to lower the value of the surface (or interfacial) tension, σ, in accordance with the Gibbs adsorption equation [4–6]

$$d\sigma = -\sum_i \Gamma_i d\mu_i \qquad (7.1)$$

where
   Γ_i is the surface concentration (adsorption) of the ith component
   μ_i is its chemical potential

The summation in Equation 7.1 is carried out over all components. Usually an equimolecular dividing surface with respect to the solvent is introduced for which the adsorption of the solvent is set zero by definition [4,5]. Then the summation is carried out over all other components. Note that Γ_i is an excess surface concentration with respect to the bulk; Γ_i is positive for surfactants, which decrease σ in accordance with Equation 7.1. On the contrary, Γ_i is negative for aqueous solutions of electrolytes, whose ions are repelled from the surface by the electrostatic image forces [5]; consequently, the addition of electrolytes increases the surface tension of water [6]. For surfactant concentrations above the critical micellization concentration (CMC) μ_i is equal to constant and, consequently, σ is also equal to constant (see Equation 7.1).

7.2.1.1 Nonionic Surfactants

7.2.1.1.1 Types of Adsorption Isotherms
Consider the boundary between an aqueous solution of a nonionic surfactant and a hydrophobic phase, air or oil. The dividing surface is usually chosen to be the equimolecular surface with respect to water, that is $\Gamma_w = 0$. Then Equation 7.1 reduces to $d\sigma = -\Gamma_1 d\mu_1$, where the subscript 1 denotes the surfactant. Because the bulk surfactant concentration is usually not too high, we can use the expression for the chemical potential of a solute in an ideal solution:

$$\mu_1 = \mu_1^{(0)} + kT \ln c_1,$$

where
   k is the Boltzmann constant
   T is the absolute temperature
   c_1 is the concentration of nonionic surfactant
   $\mu_1^{(0)}$ is its standard chemical potential, which is independent of c_1

Thus the Gibbs adsorption equation acquires the form

$$d\sigma = -kT\Gamma_1 d\ln c_1 \qquad (7.2)$$

The surfactant adsorption isotherms, expressing the connection between Γ_1 and c_1, are usually obtained by means of some molecular model of adsorption. Table 7.2 contains the six most popular surfactant adsorption isotherms, those of Henry, Freundlich [7], Langmuir [8], Volmer [9], Frumkin [10], and van der Waals [11]. For $c_1 \to 0$ all isotherms (except that of Freundlich) reduce to the Henry isotherm: $\Gamma_1/\Gamma_\infty = Kc_1$. The physical difference between the Langmuir and Volmer isotherms is that the Langmuir isotherm corresponds to a model of localized adsorption, while the Volmer corresponds to nonlocalized

TABLE 7.2

Types of Adsorption and Surface-Tension Isotherms

Type of Isotherm	Surfactant Adsorption Isotherms (for Nonionic Surfactants: $a_{1s} \equiv c_1$)
Henry	$Ka_{1s} = \dfrac{\Gamma_1}{\Gamma_\infty}$
Freundlich	$Ka_{1s} = \left(\dfrac{\Gamma_1}{\Gamma_\infty}\right)^{1/m}$
Langmuir	$Ka_{1s} = \dfrac{\Gamma_1}{\Gamma_\infty - \Gamma_1}$
Volmer	$Ka_{1s} = \dfrac{\Gamma_1}{\Gamma_\infty - \Gamma_1} \exp\left(\dfrac{\Gamma_1}{\Gamma_\infty - \Gamma_1}\right)$
Frumkin	$Ka_{1s} = \dfrac{\Gamma_1}{\Gamma_\infty - \Gamma_1} \exp\left(-\dfrac{2\beta\Gamma_1}{kT}\right)$
van der Waals	$Ka_{1s} = \dfrac{\Gamma_1}{\Gamma_\infty - \Gamma_1} \exp\left(\dfrac{\Gamma_1}{\Gamma_\infty - \Gamma_1} - \dfrac{2\beta\Gamma_1}{kT}\right)$

	Surface-Tension Isotherm $\sigma = \sigma_0 - kTJ + \sigma_d$ (for Nonionic Surfactants: $\sigma_d \equiv 0$)
Henry	$J = \Gamma_1$
Freundlich	$J = \dfrac{\Gamma_1}{m}$
Langmuir	$J = -\Gamma_\infty \ln\left(1 - \dfrac{\Gamma_1}{\Gamma_\infty}\right)$
Volmer	$J = \dfrac{\Gamma_\infty \Gamma_1}{\Gamma_\infty - \Gamma_1}$
Frumkin	$J = -\Gamma_\infty \ln\left(1 - \dfrac{\Gamma_1}{\Gamma_\infty}\right) - \dfrac{\beta\Gamma_1^2}{kT}$
Van der Waals	$J = \dfrac{\Gamma_\infty \Gamma_1}{\Gamma_\infty - \Gamma_1} - \dfrac{\beta\Gamma_1^2}{kT}$

Note: Surfactant adsorption isotherm and surface-tension isotherm, which are combined to fit experimental data, obligatorily must be of the same type.

adsorption. The Frumkin and van der Walls isotherms generalize, respectively, the Langmuir and Volmer isotherms for case, in which the interaction between neighboring adsorbed molecules is not negligible. (If the interaction parameter β is set as zero, the Frumkin and van der Walls isotherms reduce to the Langmuir and Volmer isotherms, correspondingly.) The comparison between theory and experiment shows that for air–water interfaces $\beta > 0$, whereas for oil–water interfaces we can set $\beta = 0$ [12,13]. The latter facts lead to the conclusion that for air–water interfaces β takes into account the van der Waals attraction between the hydrocarbon tails of the adsorbed surfactant molecules across air; such attraction is missing when the hydrophobic phase is oil. The adsorption parameter K in Table 7.2 characterizes the surface activity of the surfactant: the greater the K, the higher the surface activity. K is related to the standard free energy of adsorption, $\Delta f = \mu_1^0 - \mu_{1s}^0$, which is the energy gain for bringing a molecule from the bulk of the aqueous phase to a diluted adsorption layer [14,15]:

$$K = \frac{\delta_1}{\Gamma_\infty} \exp\left(\frac{\mu_1^{(0)} - \mu_{1s}^{(0)}}{kT}\right) \tag{7.3}$$

where
  δ_1 characterizes the thickness of the adsorption layer; δ_1 can be set (approximately) equal to the length of the amphiphilic molecule
  Γ_∞ represents the maximum possible value of the adsorption

In the case of localized adsorption (Langmuir and Frumkin isotherms) $1/\Gamma_\infty$ is the area per adsorption site. In the case of nonlocalized adsorption (Volmer and van der Waals isotherms) $1/\Gamma_\infty$ is the excluded area per molecule.

　　As mentioned earlier, the Freundlich adsorption isotherm, unlike the others in Table 7.2, does not become linear at low concentrations, but remains convex to the concentration axis. Moreover, it does not show saturation or limiting value. Hence, for the Freundlich adsorption isotherm in Table 7.2 Γ_∞ is a parameter scaling the adsorption (rather than saturation adsorption).

This isotherm can be derived assuming that the solid surface is heterogeneous [16,17]. Consequently, if the data fits the Freundlich equation, this is an indication, but not a proof, that the surface is heterogeneous [6].

The adsorption isotherms in Table 7.2 can be applied to both fluid and solid interfaces. The surface-tension isotherms in Table 7.2, which relate σ and Γ_1, are usually applied to fluid interfaces, although they could also be used for solid–liquid interfaces if σ is identified with the Gibbs [4] superficial tension. (The latter is defined as the force per unit length which opposes every increase of the wet area without any deformation of the solid.)

The surface-tension isotherms in Table 7.2 are deduced from the respective adsorption isotherms in the following way. The integration of Equation 7.2 yields

$$\sigma = \sigma_0 - kTJ \tag{7.4}$$

where σ_0 is the interfacial tension of the pure solvent and

$$J \equiv \int_0^{c_1} \Gamma_1 \frac{dc_1}{c_1} = \int_0^{\Gamma_1} \Gamma_1 \frac{d\ln c_1}{d\Gamma_1} d\Gamma_1 \tag{7.5}$$

The derivative $d\ln c_1/d\Gamma_1$ is calculated for each adsorption isotherm, and then the integration in Equation 7.5 is carried out analytically. The obtained expressions for J are listed in Table 7.2. Each surface-tension isotherm, $\sigma(\Gamma_1)$, has the meaning of a two-dimensional equation of state of the adsorption monolayer, which can be applied to both soluble and insoluble surfactants [6,18].

An important thermodynamic property of a surfactant adsorption monolayer is its Gibbs (surface) elasticity

$$E_G \equiv -\Gamma_1 \left(\frac{\partial \sigma}{\partial \Gamma_1} \right)_T \tag{7.6}$$

Expressions for E_G, corresponding to various adsorption isotherms, are shown in Table 7.3. The Gibbs elasticity characterizes the lateral fluidity of the surfactant adsorption monolayer. At high values of the Gibbs elasticity the adsorption monolayer behaves as tangentially immobile. In such a case, if two emulsion droplets approach each other, the hydrodynamic flow pattern, and the hydrodynamic interaction as well, is almost the same as if the droplets were solid. For lower values of the surfactant adsorption the so-called Marangoni effect appears, which is equivalent to the appearance of gradients of surface tension due to gradients of surfactant adsorption: $\nabla_s \sigma = -(E_G/\Gamma_1)\nabla_s \Gamma_1$, where ∇_s denotes surface gradient operator. The Marangoni effect can considerably affect the hydrodynamic interactions of fluid particles (drops and bubbles) (see Section 7.5).

7.2.1.1.2 Derivation from First Principles

Each surfactant adsorption isotherm (that of Langmuir, Volmer, Frumkin, etc.), and the related expressions for the surface tension and surface chemical potential, can be derived from an expression for the surface free energy, F_s, which corresponds to a given physical model. This derivation helps us obtain (or identify) the self-consistent system of equations, referring to a given

---

TABLE 7.3
Elasticity of Adsorption Monolayers at a Fluid Interface

Type of Isotherm (cf. Table 7.2)	Gibbs Elasticity E_G
Henry	$E_G = kT\Gamma_1$
Freundlich	$E_G = kT\dfrac{\Gamma_1}{m}$
Langmuir	$E_G = kT\Gamma_1 \dfrac{\Gamma_\infty}{\Gamma_\infty - \Gamma_1}$
Volmer	$E_G = kT\Gamma_1 \dfrac{\Gamma_\infty^2}{(\Gamma_\infty - \Gamma_1)^2}$
Frumkin	$E_G = kT\Gamma_1 \left(\dfrac{\Gamma_\infty}{\Gamma_\infty - \Gamma_1} - \dfrac{2\beta\Gamma_1}{kT} \right)$
van der Waals	$E_G = kT\Gamma_1 \left[\dfrac{\Gamma_\infty^2}{(\Gamma_\infty - \Gamma_1)^2} - \dfrac{2\beta\Gamma_1}{kT} \right]$

Note: Above expressions are valid for both nonionic and ionic surfactants.

TABLE 7.4

Free Energy and Chemical Potential for Surfactant Adsorption Layers

Type of Isotherm	Surface Free Energy $F_s(T, A, N_1)$ $(M = \Gamma_\infty A)$
Henry	$F_s = N_1 \mu_{1s}^{(0)} + kT[N_1 \ln(N_1/M) - N_1]$
Freundlich	$F_s = N_1 \mu_{1s}^{(0)} + \dfrac{kT}{m}[N_1 \ln(N_1/M) - N_1]$
Langmuir	$F_s = N_1 \mu_{1s}^{(0)} + kT[N_1 \ln N_1 + (M - N_1)\ln(M - N_1) - M \ln M]$
Volmer	$F_s = N_1 \mu_{1s}^{(0)} + kT[N_1 \ln N_1 - N_1 - N_1 \ln(M - N_1)]$
Frumkin	$F_s = N_1 \mu_{1s}^{(0)} + kT[N_1 \ln N_1 + (M - N_1)\ln(M - N_1) - M \ln M] + \dfrac{\beta \Gamma_\infty N_1^2}{2M}$
van der Waals	$F_s = N_1 \mu_{1s}^{(0)} + kT[N_1 \ln N_1 - N_1 - N_1 \ln(M - N_1)] + \dfrac{\beta \Gamma_\infty N_1^2}{2M}$

	Surface Chemical Potential μ_{1s} $(\theta \equiv \Gamma_1/\Gamma_\infty)$
Henry	$\mu_{1s} = \mu_{1s}^{(0)} + kT \ln \theta$
Freundlich	$\mu_{1s} = \mu_{1s}^{(0)} + \dfrac{kT}{m} \ln \theta$
Langmuir	$\mu_{1s} = \mu_{1s}^{(0)} + kT \ln \dfrac{\theta}{1 - \theta}$
Volmer	$\mu_{1s} = \mu_{1s}^{(0)} + kT\left(\dfrac{\theta}{1 - \theta} + \ln \dfrac{\theta}{1 - \theta}\right)$
Frumkin	$\mu_{1s} = \mu_{1s}^{(0)} + kT \ln \dfrac{\theta}{1 - \theta} - 2\beta\Gamma_1$
van der Waals	$\mu_{1s} = \mu_{1s}^{(0)} + kT\left(\dfrac{\theta}{1 - \theta} + \ln \dfrac{\theta}{1 - \theta}\right) - 2\beta\Gamma_1$

model, which is to be applied to interpret a set of experimental data. Combination of equations corresponding to different models (say Langmuir adsorption isotherm with Frumkin surface-tension isotherm) is incorrect and must be avoided.

The general scheme for derivation of the adsorption isotherms is the following:

1. With the help of statistical mechanics an expression is obtained, say, for the canonical ensemble partition function, Q, from which the surface free energy F_s is determined [11]:

$$F_s(T, A, N_1) = kT \ln Q(T, A, N_1) \tag{7.7}$$

where
   A is the interfacial area
   N_1 is the number of adsorbed surfactant molecules (see Table 7.4)

2. Differentiating the expression for F_s, we derive expressions for the surface pressure, π_s, and the surface chemical potential of the adsorbed surfactant molecules, μ_{1s} [11]:

$$\pi_s \equiv \sigma_0 - \sigma = -\left(\frac{\partial F_s}{\partial A}\right)_{T, N_1}, \quad \mu_{1s} = \left(\frac{\partial F_s}{\partial N_1}\right)_{T, A} \tag{7.8}$$

Combining the obtained expressions for π_s and μ_{1s}, we can deduce the respective form of the Butler equation [19] (see Equation 7.16).

3. The surfactant adsorption isotherm (Table 7.2) can be derived by setting the obtained expression for the surface chemical potential μ_{1s} equal to the bulk chemical potential of the surfactant molecules in the subsurface layer (i.e., equilibrium between surface and subsurface is assumed) [11]:

$$\mu_{1s} = \mu_1^{(0)} + kT \ln(a_{1s}\delta_1/\Gamma_\infty) \tag{7.9}$$

Where a_{1s} is the activity of the surfactant molecule in the subsurface layer; a_{1s} is scaled with the volume per molecule in a dense (saturated) adsorption layer, $v_1 = \delta_1/\Gamma_\infty$, where δ_1 is interpreted as the thickness of the adsorption layer, or the length of an adsorbed molecule. In terms of the subsurface activity, a_{1s}, Equation 7.9 can be applied to ionic surfactants and to dynamic

processes. In the simplest case of nonionic surfactants and equilibrium processes we have $a_{1s} \approx c_1$, where c_1 is the bulk surfactant concentration.

First, let us apply the above general scheme to derive the Frumkin isotherm, which corresponds to localized adsorption of interacting molecules. (Expressions corresponding to the Langmuir isotherm can be obtained by setting $\beta = 0$ in the respective expressions for the Frumkin isotherm.) Let us consider the interface as a two-dimensional lattice having M adsorption sites. The corresponding partition function is [11]

$$Q(T, M, N_1) = \frac{M!}{N_1!(M - N_1)!}[q(T)]N_1 \exp\left(-\frac{n_c w N_1^2}{2kTM}\right) \tag{7.10}$$

The first multiplier in the right-hand side of Equation 7.10 expresses the number of ways N_1 indistinguishable molecules can be distributed among M labeled sites; the partition function for a single adsorbed molecule is $q = q_x q_y q_z$, where q_x, q_y, and q_z are one-dimensional harmonic-oscillator partition functions. The exponent in Equation 7.10 accounts for the interaction between adsorbed molecules in the framework of the Bragg–Williams approximation [11]. w is the nearest-neighbor interaction energy of two molecules and n_c is the number of nearest-neighbor sites to a given site (e.g., $n_c = 4$ for a square lattice). Then, we substitute Equation 7.10 into Equation 7.7 and using the known Stirling approximation, $\ln M! = M \ln M - M$, we get the expression for the surface free energy corresponding to the Frumkin model:

$$F_s = kT[N_1 \ln N_1 + (M - N_1)\ln(M - N_1) - M \ln M - N_1 \ln q(T)] + \frac{n_c w N_1^2}{2M} \tag{7.11}$$

Note that

$$M = \Gamma_\infty A, \quad N_1 = \Gamma_1 A \tag{7.12}$$

where Γ_∞^{-1} is the area per one adsorption site in the lattice. Differentiating Equation 7.11 in accordance with Equation 7.8, we deduce expressions for the surface pressure and chemical potential [11]:

$$\pi_s = -\Gamma_\infty kT \ln(1 - \theta) - \beta\Gamma_1^2 \tag{7.13}$$

$$\mu_{1s} = \mu_{1s}^{(0)} + kT \ln\frac{\theta}{1 - \theta} - 2\beta\Gamma_1 \tag{7.14}$$

where we have introduced the notation

$$\theta = \frac{\Gamma_1}{\Gamma_\infty}, \quad \beta = -\frac{n_c w}{2\Gamma_\infty}, \quad \mu_{1s}^{(0)} = -kT \ln q(T) \tag{7.15}$$

We can check that Equation 7.13 is equivalent to the Frumkin's surface-tension isotherm in Table 7.2 for a nonionic surfactant. Furthermore, eliminating $\ln(1 - \theta)$ between Equations 7.13 and 7.14, we obtain the Butler equation in the following form [19]

$$\mu_{1s} = \mu_{1s}^{(0)} + \Gamma_\infty^{-1}\pi_s + kT \ln(\gamma_{1s}\theta) \quad \text{(Butler equation)} \tag{7.16}$$

where we have introduced the surface activity coefficient

$$\gamma_{1s} = \exp\left[-\frac{\beta\Gamma_\infty\theta(2 - \theta)}{kT}\right] \quad \text{(for Frumkin isotherm)} \tag{7.17}$$

(In the special case of Langmuir isotherm we have $\beta = 0$, and then $\gamma_{1s} = 1$.) The Butler equation is used by many authors [12,20–22] as a starting point for the development of thermodynamic adsorption models. It should be kept in mind that the specific form of the expressions for π_s and γ_{1s}, which are to be substituted in Equation 7.16, is not arbitrary, but must correspond to the same thermodynamic model (to the same expression for F_s—in our case Equation 7.11). Finally, substituting Equation 7.16 into Equation 7.9, we derive the Frumkin adsorption isotherm in Table 7.2, where K is defined by Equation 7.3.

Now, let us apply the same general scheme, but this time to the derivation of the van der Waals isotherm, which corresponds to nonlocalized adsorption of interacting molecules. (Expressions corresponding to the Volmer isotherm can be

obtained by setting $\beta = 0$ in the respective expressions for the van der Waals isotherm.) Now the adsorbed N_1 molecules are considered as a two-dimensional gas. The corresponding expression for the canonical ensemble partition function is

$$Q(T, M, N_1) = \frac{1}{N_1!} q^{N_1} \exp\left(-\frac{n_c w N_1^2}{2kTM}\right) \tag{7.18}$$

where the exponent accounts for the interaction between adsorbed molecules, again in the framework of the Bragg–Williams approximation. The partition function for a single adsorbed molecule is $q = q_{xy}\, q_z$, where q_z is one-dimensional (normal to the interface) harmonic-oscillator partition function. On the other hand, the adsorbed molecules have free translational motion in the xy-plane (the interface); therefore we have [11]

$$q_{xy} = \frac{2\pi \widetilde{m} kT}{h_p^2} \hat{A} \tag{7.19}$$

where
   $\widetilde{m}$ is the molecular mass
   h_p is the Planck constant
   $\hat{A} = A - N_1 \Gamma_\infty^{-1}$ is the area accessible to the moving molecules; the parameter Γ_∞^{-1} is the excluded area per molecule, which accounts for the molecular size

Having in mind that $M \equiv \Gamma_\infty A$, we can bring Equation 7.18 into the form

$$Q(T, M, N_1) = \frac{1}{N_1!} q_0^{N_1} (M - N_1)^{N_1} \exp\left(-\frac{n_c w N_1^2}{2kTM}\right) \tag{7.20}$$

where

$$q_0(T) \equiv \frac{2\pi \widetilde{m} kT}{h_p^2 \Gamma_\infty} q_z(T) \tag{7.21}$$

Further, we substitute Equation 7.20 into Equation 7.7, using the Stirling approximation, we determine the surface free energy corresponding to the van der Waals model [11,18,23]:

$$F_s = kT[N_1 \ln N_1 - N_1 - N_1 \ln q_0(T) - N_1 \ln (M - N_1)] + \frac{n_c w N_1^2}{2M} \tag{7.22}$$

Again, having in mind that $M \equiv \Gamma_\infty A$, we differentiate Equation 7.22 in accordance with Equation 7.8 to deduce expressions for the surface pressure and chemical potential:

$$\pi_s = \Gamma_\infty kT \frac{\theta}{1 - \theta} - \beta \Gamma_1^2 \tag{7.23}$$

$$\mu_{1s} = \mu_{1s}^{(0)} + kT\left(\frac{\theta}{1 - \theta} + \ln \frac{\theta}{1 - \theta}\right) - 2\beta \Gamma_1 \tag{7.24}$$

where $\mu_{1s}^{(0)} = kT \ln q_0(T)$ and β is defined by Equation 7.15. We can check that Equation 7.23 is equivalent to the van der Waals surface-tension isotherm in Table 7.2 for a nonionic surfactant. Furthermore, combining Equations 7.23 and 7.24, we obtain the Butler equation (Equation 7.16), but this time with another expression for the surface activity coefficient

$$\gamma_{1s} = \frac{1}{1 - \theta} \exp\left[-\frac{\beta \Gamma_\infty \theta(2 - \theta)}{kT}\right] \quad \text{(for van der Waals isotherm)} \tag{7.25}$$

(In the special case of Volmer isotherm we have $\beta = 0$, and then $\gamma_{1s} = 1/(1 - \theta)$.) Finally, substituting Equation 7.24 into Equation 7.9, we derive the van der Waals adsorption isotherm in Table 7.2, with K defined by Equation 7.3.

   In Table 7.4 we summarize the expressions for the surface free energy, F_s, and chemical potential μ_{1s}, for several thermodynamic models of adsorption. We recall that the parameter Γ_∞ is defined in different ways for the different models. On the other hand, the parameter K is defined in the same way for all models, viz. by Equation 7.3. The expressions in Tables 7.2 through 7.4 can be generalized for multicomponent adsorption layers [18,27].

At the end of this section, let us consider a general expression, which allows us to obtain the surface activity coefficient γ_{1s} directly from the surface pressure isotherm $\pi_s(\theta)$. From the Gibbs adsorption isotherm, $d\pi_s = \Gamma_1 d\mu_{1s}$, it follows that

$$\left(\frac{\partial \mu_{1s}}{\partial \Gamma_1}\right)_T = \frac{1}{\Gamma_1}\left(\frac{\partial \pi_s}{\partial \Gamma_1}\right)_T \tag{7.26}$$

By substituting μ_{1s} from the Butler's Equation 7.16 into Equation 7.26, and integrating we can derive the sought for expression:

$$\ln \gamma_{1s} = \int\limits_{0}^{\theta} \left(\frac{(1-\theta)}{\Gamma_\infty kT}\frac{\partial \pi_s}{\partial \theta} - 1\right)\frac{d\theta}{\theta} \tag{7.27}$$

We can check that substitution of π_s from Equations 7.13 and 7.23 into Equation 7.27 yields, respectively, the Frumkin and van der Waals expressions for γ_{1s}, viz. Equations 7.17 and 7.25.

7.2.1.2 Ionic Surfactants

7.2.1.2.1 Gouy Equation

The thermodynamics of adsorption of ionic surfactants [13,24–28] is more complicated (in comparison with that of nonionics) because of the presence of long-range electrostatic interactions and, in particular, electric double layer (EDL) in the system (see Figure 7.1). The electrochemical potential of the ionic species can be expressed in the form [29]

$$\mu_i = \mu_i^{(0)} + kT \ln a_i + Z_i e \psi \tag{7.28}$$

where
    e is the elementary electric charge
    ψ is the electric potential
    Z_i is the valence of the ionic component i
    a_i is its activity

In the EDL (Figure 7.1) the electric potential and the activities of the ions are dependent on the distance z from the phase boundary: $\psi = \psi(z)$, $a_i = a_i(z)$. At equilibrium the electrochemical potential, μ_i, is uniform throughout the solution, including the EDL (otherwise diffusion fluxes would appear) [29]. In the bulk of solution ($z \to \infty$) the electric potential tends to a constant value, which is usually set equal to zero, that is $\psi \to 0$ and $\partial\psi/\partial z \to 0$ for $z \to \infty$. If the expression for μ_i at $z \to \infty$ and that for μ_i at some finite z are set equal, from Equation 7.28 we obtain a Boltzmann-type distribution for the activity across the EDL [29]:

$$a_i(z) = a_{i\infty} \exp\left[-\frac{Z_i e \psi(z)}{kT}\right] \tag{7.29}$$

where $a_{i\infty}$ denotes the value of the activity of ion i in the bulk of solution. If the activity in the bulk, $a_{i\infty}$, is known, then Equation 7.29 determines the activity $a_i(z)$ in each point of the EDL. A good agreement between theory and experiment can be achieved [12,13,27] using the following expression for $a_{i\infty}$:

$$a_{i\infty} = \gamma_\pm c_{i\infty} \tag{7.30}$$

where
    $c_{i\infty}$ is the bulk concentration of the respective ion
    $\gamma_\pm$ is the activity coefficient calculated from the known formula [30]

$$\log \gamma_\pm = -\frac{A|Z_+ Z_-|\sqrt{I}}{1 + B d_i \sqrt{I}} + bI \tag{7.31}$$

which originates from the Debye–Hückel theory; I denotes the ionic strength of the solution:

$$I \equiv \frac{1}{2}\sum_i Z_i^2 c_{i\infty} \tag{7.32}$$
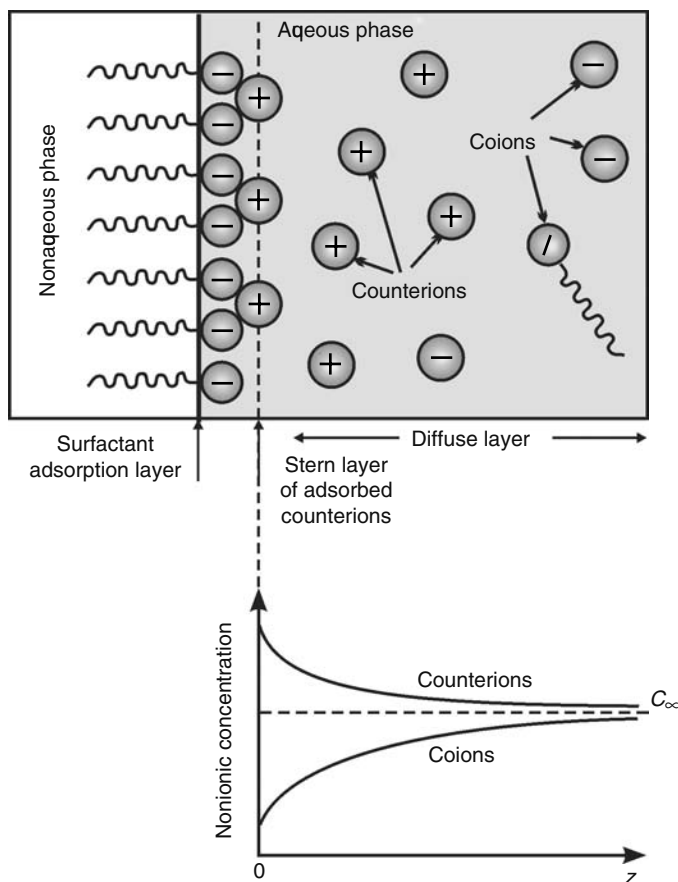
FIGURE 7.1 Electric double layer in the vicinity of an adsorption layer of ionic surfactant. (a) Diffuse layer contains free ions involved in Brownian motion, while Stern layer consists of adsorbed (bound) counterions. (b) Near the charged surface there is an accumulation of counterions and a depletion of coions.

where the summation is carried out over all ionic species in the solution. When the solution contains a mixture of several electrolytes, then Equation 7.31 defines $\gamma_{\pm}$ for each separate electrolyte, with Z_+ and Z_- being the valences of the cations and anions of this electrolyte, but with I being the total ionic strength of the solution, accounting for all dissolved electrolytes [30]. The log in Equation 7.31 is decimal, d_i is the ionic diameter, A, B, and b are parameters, whose values can be found in Ref. [30]. For example, if I is given in moles per liter (M), the parameters values are $A = 0.5115$ M$^{-1/2}$, $Bd_i = 1.316$ M$^{-1/2}$, and $b = 0.055$ M^{-1} for solutions of NaCl at 25°C.

The theory of EDL provides a connection between surface charge and surface potential (known as the Gouy equation [31,32] of Graham equation [33,34]), which can be presented in the form [27,35]

$$\sum_{i=1}^{N} = z_i \Gamma_i \frac{2}{\kappa_c} \left\{ \sum_{i=1}^{N} a_{i\infty} [\exp(-z_i \Phi_s) - 1] \right\}^{1/2} \quad \text{(Gouy equation)} \qquad (7.33)$$

where Γ_i $(i = 1, \ldots, N)$ are the adsorptions of the ionic species, $z_i = Z_i/Z_1$, and the index $i = 1$ corresponds to the surfactant ions

$$\kappa_c^2 \equiv \frac{2Z_1^2 e^2}{\varepsilon_0 \varepsilon kT}, \quad \Phi_s \equiv \frac{Z_1 e \psi_s}{kT} \qquad (7.34)$$

ε is the dielectric permittivity of the medium (water), $\psi_s = \psi(z = 0)$ is the surface potential. Note that the Debye parameter is $\kappa^2 = \kappa_c^2 I$.

For example, let us consider a solution of an ionic surfactant, which is a symmetric 1:1 electrolyte, in the presence of a symmetric, 1:1, inorganic electrolyte (salt). We assume that the counterions due to the surfactant and salt are identical. For example, this can be a solution of sodium dodecyl sulfate (SDS) in the presence of NaCl. We denote by $c_{1\infty}$, $c_{2\infty}$, and $c_{3\infty}$ the bulk concentrations of the surface-active ions, counterions, and coions, respectively (Figure 7.1). For the special system of SDS

with NaCl $c_{1\infty}$, $c_{2\infty}$, and $c_{3\infty}$ are the bulk concentration of the DS$^-$, Na$^+$, and Cl$^-$ ions, respectively. The requirement for the bulk solution to be electroneutral implies $c_{2\infty} = c_{1\infty} + c_{3\infty}$. The multiplication of the last equation by $\gamma_\pm$ yields

$$a_{2\infty} = a_{1\infty} + a_{3\infty} \tag{7.35}$$

The adsorption of the coions of the nonamphiphilic salt is expected to be equal to zero, $\Gamma_3 = 0$, because they are repelled by the similarly charged interface [27,36–38]. However, the adsorption of surfactant at the interface, Γ_1, and the binding of counterions in the Stern layer, Γ_2, are different from zero (Figure 7.1). For this system the Gouy equation (Equation 7.33) acquires the form

$$\Gamma_1 - \Gamma_2 = \frac{4}{\kappa_c} \sqrt{a_{2\infty}} \, \sinh\left(\frac{\Phi_s}{2}\right) \quad (Z_1 : Z_1 \text{ electrolyte}) \tag{7.36}$$

7.2.1.2.2 Contributions from the Adsorption and Diffuse Layers

In general, the total adsorption $\widetilde{\Gamma}_i$ of an ionic species include contributions from both the adsorption layer (surfactant adsorption layer and adsorbed counterions in the Stern layer), Γ_i, and the diffuse layer, Λ_i [13,24,26,27]:

$$\widetilde{\Gamma}_i = \Gamma_i + \Lambda_i,$$

where

$$\Lambda_i \equiv \int_0^\infty [a_i(z) - a_{i\infty}] \, dz \tag{7.37}$$

$\widetilde{\Gamma}_i$ represents a surface excess of component i with respect to the uniform bulk solution. Because the solution is electroneutral, we have $\sum_{i=1}^N z_i \widetilde{\Gamma}_i = 0$. Note, however, that $\sum_{i=1}^N z_i \Gamma_i \neq 0$, see the Gouy equation (Equation 7.33). Expressions for Λ_i can be obtained by using the theory of EDL. For example, because of the electroneutrality of the solution, the right-hand side of Equation 7.36 is equal to $\Lambda_2 - \Lambda_1 - \Lambda_3$, where

$$\Lambda_2 = 2a_{2\infty}\kappa^{-1}[\exp(\Phi_s/2) - 1]; \quad \Lambda_j = 2a_{j\infty}\kappa^{-1}[\exp(-\Phi_s/2) - 1], \quad j = 1,3. \tag{7.38}$$

($\kappa^2 = \kappa_c^2 I$; $Z_1 : Z_1$ electrolyte). In analogy with Equation 7.37, the interfacial tension of the solution, σ, can be expressed as a sum of contributions from the adsorption and diffuse layers [24,27,32]:

$$\sigma = \sigma_a + \sigma_d \tag{7.39}$$

where

$$\sigma_a = \sigma_o - kTJ \quad \text{and} \quad \sigma_d = -\varepsilon_0 \varepsilon \int_0^\infty \left(\frac{d\psi}{dz}\right)^2 dz \tag{7.40}$$

Expressions for J are given in Table 7.2 for various types of isotherms. Note that Equations 7.39 and 7.40 are valid under both equilibrium and dynamic conditions. In the special case of SDS + NaCl solution (see above), at equilibrium, we can use the theory of EDL to express $d\psi/dz$; then from Equation 7.40 we can derive [24,27,32]

$$\sigma_d = -\frac{8kT}{\kappa_c} \sqrt{a_{2\infty}} \left[\cosh\left(\frac{\Phi_s}{2}\right) - 1\right] \quad (Z_1 : Z_1 \text{ electrolyte, at equilibrium}) \tag{7.41}$$

Analytical expressions for σ_d for the cases of 2:1, 1:2, and 2:2 electrolytes can be found in Refs. [27,35].

In the case of ionic surfactant Equation 7.1 can be presented in two alternative, but equivalent forms [27,35]

$$d\sigma = -kT \sum_{i=1}^N \widetilde{\Gamma}_i d\ln a_{i\infty} \quad (T = \text{constant}) \tag{7.42}$$

$$d\sigma_a = -kT \sum_{i=1}^N \Gamma_i d\ln a_{is} \quad (T = \text{constant}) \tag{7.43}$$

where $a_{is} = a_i(z = 0)$ is the subsurface value of activity a_i. From Equations 7.29 and 7.34, we obtain

$$a_{is} = a_{i\infty} \exp(-z_i \Phi_s) \tag{7.44}$$

The comparison between Equations 7.42 and 7.43 shows that the Gibbs adsorption equation can be expressed either in terms of σ, $\widetilde{\Gamma}_i$, and $a_{i\infty}$, or in terms of σ_a, Γ_i, and a_{is}. Note that Equations 7.42 and 7.44 are valid under equilibrium conditions, while Equation 7.43 can also be used for the description of dynamic surface tension (Section 7.2.2) in the case of surfactant adsorption under diffusion control, assuming local equilibrium between adsorptions Γ_i and subsurface concentrations of the respective species.

The expression $\sigma_a = \sigma_0 - kTJ$, with J given in Table 7.2, can be used for description of both static and dynamic surface tension of ionic and nonionic surfactant solutions. The surfactant adsorption isotherms in this table can be used for both ionic and nonionic surfactants, with the only difference that in the case of ionic surfactant the adsorption constant K depends on the subsurface concentration of the inorganic counterions [27] (see Equation 7.48).

7.2.1.2.3 Effect of Counterion Binding

As an example, let us consider again the special case of SDS + NaCl solution. In this case, the Gibbs adsorption Equation 7.1, takes the form

$$d\sigma_a = -kT(\Gamma_1 d\ln a_{1s} + \Gamma_2 d\ln a_{2s}) \tag{7.45}$$

where, as before, the indices 1 and 2 refer to the DS^- and Na^+ ions, respectively. The differentials in the right-hand side of Equation 7.45 are independent (we can vary independently the concentrations of surfactant and salt), and moreover, $d\sigma_a$ is an exact (total) differential. Then, according to the Euler condition, the cross derivatives must be equal [27]:

$$\frac{\partial \Gamma_1}{\partial \ln a_{2s}} = \frac{\partial \Gamma_2}{\partial \ln a_{1s}} \tag{7.46}$$

A surfactant adsorption isotherm, $\Gamma_1 = \Gamma_1(a_{1s}, a_{2s})$, and a counterion adsorption isotherm, $\Gamma_2 = \Gamma_2(a_{1s}, a_{2s})$, are thermodynamically compatible only if they satisfy Equation 7.46. The counterion adsorption isotherm is usually taken in the form

$$\frac{\Gamma_2}{\Gamma_1} = \frac{K_2 a_{2s}}{1 + K_2 a_{2s}} \quad \text{(Stern isotherm)} \tag{7.47}$$

where K_2 is a constant parameter. The latter equation, termed the Stern isotherm [39], describes Langmuirian adsorption (binding) of counterions in the Stern layer. It can be proven that a sufficient condition Γ_2 form Equation 7.47 to satisfy the Euler's condition (Equation 7.46), together with one of the surfactant adsorption isotherms for Γ_1 in Table 7.2, is [27]

$$K = K_1(1 + K_2 a_{2s}) \tag{7.48}$$

where K_1 is another constant parameter. In other words, if K is expressed by Equation 7.48, the Stern isotherm (Equation 7.47) is thermodynamically compatible with all the surfactant adsorption isotherms in Table 7.2. In analogy with Equation 7.3, the parameters K_1 and K_2 are related to the respective standard free energies of adsorption of surfactant ions and counterions $\Delta\mu_i^{(0)}$:

$$K_i = \frac{\delta_i}{\Gamma_\infty} \exp\left(\frac{\Delta\mu_i^{(0)}}{kT}\right) \quad (i = 1, 2) \tag{7.49}$$

where δ_i stands for the thickness of the respective adsorption layer.

7.2.1.2.4 Dependence of Adsorption Parameter K on Salt Concentration

The physical meaning of Equation 7.48 can be revealed by chemical-reaction considerations. For simplicity, let us consider Langmuir-type adsorption, i.e., we treat the interface as a two-dimensional lattice. We will use the notation θ_0 for the fraction of the free sites in the lattice, θ_1 for the fraction of sites containing adsorbed surfactant ion S^-, and θ_2 for the fraction of sites containing the complex of an adsorbed surfactant ion and a bound counterion. Obviously, we can write $\theta_0 + \theta_1 + \theta_2 = 1$. The adsorptions of surfactant ions and counterions can be expressed in the form:

$$\Gamma_1/\Gamma_\infty = \theta_1 + \theta_2; \quad \Gamma_2/\Gamma_\infty = \theta_2 \tag{7.50}$$

Following Kalinin and Radke [119], we consider the reaction of adsorption of S^- ions:

$$A_0 + S^- = A_0 S^- \tag{7.51}$$

where A_0 symbolizes an empty adsorption site. In accordance with the rules of the chemical kinetics, we can express the rates of adsorption and desorption in the form:

$$r_{1,\text{ads}} = K_{1,\text{ads}}\theta_0 c_{1s}, \quad r_{1,\text{des}} = K_{1,\text{des}}\theta_1 \tag{7.52}$$

where
$\quad c_{1s}$ is the subsurface concentration of surfactant
$\quad K_{1,\text{ads}}$ and $K_{1,\text{des}}$ are the rate constants of adsorption and desorption

In view of Equation 7.50, we can write $\theta_0 = (\Gamma_\infty - \Gamma_1)/\Gamma_\infty$ and $\theta_1 = (\Gamma_1 - \Gamma_2)/\Gamma_\infty$. Thus, with the help of Equation 7.52 we obtain the net adsorption flux of surfactant:

$$Q_1 \equiv r_{1,\text{ads}} - r_{1,\text{des}} = K_{1,\text{ads}}c_{1s}(\Gamma_\infty - \Gamma_1)/\Gamma_\infty - K_{1,\text{des}}(\Gamma_1 - \Gamma_2)/\Gamma_\infty \tag{7.53}$$

Next, let us consider the reaction of counterion binding:

$$A_0 S^- + M^+ = A_0 SM \tag{7.54}$$

The rates of the direct and reverse reactions are, respectively,

$$r_{2,\text{ads}} = K_{2,\text{ads}}\theta_1 c_{2s}, \quad r_{2,\text{des}} = K_{2,\text{des}}\theta_2 \tag{7.55}$$

where
$\quad K_{2,\text{ads}}$ and $K_{2,\text{des}}$ are the respective rate constants
$\quad c_{2s}$ is the subsurface concentration of counterions

Having in mind that $\theta_1 = (\Gamma_1 - \Gamma_2)/\Gamma_\infty$ and $\theta_2 = \Gamma_2/\Gamma_\infty$, with the help of Equation 7.55 we deduce an expression for the adsorption flux of counterions:

$$Q_2 \equiv r_{2,\text{ads}} - r_{2,\text{des}} = K_{2,\text{ads}} \, c_{2s}(\Gamma_1 - \Gamma_2)/\Gamma_\infty - K_{2,\text{des}}\Gamma_2/\Gamma_\infty \tag{7.56}$$

If we can assume that the reaction of counterion binding is much faster than the surfactant adsorption, then we can set $Q_2 \equiv 0$, and Equation 7.56 reduces to the Stern isotherm (Equation 7.47) with $K_2 \equiv K_{2,\text{ads}}/K_{2,\text{des}}$. Next, a substitution of Γ_2 from Equation 7.47 into Equation 7.53 yields [35]

$$Q_1 \equiv r_{1,\text{ads}} - r_{1,\text{des}} = K_{1,\text{ads}} \, c_{1s}(\Gamma_\infty - \Gamma_1)/\Gamma_\infty - K_{1,\text{des}}(1 + K_2 c_{2s})^{-1}\Gamma_1/\Gamma_\infty \tag{7.57}$$

Equation 7.57 shows that the adsorption flux of surfactant is influenced by the subsurface concentration of counterions, c_{2s}. At last, if there is equilibrium between surface and subsurface, we have to set $Q_1 \equiv 0$ in Equation 7.57, and thus obtain the Langmuir isotherm for an ionic surfactant:

$$K c_{1s} = \Gamma_1/(\Gamma_\infty - \Gamma_1), \quad \text{with } K \equiv (K_{1,\text{ads}}/K_{1,\text{des}})(1 + K_2 c_{2s}) \tag{7.58}$$

Note that $K_1 \equiv K_{1,\text{ads}}/K_{1,\text{des}}$. This result demonstrates that the linear dependence of K on c_{2s} (Equation 7.48) can be deduced from the reactions of surfactant adsorption and counterion binding (Equations 7.51 and 7.54). (For $I < 0.1$ M we have $\gamma_\pm \approx 1$ and then activities and concentrations of the ionic species coincide.)

7.2.1.2.5 Comparison of Theory and Experiment

As illustration, we consider the interpretation of experimental isotherms by Tajima et al. [38,40,41] for the surface tension σ versus SDS concentrations at 11 fixed concentrations of NaCl (see Figure 7.2). Processing the set of data for the interfacial tension $\sigma = \sigma(c_{1\infty}, c_{2\infty})$ as a function of the bulk concentrations of surfactant (DS^-) ions and Na^+ counterions, $c_{1\infty}$ and $c_{2\infty}$, we can determine the surfactant adsorption, $\Gamma_1(c_{1\infty}, c_{2\infty})$, the counterion adsorption, $\Gamma_2(c_{1\infty}, c_{2\infty})$, the surface potential, $\psi_s(c_{1\infty}, c_{2\infty})$, and the Gibbs elasticity $E_G(c_{1\infty}, c_{2\infty})$ for every desirable surfactant and salt concentrations.

The theoretical dependence $\sigma = \sigma(c_{1\infty}, c_{2\infty})$ is determined by the following full set of equations: Equation 7.44 for $i = 1,2$; the Gouy equation (Equation 7.36), Equation 7.39 (with σ_d expressed by Equation 7.41 and J from Table 7.2), the Stern
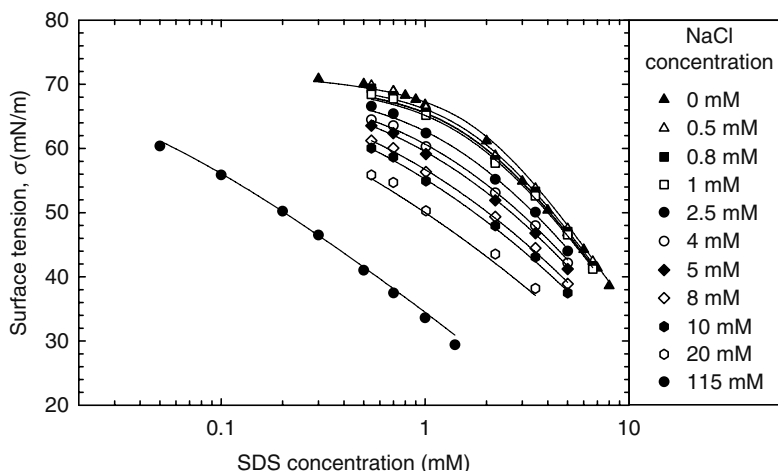
FIGURE 7.2 Plot of the surface tension σ versus the concentration of SDS, $c_{1\infty}$, for 11 fixed NaCl concentrations. The symbols are experimental data by Tajima et al. [38,40,41]. The lines represent the best fit [42] with the full set of equations specified in the text, involving the van der Waals isotherms of adsorption and surface tension (Table 7.2).

isotherm 7.47, and one surfactant adsorption isotherm from Table 7.2, say the van der Waals one. Thus we get a set of six equations for determining six unknown variables: σ, Φ_s, a_{1s}, a_{2s}, Γ_1, and Γ_2. (For $I < 0.1$ M the activities of the ions can be replaced by the respective concentrations.) The principles of the numerical procedure are described in Ref. [27].

The theoretical model contains four parameters, β, Γ_∞, K_1, and K_2, whose values are to be obtained from the best fit of the experimental data. Note that all 11 curves in Figure 7.2 are fitted simultaneously [42]. In other words, the parameters β, Γ_∞, K_1, and K_2 are the same for all curves. The value of Γ_∞, obtained from the best fit of the data in Figure 7.2, corresponds to $1/\Gamma_\infty = 29.8$ Å^2. The respective value of K_1 is 99.2 m^3 mol^{-1}, which in view of Equation 7.49 gives a standard free energy of surfactant adsorption $\Delta\mu_1^{(0)} = 12.53$ kT per DS$^-$ ion, that is 30.6 kJ mol^{-1}. The determined value of K_2 is 6.5×10^{-4} m^3/mol, which after substitution in Equation 7.49 yields a standard free energy of counterion binding $\Delta\mu_2^{(0)} = 1.64$ kT per Na$^+$ ion (i.e., 4.1 kJ mol^{-1}). The value of the parameter β is positive, $2\beta\Gamma_\infty/kT = +2.73$, which indicates the attraction between the hydrocarbon tails of the adsorbed surfactant molecules. However, this attraction is too weak to cause two-dimensional phase transition. The van der Waals isotherm predicts such transition for $2\beta\Gamma_\infty/kT > 6.75$.

Figure 7.3 shows calculated curves for the adsorptions of surfactant, Γ_1 (the full lines), and counterions, Γ_2 (the dotted lines), versus the SDS concentration, $c_{1\infty}$. These lines represent the variation of Γ_1 and Γ_2 along the experimental curves, which correspond to the lowest and highest NaCl concentrations in Figure 7.2 (viz. $c_{3\infty} = 0$ and 115 mM). We see that both Γ_1 and Γ_2
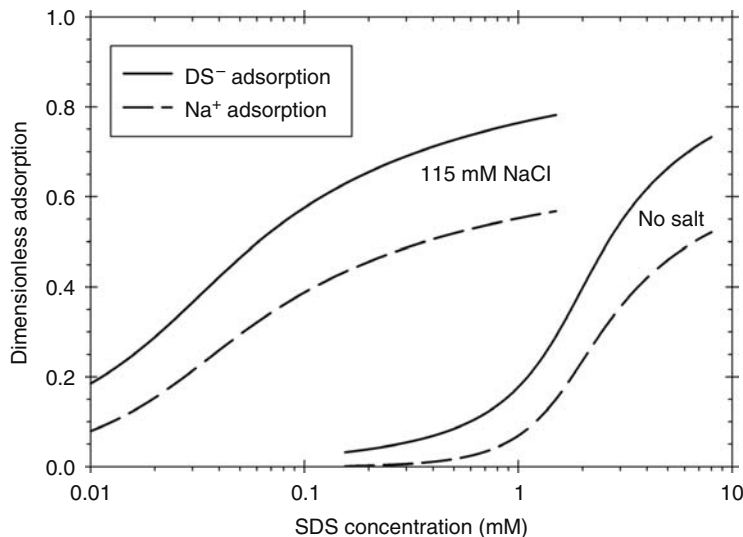
FIGURE 7.3 Plots of the dimensionless adsorptions of surfactant ions Γ_1/Γ_∞ (DS$^-$, solid lines), and counterions Γ_2/Γ_∞ (Na$^+$, dotted lines), versus the surfactant (SDS) concentration, $c_{1\infty}$. The lines are calculated [42] for NaCl concentrations 0 and 115 mM using parameter values determined from the best fit of experimental data (Figure 7.2).

are markedly greater when NaCl is present in the solution. The highest values of Γ_1 for the curves in Figure 7.3 are 4.2×10^{-6} and 4.0×10^{-6} mol m^{-2} for the solutions with and without NaCl, respectively. The latter two values compare well with the saturation adsorptions measured by Tajima et al. [40,41] for the same system by means of the radiotracer method, viz. $\Gamma_1 = 4.3 \times 10^{-6}$ mol m^{-2} and 3.2×10^{-6} mol m^{-2} for the solutions with and without NaCl.

For the solution without NaCl the occupancy of the Stern layer, Γ_2/Γ_1 rises from 0.15 to 0.73 and then exhibits a tendency to level off. The latter value is consonant with the data of other authors [43–45], who have obtained values of Γ_2/Γ_1 up to $0.70-0.90$ for various ionic surfactants; pronounced evidences for counterion binding have also been obtained in experiments with solutions containing surfactant micelles [46–50]. As it could be expected, both Γ_1 and Γ_2 are higher for the solution with NaCl. These results imply that the counterion adsorption (binding) should be always taken into account.

The fit of the data in Figure 7.2 gives also the values of the surface electric potential, ψ_s. For the solutions with 115 mM NaCl the model predicts surface potentials varying in the range $|\psi_s| = 55-95$ mV within the experimental interval of surfactant concentrations, whereas for the solution without salt the calculated surface potential is higher: $|\psi_s| = 150–180$ mV (for SDS ψ_s has a negative sign). Thus it turns out that measurements of surface tension, interpreted by means of an appropriate theoretical model, provide a method for determining the surface potential ψ_s in a broad range of surfactant and salt concentrations. The described approach could be also applied to solve the inverse problem, viz. to process data for the surface potential. In this way, the adsorption of surfactant on solid particles can be determined from the measured zeta-potential [51].

It is remarkable that the minimal (excluded) area per adsorbed surfactant molecule, $\alpha \equiv 1/\Gamma_\infty$, obtained from the best fit of surface-tension data by the van der Waals isotherm practically coincides with the value of α estimated by molecular-size considerations (i.e., from the maximal cross-sectional area of an amphiphilic molecule in a dense adsorption layer) (see Figure 7.1 in Ref. [34]). This is illustrated in Table 7.5, which contains data for alkanols, alkanoic acids, SDS, sodium dodecyl benzene sulfonate (DDBS), cocamidopropyl betaine (CAPB), and C_n-trimethyl ammonium bromides ($n = 12, 14,$ and 16). The second column of Table 7.5 gives the group whose cross-sectional area is used to calculate α. For molecules of circular cross section, we can calculate the cross-sectional area from the expression $\alpha = \pi r^2$, where r is the respective radius. For example [52], the radius of the SO_4^{2-} ion is $r = 3.09$ Å, which yields $\alpha = \pi r^2 = 30.0$ Å^2. In the fits of surface-tension data by the van der Waals isotherm, α was treated as an adjustable parameter, and the value $\alpha = 30$ Å^2 was obtained from the best fit. As seen in Table 7.5, excellent agreement between the values of α obtained from molecular size and from surface-tension fits is obtained also for many other amphiphilic molecules [52–59].

It should be noted the above result holds only for the van der Waals (or Volmer) isotherm. Instead, if the Frumkin (or Langmuir) isotherm is used, the value of α obtained from the surface-tension fits is with about 33% greater than α obtained from molecular size [42]. A possible explanation of this difference could be the fact that the Frumkin (and Langmuir) isotherm is statistically derived for localized adsorption and are more appropriate do describe adsorption at solid interfaces. In contrast, the van der Waals (and Volmer) isotherm is derived for nonlocalized adsorption, and they provide a more adequate theoretical description of the surfactant adsorption at liquid–fluid interfaces. This conclusion refers also to the calculation of surface (Gibbs) elasticity by means of the two types of isotherms [42].

The fact that α determined from molecular size coincides with α obtained from surface-tension fits (Table 7.5) is very useful for applications. Thus, when fitting experimental data, we can use the value of α from molecular size, and thus to decrease the number of adjustable parameters. This fact is especially helpful when interpreting theoretical data for the surface tension of surfactant mixtures, such as SDS + dodecanol [52], SDS + CAPB [57], and fluorinated + nonionic surfactant [59]. An additional way to decrease the number of adjustable parameters is to employ the Traube rule, which states that $\Delta\mu_1^{(0)}$ increases with $1.025\, kT$ when a CH_2 group is added to the paraffin chain (for details see Refs. [52,53,58]).

TABLE 7.5

Excluded Area per Molecule, α, Determined in Two Different Ways

Amphiphile	Group	α from Molecular Size (Å^2)	α from Surface-Tension Fits[a] (Å^2)	References
Alkanols	Paraffin chain	21.0	20.9	[52]
Alkanoic acids	COO^-	22–24	22.6	[53,54]
SDS	SO_4^{2-}	30.0	30	[42,55]
DDBS	Benzene ring	35.3	35.6	[56]
CAPB	$CH_3–N^+–CH_3$	27.8	27.8	[57]
C_nTAB ($n = 12, 14, 16$)	$N(CH_3)_4^+$	37.8	36.5–39.5	[55,58]

[a] Fit by means of the van der Waals isotherm.

7.2.2 DYNAMIC SURFACE TENSION

If the surface of an equilibrium surfactant solution is disturbed (expanded, compressed, renewed, etc.), the system will try to restore the equilibrium by exchange of surfactant between the surface and the subsurface layer (adsorption–desorption). The change of the surfactant concentration in the subsurface layer triggers a diffusion flux in the solution. In other words, the process of equilibration (relaxation) of an expanded adsorption monolayer involves two consecutive stages:

1. Diffusion of surfactant molecules from the bulk solution to the subsurface layer
2. Transfer of surfactant molecules from the subsurface to the adsorption layer; the rate of transfer is determined by the height of the kinetic barrier to adsorption

(In the case of desorption the processes have the opposite direction.) Such interfacial expansions are typical for foam generation and emulsification. The rate of adsorption relaxation determines whether the formed bubbles/drops will coalesce upon collision, and in final reckoning—how large will be the foam volume and the emulsion drop-size [60,61]. Below we focus our attention on the relaxation time of surface tension, τ_σ, which characterizes the interfacial dynamics.

The overall rate of surfactant adsorption is controlled by the slowest stage. If it is stage (i), we deal with diffusion control, while if stage (ii) is slower, the adsorption occurs under barrier (kinetic) control. Sections 7.2.2.1 through 7.2.2.4 are dedicated to processes under diffusion control (which are the most frequently observed), whereas in Section 7.2.2.5 we consider adsorption under barrier control. Finally, Section 7.2.2.6 is devoted to the dynamics of adsorption from micellar surfactant solutions.

Various experimental methods for dynamic surface-tension measurements are available. Their operational timescales cover different time intervals [62,63]. Methods with a shorter characteristic operational time are the oscillating jet method [64–66], the oscillating bubble method [67–70], the fast-formed drop technique [71,72], the surface wave techniques [73–76], and the maximum bubble pressure method (MBPM) [77–82]. Methods of longer characteristic operational time are the inclined plate method [83], the drop-weight/volume techniques [84–88], the funnel [89] and overflowing cylinder [58,90] methods, and the axisymmetric drop shape analysis [91,92] (see Refs. [62,63,93] for a more detailed review).

In this section, devoted to dynamic surface tension, we consider mostly nonionic surfactant solutions. In Section 7.2.2.4, we address the more complicated case of ionic surfactants. We will restrict our considerations to the simplest case of relaxation of an initial uniform interfacial dilatation. The more complex case of simultaneous adsorption and dilatation is considered elsewhere [62,78,82,90,93].

7.2.2.1 Adsorption under Diffusion Control

Here we consider a solution of a nonionic surfactant, whose concentration, $c_1 = c_1\,(z,t)$, depends on the position and time because of the diffusion process. (As before, z denotes the distance to the interface, which is situated in the plane $z = 0$.) Correspondingly, the surface tension, surfactant adsorption, and the subsurface concentration of surfactant vary with time: $\sigma = \sigma(t)$, $\Gamma_1 = \Gamma_1(t)$, $c_{1s} = c_{1s}(t)$. The surfactant concentration obeys the equation of diffusion:

$$\frac{\partial c_1}{\partial t} = D_1 \frac{\partial^2 c_1}{\partial z^2} \quad (z > 0,\ t > 0) \tag{7.59}$$

where D_1 is the diffusion coefficient of the surfactant molecules. The exchange of surfactant between the solution and its interface is described by the boundary conditions

$$c_1(0,t) = c_{1s}(t), \quad \frac{d\Gamma_1}{dt} = D_1 \frac{\partial c_1}{\partial z}, \quad (z = 0,\ t > 0) \tag{7.60}$$

The latter equation states that the rate of increase of the adsorption Γ_1 is equal to the diffusion influx of surfactant per unit area of the interface. Integrating Equation 7.59, along with 7.60, we can derive the equation of Ward and Tordai [94]:

$$\Gamma_1(t) = \Gamma_1(0) + \sqrt{\frac{D_1}{\pi}} \left[2c_{1\infty}\sqrt{t} - \int_0^t \frac{c_{1s}(\tau)}{\sqrt{t - \tau}} d\tau \right] \tag{7.61}$$

Solving Equation 7.61 together with some of the adsorption isotherms $\Gamma_1 = \Gamma_1(c_{1s})$ in Table 7.2, we can in principle determine the two unknown functions $\Gamma_1(t)$ and $c_{1s}(t)$. Because the relation $\Gamma_1(c_{1s})$ is nonlinear (except for the Henry isotherm), this problem, or its equivalent formulations, can be solved either numerically [95], or by employing appropriate approximations [78,96].

In many cases it is convenient to use asymptotic expressions for the functions $\Gamma_1(t)$, $c_{1s}(t)$ and $\sigma(t)$ for short times ($t \to 0$) and long times ($t \to \infty$). A general asymptotic expression for the short times can be derived from Equation 7.61 substituting $c_{1s} \approx c_{1s}(0) = $ constant:

$$\Gamma_1(t) = \Gamma_1(0) + 2\sqrt{D_1/\pi}\,[c_{1\infty} - c_{1s}(0)]\sqrt{t}\ (t \to 0) \tag{7.62}$$

Analogous asymptotic expression can be obtained also for the long times, although the derivation is not so simple. Hansen [97] derived a useful asymptotics for the subsurface concentration:

$$c_{1s}(t) = c_{1\infty} - \frac{\Gamma_{1e} - \Gamma(0)}{\sqrt{\pi D_1 t}}\ (t \to \infty) \tag{7.63}$$

where Γ_{1e} is the equilibrium value of the surfactant adsorption. The validity of Hansen's Equation 7.63 was confirmed in subsequent studies by other authors [98,99].

Below we continue our review of the asymptotic expressions considering separately the cases of small and large initial perturbations.

7.2.2.2 Small Initial Perturbation

When the deviation from equilibrium is small, then the adsorption isotherm can be linearized:

$$\Gamma_1(t) - \Gamma_{1,e} \approx \left(\frac{\partial\Gamma_1}{\partial c_1}\right)_e [c_{1s}(t) - c_e] \tag{7.64}$$

Hereafter the subscript e means that the respective quantity refers to the equilibrium state. The set of linear Equations 7.59, 7.60, and 7.64, has been solved by Sutherland [100]. The result, which describes the relaxation of a small initial interfacial dilatation, reads

$$\frac{\sigma(t) - \sigma_e}{\sigma(0) - \sigma_e} = \frac{\Gamma_1(t) - \Gamma_{1,e}}{\Gamma_1(0) - \Gamma_{1,e}} = \exp\left(\frac{t}{\tau_\sigma}\right)\mathrm{erfc}\left(\sqrt{\frac{t}{\tau_\sigma}}\right) \tag{7.65}$$

where

$$\tau_\sigma \equiv \frac{1}{D_1}\left(\frac{\partial\Gamma_1}{\partial c_1}\right)_e^2 \tag{7.66}$$

is the characteristic relaxation time of surface tension and adsorption, and

$$\mathrm{erfc}(x) \equiv \frac{2}{\sqrt{\pi}} \int\limits_x^\infty \exp\left(-x^2\right)\mathrm{d}x \tag{7.67}$$

is the so-called complementary error function [101,102]. The asymptotics of the latter function for small and large values of the argument are [101,102]:

$$\mathrm{erfc}(x) = 1 - \frac{2}{\sqrt{\pi}}x + O(x^3) \quad \text{for} \quad x \ll 1; \quad \mathrm{erfc}(x) = \frac{e^{-x^2}}{\sqrt{\pi}x}\left[1 + O\left(\frac{1}{x^2}\right)\right] \quad \text{for} \quad x \gg 1 \tag{7.68}$$

Combining Equations 7.65 and 7.68, we obtain the short-time and long-time asymptotics of the surface-tension relaxation:

$$\frac{\sigma(t) - \sigma_e}{\sigma(0) - \sigma_e} = \frac{\Gamma_1(t) - \Gamma_{1,e}}{\Gamma_1(0) - \Gamma_{1,e}} = 1 - \frac{2}{\sqrt{\pi}}\sqrt{\frac{t}{\tau_\sigma}} + O\left[\left(\frac{t}{\tau_\sigma}\right)^{3/2}\right]\ (t \ll \tau_\sigma) \tag{7.69}$$

$$\frac{\sigma(t) - \sigma_e}{\sigma(0) - \sigma_e} = \frac{\Gamma_1(t) - \Gamma_{1,e}}{\Gamma_1(0) - \Gamma_{1,e}} = \sqrt{\frac{\tau_\sigma}{\pi t}} + O\left[\left(\frac{\tau_\sigma}{t}\right)^{3/2}\right]\ (t \gg \tau_\sigma) \tag{7.70}$$

Equation 7.70 is often used as a test to verify whether the adsorption process is under diffusion control: data for $\sigma(t)$ are plotted versus $1/\sqrt{t}$ and it is checked if the plot complies with a straight line; moreover, the intercept of the line gives σ_e. We recall that Equations 7.69 and 7.70 are valid in the case of a small initial perturbation; alternative asymptotic expressions for the case of large initial perturbation are considered in the next Section 7.2.2.3.

With the help of the thermodynamic Equations 7.2 and 7.6, we derive

$$\frac{\partial \Gamma_1}{\partial c_1} = \frac{\partial \Gamma_1}{\partial \sigma}\frac{\partial \sigma}{\partial c_1} = \frac{\Gamma_1^2 kT}{c_1 E_G} \tag{7.71}$$

Thus Equation 7.66 can be expressed in an alternative form [35]:

$$\tau_\sigma = \frac{1}{D_1}\left(\frac{\Gamma_1^2 kT}{c_1 E_G}\right)_e^2 \tag{7.72}$$

Substituting E_G from Table 7.3 into Equation 7.72, we can obtain expressions for τ_σ corresponding to various adsorption isotherms. In the special case of Langmuir adsorption isotherm, we can present Equation 7.72 in the form [35]

$$\tau_\sigma = \frac{1}{D_1}\frac{(K\Gamma_\infty)^2}{(1+Kc_1)^4} = \frac{1}{D_1}\frac{(K\Gamma_\infty)^2}{(1+E_G/(\Gamma_\infty kT))^4} \quad \text{(for Langmuir isotherm)} \tag{7.73}$$

Equation 7.73 visualizes the very strong dependence of the relaxation time τ_σ on the surfactant concentration c_1; in general, τ_σ can vary with many orders of magnitude as a function of c_1. Equation 7.73 shows also that high Gibbs elasticity corresponds to short relaxation time, and vice versa.

As a quantitative example let us take typical parameter values: $K_1 = 15 \text{ m}^3 \text{ mol}^{-1}$, $1/\Gamma_\infty = 40 \text{ Å}^2$, $D_1 = 5.5\times10^{-6} \text{ cm}^2 \text{ s}^{-1}$, and $T = 298$ K. Then with $c_1 = 6.5 \times 10^{-6}$ M, from Table 7.3 (Langmuir isotherm) and Equation 7.73 we calculate $E_G \approx 1.0 \text{ mN m}^{-1}$ and $\tau_\sigma \approx 5$ s. In the same way, for $c_1 = 6.5 \times 10^{-4}$ M we calculate $E_G \approx 100 \text{ mN/m}$ and $\tau_\sigma \approx 5 \times 10^{-4}$ s.

To directly measure the Gibbs elasticity E_G, or to precisely investigate the dynamics of surface tension, we need an experimental method, whose characteristic time is smaller compared to τ_σ. Equation 7.73 and the latter numerical example show that when the surfactant concentration is higher, the experimental method should be faster.

7.2.2.3 Large Initial Perturbation

By definition, we have large initial perturbation when at the initial moment the interface is clean of surfactant:

$$\Gamma_1(0) = 0, \quad c_{1s}(0) = 0 \tag{7.74}$$

In such case, the Hansen Equation 7.63 reduces to

$$c_{1s}(t) = c_{1\infty} - \frac{\Gamma_{1,e}}{\sqrt{\pi D_1 t}} \quad (t \to \infty) \tag{7.75}$$

By substituting $c_{1s}(t)$ for c_1 in the Gibbs adsorption Equation 7.2, and integrating, we obtain the long-time asymptotics of the surface tension of a nonionic surfactant solution after a large initial perturbation:

$$\sigma(t) - \sigma_e = \left(\frac{\Gamma_1^2 kT}{c_1}\right)_e\left(\frac{1}{\pi D_1 t}\right)^{1/2} \quad \text{(large initial perturbation)} \tag{7.76}$$

with the help of Equation 7.72, we can bring Equation 7.76 into another form:

$$\sigma(t) - \sigma_e = E_G\left(\frac{\tau_\sigma}{\pi t}\right)^{1/2} \quad \text{(large initial perturbation)} \tag{7.77}$$

where E_G is given in Table 7.3. It is interesting to note that Equation 7.77 is applicable to both nonionic and ionic surfactants with the only difference that for nonionics τ_σ is given by Equation 7.66, whereas for ionic surfactants the expression for τ_σ is somewhat longer [35,103].

Equations 7.70 and 7.77 show that in the case of adsorption under diffusion control the long-lime asymptotics can be expressed in the form

$$\sigma = \sigma_e + S\, t^{-1/2} \tag{7.78}$$

In view of Equations 7.70 and 7.77, the slope S of the dependence σ versus $t^{-1/2}$ is given by the expressions [103]

$$S_s = [\sigma(0) - \sigma_e]\left(\frac{\tau_\sigma}{\pi}\right)^{1/2} \text{(small perturbation)} \tag{7.79}$$

$$S_l = E_G\left(\frac{\tau_\sigma}{\pi}\right)^{1/2} \text{(large perturbation)} \tag{7.80}$$

As known, the surfactant adsorption Γ_1 monotonically increases with the rise of the surfactant concentration, c_1. In contrast, the slope S_l is a nonmonotonic function of c_1: S_l exhibits a maximum at a certain concentration. To demonstrate that we will use the expression

$$S_l = \frac{\Gamma_{1,e}^2 kT}{c_1 \sqrt{\pi D_1}} \tag{7.81}$$

which follows from Equations 7.76 and 7.78. In Equation 7.81, we substitute the expressions for c_1 stemming from the Langmuir and Volmer adsorption isotherms (Table 7.2 with $c_1 = a_{1s}$); the result reads

$$\widetilde{S}_l = \theta(1 - \theta) \text{ (for Langmuir isotherm)} \tag{7.82}$$

$$\widetilde{S}_l = \theta(1 - \theta)\exp\left(-\frac{\theta}{1 - \theta}\right) \text{ (for Volmer isotherm)} \tag{7.83}$$

where θ and $\widetilde{S}_l$ are the dimensionless adsorption and slope coefficient:

$$\theta = \frac{\Gamma_{1,e}}{\Gamma_\infty} \quad \text{and} \quad \widetilde{S}_l = \frac{S_l \sqrt{\pi D_1}}{kT\, K\Gamma_\infty^2} \tag{7.84}$$

Figure 7.4 compares the dependencies $\widetilde{S}_l(\theta)$ given by Equations 7.82 and 7.83: we see that the former is symmetric and has a maximum at $\theta = 0.5$, whereas the latter is asymmetric with a maximum at $\theta \approx 0.29$. We recall that the Langmuir and Volmer isotherms correspond to localized and nonlocalized adsorption, respectively (see Section 7.2.1.1.2). Then Figure 7.4 shows that the symmetry/asymmetry of the plot $\widetilde{S}_l$ versus θ provides a test for verifying whether the adsorption is localized or nonlocalized. (The practice shows that the fits of equilibrium surface-tension isotherms do not provide such a test: theoretical isotherms corresponding to localized and nonlocalized adsorption are found to fit equally well surface-tension data!)
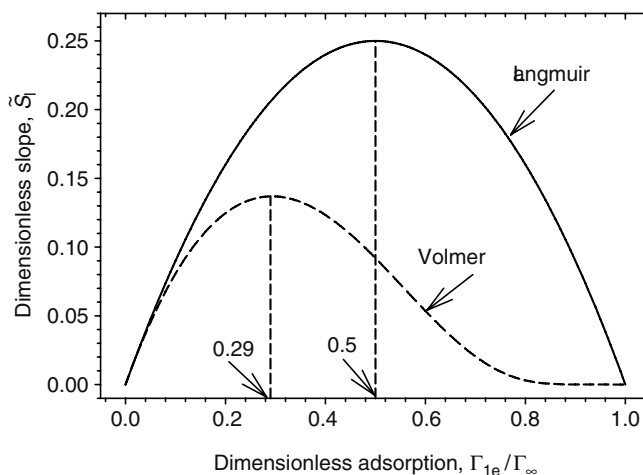

FIGURE 7.4 Plot of the dimensionless slope, $\widetilde{S}_l$, versus the dimensionless equilibrium surfactant adsorption, $\theta = \Gamma_{1e}/\Gamma_\infty$, in accordance with Equations 7.82 and 7.83, corresponding to the cases of localized and nonlocalized adsorption.

From another viewpoint, the nonmonotonic behavior of $S_I(\theta)$ can be interpreted as follows. Equation 7.80 shows that $S_I \propto E_G \sqrt{\tau_\sigma}$; then the nonmonotonic behavior stems from the fact that E_G is an increasing function of c_1, whereas τ_σ is a decreasing function of c_1. This qualitative conclusion is valid also for the case of ionic surfactant, as demonstrated in the next section.

7.2.2.4 Generalization for Ionic Surfactants

In the case of ionic surfactants the dynamics of adsorption is more complicated because of the presence of a dynamic EDL. Indeed, the adsorption of surfactant at the interface creates surface charge, which is increasing in the course of the adsorption process. The charged interface repels the new-coming surfactant molecules, but attracts the conversely charged counterions (Figure 7.1); some of them bind to the surfactant headgroups thus decreasing the surface charge density and favoring the adsorption of new surfactant molecules. The theoretical description of the overall adsorption process involves the (electro) diffusion equations for the surfactant ions, counterions and coions, and the Poisson equation from electrodynamics. Different analytical and numerical approaches to the solution of this problem have been proposed [13,58,102–111].

In Ref. [112], an approach to the dynamics of ionic surfactant adsorption was developed, which is simpler as both concept and application, but agrees very well with the experiment. Analytical asymptotic expressions for the dynamic surface tension of ionic surfactant solutions are derived in the general case of nonstationary interfacial expansion. Because the diffusion layer is much wider than the EDL, the equations contain a small parameter. The resulting perturbation problem is singular and it is solved by means of the method of matched asymptotic expansions [113]. The derived general expression for the dynamic surface tension is simplified for two important special cases, which are considered below.

The first special case refers to adsorption at an immobile interface that has been initially perturbed, and to the MBPM. The generalization of Equations 7.78 and 7.81 for this case reads [112]:

$$\sigma = \sigma_e + \frac{S_I}{(t_{age})^{1/2}}, \quad S_I \equiv \frac{kT\Gamma_{1,e}^2\lambda}{(\pi D_{eff})^{1/2}\gamma_\pm}\left(\frac{1}{c_{1\infty}} + \frac{1}{c_{2\infty}}\right) \tag{7.85a}$$

As usual, the subscript e denotes equilibrium values; t_{age} is the age of the interface, which is defined as the period of time between the minimum pressure (bubble formation) and the maximum pressure (bubble detachment) in the case of MBPM; λ is a dimensionless parameter; $\lambda = 1$ for immobile interfaces; in the case of MBPM, λ is an apparatus constant that can be determined by calibration experiments [55]; as before, $c_{1\infty}$ and $c_{2\infty}$ are the bulk concentration of surfactant ions and counterions; $\gamma_\pm$ is the activity coefficient; D_{eff} is an effective diffusivity that depends on the diffusivities and bulk concentrations of surfactant ions, counterions, and inorganic coions: $D_{eff} = D_{eff}(D_1, D_2, D_3, c_{1\infty}, c_{2\infty}, c_{3\infty})$. The latter dependence is described by explicit formulas derived in Ref. [112] (see Equations 6.19 through 6.26 therein).

In the case of the cationic surfactant dodecyl trimethyl ammonium bromide (C_{12}TAB), the calculated dependence of D_{eff} on the surfactant and salt concentrations, $c_{1\infty}$ and $c_{3\infty}$, is illustrated in Figure 7.5. Because the range $c_{1\infty} \leq$ CMC is considered,
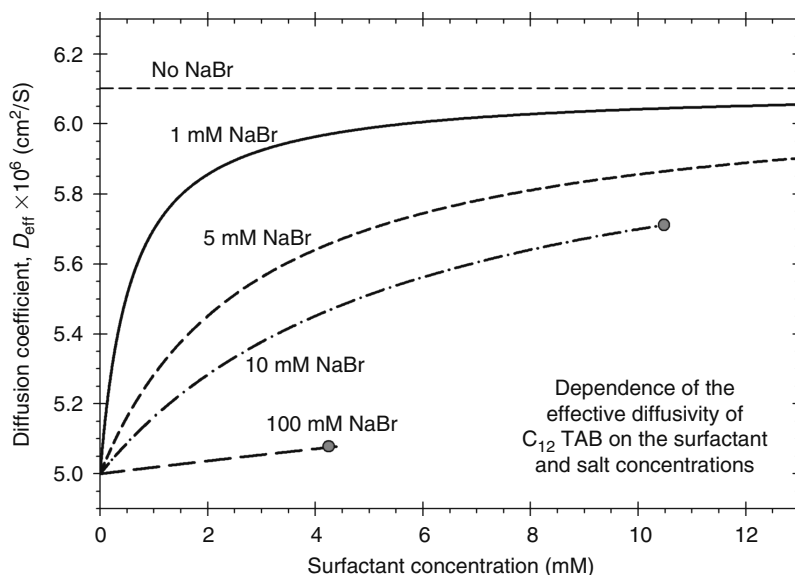

FIGURE 7.5 Dependence of the effective diffusivity, D_{eff}, on the surfactant concentration, $c_{1\infty}$, for various salt concentrations, $c_{3\infty}$, denoted in the figure. The curves are calculated by using the values of D_1, D_2, and D_3 given in Ref. [112] for the cationic surfactant C_{12}TAB. The end points of some curves correspond to the CMC.
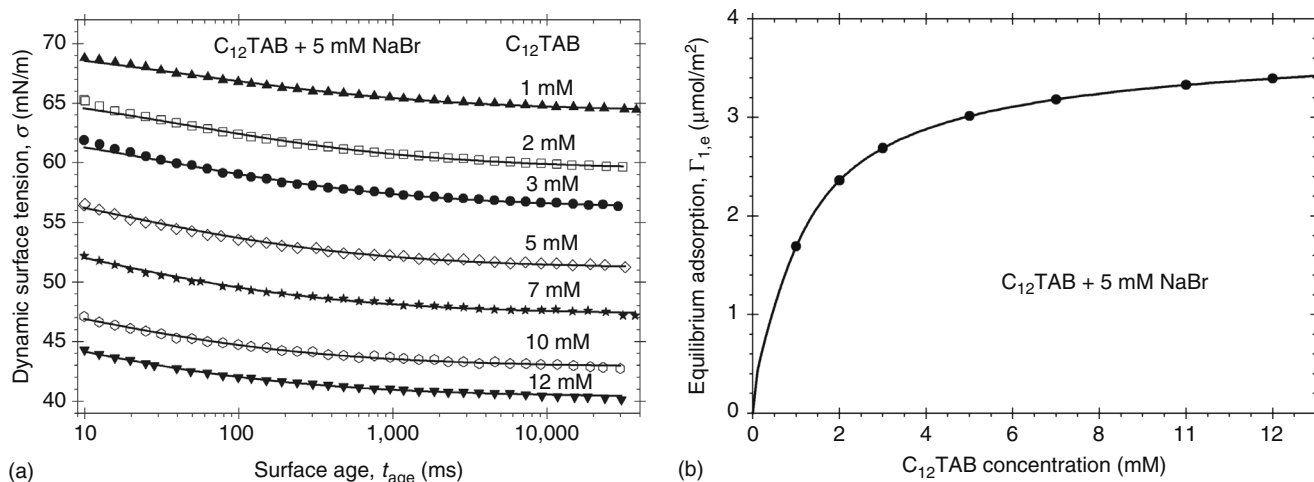
FIGURE 7.6 (a) Data for the dynamic surface tension, σ, versus the surface age, t_{age}, measured by MBPM [55] at concentrations of $C_{12}TAB$ denoted in the figure; solid lines are fits (see the text). (b) Dependence of the equilibrium surfactant adsorption, $\Gamma_{1,e}$, on the $C_{12}TAB$ concentration. The points are calculated by means of Equation 7.85a for S_1 determined from the fits in Figure 7.6a. The solid lines are calculated independently from fits of surface-tension data, σ_e versus $c_{1\infty}$, by means of the van der Waals adsorption model [112].

the calculated curves end at the CMC. At very low surfactant concentrations, $c_{1\infty} \to 0$, in the presence of salt ($c_{3\infty} > 0$), the effective diffusivity approaches its limiting value for diluted solutions, $D_{eff} \to D_1$. We see that D_{eff} increases with the rise of $c_{1\infty}$, except the case without added salt ($c_{3\infty} = 0$), for which D_{eff} is a constant: $1/D_{eff} = (1/D_1 + 1/D_2)/2$. The curves in Figure 7.5 show that D_{eff} decreases with the rise of salt concentration, $c_{3\infty}$, and becomes $\approx D_1$ for $c_{3\infty} = 100$ mM. Note that the salt concentration affects the dynamic surface tension, σ, also through $\Gamma_{1,e}$ and through the factor ($1/c_{1\infty} + 1/c_{2\infty}$) in Equation 7.85a (see Ref. [112] for details).

The accuracy of Equation 7.85a can be verified in the following way. Each of the dynamic surface-tension isotherms for $C_{12}TAB$ in Figure 7.6a are fitted by means of the equation $\sigma = \sigma_e + S_1/[a_\sigma + (t_{age})^{1/2}]$, and the parameters σ_e, a_σ, and S_1 are determined from the best fit. Next, for each value of S_1, we calculate the equilibrium surfactant adsorption, $\Gamma_{1,e}$, using Equation 7.85a and the theoretical value of D_{eff} from Figure 7.5; see the points in Figure 7.6b. For the used MBPM setup [55], the apparatus constant is $\lambda = 6.07$. The solid line in the latter figure represents the equilibrium surfactant adsorption independently calculated from the fit of equilibrium surface-tension data by means of the van der Waals isotherm [112]. The excellent agreement between the points with the line in Figure 7.6b (no adjustable parameters) confirms the accuracy of Equation 7.85a.

The case of adsorption at an interface that is subjected to stationary expansion needs a special theoretical description. This case is experimentally realized with the strip method [93,114], and the overflowing cylinder method [58,90]. It could be realized also by a Langmuir trough. The interfacial expansion is characterized by the quantity $\dot{\alpha} = dA/(Adt)$, which represents the relative rate of increase of the interfacial area, A. For stationary processes, $\dot{\alpha} = $ constant is a parameter known from the experiment. In this case, the dynamic surface tension is given by the expression [112]:

$$\sigma = \sigma_e + kT\Gamma_{1,e}^2 \left(\frac{\pi\dot{\alpha}}{2D_{eff}}\right)^{1/2} \frac{1}{\gamma_\pm}\left(\frac{1}{c_{1\infty}} + \frac{1}{c_{2\infty}}\right) \tag{7.85b}$$

where D_{eff} is given by Equations 6.19 through 6.26 in Ref. [112]. Equation 7.85b does not contain the time, t, as it should be for a stationary process. For nonionic surfactants and for ionic surfactants at high salt concentrations the term $1/c_{2\infty}$ in Equation 7.85b disappears and $D_{eff} = D_1$.

7.2.2.5 Adsorption under Barrier Control

In general, the adsorption is under barrier (kinetic, transfer) control when the surfactant transfer from the subsurface to the surface is much slower than the diffusion because of some kinetic barrier. The latter can be due to steric hindrance, spatial reorientation, or conformational changes accompanying the adsorption of molecules, including destruction of the shells of oriented water molecules wrapping the surfactant hydrocarbon tail in water [115]. We will restrict our considerations to the case of pure barrier control, without double layer effects. In such case the surfactant concentration is uniform throughout the solution, $c_1 = $ constant, and the increase of the adsorption $\Gamma_1(t)$ is solely determined by the transitions of surfactant molecules over the adsorption barrier, separating subsurface from surface:

$$\frac{d\Gamma_1}{dt} = Q \equiv r_{ads}(c_1, \Gamma_1) - r_{des}(\Gamma_1) \tag{7.86}$$

TABLE 7.6
Rate of Surfactant Adsorption for Different Kinetic Models

Type of Isotherm	Rate of Reversible Adsorption $Q = r_{ads}(c_1, \Gamma_1) - r_{des}(\Gamma_1)$
Henry	$Q = K_{ads}c_1 - K_{des}\Gamma_1/\Gamma_\infty$
Freundlich	$Q = K_{ads}K^{m-1}c_1^m - K_{des}\Gamma_1/\Gamma_\infty$
Langmuir	$Q = K_{ads}c_1\left(1 - \dfrac{\Gamma_1}{\Gamma_\infty}\right) - K_{des}\Gamma_1/\Gamma_\infty$
Frumkin	$Q = K_{ads}c_1\left(1 - \dfrac{\Gamma_1}{\Gamma_\infty}\right) - K_{des}\dfrac{\Gamma_1}{\Gamma_\infty}\exp\left(-\dfrac{2\beta\Gamma_1}{kT}\right)$
Volmer	$Q = K_{ads}c_1 - K_{des}\dfrac{\Gamma_1}{\Gamma_\infty - \Gamma_1}\exp\left(\dfrac{\Gamma_1}{\Gamma_\infty - \Gamma_1}\right)$
van der Waals	$Q = K_{ads}c_1 - K_{des}\dfrac{\Gamma_1}{\Gamma_\infty - \Gamma_1}\exp\left(\dfrac{\Gamma_1}{\Gamma_\infty - \Gamma_1} - \dfrac{2\beta\Gamma_1}{kT}\right)$

where r_{ads} and r_{des} are the rates of surfactant adsorption and desorption. The concept of barrier-limited adsorption originates from the works of Bond and Puls [116], and Doss [117], and has been further developed by other authors [118–125]. Table 7.6 summarizes some expressions for the total rate of adsorption under barrier control, Q. The quantities K_{ads} and K_{des} in Table 7.6 are the rate constants of adsorption and desorption, respectively. Their ratio is equal to the equilibrium constant of adsorption

$$K_{ads}/K_{des} = K \tag{7.87}$$

The parameters Γ_∞ and K are the same as in Tables 7.2 through 7.4. Setting $Q = 0$ (assuming equilibrium surface–subsurface), from each expression in Table 7.6 we deduce the respective equilibrium adsorption isotherm in Table 7.2. In addition, for $\beta = 0$ the expressions for Q related to the Frumkin and van der Waals model reduce, respectively, to the expressions for Q in the Langmuir and Volmer models. For $\Gamma_1 \ll \Gamma_\infty$ both the Frumkin and Langmuir expressions in Table 7.6 reduce to the Henry expression.

Substituting Q from Table 7.6 into Equation 7.86, and integrating, we can derive explicit expressions for the relaxation of surfactant adsorption:

$$\frac{\sigma(t) - \sigma_e}{\sigma(0) - \sigma_e} \approx \frac{\Gamma_1(t) - \Gamma_{1,e}}{\Gamma_1(0) - \Gamma_{1,e}} = \exp\left(-\frac{t}{\tau_\sigma}\right) \tag{7.88}$$

Equation 7.88 holds for $\sigma(t)$ only in the case of small deviations from equilibrium, whereas there is not such a restriction concerning $\Gamma_1(t)$; the relaxation time in Equation 7.88 is given by the expressions

$$\tau_\sigma = (K_{des}/\Gamma_\infty)^{-1} \text{ (Henry and Freundlich)} \tag{7.89}$$

$$\tau_\sigma = \left(\frac{K_{des}}{\Gamma_\infty} + \frac{K_{ads}c_1}{\Gamma_\infty}\right)^{-1} \text{ (Langmuir)} \tag{7.90}$$

Equation 7.88 predicts that the perturbation of surface tension, $\Delta\sigma(t) = \sigma(t) - \sigma_e$, relaxes exponentially. This is an important difference with the cases of adsorption under diffusion and electrodiffusion control, for which $\Delta\sigma(t) \propto 1/\sqrt{t}$, cf. Equations 7.70, 7.76, and 7.78. Thus a test whether or not the adsorption occurs under purely barrier control is to plot data for $\ln[\Delta\sigma(t)]$ versus t and to check if the plot complies with a straight line.

In the case of ionic surfactants the adsorption of surfactant ions is accompanied by binding of counterions. In addition, the concentrations of the ionic species vary across the EDL (even at equilibrium). These effects are taken into account in Equation 7.57, which can be used as an expression for Q in the case of Langmuir barrier adsorption of an ionic surfactant.

In fact, a pure barrier regime of adsorption is not frequently observed. It is expected that the barrier becomes more important for substances of low surface activity and high concentration in the solution. Such adsorption regime was observed with propanol, pentanol, 1,6 hexanoic acid, etc. (see Ref. [93] for details).

It may happen that the characteristic times of diffusion and transfer across the barrier are comparable. In such case we deal with mixed kinetic regime of adsorption [126]. Insofar as the stages of diffusion and transfer are consecutive, the boundary conditions at the interface are:

$$\frac{d\Gamma_1}{dt} = r_{ads}(c_1, \Gamma_1) - r_{des}(\Gamma_1) = D_1\left(\frac{\partial c_1}{\partial t}\right)_{z=0} \tag{7.91}$$

The formal transition in Equation 7.91 from mixed to diffusion control of adsorption is not trivial and demands application of scaling and asymptotic expansions. The criterion for occurrence of adsorption under diffusion control (presence of equilibrium between subsurface and surface) is

$$\frac{aK_{des}}{D_1}\left(\frac{\partial \Gamma_1}{\partial c_1}\right)_e \gg 1 \tag{7.92}$$

where a is a characteristic thickness of the diffusion layer.

An important difference between the regimes of diffusion and barrier control is in the form of the respective initial conditions. In the case of large initial deformations these are

$$\Gamma_1(0) = 0, \quad c_{1s}(0) = 0 \text{ (diffusion control)} \tag{7.93}$$

$$\Gamma_1(0) = 0, \quad c_{1s}(0) = c_{1\infty} \text{ (barrier control)} \tag{7.94}$$

Equation 7.93 reflects the fact that in diffusion regime the surface is always assumed to be equilibrated with the subsurface. In particular, if $\Gamma_1 = 0$, then we must have $c_{1s} = 0$. In contrast, Equation 7.94 stems from the presence of barrier: for time intervals shorter than the characteristic time of transfer, the removal of the surfactant from the interface ($\Gamma_1 = 0$) cannot affect the subsurface layer (because of the barrier) and then $c_{1s}(0) = c_{1\infty}$. This purely theoretical consideration implies that the effect of barrier could show up at the short times of adsorption, whereas at the long times the adsorption will occur under diffusion control [126,127]. The existence of barrier-affected adsorption regime at the short adsorption times could be confirmed or rejected by means of the fastest methods for measurement of dynamic surface tension.

7.2.2.6 Dynamics of Adsorption from Micellar Surfactant Solutions

7.2.2.6.1 Dynamic Equilibrium between Micelles and Monomers

At the higher concentrations, spherical aggregates of surfactant molecules, called micelles, appear in the aqueous surfactant solutions (Figure 7.7). The number of monomers in a micelle (the aggregation number) is typically between 50 and 100, depending on the size of the surfactant headgroup and the length of its hydrocarbon tail [34]. The micelles appear above a certain surfactant concentration termed the CMC. For concentrations above the CMC, the addition of surfactant to the solutions leads to the formation of more micelles, whereas the concentration of the monomers remains constant and equal to the CMC. In other words, the micelles, irrespective of their concentration, exist in dynamic equilibrium with a background solution of monomers with concentration equal to the CMC. (Note that at very high surfactant concentrations, the spherical micelles could undergo a transition to bigger aggregates, such as rod like or lamellar micelles [34]).
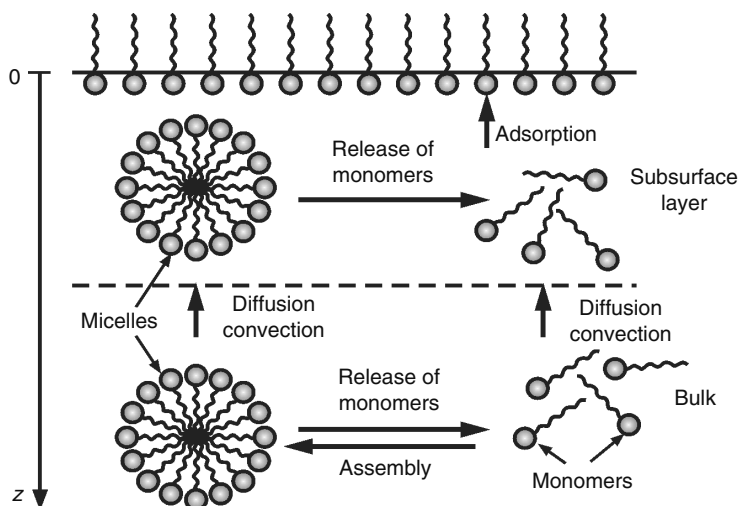
FIGURE 7.7 In the neighborhood of an expanded (nonequilibrium) adsorption monolayer, the micelles (the aggregates) release monomers to restore the equilibrium concentrations of surfactant monomers at the surface and in the bulk. The concentration gradients give rise to diffusion of both monomers and micelles. As a rule, the adsorbing component are the surfactant monomers, whereas the micelles are repelled by the interface and do not adsorb.

When surfactant molecules adsorb at an interface, the concentration of monomers in the subsurface layer decreases, which leads to release of monomers from the neighboring micelles, or to their complete decomposition. The decrease in the concentrations of monomers and micelles gives rise to corresponding diffusion fluxes from the bulk of solution toward the subsurface layer (Figure 7.7). In general, the role of the micelles as sources and carriers of monomers leads to a marked acceleration of surfactant adsorption.

The first models of micellar kinetics in spatially uniform solutions have been developed by Kresheck et al. [128] and Aniansson and Wall [129]. The existence of fast and slow processes of the micellar dynamics has been established. The fast process represents exchange of separate monomers between the micelles and the surrounding solution. If the micelle releases monomers, its aggregation number could decrease to a critical value, after which a complete decomposition of the micelle to monomers takes place. This decomposition is known as the slow demicellization process [129].

The first theoretical model of surfactant adsorption from micellar solutions, proposed by Lucassen [130], uses the simplifying assumptions that the micelles are monodisperse, and that the micellization happens as a single step, which is described as a reversible reaction of order n (the micelle aggregation number). Later, more realistic models, which account for the multistep character of the micellar process, were developed [131–133]. The assumption for a complete local dynamic equilibrium between monomers and micelles makes possible to use the equilibrium mass-action law for the micellization reaction [130,134,135]. In such a case, the surfactant transfer corresponds to a conventional diffusion-limited adsorption characterized by an effective diffusion coefficient, D_{eff}, which depends on the micelle diffusivity, concentration and aggregation number [134,135]. D_{eff} is independent of the rate constants of the fast and slow demicellization processes: k_m and k_S. Joos et al. [134,135] confirmed experimentally that in some cases the adsorption from micellar solutions could be actually described as a diffusion-limited process characterized by an apparent diffusivity, D_{eff}. In other experiments, Joos et al. [93,136] established that sometimes the dynamics of adsorption from micellar solutions exhibits a completely different kinetic pattern: the interfacial relaxation is exponential, rather than inverse square root, as it should be for diffusion-limited kinetics. The theoretical developments [93,126,136] revealed that the exponential relaxation is influenced by the kinetics of micellization, and from the data analysis we could determine the rate constant of the fast process, k_m. The observation of different kinetic regimes for different surfactants and/or experimental methods makes the physical picture rather complicated.

A realistic model of the micellar kinetics was proposed [137], and applied to investigate the dynamics of adsorption at quiescent [138] and expanding [55,139] interfaces. The theoretical analysis reveals the existence of four different consecutive relaxation regimes (stages) for a given micellar solution: two exponential regimes and two inverse-square-root regimes, following one after another in alternating order. The results of these studies are briefly described below, and the agreement between theory and experiment is illustrated.

7.2.2.6.2 Four Kinetic Regimes of Adsorption from Micellar Solutions

In the theoretical model proposed in Refs. [137] and [138], the use of the quasi equilibrium approximation (local chemical equilibrium between micelles and monomers) is avoided. The theoretical problem is reduced to a system of four nonlinear differential equations. The model has been applied to the case of surfactant adsorption at a quiescent interface [138], i.e., to the relaxation of surface tension and adsorption after a small initial perturbation. The perturbations in the basic parameters of the micellar solution are defined in the following way:

$$\xi_1 \equiv \frac{h_a}{\Gamma_{p,0}} c_{1,p}; \quad \xi_c \equiv \frac{h_a}{\beta \Gamma_{p,0}} C_{m,p}; \quad \xi_m \equiv \frac{h_a c_{1,eq}}{s_{eq}^2 \Gamma_{p,0}} m_p \tag{7.95}$$

where

$c_{1,p}$, $C_{m,p}$, and m_p are, respectively, the perturbations in the monomer concentration, c_1, micelle concentration, C_m, and the micelle mean aggregation number, m

ξ_1, ξ_c, and ξ_m are the respective dimensionless perturbations

$\Gamma_{p,0}$ is the perturbation in the surfactant adsorption at the initial moment ($t = 0$)

s_{eq} is the halfwidth of the equilibrium micelle size distribution modeled by a Gaussian bell-like curve

β and h_a are, respectively, the dimensionless bulk micelle concentration and the characteristic adsorption length, defined as follows:

$$\beta \equiv (C_{tot} - CMC)/CMC; \quad h_a = (d\Gamma/dc_1)_{eq} \tag{7.96}$$

where C_{tot} is the total surfactant concentration; Γ is the surfactant adsorption. The dimensionless fluxes of the fast and slow demicellization processes, denoted by φ_m and φ_s, respectively, can be expressed as follows [138]:

$$\varphi_m = \xi_1 - \xi_m \tag{7.97}$$
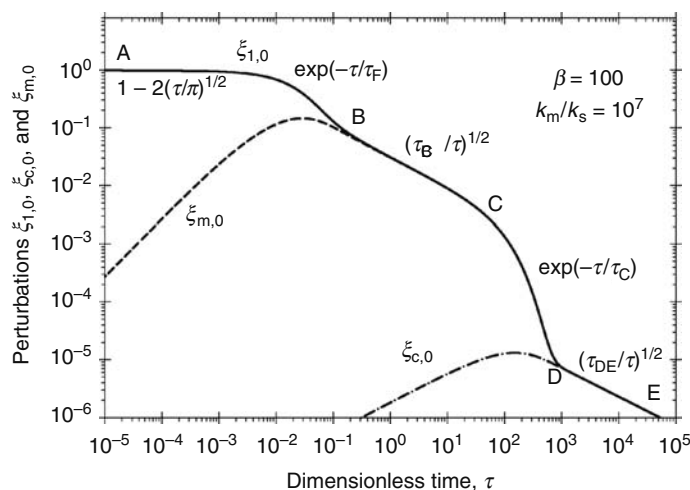
FIGURE 7.8 Time dependence of the perturbations in the subsurface monomer concentration, $\xi_{1,0}$, micelle concentration, $\xi_{c,0}$, and mean aggregation number, $\xi_{m,0}$, for $\beta = 100$. The curves are obtained by numerical solution of the general system of equations in Ref. [138].

$$\varphi_s = (m_{eq} - ws_{eq})\xi_1 - m_{eq}\xi_c + s_{eq}w\xi_m \tag{7.98}$$

(Some small terms are neglected in Equations 7.97 and 7.98.) where m_{eq} is the equilibrium micelle aggregation number, and $w = (m_{eq} - n_r)/s_{eq}$, where n_r is an aggregation number at the boundary between the regions of the rare aggregates and the abundant micelles [138].

Figure 7.8 shows results obtained by solving numerically the general system of equations in Ref. [138] for a relatively high micelle concentration, $\beta = 100$. The calculated curves $\xi_{1,0}(\tau)$, $\xi_{c,0}(\tau)$, and $\xi_{m,0}(\tau)$ represent the subsurface values (at $z = 0$, Figure 7.7) of the perturbations ξ_1, ξ_c, and ξ_m, plotted versus the dimensionless time, $\tau = (D_1/h_a^2)t$, where D_1 is the diffusion coefficient of the surfactant monomers. Note that $\xi_{1,0}$ expresses not only the perturbation in the subsurface monomer concentration, but also the perturbations in the surface tension and adsorption [138]:

$$\frac{\sigma(t) - \sigma_e}{\sigma(0) - \sigma_e} = \frac{\Gamma(t) - \Gamma_e}{\Gamma(0) - \Gamma_e} = \xi_{1,0}(\tau) \tag{7.99}$$

$\sigma(t)$ and $\Gamma(t)$ are the dynamic surface tension and adsorption; $\sigma(0)$ and $\Gamma(0)$ are their initial values, and σ_e and Γ_e are their final equilibrium values. A typical value, $k_m/k_S = 10^7$, of the ratio of the rate constants of the fast and slow demicellization processes is used to calculate the curves in Figure 7.8.

The most important feature of the relaxation curves in Figure 7.8, which represents a kinetic diagram, is that $\xi_{m,0}$ merges with $\xi_{1,0}$ at a given point, denoted by B, while $\xi_{c,0}$ merges with $\xi_{1,0}$ (and $\xi_{m,0}$) at another point, denoted by D. The time moments, corresponding to the points B and D, are denoted by τ_B and τ_D, respectively. As seen in Figure 7.8, for $\tau > \tau_B$, we have $\xi_{1,0} = \xi_{m,0}$. In view of Equation 7.97, this means that for $\tau > \tau_B$ the flux of the fast micelle relaxation process, φ_m is equal to zero. In other words, for $\tau > \tau_B$ the monomers and micelles are equilibrated with respect to the fast micellar process. For a regular relaxation process, the theoretical analysis [138] yields the expression $\tau_B = s_{eq}h_a(2k_m/D_1)^{1/2}$. In addition, for $\tau > \tau_D$ we have $\xi_{c,0} = \xi_{1,0} = \xi_{m,0}$, and then Equation 7.98 indicates that $\varphi_s = 0$, i.e., the monomers and micelles are equilibrated with respect to the slow micellar process.

The computer modeling [138] shows that $\xi_{1,0}(\tau)$ exhibits two exponential (kinetic) regimes, AB and CD, and two inverse-square-root (diffusion) regimes, BC and DE, see Figure 7.8. In particular, the point C corresponds to the moment $\tau_C = (D_1/h_a^2)t_c \approx (\beta D_1\sigma_{eq}^2)/(k_S h_a^2 m_{eq}^3)$, where t_c is the characteristic time of the slow micellar process (see Ref. [137]). τ_C serves also as a characteristic relaxation time of adsorption in the kinetic regime CD. The expressions for the other characteristic times, τ_F, τ_{BC}, and τ_{DE} (Figure 7.8) are [138]:

$$\tau_F = (m_{eq}D_1)/(\beta k_m h_a^2) \, (\text{regime AB}) \tag{7.100}$$

$$\frac{1}{\tau_{BC}} = \frac{D_{BC}}{D_1} = (1 + u\beta)(1 + u\beta B_m) \, (\text{regime BC}) \tag{7.101}$$

$$\frac{1}{\tau_{DE}} = \frac{D_{DE}}{D_1} = [1 + (u + m_{eq})\beta] \, [1 + (u + m_{eq})\beta B_m] \, (\text{regime DE}) \tag{7.102}$$
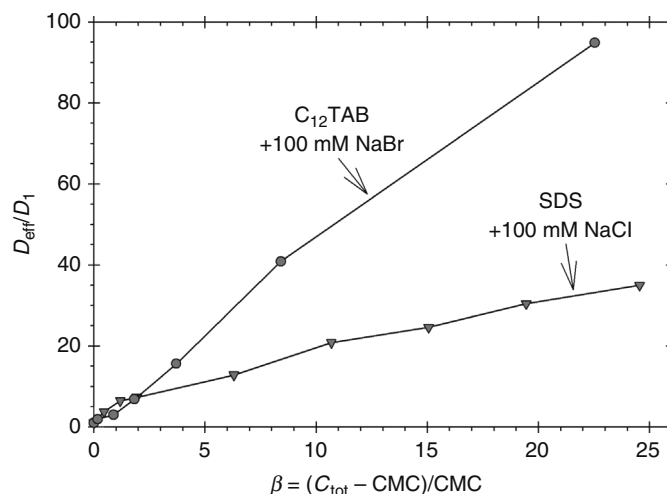
FIGURE 7.9 Plot of the dimensionless effective diffusivity of the micellar solution, d_{eff}/d_1, versus the dimensionless micelle concentration, β, obtained from dynamic-surface-tension values measured by the MBPM in reference.

where

D_{BC} and D_{DE} are the effective diffusivities of the micellar solutions in the regimes BC and DE, respectively

$u = s_{eq}^2/m_{eq}$ and $B_m = D_m/D_1$; D_m are the mean diffusivity of the micelles

$u \approx 1$ and $B_m \approx 0.2$ are the typical parameter values

It should be noted that in addition to the regular kinetic diagrams (Figure 7.8), for low micelle concentrations (β close to 1) we could observe rudimentary kinetic diagrams, characterized by merging or disappearance of the stages BC and CD [138,139].

The diffusion regimes BC and DE can be observed not only for adsorption at a quiescent interface, but also in the cases of stationary [139] and nonstationary [55] expansion of an interface. The expressions for the effective diffusivities, D_{BC} and D_{DE}, given by Equations 7.101 and 7.102, are valid in all these cases. In particular, the experimental data by Lucassen [130] correspond to the kinetic regime DE, while the experimental data by Joos et al. [135] correspond to the kinetic regime BC.

As an illustration, in Figure 7.9 we show experimental data for the ionic surfactants SDS and dodecyl trimethyl ammonium bromide (C_{12}TAB) + 100 mM added inorganic electrolyte. The data are obtained by means of the MBPM in Ref. [55]. To check whether the kinetic regime is DE, we substitute typical parameter values in Equation 7.102: $m_{eq} = 70$, $\beta = 20$, and $B_m = 0.2$, and as a result we obtain $D_{DE}/D_1 = 3.9 \times 10^5$, which is much greater than the experimental values of D_{eff}/D_1 in Figure 7.9. Consequently, the kinetic regime cannot be DE. On the other hand, a similar estimate of D_{BC}/D_1 from Equation 7.101 gives reasonable values. To demonstrate that, from the experimental values of D_{eff}/D_1 in Figure 7.9 we calculated u by means of Equation 7.101, substituting $B_m = 0.2$. For most of the concentrations we obtain values $0.4 < u < 2$, which seem reasonable. Values $u > 2$ are obtained at $\beta < 2$, which indicate that at the lowest micellar concentrations we are dealing with a rudimentary kinetic regime [138,139], rather than with the diffusion regime BC.

7.2.2.6.3 Case of Stationary Interfacial Expansion

This special case of interfacial dynamics is realized with the strip method [93,135] and the overflowing cylinder method [58,90]. Because the adsorption process is stationary, the time, t, is not a parameter of state of the system. For this reason, in the kinetic diagrams (like Figure 7.10) we plot the perturbations versus the dimensionless rate of surface expansion, $\theta = (h_a^2/D_1)(dA/dt)/A$, where A is the interfacial area, and $dA/dt = $ constant is the interfacial expansion rate. In Figure 7.10, the total perturbations, $\xi_{1,T}$, $\xi_{c,T}$, and $\xi_{m,T}$ are plotted, which represent the local perturbations, $\xi_1(z)$, $\xi_c(z)$, and $\xi_m(z)$, integrated with respect to the normal coordinate z along the whole semiaxis $z > 0$ (Figure 7.7). As seen in Figure 7.10, we observes the same kinetic regimes, as in Figure 7.8, although the diagrams in the two figures look like mirror images: the young surface age (the regime AB) corresponds to the left side of Figure 7.8, but to the right side of Figure 7.10. Analytical expressions for the adsorption and surface-tension relaxation could be found in Ref. [139]. As mentioned above, the expressions for the effective diffusivities, D_{BC} and D_{DE}, given by Equations 7.101 and 7.102, are valid also in the case of stationary interfacial expansion. In particular, it has been found [139] that the kinetic regime of adsorption from the solutions of the nonionic surfactant polyoxyethylene-20 hexadecyl ether (Brij 58), measured by means of the strip method [135], corresponds to the regime BC.
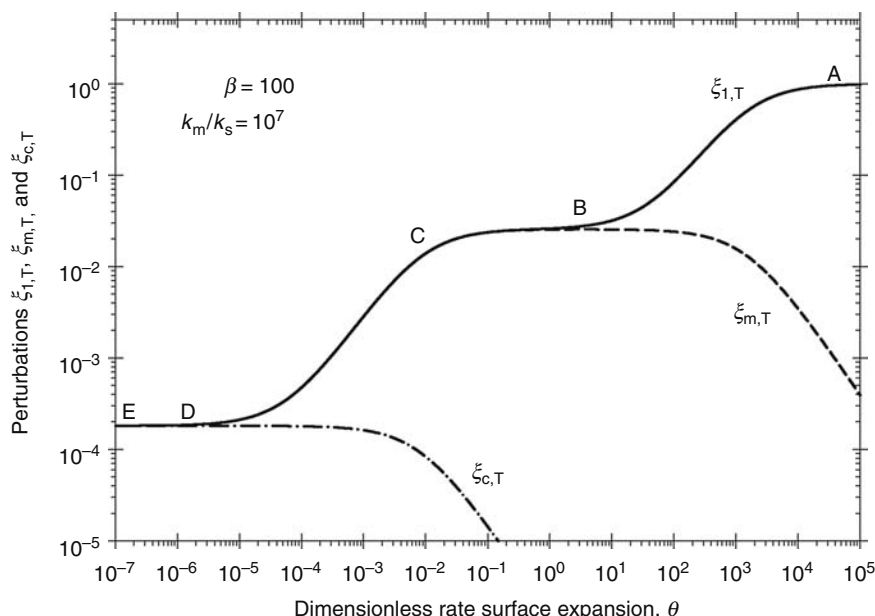
FIGURE 7.10 Total perturbations in monomer concentration, $\xi_{1,T}$, micelle concentration, $\xi_{c,T}$, and mean aggregation number, $\xi_{m,T}$, plotted versus the dimensionless rate of surface expansion, θ, at micelle dimensionless concentration $\beta = 100$. The curves are obtained by numerical solution of the linear system of equations derived in Ref. [139].

We recall that in the regime BC the rate constants of the fast and slow micellar processes, k_m and k_S, do not affect the surfactant adsorption kinetics, and cannot be determined from the fit of the data. In principle, it is possible to observe the kinetic regime AB (and to determine k_m) with faster methods or with slower surfactants.

In summary, four distinct kinetic regimes of adsorption from micellar solutions exist, called AB, BC, CD, and DE; see Figures 7.8 and 7.10. In regime AB, the fast micellar process governs the adsorption kinetics. In regime BC, the adsorption occurs under diffusion control, because the fast micellar process is equilibrated, while the slow process is negligible. In regime CD, the slow micellar process governs the adsorption kinetics. In regime DE, the adsorption occurs under diffusion control, because both the fast and slow micellar processes are equilibrated. Note that only the regimes BC and DE correspond to purely diffusion processes. For the regimes AB and CD, the rate constants of the fast and slow micellar processes, k_m and k_S, respectively, affect the surfactant adsorption kinetics, and could be in principle determined from the fit of experimental data. For the specific experimental examples considered here, the adsorption kinetics corresponds to the diffusion regime BC.

7.2.2.6.4 Kinetics of Oil Solubilization in Micellar Solutions

The term solubilization was coined by McBain [140] to denote the increased solubility of a given compound, associated with the presence of surfactant micelles or inverted micelles in the solution. The most popular solubilization process is the transfer of oil molecules into the core of surfactant micelles. Thus, oil that has no solubility (or limited solubility) in the aqueous phase becomes water-soluble in the form of solubilizate inside the micelles. This process has a central importance for washing of oily deposits from solid surfaces and porous media, and for removal of oily contaminants dispersed in water. The great practical importance of solubilization is related to its application in the everyday life: in the personal care and household detergency, as well as in various industrial processes [141].

The main actors in the solubilization process are the micelles of surfactant and/or copolymer. Their ability to uptake oil is of crucial importance [141,142]. The addition of copolymers, which form mixed micelles with the surfactants [143], is a way to control and improve the micelle solubilization performance. Two main kinetic mechanisms of solubilization have been established, whose effectuation depends on the specific system:

1. Solubilization as a bulk reaction: Molecular dissolution and diffusion of oil into the aqueous phase takes place, with a subsequent uptake of oil molecules by surfactant micelles [144–149]. This mechanism is operative for oils (like benzene, hexane, etc.), which exhibit a sufficiently high solubility in pure water. Theoretical models have been developed and verified against the experiment [145,147–149]. The bulk solubilization included the following processes. First, oil molecules are dissolved from the surface of an oil drop into water. Kinetically, this process can be characterized by a mass transfer coefficient. Next, by molecular diffusion, the oil molecules penetrate in the water

phase, where they react with the micelles. Thus, the concentration of free oil molecules diminishes with the distance from the oil–water interface. In other words, the solubilization takes place in a restricted zone around the droplet [147,148].

2. Solubilization as a surface reaction: This is the major solubilization mechanism for oils that are practically insoluble in water [144,146,148,150–158]. The uptake of such oils cannot happen in the bulk of the aqueous phase. The solubilization can be realized only at the oil–water interface. The mechanism may include (i) micelle adsorption, (ii) uptake of oil, and (iii) desorption of the swollen micelles [156–158]. Correspondingly, the theoretical description of the process involves the rate constants of the three consecutive steps. If the empty micelles are long rod, like aggregates, upon solubilization they usually break to smaller spherical aggregates [156,159]. For some systems (mostly solid solubilizates), the intermediate stages in the solubilization process may involve penetration of surfactant solution into the oily phase and formation of a liquid crystalline phase at the interface [160–164].

In the case of solubilization as surface reaction, the detailed kinetic mechanism could be multiform. Some authors [144,151] expect that the surfactant arrives at the interface in a monomeric form. Then, at the phase boundary mixed (or swollen) micellar aggregates are formed, which eventually desorb. This version of the model seems appropriate for solid solubilizates, because hemimicelles can be formed at their surfaces, even at surfactant concentrations below the bulk CMC [165]. Another concept, presented by Plucinski and Nitsch [153], includes a step of partial fusion of the micelles with the oil–water interface, followed by a step of separation. Such mechanism could take place in the case when microemulsion drops, rather than micelles, are responsible for the occurrence of solubilization.

Experiments with various surfactant systems [154,158,166] showed that the solubilization rates for solutions of ionic surfactants are generally much lower than those for nonionic surfactants. This can be attributed to the electrostatic repulsion between the micelles and the similarly charged surfactant adsorption monolayer at the oil–water interface. On the other hand, copolymers have been found to form micelles, which solubilize well various hydrophobic compounds, even in the absence of low-molecular-weight surfactants [167–175]. Moreover, appropriately chosen copolymers can act as very efficient promoters of solubilization [148,156–158].

7.3 CAPILLARY HYDROSTATICS AND THERMODYNAMICS

7.3.1 SHAPES OF FLUID INTERFACES

7.3.1.1 Laplace and Young Equations

A necessary condition for mechanical equilibrium of a fluid interface is the Laplace equation of capillarity [176–179]

$$2H\sigma = \Delta P \tag{7.103}$$

where
H is the local mean curvature of the interface
ΔP is the local jump of the pressure across the interface

If $z = z(x,y)$ is the equation of the interface in Cartesian coordinates, then H can be expressed in the form [179]

$$2H = \nabla_s \cdot \left[\frac{\nabla_s z}{(1 + |\nabla_s z|^2)^{1/2}} \right] \tag{7.104}$$

where ∇_s is the gradient operator in the plane xy. More general expressions for H can be found in the literature on differential geometry [179–181]. Equation 7.103, along with Equation 7.104, represents a second order partial differential equation which determines the shape of the fluid interface. The interface is bounded by a three-phase contact line at which the boundary conditions for the differential equation are formulated. The latter are the respective necessary conditions for mechanical equilibrium at the contact lines. When one of the three phases is solid (Figure 7.11a), the boundary condition takes the form of the Young [182] equation:

$$\sigma_{12} \cos \alpha = \sigma_{1s} - \sigma_{2s} \tag{7.105}$$
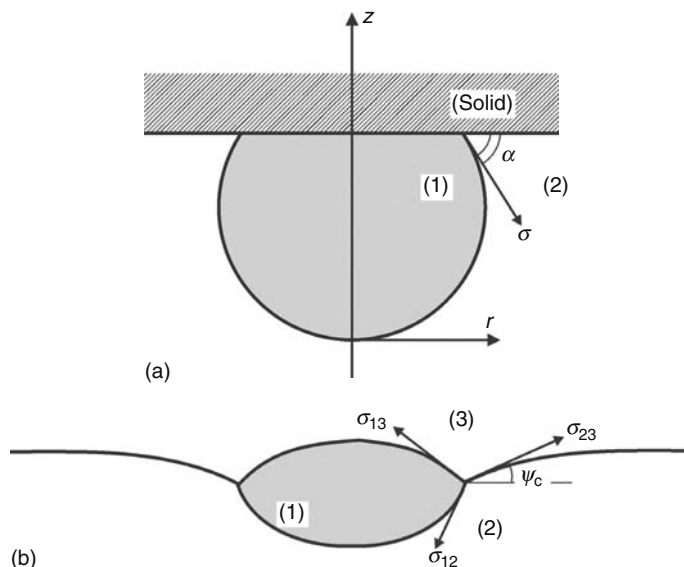
FIGURE 7.11 Sketch of fluid particle (1) attached to an interface. (a) Fluid particle attached to solid interface; α is the contact angle; σ is the interfacial tension of the boundary between the two fluid phases. (b) Fluid particle attached to a fluid interface; σ_{12}, σ_{13}, and σ_{23} are the interfacial tensions between the respective phases; ψ_c is the slope angle of the outer meniscus at the contact line.

where
  α is the three-phase contact angle
  σ_{12} is the tension of the interface between the fluid phases 1 and 2, whereas σ_{1s} and σ_{2s} are the tensions of the two fluid–solid interfaces

Insofar as the values of the three σs are determined by the intermolecular forces, the contact angle α is a material characteristics of a given three-phase system. However, when the solid is not smooth and chemically homogeneous, then the contact angle exhibits hysteresis, i.e., α has no defined equilibrium value [6,183]. Contact angle hysteresis can be observed even with molecularly smooth and homogeneous interfaces under dynamic conditions [184].

   When all the three neighboring phases are fluid, then the boundary condition takes the form of the Neumann [185] vectorial triangle (see Figure 7.11b):

$$\sigma_{12}v_{12} + \sigma_{13}v_{13} + \sigma_{23}v_{23} = 0 \tag{7.106}$$

where v_{ik} is a unit vector, which is simultaneously normal to the contact line and tangential to the boundary between phases i and k. The Laplace, Young, and Neumann equations can be derived as conditions for minimum of the free energy of the system [35,179,186]; the effect of the line tension can be also taken into account in Equations 7.105 and 7.106 [186].

   In the special case of spherical interface $H = 1/R$, with R being the sphere radius, and Equation 7.103 takes its most popular form, $2\sigma/R = \Delta P$. In the case of axisymmetric meniscus (z-axis of symmetry, Figure 7.11) the Laplace equation reduces to either of the following two equivalent forms [178,187]:

$$\frac{1}{r}\frac{d}{dr}\left[\frac{rz'}{(1+z'^2)^{1/2}}\right] = \frac{\Delta P}{\sigma}, \quad z = z(r) \tag{7.107}$$

$$-\frac{r''}{(1+r'^2)^{3/2}} + \frac{1}{r(1+r'^2)^{1/2}} = \frac{\Delta P}{\sigma}, \quad r = r(z) \tag{7.108}$$

Two equivalent parametric forms of Laplace equation are often used for calculations [178,187]:

$$\frac{d\sin\varphi}{dr} + \frac{\sin\varphi}{r} = \frac{\Delta P}{\sigma}, \quad \tan\varphi = \frac{dz}{dr} \tag{7.109}$$

or

$$\frac{d\varphi}{ds} = \frac{\Delta P}{\sigma} - \frac{\sin\varphi}{r}, \quad \frac{dr}{ds} = \cos\varphi, \quad \frac{dz}{ds} = \sin\varphi \tag{7.110}$$

where
  φ is the meniscus running slope angle
  s is the arc length along the generatrix of the meniscus

Equation 7.110 is especially convenient for numerical integration, whereas Equation 7.109 may create numerical problems at the points with $\tan\varphi = \pm\infty$, like the particle equator in Figure 7.11a. A generalized form of Equation 7.109, with account for the interfacial (membrane) bending elastic modulus, k_c,

$$\sigma\left(\frac{d\sin\varphi}{dr} + \frac{\sin\varphi}{r}\right) = \Delta P + \frac{k_c}{r}\cos\varphi\frac{d}{dr}\left\{r\cos\varphi\frac{d}{dr}\left[\frac{1}{r}\frac{d}{dr}(r\sin\varphi)\right]\right\} \tag{7.111}$$

serves for description of the axisymmetric configurations of real and model cell membranes [35,188,189]. The Laplace equation can be generalized to account also for the interfacial bending moment (spontaneous curvature), shear elasticity, etc., for review see Refs. [35,188]. The latter effects are physically important for systems or phenomena like capillary waves [190], lipid membranes [191,192], emulsions [193], and microemulsions [194].

7.3.1.2 Solutions of Laplace Equations for Menisci of Different Geometry

Very often the capillary menisci have rotational symmetry. In general, there are three types of axially symmetric menisci corresponding to the three regions denoted in Figure 7.12: (1) Meniscus meeting the axis of revolution, (2) Meniscus decaying at infinity, and (3) Meniscus confined between two cylinders, $0 < R_1 < r < R_2 < \infty$. These three cases are separately considered below.

7.3.1.2.1 Meniscus Meeting the Axis of Revolution

This includes the cases of a bubble/droplet under a plate (Figure 7.11a), the two surfaces of a floating lens (Figure 7.11b), and any kind of sessile or pendant droplets/bubbles. Such a meniscus is a part of a sphere when the effect of gravity is negligible, that is when

$$\frac{\Delta\rho g b^2}{\sigma} \ll 1 \tag{7.112}$$

where
  g is the gravity acceleration
  $\Delta\rho$ is the difference in the mass densities of the lower and the upper fluid
  b is a characteristic radius of the meniscus curvature
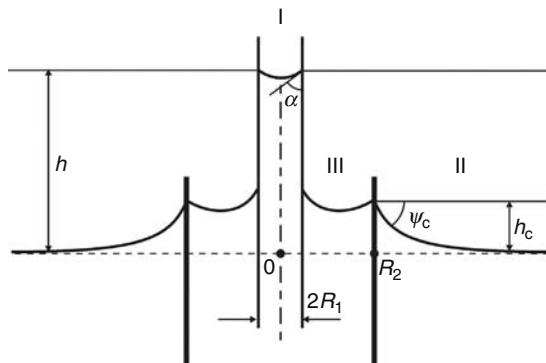
FIGURE 7.12 Capillary menisci formed around two coaxial cylinders of radii R_1 and R_2. (I) Meniscus meeting the axis of revolution; (II) meniscus decaying at infinity; (III) meniscus confined between the two cylinders. h denotes the capillary raise of the liquid in the inner cylinder; h_c is the elevation of meniscus II at the contact line $r = R_2$.

For example, if Equation 7.112 is satisfied with $b = R_1$ (see Figure 7.12), the raise, h, of the liquid in the capillary is determined by means of the equation [6]

$$h = (2\sigma \cos \alpha)/(\Delta \rho g R_1) \tag{7.113}$$

When the gravity effect is not negligible, the capillary pressure, ΔP, becomes dependent on the z-coordinate:

$$\Delta P = \frac{2\sigma}{b} + \Delta \rho g z \tag{7.114}$$

where b is the radius of curvature at the particle apex, where the two principal curvatures are equal (e.g., the bottom of the bubble in Figure 7.11a). Unfortunately, Equation 7.107, along with Equation 7.114, has no closed analytical solution. The meniscus shape can be exactly determined by numerical integration of Equation 7.110. Alternatively, various approximate expressions are available [187,195,196]. For example, if the meniscus slope is small, $z'^2 \ll 1$, Equation 7.107 reduces to a linear differential equation of Bessel type, whose solution reads

$$z(r) = 2[I_0(qr) - 1]/(bq^2), \quad q \equiv (\Delta \rho g/\sigma)^{1/2} \tag{7.115}$$

where $I_0(x)$ is the modified Bessel function of the first kind and zeroth order [197,198]. Equation 7.115 describes the shape of the lower surface of the lens in Figure 7.11b; similar expression can be derived also for the upper lens surface.

7.3.1.2.2 Meniscus Decaying at Infinity

Examples are the outer menisci in Figures 7.11b and 7.12. In this case the action of gravity cannot be neglected insofar as the gravity keeps the interface flat far from the contact line. The capillary pressure is

$$\Delta P = \Delta \rho g z \tag{7.116}$$

As mentioned above, Equation 7.107, along with Equation 7.116, has no closed analytical solution. On the other hand, the region far from the contact line has always small slope, $z'^2 \ll 1$. In this region Equation 7.107 can be linearized, and then in analogy with Equation 7.115 we derive

$$z(r) = AK_0(qr)\,(z'^2 \ll 1) \tag{7.117}$$

where

    A is a constant of integration
    $K_0(x)$ is the modified Bessel function of the second kind and zeroth order [197,198]

The numerical integration of Equation 7.110 can be carried out by using the boundary condition [187] $z'/z = -qK_1(qr)/K_0(qr)$ for some appropriately fixed $r \ll q^{-1}$ (see Equation 7.117). Alternatively, approximate analytical solutions of the problem are available [187,196,199]. In particular, Derjaguin [200] has derived an asymptotic formula for the elevation of the contact line at the outer surface of a thin cylinder,

$$h_c = -R_1 \sin \psi_c \, \ln [qR_1 \gamma_e (1 + \cos \psi_c)/4], \quad (qR_1)^2 \ll 1 \tag{7.118}$$

where

    R_1 is the radius of the contact line
    ψ_c is the meniscus slope angle at the contact line (Figure 7.12)
    q is defined by Equation 7.115
    $\gamma_e = 1.781\,072\,418\ldots$ is the constant of Euler–Mascheroni [198].

7.3.1.2.3 Meniscus Confined between Two Cylinders ($0 < R_1 < r < R_2 < \infty$)

This is the case with the Plateau borders (PBs) in real foams and emulsions, and with the model films in the Scheludko cell [201,202]; such is the configuration of the capillary bridges (Figure 7.13a) and of the fluid particles pressed between two surfaces (Figure 7.13b). When the gravitational deformation of the meniscus cannot be neglected, the interfacial shape can be determined by numerical integration of Equation 7.110, or by iteration procedure [203]. When the meniscus deformation caused by gravity is negligible, analytical solution can be found as described below.
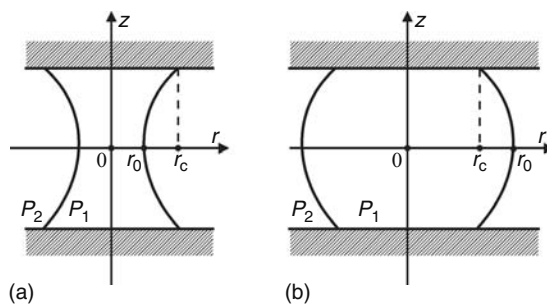
FIGURE 7.13 Concave (a) and convex (b) capillary bridges between two parallel plates. P_1 and P_2 denote the pressures inside and outside the capillary bridge, r_0 is the radius of its section with the midplane; r_c is the radius of the three-phase contact lines.

To determine the shape of the menisci depicted in Figure 7.13a and b, we integrate Equation 7.109 from r_0 to r to derive

$$\frac{dz}{dr} = \frac{k_1(r^2 - r_0^2) + r_0}{\pm[(r^2 - r_0^2)(r_1^2 - r^2)]^{1/2}|k_1|}, \quad k_1 \equiv \frac{P_1 - P_2}{2\sigma}, \quad r_1 \equiv \left|\frac{1 - k_1 r_0}{k_1}\right| \tag{7.119}$$

The pressures in phases 1 and 2, P_1 and P_2, and r_0 are shown in Figure 7.13. Equation 7.119 describes curves, which after Plateau [177,178,204–206] are called nodoid and unduloid, (see Figure 7.14). The nodoid (unlike the unduloid) has points with horizontal tangent, where $dz/dr = 0$. Then with the help of Equation 7.119, we can deduce that the meniscus generatrix is a part of nodoid if $k_1 r_0 \in (-\infty, 0) \cup (1, +\infty)$, while the meniscus generatrix is a part of unduloid if $k_1 r_0 \in (0, 1)$.

In the special case, when $k_1 r_0 = 1$, the meniscus is spherical. In the other special case, $k_1 r_0 = 0$, the meniscus has the shape of catenoid, i.e.,

$$z = \pm r_0 \ln\left\{r/r_0 + \sqrt{(r/r_0)^2 - 1}\right\}, \quad (k_1 = 0) \tag{7.120}$$

The meniscus has a neck (Figure 7.13a) when $k_1 r_0 \in (-\infty, 1/2)$; in particular, the generatrix is nodoid for $k_1 r_0 \in (-\infty, 0)$, catenoid for $k_1 r_0 = 0$, and unduloid for $k_1 r_0 \in (0, 1/2)$. For the configuration depicted in Figure 7.13a, we have $r_1 > r_0$ (in Figure 7.14 $r_a = r_0$, $r_b = r_1$) and Equation 7.119 can be integrated to yield (see tables of integrals):

$$z(r) = \pm\left\{r_0 F(\phi_1, q_1) + r_1 \text{sgn}\, k_1 \left[E(\phi_1, q_1) - \frac{1}{rr_1}\sqrt{(r^2 - r_0^2)(r_1^2 - r^2)}\right]\right\}(r_0 < r < r_1) \tag{7.121}$$
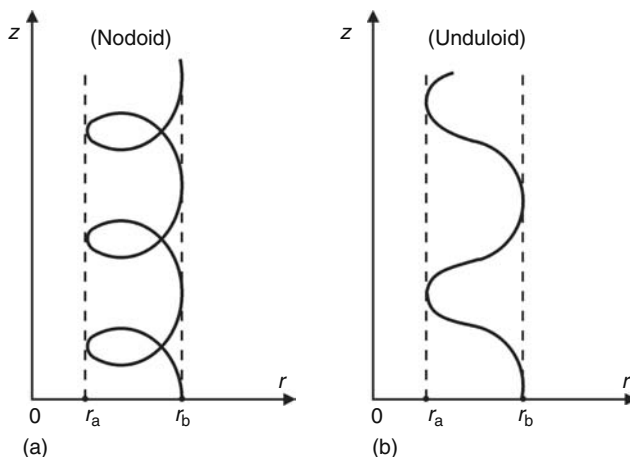
FIGURE 7.14 Typical shape of nodoid (a) and unduloid (b) Plateau curves. Note that the curves are confined between two cylinders of radii r_a and r_b.

where

sgn$x$ denotes the sign of x, $q_1 = (1 - r_0^2/r_1^2)^{1/2}$, $\sin\phi_1 = q_1^{-1}(1 - r_0^2/r^2)^{1/2}$

$F(\phi, q)$ and $E(\phi, q)$ are the standard symbols for elliptic integrals of the first and the second kind [197,198]

A convenient method for computation of $F(\phi,q)$ and $E(\phi,q)$ is the method of the arithmetic–geometric mean (see Ref. [197], Chapter 17.6).

The meniscus has a haunch (Figure 7.13b) when $k_1 r_0 \in (1/2, +\infty)$; in particular, the generatrix is unduloid for $k_1 r_0 \in (1/2, 1)$, circumference for $k_1 r_0 = 1$, and nodoid for $k_1 r_0 \in (1, +\infty)$. For the configuration depicted in Figure 7.13b, we have $r_0 > r_1$ (in Figure 7.14 $r_a = r_1$, $r_b = r_0$) and Equation 7.119 can be integrated to yield (see tables of integrals):

$$z(r) = \mp\left(\left(r_0 - \frac{1}{k_1}\right)F(\phi_2,q_2) - r_0 E(\phi_2,q_2)\right), \quad (r_1 \leq r \leq r_0) \tag{7.122}$$

where $q_2 = (1 - r_1^2/r_0^2)^{1/2}$, $\sin\phi_2 = q_2^{-1}(1 - r^2/r_0^2)^{1/2}$. Additional information about the shapes, stability and nucleation of capillary bridges, and for the capillary-bridge forces between particles, can be found in Chapter 11 of Ref. [35].

7.3.1.3 Gibbs–Thomson Equation

The dependence of the capillary pressure on the interfacial curvature leads to a difference between the chemical potentials of the components in small droplets (or bubbles) and in the large bulk phase. This effect is the driving force of phenomena like nucleation [207,208] and Ostwald ripening (see Section 7.3.1.4). Let us consider the general case of a multicomponent two-phase system; we denote the two phases by α and β. Let phase α be a liquid droplet of radius R. The two phases are supposed to coexist at equilibrium. Then we can derive [4,5,209,210]

$$(\mu_i^\beta)_R - (\mu_i^\beta)_{R=\infty} = (\mu_i^\alpha)_R - (\mu_i^\alpha)_{R=\infty} = V_i^\alpha \frac{2\sigma}{R} \tag{7.123}$$

where

μ is the chemical potential

V_i is the partial volume, the superscripts denote phase and the subscripts denote component

Equation 7.123 is derived under the following assumptions. When β is a gaseous phase, it is assumed that the partial volume of each component in the gas is much larger than its partial volume in the liquid α; this is fulfilled far enough from the critical point [210]. When phase β is liquid, it is assumed that $P^\beta(R) = P^\beta(R=\infty)$, where P denotes pressure.

When phase β is an ideal gas, Equation 7.123 yields [4,5,209,210]

$$\frac{P_i^\beta(R)}{P_i^\beta(\infty)} = \exp\left(\frac{2\sigma V_i^\alpha}{RkT}\right) \tag{7.124}$$

where $P_i^\beta(R)$ and $P_i^\beta(\infty)$ denote respectively the equilibrium vapor pressure of component i in the droplet of radius R and in a large liquid phase of the same composition. Equation 7.124 shows that the equilibrium vapor pressure of a droplet increases with the decrease of the droplet size. (For a bubble, instead of a droplet, R must be changed to $-R$ in the right-hand side of Equation 7.124 and the tendency becomes the opposite.) Equation 7.124 implies that in an aerosol of polydisperse droplets the larger droplets will grow and the smaller droplets will diminish down to complete disappearance.

The small droplets are protected against disappearance when phase α contains a nonvolatile component. Then instead of Equation 7.124 we have

$$\frac{P_i^\beta(R)}{P_i^\beta(\infty)} = \frac{1 - X(R)}{1 - X(\infty)} \exp\left(\frac{2\sigma V_i^\alpha}{RkT}\right) \tag{7.125}$$

where X denotes the molar fraction of the nonvolatile component in phase α; for $X(R) = X(\infty)$ Equation 7.125 reduces to Equation 7.124. Setting the left-hand side of Equation 7.125 equal to 1, we can determine the value $X(R)$ needed for a liquid droplet of radius R, surrounded by the gas phase β, to coexist at equilibrium with a large ($R=\infty$) liquid phase α of composition $X(\infty)$.

When both phases α and β are liquid, Equation 7.123 yields

$$\frac{X_i^\beta(R)}{X_i^\beta(\infty)} = \exp\left(\frac{2\sigma V_i^\alpha}{RkT}\right) \tag{7.126}$$

where $X_i^\beta(R)$ denotes the equilibrium molar fraction of component i in phase β coexisting with a droplet of radius R, and $X_i^\beta(\infty)$ denotes the value of $X_i^\beta(R)$ for $R \to \infty$, i.e., for phase β coexisting with a large phase α of the same composition as the droplet. In the case of O/W emulsion, X_i^β can be the concentration of the oil dissolved in the water. In particular, Equation 7.126 predicts that the large emulsion droplets will grow and the small droplets will diminish. This phenomenon is called Ostwald ripening (see the next section). If the droplets (phase α) contain a component, which is insoluble in phase β, the small droplets will be protected against complete disappearance; a counterpart of Equation 7.125 can be derived:

$$\frac{X_i^\beta(R)}{X_i^\beta(\infty)} = \frac{1 - X(R)}{1 - X(\infty)} \exp\left(\frac{2\sigma V_i^\alpha}{RkT}\right) \tag{7.127}$$

where X denotes the equilibrium concentration in phase α of the component which is insoluble in phase β. Setting the left-hand side of Equation 7.127 equal to 1, we can determine the value $X(R)$ needed for an emulsion droplet of radius R, surrounded by the continuous phase β, to coexist at equilibrium with a large ($R = \infty$) liquid phase α of composition $X(\infty)$.

7.3.1.4 Kinetics of Ostwald Ripening in Emulsions

The Ostwald ripening is observed when the substance of the emulsion droplets (we will call it component 1) exhibits at least minimal solubility in the continuous phase, β. As discussed above, the chemical potential of this substance in the larger droplets is lower than in the smaller droplets, see Equation 7.123. Then a diffusion transport of component 1 from the smaller toward the larger droplets will take place. Consequently, the size distribution of the droplets in the emulsion will change with time. The kinetic theory of Ostwald ripening was developed by Lifshitz and Slyozov [211], Wagner [212] and further extended and applied by other authors [213–216]. The basic equations of this theory are the following.

The volume of an emulsion droplet grows (or diminishes) due to the molecules of component 1 supplied (or carried away) by the diffusion flux across the continuous medium. The balance of component 1 can be presented in the form [216]

$$\frac{4\pi}{3}\frac{d}{dt}R^3(t) = 4\pi DRV_1[c_m(t) - c_{eq}(R)] \tag{7.128}$$

where
  t is the time
  D is the diffusivity of component 1 in the continuous phase
  V_1 is the volume per molecule of component 1
  c_m is the number–volume concentration of component 1 in the continuous medium far away from the droplets surfaces
  $c_{eq}(R)$ is the respective equilibrium concentration of the same component for a droplet of radius R as predicted by the Gibbs–Thomson equation

Note that Equation 7.128 is rigorous only for a diluted emulsion, in which the interdroplet concentration levels off at a constant value, $c = c_m$, around the middle of the space between each two droplets. Some authors [214] add in the right-hand side of Equation 7.128 also terms accounting for the convective mass transfer (in the case of moving droplets) and thermal contribution to the growth rate.

Because the theory is usually applied to droplets of diameter not smaller than micrometer (which are observable by optical microscope), the Gibbs–Thomson equation, Equation 7.126, can be linearized to yield [216]

$$c_{eq}(R) \approx c_\infty(1 + b/R), \quad b \equiv 2\sigma V_1/(kT) \tag{7.129}$$

with c_∞ being the value of c_{eq} for flat interface. With $\sigma = 50$ mN m^{-1}, $V_1 = 100$ Å^3, and $T = 25°C$ we estimate $b = 2.5$ nm. The latter value justifies the linearization of Gibbs–Thomson equation for droplets of micrometer size.

Let $f(R,t)$ be the size distribution function of the emulsion droplets such that $f(R,t)\,dR$ is the number of particles per unit volume in the size range from R to $(R + dR)$. The balance of the number of particles in the system reads

$$df\,dR = (j\,dt)|_R - (j\,dt)|_{R+dR}, \quad (j \equiv f\,dR/dt) \tag{7.130}$$

The term in the left-hand side of Equation 7.130 expresses the change of the number of droplets whose radius belongs to the interval $[R, R+dR]$ during a time period dt; the two terms in the right-hand side represent the number of the incoming and outgoing droplets in the size interval $[R, R+dR]$ during time period dt. Dividing both sides of Equation 7.130 by (dR/dt), we obtain the so-called continuity equation in the space of sizes [212–216]:

$$\frac{\partial f}{\partial t} + \frac{\partial j}{\partial R} = 0 \qquad (7.131)$$

One more equation is needed to determine c_m. In a closed system this can be the total mass balance of component 1:

$$\frac{d}{dt}\left[c_m(t) + \frac{4\pi}{3}\int_0^\infty dR \; R^3 f(R,t) \right] = 0 \qquad (7.132)$$

The first and the second terms in the brackets express the amount of component 1 contained in the continuous phase and in the droplets, respectively. This expression is appropriate for diluted emulsions when c_m is not negligible compared to the integral in the brackets.

Alternatively, in opened systems and in concentrated emulsions we can use a mean field approximation based on Equation 7.129 to obtain the following equation for c_m:

$$c_m(t) = c_\infty\left[1 + \frac{b}{R_m(t)} \right], \quad R_m(t) \equiv \frac{\int_{R_0}^\infty dR \; R f(R,t)}{\int_{R_0}^\infty dR f(R,t)} \qquad (7.133)$$

where R_0 is a lower limit of the experimental distribution, typically $R_0 \approx 1 \; \mu m$ as smaller droplets cannot be observed optically. The estimates show that the neglecting of the integrals over the interval $0 < R < R_0$ in Equation 7.133 does not affect significantly the value of R_m. We see that Equation 7.133 treats each emulsion droplet as being surrounded by droplets of average radius R_m, which provide a medium concentration c_m in accordance with the Gibbs–Thomson equation, Equation 7.129. From Equations 7.128 through 7.131, and 7.133 we can derive a simple expression for the flux j:

$$j(R,t) = Q\left(\frac{1}{R R_m} - \frac{1}{R^2} \right) f(R,t), \quad Q \equiv D b c_\infty V_1 \qquad (7.134)$$

In calculations, we use the set of Equations 7.128, 7.131, and 7.132 or 7.133 to determine the distribution $f(R,t)$ at known distribution $f(R,0)$ at the initial moment $t=0$. In other words, the theory predicts the evolution of the system at given initial state. From a computational viewpoint it is convenient to calculate $f(R,t)$ in a finite interval $R_0 \leq R < R_{max}$ (see Figure 7.15). The problem can be solved numerically by discretization: the interval $R_0 \leq R < R_{max}$ is subdivided into small portions of length δ, the integrals are transformed into sums and the problem is reduced to solving a linear set of equations for the unknown functions $f_k(t) \equiv f(R_k, t)$, where $R_k = R_0 + k\delta$, $k = 1, 2, \ldots$.
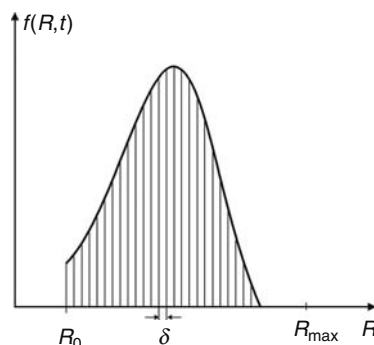
FIGURE 7.15 Sketch of the droplet size distribution function, $f(R,t)$ versus the droplet radius R at a given moment t. δ is the length of the mesh used when solving the problem by discretization.

In practice, the emulsions are formed in the presence of surfactants. At concentrations above the CMC the swollen micelles can serve as carriers of oil between the emulsion droplets of different size. In other words, surfactant micelles can play the role of mediators of the Ostwald ripening. Micelle-mediated Ostwald ripening has been observed in solutions of nonionic surfactants [217–219]. In contrast, it was found that the micelles do not mediate the Ostwald ripening in undecane-in-water emulsions at the presence of an ionic surfactant (SDS) [220]. It seems that the surface charge due to the adsorption of ionic surfactant (and the resulting double layer repulsion) prevents the contact of micelles with the oil drops, which is a necessary condition for micelle-mediated Ostwald ripening.

7.3.2 THIN LIQUID FILMS AND PBs

7.3.2.1 Membrane and Detailed Models of a Thin Liquid Film

Thin liquid films can be formed between two colliding emulsion droplets or between the bubbles in foam. Formation of thin films accompanies the particle–particle and particle–wall interactions in colloids. From a mathematical viewpoint a film is thin when its thickness is much smaller than its lateral dimension. From a physical viewpoint a liquid film formed between two macroscopic phases is thin when the energy of interaction between the two phases across the film is not negligible. The specific forces causing the interactions in a thin liquid film are called surface forces. Repulsive surface forces stabilize thin films and dispersions, whereas attractive surface forces cause film rupture and coagulation. This section is devoted to the macroscopic (hydrostatic and thermodynamic) theory of thin films, while the molecular theory of surface forces is reviewed in Section 7.4.

In Figure 7.16 a sketch of plane-parallel liquid film of thickness h is presented. The liquid in the film contacts with the bulk liquid in the PB. The film is symmetrical, i.e., it is formed between two identical fluid particles (drops, bubbles) of internal pressure P_0. The more complex case of nonsymmetrical and curved films is reviewed elsewhere [221–223].

Two different, but supplementary, approaches (models) are used in the macroscopic description of a thin liquid film. The first of them, the membrane approach, treats the film as a membrane of zero thickness and one tension, γ, acting tangentially to the membrane (see the right-hand side of Figure 7.16). In the detailed approach, the film is modeled as a homogeneous liquid layer of thickness h and surface tension σ^f. The pressure P_0 in the fluid particles is larger than the pressure, P_1, of the liquid in the PB. The difference

$$P_c = P_0 - P_1 \tag{7.135}$$

represents the capillary pressure of the liquid meniscus. By making the balance of the forces acting on a plate of unit width along the y-axis and height h placed normally to the film at $-h/2 < z < h/2$ (Figure 7.16), we derive the Rusanov [224] equation:

$$\gamma = 2\sigma^f + P_c h \tag{7.136}$$

Equation 7.136 expresses a condition for equivalence between the membrane and detailed models with respect to the lateral force. To derive the normal force balance we consider a parcel of unit area from the film surface in the detailed approach. Because the pressure in the outer phase P_0 is larger than the pressure inside the liquid, P_1, the mechanical equilibrium at the film surface is ensured by the action of an additional disjoining pressure, $\Pi(h)$ representing the surface force per unit area of the film surfaces [225]

$$\Pi(h) = P_0 - P_1 = P_c \tag{7.137}$$
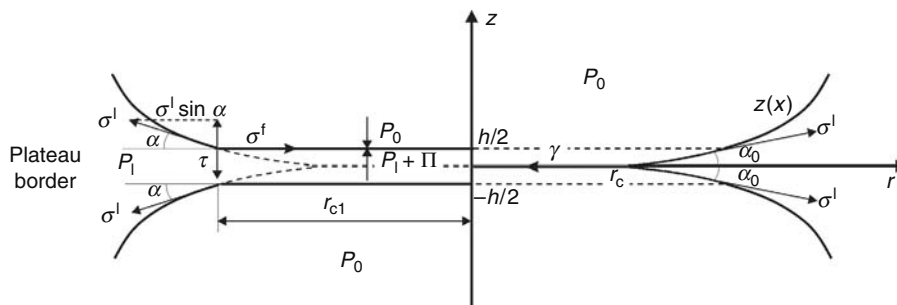
FIGURE 7.16 The detailed and membrane models of a thin liquid film (on the left- and right-hand side, respectively).
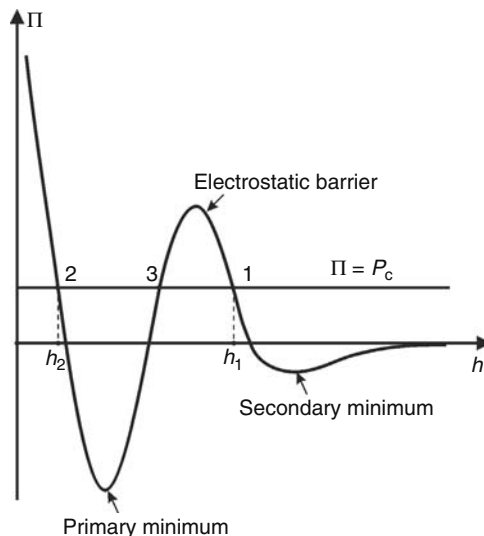
FIGURE 7.17 Sketch of a disjoining pressure isotherm of the DLVO type, Π versus h. The intersection points of the $\Pi(h)$-isotherm with the line $\Pi = P_c$ correspond to equilibrium films.

(see Figure 7.16). Note that Equation 7.137 is satisfied only at equilibrium; at nonequilibrium conditions the viscous force can also contribute to the force balance per unit film area. In general, the disjoining pressure, Π, depends on the film thickness, h. A typical $\Pi(h)$-isotherm is depicted in Figure 7.17 (for details see Section 7.4). We see that the equilibrium condition, $\Pi = P_c$, can be satisfied at three points shown in Figure 7.17. Point 1 corresponds to a film, which is stabilized by the double layer repulsion; sometimes such a film is called the primary film or common black film. Point 3 corresponds to unstable equilibrium and cannot be observed experimentally. Point 2 corresponds to a very thin film, which is stabilized by the short-range repulsion; such a film is called the secondary film or Newton black film. Transitions from common to Newton black films are often observed with foam films [226–229]. Note that $\Pi > 0$ means repulsion between the film surfaces, whereas $\Pi < 0$ corresponds to attraction.

7.3.2.2 Thermodynamics of Thin Liquid Films

In the framework of the membrane approach the film can be treated as a single surface phase, whose Gibbs–Duhem equation reads [221,230]:

$$d\gamma = -s^f dT - \sum_{i=1}^{k} \Gamma_i d\mu_i \tag{7.138}$$

where
  γ is the film tension
  T is the temperature
  s^f is the excess entropy per unit area of the film
  Γ_i and μ_i are the adsorption and the chemical potential of the ith component

The Gibbs–Duhem equations of the liquid phase (l) and the outer phase (o) read

$$dP_\chi = s_v^\chi dT + \sum_{i=1}^{k} n_i^\chi d\mu_i, \quad \chi = l, o \tag{7.139}$$

where
  s_v^χ and n_i^χ are the entropy and the number of molecules per unit volume
  P_χ is the pressure ($\chi = l, o$)

The combination of Equations 7.135 and 7.139 provides an expression for dP_c. Let us multiply this expression by h and to subtract the result from the Gibbs–Duhem equation of the film, Equation 7.138. The result reads

$$d\gamma = -\tilde{s}dT + hdP_c - \sum_{i=1}^{k} \tilde{\Gamma}_i d\mu_i \qquad (7.140)$$

where

$$\tilde{s} = s^f + (s_v^o - s_v^l)h, \quad \tilde{\Gamma}_i = \Gamma_i + (n_i^o - n_i^l)h, \quad i = 1, \ldots, k \qquad (7.141)$$

An alternative derivation of the same equations is possible [231,232]. Imagine two equidistant planes separated at a distance h. The volume confined between the two planes is thought to be filled with the bulk liquid phase (l). Taking surface excesses with respect to the bulk phases we can derive Equations 7.140 and 7.141 with $\tilde{s}$ and $\tilde{\Gamma}_i$ being the excess surface entropy and adsorption ascribed to the surfaces of this liquid layer [231,232]. A comparison between Equations 7.140 and 7.138 shows that there is one additional differential in Equation 7.140. It corresponds to one supplementary degree of freedom connected with the choice of the parameter h. To specify the model, we need an additional equation to determine h. For example, let this equation be

$$\tilde{\Gamma}_1 = 0 \qquad (7.142)$$

Equation 7.142 requires h to be the thickness of a liquid layer from phase (l), containing the same amount of component 1 as the real film. This thickness is called the thermodynamic thickness of the film [232]. It can be on the order of the real film thickness if component 1 is chosen in an appropriate way, say the solvent in the film phase.

From Equations 7.137, 7.140, and 7.142, we obtain [231]

$$d\gamma = -\tilde{s}dT + hd\Pi - \sum_{i=2}^{k} \tilde{\Gamma}_i d\mu_i \qquad (7.143)$$

A corollary of Equation 7.143 is the Frumkin [233] equation

$$\left(\frac{\partial \gamma}{\partial \Pi}\right)_{T,\mu_2,\ldots,\mu_k} = h \qquad (7.144)$$

Equation 7.144 predicts a rather weak dependence of the film tension γ on the disjoining pressure, Π, for equilibrium thin films (small h). By means of Equations 7.136 and 7.137, Equation 7.143 can be transformed to read [232]

$$2d\sigma^f = -\tilde{s}dT - \Pi dh - \sum_{i=2}^{k} \tilde{\Gamma}_i d\mu_i \qquad (7.145)$$

From Equation 7.145, we can derive the following useful relations [231]

$$2\left(\frac{\partial \sigma^f}{\partial h}\right)_{T,\mu_2,\ldots,\mu_k} = -\Pi \qquad (7.146)$$

$$\sigma^f(h) = \sigma^l + \frac{1}{2}\int_h^{\infty} \Pi(h)dh \qquad (7.147)$$

with σ^l being the surface tension of the bulk liquid. Equation 7.147 allows calculation of the film surface tension when the disjoining pressure isotherm is known.

Note that the above thermodynamic equations are, in fact, corollaries from the Gibbs–Duhem equation of the membrane approach Equation 7.138. There is an equivalent and complementary approach, which treats the two film surfaces as separate surface phases with their own fundamental equations [224,234,235]; thus for a flat symmetric film we postulate

$$dU^f = TdS^f + 2\sigma^f dA + \sum_{i=1}^{k} \mu_i dN_i^f - \Pi A dh \qquad (7.148)$$

where
A is the area
U^f, S^f, and N_i^f are the excess internal energy, entropy, and number of molecules ascribed to the film surfaces

Compared with the fundamental equation of a simple surface phase [5], Equation 7.148 contains an additional term, $\Pi A dh$, which takes into account the dependence of the film surface energy on the film thickness. Equation 7.148 provides an alternative thermodynamic definition of disjoining pressure:

$$\Pi = -\frac{1}{A}\left(\frac{\partial U^f}{\partial h}\right) \tag{7.149}$$

7.3.2.3 Transition Zone between Thin Film and PB

7.3.2.3.1 Macroscopic Description
The thin liquid films formed in foams or emulsions exist in a permanent contact with the bulk liquid in the PB, encircling the film. From a macroscopic viewpoint, the boundary between film and PB is treated as a three-phase contact line: the line, at which the two surfaces of the PB (the two concave menisci sketched in Figure 7.16) intersect at the plane of the film (see the right-hand side of Figure 7.16). The angle, α_0, subtended between the two meniscus surfaces, represents the thin film contact angle. The force balance at each point of the contact line is given by Equation 7.106 with $\sigma_{12} = \gamma$ and $\sigma_{13} = \sigma_{23} = \sigma^l$. The effect of the line tension, κ, can be also taken into account. For example, in the case of symmetrical flat film with circular contact line, like those depicted in Figure 7.16, we can write [235]

$$\gamma + \frac{\kappa}{r_c} = 2\sigma^l \cos \alpha_0 \tag{7.150}$$

where r_c is the radius of the contact line.

There are two film surfaces and two contact lines in the detailed approach (see the left-hand side of Figure 7.16). They can be treated thermodynamically as linear phases and a one-dimensional counterpart of Equation 7.148 can be postulated [235]:

$$dU^L = TdS^L + 2\widetilde{\kappa}dL + \sum_i \mu_i dN_i^L + \tau dh \tag{7.151}$$

where U^L, S^L, and N_i^L are linear excesses, $\widetilde{\kappa}$ is the line tension in the detailed approach and

$$\tau = \frac{1}{L}\left(\frac{\partial U^L}{\partial h}\right) \tag{7.152}$$

is a one-dimensional counterpart of the disjoining pressure (see Equation 7.149). The quantity τ, called the transversal tension, takes into account the interaction between the two contact lines. The general force balance at each point of the contact line can be presented in the form of the following vectorial sum [221]

$$\sigma_i^f + \sigma_i^l + \sigma_i^\kappa + \tau_i = 0, \quad i = 1, 2 \tag{7.153}$$

The vectors taking part in Equation 7.153 are depicted in Figure 7.18, where $|s_i^\kappa| = \widetilde{\kappa}_i/r_{ci}$. For the case of a flat symmetric film (Figure 7.16) the tangential and normal projections of Equation 7.153, with respect to the plane of the film, read:

$$\sigma^f + \frac{\widetilde{\kappa}}{r_{c1}} = \sigma^l \cos \alpha \tag{7.154}$$

$$\tau = \sigma^l \sin \alpha \tag{7.155}$$

Note that in general $\alpha \neq \alpha_0$ (see Figure 7.16). Besides, both α_0 and α can depend on the radius of the contact line due to line tension effects. In the case of straight contact line from Equations 7.147 and 7.154, we derive [232]

$$\cos \alpha|_{r_{c1}=\infty} = \frac{\sigma^f}{\sigma^l} = 1 + \frac{1}{2\sigma^l}\int_h^\infty \Pi(h)dh \tag{7.156}$$
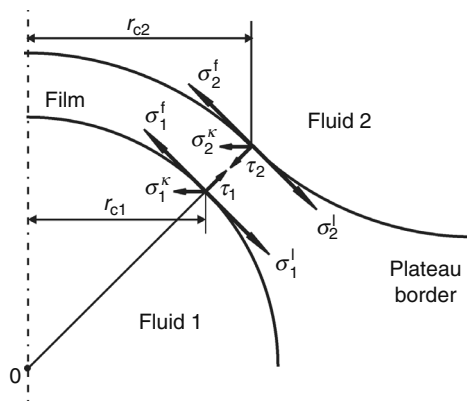
FIGURE 7.18 The force balance in each point of the two contact lines representing the boundary between a spherical film and the PB (see Equation 7.153).

Because $\cos\alpha \leq 1$, the surface tension of the film must be less than the bulk solution surface tension, $\sigma^f < \sigma^l$, and the integral term in Equation 7.156 must be negative in order for a nonzero contact angle to be formed. Hence, the contact angle, α, and the transversal tension, τ (see Equation 7.155), are integral effects of the long-range attractive surface forces acting in the transition zone between the film and PB, where $h > h_1$ (see Figure 7.17).

In the case of a fluid particle attached to a surface (Figure 7.19) the integral of the pressure $P_l = P_0 - \Delta\rho gz$ over the particle surface equals the buoyancy force, F_b, which at equilibrium is counterbalanced by the disjoining-pressure and transversal-tension forces [221,236]:

$$2\pi r_{c1}\tau = F_b + \pi r_{c1}^2 \Pi \tag{7.157}$$

F_b is negligible for bubbles of diameter smaller than ca. 300 μm. Then the forces due to τ and Π counterbalance each other. Hence, at equilibrium the role of the repulsive disjoining pressure is to keep the film thickness uniform, whereas the role of the attractive transversal tension is to keep the bubble (droplet) attached to the surface. In other words, the particle sticks to the surface at its contact line where the long-range attraction prevails (see Figure 7.17), whereas the repulsion predominates inside the film, where $\Pi = P_c > 0$. Note that this conclusion is valid not only for particle–wall attachment, but also for particle–particle interaction. For zero contact angle τ is also zero (Equation 7.155) and the particle will rebound from the surface (the other particle), unless some additional external force keeps it attached.

7.3.2.3.2 Micromechanical Description
From a microscopic viewpoint, the transition between the film surface and the meniscus is smooth, as depicted in Figure 7.20. As the film thickness increases across the transition zone, the disjoining pressure decreases and tends to zero at the PB (see Figures 7.17 and 7.20). Respectively, the surface tension varies from σ^f for the film to σ^l for the PB [237,238]. By using local
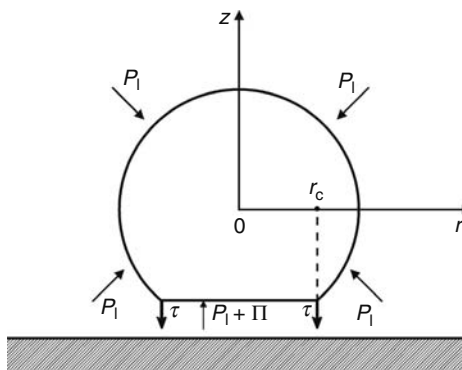
FIGURE 7.19 Sketch of the forces exerted on a fluid particle (bubble, drop, vesicle) attached to a solid surface: Π is disjoining pressure, τ is transversal tension, P_l is the pressure in the outer liquid phase.
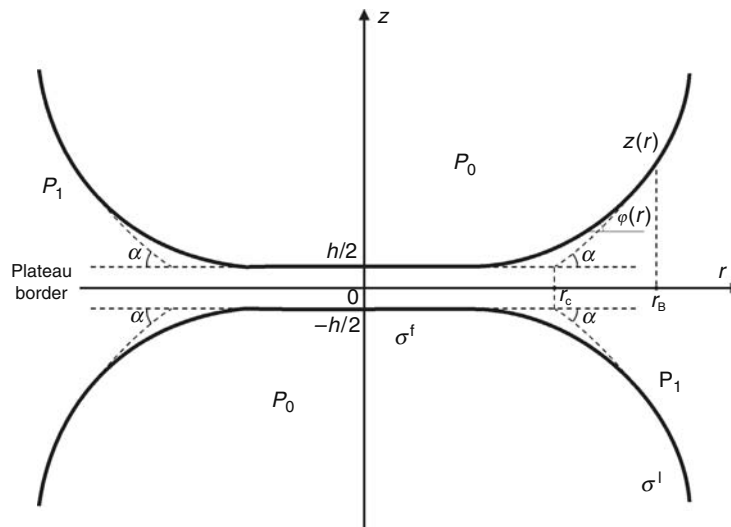
FIGURE 7.20 Liquid film between two attached fluid particles (bubbles, drops, vesicles). The solid lines represent the actual interfaces, whereas the dashed lines show the extrapolated interfaces in the transition zone between the film and the PB.

force balance considerations, we can derive the equations governing the shape of the meniscus in the transition zone; in the case of axial symmetry (depicted in Figure 7.20), these equations read [238]:

$$\frac{d}{dr}(\sigma \sin \varphi) + \frac{1}{r}\sigma(r) \sin \varphi(r) = P_c - \Pi(h(r)) \tag{7.158}$$

$$-\frac{d}{dz}(\sigma \cos \varphi) + \frac{1}{r}\sigma(r) \sin \varphi(r) = P_c, \quad \tan \varphi(r) = \frac{dz}{dr} \tag{7.159}$$

where $\varphi(r)$ and $h(r) = 2z(r)$ are the running meniscus slope angle and thickness of the gap. Equations 7.158 and 7.159 allow calculation of the three unknown functions, $z(r)$, $\varphi(r)$ and $\sigma(r)$, provided that the disjoining pressure, $\Pi(h)$, is known from the microscopic theory. By eliminating P_c between Equations 7.158 and 7.159 we can derive [238]

$$\frac{d\sigma}{dz} = -\Pi(h(r)) \cos \varphi(r) \tag{7.160}$$

This result shows that the hydrostatic equilibrium in the transition region is ensured by simultaneous variation of σ and Π. Equation 7.160 represents a generalization of Equation 7.146 for a film of uneven thickness and axial symmetry. Generalization of Equations 7.158 through 7.160 for the case of more complicated geometry is also available [221,222].

For the PB we have $z \gg h$, $\Pi \to 0$, $\sigma \to \sigma^l$ = constant, and both Equations 7.158 and 7.159 reduce to Equation 7.109 with $\Delta P = P_c$. The macroscopic contact angle, α, is defined as the angle at which the extrapolated meniscus, obeying Equation 7.109, meets the extrapolated film surface (see the dashed line in Figure 7.20). The real surface, shown by solid line in Figure 7.20, differs from this extrapolated (idealized) profile, because of the interactions between the two film surfaces, which is taken into account in Equation 7.158, but not in Equation 7.109. To compensate for the difference between the real and idealized system, the line and transversal tensions are ascribed to the contact line in the macroscopic approach. In particular, the line tension makes up for the differences in surface tension and running slope angle [238]:

$$\frac{\widetilde{\kappa}}{r_c} = \int_0^{r_B} \left[\left(\frac{\sigma \sin^2 \varphi}{r \cos \varphi}\right)^{real} - \left(\frac{\sigma \sin^2 \varphi}{r \cos \varphi}\right)^{idealized} \right] dr \tag{7.161}$$

whereas τ compensates for the differences in surface forces (disjoining pressure):

$$\tau = \frac{1}{r_c} \int_0^{r_B} [(\Pi)^{id} - \Pi(r)] r \, dr \tag{7.162}$$

where

$$(\Pi)^{id} = P_c \quad \text{For} \quad 0 < r < r_c$$

$$(\Pi)^{id} = 0 \quad \text{For} \quad r > r_c$$

The superscripts real and idealized in Equation 7.161 mean that the quantities in the respective parentheses must be calculated for the real and idealized meniscus profiles; the latter coincide for $r > r_B$ (Figure 7.20). Results for $\widetilde{\kappa}$ and τ calculated by means of Equations 7.161 and 7.162 can be found in Ref. [239].

In conclusion, it should be noted that the width of the transition region between a thin liquid film and PB is usually very small [237]—below 1 μm. That is why the optical measurements of the meniscus profile give information about the thickness of the PB in the region $r > r_B$ (Figure 7.20). Then if the data are processed by means of the Laplace equation (Equation 7.109), we determine the contact angle, α, as discussed above. In spite of being a purely macroscopic quantity, α characterizes the magnitude of the surface forces inside the thin liquid film, as implied by Equation 7.156. This has been pointed out by Derjaguin [240] and Princen and Mason [241].

7.3.2.4 Methods for Measuring Thin Film Contact Angles

Prins [242] and Clint et al. [243] developed a method of contact angle measurement for macroscopic flat foam films formed in a glass frame in contact with a bulk liquid. They measured the jump in the force exerted on the film at the moment, when the contact angle is formed. Similar experimental setup was used by Yamanaka [244] for measurement of the velocity of motion of the three-phase contact line.

An alternative method, which can be used in both equilibrium and dynamic measurements with vertical macroscopic films, was developed by Princen and Frankel [245,246]. They determined the contact angle from the data for diffraction of a laser beam refracted by the PB.

In the case of microscopic films, especially appropriate are the interferometric methods: light beams reflected or refracted from the liquid meniscus interfere and create fringes, which in turn give information about the shape of the liquid surfaces. The fringes are usually formed in the vicinity of the contact line, which provides a high precision of the extrapolation procedure used to determine the contact angle (see Figure 7.20). We can distinguish several interference techniques depending on how the interference pattern is created. In the usual interferometry the fringes are due to interference of beams reflected from the upper and lower meniscus. This technique can be used for contact angle measurements with foam films [203,247–249], emulsion films [250,251], and adherent biological cells [189]. The method is applicable for not-too-large contact angles ($\alpha < 8°-10°$); for larger meniscus slopes the region of fringes shrinks and the measurements are not possible.

The basic principle of the differential interferometry consists of an artificial splitting of the original image into two equivalent and overlapping images (see Françon [252] or Beyer [253]). Thus interferometric measurements are possible with meniscus surfaces of larger slope. The differential interferometry in transmitted light was used by Zorin et al. [254,255] to determine the contact angles of wetting and free liquid films. This method is applicable when the whole system under investigation is transparent to the light.

Differential interferometry in reflected light allows measurement of the shape of the upper reflecting surface. This method was used by Nikolov et al. [236,256–258] to determine the contact angle, film and line tension of foam films formed at the top of small bubbles floating at the surface of ionic and nonionic surfactant solutions. An alternative method is the holographic interferometry applied by Picard et al. [259,260] to study the properties of bilayer lipid membranes in solution. Film contact angles can be also determined from the Newton rings of liquid lenses, which spontaneously form in films from micellar surfactant solutions [203].

Contact angles can be also determined by measuring several geometrical parameters characterizing the profile of the liquid meniscus and processing them by using the Laplace equation (Equation 7.109) [261,262]. The computer technique allows processing of many experimental points from meniscus profile and automatic digital image analysis.

Contact angles of microscopic particles against another phase boundary can be determined interferometrically, by means of a film trapping technique (FTT) [263,264]. It consists in capturing of micrometer-sized particles, emulsion drops and biological cells in thinning free foam films or wetting films. The interference pattern around the entrapped particles allows us to reconstruct the meniscus shape, to determine the contact angles, and to calculate the particle-to-interface adhesion energy [263,264].

7.3.3 LATERAL CAPILLARY FORCES BETWEEN PARTICLES ATTACHED TO INTERFACES

7.3.3.1 Particle–Particle Interactions

The origin of the lateral capillary forces between particles captive at a fluid interface is the deformation of the interface, which is supposed to be flat in the absence of particles. The larger the interfacial deformation, the stronger the capillary interaction.
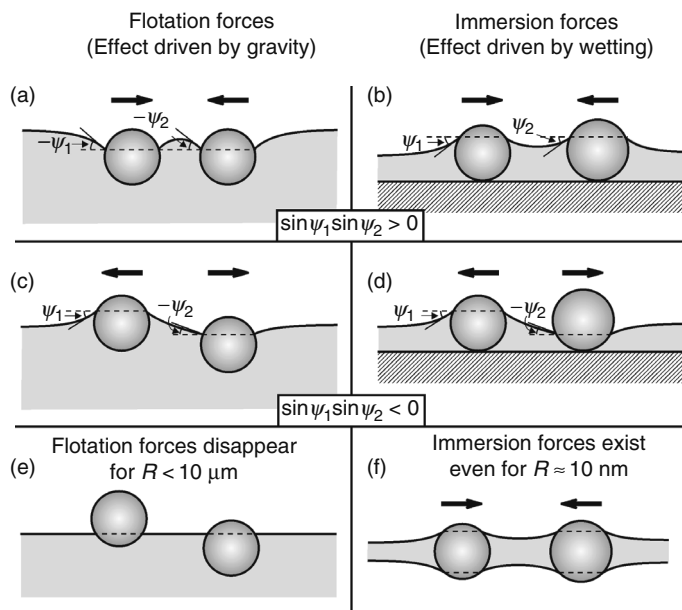
FIGURE 7.21 Flotation (a, c, e) and immersion (b, d, f) lateral capillary forces between two particles attached to fluid interface: (a) and (b) are two similar particles; (c) is a light and a heavy particle; (d) is a hydrophilic and a hydrophobic particle; (e) is small floating particles that do not deform the interface; (f) is small particles captured in a thin liquid film deforming the interfaces due to the wetting effects.

It is known that two similar particles floating on a liquid interface attract each other [265–267] (see Figure 7.21a). This attraction appears because the liquid meniscus deforms in such a way that the gravitational potential energy of the two particles decreases when they approach each other. Hence the origin of this force is the particle weight (including the Archimedes force).

A force of capillary attraction appears also when the particles (instead of being freely floating) are partially immersed in a liquid layer on a substrate [268–270] (see Figure 7.21b). The deformation of the liquid surface in this case is related to the wetting properties of the particle surface, i.e., to the position of the contact line and the magnitude of the contact angle, rather than to gravity.

To distinguish between the capillary forces in the case of floating particles and in the case of partially immersed particles on a substrate, the former are called lateral flotation forces and the latter, lateral immersion forces [267,270]. These two kinds of force exhibit similar dependence on the interparticle separation but very different dependencies on the particle radius and the surface tension of the liquid (see Refs. [35,271] for comprehensive reviews). The flotation and immersion forces can be both attractive (Figure 7.21a and b) and repulsive (Figure 7.21c and d). This is determined by the signs of the meniscus slope angles ψ_1 and ψ_2 at the two contact lines: the capillary force is attractive when $\sin \psi_1 \sin \psi_2 > 0$ and repulsive when $\sin \psi_1 \sin \psi_2 < 0$. In the case of flotation forces $\psi > 0$ for light particles (including bubbles) and $\psi < 0$ for heavy particles. In the case of immersion forces between particles protruding from an aqueous layer $\psi > 0$ for hydrophilic particles and $\psi < 0$ for hydrophobic particles. When $\psi = 0$ there is no meniscus deformation and, hence, there is no capillary interaction between the particles. This can happen when the weight of the particles is too small to create significant surface deformation (Figure 7.21e).

The immersion force appears not only between particles in wetting films (Figure 7.21b and d), but also in symmetric fluid films (Figure 7.21f). The theory provides the following asymptotic expression for calculating the lateral capillary force between two particles of radii R_1 and R_2 separated by a center-to-center distance L [35,266–271]:

$$F = 2\pi\sigma Q_1 Q_2 q K_1(qL)[1 + O(q^2 R_k^2)] \; r_k \ll L \qquad (7.163)$$

where

σ is the liquid–fluid interfacial tension
r_1 and r_2 are the radii of the two contact lines
$Q_k = r_k \sin \psi_k$ $(k = 1, 2)$ is the capillary charge of the particle [267,270]

In addition

$$q^2 = \Delta\rho g/\sigma \quad \text{(in thick film)}$$
$$q^2 = (\Delta\rho q - \Pi')/\sigma \quad \text{(in thin films)} \qquad (7.164)$$

where
    $\Delta\rho$ is the difference between the mass densities of the two fluids
    Π' is the derivative of the disjoining pressure with respect to the film thickness
    $K_1(x)$ is the modified Bessel function of the first order

The asymptotic form of Equation 7.163 for $qL \ll 1$ ($q^{-1} = 2.7$ mm for water),

$$F = 2\pi\sigma Q_1 Q_2 / L \quad r_k \ll L \ll q^{-1} \tag{7.165}$$

looks like a two-dimensional analog of Coulomb's law, which explains the name capillary charge of Q_1 and Q_2. Note that the immersion and flotation forces exhibit the same functional dependence on the interparticle distance, see Equations 7.163 and 7.165. On the other hand, their different physical origin results in different magnitudes of the capillary charges of these two kinds of capillary force. In this aspect they resemble the electrostatic and gravitational forces, which obey the same power law, but differ in the physical meaning and magnitude of the force constants (charges, masses). In the special case when $R_1 = R_2 = R$ and $r_k \ll L \ll q^{-1}$, we can derive [270,271]

$$F \propto (R^6/\sigma) K_1(qL) \quad \text{for flotation force}$$
$$F \propto \sigma R^2 K_1(qL) \quad \text{for immersion force} \tag{7.166}$$

Hence, the flotation force decreases, while the immersion force increases, when the interfacial tension σ increases. Besides, the flotation force decreases much more strongly with the decrease of R than the immersion force. Thus $F_{\text{flotation}}$ is negligible for $R < 10$ μm, whereas $F_{\text{immersion}}$ can be significant even when $R = 10$ nm. This is demonstrated in Figure 7.22 where the two types of capillary interaction are compared for a wide range of particle sizes. The values of the parameters used are: particle mass density $\rho_p = 1.05$ g cm^{-3}, surface tension $\sigma = 72$ mN m^{-1}, contact angle $\alpha = 30°$, interparticle distance $L = 2R$, and thickness of the nondisturbed planar film $l_0 = R$. The drastic difference in the magnitudes of the two types of capillary forces is due to the different deformation of the water–air interface. The small floating particles are too light to create substantial deformation of the liquid surface, and the lateral capillary forces are negligible (Figure 7.21e). In the case of immersion forces the particles are restricted in the vertical direction by the solid substrate. Therefore, as the film becomes thinner, the liquid surface deformation increases, thus giving rise to a strong interparticle attraction.

As seen in Figure 7.22, the immersion force can be significant between particles whose radii are larger than few nanometers. It has been found to promote the growth of two-dimensional crystals from colloid particles [272–275], viruses and globular proteins [276–282]. Such two-dimensional crystals have found various applications: for nanolithography [283], microcontact printing [284], as nanostructured materials in photoelectrochemical cells [285], for photocatalitic films [286], photo- and electroluminescent semiconductor materials [287], as samples for electron microscopy of proteins and viruses [288], as immunosensors [289], etc. (for reviews see Refs. [35,290]).

In the case of interactions between inclusions in lipid bilayers (Figure 7.23) the elasticity of the bilayer interior must also be taken into account. The calculated energy of capillary interaction between integral membrane proteins turns out to be of the order of several kT [192]. Hence, this interaction can be a possible explanation of the observed aggregation of membrane proteins [192,291–293]. The lateral capillary forces have been calculated also for the case of particles captured in a spherical (rather than planar) thin liquid film or vesicle [294].
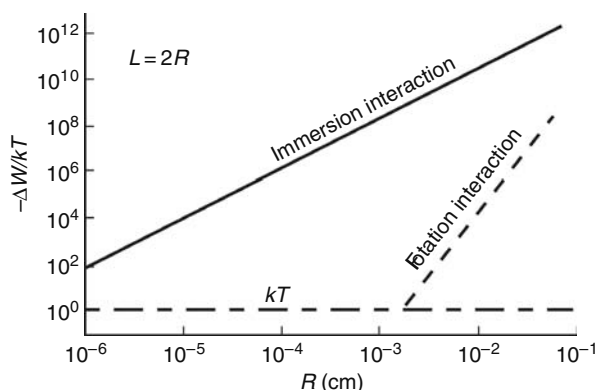
FIGURE 7.22 Plot of the capillary interaction energy in kT units, $\Delta W/kT$, versus the radius, R, of two similar particles separated at a center-to-center distance $L = 2R$.

(a)   (b)
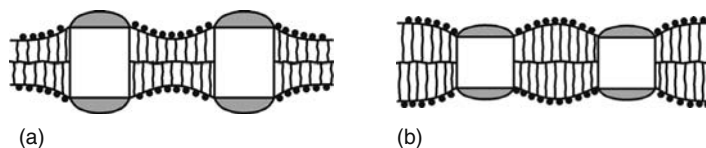
FIGURE 7.23 Inclusions (say, membrane proteins) in a lipid bilayer: the thickness of the inclusion can be greater (a) or smaller (b) than the thickness of the (nondisturbed) lipid bilayer. In both cases, the overlap of the deformations around the inclusions leads to an attraction between them [35,192].

Lateral capillary forces between vertical cylinders or between spherical particles have been measured by means of sensitive electromechanical balance [295], piezotransduser balance [296] and torsion microbalance [297]. Good agreement between theory and experiment has been established [296,297].

As already mentioned, the weight of micrometer-sized and submicrometer floating particles is not sufficient to deform the fluid interface and to bring about capillary force between the particles (Figure 7.21e). However, the situation changes if the contact line at the particle surface has undulated or irregular shape (Figure 7.24a). This may happen when the particle surface is rough, angular or heterogeneous. In such cases, the contact line sticks to an edge or to the boundary between two domains of the heterogeneous surface. The undulated contact line induces undulations in the surrounding fluid interface [290,298–301]. Let $z = \zeta(x, y)$ be the equation describing the interfacial shape around such isolated particle. Using polar coordinates (r, φ) in the xy-plane, we can express the interfacial shape as a Fourier expansion:

$$\zeta(r,\varphi) = \sum_{m=1}^{\infty} r^{-m}(A_m \cos m\varphi + B_m \sin m\varphi) \qquad (7.167)$$

where
  r is the distance from the particle centre
  A_m and B_m are the coefficients

In analogy with electrostatics, Equation 7.167 can be interpreted as a multipole expansion: the terms with $m = 1, 2, 3, \ldots$, play the role of capillary dipoles, quadrupoles, hexapoles, etc. [290,299–301]. The term with $m = 0$ (capillary charge) is missing because there is no axisymmetric contribution to the deformation (negligible particle weight). Moreover, the dipolar term with $m = 1$ is also absent because it is annihilated by a spontaneous rotation of the floating particle around a horizontal axis [299]. Therefore, the leading term becomes the quadrupolar one, with $m = 2$. The interaction between capillary quadrupoles has been investigated theoretically [299–301]. This interaction is nonmonotonic: attractive at long distances, but repulsive at short distances. Expressions for the rheological properties (surface dilatational and shear elasticity and yield stress) of Langmuir monolayers from angular particles have been derived [35,300,301]. Mesoscale capillary multipoles have been experimentally realized by Bowden et al. [302,303] by appropriate hydrophobization or hydrophilization of the sides of floating plates. Interactions between capillary quadrupoles have been observed between floating particles, which have the shape of curved disks [304] and ellipsoids [305].

At last, let us consider another type of capillary interactions—between particles surrounded by finite menisci. Such interactions appear when μm-sized or submicrometer particles are captured in a liquid film of much smaller thickness (Figure 7.24b) [306–309]. If such particles are approaching each other, the interaction begins when the menisci around the two particles overlap, $L < 2r_\text{p}$ in Figure 7.24b. The capillary force in this case is nonmonotonic: initially the attractive force

(a)   (b)
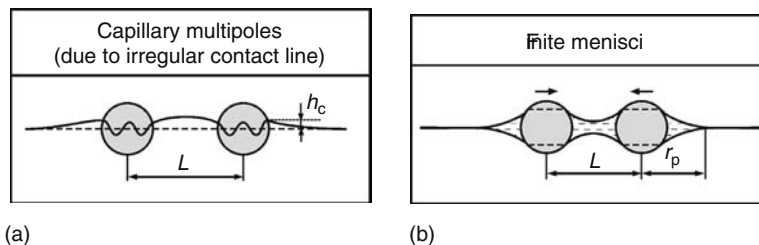
FIGURE 7.24 Special types of immersion capillary forces: (a) The contact line attachment to an irregular edge on the particle surface produces undulations in the surrounding fluid interface, which give rise to lateral capillary force between the particles. (b) When the size of particles, entrapped in a liquid film, is much greater than the nonperturbed film thickness, the meniscus surfaces meet at a finite distance, r_p; in this case, the capillary interaction begins at $L \leq 2r_\text{p}$.

increases with the increase of interparticle distance, then it reaches a maximum and further decays [309]. In addition, there are hysteresis effects: the force is different on approach and separation at distances around $L = 2r_p$ [309].

7.3.3.2 Particle–Wall Interactions

The overlap of the meniscus around a floating particle with the meniscus on a vertical wall gives rise to a particle–wall interaction, which can be both repulsive and attractive. An example for a controlled meniscus on the wall is shown in Figure 7.25, where the wall is a hydrophobic Teflon barrier whose position along the vertical can be precisely varied and adjusted.

Two types of boundary conditions at the wall are analyzed theoretically [35,310]: fixed contact line (Figure 7.25) or, alternatively, fixed contact angle. In particular, the lateral capillary force exerted on the particle depicted in Figure 7.25 is given by the following asymptotic expression [35,310]:

$$F = -\pi\sigma q[2Q_2 He^{-qx} + r_2 He^{-qx} - 2Q_2^2 K_1(qx)] \tag{7.168}$$

where

Q_2 and r_2 are the particle capillary charge and contact line radius

H characterizes the position of the contact line on the wall with respect to the nondisturbed horizontal liquid surface (Figure 7.25)

x is the particle–wall distance

q is defined by Equation 7.164 (thick films)

The first term in the right-hand side of Equation 7.168 expresses the gravity force pushing the particle to slide down over the inclined meniscus on the wall; the second term originates from the pressure difference across the meniscus on the wall; the third term expresses the so-called capillary image force, that is the particle is repelled by its mirror image with respect to the wall surface [35,310].

Static [311] and dynamic [312] measurements with particles near walls have been carried out. In the static measurements the equilibrium distance of the particle from the wall (the distance at which $F = 0$) has been measured and a good agreement with the theory has been established [311].

In the dynamic experiments [312] knowing the capillary force F (from Equation 7.168), and measuring the particle velocity, $\dot{x}$, we can determine the drag force, F_d:

$$F_d = m\ddot{x} - F, \quad F_d \equiv 6\pi\eta R_2 f_d \dot{x} \tag{7.169}$$

where

R_2, m and $\ddot{x}$ are the particle radius, mass, and acceleration

η is the viscosity of the liquid

f_d is the drag coefficient
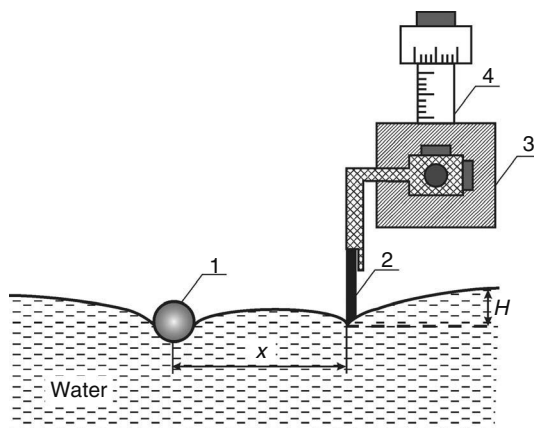
FIGURE 7.25 Experimental setup for studying the capillary interaction between a floating particle (1) and a vertical hydrophobic plate (2) separated at a distance, x. The edge of the plate is at a distance, H, lower than the level of the horizontal liquid surface far from the plate; (3) and (4) are micrometric table and screw [311,312].

If the particle were in the bulk liquid, f_d would be equal to 1 and F_d would be given by the Stokes formula. In general, f_d differs from unity because the particle is attached to the interface. The experiment [312] gives f_d varying between 0.68 and 0.54 for particle contact angle varying from 49° to 82°; the data are in good quantitative agreement with the hydrodynamic theory of the drag coefficient [313]. In other words, the less the depth of particle immersion, the less the drag coefficient, as could be expected. However, if the floating particle is heavy enough, it deforms the surrounding liquid surface; the deformation travels together with the particle, thus increasing f_d several times [312]. The addition of surfactant strongly increases f_d. The latter effect can be used to measure the surface viscosity of adsorption monolayers from low molecular weight surfactants [314], which is not accessible to the standard methods for measurement of surface viscosity.

In the case of protein adsorption layers, the surface elasticity is so strong that the particle (Figure 7.25) is arrested in the adsorption film. Nevertheless, with heavier particles and at larger meniscus slopes, it is possible to break the protein adsorption layer. Based on such experiments, a method for determining surface elasticity and yield stress has been developed [315].

7.3.3.3 Electrically Charged Particles at Liquid Interfaces

7.3.3.3.1 Particle–Interface Interaction

Let us consider a spherical dielectric particle (phase 1), which is immersed in a nonpolar medium (phase 2), near its boundary with a third dielectric medium (phase 3); see the inset in Figure 7.26. The interaction is due to electric charges at the particle surface. The theoretical problem has been solved exactly, in terms of Legendre polynomials, for arbitrary values of the dielectric constants of the three phases, and expressions for calculating the interaction force, F_z, and energy, W, have been derived [316]:

$$F_z = \frac{\beta_{23}Q^2}{4\varepsilon_2(R+s)^2}f_z, \quad W = \int_s^\infty F_z \, ds = \frac{\beta_{23}Q^2}{4\varepsilon_2(R+s)}w \qquad (7.170)$$

where
   R is the particle radius
   s is the distance between the particle surface and the fluid interface (inset in Figure 7.26)
   $Q = 4\pi R^2 \sigma_{pn}$ is the total charge at the boundary particle–nonpolar fluid, where σ_{pn} is the respective surface-charge density
   f_z and w are the dimensionless force and energy coefficients, which, in general, depend on the parameters s/R, β_{12}, and β_{23}, where $\beta_{ij} = (\varepsilon_i - \varepsilon_j)/(\varepsilon_i + \varepsilon_j)$; $i,j = 1,2,3$
   ε_1, ε_2, and ε_3 are the dielectric constants of the respective phases

At long distances, $s/R > 1$, we have $f_z \approx w \approx 1$, and then Equation 7.170 reduces to the expressions for the force and energy of interaction between a point charge Q with the interface between phases 2 and 3. This is the known image charge effect. Expressions that allow us to calculate f_z and w for shorter distances ($s/R < 1$) are derived in Ref. [316].
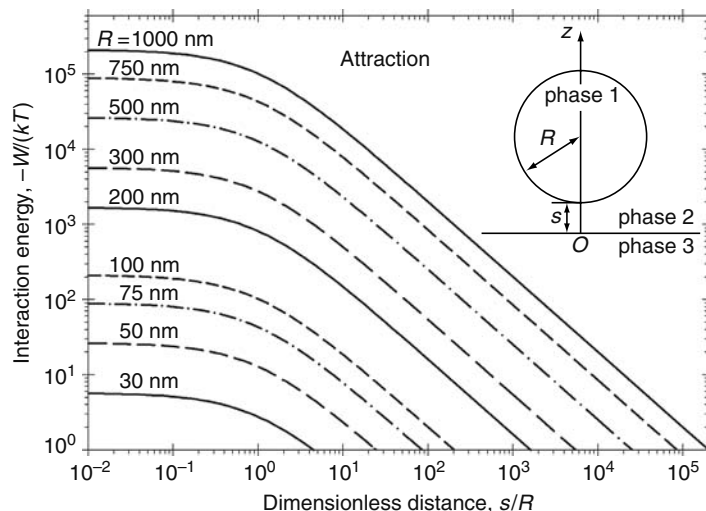
FIGURE 7.26 Plot of the interaction energy W (scaled with kT) versus the dimensionless distance, s/R, between a charged glass particle (phase 1) and a planar interface; phase 2 is tetradecane; phase 3 is water. The curves correspond to different particle radii, R, denoted in the figure.
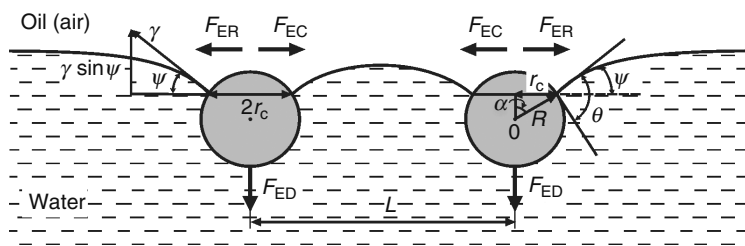
FIGURE 7.27 Sketch of two electrically charged particles attached to an oil–water interface. F_{ED} is the electrodipping force, due to the image-charge effect, that pushes the particles into water and deforms the fluid interface around the particles. F_{ER} is the direct electric repulsion between the two like-charged particles. F_{EC} is the electrocapillary attraction, related to deformations in the fluid interface created by the electric field.

In Figure 7.26, numerical results for the particle–interface interaction energy, W, scaled by the thermal energy kT, are plotted versus the relative distance, s/R, for various values of the particle radius, R. The other parameter values correspond to the following choice of the phases: phase 1 (the particle) is glass, phase 2 is tetradecane and phase 3 is water. The curves in Figure 7.26 describe a strong and long-range attraction between the particle and the interface. The interaction energy, W, becomes comparable, or smaller than the thermal energy kT for particle radius $R < 30$ nm. On the other hand, for $R > 30$ nm W strongly increases with the particle size (in Equation 7.170, $Q^2 \sim R^4$ at fixed surface charge density, σ_{pn}), and reaches $W \approx 10^5$ kT for $R = 1$ μm at close contact. In addition, the range of the interaction also strongly increases, reaching $s/R \approx 10^5$ for $R = 1$ μm. In general, this is a strong and long-range interaction [316]. For example, water drops could attract charged hydrophobic particles dispersed in the oily phase, which would favor the formation of reverse particle-stabilized emulsions.

7.3.3.3.2 Forces of Electric Origin between Particles at a Liquid Interface
Figure 7.27 shows two particles attached to the interface between water and a nonpolar fluid (oil, air). In general, the particles experience three forces of electric origin: F_{ED}, electrodipping force [317]; F_{ER}, direct electric repulsion between the two particles across the oil [318]; and F_{EC}, electric-field-induced capillary attraction [319], which is termed electrocapillary force, E_{CF}, for brevity. F_{ED} is normal to the oil–water interface and is directed toward the water phase. Physically, F_{ED} is a result of the electrostatic image-charge effect; see the previous section. F_{ED} is acting on each individual particle, while F_{ER} and F_{EC} are interaction forces between two (or more) particles. The presence of electric field leads to deformations in the fluid interface around the particles, which lead to the appearance of F_{EC}. The three forces, F_{ED}, F_{ER}, and F_{EC}, are separately considered below.

7.3.3.3.3 Electrodipping Force
At equilibrium, the electrodipping force is counterbalanced by the interfacial tension force: $F_{ED} = 2\pi r_c \gamma \sin \psi$, where γ is the interfacial tension; r_c is the radius of the contact line on the particle surface; and ψ is the meniscus slope angle at the contact line (Figure 7.27) [317,319]. Consequently, F_{ED} can be determined from the experimental values of r_c, γ, and ψ. This approach was used to obtain the values of F_{ED} for silanized glass particles of radii 200–300 μm from photographs of these particles at an oil–water or air–water interface [317]. F_{ED} was found to be much greater than the gravitational force acting on these particles.

As an illustration, Figure 7.28 compares the profiles of the liquid menisci around a noncharged particle and a charged particle. The particles represent hydrophobized glass spheres of density $\rho_p = 2.5$ g cm^{-3}. The oil phase is purified soybean oil
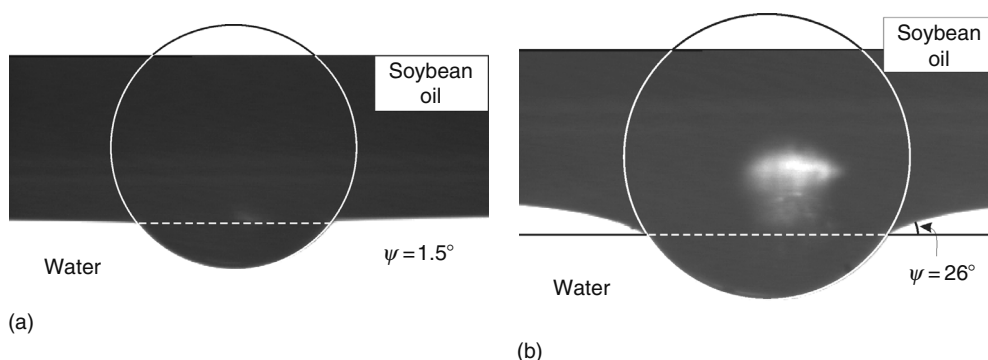
FIGURE 7.28 Side-view photographs of hydrophobized spherical glass particles at the boundary water–soybean oil (no added surfactants). (a) Noncharged particle of radius $R = 235$ μm: the meniscus slope angle due to gravity is relatively small, $\psi = 1.5°$. (b) Charged particle of radius $R = 274$ μm: the experimental meniscus slope angle is $\psi = 26°$ owing to the electrodipping force; if this electric force were missing, the gravitational slope angle would be only $\psi = 1.9°$.

of density $\rho_{oil} = 0.92$ g cm^{-3}. The oil–water interfacial tension is $\gamma = 30.5$ mN m^{-1}. Under these conditions, the calculated surface-tension force, $2\pi r_c \gamma \sin \psi$, which counterbalances the gravitational force (particle weight minus the Archimedes force) corresponds to meniscus slope angle $\psi = 1.5°$, and the deformation of the liquid interface caused by the particle is hardly visible (Figure 7.28a). In contrast, for the charged particle (Figure 7.28b), the meniscus slope angle is much greater, $\psi = 26°$. This is due to the fact that the interfacial-tension force, $2\pi r_c \gamma \sin \psi$, has to counterbalance the electrodipping force, which pushes the particle toward the water phase. Experimentally, it has been found that the angle ψ is insensitive to the concentration of NaCl in the aqueous phase, which means that (in the investigated case) the electrodipping force is due to charges situated at the particle–oil interface [317,320]. With similar particles, the magnitude of F_{ED} at the air–water interface was found to be about six times smaller than at the oil–water interface [317].

Theoretically, the electrodipping force, F_{ED}, can be calculated from the expression [320,321]:

$$F_{ED} = (4\pi/\varepsilon_n)(\sigma_{pn}R)^2(1 - \cos \alpha)f(\theta, \varepsilon_{pn}) \tag{7.171}$$

where
   ε_n is the dielectric constant of the nonpolar fluid (oil, air)
   σ_{pn} is the surface charge density at the boundary particle–nonpolar fluid
   $\varepsilon_{pn} = \varepsilon_p/\varepsilon_n$ is the ratio of the respective two dielectric constants
   α is a central angle, while $\theta = \alpha + \psi$ is the contact angle (see Figure 7.27)

We could accurately calculate the dimensionless function $f(\theta, \varepsilon_{pn})$ by means of the relation $f(\theta, \varepsilon_{pn}) = f_R(\theta, \varepsilon_{pn})/(1 - \cos\theta)$, where the function $f_R(\theta, \varepsilon_{pn})$ is tabulated in Table 7.3 of Ref. [321] on the basis of the solution of the electrostatic boundary problem. The tabulated values can be used for a convenient computer calculation of $f_R(\theta, \varepsilon_{pn})$ with the help of a four-point interpolation formula, Equation D.1 in Ref. [321]. From the experimental F_{ED} and Equation 7.171, we could determine the surface charge density, σ_{pn}, at the particle–oil and particle–air interface. Values of σ_{pn} in the range from 20 to 70 μC m^{-2} have been obtained [317,320].

7.3.3.3.4 Direct Electric Repulsion

Interactions of electrostatic origin were found to essentially influence the type of particle structures at oil–water [318,319,322–324] and air–water [325,326] interfaces. Two-dimensional hexagonal arrays of particles were observed, in which the distance between the closest neighbors was markedly greater than the particle diameter [318–327]. The existence of such structures was explained by the action of direct electrostatic repulsion between like charged particles. In many cases, the particle arrays are insensitive to the concentration of electrolyte in the aqueous phase [318,322,323]. This fact, and the direct interparticle force measurements by laser tweezers [322], lead to the conclusion that the electrostatic repulsion is due to charges at the particle–oil (or particle–air) interface, which give rise to electric repulsion across the nonpolar phase [318,322–325]. This repulsion is relatively long-ranged because of the absence of a strong Debye screening of the electrostatic forces that is typical for the aqueous phase. Evidences about the presence of electric charges on the surface of solid particles dispersed in liquid hydrocarbons could be found also in earlier studies [328,329].

For a particle in isolation, the charges at the particle–nonpolar fluid interface create an electric field in the oil that asymptotically resembles the electric field of a dipole (Figure 7.29). This field practically does not penetrate into the water phase, because it is reflected by the oil–water boundary owing to the relatively large dielectric constant of water. For a single
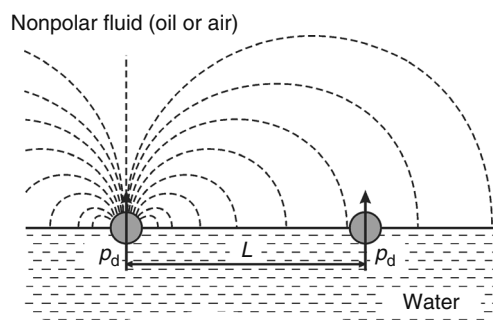
FIGURE 7.29 Two particles attached to the boundary water–nonpolar fluid and separated at a center-to-center distance L. In the nonpolar fluid (oil, air), the electric field of each particle in isolation is asymptotically identical to the field of a dipole of moment p_d. This field is created by charges at the particle–nonpolar fluid interface.

particle, the respective electrostatic problem is solved in Ref. [321]. The asymptotic behavior of the force of electrostatic repulsion between two such particles–dipoles (Figure 7.29) is [321]:

$$F_{\mathrm{ER}} = \frac{3p_{\mathrm{d}}^2}{2\varepsilon_{\mathrm{n}}L^4} \quad (R/L \ll 1) \tag{7.172}$$

L is the center-to-center distance between the two particles; $p_{\mathrm{d}} = 4\pi\sigma_{\mathrm{pn}}DR^3\sin^3\alpha$ is the effective particle dipole moment; as before, R is the particle radius and σ_{pn} is the electric charge density at the particle–nonpolar fluid interface; $D = D(\alpha,\varepsilon_{\mathrm{pn}})$ is a known dimensionless function, which can be calculated by means of Table 7.1 and Equation D.1 in Ref. [321]; $\varepsilon_{\mathrm{pn}} \equiv \varepsilon_{\mathrm{p}}/\varepsilon_{\mathrm{n}}$ is the ratio of the dielectric constants of the two phases. Equation 7.172 shows that F_{ER} asymptotically decays as $1/L^4$ like the force between two point dipoles. However, at shorter distances, the finite size of the particle is expected to lead to a Coulombic repulsion, $F_{\mathrm{ER}} \sim 1/L^2$ [322–325].

7.3.3.3.5 Electrocapillary Force

In their experiments with 1.5 μm colloidal spheres at the surfaces of water droplets in oil, Nikolaides et al. [319] observed indications about attraction between like-charged particles, and attributed the observed effect to the action of electric-field-induced capillary attraction. Their work provoked a considerable interest, because the latter force could play an important role in the micrometer and submicrometer world [330], where the effect of the gravity-induced lateral capillary force (Section 7.3.3.1) is negligible.

What concerns the theoretical description of F_{EC}, a generally accepted theory is still missing. The problem about the interplay of capillary and electric effects turned out to be rather complex. Controversial results have been reported based on the application of different truncated asymptotic expansions or other perturbation procedures [331–334]. Different approaches have lead to the conclusion that F_{EC} is attractive, but it is still unclear whether F_{EC} could prevail over F_{ER} under typical experimental conditions [335–337]. In the meantime, the number of experimental evidences about the action of attractive forces between particles at fluid interfaces keeps increasing [324,325,338–341].

As mentioned earlier, the capillary forces between particles are due to the overlap of the deformations in the liquid interface created by the particles. Hence, a necessary condition for the existence of electric-field-induced capillary force is the presence of interfacial deformations created by the electric field. As demonstrated in Figure 7.28, this necessary condition can be satisfied. The deformation is due not only to the electrodipping forces that pushes the particle toward the water (and that determines the value of the angle ψ), but also to the additional electric pressure (Maxwell stress) that is acting per unit area of the oil–water (or air–water) interface owing to the presence of electric field in the nonpolar fluid (see Figure 7.29) [317,319,320,342]. The direction of this electric force (per unit area) is from the water toward the nonpolar fluid.

The electric-field-induced deformation of a liquid interface around charged particles at the interface tetradecane-water has been quantitatively examined in Ref. [320]. An example is given in Figure 7.30. Far from the particle, the interface is flat and
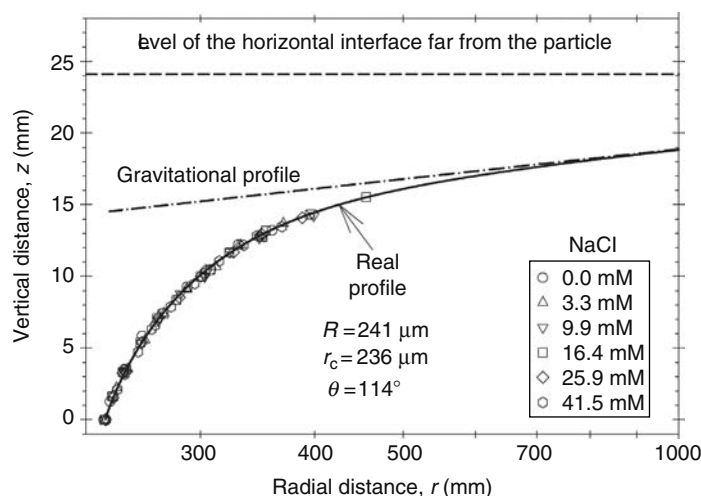
FIGURE 7.30 Profile of the oil (tetradecane)/water interface near the contact line of a charged glass particle, like that in Figure 7.28b: plot of experimental data from Ref. [320]; see Figure 7.27 for the notations. The dash-dot line shows the gravitational; profile calculated under the assumption that the particle is not charged. The difference between the real and the gravitational profiles represents the effect of electric field on the meniscus shape. The fact that the real (experimental) profile is insensitive to the concentration of NaCl in the water phase indicates that the electric charges are located at the particle–oil interface, so that the interfacial deformation is due to electric field in the oily phase.

horizontal. For particles of radii $R = 200$–300 μm, both gravitational and electric field induced deformations are present. The gravitational deformation is predominant at longer distances, whereas the electric-field deformation is significant near the particle. The latter deformation is insensitive to the variation of the concentration of NaCl in the aqueous phase (Figure 7.30), which indicates that this deformation is due to electric charges at the particle–oil interface. Good agreement between experiment (the symbols) and theory (the solid line) has been obtained.

In Ref. [343], the motion of spherical glass particles of radii 240–310 μm attached to a tetradecane–water interface was investigated. Couples of particles, which were moving toward each other under the action of lateral capillary force, are observed by optical microscopy. The analysis of the experimental results, including the comparison of the motion of charged and noncharged particles, evidences for the existence of an additional attraction between two like-charged particles at the oil–water interface. This attraction exceeds the direct electrostatic repulsion between the two particles and leads to a noticeable acceleration of their motion [343].

7.4 SURFACE FORCES

7.4.1 DERJAGUIN APPROXIMATION

The excess surface free energy per unit area of a plane-parallel film of thickness h is [14,344]

$$f(h) = \int\limits_{h}^{\infty} \Pi(h)\, dh \tag{7.173}$$

where, as before, Π denotes disjoining pressure. Derjaguin [345] derived an approximate formula, which expresses the energy of interaction between two spherical particles of radii R_1 and R_2 through integral of $f(h)$:

$$U(h_0) = \frac{2\pi R_1 R_2}{R_1 + R_2} \int\limits_{h_0}^{\infty} f(h)\, dh \tag{7.174}$$

where h_0 is the shortest distance between the surfaces of the two particles (see Figure 7.31). In the derivation of Equation 7.174 it is assumed that the interaction between two parcels from the particle surfaces, separated at the distance h, is approximately the same as that between two similar parcels in a plane-parallel film. This assumption is correct when the range of action of the surface forces and the distance h_0 are small compared to the curvature radii R_1 and R_2. It has been established, both experimentally [34] and theoretically [346], that Equation 7.174 provides a good approximation in the range of its validity.

Equation 7.174 can be generalized for smooth surfaces of arbitrary shape (not necessarily spheres). For that purpose, the surfaces of the two particles are approximated with paraboloids in the vicinity of the point of closest approach ($h = h_0$). Let the principle curvatures at this point be c_1 and c_1' for the first particle, and c_2 and c_2' for the second particle. Then the generalization of Equation 7.174 reads [344]:

$$U(h_0) = \frac{2\pi}{\sqrt{C}} \int\limits_{h_0}^{\infty} f(h)\, dh \tag{7.175}$$
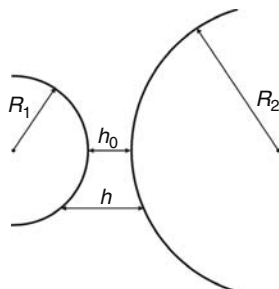
FIGURE 7.31 Two spherical particles of radii R_1 and R_2; the shortest and the running surface-to-surface distances are denoted by h_0 and h, respectively.

$$C \equiv c_1 c_1' + c_2 c_2' + (c_1 c_2 + c_1' c_2') \sin^2 \omega + (c_1 c_2' + c_1' c_2) \cos^2 \omega$$

where ω is the angle subtended between the directions of the principle curvatures of the two approaching surfaces. For two spheres, we have $c_1 = c_1' = 1/R_1$, $c_2 = c_2' = 1/R_2$, and Equation 7.175 reduces to Equation 7.174.

For two cylinders of radii r_1 and r_2 crossed at angle ω we have $c_1 = c_2 = 0$; $c_1' = 1/r_1$, $c_2' = 1/r_2$ and Equation 7.175 yields

$$U(h_0) = \frac{2\pi\sqrt{r_1 r_2}}{\sin \omega} \int_{h_0}^{\infty} f(h)\, dh \tag{7.176}$$

Equation 7.176 is often used in connection to the experiments with the surface force apparatus [34,347], in which the interacting surfaces are two crossed cylindrical mica sheets. The divergence in Equation 7.176 for $\omega = 0$ reflects the fact that the axes of the two infinitely long cylinders are parallel for $\omega = 0$ and thus the area of the interaction zone becomes infinite.

The main features of the Derjaguin approximation are the following: (1) It is applicable to any type of force law (attractive, repulsive, oscillatory), if the range of the forces is much smaller than the particles radii and (2) It reduces the problem for interactions between particles to the simpler problem for interactions in plane-parallel films.

7.4.2 VAN DER WAALS SURFACE FORCES

The van der Waals interaction between molecules i and j obeys the law:

$$u_{ij}(r) = -\frac{\alpha_{ij}}{r^6} \tag{7.177}$$

where
u_{ij} is the potential energy of interaction
r is the distance between the two molecules
α_{ij} is a constant characterizing the interaction

In fact, the van der Waals forces represent an averaged dipole–dipole interaction, which is a superposition of three main terms: (1) orientation interaction: interaction between two permanent dipoles [348]; (2) induction interaction: interaction between one permanent dipole and one induced dipole [349]; (3) dispersion interaction: interaction between two induced dipoles [350]. The theory yields [34]:

$$\alpha_{ij} = \frac{1}{(4\pi\varepsilon_0)^2} \left[\frac{p_i^2 p_j^2}{3kT} + (p_i^2 \alpha_{0j} + p_j^2 \alpha_{0i}) + \frac{3\alpha_{0i}\alpha_{0j} h_p \nu_i \nu_j}{2(\nu_i + \nu_j)} \right] \tag{7.178}$$

where
p_i and α_{i0} are the molecular dipole moment and electronic polarizability
h_p is the Planck constant
ν_i is the orbiting frequency of the electron in the Bohr atom

For van der Waals interactions between molecules in a gas phase, the orientation interaction can yield from 0% (nonpolar molecules) up to 70% (molecules of large permanent dipole moment, like H_2O) of the value of α_{ij}; the contribution of the induction interaction in α_{ij} is usually low, about 5%–10%; the contribution of the dispersion interaction might be between 24% (water) and 100% (nonpolar hydrocarbons) (for numerical data, see Ref. [34]).

According to the microscopic theory by Hamaker [351], the van der Waals interaction between two macroscopic bodies can be found by integration of Equation 7.177 over all couples of molecules, followed by subtraction of the interaction energy at infinite separation between the bodies. The result depends on the geometry of the system. For a plane-parallel film from component 3 located between two semiinfinite phases composed from components 1 and 2, the van der Waals interaction energy per unit area and the respective disjoining pressure, stemming from Equation 7.177, are [351]:

$$f_{vw} = -\frac{A_H}{12\pi h^2}, \quad \Pi_{vw} = -\frac{\partial f_{vw}}{\partial h} = -\frac{A_H}{6\pi h^3} \tag{7.179}$$

where, as usual, h is the thickness of the film and A_H is the compound Hamaker constant [14]:

$$A_H = A_{33} + A_{12} - A_{13} - A_{23} \quad (A_{ij} = \pi^2 \rho_i \rho_j \alpha_{ij},\ i,j = 1,2,3) \tag{7.180}$$

A_{ij} is the Hamaker constant of components i and j; ρ_i and ρ_j are the molecular number densities of phases i and j built up from components i and j, respectively. If A_{ii} and A_{jj} are known, we can calculate A_{ij} by using the Hamaker approximation

$$A_{ij} = (A_{ii} A_{jj})^{1/2} \tag{7.181}$$

In fact, Equation 7.181 is applicable to the dispersion contribution in the van der Waals interaction [34].

When components 1 and 2 are identical, A_H is positive (see Equation 7.180), therefore, the van der Waals interaction between identical bodies, in any medium, is always attractive. Besides, two dense bodies (even if nonidentical) will attract each other when placed in medium 3 of low density (gas, vacuum). When the phase in the middle (component 3) has intermediate Hamaker constant between those of bodies 1 and 2, A_H can be negative and the van der Waals disjoining pressure can be repulsive (positive). Such is the case of an aqueous film between mercury and gas [352].

Lifshitz et al. [353,354] developed an alternative approach to the calculation of the Hamaker constant A_H in condensed phases, called the macroscopic theory. The latter is not limited by the assumption for pairwise additivity of the van der Waals interaction [34,344,355]. The Lifshitz theory treats each phase as a continuous medium characterized by a given uniform dielectric permittivity, which is dependent on the frequency, ν, of the propagating electromagnetic waves. For the symmetric configuration of two identical phases i interacting across a medium j, the macroscopic theory provides the expression [34]

$$A_H \equiv A_{iji} = A_{iji}^{(\nu=0)} + A_{iji}^{(\nu>0)} = \frac{3}{4} kT \left(\frac{\varepsilon_i - \varepsilon_j}{\varepsilon_i + \varepsilon_j} \right)^2 + \frac{3 h_p \nu_e (n_i^2 - n_j^2)^2}{16 \sqrt{2} (n_i^2 + n_j^2)^{3/2}} \tag{7.182}$$

where
  ε_i and ε_j are the dielectric constants of phases i and j; n_i and n_j are the respective refractive indices for visible light
  h_p is the Planck constant
  ν_e is the main electronic absorption frequency which is $\approx 3.0 \times 10^{15}$ Hz for water and the most organic liquids [34]

The first term in the right-hand side of Equation 7.182, $A_{iji}^{(\nu=0)}$, is the so-called zero-frequency term, expressing the contribution of the orientation and induction interactions. Indeed, these two contributions to the van der Waals force represent electrostatic effects. Equation 7.182 shows that the zero-frequency term can never exceed $3/4kT \approx 3 \times 10^{-21}$ J. The last term in Equation 7.182, $A_{iji}^{(\nu>0)}$, accounts for the dispersion interaction. If the two phases, i and j, have comparable densities (as for emulsion systems, say oil–water–oil), then $A_{iji}^{(\nu>0)}$ and $A_{iji}^{(\nu=0)}$ are comparable by magnitude. If one of the phases, i or j, has a low density (gas, vacuum), we obtain $A_{iji}^{(\nu>0)} \gg A_{iji}^{(\nu=0)}$. In the latter case, the Hamaker microscopic approach may give comparable $A_{iji}^{(\nu>0)}$ and $A_{iji}^{(\nu=0)}$ in contradiction to the Lifshitz macroscopic theory, which is more accurate for condensed phases.

A geometrical configuration, which is important for disperse systems, is the case of two spheres of radii R_1 and R_2 interacting across a medium (component 3). Hamaker [351] has derived the following expression for the van der Waals interaction energy between two spheres:

$$U(h_0) = -\frac{A_H}{12} \left(\frac{y}{x^2 + xy + x} + \frac{y}{x^2 + xy + x + y} + 2 \ln \frac{x^2 + xy + x}{x^2 + xy + x + y} \right) \tag{7.183}$$

where

$$x = h_0/2R_1, \quad y = R_2/R_1 \leq 1 \tag{7.184}$$

and h_0 is the same as in Figure 7.31. For $x \ll 1$ Equation 7.183 reduces to

$$U(h_0) \approx -\frac{A_H}{12} \frac{y}{(1+y)x} = -\frac{2\pi R_1 R_2}{R_1 + R_2} \frac{A_H}{12\pi h_0} \tag{7.185}$$

Equation 7.185 can be also derived by combining Equation 7.179 with the Derjaguin approximation (Equation 7.174). It is worthwhile noting, that the logarithmic term in Equation 7.183 can be neglected only if $x \ll 1$. For example, even when $x = 5 \times 10^{-3}$, the contribution of the logarithmic term amounts to about 10% of the result (for $y = 1$); consequently, for larger values of x this term must be retained.
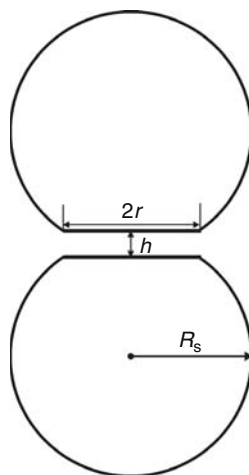
FIGURE 7.32 Thin film of radius r and thickness h formed between two attached fluid particles; the spherical part of the particle surface has radius R_s.

Another geometrical configuration, which corresponds to two colliding deformable emulsion droplets, is sketched in Figure 7.32. In this case the interaction energy is given by the expression [356]

$$U(h,r) = -\frac{A_H}{12}\left[\frac{3}{4} + \frac{R_s}{h} + 2\ln\left(\frac{h}{R_s}\right) + \frac{r^2}{h^2} - \frac{2r^2}{R_s h}\right] \quad (h, r \ll R_s) \tag{7.186}$$

where
    h and r are the thickness and the radius of the flat film formed between the two deformed drops, respectively
    R_s is the radius of the spherical part of the drop surface (see Figure 7.32)

Equation 7.186 is a truncated series expansion; the exact formula, which is more voluminous, can be found in Ref. [356]. Expressions for U for other geometrical configurations are also available [35,355].

The asymptotic behavior of the dispersion interaction at large intermolecular separations does not obey Equation 7.177; instead $u_{ij} \propto 1/r^7$ due to the electromagnetic retardation effect established by Casimir and Polder [357]. Several different expressions have been proposed to account for this effect in the Hamaker constant [355].

The orientation and induction interactions are electrostatic effects, so they are not subjected to electromagnetic retardation. Instead, they are subject to Debye screening due to the presence of electrolyte ions in the liquid phases. Thus for the interaction across an electrolyte solution the screened Hamaker constant is given by the expression [34,358]

$$A_H = 2\kappa h A_0 e^{-2\kappa h} + A_d \tag{7.187}$$

where
    A_0 denotes the contribution of the (nonscreened) orientation and induction interactions to the Hamaker constant
    A_d is the contribution of the dispersion interaction
    κ is the Debye screening parameter: $\kappa = \kappa_c I^{1/2}$ (see Equation 7.34)

Equation 7.187 is accurate to within 15% for $\kappa h > 2$ [34].

7.4.3 ELECTROSTATIC SURFACE FORCES

7.4.3.1 Two Identically Charged Planes

First we consider the electrostatic (double layer) interaction between two identical charged plane parallel surfaces across solution of symmetrical $Z:Z$ electrolyte. The charge of a counterion (i.e., ion with charge opposite to that of the surface) is $-Ze$, whereas the charge of a coion is $+Ze$ ($Z = \pm 1, \pm 2, \ldots$) with e being the elementary charge. If the separation between the two planes is very large, the number concentration of both counterions and coions would be equal to its bulk value, n_0, in the middle of the film. However, at finite separation, h, between the surfaces the two EDLs overlap and the counterion and coion concentrations in the middle of the film, n_{10} and n_{20}, are no longer equal. Because the solution inside the film is supposed to be

in electrochemical (Donnan) equilibrium with the bulk electrolyte solution of concentration n_0, we can write [359] $n_{10}n_{20} = n_0^2$, or alternatively

$$n_{10} = n_0/\sqrt{m}, \quad n_{20} = n_0\sqrt{m}, \quad m \equiv n_{20}/n_{10} \tag{7.188}$$

As pointed out by Langmuir [360], the electrostatic disjoining pressure, Π_{el}, can be identified with the excess osmotic pressure in the middle of the film:

$$\Pi_{el} = kT(n_{10} + n_{20} - 2n_0) = n_0 kT(m^{1/4} - m^{-1/4})^2 \tag{7.189}$$

Equation 7.189 demonstrates that for two identically charged surfaces Π_{el}, is always positive, i.e., corresponds to repulsion between the surfaces. In general, we have $0 < m \leq 1$, because the coions are repelled from the film due to the interaction with the film surfaces. To find the exact dependence of Π_{el} on the film thickness, h, we have to solve the Poisson–Boltzmann equation for the distribution of the electrostatic potential inside the film. The solution provides the following connection between Π_{el} and h for symmetric electrolytes [344,361]:

$$\Pi_{el} = 4n_0 kT \cot^2 \theta, \quad \kappa h = 2F(\varphi,\theta) \sin \theta \tag{7.190}$$

where $F(\varphi,\theta)$ is an elliptic integral of the first kind, and φ is related with θ as follows:

$$\cos \varphi = \frac{\cot\theta}{\sinh\left(\dfrac{Z\Phi_s}{2}\right)} \quad \text{(fixed surface potential } \Phi_s) \tag{7.191}$$

$$\tan \varphi = (\tan \theta)\sinh\left(\frac{Z\Phi_\infty}{2}\right) \quad \text{(fixed surface charge } \sigma_s) \tag{7.192}$$

$$\cosh(Z\Phi_\infty) = 1 + \frac{1}{2}\left(\frac{Ze\sigma_s}{\varepsilon\varepsilon_0 kT\kappa}\right)^2, \quad \Phi_s \equiv \frac{e\psi_s}{kT} \tag{7.193}$$

where
  Φ_s is the dimensionless surface potential
  Φ_∞ is the value of Φ_s for $h \to \infty$

Equation 7.190 expresses the dependence $\Pi_{el}(h)$ in a parametric form: $\Pi_{el}(\theta)$, $h(\theta)$. Fixed surface potential or charge means that Φ_s or σ_s does not depend on the film thickness h. The latter is important to be specified when integrating $\Pi(h)$ or $f(h)$ (in accordance with Equations 7.173 or 7.176) to calculate the interaction energy.

In principle, it is possible neither the surface potential nor the surface charge to be constant [362]. In such case a condition for charge regulation is applied, which in fact represents the condition for dynamic equilibrium of the counterion exchange between the Stern and diffuse parts of the EDL (i.e., condition for constant electrochemical potentials of the ionic species). As discussed in Section 7.2.1.2.3, the Stern layer itself can be considered as a Langmuir adsorption layer of counterions. We can relate the maximum possible surface charge density (due to all surface ionizable groups) to Γ_1 in Equation 7.47: $\sigma_{max} = Ze\Gamma_1$. Likewise, the effective surface charge density, σ_s, which is smaller by magnitude than σ_{max} (because some ionizable groups are blocked by adsorbed counterions) can be expressed as $\sigma_s = Ze(\Gamma_1 - \Gamma_2)$. Then, with the help of Equation 7.44, the Stern isotherm (Equation 7.47) can be represented in the form

$$\frac{\sigma_{max} - \sigma_s}{\sigma_{max}} = [1 + (K_2 I)^{-1} \exp(Z\Phi_s)]^{-1} \tag{7.194}$$

The product $Z\Phi_s$ is always positive. At high surface potential, $Z\Phi_s \to \infty$, from Equation 7.194 we obtain $\sigma_s \to \sigma_{max}$, i.e., there is no blocking of surface ionizable groups by adsorbed counterions.

When the film thickness is large enough ($\kappa h \geq 1$) the difference between the regimes of constant potential, constant charge and charge regulation becomes negligible, i.e., the usage of each of them leads to the same results for $\Pi_{el}(h)$ [14].

When the dimensionless electrostatic potential in the middle of the film

$$\Phi_m = \frac{e}{kT}\psi_m = -\frac{1}{2Z}\ln m \tag{7.195}$$

is small enough (the film thickness, h, is large enough), we could use the superposition approximation, i.e., we could assume that $\Phi_m \approx 2\Phi_1(h/2)$, where Φ_1 is the dimensionless electric potential at a distance $h/2$ from the surface (of the film) when the other surface is removed at infinity. Because

$$Z\Phi_1(h/2) = 4e^{-\kappa h/4}\,\tanh(Z\Phi_s/4) \tag{7.196}$$

from Equations 7.189, 7.195, and 7.196 we obtain a useful asymptotic formula [363]

$$\Pi_{el} \approx n_0 kTZ^2\Phi_m^2 \approx 64n_0 kT\left(\tanh\frac{Z\Phi_s}{4}\right)^2 e^{-\kappa h} \tag{7.197}$$

It should be noted that if Φ_s is large enough, the hyperbolic tangent in Equation 7.197 is identically 1, and Π_{el} (as well as f_{el}) becomes independent of the surface potential (or charge). Equation 7.197 can be generalized for the case of 2:1 electrolyte (bivalent counterion) and 1:2 electrolyte (bivalent coion) [364]:

$$\Pi_{el} = 432n_{(2)}kT\left(\tanh\frac{v_{i:j}}{4}\right)^2 e^{-\kappa h} \tag{7.198}$$

where $n_{(2)}$ is the concentration of the bivalent ions, the subscript $i{:}j$ takes the value 2:1 or 1:2, and

$$v_{2:1} = \ln\left[3/(1 + 2e^{-\Phi_s})\right], \quad v_{1:2} = \ln\left[(2e^{\Phi_s} + 1)/3\right] \tag{7.199}$$

7.4.3.2 Two Nonidentically Charged Planes

Contrary to the case of two identically charged surfaces, which always repel each other (see Equation 7.189), the electrostatic interaction between two plane-parallel surfaces of different potentials, ψ_{s1} and ψ_{s2}, can be either repulsive or attractive [344,365]. Here, we will restrict our considerations to the case of low surface potentials, when the Poisson–Boltzmann equation can be linearized. Despite that it is not too general quantitatively, this case exhibits qualitatively all features of the electrostatic interaction between different surfaces.

If $\psi_{s1} = $ constant, and $\psi_{s2} = $ constant, then the disjoining pressure at constant surface potential reads [344]:

$$\Pi_{el}^\psi = \frac{\varepsilon\varepsilon_0\kappa^2}{2\pi}\,\frac{2\psi_{s1}\psi_{s2}\,\cosh\kappa h - (\psi_{s1}^2 + \psi_{s2}^2)}{\sinh^2\kappa h} \tag{7.200}$$

When the two surface potentials have opposite signs, i.e., when $\psi_{s1}\psi_{s2} < 0$, Π_{el}^ψ is negative for all h and corresponds to electrostatic attraction (see Figure 7.33a). This result could have been anticipated, because two charges of opposite sign attract each other. More interesting is the case, when $\psi_{s1}\psi_{s2} > 0$, but $\psi_{s1} \neq \psi_{s2}$. In the latter case, the two surfaces repel each other for
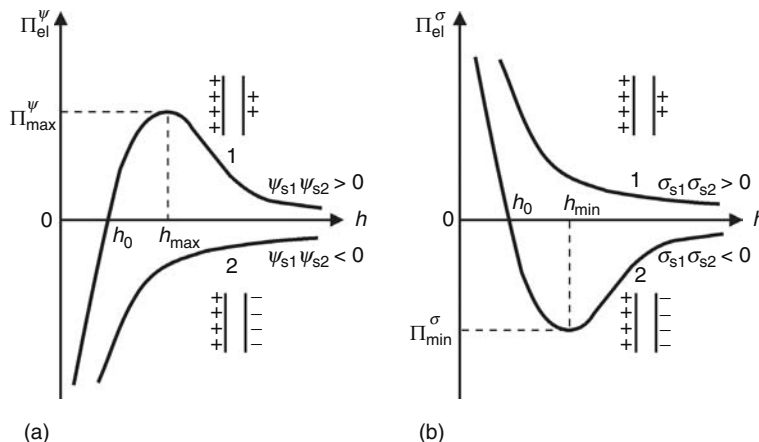
FIGURE 7.33 Electrostatic disjoining pressure at (a) fixed surface potential, Π_{el}^ψ, and (b) fixed surface charge density, Π_{el}^σ, both of them plotted versus the film thickness h. ψ_{s1} and ψ_{s2} are the potentials of the two surfaces; σ_{s1} and σ_{s2} are the respective surface charge densities.

$h > h_0$, whereas they attract each other for $h < h_0$ (Figure 7.33a); h_0 is determined by the equation $\kappa h_0 = \ln(\psi_{s2}/\psi_{s1})$; $\psi_{s2} > \psi_{s1}$. In addition, the electrostatic repulsion has a maximum value of

$$\Pi^{\psi}_{el}(\max) = \frac{\varepsilon\varepsilon_0\kappa^2}{2\pi}\psi_{s1}^2 \quad \text{at} \quad h_{\max} = \frac{1}{\kappa}\operatorname{arccosh}\frac{\psi_{s2}}{\psi_{s1}}, \quad \psi_{s2} > \psi_{s1} \tag{7.201}$$

Similar electrostatic disjoining pressure isotherm has been used to interpret the experimental data for aqueous films on mercury [147]. It is worthwhile noting, that $\Pi^{\psi}_{el}(\max)$ depends only on ψ_{s1}, i.e., the maximum repulsion is determined by the potential of the surface of lower charge.

If $\sigma_{s1} = $ constant, and $\sigma_{s2} = $ constant, then instead of Equation 7.200 we have [344]

$$\Pi^{\sigma}_{el}(h) = \frac{1}{2\varepsilon\varepsilon_0}\frac{2\sigma_{s1}\sigma_{s2}\cosh\kappa h + \sigma_{s1}^2 + \sigma_{s2}^2}{\sinh^2\kappa h} \tag{7.202}$$

When $\sigma_1\sigma_2 > 0$ Equation 7.202 yields $\Pi^{\sigma}_{el} > 0$ for every h (see Figure 7.33b). However, when $\sigma_1\sigma_2 < 0$, Π^{σ}_{el} is repulsive for small thickness, $h < h_0$ and attractive for larger separations, $h > h_0$; h_0 is determined by the equation $\kappa h_0 = \ln(-\sigma_{s2}/\sigma_{s1})$; $|\sigma_{s2}| > |\sigma_{s1}|$. The electrostatic disjoining pressure in this case has a minimum value

$$\Pi^{\sigma}_{el}(\min) = \frac{1}{\varepsilon\varepsilon_0}\sigma_{s1}\sigma_{s2}, \quad \text{at} \quad h_{\min} = \frac{1}{\kappa}\operatorname{arccosh}\left(-\frac{\sigma_{s2}}{\sigma_{s1}}\right) \tag{7.203}$$

Finally, it should be noted, that all curves depicted in Figure 7.24 decay exponentially at $h \to \infty$. An asymptotic expression for $Z:Z$ electrolytes, which generalizes Equation 7.197, holds [344,363]:

$$\Pi_{el}(h) = 64n_0kT\gamma_1\gamma_2 e^{-\kappa h}, \quad \gamma_k \equiv \tanh\left(\frac{Ze\psi_{sk}}{4kT}\right), \quad k = 1, 2 \tag{7.204}$$

Equation 7.204 is valid for both low and high surface potentials, only if $\exp(-\kappa h) \ll 1$.

7.4.3.3 Two Charged Spheres

When the EDLs are thin compared with the particle radii ($\kappa^{-1} \ll R_1, R_2$) and the gap between the particles is small ($h_0 \ll R_1, R_2$), we can use Equation 7.204 in conjunction with the Derjaguin approximation, Equations 7.173 and 7.174. The result for the energy of electrostatic interaction between two spheres reads:

$$U_{el}(h_0) = \frac{128\pi R_1 R_2}{\kappa^2(R_1 + R_2)}n_0kT\gamma_1\gamma_2 e^{-\kappa h} \tag{7.205}$$

Equation 7.205 is valid for any surface potentials ψ_{s1} and ψ_{s2} but only for $\exp(\kappa h) \gg 1$. Complementary expressions, which are valid for every $h \ll R_1, R_2$, but for small surface potentials, can be derived by integrating Equations 7.200 and 7.202, instead of Equation 7.204. In this way, for $\psi_{s1} = $ constant and $\psi_{s2} = $ constant, we can derive [366]:

$$U^{\psi}_{el}(h_0) = \frac{\pi\varepsilon\varepsilon_0 R_1 R_2}{R_1 + R_2}[(\psi_{s1} + \psi_{s2})^2\ln(1 + e^{-\kappa h_0}) + (\psi_{s1} - \psi_{s2})^2\ln(1 - e^{-\kappa h_0})] \tag{7.206}$$

or, alternatively, for $\sigma_{s1} = $ constant and $\sigma_{s2} = $ constant we obtain [367]

$$U^{\sigma}_{el}(h_0) = \frac{-\pi R_1 R_2}{\varepsilon\varepsilon_0\kappa^2(R_1 + R_2)}[(\sigma_{s1} + \sigma_{s2})^2\ln(1 - e^{-\kappa h_0}) + (\sigma_{s1} - \sigma_{s2})^2\ln(1 + e^{-\kappa h_0})] \tag{7.207}$$

The range of validity of the different approximations involved in the derivations of Equations 7.205 through 7.207 is discussed in the book by Russel et al. [368]

As mentioned above, Equations 7.205 through 7.207 hold for $h_0 \ll R$. In the opposite case, when h_0 is comparable to or larger than the particle radius R, we can use the equation [14]

$$U_{el}(h_0) = \frac{4\pi\varepsilon\varepsilon_0\psi_s^2 R^2}{2R + h_0}e^{-\kappa h_0} \tag{7.208}$$

stemming from the theory of Debye and Hückel [369] for two identical particles. Equation 7.208 was derived by using the superposition approximation (valid for weak overlap of the two EDLs) and the linearized Poisson–Boltzmann equation. A simple approximate formula, representing in fact interpolation between Equations 7.208 and 7.206 (the latter for $R_1 = R_2 = R$), has been derived by McCartney and Levine [370]

$$U_{el}^{\psi}(h_0) = 4\pi\varepsilon\varepsilon_0 R\psi_s^2 \frac{R+h_0}{2R+h_0} \ln\left(1 + \frac{Re^{-\kappa h_0}}{R+h_0}\right) \tag{7.209}$$

Equation 7.209 has the advantage to give a good approximation for every h_0 provided that the Poisson–Boltzmann equation can be linearized. Similar expressions for the energy of electrostatic interaction between two deformed droplets or bubbles (Figure 7.32) can be derived [356].

7.4.4 DERJAGUIN–LANDAU–VERWEY–OVERBEEK (DLVO) THEORY

The first quantitative theory of interactions in thin liquid films and dispersions is the DLVO theory called after the names of the authors: Derjaguin and Landau [371] and Verwey and Overbeek [363]. In this theory, the total interaction is supposed to be a superposition of van der Waals and double layer interactions. In other words, the total disjoining pressure and the total interaction energy are presented in the form:

$$\Pi = \Pi_{vw} + \Pi_{el}, \quad U = U_{vw} + U_{el} \tag{7.210}$$

A typical curve, Π versus h, exhibits a maximum representing a barrier against coagulation, and two minima, called primary and secondary minimum (see Figure 7.17); the U versus h curve has a similar shape. The primary minimum appears if strong short-range repulsive forces (e.g., steric forces) are present. With small particles, the depth of the secondary minimum is usually small ($U_{min} < kT$). If the particles cannot overcome the barrier, coagulation (flocculation) does not take place, and the dispersion is stable due to the electrostatic repulsion, which gives rise to the barrier. With larger colloidal particles ($R > 0.1$ μm) the secondary minimum could be deep enough to cause coagulation and even formation of ordered structures of particles [372].

By addition of electrolyte or by decreasing the surface potential of the particles, we can suppress the electrostatic repulsion and thus decrease the height of the barrier. According to DLVO theory, the critical condition determining the onset of rapid coagulation is

$$U(h_{max}) = 0, \quad \left.\frac{dU}{dh}\right|_{h_{max}} = 0 \tag{7.211}$$

where $h = h_{max}$ denotes the position of the barrier.

By using Equation 7.185 for U_{vw} and Equation 7.205 for U_{el} we derive from Equations 7.210 and 7.211 the following criterion for the threshold of rapid coagulation of identical particles ($R_1 = R_2 = R$; $\gamma_1 = \gamma_2 = \gamma$):

$$\frac{\kappa^6}{n_0^2} = \left[\frac{768\pi}{A_H}kTe^{-1}\tanh^2\left(\frac{Ze\psi_s}{4kT}\right)\right]^2 \tag{7.212}$$

For a Z:Z electrolyte, substituting $\kappa^2 = (2Z^2e^2n_0)/(\varepsilon_0\varepsilon kT)$ into Equation 7.212, we obtain:

$$n_0(\text{critical}) \propto \frac{1}{Z^6}\tanh^4\left(\frac{Ze\psi_s}{4kT}\right) \tag{7.213}$$

When ψ_s is high enough, the hyperbolic tangent equals 1 and Equation 7.213 yields $n_0(\text{critical}) \propto Z^{-6}$ which is, in fact, the empirical rule established earlier by Schulze [373] and Hardy [374].

7.4.5 NON-DLVO SURFACE FORCES

After 1980, a number of surface forces have been found out which are not taken into account by conventional DLVO theory. They are considered separately below.

7.4.5.1 Ion Correlation Forces

As shown by Debye and Hückel [369], due to the strong electrostatic interaction between the ions in a solution, the positions of the ions are correlated in such a way that a counterion atmosphere appears around each ion, thus screening its Coulomb

potential. The energy of formation of the counterion atmospheres gives a contribution to the free energy of the system called correlation energy [23]. The correlation energy affects also a contribution to the osmotic pressure of the electrolyte solution, which can be presented in the form [23]

$$\Pi_{\text{osm}} = kT \sum_{i=1}^{k} n_i - \frac{kT\kappa^2}{24\pi} \tag{7.214}$$

The first term in the right-hand side of the Equation 7.214 corresponds to an ideal solution, whereas the second term takes into account the effect of electrostatic interactions between the ions (the same effect is accounted for thermodynamically by the activity coefficient, see Equation 7.31).

The expression for Π_{el} in the DLVO theory (Equation 7.189) obviously corresponds to an ideal solution, the contribution of the ionic correlations being neglected. Hence, in a more general theory instead of Equation 7.210 we could write:

$$\Pi = \Pi_{\text{vw}} + \Pi_{\text{el}} + \Pi_{\text{cor}} \tag{7.215}$$

where Π_{cor} is the contribution of the ionic correlations to the disjoining pressure. The theory of Π_{cor} takes into account the following effects: (1) the different ionic concentration (and hence the different Debye screening) in the film compared to that in the bulk solution; (2) the energy of deformation of the counterion atmosphere due to the image forces; (3) the energy of the long-range correlations between charge-density fluctuations in the two opposite EDLs. For calculating Π_{cor} both numerical solutions [375,376] and analytical expressions [377–379] have been obtained. For example, in the case when the electrolyte is symmetrical (Z:Z) and $\exp(-\kappa h) \ll 1$ we can use the asymptotic formula [377]

$$\Pi_{\text{cor}} = \Pi_{\text{el}} \frac{Z^2 e^2 \kappa}{16\pi\varepsilon\varepsilon_0 kT} (\ln 2 + 2I_C) + O(e^{-\kappa h}) \tag{7.216}$$

where Π_{el} is the conventional DLVO electrostatic disjoining pressure,

$$I_C = \frac{1}{2}(1 + J)\ln 2 + \frac{2 - 2z^3 + z}{2z(2z^2 - 1)^2} - \frac{1}{2}(1 - J)\ln(z + z^2)$$

$$- \frac{\sqrt{z^2 - 1}}{z}[1 + J + 4(2z^2 - 1)^{-3}]\arctan\sqrt{\frac{z - 1}{z + 1}}$$

$$J \equiv \frac{2z^2 - 3}{(2z^2 - 1)^3}, \quad z \equiv \left[1 + \left(\frac{e\sigma_s}{2\varepsilon\varepsilon_0 kT\kappa}\right)^2\right]^{1/2}$$

The results for the case of symmetric electrolytes are the following. Π_{cor} is negative and corresponds to attraction, which can be comparable by magnitude with Π_{vw}. In the case of 1:1 electrolyte Π_{cor} is usually a small correction to Π_{el}. In the case of 2:2 electrolyte, however, the situation can be quite different: the attractive forces, $\Pi_{\text{cor}} + \Pi_{\text{vw}}$, prevails over Π_{el} and the total disjoining pressure, Π, becomes negative. The effect of Π_{cor} is even larger in the presence of ions of higher valence. Short-range net attractive ion-correlation forces have been measured by Marra [380,381] and Kjellander et al. [382,383] between highly charged anionic bilayer surfaces in $CaCl_2$ solutions. These forces are believed to be responsible for the strong adhesion of some surfaces (clay and bilayer membranes) in the presence of divalent counterions [34,382,384]. On the other hand, Kohonen et al. [385] measured a monotonic repulsion between two mica surfaces in 4.8×10^{-3} M solution of $MgSO_4$. Additional work is necessary to verify the theoretical predictions and to clarify the physical significance of the ion-correlation surface force.

Note that the theory predicts ion-correlation attraction not only across water films with overlapping EDLs, but also across *oily* films intervening between two water phases. In the latter case, Π_{cor} is not zero because the ions belonging to the two outer double layers interact across the thin dielectric (oil) film. The theory for such a film [386] predicts that Π_{cor} is negative (attractive) and strongly dependent on the dielectric permittivity of the oil film; Π_{cor} can be comparable by magnitude with Π_{vw}; $\Pi_{\text{el}} = 0$ in this case.

7.4.5.2 Steric Interaction

7.4.5.2.1 Physical Background
The steric interaction between two surfaces appears when chain molecules, attached at some point(s) to a surface, dangle out into the solution (see Figure 7.34). When two such surfaces approach each other, the following effects take place [34,387–389]:
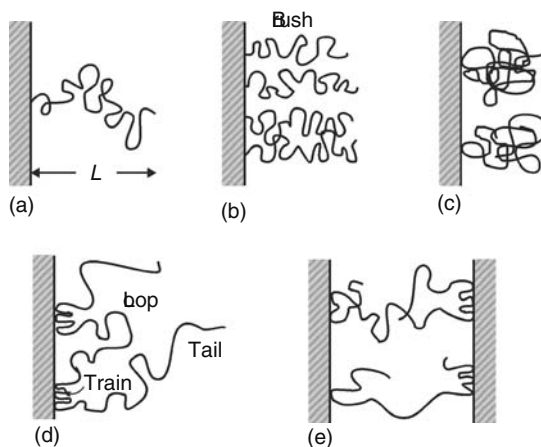
FIGURE 7.34 Polymeric chains adsorbed at an interface: (a) terminally anchored polymer chain of mean end-to-end distance *L*; (b) a brush of anchored chains; (c) adsorbed (but not anchored) polymer coils; (d) configuration with a loop, trains and tails; (e) bridging of two surfaces by adsorbed polymer chains.

(1) The entropy decreases due to the confining of the dangling chains which results in a repulsive osmotic force known as steric or overlap repulsion. (2) In a poor solvent, the segments of the chain molecules attract each other; hence the overlap of the two approaching layers of polymer molecules will be accompanied with some intersegment attraction; the latter can prevail for small overlap, however at the distance of larger overlap it becomes negligible compared with the osmotic repulsion. (3) Another effect, known as the bridging attraction, occurs when two opposite ends of chain molecule can attach (adsorb) to the opposite approaching surfaces, thus forming a bridge between them (see Figure 7.34e).

Steric interaction can be observed in foam or emulsion films stabilized with nonionic surfactants or with various polymers, including proteins. The usual nonionic surfactants molecules are anchored (grafted) to the liquid interface by their hydrophobic moieties. When the surface concentration of adsorbed molecules is high enough, the hydrophilic chains are called to form a brush (Figure 7.34b). The coils of macromolecules, like proteins, can also adsorb at a liquid surface (Figure 7.34c). Sometimes the configurations of the adsorbed polymers are very different from the statistical coil: loops, trains, and tails can be distinguished (Figure 7.34d).

The osmotic pressure of either dilute or concentrated polymer solutions can be expressed in the form [390]:

$$\frac{P_{\text{osm}}}{nkT} = \frac{1}{N} + \frac{1}{2}nv + \frac{1}{3}n^2w + \cdots \tag{7.217}$$

where
   N is the number of segments in the polymer chain
   n is the number segment density
   v and *w* account for the pair and triplet interactions, respectively, between segments

In fact, *v* and *w* are counterparts of the second and third virial coefficients in the theory of imperfect gases [11]; *v* and *w* can be calculated if information about the polymer chain and the solvent is available [368]:

$$w^{1/2} = \bar{v}m/N_{\text{A}}, \quad v = w^{1/2}(1 - 2\chi) \tag{7.218}$$

where
   $\bar{v}$ (m^3/kg) is the specific volume per segment
   m (kg/mol) is the molecular weight per segment
   N_{A} is the Avogadro number
   χ is the Flory parameter

The latter depends on both the temperature and the energy of solvent–segment interaction. Then, *v* can be zero (see Equation 7.218) for some special temperature, called the theta temperature. The solvent at the theta temperature is known as the theta solvent or ideal solvent. The theta temperature in polymer solutions is a counterpart of the Boil temperature in imperfect gases: this is the temperature at which the intermolecular (intersegment) attraction and repulsion are exactly counterbalanced. In a

good solvent, however, the repulsion due mainly to the excluded volume effect dominates the attraction and $v > 0$. In contrast, in a poor solvent the intersegment attraction prevails, so $v < 0$.

7.4.5.2.2 Thickness of the Polymer Adsorption Layer

The steric interaction between two approaching surfaces appears when the film thickness becomes of the order of, or smaller than $2L$ where L is the mean-square end-to-end distance of the hydrophilic portion of the chain. If the chain was entirely extended, then L would be equal to Nl with l being the length of a segment; however, due to the Brownian motion $L < Nl$. For an anchored chain, like that depicted in Figure 7.34a, in a theta solvent, L can be estimated as [368]:

$$L \approx L_0 \equiv l\sqrt{N} \tag{7.219}$$

In a good solvent $L > L_0$, whereas in a poor solvent $L < L_0$. In addition, L depends on the surface concentration, Γ, of the adsorbed chains, i.e., L is different for an isolated molecule and for a brush (see Figures 7.34a and b). The mean field approach [368,391] applied to polymer solutions provides the following equation for calculating L

$$\widetilde{L}^3 - \left(1 + \frac{1}{9}\widetilde{\Gamma}^2\right)\widetilde{L}^{-1} = \frac{1}{6}\widetilde{v} \tag{7.220}$$

where $\widetilde{L}, \widetilde{\Gamma}$, and $\widetilde{v}$ are the dimensionless values of L, Γ, and v defined as follows:

$$\widetilde{L} = L/(l\sqrt{N}), \quad \widetilde{\Gamma} = \Gamma N\sqrt{w}/l, \quad \widetilde{v} = v\Gamma N^{3/2}/l \tag{7.221}$$

For an isolated adsorbed molecule ($\widetilde{\Gamma} = 0$) in an ideal solvent ($\widetilde{v} = 0$) Equation 7.220 predicts $\widetilde{L} = 1$, i.e., $L = L_0$.

7.4.5.2.3 Overlap of Adsorption Layers

We now consider the case of terminally anchored chains, like those depicted in Figures 7.34a and b. Dolan and Edwards [392] calculated the steric interaction free energy per unit area, f, as a function on the film thickness, h, in a theta solvent:

$$f(h) = \Gamma kT\left[\frac{\pi^2}{3}\frac{L_0^2}{h^2} - \ln\left(\frac{8\pi}{3}\frac{L_0^2}{h^2}\right)\right] \quad \text{for} \quad h < L_0\sqrt{3} \tag{7.222}$$

$$f(h) = 4\Gamma kT \exp\left(-\frac{3h^2}{2L_0^2}\right) \quad \text{for} \quad h > L_0\sqrt{3} \tag{7.223}$$

where L_0 is the end-to-end distance as defined by Equation 7.219. The boundary between the power-law regime ($f \propto 1/h^2$) and the exponential decay regime is at $h = L_0\sqrt{3} \approx 1.7L_0$, the latter being slightly less than $2L_0$, which is the intuitively expected onset of the steric overlap. The first term in the right-hand side of Equation 7.222 comes from the osmotic repulsion between the brushes, which opposes the approach of the two surfaces; the second term is negative and accounts effectively for the decrease of the elastic energy of the initially extended chains when the thickness of each of the two brushes, pressed against each other, decreases.

In the case of good solvent the disjoining pressure $\Pi = -\mathrm{d}f/\mathrm{d}h$ can be calculated by means of Alexander-de Gennes theory as [393,394]:

$$\Pi(h) = kT\Gamma^{3/2}\left[\left(\frac{2L_g}{h}\right)^{9/4} - \left(\frac{h}{2L_g}\right)^{3/4}\right] \quad \text{for} \quad h < 2L_g, \quad L_g = N(\Gamma l^5)^{1/3} \tag{7.224}$$

where L_g is the thickness of a brush in a good solvent [395]. The positive and the negative terms in the right-hand side of Equation 7.224 correspond to osmotic repulsion and elastic attraction. The validity of Alexander-de Gennes theory was experimentally confirmed by Taunton et al. [396] who measured the forces between two brush layers grafted on the surfaces of two crossed mica cylinders.

In the case of adsorbed molecules, like these in Figure 7.34c, which are not anchored to the surface, the measured surface forces depend significantly on the rate of approaching of the two surfaces [397,398]. The latter effect can be attributed to the comparatively low rate of exchange of polymer between the adsorption layer and the bulk solution. This leads to a hysteresis of the surface force: different interaction on approach and separation of the two surfaces [34]. In addition, we can observe two regimes of steric repulsion: (1) weaker repulsion at larger separations due to the overlap of the tails (Figure 7.34d) and (2) stronger repulsion at smaller separations indicating overlap of the loops [399].

7.4.5.3 Oscillatory Structural Forces

7.4.5.3.1 Origin of the Structural Forces

Oscillatory structural forces appear in two cases: (1) in thin films of pure solvent between two smooth solid surfaces; (2) in thin liquid films containing colloidal particles (including macromolecules and surfactant micelles). In the first case, the oscillatory forces are called the solvation forces [34,400]; they are important for the short-range interactions between solid particles and dispersions. In the second case, the structural forces affect the stability of foam and emulsion films as well as the flocculation processes in various colloids. At higher particle concentrations, the structural forces stabilize the liquid films and colloids [401–405]. At lower particle concentrations, the structural forces degenerate into the so-called depletion attraction, which is found to destabilize various dispersions [406,407].

In all cases, the oscillatory structural forces appear when monodisperse spherical (in some cases ellipsoidal or cylindrical) particles are confined between the two surfaces of a thin film. Even one hard wall can induce ordering among the neighboring molecules. The oscillatory structural force is a result of overlap of the structured zones at two approaching surfaces [408–411]. A simple connection between density distribution and structural force is given by the contact value theorem [34,411,412]:

$$\Pi_{os}(h) = kT[n_s(h) - n_s(\infty)] \tag{7.225}$$

where

Π_{os} is the disjoining pressure component due to the oscillatory structural forces
$n_s(h)$ is the particle number density in the subsurface layer as a function of the distance between the walls, h

Figure 7.35 illustrates the variation of n_s with h and the resulting disjoining pressure, Π_{os}. We see that in the limit of very small separations, as the last layer of particles is eventually squeezed out, $n_s \to 0$ and

$$\Pi_{os}(h) \to -kTn_s(\infty) \quad \text{for } h \to 0 \tag{7.226}$$

In other words, at small separations Π_{os} is negative (attractive). Equation 7.226 holds for both solvation forces and colloid structural forces. In the latter case, Equation 7.226 represents the osmotic pressure of the colloid particles and the resulting attractive force is known as the depletion force (Section 7.4.5.3.3).

It is worthwhile noting that the wall can induce structuring in the neighboring fluid only if the magnitude of the surface roughness is negligible compared with the particle diameter, d. Indeed, when surface irregularities are present, the oscillations are smeared out and oscillatory structural force does not appear. If the film surfaces are fluid, the role of the surface roughness is played by the interfacial fluctuation capillary waves, whose amplitude (usually between 1 and 5 Å) is comparable to the
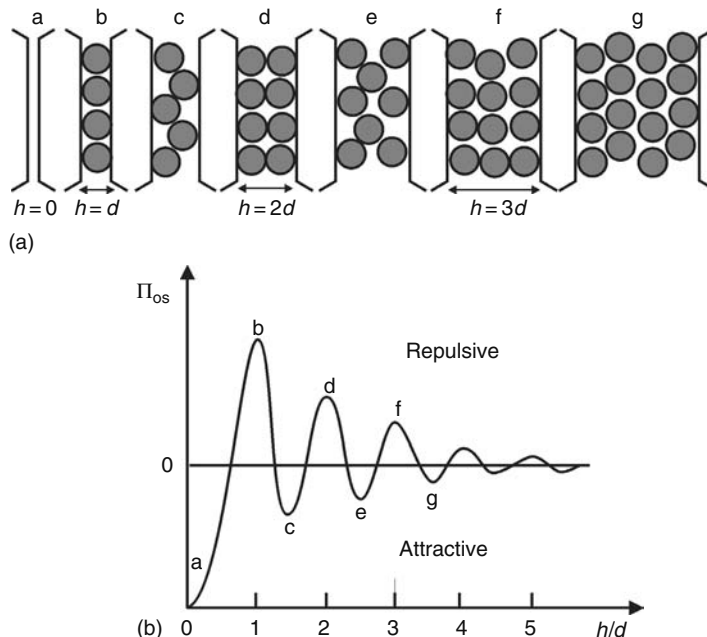

FIGURE 7.35 (a) Sketch of the consecutive stages of the thinning of a liquid film containing spherical particles; (b) Plot of the related oscillatory structural component of disjoining pressure, Π_{os}, versus the film thickness h [34].

diameter of the solvent molecules. That is why oscillatory solvation forces (due to structuring of solvent molecules) are observed only with liquid films, which are confined between smooth solid surfaces [34]. In order for structural forces to be observed in foam or emulsion films, the diameter of the colloidal particles must be much larger than the amplitude of the surface corrugations. The period of the oscillations is always about the particle diameter [34,405].

The theories developed for calculating the oscillatory force are based on modeling by means of the integral equations of statistical mechanics [413–417] or numerical simulations [418–421]. As a rule, these approaches are related to complicated theoretical expressions or numerical procedures, in contrast with the DLVO theory, one of its main advantages being its simplicity [34]. To overcome this difficulty, some relatively simple semiempirical expressions have been proposed [422,423] on the basis of fits of theoretical results for hard-sphere fluids.

A semiempirical formula for the oscillatory structural component of disjoining pressure reads [422]:

$$
\begin{aligned}
\Pi_{\text{os}}(h) &= P_0 \cos\left(\frac{2\pi h}{d_1}\right) \exp\left(\frac{d^3}{d_1^2 d_2} - \frac{h}{d_2}\right) \quad \text{for} \quad h > d \\
&= -P_0 \quad \text{for} \quad 0 < h < d
\end{aligned}
\tag{7.227}
$$

where

d is the diameter of the hard spheres
d_1 and d_2 are the period and the decay length of the oscillations which are related to the particle volume fraction, ϕ, as follows [422]

$$
\frac{d_1}{d} = \sqrt{\frac{2}{3}} + 0.237\Delta\phi + 0.633(\Delta\phi)^2; \quad \frac{d_2}{d} = \frac{0.4866}{\Delta\phi} - 0.420
\tag{7.228}
$$

where
$\Delta\phi = \phi_{\text{max}} - \phi$ with $\phi_{\text{max}} = \pi/(3\sqrt{2})$ is the value of ϕ at close packing
P_0 is the particle osmotic pressure determined by means of Carnahan–Starling formula [424]:

$$
P_0 = nkT \frac{1 + \phi + \phi^2 - \phi^3}{(1 - \phi)^3}, \quad n = \frac{6\phi}{\pi d^3}
\tag{7.229}
$$

where n is the particle number density. For $h < d$, when the particles are expelled from the slit into the neighboring bulk suspension, Equation 7.227 describes the depletion attraction. On the other hand, for $h > d$ the structural disjoining pressure oscillates around P_0 as defined by Equation 7.229 in agreement with the finding of Kjellander and Sarman [415]. The finite discontinuity of Π_{os} at $h = d$ is not surprising as, at this point, the interaction is switched over from oscillatory to depletion regime. It should be noted that in an oscillatory regime, the concentration dependence of Π_{os} is dominated by the decay length d_2 in the exponent (see Equations 7.227 and 7.228). Roughly speaking, for a given distance h, the oscillatory disjoining pressure Π_{os} increases five times when ϕ is increased with 10% [422]. The comparison with available numerical data showed that Equation 7.227 is accurate everywhere except in the region of the first (the highest) oscillatory maximum.

A semiempirical expression for $\Pi_{\text{os}}(H)$, which is accurate in the whole region $0 \leq H < \infty$, including the region of the first maximum, was proposed by Trokhymchuk et al. [423]:

$$
\begin{aligned}
\Pi_{\text{os}} &= \Pi_0 \cos(\omega h + \varphi_2)e^{-\kappa h} + \Pi_1 e^{(d-h)\delta} \quad \text{for} \quad h \geq d \\
\Pi_{\text{os}} &= -P_0 \quad \text{for} \quad 0 < h < d
\end{aligned}
\tag{7.230}
$$

where, Π_0, Π_1, ω, φ_2, κ, and δ are universal functions of particle volume fraction, ϕ, tabulated in Ref. [423]. Equation 7.230 compares very well with existing computer simulation data [423].

The interactions between the micelles in a nonionic surfactant solution can be adequately described as interactions in a hard-sphere fluid. Experiments with foam films formed from aqueous solutions of two nonionic surfactants, Brij 35 and Tween 20, which contain spherical micelles of diameters in the range 7–9 nm, have been carried out [425]. From the measured contact angles, the micelle aggregation number and volume fraction have been determined. In addition, from the measured disjoining-pressure isotherms the micelle diameter has been found. In other words, the liquid-film measurements could give information about the micelles, which is analogous to that obtainable by dynamic and static light scattering (DLS and SLS). As an illustration, Figure 7.36 shows the comparison of theory and experiment for the nonionic surfactant Tween 20. The experimental $\Pi_{\text{os}}(h)$ dependence is obtained by using the porous-plate cell by Mysels and Jones [426]. The points on the horizontal axis correspond to the thickness of the metastable states of the film measured by the Scheludko capillary cell
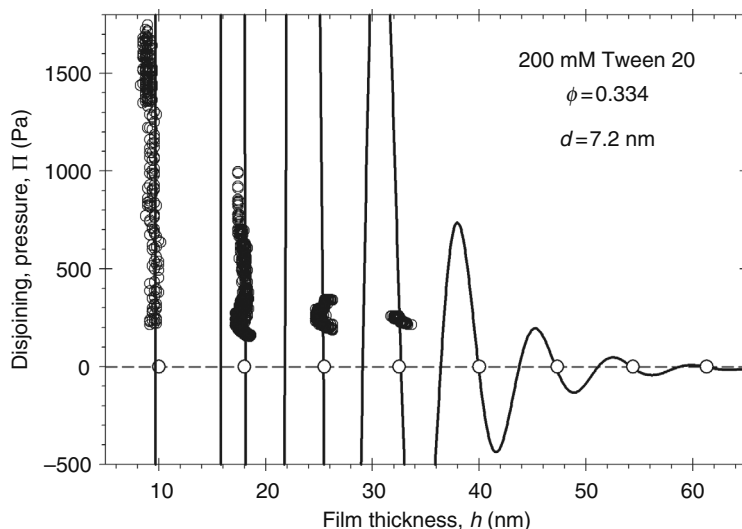
FIGURE 7.36 Plot of disjoining pressure, Π, versus film thickness, h: Comparison of experimental data for a foam film [425] (porous-plate cell) with the theoretical curve (solid line) calculated by means of Equation 7.230. The film is formed from 200 mM aqueous solution of the nonionic surfactant Tween 20. The volume fraction of the micelles ($\phi = 0.334$) is determined from the film contact angle; the micelle diameter ($d = 7.2$ nm) is determined by DLS. The points on the horizontal axis denote the respective values of h for the stratification steps measured by a Scheludko capillary cell.

[201,202]. The solid line is calculated by means of Equation 7.230 for particle (micelle) diameter determined by light scattering and micelle volume fraction determined from the contact angle of the thin liquid film [425]. Note that the short-range repulsion at $h \approx 10$ nm (Figure 7.36) corresponds to the steric repulsion between the hydrophilic headgroups of the surfactant molecules.

The predictions of different quantitative criteria for stability–instability transitions were investigated [425], having in mind that the oscillatory forces exhibit both maxima, which play the role of barriers to coagulation, and minima that could produce flocculation or coalescence in colloidal dispersions (emulsions, foams, suspensions). The interplay of the oscillatory force with the van der Waals surface force was taken into account. Two different kinetic criteria were considered, which give similar and physically reasonable results about the stability–instability transitions. Diagrams were constructed, which show the values of the micelle volume fraction, for which the oscillatory barriers can prevent the particles from coming into close contact, or for which a strong flocculation in the depletion minimum or a weak flocculation in the first oscillatory minimum could be observed [425].

It should be noted that Equations 7.227 and 7.230 refer to hard spheres of diameter d. In practice, however, the interparticle potential can be soft because of the action of long-range repulsive forces. If such is the case, we can obtain an estimation of the structural force by introducing an effective hard-core diameter [404]

$$d(T) = \left[\frac{3}{4\pi} \beta_2(T) \right]^{1/3} \qquad (7.231)$$

where β_2 is the second virial coefficient in the virial expansion of the particle osmotic pressure: $P_{osm}/(nkT) = 1 + \beta_2 n/2 + \ldots$ When the particles are ionic surfactant micelles (or other electrically charged particles), the diameter of the effective hard sphere can be approximated as $d \approx d_H + 2\kappa^{-1}$, where d_H is the micelle hydrodynamic diameter (usually measured by dynamic light scattering [DLS]); the Debye screening length κ^{-1}, involves contributions from both the background electrolyte and the counterions dissociated from the micelles [402,403,427,428]:

$$\kappa^2 = \frac{e^2}{\varepsilon_0 \varepsilon kT} [2(\text{CMC} + I_a) + (C_s - \text{CMC})\alpha_d] \qquad (7.232)$$

CMC, C_s is the total concentration of ionic surfactant; I_a is the ionic strength due to added inorganic electrolyte (if any), and α_d is the degree of ionization of the micelle surface ionizable groups (nonneutralized by bound counterions).

7.4.5.3.2 Oscillatory Solvation Forces
When the role of hard spheres, like those depicted in Figure 7.35, is played by the molecules of solvent, the resulting volume exclusion force is called the oscillatory solvation force, or sometimes when the solvent is water, oscillatory hydration
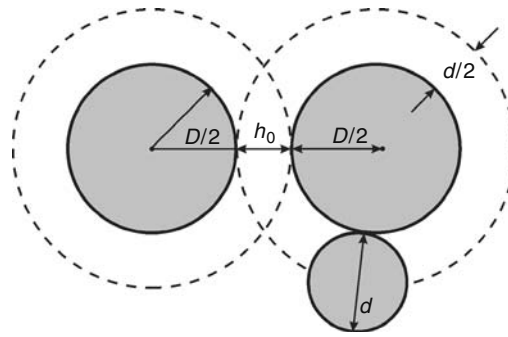
FIGURE 7.37 Overlap of the depletion zones around two particles of diameter D separated at a surface-to-surface distance h_0; the smaller particles have diameter d.

force [34]. The latter should be distinguished from the monotonic hydration force, which has different physical origin and is considered separately in Section 7.4.5.4.

Measurement of the oscillatory solvation force became possible after the precise surface force apparatus had been constructed [34]. This apparatus allowed to measure the surface forces in thin liquid films confined between mica (or modified mica) surfaces and in this way to check the validity of the DLVO theory down to thickness of about 5 Å and even smaller. The experimental results with nonaqueous liquids of both spherical (CCl_4) or cylindrical (linear alkanes) molecules showed that at larger separations the DLVO theory is satisfied, whereas at separations on the order of several molecular diameters an oscillatory force is superimposed over the DLVO force law. In aqueous solutions, oscillatory forces were observed at higher electrolyte concentrations with periodicity of 0.22–0.26 nm, about the diameter of the water molecule [34]. As mentioned above, the oscillatory solvation forces can exist only between smooth solid surfaces.

7.4.5.3.3 Depletion Force

Bondy [429] observed coagulation of rubber latex in presence of polymer molecules in the disperse medium. Asakura and Oosawa [406] published a theory, which attributed the observed interparticle attraction to the overlap of the depletion layers at the surfaces of two approaching colloidal particles (see Figure 7.37). The centers of the smaller particles, of diameter, d, cannot approach the surface of a bigger particle (of diameter D) at a distance shorter than $d/2$, which is the thickness of the depletion layer. When the two depletion layers overlap (Figure 7.37), some volume between the large particles becomes inaccessible for the smaller particles. This gives rise to an osmotic pressure, which tends to suck out the solvent between the bigger particles, thus forcing them against each other. The total depletion force experienced by one of the bigger particles is [406]

$$F_{\text{dep}} = -kTnS(h_0) \tag{7.233}$$

where the effective depletion area is

$$
S(h_0) = \frac{\pi}{4}(2D + d + h_0)(d - h_0) \quad \text{for} \quad 0 \leq h_0 \leq d
$$
$$
S(h_0) = 0 \quad \text{for} \quad d \leq h_0 \tag{7.234}
$$

where
  h_0 is the shortest distance between the surfaces of the larger particles
  n is the number density of the smaller particles

By integrating Equation 7.233, we can derive an expression for the depletion interaction energy between the two larger particles, $U_{\text{dep}}(h_0)$. For $D \gg d$, this expression reads:

$$U_{\text{dep}}(h_0)/kT \approx -\frac{3}{2}\phi\frac{D}{d^3}(d - h_0)^2 \quad 0 \leq h_0 \leq d \tag{7.235}$$

where $\phi = \pi nd^3/6$ is the volume fraction of the small particles. The maximum value of U_{dep} at $h_0 = 0$ is $U_{\text{dep}}(0)/kT \approx -3\phi D/(2d)$. For example, if $D/d = 50$ and $\phi = 0.1$, then $U_{\text{dep}}(0) = 7.5\ kT$. This depletion attraction turns out to be large enough to cause flocculation in dispersions. De Hek and Vrij [407] studied systematically the flocculation of sterically stabilized silica

suspensions in cyclohexane by polystyrene molecules. Patel and Russel [430] investigated the phase separation and rheology of aqueous polystyrene latex suspensions in the presence of polymer (Dextran T-500). The stability of dispersions is often determined by the competition between electrostatic repulsion and depletion attraction [431]. An interplay of steric repulsion and depletion attraction was studied theoretically by van Lent et al. [432] for the case of polymer solution between two surfaces coated with anchored polymer layers. Joanny et al. [433] and Russel et al. [368] reexamined the theory of depletion interaction by taking into account the internal degrees of freedom of the polymer molecules; their analysis confirmed the earlier results of Asakura and Oosawa [406].

In the case of plane-parallel films the depletion component of disjoining pressure is

$$\Pi_{dep}(h) = -nkT \quad h < d$$
$$\Pi_{dep}(h) = 0 \quad h > d$$

(7.236)

which is similar to Equation 7.226. This is not surprising because in both case we are dealing with the excluded volume effect. Evans and Needham [434] succeeded to measure the depletion energy of two interacting bilayer surfaces in a concentrated Dextran solution; their results confirm the validity of Equation 7.236.

The depletion interaction is present always when a film is formed from micellar surfactant solution; the micelles play the role of the smaller particles. At higher micellar concentrations, the volume exclusion interaction becomes more complicated: it follows the oscillatory curve depicted in Figure 7.35. In this case only, the first minimum (that at $h \to 0$) corresponds to the conventional depletion force.

7.4.5.3.4 Colloid Structural Forces

In the beginning of the twentieth century, Johnott [435] and Perrin [436] observed that foam films decrease their thickness by several stepwise transitions. The phenomenon was called stratification. Bruil and Lyklema [437] and Friberg et al. [438] studied systematically the effect of ionic surfactants and electrolytes on the occurrence of the stepwise transitions. Keuskamp and Lyklema [439] anticipated that some oscillatory interaction between the film surfaces must be responsible for the observed phenomenon. Kruglyakov et al. [440,441] reported the existence of stratification with emulsion films.

It should be noted that the explanation of the stepwise transitions in the film thickness as a layer-by-layer thinning of an ordered structure of spherical micelles within the film (see Figure 7.35) was first given by Nikolov et al. [401–405]. (Before that it was believed that the stepwise transitions are due to the formation of a lamella-liquid-crystal structures of surfactant molecules in the films.) One of the direct proofs was given by Denkov et al. [442,443] who succeeded in freezing foam films at various stages of stratification. The electron microscope pictures of such vitrified stratifying films containing latex particles (144 nm in diameter) and bacteriorhodopsin vesicles (44 nm in diameter) showed ordered particle arrays of hexagonal packing [443]. The mechanism of stratification was studied theoretically in Ref. [444], where the appearance and expansion of black spots in the stratifying films were described as being a process of condensation of vacancies in a colloid crystal of ordered micelles within the film.

The stable branches of the oscillatory curves have been detected by means of a thin-film-pressure balance [425,445,446]. Oscillatory forces due to surfactant micelles and microemulsion droplets have been measured also by means of a surface-force apparatus [428,447]; by atomic force microscopy [448]; by light-scattering method [449], in asymmetric films [450], in emulsion films [451], and in films containing solid colloidal spheres [401,402,452–455]. Such forces are observed also in more complex systems like protein solutions, surfactant–polymer mixtures, and ABA amphiphilic block copolymers [456–464].

7.4.5.4 Repulsive Hydration and Attractive Hydrophobic Forces

These two surface forces are observed in thin aqueous films. Their appearance is somehow connected with the unique properties of the water as solvent: small molecular size, large dipole moment, high dielectric constant, and formation of an extensive hydrogen-bonding network [34,465].

7.4.5.4.1 Repulsive Hydration Forces

In their experiments with films from aqueous electrolyte solutions confined between two mica surfaces, Israelachvili et al. [466,467] and Pashley [468,469] examined the validity of the DLVO theory at small film thickness. At electrolyte concentrations below 10^{-4} mol L^{-1} (KNO$_3$ or KCl), they observed the typical DLVO maximum (see Figure 7.17); however, at electrolyte concentrations higher than 10^{-3} M they did not observe the expected DLVO maximum and primary minimum. Instead a strong short-range repulsion was detected. Empirically, this force, called the hydration repulsion, appears to follow an exponential law [34]

$$f_{hydr}(h) = f_0 e^{-h/\lambda_0}$$

(7.237)

where the decay length $\lambda_0 \approx 0.6$–1.1 nm for 1:1 electrolytes and f_0 depends on the hydration of the surfaces but is usually about 3–30 mJ m^{-2}.

The physical importance of the hydration force is that it stabilizes some dispersions preventing coagulation in the primary minimum. It is believed that the hydration force is connected with the binding of strongly hydrated ions at the interface. This is probably the explanation of the experimental results of Healy et al. [470] who found that even high electrolyte concentrations cannot cause coagulation of amphoteric latex particles due to binding of strongly hydrated Li$^+$ ions at the particle surfaces. If the Li$^+$ ions are replaced by weakly hydrated Cs$^+$ ions, the hydration repulsion becomes negligible, compared with the van der Waals attraction, and the particles coagulate as predicted by the DLVO theory. Hence, the hydration repulsion can be regulated by ion exchange.

For the time being, there is no generally accepted theory of the repulsive hydration forces. The first quantitative theory by Marčelja and Radič [471] attributes the hydration repulsion to the water structuring in the vicinity of a surface, which leads to the appearance of a decaying polarization profile. This model was further developed by other authors [472,473]. A different approach was proposed by Jönsson and Wennerström [474], who developed an explicit electrostatic model based on the image charge concept. Leikin and Kornyshev [475] combined the main features of the solvent polarization [471] and image charge [474] models in a nonlocal electrostatic theory of the repulsion between electroneutral lipid bilayers. On the other hand, Israelachvili and Wennerström [476] demonstrated that the short-range repulsion between lipid membranes may also be a manifestation of undulation, peristaltic and protrusion forces, which are due to thermally excited fluctuations at the interfaces (see Section 7.4.5.5).

In the case of charged surfaces, Henderson and Losada-Cassou [413,477] pointed out that the physical origin of the hydration repulsion can be attributed to the presence of a layer of lower dielectric constant, ε, in the vicinity of the interface. It was demonstrated that the DLVO theory complemented with such a layer correctly predicts the dependence of hydration repulsion on the electrolyte concentration. A further extension of this approach was given by Basu and Sharma [478], who incorporated the effect of the variation of ε in the theory of electrostatic disjoining pressure. Their model provides quantitative agreement with the experimental data at low electrolyte concentration and pH, and qualitative agreement at higher electrolyte concentration and pH.

A further development of the theory [479] demonstrates that if the theory of Basu and Sharma [478] is further extended by taking into account the finite size of the ions, then quantitative agreement between theory and experiment can be achieved for all electrolyte concentrations and pH. In summary, the hydration repulsion can be attributed to the interplay of the following two effects, which are neglected in the conventional DLVO theory.

The effect of the dielectric saturation is due to the presumed preferential alignment of the solvent dipoles near a charged surface. From the viewpoint of the macroscopic continuum theory, this effect is represented by a reduced dielectric permittivity, ε, in the vicinity of the interface [478,479]. We can use the Booth [480] formula to relate ε with the intensity of the electric field, $E = |\mathrm{d}\psi/\mathrm{d}x|$:

$$\varepsilon(E) = n_{\mathrm{r}}^2 + (\varepsilon_{\mathrm{b}} - n_{\mathrm{r}}^2)\frac{3}{\beta E}\left(\coth \beta E - \frac{1}{\beta E}\right), \quad \beta \equiv \frac{5\mu(n_{\mathrm{r}}^2 + 2)}{2kT} \tag{7.238}$$

where
$n_{\mathrm{r}} = 1.33$ is the refractive index of water
ε_{b} is the bulk dielectric constant (for $E = 0$)
$\mu = 1.85 \times 10^{-18}$ CGSE units is the dipole moment of water

Equation 7.238 is used by Basu and Sharma [478] to calculate the hydration repulsion. However, it turns out that the finite size of the ions also gives a considerable contribution to the hydration repulsion.

The volume excluded by the ions becomes important in relatively thin films, insofar as the counterion concentration is markedly higher in the vicinity of a charged surface. This effect was taken into account [479] by means of the Bikerman equation [481,482]:

$$n_i(x) = \frac{1 - v\sum_k n_k(x)}{1 - v\sum_k n_{k0}} n_{i0} \exp U_i \tag{7.239}$$

Here, x is the distance to the charged surface; n_i and U_i are, respectively, the number density and the potential energy (in kT units) of the ith ion in the double electric layer; n_{i0} is the value of n_i in the bulk solution; the summation is carried out over all ionic species; v is the average excluded volume per counterion and can be theoretically estimated [479] as being equal to eight times the volume of the hydrated counterion.

The electrostatic boundary problem accounting for the effects of dielectric saturation and ionic excluded volume can be formulated as follows [479]. The electric potential in the film, $\psi(x)$, satisfies the Poisson equation

$$\varepsilon_0 \frac{\mathrm{d}}{\mathrm{d}x}\left(\varepsilon \frac{\mathrm{d}\psi}{\mathrm{d}x}\right) = -\rho(x) \tag{7.240}$$

where ε is given by Equation 7.238 and the surface charge density, $\rho(x)$, is determined from Equation 7.239:

$$\rho(x) = \frac{\sum_i Z_i e n_i^* \exp U_i}{1 + v \sum_i n_i^* \exp U_i}, \quad n_i^* \equiv \frac{n_{i0}}{1 + v \sum_k n_{k0}} \tag{7.241}$$

The potential energy U_i accounts for both the mean-field electrostatic energy and the energy of hydration [478]

$$U_i = -\frac{Z_{ie}\psi + W_i}{kT}, \quad W_i \equiv \frac{Z_i^2 e^2}{d_i}\left[\frac{1}{\varepsilon(E)} - \frac{1}{\varepsilon_b}\right] \tag{7.242}$$

where d_i is the diameter of the ith ion. The boundary condition of the charged surface reads:

$$\left.\frac{\mathrm{d}\psi}{\mathrm{d}x}\right|_{x=0} = -\frac{\sigma_s}{\varepsilon_0 \varepsilon_s}, \quad \varepsilon_s \equiv \varepsilon|_{x=0} \tag{7.243}$$

where σ_s is determined by the Stern isotherm, Equation 7.194. The boundary problem (Equations 7.240 through 7.243) can be solved numerically. Then, the total electrostatic disjoining pressure can be calculated by means of the expression [479]

$$\Pi_{el}^{tot} \equiv -\int_0^{\psi_m} \rho_m \mathrm{d}\psi = \frac{kT}{v}\ln\left[\frac{1 + v\sum_k n_k^* \exp(-Z_i e \psi_m/kT)}{1 + v\sum_k n_k^*}\right] \tag{7.244}$$

where the subscript m denotes values of the respective variables at the midplane of the film. Finally, the non-DLVO hydration force can be determined as an excess over the conventional DLVO electrostatic disjoining pressure:

$$\Pi_{hr} \equiv \Pi_{el}^{tot} - \Pi_{el}^{DLVO} \tag{7.245}$$

where Π_{el}^{DLVO} is defined by Equation 7.189, which can be deduced from Equation 7.244 for $v \to 0$ and $\varepsilon \equiv \varepsilon_b$. Note that both the effect of $v \neq 0$ and $\varepsilon \neq \varepsilon_b$ lead to a larger value of ψ_m, which contributes to a positive (repulsive) Π_{hr}.

The theory [479] based on Equations 7.238 through 7.245 is in excellent numerical agreement with the experimental data of Pashley [469,470], Claesson et al. [483], and Horn et al. [484]. An illustration is given in Figure 7.38, where v is equal to eight times the volume of the hydrated Na^+ ion. In all cases, acceptable values of the adjustable parameters, σ_{max} and $\Phi_a = -\Delta\mu_2^{(0)}$ in the Stern isotherm are obtained (see Equations 7.49 and 7.194). It is interesting to note that in all investigated cases the effect of $v \neq 0$ gives about four times larger contribution in Π_{hr} compared to the effect of $\varepsilon \neq \varepsilon_b$.

7.4.5.4.2 Hydrophobic Attraction

The water does not spread spontaneously on hydrocarbons and the aqueous films on hydrophobic surfaces are rather unstable [485]. The cause for these effects is an attractive hydrophobic force, which is found to appear in aqueous films in contact with hydrophobic surfaces. The experiments showed, that the nature of the hydrophobic surface force is different from the van der Waals and double layer interactions [486–490]. The measurements indicate that the hydrophobic interaction decays exponentially with the increase of the film thickness, h. The hydrophobic free energy per unit area of the film can be described by means of the equation [34]

$$f_{\text{hydrophobic}} = -2\gamma e^{-h/\lambda_0} \tag{7.246}$$

where typically $\gamma = 10$–50 mJ/m^2, and $\lambda_0 = 1$–2 nm in the range $0 < h < 10$ nm. Larger decay length, $\lambda_0 = 12$–16 nm, was reported by Christenson et al. [490] for the range $20 < h < 90$ nm. This long-range attraction could entirely dominate the
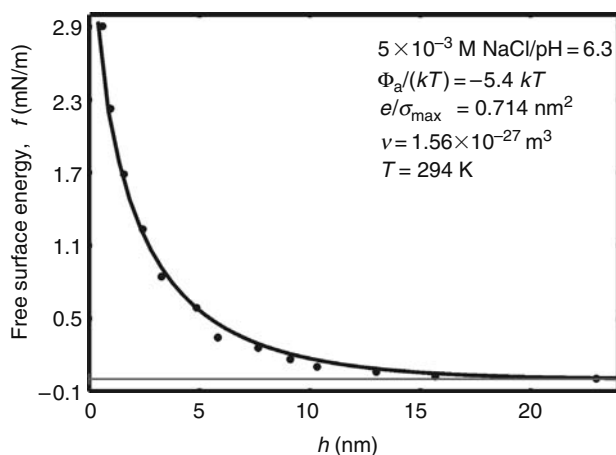
FIGURE 7.38 Comparison of theory [479] with experimental data [468] measured with solution of 5 mM NaCl at pH $= 6.3$ between mica surfaces: the total interaction free energy, $f = f_{vw} + f_{el} + f_{hr}$, is plotted against the film thickness h (see Equations 7.173 and 7.244). The solid line is the best fit calculated with adsorption energy $\Phi_a = -5.4~kT$ per Na^+ ion, and area per surface ionizable group 0.714 nm^2.

van der Waals forces. Ducker et al. [491] measured the force between hydrophobic and hydrophilic silica particles and air bubbles by means of an atomic force microscope.

It was found experimentally that 1:1 and 2:2 electrolytes reduce considerably the long-range part of the hydrophobic attraction [489,490]. The results suggest that this reduction could be due to ion adsorption or ion exchange at the surfaces rather than to the presence of electrolyte in the solution itself. Therefore, the physical implication (which might seem trivial) is that the hydrophobic attraction across aqueous films can be suppressed by making the surfaces more hydrophilic. Besides, some special polar solutes are found to suppress the hydrophobic interaction at molecular level in the bulk solution, e.g., urea, $(NH_2)_2CO$, dissolved in water can cause proteins to unfold. The polar solutes are believed to destroy the hydrogen-bond structuring in water; therefore they are sometimes called chaotropic agents [34].

There is no generally accepted explanation of the hydrophobic surface force. One of the possible explanations is that the hydrogen bonding in water (and other associated liquids) could be the main underlying factor [34,492]. The related qualitative picture of the hydrophobic interaction is the following. If there were no thermal motion, the water molecules would form an ice-like tetrahedral network with four nearest neighbors per molecule (instead of 12 neighbors at close packing), because this configuration is favored by the formation of hydrogen bonds. However, due to the thermal motion a water molecule forms only about 3–3.5 transient hydrogen bonds with its neighbors in the liquid [493] with lifetime of a hydrogen bond being about 10^{-11} s. When a water molecule is brought in contact with a nonhydrogen-bonding molecule or surface, the number of its possible favorable configurations is decreased. This effect also reduces the number of advantageous configurations of the neighbors of the subsurface water molecules and some ordering propagates in the depth of the liquid. This ordering might be initiated by the orientation of the water dipoles at a water–air or water–hydrocarbon interface with the oxygen atom being oriented toward the hydrophobic phase [494–497]. Such ordering in the vicinity of the hydrophobic wall is entropically unfavorable. When two hydrophobic surfaces approach each other, the entropically unfavored water is ejected into the bulk, thereby reducing the total free energy of the system. The resulting attraction could in principle explain the hydrophobic forces. The existing phenomenological theory [492] has been generalized to the case of asymmetric films [498], and has been applied to interpret experimental data for breakage of emulsion and foam films at low surfactant and high electrolyte concentrations [499,500].

Another hypothesis for the physical origin of the hydrophobic force considers a possible role of formation of gaseous capillary bridges between the two hydrophobic surfaces (see Figure 7.13a) [34,501,502]. In this case, the hydrophobic force would be a kind of capillary-bridge force (see e.g., Chapter 11 in Ref. [35]). Such bridges could appear spontaneously, by nucleation (spontaneous dewetting), when the distance between the two surfaces becomes smaller than a certain threshold value, of the order of several hundred nanometers. Gaseous bridges could appear even if there is no dissolved gas in the water phase; the pressure inside a bridge can be as low as the equilibrium vapor pressure of water (23.8 mm Hg at 25°C) owing to the high interfacial curvature of nodoid-shaped bridges (see Section 7.3.1.2.3 and Ref. [35]). A number of studies [503–511] provides evidence in support of the capillary-bridge origin of the long-range hydrophobic surface force. In particular, the observation of steps in the experimental data was interpreted as an indication for separate acts of bridge nucleation [507].

In summary, it is more likely that two different effects are called hydrophobic interaction: (1) the known molecular hydrophobic effect [34,512,513] which could bring about an attractive surface force of decay length about 15 nm [492,498–500], and (2) formation of capillary-bridge cavities between two hydrophobic surfaces [501–511]. For the time being, there are sufficiently evidences showing that both effects exist in reality.

7.4.5.5 Fluctuation Wave Forces

All fluid interfaces, including liquid membranes and surfactant lamellas, are involved in a thermal fluctuation wave motion. The configurational confinement of such thermally exited modes within the narrow space between two approaching interfaces gives rise to short-range repulsive surface forces, which are considered below.

7.4.5.5.1 Undulation Forces

The undulation force arises from the configurational confinement related to the bending mode of deformation of two fluid bilayers. This mode consists in undulation of the bilayer at constant bilayer area and thickness (Figure 7.39a). Helfrich et al. [514,515] established that two such bilayers, apart at a mean distance h, experience a repulsive disjoining pressure given by the expression:

$$\Pi_{und}(h) = \frac{3\pi^2 (kT)^2}{64 k_t h^3} \tag{7.247}$$

where k_t is the bending elastic modulus of the bilayer as a whole. The experiment [516] and the theory [35,192] show that k_t is of the order of 10^{-19} J for lipid bilayers. The undulation force has been measured, and the dependence $\Pi_{und} \propto h^{-3}$ confirmed experimentally [517–519].

7.4.5.5.2 Peristaltic Force

The peristaltic force [476] originates from the configurational confinement related to the peristaltic (squeezing) mode of deformation of a fluid bilayer (Figure 7.39b). This mode of deformation consists in fluctuation of the bilayer thickness at fixed position of the bilayer midsurface. The peristaltic deformation is accompanied with extension of the bilayer surfaces. Israelachvili and Wennerstöm [476] demonstrated that the peristaltic disjoining pressure is related to the stretching modulus, k_s, of the bilayer:

$$\Pi_{per}(h) \approx \frac{2(kT)^2}{\pi^2 k_s h^5} \tag{7.248}$$

The experiment [520] gives values of k_s varying between 135 and 500 mN m^{-1}, depending on temperature and composition of the lipid membrane.
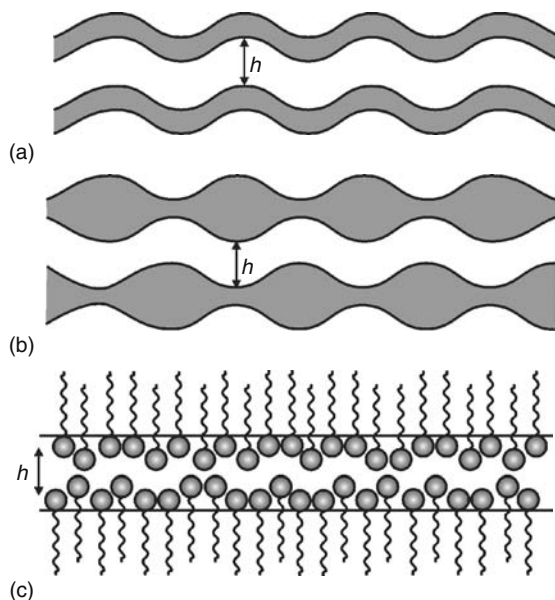
**FIGURE 7.39** Surface forces due to configurational confinement of thermally exited modes into a narrow region of space between two approaching interfaces: (a) bending mode of membrane fluctuations giving rise to the undulation force; (b) squeezing mode of membrane fluctuations producing the peristaltic force; (c) fluctuating protrusion of adsorbed amphiphilic molecules engendering the protrusion surface force.

7.4.5.5.3 Protrusion Force

Due to the thermal motion, the protrusion of an amphiphilic molecule in an adsorption monolayer (or micelle) may fluctuate about the equilibrium position of the molecule (Figure 7.39c). In other words, the adsorbed molecules are involved in a discrete wave motion, which differs from the continuous modes of deformation considered above. Aniansson et al. [521,522] analyzed the energy of protrusion in relation to the micelle kinetics. They assumed the energy of molecular protrusion to be of the form $u(z) = \alpha z$, where z is the distance out of the surface ($z > 0$) and determined $\alpha \approx 3 \times 10^{-11}$ J m^{-1} for single-chained surfactants. The average length of the Brownian protrusion of the amphiphilic molecules is on the order of $\lambda \equiv kT/\alpha$ [476].

By using a mean-field approach Israelachvili and Wennerström [476] derived the following expression for the protrusion disjoining pressure which appears when two protrusion zones overlap (Figure 7.39c):

$$\Pi_{\text{protr}}(h) = \frac{\Gamma kT}{\lambda} \frac{(h/\lambda) \exp(-h/\lambda)}{1 - (1 + h/\lambda) \exp(-h/\lambda)} \tag{7.249}$$

where

λ is the characteristic protrusion length; $\lambda = 0.14$ nm at 25°C for surfactants with paraffin chain
Γ is the number of protrusion sites per unit area

Note that Π_{protr} decays exponentially for $h \gg \lambda$, but $\Pi_{\text{protr}} \propto h^{-1}$ for $h < \lambda$, i.e., Π_{protr} is divergent at $h \to 0$. The respective interaction free energy (per unit film area) is

$$f_{\text{protr}} = \int_{h}^{\infty} \Pi_{\text{protr}}(\hat{h}) d\hat{h} = -\Gamma kT \ln[1 - (1 + h/\lambda) \exp(-h/\lambda)] \tag{7.250}$$

Equation 7.249 was found to fit well experimental data for the disjoining pressure of liquid films stabilized by adsorbed protein molecules: bovine serum albumin (BSA) [523]. In that case, Γ was identified with the surface density of the loose secondary protein adsorption layer, while λ turned out to be about the size of the BSA molecule [523]. A more detailed statistical approach to the theoretical modeling of protrusion force was recently proposed [524].

7.5 HYDRODYNAMIC INTERACTIONS IN DISPERSIONS

7.5.1 BASIC EQUATIONS AND LUBRICATION APPROXIMATION

In addition to the surface forces (see Section 7.4), two colliding particles in a liquid medium also experience hydrodynamic interactions due to the viscous friction, which can be rather long range (operative even at distances above 100 nm). The hydrodynamic interaction among particles depends on both the type of fluid motion and the type of interfaces. The quantitative description of this interaction is based on the classical laws of mass conservation and momentum balance for the bulk phases [525–530]:

$$\frac{\partial \rho}{\partial t} + \text{div}(\rho \mathbf{v}) = 0 \tag{7.251}$$

$$\frac{\partial}{\partial t}(\rho \mathbf{v}) + \text{div}(\rho \mathbf{v}\mathbf{v} - \mathbf{P} - \mathbf{P}_{\text{b}}) = 0 \tag{7.252}$$

where

ρ is the mass density
$\mathbf{v}$ is the local mass average velocity
$\mathbf{P}$ is the hydrodynamic stress tensor
$\mathbf{P}_{\text{b}}$ is the body-force tensor which accounts for the action of body forces such as gravity, electrostatic forces (the Maxwell tensor), etc.

In a fluid at rest, and in the absence of body forces, the only contact force given by the hydrodynamic stress tensor is the scalar thermodynamic pressure, p, and $\mathbf{P}$ can be written as $\mathbf{P} = -p\mathbf{I}$, where $\mathbf{I}$ is the unit tensor in space. For a fluid in motion, the viscous forces become operative and

$$\mathbf{P} = -p\mathbf{I} + \mathbf{T} \tag{7.253}$$

where $\mathbf{T}$ is the viscous stress tensor. From the definition of the stress tensor (Equation 7.253), it follows that the resultant hydrodynamic force, $\mathbf{F}$, exerted by the surrounding fluid on the particle surface, S, and the torque, $\mathbf{M}$, applied to it are given by the expressions [525,527]

$$\mathbf{F} = \int_S \mathbf{P} \cdot \mathbf{n}\, dS, \quad \mathbf{M} = \int_S \mathbf{r}_0 \times \mathbf{P} \cdot \mathbf{n}\, dS \tag{7.254}$$

where
  $\mathbf{r}_0$ is the position vector of a point of S with respect to an arbitrarily chosen coordinate origin
  $\mathbf{n}$ is the vector of the running unit normal to the surface S

In the presence of body forces, the total force, $\mathbf{F}_{\text{tot}}$, and torque, $\mathbf{M}_{\text{tot}}$, acting on the particle surface are

$$\mathbf{F}_{\text{tot}} = \mathbf{F} + \int_S \mathbf{P}_b \cdot \mathbf{n}\, dS, \quad \mathbf{M}_{\text{tot}} = \mathbf{M} + \int_S \mathbf{r}_0 \times \mathbf{P}_b \cdot \mathbf{n}\, dS \tag{7.255}$$

The dependence of the viscous stress on the velocity gradient in the fluid is a constitutive law, which is usually called the bulk rheological equation. The general linear relation between the viscous stress tensor, $\mathbf{T}$, and the rate of strain tensor,

$$\mathbf{D} = \frac{1}{2}[\nabla \mathbf{v} + (\nabla \mathbf{v})^{\mathsf{T}}] \tag{7.256}$$

(the superscript T denotes conjugation) reads

$$\mathbf{T} = \zeta(\text{div } \mathbf{v})\mathbf{I} + 2\eta\left[\mathbf{D} - \frac{1}{3}(\text{div } \mathbf{v})\mathbf{I}\right] \tag{7.257}$$

The latter equation is usually referred as the Newtonian model or Newton's law of viscosity. In Equation 7.257, ζ is the dilatational bulk viscosity and η is the shear bulk viscosity. The usual liquids comply well with the Newtonian model. On the other hand, some concentrated macromolecular solutions, colloidal dispersions, gels, etc., may exhibit non-Newtonian behavior; their properties are considered in detail in some recent review articles and books [530–533]. From Equations 7.252 and 7.257, one obtains the Navier–Stokes equation [534,535]:

$$\rho\frac{d\mathbf{v}}{dt} = -\nabla p + \left(\zeta + \frac{1}{3}\eta\right)\nabla(\nabla \cdot \mathbf{v}) + \eta\nabla^2\mathbf{v} + \mathbf{f}, \quad (\mathbf{f} \equiv \Delta\mathbf{P}_b) \tag{7.258}$$

for homogeneous Newtonian fluids, for which the dilatational and shear viscosities, ζ and η, do not depend on the spatial coordinates. In Equation 7.258, the material derivative d/dt can be presented as a sum of a local time derivative and a convective term:

$$\frac{d}{dt} = \frac{\partial}{\partial t} + (\mathbf{v} \cdot \nabla) \tag{7.259}$$

If the density, ρ, is constant, the equation of mass conservation (Equation 7.251) and the Navier–Stokes Equation 7.258 reduce to

$$\text{div } \mathbf{v} = 0, \quad \rho\frac{d\mathbf{v}}{dt} = -\nabla p + \eta\nabla^2\mathbf{v} + \mathbf{f} \tag{7.260}$$

For low shear stresses in the dispersions, the characteristic velocity, V_z, of the relative particle motion is small enough in order for the Reynolds number, $\text{Re} = \rho V_z L/\eta$, to be a small parameter, where L is a characteristic length scale. In this case, the inertia terms in Equations 7.258 and 7.260 can be neglected. Then, the system of equations becomes linear and the different types of hydrodynamic motion become additive [368,536,537]; e.g., the motion in the liquid flow can be presented as a superposition of elementary translation and rotational motions.

The basic equations can be further simplified in the framework of the lubrication approximation, which can be applied to the case when the Reynolds number is small and when the distances between the particle surfaces are much smaller than their
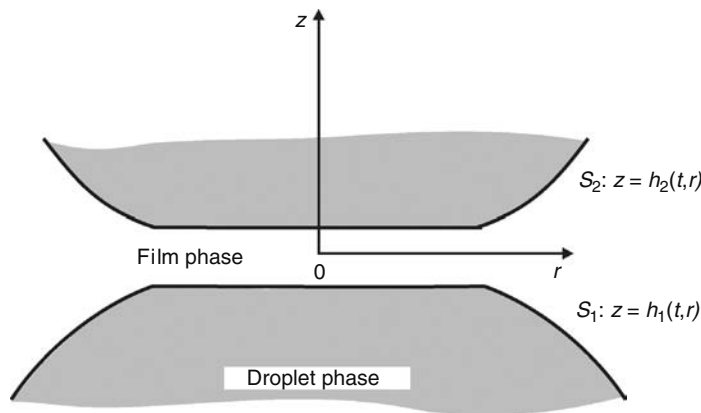
FIGURE 7.40 Sketch of a plane-parallel film formed between two identical fluid particles.

radii of curvature (Figure 7.40) [538,539]. There are two ways to take into account the molecular interactions between the two particles across the liquid film intervening between them: (1) the body force approach; (2) the disjoining pressure approach. The former approach treats the molecular forces as components of the body force, $\mathbf{f}$ (Equation 7.258); consequently, they give contributions to the normal and tangential stress boundary conditions [540,541]. In the case (2), the molecular interactions are incorporated only in the normal stress boundary conditions at the particle surfaces. When the body force can be expressed as a gradient of potential, $\mathbf{f} = \nabla U$ (that is $\mathbf{P}_b = U\mathbf{I}$), the two approaches are equivalent [542].

If two particles are interacting across an electrolyte solution, the equations of continuity and the momentum balance, Equation 7.260, in lubrication approximation read [543]

$$\nabla_{II} \cdot \mathbf{v}_{II} + \frac{\partial v_z}{\partial z} = 0, \quad \eta \frac{\partial^2 \mathbf{v}_{II}}{\partial z^2} = \nabla_{II} p + kT \sum_{i=1}^{N} z_i c_i \nabla_{II} \Phi, \quad \frac{\partial p}{\partial z} + kT \sum_{i=1}^{N} z_i c_i \frac{\partial \Phi}{\partial z} = 0 \tag{7.261}$$

where $\mathbf{v}_{II}$ and ∇_{II} are the projection of the velocity and the gradient operator on the plane xy; the z-axis is (approximately) perpendicular to the film surfaces S_1 and S_2 (see Figure 7.40); $c_i = c_i(r, z, t)$ is the ion concentration ($i = 1, 2, \ldots, N$); Φ is the dimensionless electric potential (see Sections 7.2.1.2 and 7.2.2). It turns out that in lubrication approximation, the dependence of the ionic concentrations on the z coordinate comes through the electric potential $\Phi(r, z, t)$: we obtain a counterpart of the Boltzmann equation $c_i = c_{i,n}(r, z, t) \exp(-z_i \Phi)$, where $c_{i,n}$ refers to an imaginary situation of switched off electric charges ($\Phi \equiv 0$). The kinematic boundary condition for the film surfaces has the form:

$$\frac{\partial h_j}{\partial t} + \mathbf{u}_j \cdot \nabla_{II} h_j = (v_z)_j \quad \text{at} \quad S_j(j = 1,2) \tag{7.262}$$

where $\mathbf{u}_i$ is the velocity projection in the plane xy at the corresponding film surface, S_i, which is close to the interfacial velocity; $(v_z)_i$ is the z component of the velocity at the surface S_i. The general solution of Equations 7.261 and 7.262 could be written as:

$$p = p_n + kT \sum_{i=1}^{N} (c_i - c_{i,n}) \tag{7.263}$$

$$\mathbf{v}_{II} = \frac{(z - h_1)(z - h_2)}{2\eta} \nabla_{II} p_n + \frac{h_2 - z}{h} \mathbf{u}_1 + \frac{z - h_1}{h} \mathbf{u}_2$$

$$+ \frac{kTh^2}{4\eta} \sum_{i=1}^{N} \left[m_{2,i}(z) - \frac{h_2 - z}{h} m_{2,i}(h_1) - \frac{z - h_1}{h} m_{2,i}(h_2) \right] \nabla_{II} c_{i,n} \tag{7.264}$$

Here $h = h_2 - h_1$ is the local film thickness; the meaning of $p_n(x, y, t)$ is analogous to that of $c_{i,n}(x, y, t)$; the functions, $m_{k,i}(z)$, account for the distribution of the ith ionic species in the EDL:

$$m_{0,i} \equiv \exp(-z_i \Phi) - 1, \quad m_{k,i}(z) \equiv \frac{2}{h} \int_0^z m_{k-1,i}(\hat{z}) d\hat{z} \ (k = 1, 2, 3, \ i = 1, 2, \ldots, N) \tag{7.265}$$

The equation determining the local thickness, h, of a film with fluid surfaces (or, alternatively, determining the pressure distribution at the surfaces of the gap between two solid particles of known shape) is

$$\frac{\partial h}{\partial t} + \nabla_{\mathrm{II}} \cdot \left[\frac{h}{2}(\mathbf{u}_1 + \mathbf{u}_2) \right] = \frac{1}{12\eta} \nabla_{\mathrm{II}} \cdot (h^3 \nabla_{\mathrm{II}} p) + \frac{kT}{8\eta} \nabla_{\mathrm{II}} \cdot \left[h^3 \sum_{i=1}^{N} [m_{2,i}(h_1) + m_{2,i}(h_2) - m_{3,i}(h_2) + m_{3,i}(h_1)] \nabla_{\mathrm{II}} c_{i,\mathrm{n}} \right] \quad (7.266)$$

The problem for the interactions upon central collisions of two axisymmetric particles (bubbles, droplets, or solid spheres) at small surface-to-surface distances was first solved by Reynolds [538] and Taylor [544,545] for solid surfaces and by Ivanov et al. [546,547] for films of uneven thickness. Equation 7.266 is referred to as the general equation for films with deformable surfaces [546,547] (see also the more recent reviews [223,548,549]). The asymptotic analysis [550–552] of the dependence of the drag and torque coefficient of a sphere, which is translating and rotating in the neighborhood of a solid plate, is also based on Equation 7.266 applied to the special case of stationary conditions.

Using Equation 7.255, one can obtain expressions for the components of the total force exerted on the particle surface, S, in the lubrication approximation:

$$F_{\mathrm{tot},z} = \int_S \left[p_{\mathrm{n}} + kT \sum_{i=1}^{N} (c_{is} - c_{i,\mathrm{n}}) + \Pi_{\mathrm{nel}} - p_{\infty} \right] dS \quad (7.267)$$

$$\mathbf{F}_{\mathrm{tot},\mathrm{II}} = -\int_S \left(\eta \frac{\partial \mathbf{v}_{\mathrm{II}}}{\partial z} + \frac{2kT}{\kappa_{\mathrm{c}}^2} \frac{\partial \Phi}{\partial z} \nabla_{\mathrm{II}} \Phi \right) dS \quad (7.268)$$

where p_{∞} is the pressure at infinity in the meniscus region (Figure 7.40) and $\Pi_{\mathrm{nel}} \equiv \Pi - \Pi_{\mathrm{el}}$ accounts for the contribution of nonelectrostatic (nondouble layer) forces to the disjoining pressure (see Section 7.4). The normal and the lateral force resultants, F_z and $\mathbf{F}_{\mathrm{II}}$, are the hydrodynamic resistance and shear force, respectively.

7.5.2 INTERACTION BETWEEN PARTICLES OF TANGENTIALLY IMMOBILE SURFACES

The surfaces of fluid particles can be treated as tangentially immobile when they are covered by dense surfactant adsorption monolayers that can resist tangential stresses [223,548,549,553,554]. In such a case, the bubbles or droplets behave as flexible balls with immobile surfaces. When the fluid particles are rather small (say, microemulsion droplets), they can behave like hard spheres; therefore, some relations considered below, which were originally derived for solid particles, can be also applied to fluid particles.

7.5.2.1 Taylor and Reynolds Equations, and Influence of the Particle Shape

In the case of two axisymmetric particles moving along the z-axis toward each other with velocity $V_z = -dh/dt$ Equation 7.266 can be integrated, and from Equation 7.267 the resistance force can be calculated. The latter turns out to be proportional to the velocity and bulk viscosity and depends on the shape in a complex way. For particles with tangentially immobile surfaces and without surface electric charge ($\mathbf{u}_1 = \mathbf{u}_2 = 0$, $\Phi = 0$) Charles and Mason [555] have derived

$$F_z = 6\pi\eta V_z \int_0^{\infty} \frac{r^3}{h^3} dr \quad (7.269)$$

where r is the radial coordinate in a cylindrical coordinate system. In the case of two particles of different radii, R_1 and R_2, film radius R, and uniform film thickness h (see Figure 7.41), from Equation 7.269 the following expression can be derived [556,557]:

$$F_z = \frac{3}{2}\pi\eta V_z \frac{R_*^2}{h} \left(1 + \frac{R^2}{hR_*} + \frac{R^4}{h^2 R_*^2} \right), \quad R_* \equiv \frac{2R_1 R_2}{(R_1 + R_2)} \quad (7.270)$$

This geometrical configuration has proved to be very close to the real one in the presence of electrostatic disjoining pressure [239]. The Charles–Mason formula (Equation 7.269) and Equation 7.267 have been used to calculate the velocity of film
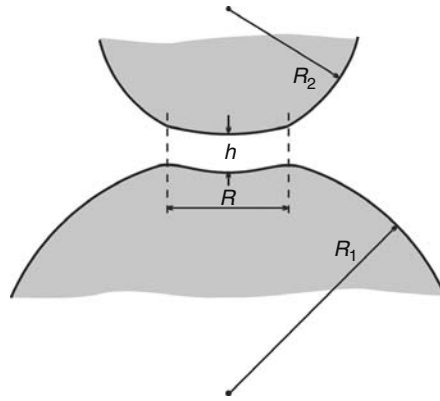
FIGURE 7.41 Sketch of a film between two nonidentical fluid particles of radii R_1 and R_2. The film thickness and radius are denoted by h and R.

thinning for a large number of cases, summarized by Hartland [558] in tables for more than 50 cases (two- and three-dimensional small drops, fully deformed large drops subjected to large forces, two-dimensional hexagonal drops, etc.).

Setting $R = 0$ in Equation 7.270, we can derive a generalized version of the Taylor formula [544,545] for the velocity of approach of two nondeformable spheres under the action of an external (nonviscous) force, F_z [557]:

$$V_{Ta} = \frac{2hF_z}{3\pi\eta R_*^2} \tag{7.271}$$

When a solid sphere of radius R_c approaches a flat solid surface, we may use the Taylor formula with $R_* = 2R_c$ when the gap between the two surfaces is small compared to R_c. In fact Equation 7.271 does not appear in any G.I. Taylor's publications but in the article by Hardy and Bircumshaw [544] it was published (see Ref. [545]).

In the case when two plane-parallel ellipsoidal discs of tangentially immobile surfaces are moving against each other under the action of an external force, $F_{tot,z}$, from Equations 7.266 and 7.267, we can derive the Reynolds equation [538] for the velocity of film thinning:

$$V_{Re} = \frac{F_z h^3 (a^2 + b^2)}{3\pi\eta a^3 b^3} \tag{7.272}$$

where a and b are the principal radii of curvature. If there is a contribution of the disjoining pressure, Π, the Reynolds equation for a flat axisymmetrical film ($a = b = R$) between two fluid particles of capillary pressure P_c can be written in the form [202]:

$$V_{Re} = \frac{2F_z h^3}{3\pi\eta R^4} = \frac{2(P_c - \Pi)h^3}{3\eta R^2} \tag{7.273}$$

From Equations 7.270 and 7.273 the ratio between the Reynolds velocity and the velocity of film thinning for a given force is obtained. In Figure 7.42, this ratio is plotted as a function of the film thickness, h, divided by inversion thickness, $h_i = R^2/R_*$ [548]. We see that the influence of the viscous friction in the zone encircling the film (this influence is not accounted for in Equation 7.273) decreases the velocity of thinning about three times for the larger distances, whereas for the small distances this influence vanishes. From Equations 7.270 and 7.271, the ratio between the Taylor velocity (corresponding to nondeformable spheres) and the approaching velocity of two deformable particles can be calculated. The dependence of this ratio on the distance between the particles for different film radii is illustrated in Figure 7.43. We see that an increase of the film radius, R, and a decrease of the distance, h, lead to a decrease in the velocity. The existence of a film between the particles can decrease the velocity of particle approach, V_z, by several orders of magnitude.

7.5.2.2 Interactions among Nondeformable Particles at Large Distances

The hydrodynamic interaction between members of a group of small particles suspended in a viscous fluid has fundamental importance for the development of adequate models for calculating the particle collective diffusion coefficient and the effective viscosity of suspension [368,536,554,559,560]. The Stokesian resistance is determined for a number of specific particle shapes
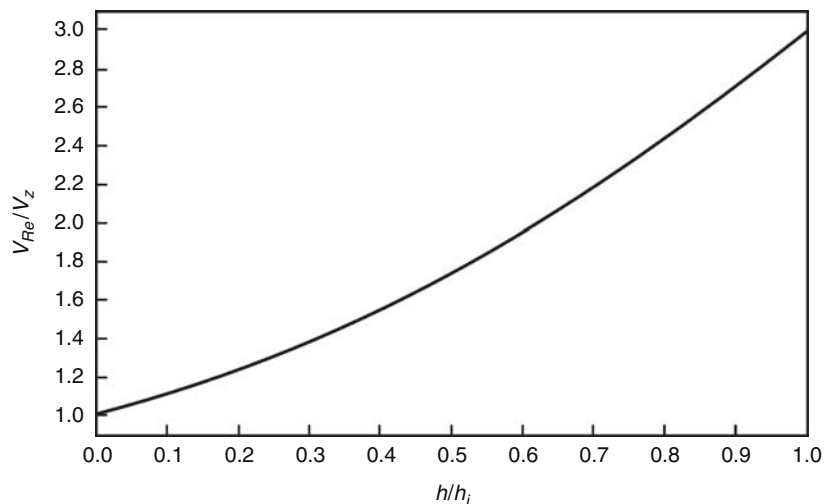
FIGURE 7.42 Plot of V_{Re}/V_z versus h/h_i for two fluid particles (Equation 7.270) which are deformed because of the viscous friction in the transition zone between the film and the bulk phase (see Figure 7.41).

under the condition that the particles are located so far apart that the hydrodynamic interactions can be ignored [536]. A general theory applicable to a single particle of arbitrary shape has been developed by Brenner [561,562]. This method gives the first-order correction (with respect to the particle volume fraction) of the viscosity and diffusivity. Matrix relations between resistance and velocity for the pure translational and rotational motions of the members of a general multiparticle system involved in a linear shear flow are given by Brenner and O'Neill [563]. In principle, from these relations we can further obtain the higher order terms in the series expansion of the viscosity and diffusivity with respect to the powers of the particle volume fraction.

At present, the only multiparticle system for which exact values of the resistance tensors can be determined is that of two spheres. It turns out that all types of hydrodynamic flows related to the motion of two spherical particles (of radii R_1 and R_2) can be expressed as superpositions of the elementary processes depicted in Figure 7.44 [368,527,536,537,564–573].

The first particle moves toward the second immobile particle and rotates around the line of centers (see Figure 7.44a). This is an axisymmetric rotation problem (a two-dimensional hydrodynamic problem) which was solved by Jeffery [565] and Stimson and Jeffery [566] for two identical spheres moving with equal velocities along their line of centers. Cooley and O'Neill [567,568] calculated the forces for two nonidentical spheres moving with the same speed in the same direction,
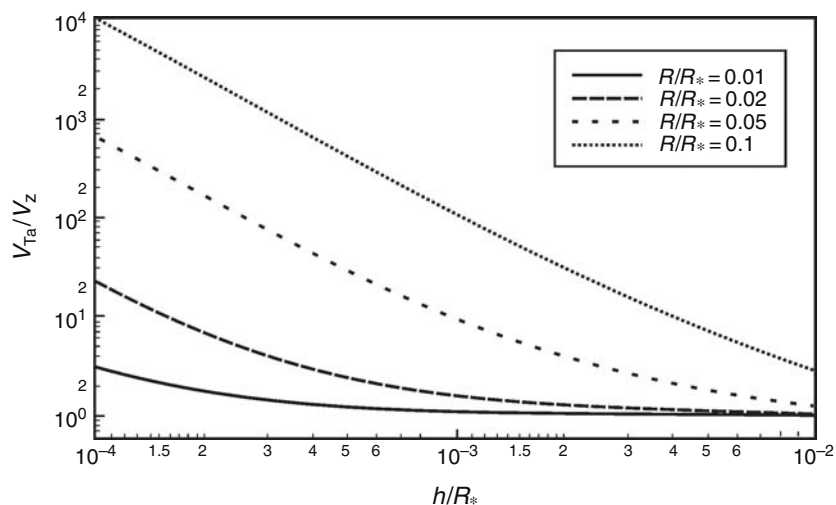
FIGURE 7.43 Plot of V_{Ta}/V_z versus h/R_* for various values of the dimensionless film radius, R/R_*. V_{Ta} corresponds to two nondeformed (spherical) particles (Equation 7.271), whereas V_z is the velocity of approach of two deformed particles (Equation 7.270).
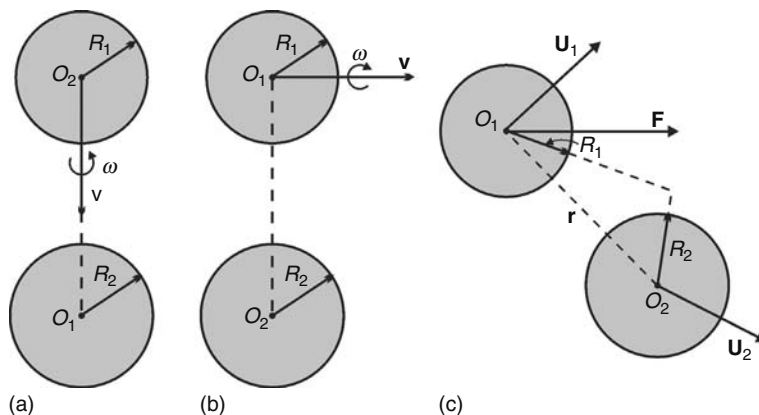
FIGURE 7.44 Types of hydrodynamic interactions between two spherical particles: (a) motion along and rotation around the line of centers; (b) motion along and rotation around an axis perpendicular to the line of centers; (c) the first particle moves under the action of an applied external force, **F**, whereas the second particle is subjected to the hydrodynamic disturbance created by the motion of the first particle.

or alternatively, moving toward each other. A combination of these results permits evaluation of the total forces and torques acting on the particles.

The first particle then moves along an axis perpendicular to the center line and rotates around this axis, whereas the second particle is immobile; see Figure 7.44b (this is a typical three-dimensional hydrodynamic problem). The contribution of this asymmetric motion of the spheres to the resistance tensors was determined by Davis [569] and O'Neill and Majumdar [570].

The first particle moves with linear velocity, $\mathbf{U}_1$, under the action of an applied external force, **F**, whereas the second particle is subjected to the hydrodynamic disturbances (created by the motion of the first particle) and moves with a linear velocity, $\mathbf{U}_2$ (see Figure 7.44c). As a rule, this is a three-dimensional hydrodynamic problem. For this case, Batchelor [574] and Batchelor and Wen [575] have derived the following expressions for the instantaneous translational velocities of the two particles in an otherwise quiescent and unbounded fluid:

$$\mathbf{U}_1 = \frac{\mathbf{F}}{6\pi\eta R_1} \cdot \left[A_{11}(r)\frac{\mathbf{rr}}{r^2} + B_{11}(r)\left(\mathbf{I} - \frac{\mathbf{rr}}{r^2}\right)\right] \tag{7.274}$$

$$\mathbf{U}_2 = \frac{\mathbf{F}}{6\pi\eta(R_1 + R_2)} \cdot \left[A_{12}(r)\frac{\mathbf{rr}}{r^2} + B_{12}(r)\left(\mathbf{I} - \frac{\mathbf{rr}}{r^2}\right)\right] \tag{7.275}$$

where **r** is the vector connecting the particle centers and $r = |\mathbf{r}|$. Expressions for the mobility functions A_{ij} and B_{ij} $(i, j = 1, 2)$ at large values of the dimensionless distance $s = 2r/(R_1 + R_2)$ and comparable particle radii $\lambda = R_2/R_1 = O(1)$ have been derived by Jeffrey and Onishi [576] and Davis and Hill [573]. The derived far-field expansions are

$$1 - B_{11} = \frac{68\lambda^5}{(1+\lambda)^6 s^6} + \frac{32\lambda^3(10 - 9\lambda^2 + 9\lambda^4)}{(1+\lambda)^8 s^8} + \frac{192\lambda^5(35 - 18\lambda^2 + 6\lambda^4)}{(1+\lambda)^{10} s^{10}} + O(s^{-12})$$

$$B_{11} - A_{11} = \frac{60\lambda^3}{(1+\lambda)^4 s^4} - \frac{60\lambda^3(8 - \lambda^2)}{(1+\lambda)^6 s^6} + \frac{32\lambda^3(20 - 123\lambda^2 + 9\lambda^4)}{(1+\lambda)^8 s^8} + \frac{64\lambda^2(175 + 1500\lambda - 426\lambda^2 + 18\lambda^4)}{(1+\lambda)^{10} s^{10}} + O(s^{-12})$$

$$A_{11} - \frac{2A_{12}}{1+\lambda} = 1 - \frac{3}{(1+\lambda)s} + \frac{4(1+\lambda^2)}{(1+\lambda)^3 s^3} - \frac{60\lambda^3}{(1+\lambda)^4 s^4} + \frac{32\lambda^3(15 - 4\lambda^2)}{(1+\lambda)^6 s^6} - \frac{2400\lambda^3}{(1+\lambda)^7 s^7}$$

$$- \frac{192\lambda^3(5 - 22\lambda^2 + 3\lambda^4)}{(1+\lambda)^8 s^8} + \frac{1920\lambda^3(1 + \lambda^2)}{(1+\lambda)^9 s^9} - \frac{256\lambda^5(70 - 375\lambda - 120\lambda^2 + 9\lambda^3)}{(1+\lambda)^{10} s^{10}}$$

$$- \frac{1536\lambda^3(10 - 151\lambda^2 + 10\lambda^4)}{(1+\lambda)^{11} s^{11}} + O(s^{-12}) \tag{7.276}$$

$$B_{11} - \frac{2B_{12}}{1+\lambda} = 1 - \frac{3}{2(1+\lambda)s} - \frac{2(1+\lambda^2)}{(1+\lambda)^3 s^3} - \frac{68\lambda^5}{(1+\lambda)^6 s^6} - \frac{32\lambda^3(10 - 9\lambda^2 + 9\lambda^4)}{(1+\lambda)^8 s^8}$$

$$- \frac{192\lambda^5(35 - 18\lambda^2 + 6\lambda^4)}{(1+\lambda)^{10} s^{10}} - \frac{16\lambda^3(560 - 553\lambda^2 + 560\lambda^4)}{(1+\lambda)^{11} s^{11}} + O(s^{-12})$$

In the case of a small heavy sphere falling through a suspension of large particles (fixed in space), we have $\lambda \gg 1$; the respective expansions, corresponding to Equation 7.276, were obtained by Fuentes et al. [577]. In the opposite case, when $\lambda \ll 1$, the suspension of small background spheres will reduce the mean velocity of a large heavy particle (as compared with its Stokes velocity [578]) because the suspension behaves as an effective fluid of larger viscosity as predicted by the Einstein viscosity formula [574,577].

7.5.2.3 Stages of Thinning of a Liquid Film

Experimental and theoretical investigations [221,229,548,549,554,579,580] show that during the approach of two fluid colloidal particles, a flat liquid film can appear between their closest regions (see Figure 7.32). The hydrodynamic interactions as well as the buoyancy, the Brownian, electrostatic, van der Waals, and steric forces and other interactions can be involved in film formation [193,239,556,581,582]. The formation and the evolution of a foam or emulsion film usually follows the stages shown in Figure 7.45.

Under the action of an outer driving force, the fluid particles approach each other. The hydrodynamic interaction is stronger at the front zones and leads to a weak deformation of the interfaces in this front region. In this case, the usual hydrodynamic capillary number, $Ca = \eta V_z/\sigma$, which is a small parameter for nondeformable surfaces, should be modified to read $Ca = \eta V_z R_*/\sigma h$, where the distance, h, between the interfaces is taken into account. The shape of the gap between two drops for different characteristic times was calculated numerically by many authors [582–602]. Experimental investigation of these effects for symmetric and asymmetric drainage of foam films were carried out by Joye et al. [591,592]. In some special cases, the deformation of the fluid particle can be very fast: for example, the bursting of a small air bubble at an air–water interface is accompanied by a complex motion resulting in the production of a high-speed liquid jet (see Boulton-Stone and Blake [602]).

When a certain small separation, h_i, the inversion thickness, is reached, the sign of the curvature in the contact of the fluid particles (drops, bubbles) changes. A concave lens-shaped formation called a dimple is formed (see Frankel and Mysels [603]). This stage is also observed for asymmetric films [592]. A number of theoretical studies have described the development of a dimple at the initial stage of film thinning [582–602]. The inversion thickness can be calculated from a simple equation in which the van der Waals interaction is explicitly taken into account (see Section 7.4.2) [223,547,582]

$$h_i = \frac{F_z(\sigma_1 + \sigma_2)}{4\pi\sigma_1\sigma_2}\left(1 - \frac{A_H R_*}{12 F_z h_i}\right) \tag{7.277}$$

where σ_1 and σ_2 are the interfacial tensions of the phase boundaries S_1 and S_2; in this case F_z is the external force (of nonviscous and non-van der Waals origin) experienced by the approaching particles; A_H is the Hamaker constant. In the case,
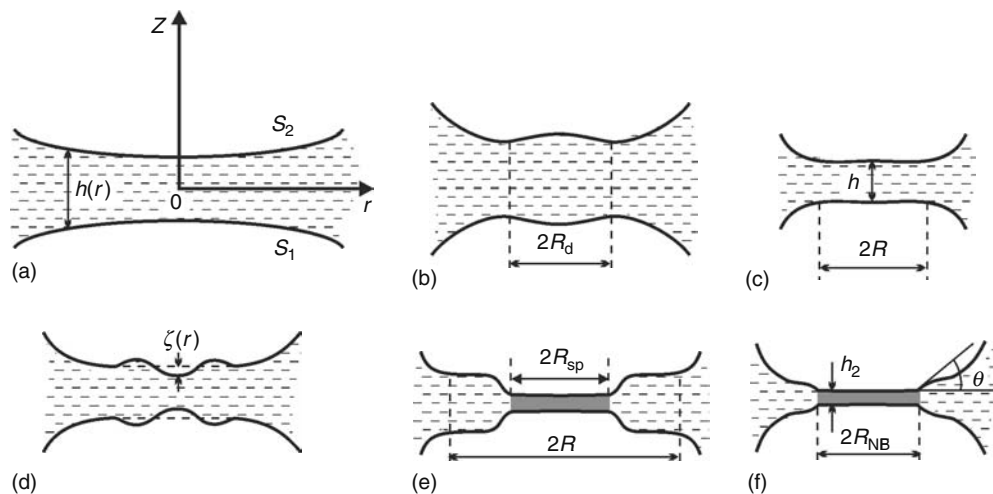
FIGURE 7.45 Main stages of formation and evolution of a thin liquid film between two bubbles or drops: (a) mutual approach of slightly deformed surfaces; (b) at a given separation, the curvature at the center inverts its sign and a dimple arises; (c) the dimple disappears, and eventually an almost plane-parallel film forms; (d) due to thermal fluctuations or other disturbances the film either ruptures or transforms into a thinner Newton black film (e), which expands until reaching the final equilibrium state (f).

when the van der Waals force is negligible, Equation 7.277 reduces to $h_i = F_z(\sigma_1 + \sigma_2)/(4\pi\sigma_1\sigma_2)$ [223,547]. Danov et al. [556] have shown that in the case of Brownian flocculation of identical small droplets, h_i obeys the following transcendental equation:

$$h_i = \frac{kT}{2\pi\sigma z_i}\left\{\int_0^{z_i}\left(\frac{z_i}{z}\right)^2 \frac{\gamma(z)}{\gamma(z_i)}\exp\left[\frac{U(z)-U(z_i)}{kT}\right]\frac{dz}{z_i}\right\}^{-1} \tag{7.278}$$

where

    kT is the thermal energy; $\gamma(z) = F_z/V_z$ is the hydrodynamic resistance given by Equation 7.270
    U is the potential energy due to the surface forces (see Equation 7.175)
    z is the distance between the droplet mass centers

These authors pointed out that with an increase of droplet size the role of the Brownian force in the film formation decreases, but for micrometer-sized liquid droplets the Brownian force is still by several orders of magnitude greater than the buoyancy force due to gravity. If the driving force is large enough, so that it is able to overcome the energy barrier created by the electrostatic repulsion and/or the increase of the surface area during the droplet deformation, then film with a dimple will be formed. On the contrary, at low electrolyte concentration (i.e., strong electrostatic repulsion) such a dimple might not appear. Parallel experiments [604] on the formation and thinning of emulsion films of macroscopic and microscopic areas, prepared in the Scheludko cell [202] and in a miniaturized cell, show that the patterns and the time scales of the film evolution in these two cases are significantly different. There is no dimple formation in the case of thin liquid films of small diameters [604].

In the case of predominant van der Waals attraction, instead of a dimple, a reverse bell-shape deformation, called a pimple, appears and the film quickly ruptures [582,589,598,601]. The thickness, h_p, at which the pimple appears can be calculated from the relationship [582]:

$$h_p = \left(\frac{A_H R_*}{12 F_z}\right)^{1/2} \tag{7.279}$$

The pimple formation thickness depends significantly on the radius, R_*. If a drop of tangentially immobile surfaces and radius R_d is driven by the buoyancy force, then we have:

$$F_z = \frac{4}{3}\pi R_d^3 \Delta\rho g \tag{7.280}$$

where

    $\Delta\rho$ is the density difference
    g is the gravity acceleration

For the collision of this drop with another immobile one, we have $h_p^2 = A_H/(16\pi\Delta\rho g R_d^2)$. We see that h_p is inversely proportional to the drop radius. For typical values of the Hamaker constant $A_H = 4 \times 10^{-20}$ J, density difference $\Delta\rho = 0.12$ g cm^{-3}, and $R_d = 10$ μm, the thickness of pimple formation is $h_p = 82.3$ nm. Note that this thickness is quite large. The pimple formation can be interpreted as the onset of instability without fluctuations (stability analysis of the film intervening between the drops has been carried out elsewhere [60]).

As already mentioned, if the van der Waals force (or other attractive force) is not predominant, first a dimple forms in the thinning liquid films. Usually the dimple exists for a short period of time; initially it grows, but as a result of the swift outflow of liquid it decreases and eventually disappears. The resulting plane-parallel film thins at almost constant radius R. When the electrostatic repulsion is strong, a thicker primary film forms (see point 1 in Figure 7.17). From the viewpoint of conventional DLVO theory, this film must be metastable. Indeed, the experiments with microscopic foam films, stabilized with sodium octyl sulfate or SDS in the presence of different amount of electrolyte [605], show that a black spot may suddenly form and a transition to secondary (Newton black) film may occur (see point 2 in Figure 7.17). The rate of thinning depends not only on the capillary pressure (the driving force) but also very strongly on the surfactant concentration (for details, see Section 7.5.3.2).

The appearance of a secondary film (or film rupture, if the secondary film is not stable) is preceded by corrugation of the film surfaces due to thermally excited fluctuations or outer disturbances. When the derivative of the disjoining pressure, $\partial\Pi/\partial h$, is positive, the amplitude of the fluctuations (ζ in Figure 7.45d) spontaneously grows. As already mentioned, the instability leads to rupture of the film or to formation of black spots. The theory of film stability was developed by de Vries [606], Vrij [607], Felderhof [540], Sche and Fijnaut [541], Ivanov et al. [608], Gumerman and Homsy [609], Malhotra and Wasan [610],

Maldarelli and Jain [542], and Valkovska et al. [611]. On the basis of the lubrication approximation for tangentially immobile surfaces, Ivanov et al. [608] and Valkovska et al. [611] derived a general expression for the critical film thickness, h_{cr}, by using long-waves stability analysis:

$$h_{cr} = h_{tr} \left(\frac{\sigma h_{tr}^2}{kT} \right)^{1/4} \exp \left(-\frac{k_{cr}^2 R^2}{32 h_{cr}^3} \int_{h_{cr}}^{h_{tr}} \frac{h^3 \Pi'}{P_c - \Pi} dh \right) \tag{7.281}$$

where k_{cr} is the wave number of the critical wave defined as

$$k_{cr}^2 = \frac{\dfrac{1}{\sigma} \displaystyle\int_{h_{cr}}^{h_{tr}} \dfrac{h^3 \Pi'}{P_c - \Pi} dh}{\displaystyle\int_{h_{cr}}^{h_{tr}} \dfrac{h^6}{P_c - \Pi} dh} \tag{7.282}$$

In Equation 7.282, h_{tr} is the so-called transitional thickness [607,608,611] at which the increase of free energy due to the increased film area and the decrease of free energy due to the van der Waals interaction in the thinner part (Figure 7.45d) compensate each other. At h_{tr} the most rapidly growing fluctuation (the critical wave) becomes unstable. The transitional thickness obeys the following equation [608,611]:

$$\frac{24 h_{cr}^3 [P_c - \Pi(h_{tr})]}{R^2 k_{cr}^2 h_{tr}^4} + \frac{\sigma k_{cr}^2 h_{tr}^3}{2 h_{cr}^3} = \Pi'(h_{tr}) \tag{7.283}$$

Figures 7.46 and 7.47 show the critical thicknesses of rupture, h_{cr}, for foam and emulsion films, respectively, plotted versus the film radius [612]. In both cases the film phase is the aqueous phase, which contains 4.3×10^{-4} M SDS + added NaCl. The emulsion film is formed between two toluene drops. Curve 1 is the prediction of a simpler theory, which identifies the critical thickness with the transitional one [610]. Curve 2 is the theoretical prediction of Equations 7.281 through 7.283 (no adjustable parameters); in Equation 7.182 for the Hamaker constant the electromagnetic retardation effect has also been taken into account [368]. In addition, Figure 7.48 shows the experimental dependence of the critical thickness versus the concentration of surfactant (dodecanol) for aniline films. Figures 7.46 through 7.48 demonstrate that when the film area increases and/or the electrolyte concentration decreases the critical film thickness becomes larger. Figure 7.49 show the critical thickness of foam film rupture for three concentrations of SDS in the presence of 0.3 M NaCl [500]. The dashed and dash-dotted lines, for 1 and 10 μM SDS, respectively, are computed assuming only the van der Waals attraction (no adjustable parameter). The deviation of
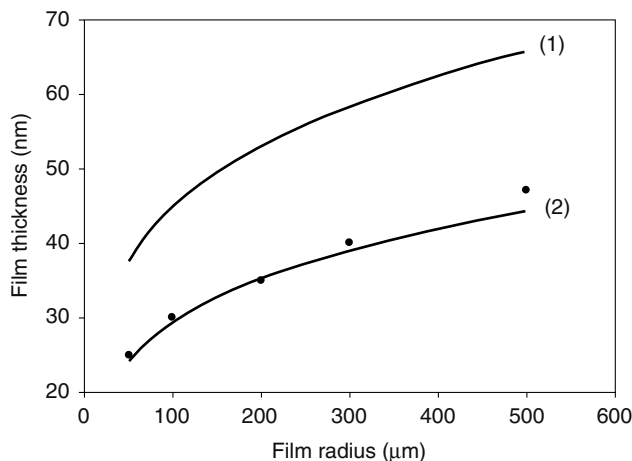
FIGURE 7.46 Dependence of the critical thickness, h_{cr}, on the radius, R, of foam films. The experimental points are data from Ref. [612]; the films are formed from a solution of 4.3×10^{-4} M SDS + 0.25 M NaCl. Curve 1 is the prediction of the simplified theory [610], whereas Curve 2 is calculated using Equations 7.281 through 7.283; no adjustable parameters.
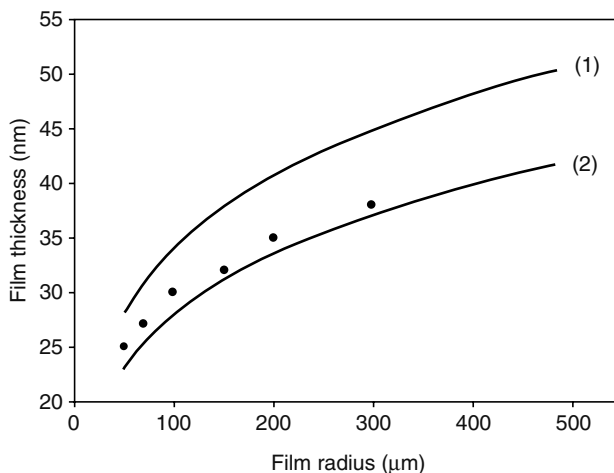
FIGURE 7.47 Critical thickness, h_{cr}, versus radius, R, of emulsion films, toluene/water/toluene. The experimental points are data from Ref. [612]; the films are formed from a solution of 4.3×10^{-4} M SDS + 0.1 M NaCl. Curve 1 is the prediction of the simplified theory [610], whereas Curve 2 is calculated using Equations 7.281 through 7.283; no adjustable parameters.

the predicted values of h_{cr} from the measured is because of the hydrophobic interaction (Section 7.4.5.4.2). The solid lines represent fits with the decay length of the hydrophobic interactions $\lambda_0 = 15.8$ nm using Equations 7.281 through 7.283.

The surface corrugations do not necessarily lead to film rupture. Instead, black spots (secondary films of very low thickness; h_2 in Figure 7.17) can be formed. The typical thickness of plane-parallel films at stage c (Figure 7.45c) is about 200 nm, while the characteristic thickness h_2 of the Newton black film (Figures 7.45e and f) is about 5–10 nm. The black spots either coalesce or grow in diameter, forming an equilibrium secondary (Newton black) film with a thickness h_2 and radius R_{sp}. These spots grow until they cover the whole film area.

After the entire film area is occupied by the Newton black film, the film radius increases until it reaches its equilibrium value, $R = R_{NBF}$ (Figure 7.45f). Finally, the equilibrium contact angle is established. For more details about this last stage of film thinning, see part IV.C of Ref. [223].

7.5.2.4 Dependence of Emulsion Stability on the Droplet Size

Experimental data [614,615] show that the emulsion stability correlates well with the lifetime of separate thin emulsion films or of drops coalescing with their homophase. To simplify the treatment we will consider here the lifetime of a single drop pressed against its homophase under the action of gravity. To define the lifetime (or drainage time) τ, we assume that in the initial and final moments the film has some known thicknesses h_{in} and h_f:
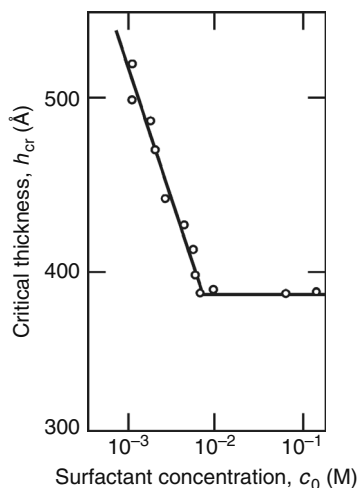
FIGURE 7.48 Dependence of the critical thickness, h_{cr}, of aniline films on the concentration of dodecanol, c_0. (Modified from Ivanov, I.B., *Pure Appl. Chem.*, 52, 1241, 1980. With permission.)
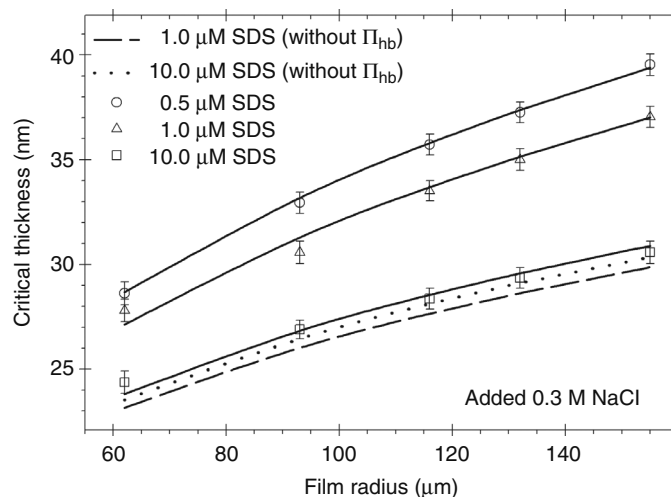
FIGURE 7.49 Critical thickness, h_{cr}, versus the film radius at a 0.3 M fixed concentration of NaCl for three SDS concentrations: 0.5, 1, and 10 μM. The dashed and dash-dotted lines, for 1 and 10 μM SDS, respectively, are computed using an absence of the hydrophobic attraction. The solid lines are fits of the experimental points with $\lambda_0 = 15.8$ nm.

$$\tau = \int_{h_f}^{h_{in}} \frac{dh}{V_z} = \frac{3\pi\eta R_*^2}{2F_z}\left[\ln\left(\frac{h_{in}}{h_f}\right) + \frac{R^2}{h_f R_*}\left(1 - \frac{h_f}{h_{in}}\right) + \frac{R^4}{2h_f^2 R_*^2}\left(1 - \frac{h_f^2}{h_{in}^2}\right)\right] \tag{7.284}$$

The final thickness, h_f, may coincide with the critical thickness of film rupture. Equation 7.284 is derived for tangentially immobile interfaces from Equation 7.270 at a fixed driving force (no disjoining pressure).

In the case of gravity-driven coalescence of a droplet with its homophase, the driving force is given by Equation 7.280 and the mean drop radius is $R_* = 2R_d$. Then from Equations 7.280 and 7.284 we can deduce the droplet lifetime in the so-called Taylor regime, corresponding to nondeformed droplets ($R = 0$):

$$\tau_{Ta} = \frac{6\pi\eta R_d^2}{F_z}\ln\left(\frac{h_{in}}{h_f}\right) = \frac{9\eta}{2gR_d\Delta\rho}\ln\left(\frac{h_{in}}{h_f}\right) \tag{7.285}$$

We see that τ_{Ta} depends logarithmically on the ratio of the initial and final thickness. Moreover, in the Taylor regime the lifetime, τ, decreases with the increase of the driving force, F_z, and the drop radius, R_d. The latter fact is confirmed by the experimental data of Dickinson et al. [616].

In the case of deformed drops ($R \neq 0$), the drainage time, τ, is determined by Equation 7.284, and in such a case the fluid particles approach each other in the Reynolds regime [548,613]. The dependence of τ on R_d in Equation 7.284 is very complex, because the driving force, F_z, and the film radius, R, depend on R_d. The film radius can be estimated from the balance of the driving and capillary force [548,613]:

$$R^2 = \frac{F_z R_d}{2\pi\sigma} \tag{7.286}$$

In this regime, the lifetime, τ, increases with an increase of the driving force, F_z. This is exactly the opposite trend compared to results for the Taylor regime (see Equation 7.285). The result can be rationalized in view of Reynolds equation (Equation 7.273). In the numerator of this equation, $F_z \propto R_d^3$, whereas in the denominator $R^4 \propto R_d^8$ (see Equation 7.286); as a result, the drainage rate becomes proportional to R_d^{-5}, i.e., V_z decreases as the droplet radius increases.

The numerical results from Equations 7.284 through 7.286 for the lifetime or drainage time, τ, versus the droplet radius, R_d, are plotted in Figure 7.50 for parameter values typical for emulsion systems: $\Delta\rho = 0.2$ g cm^{-3}, $\eta = 1$ cP, $h_f = 5$ nm, and $h_{in} = R_d/10$. The various curves in Figure 7.50 correspond to different values of the surface tension, σ, shown in the figure. The left branches of the curves correspond to the Taylor regime (nondeformed droplets), whereas the right branches correspond to the Reynolds regime (formation of film between the droplets). The presence of a deep minimum on the τ versus R_d curve was first pointed out by Ivanov [617,618]. The theoretical dependencies in Figure 7.50 agree well with experimental data [619–621] for the lifetime of oil droplets pressed by the buoyancy force against a large oil–water interface in a system containing protein BSA (Figure 7.51).
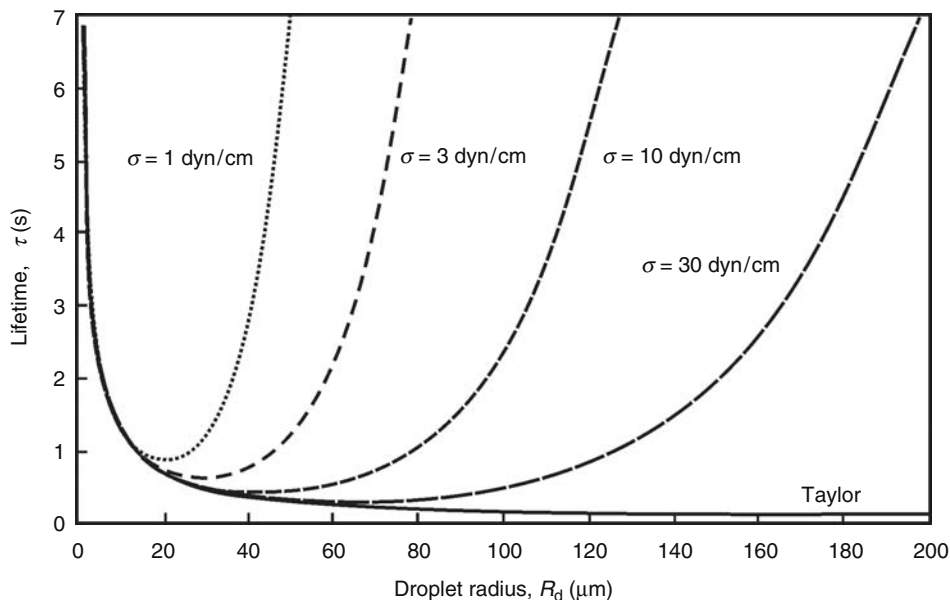
FIGURE 7.50 Calculated lifetime, τ, of drops approaching a fluid interface in Taylor regime (the solid line) and in Reynolds regime (the other lines) as a function of the droplet radius, R_d.

7.5.3 EFFECT OF SURFACE MOBILITY

The hydrodynamic interactions between fluid particles (drops, bubbles) suspended in a liquid medium depend on the interfacial mobility. In the presence of surfactants, the bulk fluid motion near an interface disturbs the homogeneity of the surfactant adsorption monolayer. The ensuing surface-tension gradients act to restore the homogeneous equilibrium state of the monolayer. The resulting transfer of adsorbed surfactant molecules from the regions of lower surface tension toward the regions of higher surface tension constitutes the Marangoni effect. The analogous effect, for which the surface-tension gradient is caused by a temperature gradient, is known as the Marangoni effect of thermocapillarity. In addition, the interfaces possess specific surface rheological properties (surface elasticity and dilatational and shear surface viscosities), which give rise to the so-called Boussinesq effect (see below) [622].
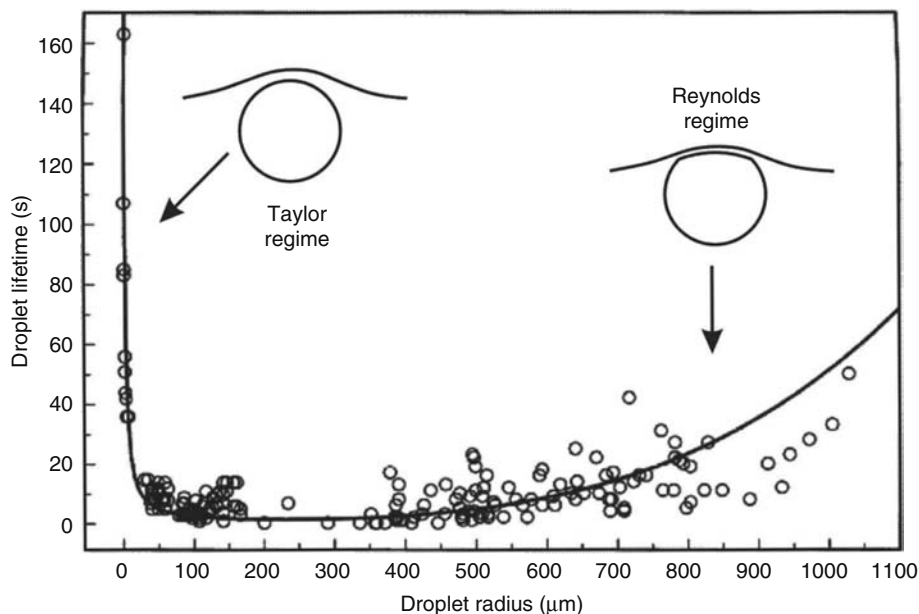
FIGURE 7.51 Stability of oil drops pressed by buoyancy against a large oil/water interface. Measured lifetime, (the points), is plotted versus droplet radius in a system consisting of soybean oil and aqueous solution of $4 \cdot 10^{-4}$ wt% BSA $+ 0.15$ M NaCl (pH $= 6.4$). The solid line is drawn in accordance to Equation 7.284.

7.5.3.1 Diffusive and Convective Fluxes at an Interface—Marangoni Effect

To take into account the influence of surfactant adsorption, Equations 7.251 and 7.252 are to be complemented with transport equations for each of the species ($k = 1,2,\ldots, N$) in the bulk phases [525,528,553,554]

$$\frac{\partial c_k}{\partial t} + \mathrm{div}(c_k\mathbf{v} + \mathbf{j}_k) = r_k \quad (k = 1, 2, \ldots, N) \tag{7.287}$$

where c_k and $\mathbf{j}_k$ are bulk concentration and flux, respectively, of the kth species—note that $\mathbf{j}_k$ includes the molecular diffusive flux, the flux driven by external forces (e.g., electrodiffusion [543,553,554]) and the thermodiffusion flux [553]; and r_k is the rate of production due to chemical reactions, including surfactant micellization or micelle decay. The surface mass-balance equation for the adsorption, Γ_k, has the form [543,553,554]:

$$\frac{\partial \Gamma_k}{\partial t} + \nabla_s \cdot (\Gamma_k\mathbf{v}_s + \mathbf{j}_k^s) = r_k^s + \mathbf{n} \cdot <\mathbf{j}_k> \tag{7.288}$$

where
  $\mathbf{n}$ is the unit normal to the interface directed from phase 1 to 2
  $<>$ denotes the difference between the values of a given physical quantity at the two sides of the interface
  ∇_s is the surface gradient operator [623]
  $\mathbf{v}_s$ is the local material surface velocity
  $\mathbf{j}_k^s$ is the two-dimensional flux of the kth component along the interface
  r_k^s accounts for the rate of production of the kth component due to interfacial chemical reactions and could include conformational changes of adsorbed proteins

Equation 7.288 provides a boundary condition for the normally resolved flux, $\mathbf{j}_k$. From another viewpoint, Equation 7.288 represents a two-dimensional analog of Equation 7.287. The interfacial flux, $\mathbf{j}_k^s$, can also contain contributions from the interfacial molecular diffusion, electrodiffusion, and thermodiffusion. A simple derivation of the time-dependent convective-diffusion equation for surfactant transport along a deforming interface is given by Brenner and Leal [624–627], Davis et al. [560], and Stone [628]. If the molecules are charged, the bulk and surfaces electrodiffusion fluxes can be expressed in the form [543,629,630]:

$$\mathbf{j}_k = -D_k(\nabla c_k + z_k c_k \nabla\Phi), \quad \mathbf{j}_k^s = -D_k^s(\nabla_s\Gamma_k + z_k\Gamma_k\nabla_s\Phi) \tag{7.289}$$

for the bulk and interfacial phase. Here, D_k and D_k^s are the bulk and surface collective diffusion coefficients, respectively, which are connected with the diffusion coefficients of individual molecules, $D_{k,0}$ and $D_{k,0}^s$, through the relationship [630]

$$D_k = \frac{D_{k,0}}{kT}\frac{K_b(\phi_k)}{(1-\phi_k)}\frac{\partial\mu_k}{\partial\ln\phi_k}, \quad D_k^s = \frac{D_{k,0}^s}{kT}K_s(\Gamma_k)\frac{\partial\mu_k^s}{\partial\ln\Gamma_k} \tag{7.290}$$

where μ_k and μ_k^s are the bulk and surface chemical potentials, respectively. The dimensionless bulk friction coefficient, K_b, accounts for the change in the hydrodynamic friction between the fluid and the particles (created by the hydrodynamic interactions between the particles). The dimensionless surface mobility coefficient, K_s, accounts for the variation of the friction of a molecule in the adsorption layer. Feng [631] has determined the surface diffusion coefficient, the dilatational elasticity, and the viscosity of a surfactant adsorption layer by theoretical analysis of experimental data. Stebe and Maldarelli [632,633] studied theoretically the surface diffusion driven by large adsorption gradients. The determination of bulk and surface diffusion coefficients from experimental data for the drainage of nitrobenzene films stabilized by different concentrations of dodecanol was reported [629].

Note that the adsorption isotherms, relating the surface concentration, Γ_k, with the subsurface value of the bulk concentration, c_k (see Section 7.2.2.1), or the respective kinetic Equation 7.86 for adsorption under barrier control (see Section 7.2.2.5), should also be employed in the computations based on Equations 7.287 through 7.290 for a complete set of equations to be obtained.

Another boundary condition is the equation of the interfacial momentum balance [529,548,554]:

$$\nabla_s \cdot \boldsymbol{\sigma} = \mathbf{n} \cdot <\mathbf{P} + \mathbf{P}_b> \tag{7.291}$$

where $\boldsymbol{\sigma}$ is the interfacial stress tensor, which is a two-dimensional counterpart of the bulk stress tensor, $\mathbf{P}$. Moreover, a two-dimensional analog of Equations 7.253, 7.256, and 7.257, called the Boussinesq–Scriven constitutive law, can be postulated for a fluid interface [223,554,622,634–638]:

$$\boldsymbol{\sigma} = \sigma_a \mathbf{I}_s + (\eta_{dl} - \eta_{sh})(\nabla_s \cdot \mathbf{v}_s)\mathbf{I}_s + \eta_{sh}\left[(\nabla_s \cdot \mathbf{v}_s)\mathbf{I}_s + \mathbf{I}_s(\nabla_s \cdot \mathbf{v}_s)^T\right] \tag{7.292}$$

where
  η_{dl} and η_{sh} are the interfacial dilatational and shear viscosities, respectively
  $\mathbf{I}_s$ is the unit surface idemfactor [623]
  σ_a is the scalar adsorption part of the surface tension (see Section 7.2.1.2.2)

In view of the term $\sigma_a \mathbf{I}_s$ in Equation 7.292, the Marangoni effects are hidden in the left-hand side of the boundary condition (Equation 7.291) through the surface gradient of σ_a:

$$\nabla_s \sigma_a = -\sum_{k=1}^{N} \frac{E_k}{\Gamma_k} \nabla_s \Gamma_k - \frac{E_T}{T} \nabla_s T, \quad E_k = -\left(\frac{\partial \sigma_a}{\partial \ln \Gamma_k}\right)_{T,\Gamma_{j\neq k}}, \quad E_T = -\left(\frac{\partial \sigma_a}{\partial \ln T}\right)_{\Gamma_k} \tag{7.293}$$

where
  E_k is the Gibbs elasticity for the kth surfactant species (see Equation 7.6)
  E_T represents the thermal analog of the Gibbs elasticity

The thermocapillary migration of liquid drops or bubbles and the influence of E_T on their motion are investigated in a number of works [639–641].

   In fact, Equation 7.292 describes an interface as a two-dimensional Newtonian fluid. On the other hand, a number of non-Newtonian interfacial rheological models have been described in the literature [642–645]. Tambe and Sharma [646] modeled the hydrodynamics of thin liquid films bounded by viscoelastic interfaces, which obey a generalized Maxwell model for the interfacial stress tensor. These authors [647,648] also presented a constitutive equation to describe the rheological properties of fluid interfaces containing colloidal particles. A new constitutive equation for the total stress was proposed by Horozov et al. [649], Danov et al. [650], and Ivanov et al. [651] who applied a local approach to the interfacial dilatation of adsorption layers.

   When the temperature is not constant, the bulk heat transfer equation complements the system and involves Equations 7.251, 7.252, and 7.287. The heat transfer equation is a special case of the energy balance equation. It should be noted that more than 20 various forms of the overall differential energy balance for multicomponent systems are available in the literature [525,528]. The corresponding boundary condition can be obtained as an interfacial energy balance [554,638]. Based on the derivation of the bulk [652] and interfacial [650,653] entropy inequalities (using the Onsager theory), various constitutive equations for the thermodynamic mass, heat, and stress fluxes have been obtained.

7.5.3.2 Fluid Particles and Films of Tangentially Mobile Surfaces

When the surface of an emulsion droplet is mobile, it can transmit the motion of the outer fluid to the fluid within the droplet. This leads to a special pattern of the fluid flow and affects the dissipation of energy in the system. The problem concerning the approach of two nondeformed (spherical) drops or bubbles of pure phases has been investigated by many authors [548,576,577,583,584,654–659]. A number of solutions, generalizing the Taylor equation (Equation 7.271), have been obtained. For example, the velocity of central approach, V_z, of two spherical drops in pure liquid is related to the hydrodynamic resistance force, F_z, by means of a Padé-type expression derived by Davis et al. [583]

$$V_z = \frac{2hF_z}{3\pi\eta R_*^2} \frac{1 + 1.711\xi + 0.461\xi^2}{1 + 0.402\xi}, \quad \xi = \frac{\eta}{\eta_d}\sqrt{\frac{R_*}{2h}} \tag{7.294}$$

where
  h is the closest surface-to-surface distance between the two drops
  η_d is the viscosity of the disperse phase (the liquid in the droplets)

In the limiting case of solid particles, we have $\eta_d \to \infty$, and Equation 7.294 reduces to the Taylor equation (Equation 7.271). Note that in the case of close approach of two drops ($\xi \gg 1$), the velocity V_z is proportional to $\sqrt{h}$. This implies that the two drops can come into contact ($h = 0$) in a finite period of time ($\tau < \infty$) under the action of a given force, F_z, because the integral

in Equation 7.284 is convergent for $h_f = 0$. This is in contrast to the case of immobile interfaces ($\xi \ll 1$), when $V_z \propto h$ and $\tau \to \infty$ for $h_f \to 0$.

In the other limiting case, that of two nondeformed gas bubbles ($\eta_d \to 0$) in pure liquid, Equation 7.294 cannot be used; instead, V_z can be calculated from the expression due to Beshkov et al. [659]

$$V_z = \frac{F_z}{2\pi\eta R_d \ln(R_d/h)} \tag{7.295}$$

Note that in this case $V_z \propto (\ln h)^{-1}$, and the integral in Equation 7.284 is convergent for $h_f \to 0$. In other words, the theory predicts that the lifetime, τ, of a doublet of two colliding spherical bubbles in pure liquid is finite. Of course, the real lifetime of a doublet of bubbles or drops is affected by the surface forces for $h < 100$ nm, which should be accounted for in F_z and which may lead to the formation of thin film in the zone of contact [193,356].

Let us proceed with the case of deformed fluid particles (Figure 7.32). A number of theoretical studies [660–663] have been devoted to the thinning of plane-parallel liquid films of pure liquid phases (no surfactant additives). Ivanov and Traykov [662] derived the following exact expressions for the velocity of thinning of an emulsion film:

$$V_z = \left(\frac{32\Delta P^2}{\rho_d \eta_d R^4}\right)^{1/3} h^{5/3}, \quad \frac{V_z}{V_{Re}} = \frac{1}{\varepsilon_e}, \quad \varepsilon_e \equiv \left(\frac{\rho_d \eta_d h^4 F_z}{108\pi\eta^3 R^4}\right)^{1/3} \tag{7.296}$$

where
  ρ_d is the density of the disperse phase
  V_{Re} is the Reynolds velocity defined by Equation 7.273
  ε_e is the so-called emulsion parameter

Substituting typical parameter values in Equations 7.294 and 7.296, we can check that at a given constant force the velocity of thinning of an emulsion film is smaller than the velocity of approach of two nondeformed droplets and much larger than V_{Re}. It is interesting to note that the velocity of thinning as predicted by Equation 7.296 does not depend on the viscosity of the continuous phase, η, and its dependence on the drop viscosity, η_d, is rather weak. There are experimental observations confirming this prediction (see Ref. [32], p. 381).

The presence of surfactant adsorption monolayers decreases the mobility of the droplet (bubble) surfaces. This is due to the Marangoni effect (see Equation 7.293). From a general viewpoint, we may expect that the interfacial mobility will decrease with the increase of surfactant concentration until eventually the interfaces become immobile at high surfactant concentrations (see Section 7.5.2); therefore, a pronounced effect of surfactant concentration on the velocity of film drainage should be expected. This effect really exists (see Equation 7.297), but in the case of emulsions it is present only when the surfactant is predominantly soluble in the continuous phase.

Traykov and Ivanov [663] established (both theoretically and experimentally) the interesting effect that when the surfactant is dissolved in the disperse phase (that is, in the emulsion droplets), the droplets approach each other just as in the case of pure liquid phases, i.e., Equation 7.296 holds. Qualitatively, this effect can be attributed to the fact that the convection-driven surface-tension gradients are rapidly damped by the influx of surfactant from the drop interior; in this way, the Marangoni effect is suppressed. Indeed, during the film drainage the surfactant is carried away toward the film border, and a nonequilibrium distribution depicted in Figure 7.52a appears. Because, however, the mass transport is proportional to the perturbation, the larger the deviation from equilibrium, the stronger the flux tending to eliminate the perturbation (the surfactant flux is denoted by thick arrows in Figure 7.52b). In this way, any surface concentration gradient (and the related Marangoni effect) disappears. The emulsion films in this case behave as if surfactant is absent.
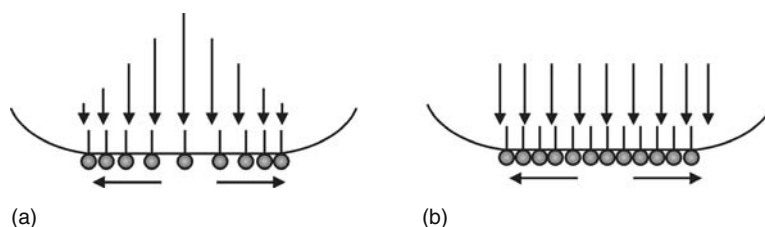

FIGURE 7.52 Damping of convection-driven surface-tension gradients by influx of surfactant from the drop interior. (a) Since the mass transport is proportional to the perturbation, the larger the perturbation, the stronger the flux tending to eliminate it. (b) Uniform surfactant distribution is finally reached.

In the opposite case, when the surfactant is soluble in the continuous phase, the Marangoni effect becomes operative and the rate of film thinning becomes dependent on the surface (Gibbs) elasticity (see Equation 7.293). Moreover, the convection-driven local depletion of the surfactant monolayers in the central area of the film surfaces gives rise to fluxes of bulk and surface diffusion of surfactant molecules. The exact solution of the problem [543,546,579,629,630,663] gives the following expression for the rate of thinning of symmetrical planar films (of both foam and emulsion type):

$$\frac{V_z}{V_{Re}} = 1 + \frac{1}{\varepsilon_e + \varepsilon_f}, \quad \frac{1}{\varepsilon_f} = \frac{6\eta D_s}{hE_G} + \frac{3\eta D}{\Gamma(\partial\sigma/\partial c)} \tag{7.297}$$

where

D and D_s are the bulk and interfacial collective diffusion coefficients (see Equation 7.290)
E_G is the Gibbs elasticity
ε_f is the so-called foam parameter [613]

In the special case of foam film, one substitutes $\varepsilon_e = 0$ in Equation 7.297. Note that the diffusive surfactant transport, which tends to restore the uniform adsorption monolayers, damps the surface-tension gradients (which oppose the film drainage) and thus accelerates the film thinning. However, at large surfactant concentrations, the surface elasticity, E_G, prevails, ε_f increases, and, consequently, the thinning rate decreases down to the Reynolds velocity, $V_z \rightarrow V_{Re}$ (see Equation 7.297). Similar expressions for the rate of film thinning, which are appropriate for various ranges of values of the interfacial parameters, can be found in the literature [223,547,548,594,664,665]. A table describing the typical ranges of variation of the interfacial properties (Γ, E_G, D, D_s, $\partial\sigma/\partial c$, etc.) for emulsion and foam systems can be found in Ref. [223], Table 7.2 therein. For $h < 100$ nm, the influence of the disjoining pressure should be taken into account (see Equation 7.273). In some studies [223,557,646,666–669], the effect of the interfacial viscosity on the rate of thinning and the lifetime of plane-parallel films is investigated; this effect is found to decrease when the film thickness, h, becomes smaller and the film radius, R, becomes larger.

Note that Equation 7.297 does not hold in the limiting case of foam films ($\varepsilon_e = 0$) at low surfactant concentration, $\varepsilon_f \rightarrow 0$. The following expression is available for this special case [613]:

$$V_z/V_{Re} = (1 + 1/\varepsilon_f)/[1 + 4h^2/(3R^2\varepsilon_f)] \tag{7.298}$$

The merit of Equation 7.298 is that it gives as limiting cases both V_z/V_{Re} for foam films without surfactant, $\varepsilon_f \rightarrow 0$, and Equation 7.297 with $\varepsilon_e = 0$ (note that in the framework of the lubrication approximation, used to derive Equation 7.297, the terms $\propto h^2/R^2$ are being neglected). Equation 7.298 has also some shortcomings, which are discussed in Ref. [613].

Another case, which is not described by Equations 7.297 and 7.298, is the approach of two nondeformed (spherical) bubbles in the presence of surfactant. The velocity of approach in this case can be described by means of the expression [547,557,618,630]:

$$\frac{V_z}{V_{Ta}} = \frac{h_s}{z_h}\left\{\left[\frac{h(1+b)}{h_s} + 1\right]\text{Ln}\left[\frac{h_s}{h(1+b)} + 1\right] - 1\right\}^{-1} \tag{7.299}$$

where the parameters b and h_s account for the influence of bulk and surface diffusivity of surfactants, respectively. From Equation 7.290 these parameters are calculated to be [630]

$$b \equiv \frac{3\eta c D_0 K_b(\phi)}{kT\Gamma^2(1-\phi)}, \quad h_s \equiv \frac{6\eta D_0^s K_s(\Gamma)}{kT\Gamma} \tag{7.300}$$

Generalization of Equation 7.299 to the more complicated case of two nondeformed (spherical) emulsion droplets with account for the influence of surface viscosity has been published in Ref. [557].

Returning to the parameter values, we note that usually $\varepsilon_e \ll \varepsilon_f$ and $\varepsilon_e \ll 1$. Then, comparing the expressions for V_z/V_{Re} as given by Equations 7.296 and 7.297, we conclude that the rate of thinning is much greater when the surfactant is dissolved in the droplets (the disperse phase) in comparison with the case when the surfactant is dissolved in the continuous phase. This prediction of the theory was verified experimentally by measuring the number of films that rupture during a given period of time [670], as well as the rate of thinning. When the surfactant was dissolved in the drop phase, the average lifetime was the same for all surfactant concentrations (Figure 7.53a), in agreement with Equation 7.296. For the emulsion film with the same, but
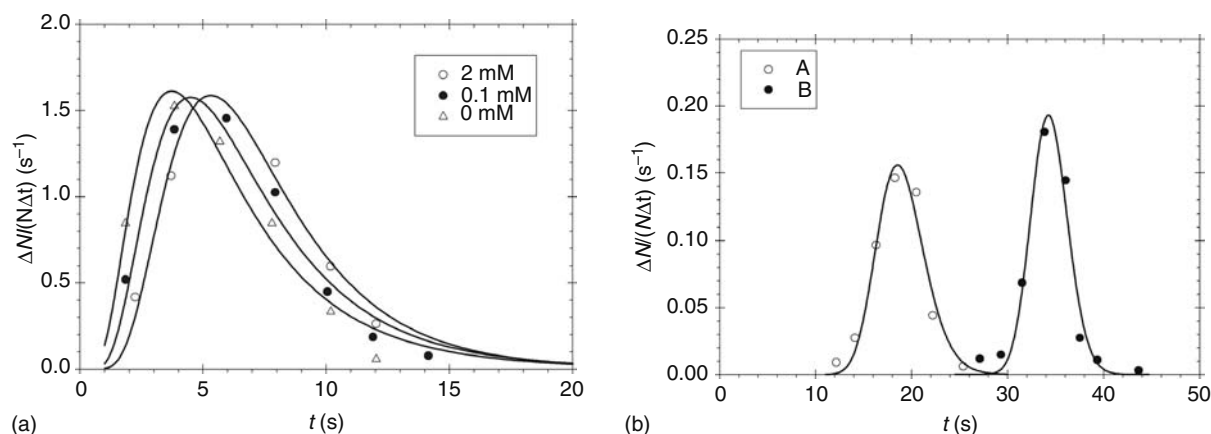
FIGURE 7.53 Histograms for the lifetimes of emulsion films: $\Delta N/N$ is the relative number of films that have ruptured during a time interval Δt. (a) Surfactant in the drops: benzene films between water drops containing surfactant sodium octylsulfonate of concentration: 0 M, 0.1 mM, and 2 mM; (b) Surfactant in the film: (a) benzene film with 0.1 M of lauryl alcohol dissolved in the film, (b) water film with 2 mM of sodium octylsulfonate inside [670].

inverted, liquid phases (the former continuous phase becomes disperse phase, and vice versa), i.e., the surfactant is in the film phase, the average lifetime is about 70 times longer—compare curves in Figure 7.53a with curve B in Figure 7.53b. The theoretical conclusions have been also checked and proved in experimental measurements with nitroethane droplets dispersed in an aqueous solution of the cationic surfactant hexadecyl trimethyl ammonium chloride (HTAC) [615].

7.5.3.3 Bancroft Rule for Emulsions

There have been numerous attempts to formulate simple rules connecting the emulsion stability with the surfactant properties. Historically, the first one was the Bancroft rule [671], which states that "to have a stable emulsion the surfactant must be soluble in the continuous phase." A more sophisticated criterion was proposed by Griffin [672] who introduced the concept of hydrophilic–lipophilic balance (HLB). As far as emulsification is concerned, surfactants with an HLB number in the range of 3–6 must form water in oil (W/O) emulsions, whereas those with HLB numbers from 8 to 18 are expected to form O/W emulsions. Different formulae for calculating the HLB numbers are available; for example, the Davies expression [673] reads

$$\text{HLB} = 7 + (\text{hydrophilic group number}) - 0.475 n_c \tag{7.301}$$

where n_c is the number of –CH_2– groups in the lipophilic part of the molecule. Schinoda and Friberg [674] proved that the HLB number is not only a property of the surfactant molecules, but also depends strongly on the temperature (for nonionic surfactants), on the type and concentration of added electrolytes, on the type of oil phase, etc. They proposed using the phase inversion temperature (PIT) instead of HLB for characterization of the emulsion stability.

Davis [675] summarized the concepts of HLB, PIT, and Windsor's ternary phase diagrams for the case of microemulsions and reported topological ordered models connected with the Helfrich membrane bending energy. Because the curvature of surfactant lamellas plays a major role in determining the patterns of phase behavior in microemulsions, it is important to reveal how the optimal microemulsion state is affected by the surface forces determining the curvature energy [222,676,677]. It is hoped that lattice models [678,679] and membrane curvature models [680,681] will lead to predictive formulae for the microemulsion design.

Ivanov et al. [613,617,618,682] have proposed a semiquantitative theoretical approach that provides a straightforward explanation of the Bancroft rule for emulsions. This approach is based on the ideas of Davies and Rideal [32] that both types of emulsions are formed during the homogenization process, but only the one with lower coalescence rate survives. If the initial drop concentration for both emulsions is the same, the coalescence rates for the two emulsions—$(\text{Rate})_1$ for emulsion 1 and $(\text{Rate})_2$ for emulsion 2 (Figure 7.54)—will be proportional to the respective coalescence rate constants, $k_{c,1}$ and $k_{c,2}$ (see Section 7.6), and inversely proportional to the film lifetimes, τ_1 and τ_2:

$$\frac{(\text{Rate})_1}{(\text{Rate})_2} \approx \frac{k_{c,1}}{k_{c,2}} \approx \frac{\tau_2}{\tau_1} \approx \frac{V_1}{V_2} \tag{7.302}$$
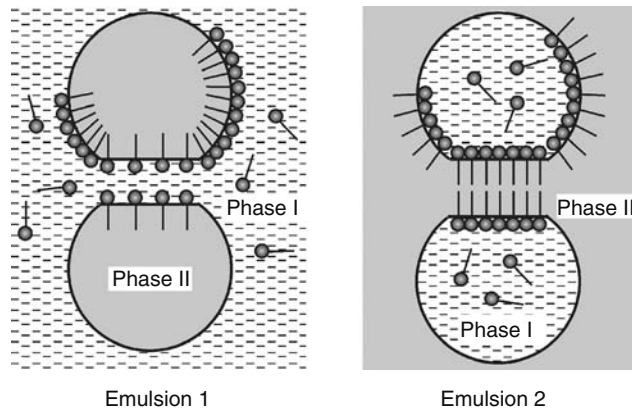
FIGURE 7.54 The two possible types of emulsions obtained just after the homogenization; the surfactant is soluble into phase I.

where V_1 and V_2 denote the respective velocities of film thinning. After some estimates based on Equations 7.273, 7.284, 7.296, and 7.297, we can express the ratio in Equation 7.302 in the form:

$$\frac{(\text{Rate})_1}{(\text{Rate})_2} \approx (486\rho_d D_s^3)^{1/3} \left(\frac{h_{cr,1}^3}{h_{cr,2}^2}\right)^{1/3} \left(\frac{\eta_d}{R^2}\right)^{1/3} \frac{P_c - \Pi_1}{E_G(P_c - \Pi_2)^{2/3}} \tag{7.303}$$

where $h_{cr,1}$ and $h_{cr,2}$ denote the critical thickness of film rupture for the two emulsions in Figure 7.54. Many conclusions can be drawn, regarding the type of emulsion to be formed:

1. If the disjoining pressures, Π_1 and Π_2, are zero, the ratio in Equation 7.303 will be very small. Hence, emulsion 1 (surfactant soluble in the continuous phase) will coalesce much more slowly and it will survive. This underlines the crucial importance of the surfactant location (which is connected with its solubility), thus providing a theoretical foundation for Bancroft's rule. The emulsion behavior in this case will be controlled almost entirely by the hydrodynamic factors (kinetic stability).
2. Disjoining pressure, Π, plays an important role. It can substantially change and even reverse the behavior of the system if it is comparable by magnitude with the capillary pressure, P_c. For example, if $(P_c - \Pi_2) \to 0$ at a finite value of $P_c - \Pi_1$ (which may happen, for example, for an O/W emulsion with oil soluble surfactant), the ratio in Equation 7.303 may become much larger than unity, which means that emulsion 2 will become thermodynamically stable. In some cases the stabilizing disjoining pressure is large enough for emulsions with a very high volume fraction of the disperse phase (above 95% in some cases) to be formed [683].
3. Gibbs elasticity, E_G, favors the formation of emulsion 1, because it slows down the film thinning. On the other hand, increased surface diffusivity, D_s, decreases this effect, because it helps the interfacial tension gradients to relax, thus facilitating the formation of emulsion 2.
4. Film radius, R, increases and capillary pressure, P_c, decreases with the drop radius, R_d. Therefore, larger drops will tend to form emulsion 1, although the effect is not very pronounced.
5. Difference in critical thicknesses of the two emulsions only slightly affects the rate ratio in Equation 7.303, although the value of h_{cr} itself is important.
6. Viscosity of the continuous phase, η, has no effect on the rate ratio, which depends only slightly on the viscosity of the drop phase, η_d. This is in agreement with the experimental observations [32].
7. Interfacial tension, σ, affects the rate ratio directly only through the capillary pressure, $P_c = 2\sigma/R_d$. The electrolyte primarily affects the electrostatic disjoining pressure, Π, which decreases as the salt content increases, thus destabilizing the O/W emulsion. It can also influence the stability by changing the surfactant adsorption (including the case of nonionic surfactants).
8. Temperature strongly affects the solubility and surface activity of nonionic surfactants [3]. It is well known that at higher temperature nonionic surfactants become more oil soluble, which favors the W/O emulsion. Thus, solubility may change the type of emulsion formed at the PIT. The surface activity has numerous implications, the most important is the change of the Gibbs elasticity, E_G, and the interfacial tension, σ.

9. Surface-active additives (cosurfactants, demulsifiers, etc.), such as fatty alcohols in the case of ionic surfactants, may affect the emulsifier partitioning between the phases and its adsorption, thereby changing the Gibbs elasticity and the interfacial tension. The surface-active additive may also change the surface charge (mainly by increasing the spacing among the emulsifier ionic headgroups), thus decreasing the repulsive electrostatic disjoining pressure and favoring the W/O emulsion. Polymeric surfactants and adsorbed proteins increase the steric repulsion between the film surfaces. They may favor either O/W or W/O emulsions, depending on their conformation at the interface and their surface activity.

10. Interfacial bending moment, B_0, can also affect the type of the emulsion, although this is not directly visible from Equation 7.303. (Note that $B_0 = -4k_cH_0$, where H_0 is the so-called spontaneous curvature and k_c is the interfacial curvature elastic modulus [188]. Typically, B_0 is of the order of 5×10^{-11} N.) Usually, for O/W emulsions, B_0 opposes the flattening of the droplet surfaces in the zone of collision (Figure 7.32), but for W/O emulsions it favors flattening [193]. This effect might be quantified by the expression for the curvature contribution in the energy of droplet–droplet interaction [193]:

$$W_c = -2\pi R^2 B_0/R_d, \quad (R/R_d)^2 \ll 1 \tag{7.304}$$

It turns out that $W_c > 0$ for the droplet collisions in an O/W emulsion, while $W_c < 0$ for a W/O emulsion [193]. Consequently, the interfacial bending moment stabilizes the O/W emulsions but destabilizes the W/O ones. There is supporting experimental evidence [684] for microemulsions, i.e., for droplets of rather small size. Moreover, the effect of the bending moment can be important even for micrometer-sized droplets [193]. This is because the bent area increases faster ($R^2 \propto R_d^2$) than the bending energy per unit area decreases ($W_c/R^2 \propto 1/R_d$) when the droplet radius, R_d, increases (see Equation 7.304).

For micron-sized emulsion droplets the capillary pressure can be so high that a film may not appear between the drops. In such case, instead of Equation 7.303, we can use analogous expression for nondeformed (spherical) drops [685].

7.5.3.4 Demulsification

It has been known for a long time [32] that one way to destroy an emulsion is to add a surfactant, which is soluble in the drop phase—this method is termed chemical demulsification. To understand the underlying process, let us consider two colliding emulsion droplets with film formed in the zone of collision (see Figures 7.32 and 7.55). As discussed above, when the liquid is flowing out of the film, the viscous drag exerted on the film surfaces (from the side of the film interior) carries away the adsorbed emulsifier toward the film periphery. Thus, a nonuniform surface distribution of the emulsifier (shown in Figure 7.55a by empty circles) is established. If demulsifier (the closed circles in Figure 7.55b) is present in the drop phase, it will occupy the interfacial area freed by the emulsifier. The result will be saturation of the adsorption layer, as shown in Figure 7.55b. If the demulsifier is sufficiently surface active, its molecules will be able to decrease substantially, and even to eliminate completely, the interfacial tension gradients, thus changing the emulsion to type 2 (see Figure 7.54 and Section 7.5.3.2). This leads to a
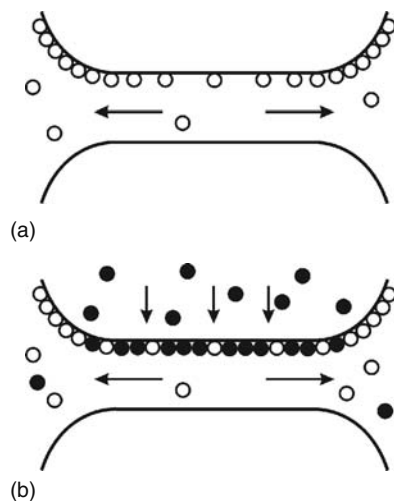
FIGURE 7.55 (a) Nonuniform surface distribution of an emulsifier due to drag from the draining film. (b) Suppression of the surface-tension gradients by a demulsifier added in the drop phase.

strong increase in the rate of film thinning, rapid drop coalescence, and emulsion destruction [617,618]. The above mechanism suggests that the demulsifier has to possess the following properties:

1. Soluble in the drop phase or in both phases, but in the latter case its solubility in the drop phase must be much higher.
2. Diffusivity and concentration must be large enough to provide a sufficiently large demulsifier flux toward the surfaces and thus eliminate the gradients of the interfacial tension.
3. Surface activity must be comparable and even higher than that of the emulsifier; otherwise, even though it may adsorb, it will not be able to suppress the interfacial tension gradients.

In regard to defoaming, various mechanisms are possible, which are discussed in Section 7.7.

7.5.4 INTERACTIONS IN NONPREEQUILIBRATED EMULSIONS

The common nonionic surfactants are often soluble in both water and oil phases. In the practice of emulsion preparation, the surfactant (the emulsifier) is initially dissolved in one of the liquid phases and then the emulsion is prepared by homogenization. In such a case, the initial distribution of the surfactant between the two phases of the emulsion is not in equilibrium; therefore, surfactant diffusion fluxes appear across the surfaces of the emulsion droplets. The process of surfactant redistribution usually lasts from several hours to days, until finally equilibrium distribution is established. The diffusion fluxes across the interfaces, directed either from the continuous phase toward the droplets or the reverse, are found to stabilize both thin films and emulsions. In particular, even films, which are thermodynamically unstable, may exist several days because of the diffusion surfactant transfer; however, they rupture immediately after the diffusive equilibrium has been established. Experimentally, this effect manifests itself in phenomena called cyclic dimpling [686] and osmotic swelling [687]. These two phenomena, as well as the equilibration of two phases across a film [688,689], are described and interpreted below.

7.5.4.1 Surfactant Transfer from Continuous to Disperse Phase (Cyclic Dimpling)

The phenomenon of cyclic dimpling was first observed [618,686] with xylene films intervening between two water droplets in the presence of the nonionic emulsifier Tween 20 or Tween 80 (initially dissolved in water but also soluble in oil). The same phenomenon also has been observed with other emulsion systems.

After the formation of such an emulsion film, it thins down to an equilibrium thickness (approximately 100 nm), determined by the electrostatic repulsion between the interfaces. As soon as the film reaches this thickness, a dimple spontaneously forms in the film center and starts growing (Figure 7.56a). When the dimple becomes bigger and approaches the film periphery, a channel forms connecting the dimple with the aqueous phase outside the film (Figure 7.56b). Then, the water contained in the dimple flows out leaving an almost plane-parallel film behind. Just afterward, a new dimple starts to grow and the process repeats again. The period of this cyclic dimpling remains approximately constant for many cycles and could be from a couple of minutes up to more than 10 min. It was established that this process is driven by the depletion of the
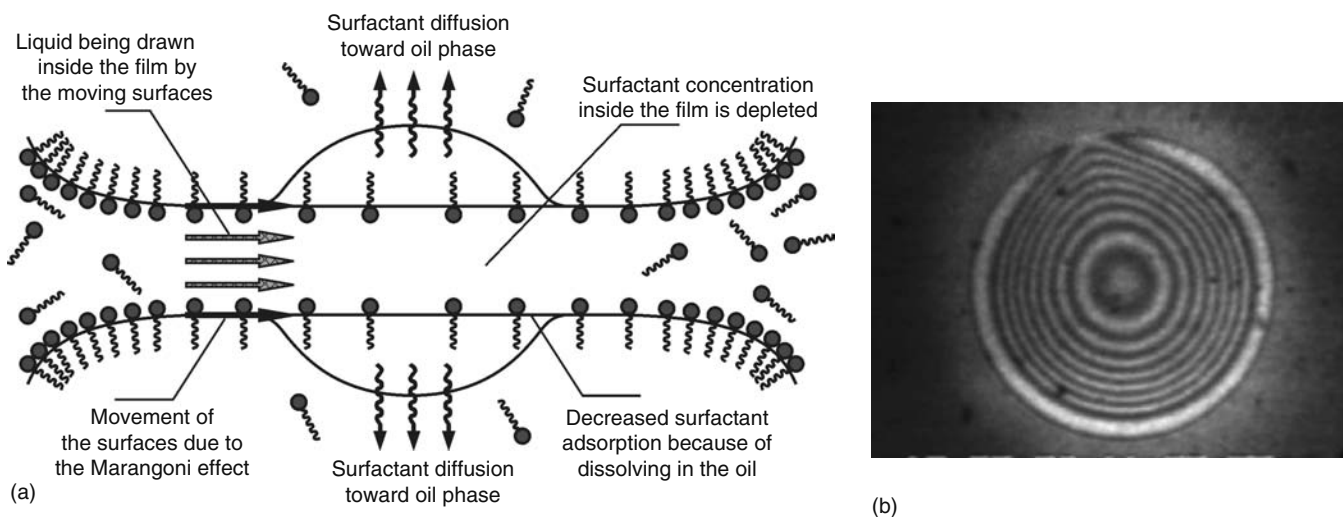
FIGURE 7.56 Spontaneous cyclic dimpling caused by surfactant diffusion from the aqueous film toward the two adjacent oil phases. (a) Schematic presentation of the process. (b) Photograph of a large dimple just before flowing out; the interference fringes in reflected light allow determination of the dimple shape.

surfactant concentration on the film surfaces due to the dissolving of surfactant in the adjacent drop phases. The depletion triggers a surface convection flux along the two film surfaces and a bulk diffusion flux in the film interior. Both fluxes are directed toward the center of the film. The surface convection causes a tangential movement of the film surfaces; the latter drag along a convective influx of solution in the film, which feeds the dimple. Thus, the cyclic dimpling appears to be a process leading to stabilization of the emulsion films and emulsions due to the influx of additional liquid in the region between the droplets, which prevents them from a closer approach, and eventually, from coalescence.

Combining the general equation of films with deformable interfaces (Equation 7.266), the mass balance (Equations 7.287 and 7.288), and the boundary condition for the interfacial stresses (Equation 7.292), we can derive [690]:

$$\frac{\partial h}{\partial t} + \frac{1}{3\eta r}\frac{\partial}{\partial r}\left\{ rh^3 \frac{\partial}{\partial r}\left[\frac{\sigma}{r}\frac{\partial}{\partial r}\left(r\frac{\partial h}{\partial r}\right) + \Pi(h)\right]\right\} = \frac{1}{2r}\frac{\partial}{\partial r}\left(\frac{jhr^2}{\Gamma}\right) \tag{7.305}$$

where
  j is the diffusion flux in the drop phase
  r is the radial coordinate
  $h(r,t)$ is the film thickness
  σ is the surface tension
  Γ is the adsorption
  Π is the disjoining pressure

The comparison between the numerical calculations based on Equation 7.305 and the experimental data for the cyclic dimpling with the anionic surfactant sodium nonylphenol polyoxyethylene-25 sulfate shows a very good agreement (Figure 7.57). The experimental points are obtained from the interference fringes (see Figure 7.56). The shape in the initial moment, $t = 0$, serves as an initial condition for determining $h(r,t)$ by solving Equation 7.305. The curves for $t = 3$, 9, 17, and 29 s represent theoretical predictions. The scaling parameters along the h and r axes in Figure 7.57 are $h_0 = 350$ nm and $R = 320$ μm, with the latter the film radius; the only adjustable parameter is the diffusion flux, j.

7.5.4.2 Surfactant Transfer from Disperse to Continuous Phase (Osmotic Swelling)

Velev et al. [615] reported that emulsion films, formed from preequilibrated phases containing the nonionic surfactant Tween and 0.1 M NaCl, spontaneously thin to Newton black films (thickness ≈ 10 nm) and then rupture. However, when the nonionic surfactant Tween 20 or Tween 60 is initially dissolved in the xylene drops and the film is formed from the nonpreequilibrated phases, no black film formation and rupture are observed [618,687]. Instead, the films have a thickness above 100 nm, and we observe formation of channels of larger thickness connecting the film periphery with the film center (Figure 7.58). We may observe that the liquid is circulating along the channels for a period from several hours to several days. The phenomenon continues until the redistribution of the surfactant between the phases is accomplished. This phenomenon occurs only when the background surfactant concentration in the continuous (the aqueous) phase is not lower than the CMC. These observations can be interpreted in the following way.
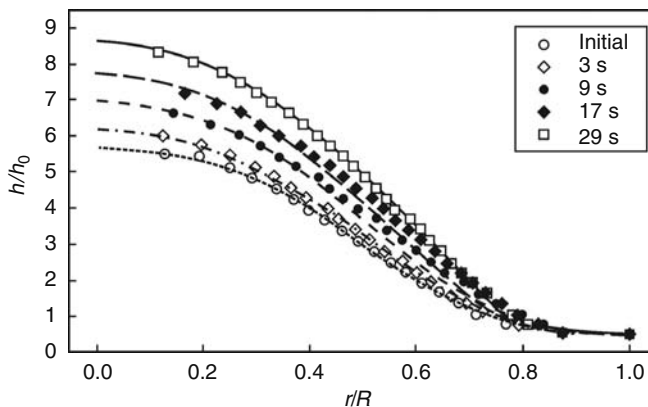
FIGURE 7.57 Comparison between the theory of cyclic dimpling (the lines) and the experimental data (the points) for the dimple shape, $h(r)$, determined from the interference fringes (see Figure 7.56b); emulsifier is anionic surfactant sodium nonylphenol polyoxyethylene-25 sulfate and the oil phase is styrene.

(a)   (b)
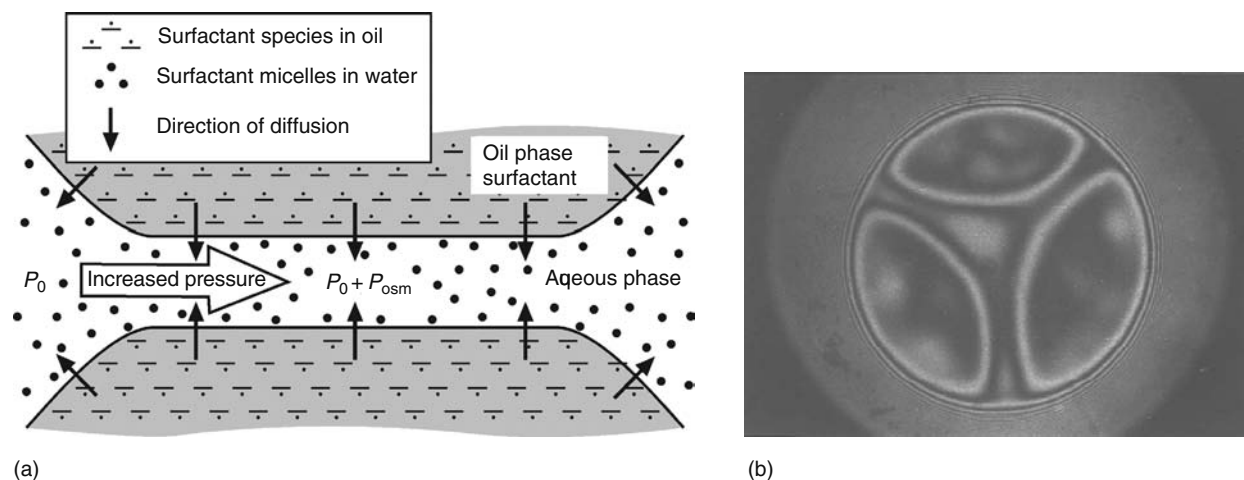
FIGURE 7.58 Osmotic swelling of an aqueous film formed between two oil droplets. (a) The surfactant dissolved in the oil is transferred by diffusion toward the film, where it forms micelles, the osmotic effects of which increase the local pressure. (b) Photograph of a typical pattern from a circular film with channels.

Because the surfactant concentration in the oil phase (the disperse phase) is higher than the equilibrium concentration, surfactant molecules cross the oil–water interface toward the aqueous phase. Thus, surfactant accumulates within the film, because the bulk diffusion throughout the film is not fast enough to transport promptly the excess surfactant into the PB. As the background surfactant concentration in the aqueous phase is not less than CMC, the excess surfactant present in the film is packed in the form of micelles (denoted by black dots in Figure 7.58a). This decreases the chemical potential of the surfactant inside the film. Nevertheless, the film is subjected to osmotic swelling because of the increased concentration of micelles within. The excess osmotic pressure

$$P_{osm} = kTC_{mic} \geq P_c \qquad (7.306)$$

counterbalances the outer capillary pressure and arrests further thinning of the film. Moreover, the excess osmotic pressure in the film gives rise to a convective outflow of solution: this is the physical origin of the observed channels (Figure 7.58b).

Experimental data [618,687] show that the occurrence of the above phenomenon is the same for initial surfactant concentration in the water varying from 1 up to 500 times the CMC, if only some amount of surfactant is also initially dissolved also in the oil. This fact implies that the value of the surfactant chemical potential inside the oil phase is much greater than that in the aqueous phase, with the latter closer to its value at the CMC in the investigated range of concentrations.

7.5.4.3   Equilibration of Two Droplets across a Thin Film

In the last two sections, we considered mass transfer from the film toward the droplets and the reverse, from droplets toward the film. In both cases, the diffusion fluxes lead to stabilization of the film. Here, we consider the third possible case corresponding to mass transfer from the first droplet toward the second one across the film between them. In contrast with the former two cases, in the last case the mass transfer is found to destabilize the films. Experimentally, the diffusion transfer of alcohols, acetic acid, and acetone was studied [691,692]. The observed destabilization of the films can be attributed to the appearance of Marangoni instability [688], which manifests itself through the growth of capillary waves at the interfaces, which eventually can lead to film rupture.

The Marangoni instabilities can appear not only in thin films, but also in the simpler case of a single interface. In this case, the Marangoni instability may bring about spontaneous emulsification. This effect has been theoretically investigated by Sterling and Scriven [693], whose work stimulated numerous theoretical and experimental studies on spontaneous emulsification. Lin and Brenner [694] examined the role of the heat and mass transfer in an attempt to check the hypothesis of Holly [695] that the Marangoni instability can cause the rupture of tear films. Their analysis was extended by Castillo and Velarde [696], who accounted for the tight coupling of the heat and mass transfer and showed that it drastically reduces the threshold for Marangoni convection. Instability driven by diffusion flux of dissolved oil molecules across an asymmetric liquid film (oil–water–air film) has been theoretically investigated [689]. It was found that even small decrements of the water–air surface tension, caused by the adsorbed oil, are sufficient to trigger the instability.

7.5.5 HYDRODYNAMIC INTERACTION OF A PARTICLE WITH AN INTERFACE

There are various cases of particle–interface interactions, which require separate theoretical treatment. The simpler case is the hydrodynamic interaction of a solid particle with a solid interface. Other cases are the interactions of fluid particles (of tangentially mobile or immobile interfaces) with a solid surface; in these cases, the hydrodynamic interaction is accompanied by deformation of the particle. On the other hand, the colloidal particles (both solid and fluid) may hydrodynamically interact with a fluid interface, which thereby undergoes a deformation. In the case of fluid interfaces, the effects of surfactant adsorption, surface diffusivity, and viscosity affect the hydrodynamic interactions. A special class of problems concerns particles attached to an interface, which are moving throughout the interface. Another class of problems is related to the case when colloidal particles are confined in a restricted space within a narrow cylindrical channel or between two parallel interfaces (solid and fluid); in the fluid case, the particles interact simultaneously with both film surfaces.

The theoretical contributions are limited to the case of low Reynolds number [536,537,613,697–699] (mostly for creeping flows, see Section 7.5.1), avoiding the difficulties arising from the nonlinearity of the equations governing the fluid motion at higher velocities. Indeed, for low Reynolds numbers, the term $\mathbf{v} \cdot \nabla \mathbf{v}$ in the Navier–Stokes equation (see Equations 7.258 through 7.260) is negligible, and we may apply the method of superposition to solve the resulting linear set of equations. This means that we may first solve the simpler problems about the particle elementary motions: (1) particle translation (without rotation) in an otherwise immobile liquid, (2) particle rotation (without translation) in an otherwise immobile liquid, and (3) streamlining of an immobile particle by a Couette or Poiseuille flow. Once the problems about the elementary motions have been solved, we may obtain the linear and angular velocity of the real particle motion combining the elementary flows. The principle of combination is based on the fact that for low Reynolds numbers the particle acceleration is negligible, and the net force and torque exerted on the particle must be zero. In other words, the hydrodynamic drag forces and torques originating from the particle translation and rotation are counterbalanced by those originating from the streamlining:

$$\mathbf{F}_{\text{translation}} + \mathbf{F}_{\text{rotation}} + \mathbf{F}_{\text{streamlining}} = \mathbf{0}, \quad \mathbf{M}_{\text{translation}} + \mathbf{M}_{\text{rotation}} + \mathbf{M}_{\text{streamlining}} = \mathbf{0} \tag{7.307}$$

That is the reason why we will now consider expressions for $\mathbf{F}$ and $\mathbf{M}$ for various types of elementary motions.

7.5.5.1 Particle of Immobile Surface Interacting with a Solid Wall

The force and torque exerted on a solid particle were obtained in the form of a power series with respect to R_d/l, where R_d is the particle radius and l is the distance from the center of the particle to the wall. Lorentz [700] derived an asymptotic expression for the motion of a sphere along the normal to a planar wall with an accuracy of up to R_d/l. Faxen [701] developed the method of reflection for a sphere moving between two parallel planes in a viscous fluid. Using this method, Wakiya [702] considered the cases of motion in flow of Couette and Poiseuille; however, the method employed by him, cannot be applied to small distances to the wall [559]. The next important step was taken by Dean and O'Neil [703] and O'Neil [704], who found an exact solution for the force and the torque acting on a spherical particle moving tangentially to a planar wall at an arbitrary distance from the wall. The limiting case of small distances between the particle and the wall was examined by several authors [550–552,705]. Instead of an exact solution of the problem, the authors derived asymptotic formulae for the force and torque. Keh and Tseng [706] presented a combined analytical–numerical study for the slow motion of an arbitrary axisymmetric body along its axis of revolution, with the latter normal to a planar surface. The inertial migration of a small solid sphere in a Poiseuille flow was calculated by Schonberg and Hinch [707] for the case when the Reynolds number for the channel is of the order of unity.

Below, we present expressions for the forces and torques for some of the elementary motions. In all cases we assume that the Reynolds number is small, the coordinate plane xy is parallel to the planar wall and h is the shortest surface-to-surface distance from the particle to the wall.

First, we consider the case of a pure translational motion: a solid spherical particle of radius R_d that translates along the y-axis with a linear velocity U and angular velocity $\omega \equiv 0$ in an otherwise quiescent fluid. In spite of the fact that the particle does not rotate, it experiences a torque, $\mathbf{M}$, directed along the x-axis, due to friction with the viscous fluid. The respective asymptotic expressions [550–552] for the components of the drag force, $\mathbf{F}$, and torque, $\mathbf{M}$, read

$$F_x = 0, \quad F_y = -6\pi\eta U R_d f_y, \quad M_x = -8\pi\eta U R_d^2 m_x, \quad M_y = 0 \tag{7.308}$$

$$f_y = \left(\frac{8}{15} + \frac{16}{375}\frac{h}{R_d}\right)\ln\left(\frac{2R_d}{h}\right) + 0.58461 + O\left(\frac{h}{R_d}\right) \tag{7.309}$$

$$m_x = \left(\frac{1}{10} + \frac{43}{250}\frac{h}{R_d}\right)\ln\left(\frac{2R_d}{h}\right) - 0.26227 + O\left(\frac{h}{R_d}\right) \tag{7.310}$$

where f_y and m_x are dimensionless drag force and torque coefficients, respectively.

Second, we consider the case of pure rotation: a solid spherical particle of radius R_d is situated at a surface-to-surface distance, h, from a planar wall and rotates with angular velocity, ω, around the x-axis in an otherwise quiescent fluid. The corresponding force and torque resultants are [550–552]

$$F_x = 0, \quad F_y = -6\pi\eta\omega R_d^2 f_y, \quad M_x = -8\pi\eta\omega R_d^3 m_x, \quad M_y = 0 \tag{7.311}$$

$$f_y = \frac{2}{15}\ln\left(\frac{R_d}{h}\right) - 0.2526 + O\left(\frac{h}{R_d}\right), \quad m_x = \frac{2}{5}\ln\left(\frac{R_d}{h}\right) + 0.3817 + O\left(\frac{h}{R_d}\right) \tag{7.312}$$

From Equations 7.308 through 7.312, it follows that the force and the torque depend weakly (logarithmically) on the distance, h, as compared to the Taylor or Reynolds laws (Equations 7.271 and 7.272).

As discussed in Sections 7.5.2.1 and 7.5.3.2, a fluid particle in the presence of high surfactant concentration can be treated as a deformable particle of tangentially immobile surfaces. Such a particle deforms when pressed against a solid wall (see the inset in Figure 7.59). To describe the drag due to the film intervening between the deformed particle and the wall, we may use the expression derived by Reynolds [538] for the drag force exerted on a planar solid ellipsoidal disc, which is parallel to a solid wall and is moving along the y-axis at a distance h from the wall:

$$F_x = 0, \quad F_y = -\pi\eta U\frac{h}{ab} \tag{7.313}$$

Here, a and b are the semiaxes of the ellipse; for a circular disc (or film), we have $a = b = R$. By combining Equations 7.308 and 7.309 with Equation 7.313, we can derive an expression for the net drag force experienced by the deformed particle (the inset in Figure 7.59) when it moves along the y-axis with a linear velocity U:

$$F_y = -6\pi\eta U R_d f_y, \quad f_y = \frac{R^2}{6hR_d} + \left(\frac{8}{15} + \frac{16}{375}\frac{h}{R_d}\right)\ln\left(\frac{2R_d}{h}\right) + 0.58461 + O\left(\frac{h}{R_d}\right) \tag{7.314}$$

where
   h and R denote film thickness and radius
   R_d is the curvature radius of the spherical part of the particle surface

The dependence of the dimensionless drag coefficient, f_y, on the distance h for different values of the ratio R/R_d is illustrated in Figure 7.59. The increase of R/R_d and the decrease of h/R_d may lead to an increase of the drag force, f_y, by an order of magnitude. The reason why the film between a deformed particle and a wall can be responsible for the major part of the energy dissipation. Moreover, the formation of doublets and flocks of droplets separated by liquid films seems to be of major importance for the rheological behavior of emulsions.
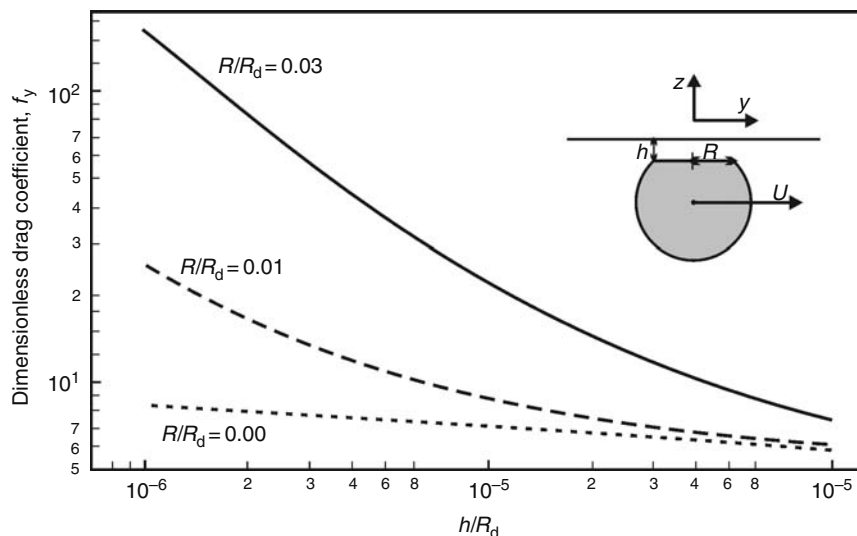

FIGURE 7.59 Deformed fluid particle (the inset) moving tangentially to an immobile solid surface: plot of the dimensionless drag coefficient, f_y, versus the dimensionless film thickness, h/R_d, for three values of the dimensionless film radius, R/R_d (see Equation 7.314).

7.5.5.2 Fluid Particles of Mobile Surfaces

Let us start with the case of pure phases, when surfactant is missing and the fluid–liquid interfaces are mobile. Under these conditions, the interaction of an emulsion droplet with a planar solid wall was investigated by Ryskin and Leal [708], and numerical solutions were obtained. A new formulation of the same problem was proposed by Liron and Barta [709]. The case of a small droplet moving in the restricted space between two parallel solid surfaces was solved by Shapira and Haber [710,711]. These authors used the Lorentz reflection method to obtain analytical solutions for the drag force and the shape of a small droplet moving in Couette flow or with constant translational velocity.

The more complicated case, corresponding to a viscous fluid particle approaching the boundary between two pure fluid phases (all interfaces deformable), was investigated by Yang and Leal [712,713] who succeeded in obtaining analytical results.

Next, we proceed with the case when surfactant is present and the Marangoni effect becomes operative. Classical experiments carried out by Lebedev [714] and Silvey [715] show that the measured velocity of sedimentation, U, of small fluid droplets in a viscous liquid (pure liquid phases assumed) does not obey the Hadamar [716] and Rybczynski [717] equation:

$$F = 2\pi\eta U R_d \frac{3\eta_d + 2\eta}{\eta_d + \eta} \tag{7.315}$$

where F is the drag force. The limiting case $\eta_d \to 0$ corresponds to bubbles, whereas in the other limit, $\eta_d \to \infty$, Equation 7.315 describes solid particles. Note that Equation 7.315 is derived for the motion of a spherical fluid particle (drop or bubble) of viscosity η_d in a liquid of viscosity η in the absence of any surfactant. The explanation of the contradiction between theory and experiment [714,715] turned out to be very simple: even liquids that are pure from the viewpoint of the spectral analysis may contain some surface-active impurities, whose bulk concentration might be vanishingly low, but which can provide a dense adsorption layer at the restricted area of the fluid particle surface. Then, the effects of Gibbs elasticity and interfacial viscosity substantially affect the drag coefficient of the fluid particle. The role of the latter two effects was investigated by Levich [553], Edwards et al. [554], and He et al. [718] for the motion of an emulsion droplet covered with a monolayer of nonsoluble surfactant (adsorption and/or desorption not present). These authors used the Boussinesq–Scriven constitutive law of a viscous fluid interface (Equation 7.292), and established that only the dilatational interfacial viscosity, η_{dl}, but not the shear interfacial viscosity, η_{sh}, influences the drag force. If the surfactant is soluble in both phases and the process of adsorption is diffusion controlled (see Section 7.2.2.1) the generalization of Equation 7.315 is

$$F = 2\pi\eta U R_d \left[3 - \left(1 + \frac{\eta_d}{\eta} + \frac{2\eta_{dl}}{\eta R_d} + \frac{R_d E_G}{3\eta D_s} \frac{2}{2 + 2\dfrac{R_d D}{h_a D_s} + \dfrac{R_d D_d}{h_{d,a} D_s}} \right)^{-1} \right] \tag{7.316}$$

where
D_d is the surfactant diffusion coefficient in the drop phase
c and c_d are the concentrations of surfactant in the continuous and drop phases, respectively
$h_a = \partial\Gamma/\partial c$ and $h_{d,a} = \partial\Gamma/\partial c_d$ are the slopes of adsorption isotherms with respect to the surfactant concentration

In the limiting case without surfactant Equation 7.316 is reduced to the Hadamar [716] and Rybczynski [717] equation (Equation 7.315).

Danov et al. [313,719–722] investigated theoretically the hydrodynamic interaction of a fluid particle with a fluid interface in the presence of surfactant. The numerical results of these authors reveal that there is a strong influence of both shear and dilatational interfacial viscosities on the motion of the fluid particle when the particle–interface distance, h, is approximately equal to or smaller than the particle radius, R_d. For example, in the presence of an external force acting parallel to the interface (along the y-axis), the stationary motion of the spherical particle close to the viscous interface is a superposition of a translation along the y-axis with velocity V_y and a rotation (around the x-axis) with an angular velocity, ω_x (see the inset in Figure 7.50a). The numerical results of Danov et al. [721,722] for V_y and ω_x normalized by the Stokes velocity, $V_{Stokes} = F/(6\pi\eta R_d)$, are plotted in Figures 7.60a and b versus h/R_d for four different types of interfaces: (1) solid particle and solid wall (see Equations 7.308 through 7.310); (2) fluid particle and fluid interface for $K = E = 100$; (3) the same system as (2) but for $K = E = 10$; (4) the same system as (2) but for $K = E = 1$, where

$$K \equiv \eta_{dl}/(\eta R_d), \quad E \equiv \eta_{sh}/(\eta R_d) \tag{7.317}$$
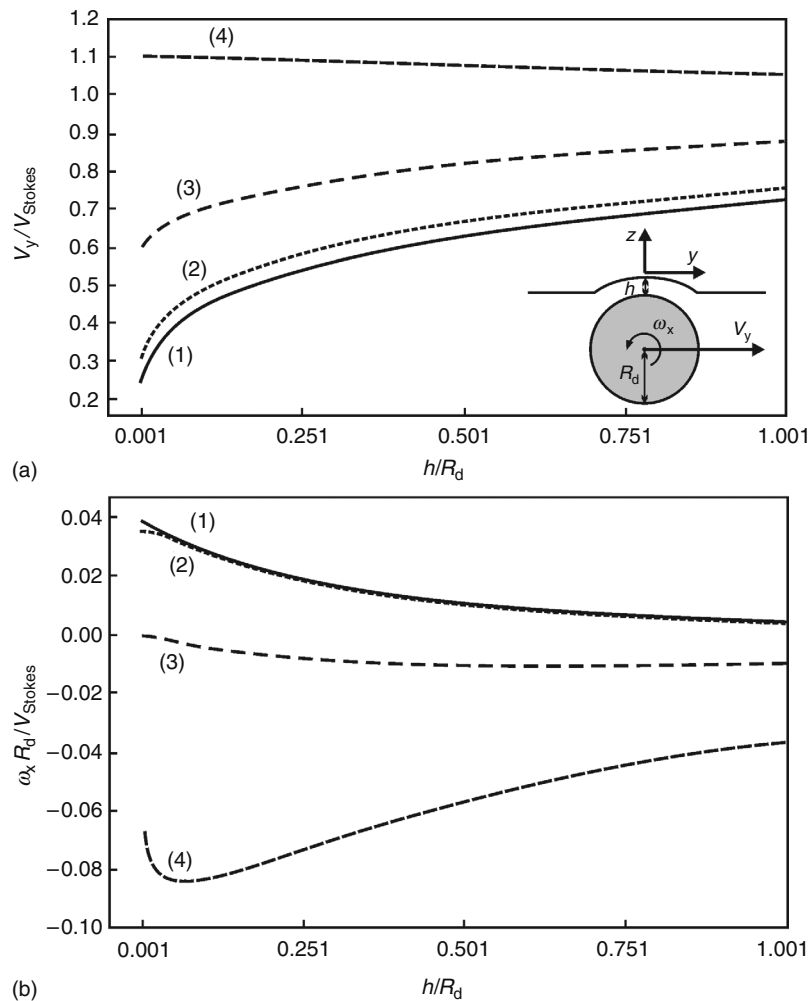
FIGURE 7.60 Spherical particle moving tangentially to a viscous interface: plots of the stationary dimensionless linear (V_y/V_{Stokes}) (a) and angular ($\omega_x R_d/V_{Stokes}$) (b) velocities versus the dimensionless thickness, h/R_d. The curves correspond to various surface viscosities: (1) $K = E = \infty$ (solid surfaces); (2) $K = E = 100$; (3) $K = E = 10$, and (4) $K = E = 1$ (see Equation 7.317).

(For the definition of the interfacial viscosities, η_{dl} and η_{sh}, see Equation 7.292). As seen in Figure 7.60a, the velocity of the sphere, V_y, is less than V_{Stokes} for the solid (1) and the highly viscous (2) interfaces, and V_y noticeably decreases when the distance h decreases. However, in case (4), corresponding to low surface viscosities, the effect is quite different: V_y/V_{Stokes} is greater than unity (the sphere moves faster near the interface than in the bulk), and its dependence on h is rather weak. The result about the angular velocity, ω_x, is also intriguing (Figure 7.60b). The stationary rotation of a sphere close to a solid (1) or highly viscous (2) interface is in positive direction, i.e., $\omega_x > 0$. For the intermediate interfacial viscosity (3), the sphere practically does not rotate, whereas, for the interfaces of low viscosity (4), the drop rotates in the opposite direction, i.e., $\omega_x < 0$. The inversion of the sign of ω_x is due to the fact that the friction of the particle with the bulk fluid below it (see the inset in Figure 7.60a) becomes stronger than the friction with the interface above the particle.

Finally, we consider the case of a solid particle attached to a liquid–fluid interface. This configuration is depicted in Figure 7.21e; note that the position of the particle along the normal to the interface is determined by the value of the three-phase contact angle. Stoos and Leal [723] investigated the case when such an attached particle is subjected to a flow directed normally to the interface. These authors determined the critical capillary number, beyond which the captured particle is removed from the interface by the flow.

Danov et al. [313] examined the case of an attached particle moving along a liquid–gas interface under the action of an applied force directed tangentially to the interface. The effect of the contact angle (the depth of immersion), as well as the effect of adsorbed surfactant on the drag force, was investigated. These authors also calculated the surface diffusion coefficient of a Brownian particle attached to the liquid surface. Let D_p and D_{p0} be the particle surface diffusion coefficient in the presence and in the absence of surfactant, respectively. In Figure 7.61a, we plot the results for D_p/D_{p0} versus the solid–liquid–gas contact angle, θ, for three different values of the parameters K and E characterizing the surface viscosities (see Equation 7.317):
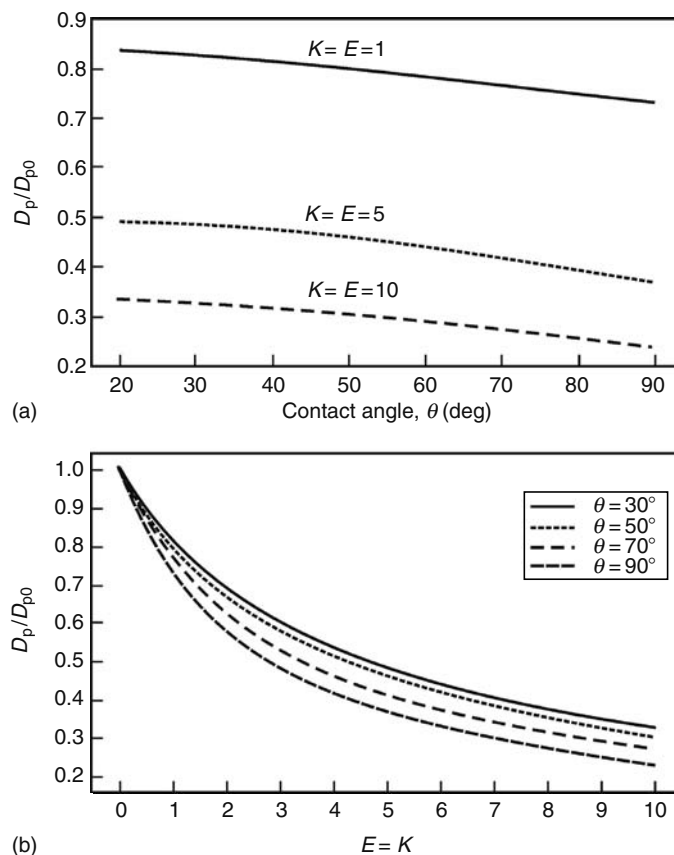
FIGURE 7.61 Effect of adsorbed surfactant on the surface diffusivity, D_p, of a Brownian particle attached to a fluid interface: (a) plot of D_p/D_{p0} versus particle contact angle, θ, for various surface viscosities, (see Equation 7.317); (b) plot of D_p/D_{p0} versus the dimensionless surface viscosity, $K = E$, for various θ.

(1) $K = E = 1$; (2) $K = E = 5$, and (3) $K = E = 10$. The relatively small slope of the curves in Figure 7.61a indicates that D_p/D_{p0} depends less significantly on the contact angle, θ, than on the surface viscosity characterized by K and E. Note, however, that D_{p0} itself depends markedly on θ: the absolute value of D_{p0} is smaller for the smaller values of θ (for deeper immersion of the particle in the liquid phase). Figure 7.61b presents the calculated dependence of D_p/D_{p0} on the surface viscosity characterized by K and E ($K = E$ is used in the calculations) for various fixed values of the contact angle, θ. Apparently, the particle mobility decreases faster for the smaller values of K and then tends to zero insofar as the fluid surface solidifies for the higher values of the surface viscosities. The experimental data from measurements of the drag coefficient of spherical particles attached to fluid interfaces [312] showed very good agreement with the predictions of the theory [313].

The role of surface viscosity and elasticity on the motion of a solid particle trapped in a thin film, at an interface, or at a membrane of a spherical vesicle has been recently investigated in Refs. [724,725]. The theoretical results [724,725] have been applied to process the experimental data for the drag coefficient of polystyrene latex particles moving throughout the membrane of a giant lipid vesicle [726–732]. Thus, the interfacial viscosity of membranes has been determined.

7.5.6 BULK RHEOLOGY OF DISPERSIONS

The description of the general rheological behavior of colloidal dispersions requires information regarding the drag forces and torques experienced by the individual particles [368,733,734]. In dilute systems, the hydrodynamic interactions between the particles can be neglected and their motion can be treated independently. In contrast, when the particle concentration is higher, the effect of hydrodynamic interactions between a spherical particle and an interface on the drag force and torque acquires considerable importance. The viscosity and the collective diffusion coefficient of colloidal dispersions can be strongly affected also by long-range surface forces, like the electrostatic double layer force (see Section 7.9.2.4).

Long ago Einstein [735] obtained a formula for the diffusion coefficient for solid spheres in the dilute limit:

$$D = kT/(6\pi\eta_m R_p) \tag{7.318}$$

where

R_p is the particle radius
η_m is the viscosity of the liquid medium

This relation was later generalized by Kubo [736] for cases when the hydrodynamic resistance becomes important. The further development in this field is reviewed by Davis [697].

The particle–particle interactions lead to a dependence of the viscosity, η, of a colloidal dispersion on the particle volume fraction, ϕ. Einstein [737] showed that for a suspension of spherical particles in the dilute limit:

$$\eta = \eta_m[1 + 2.5\phi + O(\phi^2)] \tag{7.319}$$

Later Taylor [738] generalized Equation 7.319 for emulsion systems taking into account the viscous dissipation of energy due to the flow inside the droplets. Oldroyd [739] took into account the effect of surface viscosity and generalized the theory of Taylor [738] to diluted monodisperse emulsions whose droplets have viscous interfaces. Taylor [740], Fröhlich and Sack [741], and Oldroyd [742] applied asymptotic analysis to derive the next term in Equation 7.319 with respect to the capillary number. Thus, the effect of droplet interfacial tension was included. This generalization may be important at high shear rates. Another important generalization is the derivation of appropriate expressions for the viscosity of suspensions containing particles with different shapes [536,537]. A third direction of generalization of Equation 7.319 is to calculate the next term in the series with respect to the volume fraction, ϕ. Batchelor [743] took into account the long-range hydrodynamic interaction between the particles to derive:

$$\eta = \eta_m[1 + 2.5\phi + 6.2\phi^2 + O(\phi^3)] \tag{7.320}$$

From a mathematical viewpoint, Equation 7.320 is an exact result; however, from a physical viewpoint, Equation 7.320 is not entirely adequate to the real dispersions, as not only the long-range hydrodynamic interactions are operative in colloids. A number of empirical expressions have been proposed in which the coefficient multiplying ϕ^2 varies between 5 and 15 [744]. The development of new powerful numerical methods during the last 10 years helped for a better understanding of the rheology of emulsions [745–753]. The simple shear and Brownian flow of dispersions of elastic capsules, rough spheres, and liquid droplets were studied in Refs. [746,750,752,753]. The effect of insoluble surfactants and the drop deformation on the hydrodynamic interactions and on the rheology of dilute emulsions are the subject of investigation in Refs. [747,749,751]. Loewenberg and Hinch [745,748] discussed the basic ideas of the numerical simulations of concentrated emulsion flows. These works are aimed at giving a theoretical interpretation of various experimental results for dilute and concentrated dispersions. When the Peclet number is not small, the convective term in the diffusion equation (Equations 7.287 and 7.288) cannot be neglected and the respective problem has no analytical solution. Thus, a complex numerical investigation has to be applied [754,755].

The formulae of Einstein [735,737], Taylor [738], and Oldroyd [739] have been generalized for dilute emulsions of mobile surfaces with account for the Gibbs elasticity and the bulk and surface diffusion and viscosity [756]:

$$\frac{\eta}{\eta_m} = 1 + \left(1 + \frac{3}{2}<\varepsilon_m>\right)\phi + O(\phi^2), \quad <\varepsilon_m> \equiv \sum R_d^3 \varepsilon_m \Big/ \sum R_d^3 \tag{7.321}$$

where $<\varepsilon_m>$ is the average value of the interfacial mobility parameter, ε_m, for all droplets in the control volume. The mobility parameter of individual drops, ε_m, and the effective surfactant diffusion coefficient, D_{eff}, are [756]

$$\varepsilon_m \equiv \frac{\left[\dfrac{\eta_d}{\eta_m} + \dfrac{2}{5}\left(\dfrac{R_d E_G}{2\eta_m D_{eff}} + \dfrac{3\eta_{dl} + 2\eta_{sh}}{R_d \eta_m}\right)\right]}{\left[1 + \dfrac{\eta_d}{\eta_m} + \dfrac{2}{5}\left(\dfrac{R_d E_G}{2\eta_m D_{eff}} + \dfrac{3\eta_{dl} + 2\eta_{sh}}{R_d \eta_m}\right)\right]} \tag{7.322}$$

$$D_{eff} \equiv D_s + \frac{R_d D}{2h_a} + \frac{R_d D_d}{3h_{d,a}} \tag{7.323}$$

(see Equation 7.316). If the droplet size distribution in the emulsion, and the interfacial rheological parameters are known, then the average value $<\varepsilon_m>$ can be estimated. For monodisperse emulsions the average value, $<\varepsilon_m>$, and the interfacial mobility parameter, ε_m, are equal. In the special case of completely mobile interfaces, that is, $R_d E_G/(\eta_m D_{eff}) \to 0$ and $(3\eta_{dl} + 2\eta_{sh})/(R_d \eta_m) \to 0$, the mobility parameter, ε_m, does not depend on the droplet size, and from Equations 7.322 and 7.323 the Taylor
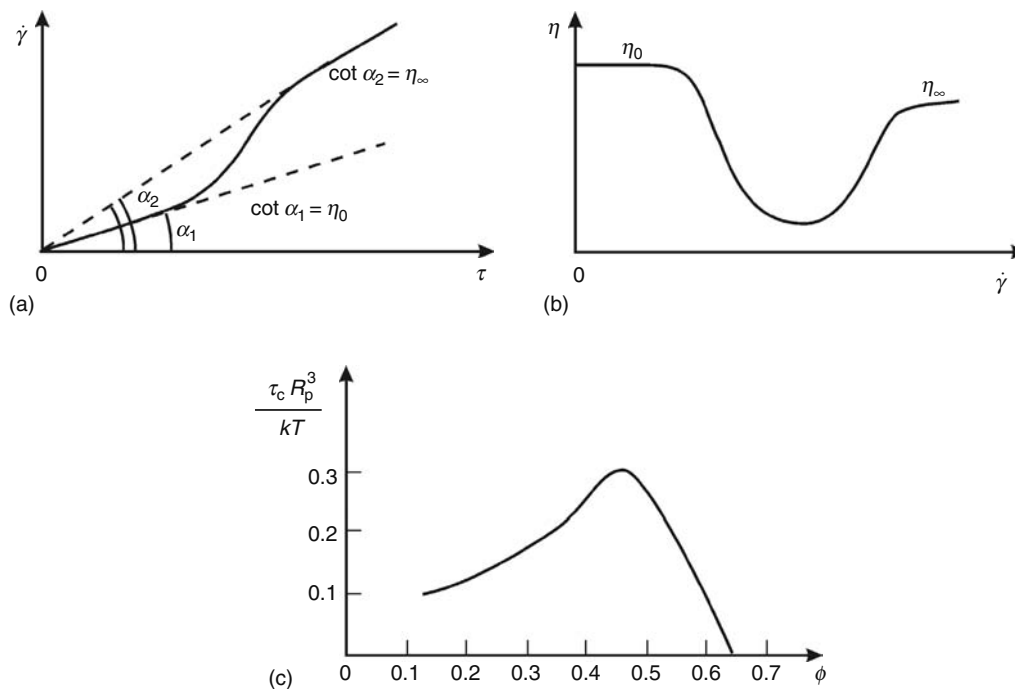
FIGURE 7.62 Qualitative presentation of basic relations in rheology of suspensions: (a) rate of strain, $\dot{\gamma}$, versus applied stress, τ, (see Equation 7.324); (b) average viscosity of a suspension, η, versus rate of strain, $\dot{\gamma}$; (c) dimensionless parameter τ_c (Equation 7.328) versus particle volume fraction ϕ.

[738] formula is obtained. It is important to note that the Taylor formula takes into account only the bulk properties of the phases (characterized by η_d/η_m); in such a case ε_m is independent of R_d and the Taylor equation is applicable also to polydisperse emulsions. If only the Marangoni effect is neglected ($E_G \rightarrow 0$), then Equations 7.322 and 7.323 become equivalent to the Oldroyd [739] formula, which is originally derived only for monodisperse emulsions.

For higher values of the particle volume fraction, the rheological behavior of the colloidal dispersions becomes rather complex. We will consider qualitatively the observed phenomena, and next we will review available semiempirical expressions.

For a simple shear (Couette) flow, the relation between the applied stress, τ, and the resulting shear rate, $\dot{\gamma}$, can be expressed in the form:

$$\tau = \eta\dot{\gamma} \tag{7.324}$$

(For example, when a liquid is sheared between two plates parallel to the xy plane, we have $\dot{\gamma} = \partial v_x/\partial z$.) A typical plot of $\dot{\gamma}$ versus τ is shown in Figure 7.62a. For low and high shear rates, we observe Newtonian behavior ($\eta = \text{constant}$), whereas in the intermediate region a transition from the lower shear rate viscosity, η_0, to the higher shear rate viscosity, η_∞, takes place. This is also visualized in Figure 7.62b, where the viscosity of the colloidal dispersion, η, is plotted versus the shear rate, $\dot{\gamma}$; note that in the intermediate zone η has a minimum [530].

Also note that both η_0 and η_∞ depend on the particle volume fraction, ϕ. De Kruif et al. [744] proposed the semiempirical expansions:

$$\frac{\eta_0}{\eta_m} = 1 + 2.5\phi + (4 \pm 2)\phi^2 + (42 \pm 10)\phi^3 + \cdots \tag{7.325}$$

$$\frac{\eta_\infty}{\eta_m} = 1 + 2.5\phi + (4 \pm 2)\phi^2 + (25 \pm 7)\phi^3 + \cdots \tag{7.326}$$

as well as two empirical expressions which can be used in the whole range of values of ϕ:

$$\frac{\eta_0}{\eta_m} = \left(1 - \frac{\phi}{0.63}\right)^{-2}, \quad \frac{\eta_\infty}{\eta_m} = \left(1 - \frac{\phi}{0.71}\right)^{-2} \tag{7.327}$$

In regard to the dependence of η on the shear stress, τ, Russel et al. [368] reported that for the intermediate values of τ, corresponding to non-Newtonian behavior (Figures 7.62a and b), the experimental data correlate reasonably well with the expression:

$$\frac{\eta - \eta_\infty}{\eta - \eta_0} = \frac{1}{1 + (\tau/\tau_c)^n} \tag{7.328}$$

with $1 \le n \le 2$, where τ_c is the value of τ for which $\eta = (\eta_0 + \eta_\infty)/2$. In its own turn, τ_c depends on the particle volume fraction ϕ (see Figure 7.62c). We see that τ_c increases with the volume fraction, ϕ, in dilute dispersions then passes through a maximum and finally decreases down to zero; note that $\tau_c \to 0$ corresponds to $\eta_0 \to \infty$. The peak at $\phi \approx 0.5$ is the only indication that the hard-sphere disorder–order transition either occurs or is rheologically significant in these systems [368].

The restoring force for a dispersion to return to a random, isotropic situation at rest is either Brownian (thermal fluctuations) or osmotic [757]. The former is the most important for submicrometer particles and the latter for larger particles. Changing the flow conditions changes the structure, and this leads to thixotropic effects, which are especially strong in flocculated systems.

Krieger and Dougherty [758] applied the theory of corresponding states to obtain the following expression for the viscosity of hard-sphere dispersions:

$$\frac{\eta}{\eta_m} = \left(1 - \frac{\phi}{\phi_{max}}\right)^{-[\eta]\phi_{max}} \tag{7.329}$$

where
    $[\eta]$ is the dimensionless intrinsic viscosity, which has a theoretical value of 2.5 for monodisperse rigid spheres
    ϕ_{max} is the maximum packing volume fraction for which the viscosity η diverges

The value of ϕ_{max} depends on the type of packing of the particles [530] (Table 7.7). The maximum packing fraction, ϕ_{max}, is very sensitive to particle-size distribution and particle shape [759]. Broader particle-size distributions have greater values of ϕ_{max}. On the other hand, nonspherical particles lead to poorer space-filling and hence lower ϕ_{max}. Table 7.8 presents the values of $[\eta]$ and ϕ_{max} obtained by fitting the results of a number of experiments on dispersions of asymmetric particles using Equation 7.329. The trend of $[\eta]$ to increase and ϕ_{max} to decrease with increasing asymmetry is clearly seen, but the product, $[\eta]\phi_{max}$, is almost constant; $[\eta]\phi_{max}$ is about 2 for spheres and about 1.4 for fibers. This fact can be utilized to estimate the viscosity of a wide variety of dispersions.

A number of rheological experiments with foams and emulsions are summarized in the reviews by Prud'home and Khan [760] and Tadros [761]. These experiments demonstrate the influence of films between the droplets (or bubbles) on the shear viscosity of the dispersion as a whole. Unfortunately, there is no consistent theoretical explanation of this effect accounting for the different hydrodynamic resistance of the films between the deformed fluid particles as compared to the nondeformed spherical particles (see Sections 7.5.2 and 7.5.3). In the case of emulsions and foams, the deformed droplets or bubbles have a polyhedral shape, and maximum packing fraction can be $\phi_{max} \approx 0.9$ and even higher. For this case, a special geometrical rheological theory has been developed [554,762,763].

Wessel and Ball [764] and Kanai et al. [765] studied in detail the effects of shear rate on the fractal structure of flocculated emulsion drops. They showed that the size of the flocs usually decreases with the increase of the shear stress; often the flocs are split to single particles at high shear rates. As a result, the viscosity decreases rapidly with the increase of the shear rate.

Interesting effects are observed when a dispersion contains both larger and smaller particles; the latter are usually polymer coils, spherical or cylindrical surfactant micelles, or microemulsion droplets. The presence of the smaller particles may induce clustering of the larger particles due to the depletion attraction (see Section 7.4.5.3.3); such effects are described in the works on

TABLE 7.7

Maximum Packing Volume Fraction, ϕ_{max}, for Various Arrangements of Monodisperse Spheres

Arrangement	ϕ_{max}
Simple cubic	0.52
Minimum thermodynamically stable configuration	0.548
Hexagonally packed sheets just touching	0.605
Random close packing	0.637
Body-centered cubic packing	0.68
Face-centered cubic/hexagonal close packed	0.74

TABLE 7.8
Values of $[\eta]$ and ϕ_{max} for a Number of Dispersions Obtained by Fitting
Experimental Data by Means of Equation 7.329

System	$[\eta]$	ϕ_{max}	$[\eta]\phi_{max}$	Reference
Spheres (submicron)	2.7	0.71	1.92	[744]
Spheres (40 μm)	3.28	0.61	2.00	[771]
Ground gypsum	3.25	0.69	2.24	[772]
Titanium dioxide	5.0	0.55	2.75	[772]
Glass rods (30×700 μm)	9.25	0.268	2.48	[773]
Quartz grains (53–76 μm)	5.8	0.371	2.15	[773]
Glass fibers:				
Axial ratio-7	3.8	0.374	1.42	[771]
Axial ratio-14	5.03	0.26	1.31	[771]
Axial ratio-21	6.0	0.233	1.40	[771]

surfactant-flocculated and polymer-flocculated emulsions [766–769]. Other effects can be observed in dispersions representing mixtures of liquid and solid particles. Yuhua et al. [770] have established that if the size of the solid particles is larger than three times the size of the emulsion drops, the emulsion can be treated as a continuous medium (of its own average viscosity), in which the solid particles are dispersed; such treatment is not possible when the solid particles are smaller.

7.6 KINETICS OF COAGULATION

There are three scenarios for the occurrence of a two-particle collision in a dispersion depending on the type of particle–particle interactions. (1) If the repulsive forces are predominant, the two colliding particles will rebound and the colloidal dispersion will be stable. (2) When at a given separation the attractive and repulsive forces counterbalance each other (the film formed upon particle collision is stable), aggregates or flocs of attached particles can appear. (3) When the particles are fluid and the attractive interaction across the film is predominant, the film is unstable and ruptures; this leads to coalescence of the drops in emulsions or of the bubbles in foams.

To a great extent, the occurrence of coagulation is determined by the energy, U, of particle–particle interaction. U is related to the disjoining pressure, Π, by means of Equations 7.173 and 7.174. Qualitatively, the curves Π versus h (see Figure 7.17) and U versus h are similar. The coagulation is called fast or slow depending on whether the electrostatic barrier (see Figure 7.17) is less than kT or much higher than kT. In addition, the coagulation is termed reversible or irreversible depending on whether the depth of the primary minimum (see Figure 7.17) is comparable with kT or much greater than kT.

Three types of driving forces can lead to coagulation. (1) The body forces, such as gravity and centrifugal force, cause sedimentation of the heavier particles in suspensions or creaming of the lighter droplets in emulsions. (2) For the particles that are smaller than about 1 μm, the Brownian stochastic force dominates the body forces, and the Brownian collision of two particles becomes a prerequisite for their attachment and coagulation. (3) The temperature gradient in fluid dispersions causes thermocapillary migration of the particles driven by the Marangoni effect. The particles moving with different velocities can collide and form aggregates.

7.6.1 IRREVERSIBLE COAGULATION

The kinetic theory of fast irreversible coagulation was developed by Smoluchowski [774,775]. Later the theory was extended to the case of slow and reversible coagulation. In any case of coagulation (flocculation), the general set of kinetic equations reads:

$$\frac{dn_k}{dt} = \frac{1}{2} \sum_{i=1}^{k-1} a_f^{i,k-i} n_i n_{k-i} - n_k \sum_{i=1}^{\infty} a_f^{k,i} n_i + q_k \quad (k = 1, 2, \dots) \tag{7.330}$$

where
   t is the time
   n_1 is the number of single particles per unit volume
   n_k is the number of aggregates of k particles ($k = 2, 3, \dots$) per unit volume
   $a_f^{i,j}$ ($i,j = 1, 2, 3, \dots$) are the rate constants of flocculation (coagulation; see Figure 7.63)
   q_k is the flux of aggregates of size k which are products of other processes, different from the flocculation itself (say, the
      reverse process of aggregate disassembly or the droplet coalescence in emulsions; see Equations 7.342 and 7.346)
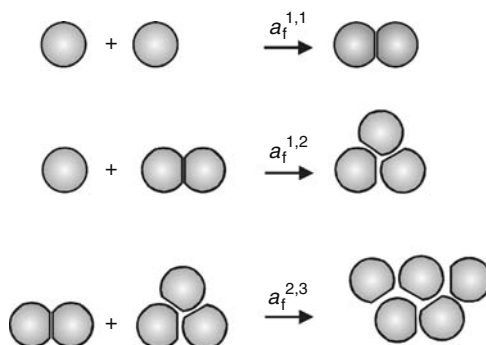
FIGURE 7.63 Elementary acts of flocculation according to the Smoluchowski scheme; $a_f^{i,j}$ ($i,j = 1, 2, 3, \ldots$) are rate constants of flocculation.

In the special case of irreversible coagulation without coalescence, we have $q_k \equiv 0$. The first term in the right-hand side of Equation 7.330 is the rate of formation of k aggregates by the merging of two smaller aggregates, whereas the second term expresses the rate of loss of k aggregates due to their incorporation into larger aggregates. The total concentration of aggregates (as kinetically independent units), n, and the total concentration of the constituent particles (including those in aggregated form), n_{tot}, can be expressed as

$$n = \sum_{k=1}^{\infty} n_k, \quad n_{\text{tot}} = \sum_{k=1}^{\infty} k n_k \tag{7.331}$$

The rate constants can be expressed in the form:

$$a_f^{i,j} = 4\pi D_{i,j}^{(0)}(R_i + R_j)E_{i,j} \tag{7.332}$$

where
  $D_{i,j}^{(0)}$ is the relative diffusion coefficients for two flocks of radii R_i and R_j and aggregation number i and j, respectively
  $E_{i,j}$ is the so-called collision efficiency [587,776]

Below we give expressions for $D_{i,j}^{(0)}$ and $E_{i,j}$ appropriate for various physical situations.
    The Einstein approach (see Equation 7.318), combined with the Rybczynski–Hadamar equation (Equation 7.315) leads to the following expression for the relative diffusivity of two isolated Brownian droplets:

$$D_{i,j}^{(0)} = \frac{kT}{2\pi\eta} \frac{\eta_d + \eta}{3\eta_d + 2\eta} \left(\frac{1}{R_i} + \frac{1}{R_j} \right) \text{ (perikinetic coagulation)} \tag{7.333}$$

The limiting case $\eta_d \to 0$ corresponds to two bubbles, whereas in the other limit ($\eta_d \to \infty$) Equation 7.333 describes two solid particles or two fluid particles of tangentially immobile surfaces.
    When the particle relative motion is driven by a body force or by the thermocapillary migration (rather than by self-diffusion), Equation 7.333 is no longer valid. Instead, in Equation 7.332, we have to formally substitute the following expression for $D_{i,j}^{(0)}$ (see Rogers and Davis [777]):

$$D_{i,j}^{(0)} = \frac{1}{4}(R_i + R_j)|\mathbf{v}_i - \mathbf{v}_j| \text{ (orthokinetic coagulation)} \tag{7.334}$$

Here $\mathbf{v}_j$ denotes the velocity of a flock of aggregation number j. Physically, Equation 7.334 accounts for the fact that some particle (usually a larger one) moves faster than the remaining particles and can capture them upon collision. This type of coagulation is called orthokinetic to distinguish it from the self-diffusion-driven perikinetic coagulation described by Equation 7.333. In the case of gravity-driven flocculation, we can identify $\mathbf{v}_j$ with the velocity U in Equation 7.315, where F is to be set equal to the gravitational force exerted on the particle; for a solid particle or a fluid particle of tangentially immobile surface, this yields $\mathbf{v}_j = 2g\Delta\rho R_j^2/(9\eta)$ with g the acceleration due to gravity and $\Delta\rho$ the density difference between the two phases.
    In the case of orthokinetic coagulation of liquid drops driven by the thermocapillary migration, the particle velocity $\mathbf{v}_j$ is given by the expression (see Young et al. [778]):

$$\mathbf{v}_j = \frac{2R_j E_T \lambda}{(3\eta_d + 2\eta)(\lambda_d + 2\lambda)} \nabla(\ln T) \text{ (thermocapillary velocity)} \tag{7.335}$$

where the thermal conductivity of the continuous and disperse phases are denoted by λ and λ_d, respectively. The interfacial thermal elasticity, E_T, is defined by Equation 7.293.

The collision efficiency, $E_{i,j}$, in Equation 7.332 accounts for the interactions (of both hydrodynamic and intermolecular origin) between two colliding particles. The inverse of $E_{i,j}$ is often called the stability ratio or the Fuchs factor [779] and can be expressed in the following general form [14,587]:

$$W_{i,j} = \frac{1}{E_{i,j}} = 2 \int_0^\infty \frac{\beta(s)}{(s+2)^2} \exp\left[\frac{U_{i,j}(s)}{kT}\right] ds, \quad s \equiv \frac{2h}{R_i + R_j} \tag{7.336a}$$

$$\beta \equiv \left(2\pi\eta R_* \frac{3\eta_d + 2\eta}{\eta_d + \eta}\right)^{-1} \frac{F_z}{V_z}$$

where
  h is the closest surface-to-surface distance between the two particles
  R^* is defined by Equation 7.270
  $U_{i,j}(s)$ is the energy of (nonhydrodynamic) interactions between the particles (see Section 7.4)
  $\beta(s)$ accounts for the hydrodynamic interactions
  F_z/V_z is the particle friction coefficient

Thus, $\beta \to 1$ for $s \to \infty$, insofar as for large separations the particles obey the Rybczynski–Hadamar equation (Equation 7.315). In the opposite limit, $s \ll 1$, i.e., close approach of the two particles, F_z/V_z can be calculated from Equation 7.271, 7.294, 7.295, or 7.299, depending on the specific case. In particular, for $s \ll 1$, we have $\beta \propto 1/s$ for two solid particles (or fluid particles of tangentially immobile surfaces), $\beta \propto s^{-1/2}$ for two liquid droplets, and $\beta \propto \ln s$ for two gas bubbles. We see that for two solid particles ($\beta \propto 1/s$), the integral in Equation 7.336a may be divergent. To overcome this problem, one usually accepts that for the smallest separations $U_{i,j}$ is dominated by the van der Waals interaction, as given by Equation 7.185, i.e., $U_{i,j} \to -\infty$, and, consequently, the integrand in Equation 7.336a tends to zero for $s \to 0$.

Note that the value of $W_{i,j}$ is determined mainly by the values of the integrand in the vicinity of the electrostatic maximum (barrier) of $U_{i,j}$ (see Figure 7.17), insofar as $U_{i,j}$ enters Equation 7.336a as an exponent. By using the method of the saddle point, Derjaguin [14] estimated the integral in Equation 7.336a:

$$W_{i,j} \equiv \frac{1}{E_{i,j}} \approx \left[\frac{8\pi kT}{-U_{i,j}''(s_m)}\right]^{1/2} \frac{\beta(s_m)}{(s_m + 2)^2} \exp\left[\frac{U_{i,j}(s_m)}{kT}\right] \tag{7.336b}$$

where s_m denotes the value of s corresponding to the maximum. We see that the larger the barrier, $U_{i,j}(s_m)$, the smaller the collision efficiency, $E_{i,j}$, and the slower the coagulation.

Note also that for imaginary particles, which experience neither long-range surface forces ($U_{i,j} = 0$) nor hydrodynamic interactions ($\beta = 1$), Equation 7.336a yields a collision efficiency $E_{i,j} = 1$ and Equation 7.332 reduces to the Smoluchowski [774,775] expression for the rate constant of the fast irreversible coagulation. In this particular case, Equation 7.330 represents an infinite set of nonlinear differential equations. If all flocculation rate constants are the same and equal to a_f, the problem has a unique exact solution [774,775]:

$$n = \frac{n_0}{1 + a_f n_0 t/2}, \quad n_k = n_0 \frac{(a_f n_0 t/2)^{k-1}}{(1 + a_f n_0 t/2)^{k+1}} \quad (k = 1, 2, \ldots) \tag{7.337}$$

It is supposed that the total average concentration of the constituent particles (in both singlet and aggregated form), n_{tot}, does not change and is equal to the initial number of particles, n_0. Unlike n_{tot}, the concentration of the aggregates, n, decreases with time, while their size increases. Differentiating Equation 7.337 we obtain

$$\frac{dn}{dt} = -\frac{a_f}{2} n^2, \quad \frac{d\overline{V}}{dt} = \frac{a_f}{2} \phi_0, \quad \overline{V} \equiv \frac{\phi_0}{n} \tag{7.338}$$

where
$\quad \overline{V}$ is the average volume per aggregate
$\quad \phi_0$ is the initial volume fraction of the constituent particles

Combining Equations 7.332 and 7.338, we obtain the following result for perikinetic (Brownian) coagulation:

$$\frac{\overline{V}}{V_0} = 1 + \frac{t}{t_{Br}}, \quad t_{Br} = \frac{R_0^2}{3\phi_0 D_0 E_0} \qquad (7.339)$$

where
$\quad V_0 = 4\pi R_0^3/3$ is the volume of a constituent particle
$\quad t_{Br}$ is the characteristic time of the coagulation process in this case
$\quad E_0$ is an average collision efficiency
$\quad D_0$ is an average diffusion coefficient

In contrast, $\overline{V}$ is not a linear function of time for orthokinetic coagulation. When the flocculation is driven by a body force, i.e., in case of sedimentation or centrifugation, we obtain [776]:

$$\frac{\overline{V}}{V_0} = \left(1 - \frac{t}{3t_{bf}}\right)^{-3}, \quad t_{bf} = \frac{2R_0}{3\phi_0 v_{bf} E_0} \qquad (7.340)$$

where
$\quad t_{bf}$ is the characteristic time in this case
$\quad v_{bf}$ is an average velocity of aggregate motion

As discussed above, when the body force is gravitational, we have $v_{bf} = 2g\Delta\rho R_0^2/(9\eta)$.

When the orthokinetic coagulation is driven by the thermocapillary migration, the counterpart of Equation 7.340 reads [776]

$$\frac{\overline{V}}{V_0} = \exp\left(\frac{t}{t_{tm}}\right), \quad t_{tm} = \frac{2R_0}{3\phi_0 v_{tm} E_0} \qquad (7.341)$$

where
$\quad v_{tm}$ is an average velocity of thermocapillary migration
$\quad t_{tm}$ is the respective characteristic time

Note that $D_0 \propto R_0^{-1}$, $v_{bf} \propto R_0^2$ and $v_{tm} \propto R_0$ (see Equations 7.318 and 7.335). Then, from Equations 7.339 through 7.341, it follows that the three different characteristic times exhibit different dependencies on particle radius: $t_{Br} \propto R_0^3$, $t_{bf} \propto R_0^{-1}$, while t_{tm} is independent of R_0. Thus, the Brownian coagulation is faster for the smaller particles, the body force-induced coagulation is more rapid for the larger particles, whereas the thermocapillary-driven coagulation is not so sensitive to the particle size [780].

The Smoluchowski scheme based on Equations 7.337 and 7.338 has found numerous applications [278]. An example for biochemical application is the study [781,782] of the kinetics of flocculation of latex particles caused by human gamma globulin in the presence of specific key–lock interactions. The infinite set of Smoluchowski equations (Equation 7.330) was solved by Bak and Heilmann [783] in the particular case when the aggregates cannot grow larger than a given size; an explicit analytical solution was obtained by these authors.

7.6.2 REVERSIBLE COAGULATION

In the case of reversible coagulation, the flocs can disaggregate because the primary minimum (Figure 7.17) is not deep enough [14]. For example, an aggregate composed of $i+j$ particles can be split on two aggregates containing i and j particles. We denote the rate constant of this reverse process by $a_r^{i,j}$ (Figure 7.64a). It is assumed that both the straight process of flocculation (Figure 7.63) and the reverse process (Figure 7.64a) take place. The kinetics of aggregation in this more general case is described by the Smoluchowski set of equations, Equation 7.330, where we have to substitute:

$$q_1 = \sum_{i=1}^{\infty} a_r^{1,i} n_{i+1}, \quad q_k = \sum_{i=1}^{\infty} a_r^{k,i} n_{i+k} - \frac{1}{2} n_k \sum_{i=1}^{k-1} a_r^{i,k-i} \quad (k = 2, 3, \ldots) \qquad (7.342)$$
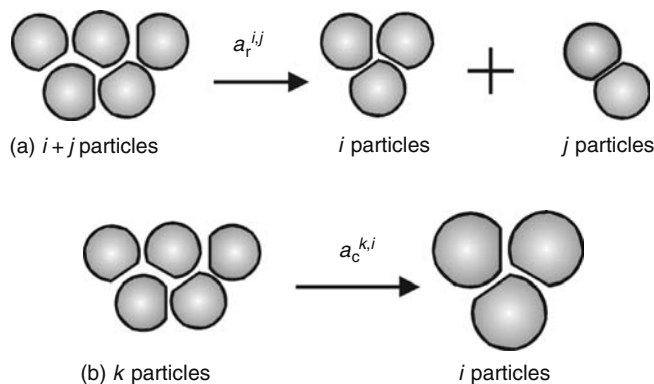
FIGURE 7.64 Elementary acts of aggregate splitting (a) and droplet coalescence within an aggregate (b); $a_r^{i,j}$ and $a_c^{k,i}$ ($i, j, k = 1, 2, 3, \ldots$) are the rate constants of the respective processes.

In Equation 7.342, q_k equals the rate of formation of k aggregates in the process of disassembly of larger aggregates minus the rate of decay of the k aggregates. As before, the total number of constituent particles, n_{tot}, does not change. However, the total number of the aggregates, n, can either increase or decrease depending on whether the straight or the reverse process prevails. Summing up all Equations in 7.330 and using Equation 7.342, we derive the following equation for n:

$$\frac{dn}{dt} = \frac{1}{2} \sum_{i=1}^{\infty} \sum_{j=1}^{\infty} (a_r^{i,j} n_{i+j} - a_f^{i,j} n_i n_j) \tag{7.343}$$

Martinov and Muller [784] reported a general expression for the rate constants of the reverse process:

$$a_r^{i,j} = \frac{D_{i,j}^{(0)} E_{i,j}}{Z_{i,j}} \frac{1}{(R_i + R_j)^2} \tag{7.344}$$

where $Z_{i,j}$ is the so-called irreversible factor, which can be presented in the form

$$Z_{i,j} = \frac{1}{8} \int_{U_{i,j}^{<0}} (s+2)^2 \exp\left[-\frac{U_{i,j}(s)}{kT}\right] ds \tag{7.345}$$

The integration in Equation 7.345 is carried out over the region around the primary minimum, where $U_{i,j}$ takes negative values (see Figure 7.17). In other words, $Z_{i,j}$ is determined by the values of $U_{i,j}$ in the region of the primary minimum, whereas $E_{i,j}$ is determined by the values of $U_{i,j}$ in the region of the electrostatic maximum (see Equations 7.336b and 7.345). When the minimum is deeper, $Z_{i,j}$ is larger, and the rate constant in Equation 7.344 is smaller. In addition, as seen from Equations 7.336b and 7.344, the increase of the height of the barrier also decreases the rate of the reverse process. The physical interpretation of this fact is that to detach from an aggregate a particle has first to go out from the well and then jump over the barrier (Figure 7.17).

To illustrate the effect of the reverse process on the rate of flocculation, we solved numerically the set of Equations 7.330, 7.342, and 7.343. To simplify the problem, we used the following assumptions: (1) the von Smoluchowski assumption that all rate constants of the straight process are equal to a_f; (2) aggregates containing more than M particles cannot decay; (3) all rate constants of the reverse process are equal to a_r; and (4) at the initial moment, only single constituent particles of concentration n_0 are available. In Figure 7.65, we plot the calculated curves of n_0/n versus the dimensionless time, $\tau = a_f n_0 t/2$, for a fixed value, $M = 4$, and various values of the ratio of the rate constants of the straight and the reverse process, $b = 2a_r/(n_0 a_f)$. Note that n is defined by Equation 7.331. We see that in an initial time interval all curves in Figure 7.65 touch the von Smoluchowski distribution (corresponding to $b = 0$), but after this period we observe a reduction in the rate of flocculation, which is larger for the curves with larger values of b (larger rate constants of the reverse process). These S-shaped curves are typical for the case of reversible coagulation, which is also confirmed by the experiment [14,785].

7.6.3 KINETICS OF SIMULTANEOUS FLOCCULATION AND COALESCENCE IN EMULSIONS

When coalescence is present, in addition to the flocculation, the total number of constituent drops, n_{tot} (see Equation 7.331), does change, in contrast to the case of pure flocculation considered above [32]. Hartland and Gakis [786], and Hartland and
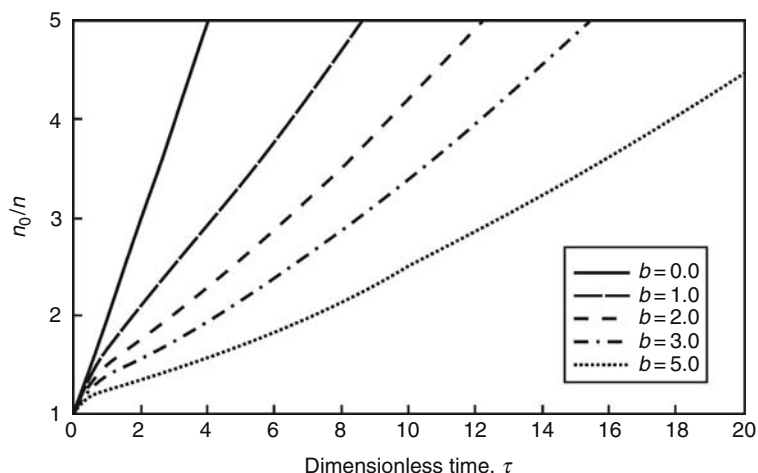
FIGURE 7.65 Reversible coagulation: theoretical plot of the inverse dimensionless aggregate concentration, n_0/n, versus the dimensionless time, $\tau = a_f n_0 t/2$, in the case of $M = 4$ and various values of the dimensionless ratio, $b = 2a_r/(n_0 a_f)$, of the rate constants of the reverse and straight process, a_r and a_f.

Vohra [787] were the first to develop a model of coalescence that relates the lifetime of single films to the rate of phase separation in emulsions of fairly large drops (approximately 1 mm) in the absence of surfactant. Their analysis was further extended by Lobo et al. [788] to quantify the process of coalescence within an already creamed or settled emulsion (or foam) containing drops of size less than 100 μm; these authors also took into account the effect of surfactants, which are commonly used as emulsifiers. Danov et al. [789] generalized the Smoluchowski scheme to account for the fact that the droplets within the flocs can coalesce to give larger droplets, as illustrated in Figure 7.64b. In this case, in the right-hand side of Equation 7.330 we have to substitute [789]

$$q_1 = \sum_{i=2}^{\infty} a_c^{i,1} n_i, \quad q_k = \sum_{i=k+1}^{\infty} a_c^{i,k} n_i - n_k \sum_{i=1}^{k-1} a_c^{k,i} \ (k = 2, 3, \dots) \tag{7.346}$$

where $a_c^{k,i}$ is the rate constant of transformation (by coalescence) of an aggregate containing k droplets into an aggregate containing i droplets (see Figure 7.64b). The newly formed aggregate is further involved in the flocculation scheme, which thus accounts for the fact that the flocculation and coalescence processes are interdependent. In this scheme, the total coalescence rate, $a_{c,tot}^i$, and the total number of droplets, n_{tot}, obey the following equations [789]:

$$\frac{dn_{tot}}{dt} = -\sum_{i=2}^{\infty} a_{c,tot}^i n_i, \quad a_{c,tot}^i = \sum_{k=1}^{i-1} (i - k) a_c^{i,k} \ (i = 2, 3, \dots) \tag{7.347}$$

To determine the rate constants of coalescence, $a_c^{k,i}$, Danov et al. [556] examined the effects of droplet interactions and Brownian motion on the coalescence rate in dilute emulsions of micrometer- and submicrometer-sized droplets. The processes of film formation, thinning, and rupture were included as consecutive stages in the scheme of coalescence. Expressions for the interaction energy due to the various DLVO and non-DLVO surface forces between two deformed droplets were obtained [356] (see also Section 7.4).

Average models for the total number of droplets are also available [790,791]. The average model of van den Tempel [790] assumes linear structure of the aggregates. The coalescence rate is supposed to be proportional to the number of contacts within an aggregate. To simplify the problem, van den Tempel has used several assumptions, one of them is that the concentration of the single droplets, n_1, obeys the Smoluchowski distribution (Equation 7.337) for $k = 1$. The average model of Borwankar et al. [791] is similar to that of van den Tempel but is physically more adequate. The assumptions used by the latter authors [791] make their solution more applicable to cases in which the flocculation (rather than the coalescence) is slow and is the rate determining stage. This is confirmed by the curves shown in Figure 7.66 which are calculated for the same rate of coalescence, but for three different rates of flocculation. For relatively high rates of flocculation (Figure 7.66a), the predictions of the three theories differ. For the intermediate rates of flocculation (Figure 7.66b), the prediction of the model by Borwankar et al. [791]
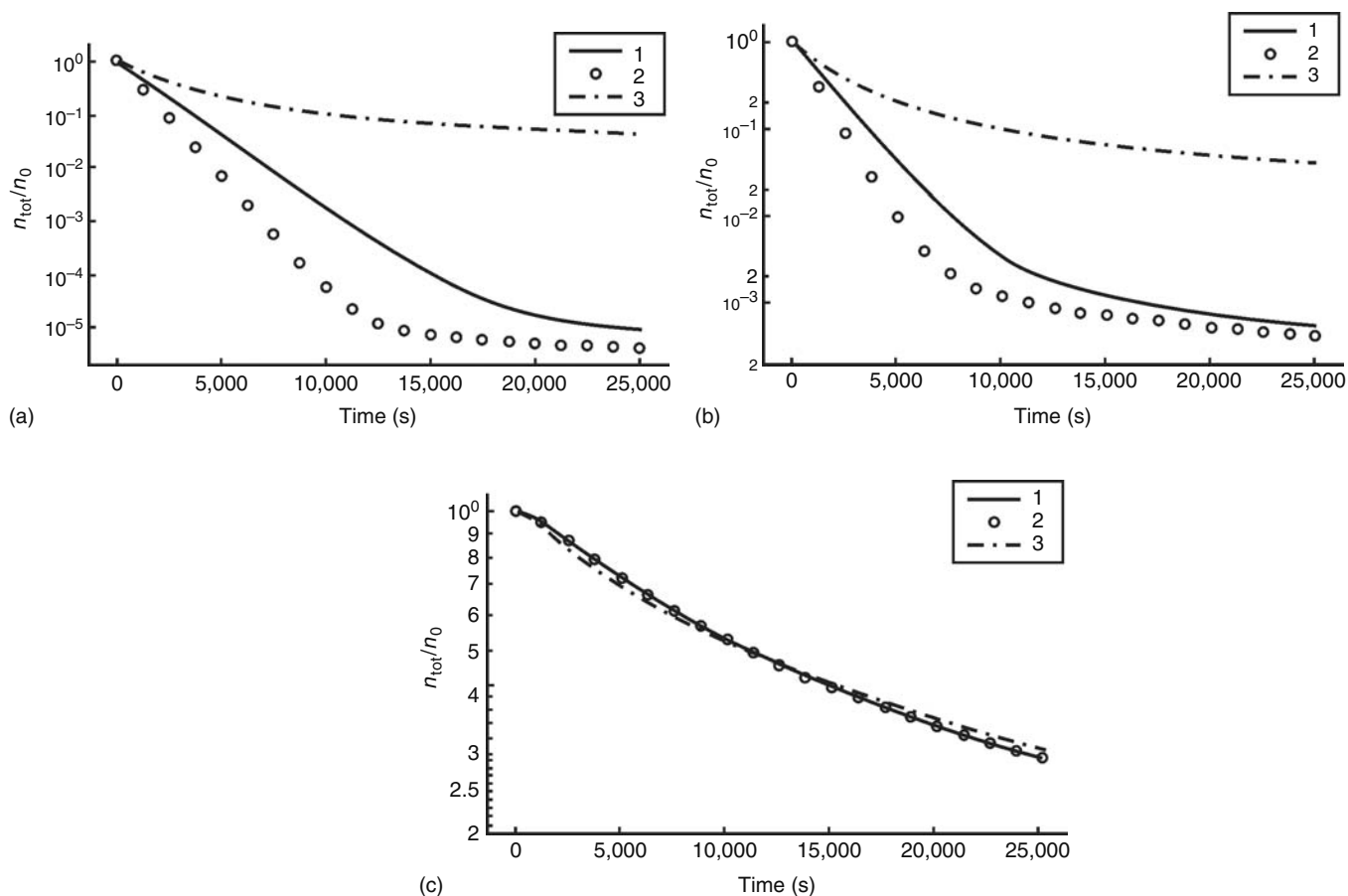
FIGURE 7.66 Relative change in the total number of drops, n_{tot}, versus time, t; initial number of primary drops $n_0 = 10^{12}$ cm^{-3}; coalescence rate constant $k_c^{2,1} = 10^{-3}$ s^{-1}. Curve 1: numerical solution of Equation 7.347. Curve 2: output of the model of Borwankar et al. [791]. Curve 3: output of the model of van den Tempel [790]. The values of the flocculation rate constant are (a) $a_f = 10^{-11}$ cm^3 s^{-1}; (b) $a_f = 10^{-13}$ cm^3 s^{-1}; (c) $a_f = 10^{-16}$ cm^3 s^{-1}.

is close to that of the more detailed model by Danov et al. [789]. For very low values of the flocculation rate constant, a_f, for which the coalescence is not the rate-determining stage, all three theories [789–791] give numerically close results (Figure 7.66c). (For more details about the coupling of coalescence and flocculation in dilute O/W emulsions see Ref. [792].)

7.7 MECHANISMS OF ANTIFOAMING

In Sections 7.4 through 7.6 we considered the main interparticle forces which govern the stability of colloidal systems and some of the mechanisms, which result in destabilization of suspensions and emulsions (coagulation, demulsification). In various technologies (such as pulp and paper production, drug manufacturing, textile dying, crude oil processing, and many others) very voluminous and stable foams can appear, which impede the normal technological process and are, therefore, rather undesired. In these cases, various oils and oil–solid mixtures are introduced as additives to the foaming media for an efficient foam control [793]. Such oils and oil–silica mixtures are commonly termed as antifoams or defoamers [793–797]. Antifoams are used in consumer products as well (e.g., in washing powders and anti-dyspepsia drugs). Sometimes, oils are introduced in surfactant solutions for other reasons and the observed foam destabilization effect is undesired—a typical example is the use of silicone oils as hair conditioners in shampoos [798–799]. The mechanisms responsible for the foam destruction effect of oil-based antifoams are still not entirely understood and are the subject of intensive studies.

A typical antifoam consists of an oil (polydimethylsiloxane or hydrocarbon), dispersed hydrophobic solid particles (e.g., hydrophobized silica), or a mixture of both [794]. The oil–solid mixtures are often called antifoam compounds. The weight concentration of the solid particles in compounds is around several percent (typically between two and eight). A strong synergistic effect between the oil and the solid particles is observed in the compounds—in most cases, the latter are much more efficient than either of their individual components, if taken separately [794,795]. The compounds are used at a concentration

below 0.1 wt%, whereas the oils are used at higher concentrations (up to several percent) due to their lower antifoam efficiency. The antifoams are usually preemulsified in the form of oil drops or mixed oil–solid globules of micrometer size.

A detailed discussion on many aspects of the mechanisms of antifoaming can be found in review articles by Garrett [794], Wasan and Christiano [796], as well as in the books by Exerowa and Kruglyakov [795], and Kralchevsky and Nagayama [797]. In the present section, we compare the mechanisms of foam destruction by oils and oil–silica compounds. The discussion is based on results obtained during the last ten years, which are summarized in the recent review by Denkov [800].

7.7.1   LOCATION OF ANTIFOAM ACTION—FAST AND SLOW ANTIFOAMS

An important question about the mechanism of foam destruction is which is the structural element (foam film or Plateau borders, PB) actually destroyed by the antifoam globules. This question has a practical importance, because the diameter of the globules in the commercial antifoams should fit the typical size of the structural element to be destroyed—the film thickness or the cross section of the PB, respectively [798]. Most of the researchers consider that the antifoam globules rupture the foam films [794,795], whereas Koczo et al. [801] suggest that the antifoam globules first escape from the foam films into the neighboring PB and get trapped there; only afterward, the globules are assumed to destroy the PB and the neighboring foam films.

Direct microscopic observations by a high-speed video camera showed that the foam destruction by typical antifoam compounds (comprising silicone oil and silica) occurred through rupture of the foam lamellae [802,803]. Experiments with small (millimeter-sized) and large (centimeter-sized) foam films showed that the compounds induced the formation of a hole in the foam films at the early stages of the film thinning process (Figure 7.67). This is possible, because the foam films stabilized by low molecular mass surfactants thin rapidly, within several seconds, down to a thickness of one to several micrometers which is comparable to the diameter of the antifoam globules [802]. As a result, the foam films rupture within several seconds after their formation. Accordingly, the foam produced from such solutions disappear completely for less than 10 s in a standard shake test [802].

For this reason, the antifoams that are able to break the foam films are termed "the fast antifoams" [800]. Experiments with several ionic and nonionic surfactants have confirmed that the observed foam film destruction is rather typical for mixed oil–silica antifoams [800,802–805].

On the other hand, similar experimental methods showed [798,799,806,807] that the foam destruction occurred in a different manner when pure oils (without silica particles) were used as antifoams. The oil drops were seen to leave the foam films (without rupture) during the film thinning process. The antifoam drops were accumulated in the PBs and remained trapped there for a certain period of time [798,799], as presumed by Koczo et al. [801]. The slow process of water drainage from the foam led to a gradual narrowing of the PBs and the oil drops became strongly compressed with time. When the compressing capillary pressure exceeded some critical value, the oil drops entered the walls of the PB, inducing its destruction and the rupture of the neighboring foam films (Figure 7.68) [798]. Much longer time was needed for foam destruction in this case, typically, more than several minutes. That is why, these antifoams were termed the "slow antifoams" [800]. Furthermore, a residual foam of well-defined height, which remained stable for many hours, was observed in such systems.
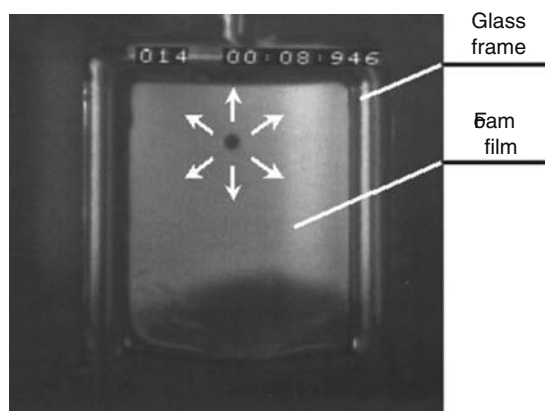
FIGURE 7.67   Image of a large foam film in the moment of its rupture by preemulsified globules of an antifoam compound (4.2 wt% of hydrophobic silica dispersed in silicone oil). The film is formed on a rectangular glass frame which is rapidly withdrawn from 10 mM solution of the anionic surfactant dioctyl sulfosuccinate (hereafter denoted for brevity as AOT). One sees a hole (the black circle in the upper part of the film) which, in reality, rapidly expands with time. The film ruptures 0.5 s after its formation at a thickness about several micrometers. The image is taken by a high-speed video camera as explained in Ref. [802].
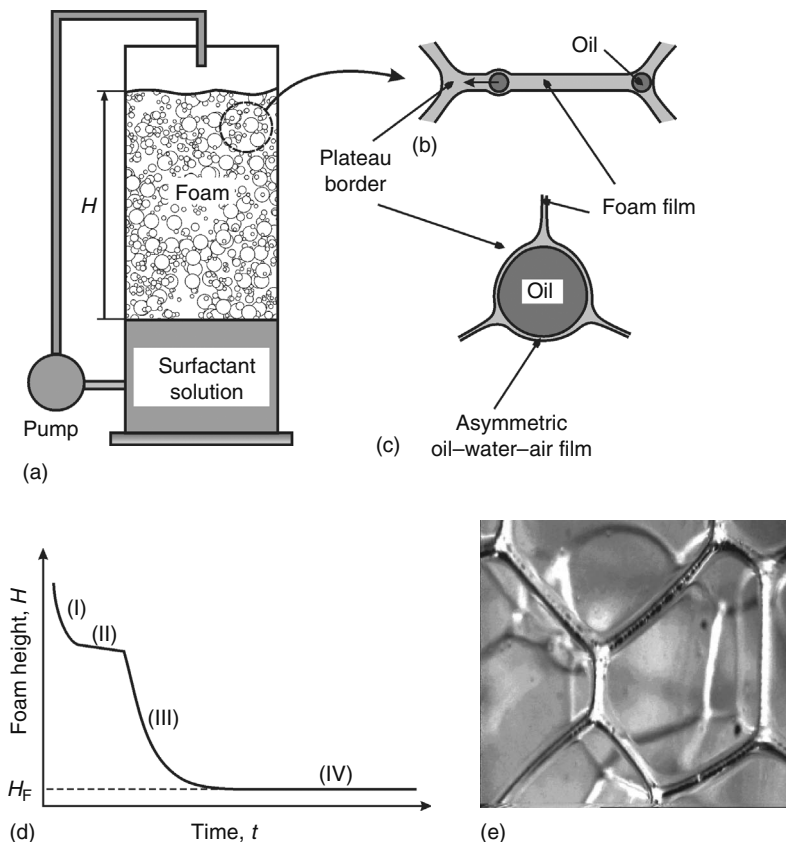
FIGURE 7.68 Foam destruction by oil drops (slow antifoams) [798,799,818]: (a, b) The oil drops are rapidly expelled from the foam films into the neighboring PBs soon after the foam is formed; (c) The drops are strongly compressed in the narrowing PBs and asymmetric oil–water–air films are formed. The drop entry and foam destruction occur when the compressing pressure exceeds a certain critical value, which depends on the particular system; (d) Schematic presentation of the main stages of foam evolution in the presence of oil drops—(I) drainage of liquid from the foam without bubble coalescence; (II) stable foam due to the insufficient compression of the oil drops; (III) foam destruction as a result of drop entry in the PBs; (IV) long-living residual foam with final height H_F; (e) Photograph of real foam cells with many oil drops trapped in the PBs (the drops are visualized by the wavy profile of the PBs).

These studies show that the foam destruction may occur through rupture of either the foam films or the PBs, depending on the particular system. Further experiments have shown that the main factor determining the position of foam destruction, and whether a given antifoam behaves as fast or slow, is the magnitude of the so-called entry barrier (see Section 7.7.3).

7.7.2 BRIDGING–STRETCHING MECHANISM

As mentioned above, microscopic observations by a high-speed video camera were made [802] to clarify the detailed mechanism of foam film rupture by mixed antifoams. They showed that when an antifoam globule connected (bridged) the surfaces of a foam film, an unstable oil bridge was formed, which stretched with time due to uncompensated capillary pressures at the oil–air and oil–water interfaces, and eventually ruptured the entire foam film (Figure 7.69). The term "bridging–stretching" was suggested [802,808] to describe this mechanism. The bridging–stretching mechanism explains why the typical antifoam compounds contain a high excess of oil—the antifoam globules should be able to deform for effectuation of the bridge stretching and rupture.

The stability of oil bridges in foam films was theoretically studied by Garrett [794,809] on the basis of the theory of capillarity. The analysis showed that a necessary condition for having an unstable bridge is that the bridging coefficient:

$$B = \sigma_{AW}^2 + \sigma_{OW}^2 - \sigma_{OA}^2 \tag{7.348}$$

should be positive. Here, σ is interfacial tension and the subscripts AW, OW, and OA denote the air–water, oil–water, and oil–air interfaces, respectively. A more refined capillary model [808] showed that oil bridges, formed from oil drops of diameter comparable to, or smaller than the film thickness, might be metastable even at positive values of B. Therefore, the size of the oil bridges should be above a certain critical value (which depends on the film thickness and the interfacial tensions) for having an
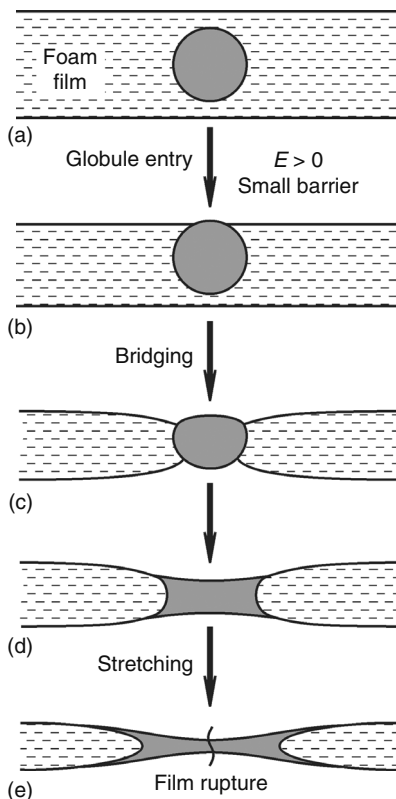
FIGURE 7.69 Schematic presentation of the bridging–stretching mechanism of foam film rupture by antifoam globules [802,808]: After an oil bridge is formed (a–c), it stretches due to uncompensated capillary pressures at the oil–water and oil–air interfaces (c–e). Finally, the bridge ruptures in its thinnest central region (the vertical wavy line in e). The globule entry is possible only if the entry coefficient, $E > 0$, and the entry barrier is low (see Section 7.7.3).

unstable oil bridge. This theoretical result was invoked to explain the reduced stability of the foam films in the presence of a spread oil layer (for details see Ref. [808]).

7.7.3 ROLE OF THE ENTRY BARRIER

Any mechanism of foam destruction by preemulsified antifoam globules requires an entry of these globules at the surface of the foam film or the PB (e.g., Figures 7.68 and 7.69). The entry event depends on two major factors: (1) The equilibrium position of an oil drop (lens) on the air–water interface, which is determined by the values of the interfacial tensions σ_{AW}, σ_{OW}, and σ_{OA} (see Figure 7.11). (2) The repulsive forces (e.g., of electrostatic origin), which stabilize the asymmetric oil–water–air film, formed when an antifoam globule approaches the foam film surface; the barrier created by these forces should be overcome for the globule entry to occur [794,796,800,801,810–814].

A theoretical analysis shows [794] that if the so-called entry coefficient:

$$E = \sigma_{AW} + \sigma_{OW} + \sigma_{OA} \tag{7.349}$$

is negative (as it is the case with some oils and surfactant solutions), the oil drops do not have a stable equilibrium position at the surface and spontaneously submerge into the surfactant solution. Such oils are inactive as antifoams because no oil bridges can be formed (factor 1 is decisive). One of the main reasons to use silicone oils in various antifoam formulations is that these oils usually have positive values of B and E coefficients in the solutions of most conventional (hydrocarbon-based) surfactants [794,815]. Besides, it was theoretically shown that a positive value of B necessarily corresponds to a positive value of E (the reverse is not always true) [797,816].

The experiments show, however, that many oils with positive B and E coefficients might have low antifoam efficiency [798,799,806,807]. In these cases, the stability of the asymmetric oil–water–air films is very high, and the formation of unstable oil bridges becomes impossible for kinetic reasons (factor 2 is decisive). The repulsive interaction that should be overcome for effectuation of the antifoam globules entry on the solution surface is usually termed "the entry barrier." A recently developed method FTT [807,817,818] allowed one to quantify precisely the entry barrier with actual micrometer-sized antifoam globules,
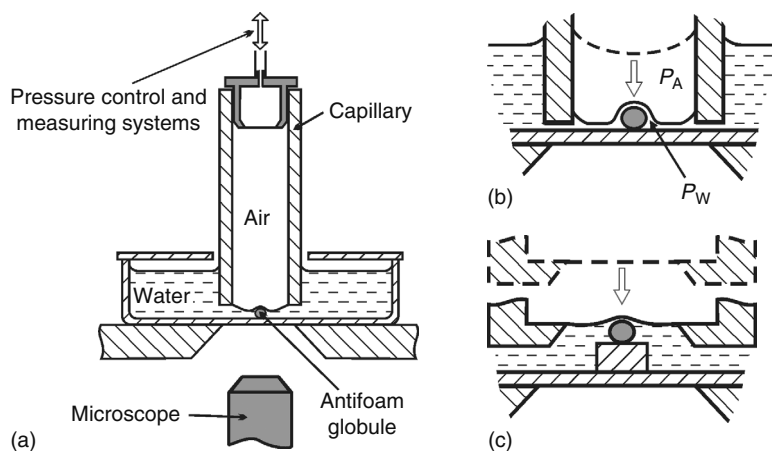
FIGURE 7.70 Scheme of the experimental setup and the basic principle of the FTT [817]. (a) Vertical capillary, partially immersed in surfactant solution containing antifoam globules, is held close to the bottom of the experimental vessel. (b) The air pressure inside the capillary, P_A, is increased and the convex air–water meniscus in the capillary is pressed against the glass substrate. Some of the antifoam globules remain trapped in the formed glass–water–air film and are compressed by the meniscus. At a given critical capillary pressure, $P_C^{CR} = P_A - P_W$, the asymmetric film formed between the antifoam globule and the solution surface ruptures and an event of globule entry is observed by an optical microscope. (c) Another modification called gentle FTT is used for measuring entry barriers lower than 20 Pa—an initially flat meniscus is formed, which allows the trapping of antifoam globules at a virtually zero capillary pressure.

and a number of important results have been obtained. The principle of the FTT and some of the main conclusions, drawn from the results obtained by this technique, are briefly discussed below.

7.7.3.1 Film Trapping Technique (FTT)

The principle and the experimental setup of the FTT are illustrated in Figure 7.70 [807,817,818]. Briefly, a vertical glass capillary is positioned at a small distance above the flat bottom of a glass vessel. The lower end of the capillary is immersed in the working surfactant solution which contains dispersed antifoam globules. The capillary is connected to a pressure control system which allows one to vary and to measure the air pressure in the capillary, P_A. When P_A increases, the air–water meniscus in the capillary is pushed against the glass substrate and a wetting film (glass–water–air) is formed which traps some of the antifoam globules. The setup allows one to determine the capillary pressure of the air–water meniscus around the trapped drops, $P_C = P_A - P_W$, where P_W is the pressure in the aqueous film (for details, see Refs. [817,818]). The experiments show that the trapped antifoam globules enter (pierce) the surface of the wetting film at a given, critical capillary pressure, P_C^{CR}. Therefore, the equipment allows one to measure P_C^{CR} as a function of various parameters, such as the types of oil and surfactant, concentration of solid particles in the compound, size of the antifoam globules, etc. A larger value of P_C^{CR} corresponds to a higher entry barrier (more difficult drop entry) and vice versa. For compounds having very low entry barriers, a special version of the FTT was developed [817] (gentle FTT) (see Figure 7.70c). Experiments in the presence and absence of a prespread oil layer can be performed, which allows one to evaluate the effect of oil spreading on the entry barrier.

7.7.3.2 Critical Entry Pressure for Foam Film Rupture

Experiments with a large set of systems (various oils, compounds, and surfactants) showed [800,818] that there is a well-defined threshold value, $P_{TR} \approx 15$ Pa, which separates the fast (foam film breaking) from the slow (PB breaking) antifoams. Some of the results from these experiments are summarized in Figure 7.71, where the relationship between the foam lifetime and the entry barrier, P_C^{CR}, is shown. One sees from this figure that all experimental points fall into two distinct regions: (1) Systems in which the foam is destroyed for less than 10 s, i.e., these correspond to fast antifoams; for them $P_C^{CR} < 15$Pa; (2) Systems for which the defoaming time is longer than 5 min (slow antifoams); for them $P_C^{CR} > 20$Pa. Therefore, the magnitude of the entry barrier is of crucial importance for the time scale of foam destruction by oil-based antifoams. Another relation of P_C^{CR} with the antifoam activity (more precisely, with the height of the residual foam, H_F, in the presence of oil drops; see Figure 7.68d) was discussed in Refs. [798,818].

One should note that at high surfactant concentrations, only oil–solid compounds have been observed to behave as fast antifoams, whereas both oils and compounds could behave as slow antifoams depending on the magnitude of the entry barrier (at low surfactant concentrations, the pure oils could also act as fast antifoams). In all experiments it was found that the hydrophobic solid particles reduce the entry barrier by one to two orders of magnitude, but sometimes P_C^{CR} remains higher than
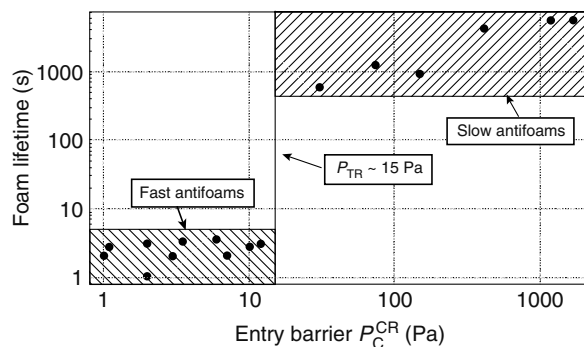
FIGURE 7.71 Correlation between the entry barrier, P_C^{CR}, and the foam lifetime measured for various surfactant–antifoam systems: The experimental data (solid circles) fall into two distinct regions: systems in which the foam is destroyed in less than 5 s (fast antifoams) and $P_C^{CR} < 15$ Pa; and systems for which the defoaming time is longer than 8 min (slow antifoams) and $P_C^{CR} > 20$ Pa. The composition of the various systems is given in Ref. [818].

the threshold value, P_{TR}, and the compound is unable to break the foam films. In the latter cases, the compound globules are expelled into the neighboring PBs during the process of foam film drainage. These results confirm the idea of Garrett [794] that the main role of the solid particles in the antifoam compounds is to reduce the entry barrier of the globules.

7.7.3.3 Optimal Hydrophobicity of Solid Particles

Some authors accept [815,819] that the use of more hydrophobic solid particles results in more active antifoam compounds. In a recent study [805], this idea was experimentally tested by applying the following procedure for a gradual increase of silica hydrophobicity: initially hydrophilic silica particles were mixed with silicone oil at a room temperature, and this mixture was stored under mild stirring for a long period of time. Under these conditions, the adsorption of silicone oil on the silica surface is a slow process which takes weeks before the final, most hydrophobic state of the particles is reached. The antifoam efficiency of the compound was tested every day, and the results obtained with various systems unambiguously showed the presence of a well pronounced, optimal silica hydrophobicity corresponding to highest antifoam efficiency.

The antifoam efficiency in these experiments was evaluated [805] by an automatic shake test. Briefly, 100 mL of the foaming solution was placed in a standard 250 mL glass bottle and 0.01% of the compound was introduced into this sample. The bottle was then mechanically agitated in a series of consecutive shake cycles. After each cycle of agitation for 10 s, the solution remained quiescent for another 60 s and the defoaming time was measured (defined as the time for appearance of a clean water–air interface without bubbles). Afterward, a new shaking cycle was performed and this procedure was repeated until the defoaming time exceeded 60 s in three consecutive cycles—this was considered as the moment of compound exhaustion (see Section 7.7.4 and Figure 7.74 for further explanations). Larger number of cycles before the compound exhaustion corresponds to better antifoam durability (efficiency) and vice versa.

The observed maximum (see the illustrative result presented in Figure 7.72a) was explained [805] as a result of two requirements which stem from the main role of the silica particles, namely, to assist the globule entry by rupturing the asymmetric oil–water–air films (see Figure 7.73). The first requirement, formulated by Garrett [794], is that the particles should be sufficiently hydrophobic to be dewetted by the oil–water and air–water interfaces (otherwise, the solid particles would stabilize, rather than destabilize the asymmetric film). The other requirement [805] is that the particles should protrude sufficiently deep into the aqueous phase in order to bridge the surfaces of the asymmetric oil–water–air film, and it is better satisfied by more hydrophilic particles. Therefore, an optimal hydrophobicity is expected, at which both requirements are balanced, the entry barrier is low, and the antifoam is most active. Indeed, a straightforward correlation between the antifoam efficiency and the magnitude of the entry barrier, P_C^{CR}, was observed in the studied systems (Figure 7.72b). For spherical particles, the optimal hydrophobicity was expressed as a most favorable three-phase contact angle solid–water–oil [805]:

$$\cos \theta_O \approx h_{AS}/R_P - 1 \tag{7.350}$$

where
 h_{AS} is the thickness of the asymmetric oil–water–air film
 R_P is the particle radius (see Figure 7.73)

This angle corresponds to the condition $h_{AS} = d_{PR}$, where $d_{PR} = R_P(1 + \cos \theta_O)$ is the equilibrium protrusion depth of the solid particle into the aqueous phase.
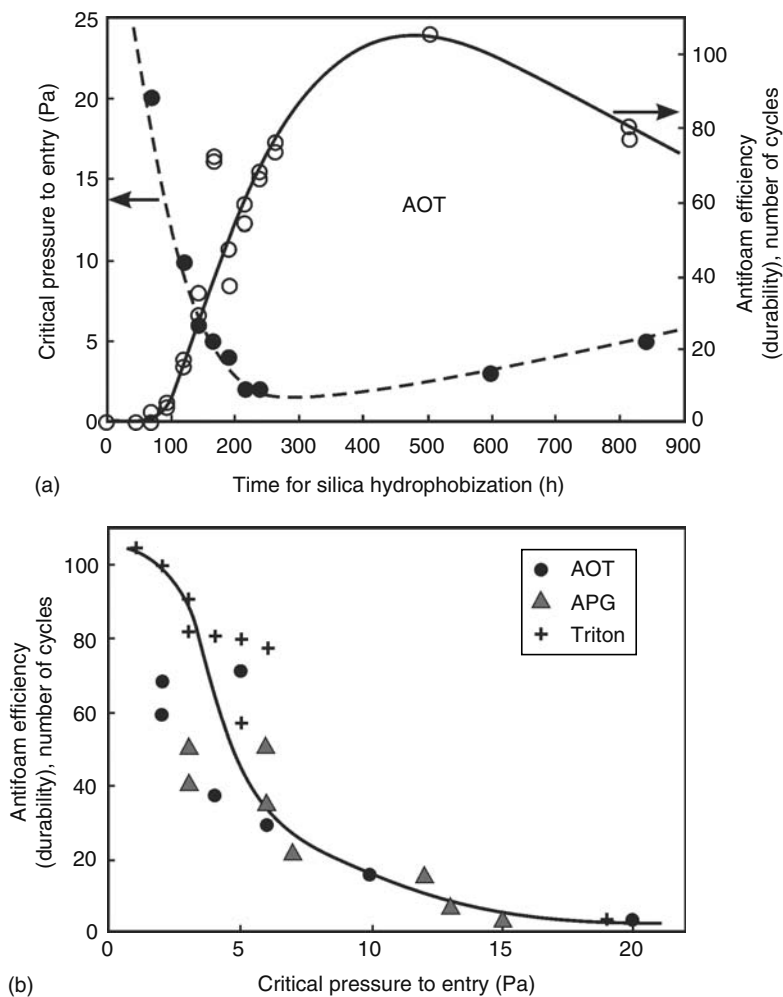
FIGURE 7.72 (a) Critical pressure for globule entry, P_C^{CR} (full circles), and efficiency (empty circles) of a silicone oil–silica compound in 10 mM AOT solution, as functions of the time of silica hydrophobization. (b) The dependence of the compound efficiency on P_C^{CR} for solutions of three different surfactants: 10 mM anionic AOT, 0.6 mM nonionic APG; and 1 mM nonionic Triton X-100. (Adapted from Marinova, K.M., Denkov, N.D., Branlard, P., Giraud, Y., and Deruelle, M., *Langmuir*, 2001 [805]. With permission.)

7.7.3.4 Role of the Prespread Oil Layer

It has been known for many years [794,820,821] that some correlation exists between the spreading behavior of the oils and their antifoam activity. The value of the spreading coefficient:

$$S = \sigma_{AW} - \sigma_{OW} - \sigma_{OA} \tag{7.351}$$

which characterizes the mode of spreading of the oil on the surface of the solution, and the rate of oil spreading have been often considered as important factors for the antifoam activity. However, as shown by Garrett et al. [822] the oil spreading is not a necessary condition for having an active antifoam, and many studies [798,799,806] have confirmed that the correlation is not always present.

The effect of the spread oil on the entry barriers of various oils and oil–silica compounds was studied by the FTT [800,804,807]. The experimental results showed that the presence of a prespread oil layer on the surface of the solution reduces by several times the entry barrier for mixed oil–silica compounds (see Table 7.9). Furthermore, it was found [804] that the entry barrier in many systems is below the threshold value $P_{TR} \approx 15$ Pa (which separates the fast from slow antifoams, see Figure 7.71), only in the presence of a prespread layer of oil. In other words, these antifoams behave as fast ones only because the oil spreads rapidly on the solution surface during foaming, reducing in this way the entry barrier below P_{TR}. The results for the entry barrier of oil drops (without silica) also showed a moderate reduction of the entry barrier by a prespread oil in most systems [804,807]. However, at least in one of the studied systems (hexadecane drops in solutions of the anionic surfactant sodium dodecyl-benzenesulfonate; see Table 7.9) a significant increase of the entry barrier upon oil spreading was
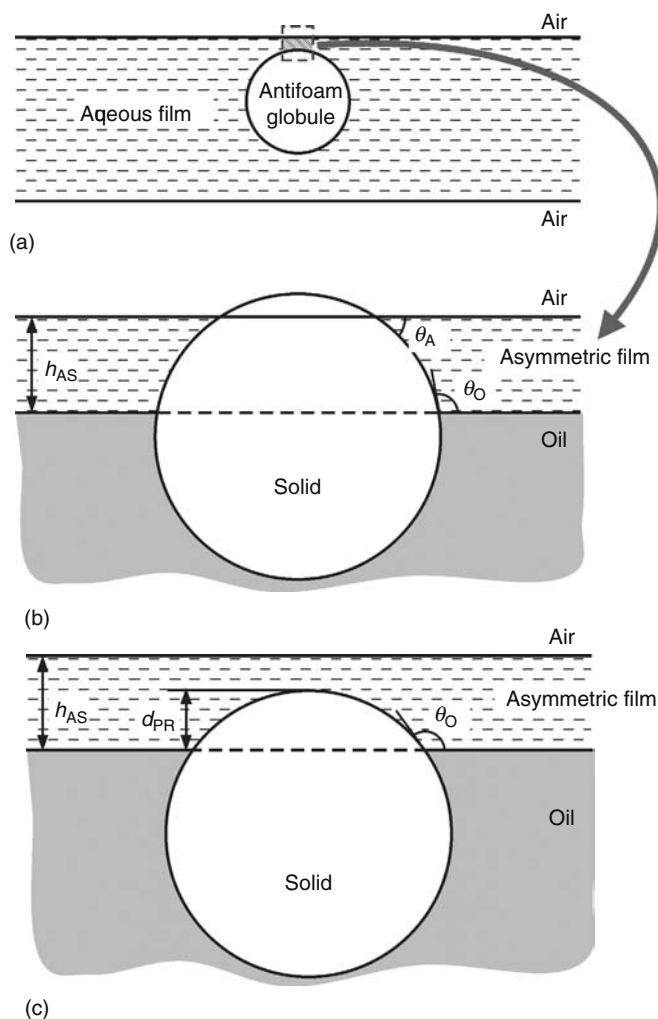
FIGURE 7.73 Schematic explanation of the optimal hydrophobicity of the solid particles in oil–solid antifoam compounds: (a) When an antifoam globule approaches the foam film surface, an asymmetric oil–water–air film of thickness h_{AS} forms. (b) The zone of contact in an enlarged scale. If the protrusion depth, d_{PR}, of the solid particle is larger than h_{AS}, the particle should be sufficiently hydrophobic $(\theta_A + \theta_O > 180°)$ in order to pierce the air/water interface and induce a film rupture; however, if the particle is insufficiently hydrophobic $(\theta_A + \theta_O < 180°)$, it would stabilize the film [794]. (c) On the other side, if the solid particles is over-hydrophobized, then $d_{PR} < h_{AS}$ and the particle is again unable to pierce the asymmetric film [805].

observed [807]. The entry barrier of the oils in surfactant solutions above their critical micellization concentration (CMC) is higher than P_{TR} both in the presence and absence of spread oil, which explains why the pure oils behave as slow antifoams at typical surfactant concentrations.

We can conclude from the results shown in Table 7.9, that there is a well-pronounced synergistic effect between the solid particles present in compounds and the spread oil. Most of the studied fast antifoams have sufficiently low entry barriers exclusively as a result of the combined action of the solid particles and the spread oil layer [804].

As mentioned in Section 7.7.2, the spread layer of oil has another important role as well. The spread oil is able to feed the oil bridges, formed in foam films, by a mechanism explained in Ref. [808], as a result, larger and less stable oil bridges are formed.

7.7.4 MECHANISMS OF COMPOUND EXHAUSTION AND REACTIVATION

The process of antifoam exhaustion (deactivation) is illustrated in Figure 7.74—the time for foam destruction in a standard shake test is shown as a function of the number of the shaking cycle (see Section 7.7.3.3 for the used shake test) [823]. Shorter defoaming time means more active antifoam and vice versa. As seen from Figure 7.74, the initial high activity of the antifoam deteriorates with the foaming cycles and the defoaming time becomes longer than 60 s after 45 cycles—the antifoam has been exhausted. This process is very undesired from practical viewpoint, and more durable antifoams (able to sustain a larger number of foam destruction cycles) are searched by the manufacturers.

TABLE 7.9
Entry Barriers, P_C^{CR}, of Different Antifoams in Surfactant Solutions in the Presence and Absence of a Prespread Layer of Oil, from which the Antifoam is Prepared

Antifoam	Surfactant	Spread Layer	P_C^{CR}, Pa
Dodecane	2.6 mM SDDBS	No	96 ± 5
		Yes	48 ± 5
Hexadecane	2.6 mM SDDBS	No	80 ± 5
		Yes	400 ± 10
Silicone oil	10 mM AOT	No	28 ± 1
		Yes	19 ± 2
Compound 1	10 mM AOT	No	8 ± 1
		Yes	3 ± 2
Compound 2	10 mM AOT	No	20 ± 5
		Yes	4 ± 1
Compound 1	1 mM Triton X-100	No	30 ± 1
		Yes	5 ± 2
Compound 2	1 mM Triton X-100	No	22 ± 1
		Yes	7 ± 1

Sources: Data from Denkov, N.D., Tcholakova, S., Marinova, K., and Hadjiiski, A., Role of oil spreading for the efficiency of mixed oil-solid antifoams, *Langmuir*, 2001. submitted; Hadjiiski, A., Tcholakova, S., Denkov, N.D., Durbut, P., Broze, G., and Mehreteab, A., *Langmuir*, 17, 7011, 2001.

Notes: SDDBS and AOT denote the anionic surfactants sodium dodecyl-benzenesulfonate and sodium dioctyl-sulfosuccinate, respectively. Triton X-100 is the nonionic surfactant nonylphenol deca (ethyleneglycolether). Compound 1 is a mixture of silicone oil and hydrophobized silica; Compound 2 is an emulsion of Compound 1, which contains also solid particles of Span 60.

Interestingly, the addition of a new portion of oil (without silica particles) leads to a complete restoration of the antifoam activity (Figure 7.74). Note that the oil itself has a very weak antifoam activity in the absence of silica. Therefore, the antifoam reactivation certainly involves the solid particles that have been introduced with the first portion of mixed antifoam. The subsequent foaming cycles lead to a second exhaustion series, and such consecutive periods of exhaustion/reactivation can be repeated several times.
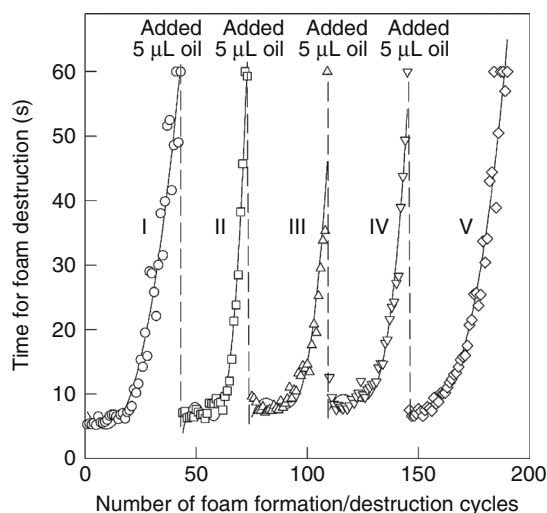
FIGURE 7.74 Consecutive cycles of exhaustion and reactivation of mixed oil–silica compound in 10 mM solution of the anionic surfactant sodium dioctyl-sulfosuccinate (AOT). An initially active antifoam (defoaming time ≈ 5 s) gradually looses its activity with the number of foam formation/destruction cycles in a standard shake test [823]. The introduction of silicone oil results in a perfect restoration of the antifoam activity. Five exhaustion curves (indicated by roman numbers; the symbols indicate the experimentally measured defoaming time) and the corresponding four reactivation events (the vertical dashed lines) are shown. (Adapted from Ref. [823].)
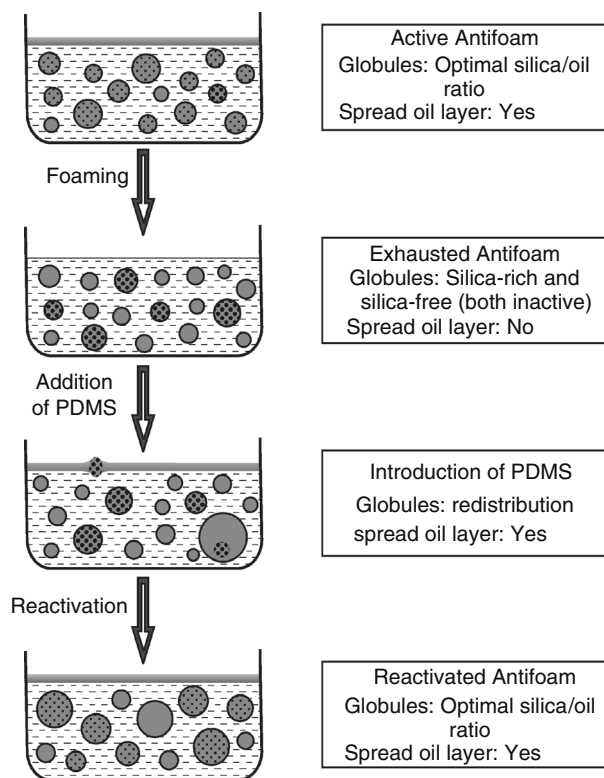
FIGURE 7.75 Schematic presentation of the processes of antifoam exhaustion and reactivation of emulsified oil–silica antifoam compound.

Systematic experiments [823] with solutions of the anionic surfactant sodium dioctyl-sulfosuccinate (AOT) showed that the exhaustion of mixed silica–silicone oil antifoams is due to two closely interrelated processes: (1) partial segregation of the oil and silica into two distinct, inactive populations of antifoam globules, silica-free and silica-enriched; (2) disappearance of the spread oil layer from the solution surface (Figure 7.75). The oil drops deprived of silica, which appear in process 1, are unable to enter the air–water interface and to destroy the foam lamellae, because the entry barrier is too high for them. On the other hand, the antifoam globules enriched in silica trap some oil, which is not available for spreading on the solution surface. As a result, the spread oil layer gradually disappears from the solution surface (process 2) due to oil emulsification in the moment of foam film rupture. Ultimately, both types of globules, silica-enriched and silica-free, become unable to destroy the foam films, and the antifoam transforms into an exhausted state. Accordingly, the reactivation process is due to: (1) restoration of the spread oil layer, and (2) rearrangement of the solid particles from the exhausted antifoam with the fresh oil into new antifoam globules having optimal silica concentration. No correlation between the size of the antifoam globules and their activity was established in these experiments, which showed that the reduction of the globule size (which is often considered as the main factor in the antifoam exhaustion) was a second-order effect in the studied systems. Similar conclusions were drawn from experiments with nonionic surfactants as well [803].

In conclusion, a progress has been achieved during the last years in revealing the mechanisms of foam destruction by oil-based antifoams. This progress has been greatly facilitated by the various methods for direct microscopic observations of the foams and foam films (including some of the foam destruction events), and by the implementation of the FTT for a direct measurement of the entry barriers of the antifoam globules.

7.8 ELECTROKINETIC PHENOMENA IN COLLOIDS

The term "electrokinetic phenomena" refers to several processes which appear when a charged surface (or colloidal particle) is set in a relative motion with respect to the adjacent liquid phase. Classically, four types of electrokinetic phenomena are distinguished: electroosmosis, streaming potential, electrophoresis, and sedimentation potential (Figure 7.76). These will be discussed in Sections 7.8.2 through 7.8.6. Nowadays, the electrical conductivity (at constant electrical field) and the dielectric response (at alternating electrical field) of the disperse systems are often considered together with the electrokinetic phenomena, because the theoretical approaches and the governing equations are similar (Section 7.8.7). Experimental methods based on all these phenomena are widely used for characterization of the electrical surface potential in dispersions. A comprehensive presentation of the topic until the end of 1980s can be found in review articles [824–834] and monographs [835–837].

Driving force / Moving phase	Electric field creates mechanical flux	Mechanical flux creates electric field
Solid phase is Immobile	(a) Electroosmosis	(b) Streaming potential
Solid particles (or liqid droplets) are moving	(c) Electrophoresis	(d) Sedimentation potential
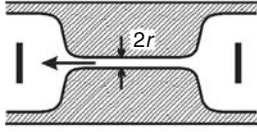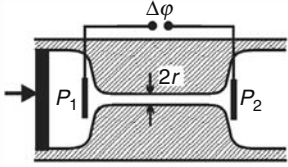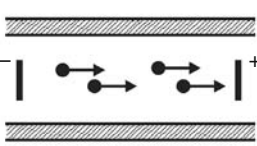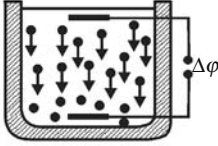
FIGURE 7.76 The four basic electrokinetic phenomena: (a) Electroosmotic liquid flow through a capillary (of charged walls) appears when an electric potential difference is applied; (b) Streaming electric potential appears when a pressure drop drives the liquid to flow through the capillary; (c) Electrophoretic motion of charged particles is observed in an external electric field; (d) Sedimentation potential is established when charged particles are moving under the action of gravity.

The recent development of the area is reviewed in the collective monograph [838]. The major experimental techniques are described in Chapter 4 of Ref. [836] and Chapters 8 through 14 in Ref. [838]. Recently, a substantial interest has been raised by the apparent discrepancy between the results obtained by different electrokinetic methods for one and the same system. This problem is discussed in Section 7.8.8. Finally, the electrokinetic properties of air–water and oil–water interfaces are briefly described in Section 7.8.9.

7.8.1 POTENTIAL DISTRIBUTION AT A PLANAR INTERFACE AND AROUND A SPHERE

When a dielectric phase (solid or fluid) is placed in contact with polar liquid, such as water, the interface gets charged due to either specific adsorption of ions initially dissolved in the polar liquid, or dissociation of surface ionizable groups [14,34,837]. The final result of these two processes is the formation of an electrical double layer (see Figure 7.77), which may contain three types of ions:

1. Ions attached to the surface by chemical bond are those parts of the ionized groups which remain bound after the dissociation process.
2. Ions bound by very strong Coulomb attraction (after partial loss of molecules from the ion solvating shell) or by some other noncovalent specific, short-range attraction build up the so-called Stern layer.
3. Ions that are involved in more or less free Brownian motion present the diffuse part of the electrical double layer.

The ions from groups (1) and (2), considered together, determine the effective surface charge density, σ_s, which must be balanced by an excess of counterions in the diffuse layer (equal in magnitude and opposite in sign). The distribution of electrical potential in the diffuse layer is usually rather accurately described by the Poisson–Boltzmann (PB) equation:

$$\nabla^2 \psi = -\frac{e}{\varepsilon \varepsilon_0} \sum_j Z_j n_{b,j} \exp\left[-\frac{eZ_j\psi}{kT}\right] \tag{7.352}$$

where
  ψ is the local (average) value of the electrical potential
  e is the elementary charge
  ε is the relative dielectric permittivity of the liquid
  ε_0 is the electrical permittivity in vacuo
  Z_j and $n_{b,j}$ are the number of charges and the bulk number concentration, respectively, of ion j
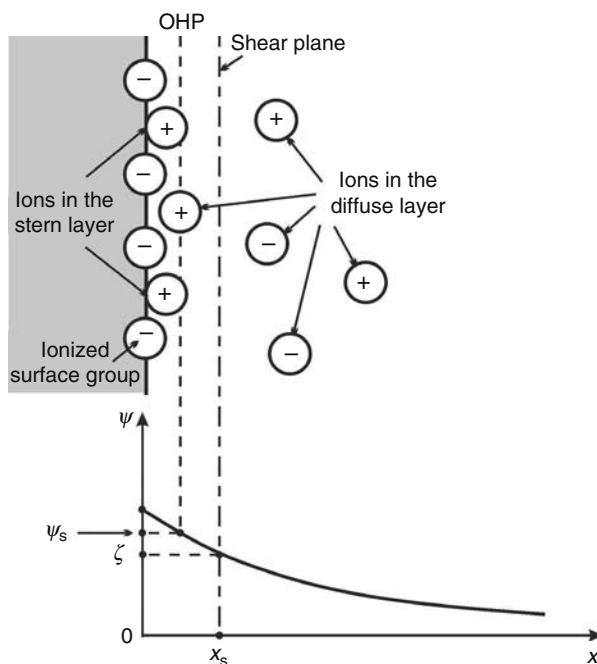
FIGURE 7.77 Schematic presentation of the structure of the electrical double layer (EDL). The surface charge is created by ionized surface groups and/or by ions tightly adsorbed in the Stern layer. The plane of closest approach of the ions from the diffuse part of the electrical double layer is called the outer Helmholtz plane (OHP). The electric potential in the OHP plane is referred to as the surface potential, ψ_s, in the text. The shear plane, $x = x_s$, separates the hydrodynamically immobile liquid that moves together with the surface, $x < x_s$, from the mobile liquid, $x > x_s$, which has nonzero relative velocity with respect to the surface. Note that the ions in the immobile part of the EDL can move with respect to the surface under an applied electric field, which gives rise to the anomalous surface conductivity (Section 7.8.8).

The model of the electrical double layer based on Equation 7.352 is called in the literature Gouy–Chapmen or Gouy–Stern model. For symmetrical ($Z:Z$) electrolyte, the PB equation can be written in the form:

$$\nabla^2 \psi = \frac{2eZn_0}{\varepsilon\varepsilon_0} \sinh\left(\frac{eZ\psi}{kT}\right) \tag{7.353}$$

where n_0 is the bulk electrolyte number concentration. For a flat interface (see Figure 7.77), Equation 7.353 has an exact analytical solution [34,368,837]:

$$\psi(x) = \frac{2kT}{eZ} \ln\left[\frac{1 + \gamma_s \exp(-\kappa x)}{1 - \gamma_s \exp(-\kappa x)}\right] \tag{7.354}$$

where

$$\gamma_s \equiv \tanh\left(\frac{ze\psi_s}{4kT}\right), \quad \kappa^2 \equiv \frac{2e^2 Z^2 n_0}{\varepsilon\varepsilon_0 kT}$$

and ψ_s is the electrical potential at the surface of closest approach of the ions from the diffuse layer to the interface. This surface is called the outer Helmholtz plane and ψ_s is called the surface potential. The surface charge and potential are interrelated by the expression:

$$\sigma_s = -\varepsilon\varepsilon_0 \left(\frac{d\psi}{dx}\right)_{x=0} = (8\varepsilon\varepsilon_0 kTn_0)^{1/2} \sinh\left(\frac{eZ\psi_s}{2kT}\right) \tag{7.355}$$

which is a direct corollary [14,34] from Equation 7.353 and the condition for overall electroneutrality of the interface.

If the surface potential is small, one can expand in series the logarithm in the right-hand-side of Equation 7.354 and derive the Debye–Hückel equation:

$$\psi(x) = \psi_s \exp(-\kappa x), \quad \frac{Ze\psi_s}{kT} < 1 \tag{7.356}$$

On the other hand, the potential always decays exponentially far from the interface ($\kappa x \gg 1$) at an arbitrary magnitude of ψ_s (see Equation 7.354):

$$\psi(x) = \frac{4kT}{eZ} \gamma_s \exp(-\kappa x), \quad \kappa x \gg 1 \tag{7.356a}$$

The potential distribution around a spherical particle can be found from the PB equation (Equation 7.352), which in this case reads:

$$\frac{1}{r^2} \frac{d}{dr}\left(r^2 \frac{d\psi}{dr}\right) = -\frac{e}{\varepsilon\varepsilon_0} \sum_j Z_j n_{b,j} \exp\left[-\frac{eZ_j\psi(r)}{kT}\right] \tag{7.357}$$

The respective boundary conditions are

$$\psi(r = R) = \psi_s, \quad \psi(r \to \infty) = 0$$

Equation 7.357 has an analytical solution only in the case of small surface potential:

$$\psi(r) = \psi_s \frac{R \exp[-\kappa(r - R)]}{r}, \quad \frac{Ze\psi_s}{kT} < 1 \tag{7.358}$$

In this case, the surface charge density is a linear function of ψ_s:

$$\sigma_s = \frac{\varepsilon\varepsilon_0(1 + \kappa R)}{R} \psi_s, \quad \frac{Ze\psi_s}{kT} < 1 \tag{7.359}$$

For a large surface potential, ψ_s, the potential distribution can be found by numerical integration of the PB equation. Far from the sphere surface, the potential always obeys the law:

$$\psi(r) = \psi_s^* \frac{R \exp[-\kappa(r - R)]}{r}, \quad \kappa(r - R) \gg 1 \tag{7.360}$$

where $\psi_s^*(\kappa R, \psi_s)$ is an effective potential, which can be found by numerical solution of the PB equation. By using the method of matched asymptotic expansions, Chew and Sen [839] obtained for a thin electrical double layer ($\kappa R > 1$):

$$\psi_s^* = \frac{4kT}{Ze}\left(\gamma_s + \frac{\gamma_s^3}{2\kappa R}\right) \tag{7.361}$$

A useful relationship between ψ_s and σ_s for a sphere was proposed by Loeb et al. [840]:

$$\sigma_s = \frac{\varepsilon\varepsilon_0 \kappa kT}{Ze}\left[2\sin h\left(\frac{Ze\psi_s}{2kT}\right) + \frac{4}{\kappa R}\tan h\left(\frac{Ze\psi_s}{4kT}\right)\right] \tag{7.362}$$

and was theoretically justified by other authors [838,841–844]. Equation 7.362 coincides with the exact numerical results within an accuracy of a few percent for $\kappa R > 0.5$ and arbitrary surface potential [836,840]. A general approach for derivation of approximate (but accurate) expressions relating ψ_s and σ_s, including for systems containing nonsymmetric electrolytes, has been proposed by Ohshima [844,845].

7.8.2 ELECTROOSMOSIS

When an electrical field of intensity E is applied in parallel to a charged flat interface, the excess of counterions in the diffuse layer gives rise to a body force exerted on the liquid. The liquid starts moving with local velocity varying from zero in the plane of shear ($x = x_s$) to some maximal value, V_{EO}, at a large distance from the wall (see Figure 7.77). The magnitude of this electroosmotic velocity was calculated by Smoluchowski [846] under the assumptions that: (1) the ion distribution in the

diffuse layer obeys the PB equation, (2) at each point the electrical force is balanced by the viscous friction, and (3) the liquid viscosity in the diffuse layer is equal to that of the bulk liquid, η. The final result reads [846]:

$$V_{EO} = -\frac{\varepsilon\varepsilon_0\zeta}{\eta}E \tag{7.363}$$

where ζ is the electrical potential in the shear plane, i.e., $\zeta \equiv \psi(x = x_s)$. The quantity

$$\mu_{EO} = \frac{V_{EO}}{E} = -\frac{\varepsilon\varepsilon_0\zeta}{\eta} \tag{7.364}$$

is called electroosmotic mobility. The Smoluchowski consideration is also applicable to capillaries of a radius much larger than the Debye screening length, κ^{-1}. Therefore, by measuring the liquid flow through a capillary, like that shown in Figure 7.76, one can determine the ζ potential of the capillary surface. It is usually acceptable [836] to measure the liquid flux (volume displaced per unit time), J_{EO}, along with the electric current transported by the liquid, I_{EO}:

$$J_{EO} = \pi r^2 V_{EO} \quad \text{and} \quad I_{EO} = \pi r^2 \chi_b E \tag{7.365}$$

where
   r is the capillary radius
   χ_b is the bulk conductivity of the liquid

The ratio

$$J_{EO}\ I_{EO} = V_{EO}\ x_b E = -\frac{\varepsilon\varepsilon_0\zeta}{\eta x_b} \tag{7.366}$$

does not depend on the capillary radius and can be used to determine ζ. Quite often, however, the high concentration of ions in the double electric layer leads to a much higher conductivity in the surface region, compared to that in the bulk electrolyte solution. To account for this effect Bikerman [847] introduced the term "specific surface conductivity," χ_s, which presents an excess quantity over the bulk conductivity. Then, Equation 7.365 is modified to read:

$$I_{EO} = (\pi r^2 \chi_b + 2\pi r \chi_s)E \tag{7.367}$$

and Equation 7.366 acquires the form:

$$|J_{EO}/I_{EO}| = \frac{\varepsilon\varepsilon_0\zeta}{\eta(\chi_b + 2\chi_s/r)} \tag{7.368}$$

Alternatively, instead of measuring the electroosmotic liquid flux at zero pressure difference across the capillary, one can determine [836] ζ by measuring the counterpressure, ΔP_{EO}, necessary to completely stop the net liquid transport through the capillary:

$$\Delta P_{EO} = \frac{8\varepsilon\varepsilon_0\zeta}{\pi r^4(\chi_b + 2\chi_s/r)}I_{EO} \tag{7.369}$$

Bikerman [847] obtained the following expression for χ_s in the case of a symmetrical (Z:Z) electrolyte, under the assumption that the surface conductivity is due only to the ions located in the movable part of the diffuse layer:

$$\chi_s = \frac{2Z^2e^2n_0}{kT\kappa}\left\{D^+\left[\exp\left(-\frac{Ze\zeta}{2kT}\right)-1\right]\left(1+\frac{3m^+}{Z^2}\right) + D^-\left[\exp\left(\frac{Ze\zeta}{2kT}\right)-1\right]\left(1+\frac{3m^-}{Z^2}\right)\right\} \tag{7.370}$$

where $D^{\pm}$ are ion diffusion coefficients, while $m^{\pm}$ are dimensionless ion mobilities, defined as

$$m^{\pm} = \frac{2}{3}\left(\frac{kT}{e}\right)^2\frac{\varepsilon\varepsilon_0}{\eta}\frac{Z^2}{D^{\pm}} = \frac{2\varepsilon\varepsilon_0 N_A kT}{3\eta}\frac{Z^2}{\Lambda^0} = 12.84 \times 10^{-4}\left(\frac{Z^2}{\Lambda^0}\right) \quad \text{at } 25°C \text{ in water} \tag{7.371}$$

Λ° (m^2 ohm^{-1} mol^{-1}) is the limiting molar conductivity of ions at infinite dilution. The typical values of χ_s are around 10^{-9} ohm^{-1}. For comparison, the bulk conductivity, χ_b, is given by

$$\chi_b = \frac{e^2}{kT} \sum D_j Z_j^2 n_{b,j} \tag{7.372}$$

and can vary within a wide range (note that χ_s and χ_b have different dimensions).

Equation 7.368 shows that for determination of ζ and χ_s, one needs measurements with several capillaries made of the same material, but having different radii. The effect of the surface conductivity can be neglected when the criterion

$$\frac{2\chi_s}{\chi_b r} \sim \frac{1}{\kappa r} \exp\left(\frac{Ze\psi_s}{2kT}\right) \ll 1 \tag{7.373}$$

is satisfied [836,837,848]. In other words, the surface conductivity is negligible at low surface potential and high ionic strength. Besides, Equation 7.366 can be applied [836,848,849] also to electroosmotic flow in porous plugs or membranes if: (1) the typical pore size is much larger than κ^{-1} (2) the effects of the surface conductivity, χ_s, are negligible, and (3) the flow is laminar.

This consideration can be extended to include capillaries of radii comparable to κ^{-1} and the cases when the potential distribution cannot be approximated using the results for a planar wall [827,836].

The so-called plane interface technique [850–852] is a modification of the electroosmotic method, in which submicrometer particles are used as probes to visualize the osmotic velocity profile close to an interface. The method allowed precise determination of the ζ potential at mica, quartz, sapphire, and fused-silica surfaces as a function of pH [851,852]. The attempt [850,852,853] to apply the plane interface technique to the air–water interface, however, gave ambiguous results, probably due to the interfacial fluidity.

7.8.3 STREAMING POTENTIAL

If a pressure drop, $\Delta P = P_1 - P_2$, is imposed at the ends of a capillary, like that shown in Figure 7.76, the liquid starts moving through the capillary [836,843]. The charges in the mobile part of the double layer at the capillary wall are thus forced to move toward the end of the capillary. As a result, a streaming current, I_{ST}, appears which leads to the accumulation of excess charge at the capillary end. This excess charge gives rise to an electric potential difference between the ends of the capillary, called streaming potential, E_{ST}. On its own, the streaming potential causes a current flow, I_C, in a direction opposite to I_{ST}. Finally, a steady state is established when $|I_C| = |I_{ST}|$ and the net electric current across the capillary becomes zero. One can directly measure E_{ST} by probe electrodes, and the following relationship is used to determine the ζ potential of the capillary walls [836]:

$$\frac{E_{ST}}{\Delta P} = \frac{\varepsilon \varepsilon_0 \zeta}{\eta(\chi_b + 2\chi_s/r)} \tag{7.374}$$

Alternatively, instead of measuring E_{ST}, one can measure the streaming current, I_{ST}, by using the appropriate electrical circuit [836]:

$$I_{ST} = -\frac{\varepsilon \varepsilon_0}{\eta} \frac{\pi r^2}{L} \Delta P \zeta \tag{7.375}$$

where, L denotes the length of the capillary. An important advantage of the streaming current measurement is that the surface conductivity does not matter for the calculation (see Equation 7.375), and experimental determination of χ_s is not necessary. Similar experiments were performed by Scales et al. [854] to determine the ζ potential of mica surface.

Equations 7.374 and 7.375 are valid only if the capillary radius is much larger than the thickness of the diffuse layer. A number of modifications were suggested in the literature to extend the theoretical consideration to narrower capillaries and porous plugs (see, for example, the review article by Dukhin and Derjaguin [827] and the book of Hunter [836]). Measurements of the streaming potential, streaming current, and electrical conductance of plugs made of latex particles were performed and analyzed by van den Hoven and Bijsterbosch [855].

7.8.4 ELECTROPHORESIS

The movement of a charged colloidal particle in an external electrical field is called electrophoretic motion and the respective phenomenon is electrophoresis. The electrophoretic velocity in the two limiting cases, of a thin and thick electrical double layer around a spherical particle, can be calculated by Smoluchowski [856] and Hückel [857] formulas:

$$V_{EL} = \frac{\varepsilon\varepsilon_0 \zeta}{\eta} E, \quad \kappa R \gg 1 \text{ (Smoluchowski)} \tag{7.376}$$

$$V_{EL} = \frac{2}{3} \frac{\varepsilon\varepsilon_0 \zeta}{\eta} E, \quad \kappa R \ll 1 \text{ (Huckel)} \tag{7.377}$$

It is important to note that Equation 7.376 is valid for particles of arbitrary shape and size, if the following requirement is fulfilled: The dimensions of the particle and the local radii of curvature of the particle surface are much larger than the Debye screening length.

The problem for spherical particles at arbitrary κR was solved by Henry [858] who obtained

$$\mu_{EL} = \frac{V_{EL}}{E} = \frac{2}{3} \frac{\varepsilon\varepsilon_0 \zeta}{\eta} f_1(\kappa R) = \frac{Q}{6\pi\eta R(1 + \kappa R)} f_1(\kappa R) \text{ (Henry)} \tag{7.378}$$

where
   μ_{EL} is the particle electrophoretic mobility
   Q is the particle charge
   $f_1(\kappa R)$ is a correction factor given by

$$f_1(\kappa R) = \frac{3}{2} - \frac{9}{2}(\kappa R)^{-1} + \frac{75}{2}(\kappa R)^{-2} - 330(\kappa R)^{-3}, \quad \kappa R > 1$$

$$f_1(\kappa R) = 1 + \frac{1}{16}(\kappa R)^2 - \frac{5}{48}(\kappa R)^3 - \frac{1}{96}[(\kappa R)^4 - (\kappa R)^5]$$

$$+ \left[\frac{1}{8}(\kappa R)^4 - \frac{1}{96}(\kappa R)^6\right]\exp(\kappa R)E_1(\kappa R), \quad \kappa R < 1 \tag{7.379}$$

and $E_1(x) \equiv \int_1^\infty e^{-sx}\frac{ds}{s}$ is an integral exponent of the first order. The limiting values, $f_1(\kappa R \to \infty) = 3/2$ and $f_1(\kappa R \to 0) = 1$, reduce Henry's equation to the equations of Smoluchowski and Hückel, respectively. The effect of the surface conductivity, χ_s, can be phenomenologically included in this approach, as shown by Henry [859]. Also, if the material of the particle has finite electrical conductivity, χ_p, its electrophoretic mobility is given by [858]:

$$\mu_{EL} = \frac{2}{3} \frac{\varepsilon\varepsilon_0 \zeta}{\eta} f_2(\kappa R, \chi_p/\chi_b) \tag{7.380}$$

where

$$f_2(\kappa R, \chi_p/\chi_b) = 1 + 2\frac{(\chi_b - \chi_p)}{(2\chi_b + \chi_p)}[f_1(\kappa R) - 1] \tag{7.381}$$

It was shown [827,828,835], however, that the approach of Henry is strictly valid only for small values of the ζ potential, $Ze\zeta/kT < 1$, because it neglects the relaxation and the retardation effects, connected with distortion of the counterion atmosphere around the moving particle. Solutions of the problem for not-too-high ζ potentials were suggested by Overbeek [860] and Booth [861]. The mobility of a spherical, nonconducting particle of arbitrary ζ potential and arbitrary κR was rigorously calculated by Wiersema et al. [862] and by O'Brien and White [863]. In Figure 7.78, the results of O'Brien and White [863] for the particle mobility as a function of the ζ potential at different values of κR are represented. One interesting conclusion from these calculations is that the mobility has a maximum for $\kappa R > 3$, i.e., a given value of μ_{EL} may result from two different values of ζ. The maximum in these curves appears at $\zeta \sim 150$ mV. The numerical algorithm of O'Brien and White [863] is sufficiently rapid to allow application to individual sets of experimental data.

Explicit approximate expressions were suggested by several authors. For a thin electrical double layer, Dukhin and Derjaguin [827] derived a formula, which was additionally simplified (without loss of accuracy) by O'Brien and Hunter [864]:

$$\mu_{EL} = \frac{\varepsilon\varepsilon_0}{\eta}\zeta - 4\frac{\varepsilon\varepsilon_0 kT}{e}\left\{\frac{\frac{\tilde{\zeta}}{2} - \frac{\ln 2}{Z}\left[1 - \exp\left(-Z\tilde{\zeta}\right)\right]}{2 + \frac{\kappa R}{M}\exp\left(-\frac{Z\tilde{\zeta}}{2}\right)}\right\}, \quad \kappa R \gg 1 \tag{7.382}$$
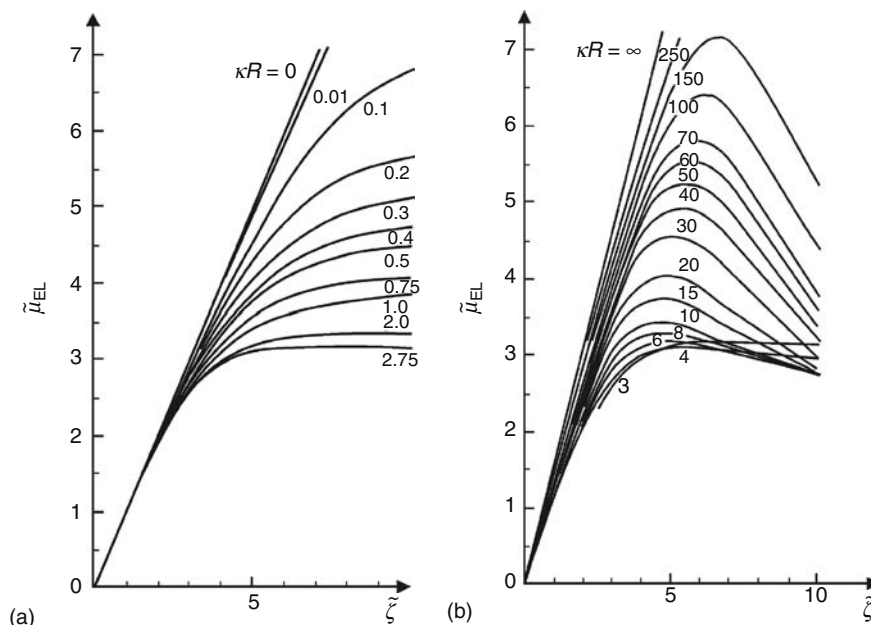
FIGURE 7.78 The dimensionless electrophoretic mobility of spherical particles, $\tilde{\mu}_{EL} = 3\,\eta e\mu_{EL}/(2\varepsilon\varepsilon_0 kT)$, versus the dimensionless zeta-potential, $\tilde{\xi} = e\zeta/(kT)$, for various values of κR: (a) κR varies between 0 and 2.75; (b) κR varies between three and infinity [863].

where
 $\tilde{\zeta} \equiv \frac{e\zeta}{kT}$ is the dimensionless ζ potential, $\widetilde{M} = (1 + 3m/Z^2)$
 m is the dimensionless mobility of the ions (see Equation 7.371)

Equation 7.382 was derived assuming equal valency and mobility of the counter- and coions. The comparison with the exact numerical calculations showed that Equation 7.382 is rather accurate for $\kappa R > 30$ and arbitrary ζ potential. Another explicit formula of high accuracy (less than 1% for arbitrary ζ potential) and wider range of application ($\kappa R > 10$) was suggested by Ohshima et al. [865]

For low values of the ζ potential, Ohshima [866] suggested an approximate expression for the Henry's function (Equations 7.378 and 7.379), which has a relative error of less than 1% for arbitrary values of κR:

$$\mu_{EL} = \frac{2}{3}\frac{\varepsilon\varepsilon_0\zeta}{\eta}\left(1 + \frac{1}{2\{1 + 2.5/[\kappa R(1 + 2e^{-\kappa R})]\}^3}\right) \tag{7.383}$$

Recently, Ohshima [867] derived an extension of Equation 7.383, which is accurate for $\tilde{\zeta} < 3$ at arbitrary values of κR.

The electrophoretic mobility of particles having a cylindrical or ellipsoidal shape was studied theoretically by Stigter [868], van der Drift et al. [869], and Ohshima [870]. The polyelectrolytes [871–873] and the spherical particles covered by a layer of polymer [874,875] (or polyelectrolyte) are two other types of systems that have been matters of great interest. In a recent series of papers Ohshima and Kondo [876–878] derived a general analytic formula for the case of a hard particle, covered by a layer of polyelectrolyte. In the corresponding limiting cases, the general expression reduces to the known expressions for a hard spherical particle, a plate-like particle covered by a polyelectrolyte layer, or a charged porous sphere [876,877].

Churaev and Nikologorskaja [879] performed measurements of the electrophoretic mobility and the diffusion coefficient of silica particles before and after adsorption of polyethylenoxides. They found that the experimental data can be explained only by assuming that the adsorbed polymer layer not only shifts the shear plane apart from the particle surface (thus increasing the hydrodynamic radius of the particles) but also substantially reduces the particle surface potential. According to the authors [879] the decrease in the surface charge could be due to the lower dielectric permittivity in the adsorption layer compared to that of water. It is rather possible that a similar effect played a role in the experiments of Furusawa et al. [880] who showed that the adsorption of hydroxylpropylcellulose on latex particles may completely shield their charge (the particle ζ potential becomes zero). Since the adsorption layer was shown to be very stable in a wide range of pH and electrolyte concentrations, such particles can be used as a reference sample for electrophoretic measurements. These particles exactly follow the electroosmotic liquid flow in the cell and, hence, represent a convenient probe sample for the plane interface technique mentioned in Section 7.8.2.

The effect of the interparticle interactions on the electrophoretic mobility in concentrated dispersions was theoretically studied by Levine and Neale [881]. They used a cell model with two alternative boundary conditions at the cell boundary to describe the hydrodynamic flow: the free surface model of Happel [882] and the zero vorticity model of Kuwabara [883]. The results [881] suggested that the zero vorticity model is more appropriate, because it represents in a more correct way the limit to low particle concentration. Experiments at very low electrolyte concentrations, when the electrostatic interactions between the particles are very strong, were performed by Deggelmann et al. [884]. They observed a strong increase in the electrophoretic mobility at lower ionic strength (when the electrostatic interaction is stronger and the particles form a liquid-like structure) which was in apparent contradiction with the predictions of the Levine and Neale's theory [881]. One possible explanation of this surprising result could be that the decrease of the ionic strength leads to a simultaneous increase in the surface potential [34], and this effect prevails over the increased interparticle interactions. Further development of the electrokinetic theory for concentrated dispersions was presented by Kozak and Davis [885], and Ohshima [877,886].

Another interesting experimental study of concentrated suspensions of human erythrocytes was performed by Zukoski and Saville [887]. Although volume fractions as high as 75% were employed, the electrophoretic mobility changed by the factor $(1 - \phi)$ in the whole concentration range, which was simply explained by the backflow of liquid necessary to conserve the suspension volume. The electrostatic and hydrodynamic particle–particle interactions apparently canceled each other in these experiments. One should note that the electrolyte concentration was relatively high and, contrary to the experiments of Deggelmann et al. [884] the electrical double layers were thin in comparison with the particle size.

A recent progress was achieved in the theoretical description of the electrophoretic mobility of spherical particles in oscillating electrical field [888], the so-called dynamic mobility (see also Section 7.8.7.2). General equations at an arbitrary frequency, ζ potential, and κR, as well as analytical formulas for low ζ potentials, were derived by Mangelsdorf and White [888]. Theory and experiment [889] demonstrated rather strong frequency dependence of the electrophoretic response of the particles in the hertz and kilohertz regions. A general theoretical expressions, along with explicit approximate formulas, for the dynamic electrophoretic mobility of spheres and cylinders were derived by Ohshima [877,890,891]. The electrophoretic measurements in oscillating fields are stimulated also by the fact that the undesirable effect of the electroosmotic flow in the experimental cell, created by the charge at the cell walls, is strongly suppressed in this type of equipment [889,892].

Another important recent development is the construction of equipment capable of measuring the mobility of nanometer-sized particles, such as micelles and protein molecules. The different mobility of proteins in polymer gels is widely used for their separation and identification [893], but this method is not suitable for the physicochemical study of proteins, because the interactions of the protein molecules with the polymer gel matrix could be rather specific. For a long time the electrophoretic mobility of proteins in a free solution was studied by the moving boundary method of Tiselius [894], since electrophoretic equipment based on DLS (Section 7.9.2.1) is limited to particles of a size between approximately 50 nm and 10 μm. The method of Tiselius is not so easy and, in principle, it is not very suitable for micellar solutions, because a boundary between solutions of different concentrations must be formed. Imae et al. [895,897–900] described an improved version of electrophoretic light scattering equipment applicable to particles of a diameter as small as several nanometers. The feasibility of this equipment was demonstrated [896] by measuring the electrophoretic mobility of micelles of sodium dodecylsulfate (SDS) and of mixed micelles of SDS with nonionic surfactants. The electrokinetic properties of micelles are discussed in the recent review by Imae [900]. This experimental advance is accompanied by progress in the theoretical analysis of the electrophoretic mobility of nonspherical and nonuniformly charged particles (such as proteins) with some spatial charge distribution on the particle surface [901–904]. One quite interesting conclusion from the work of Yoon [904] was that Henry's formula, Equations 7.378 through 7.379, is correct for spherical particles of arbitrary charge distribution (with Q being the net particle charge in this case), provided that the electrical potential is low and can be described by the linearized PB equation.

More details about the method of electrophoretic mobility measurement by means of DLS are given in Section 7.9.2.1.

7.8.5 Sedimentation Potential

When a charged particle is sedimenting under the action of gravity (Figure 7.76d) the ions in the electrical double layer are not obliged to follow the particle motion. Instead, a continuous flow of ions enters the lower half of the particle diffuse layer and leaves its upper half. The net effect is a spatial separation of the negative and positive charges which creates the sedimentation potential of intensity, E_{SED}. At a steady state, the electrical current caused by the particle motion must be counterbalanced by an equal-in-magnitude (but opposite-in-direction) current created by E_{SED}. The intensity, E_{SED}, can be directly measured by means of electrode probes placed at two different levels in the suspension of settling particles. Smoluchowski [905] derived the following equation connecting E_{SED} and the ζ potential of spherical non conducting particles:

$$E_{SED} = \frac{\varepsilon \varepsilon_0}{\eta} \frac{F_g \rho_p}{\chi_b} \quad \text{at} \quad \kappa R \gg 1 \tag{7.384}$$

where

$F_g = gV_p(d_p - d_0)$ is the gravity force (with subtracted Archimedes' force) acting on a particle

ρ_p is the particle number concentration; g is gravity acceleration

V_p is the particle volume

d_p is the particle mass density

d_0 is the mass density of the disperse medium

Generalization of the theoretical consideration to arbitrary values of κR was given by Booth [906]. The theory was later refined by Ohshima et al. [907] who performed exact numerical calculations and proposed explicit formulas for the cases of not-too-high surface potential and for thin electrical double layers. The effect of particle concentration was considered by Levine et al. [908] who used a cell model to account for the hydrodynamic interaction between the particles. The theory of Levine et al. [908] is restricted to thin double layers ($\kappa R > 10$) and low surface potentials.

7.8.6 ELECTROKINETIC PHENOMENA AND ONZAGER RECIPROCAL RELATIONS

All electrokinetic phenomena include the coupled action of an electrical force (with the respective electrical current) and a hydrodynamic force (with the respective hydrodynamic flux). Therefore, one can apply the general approach of the linear thermodynamics of irreversible processes to write [909,910]:

$$
\begin{aligned}
J_1 &= \alpha_{11}F_1 + \alpha_{12}F_2 \\
J_2 &= \alpha_{21}F_1 + \alpha_{22}F_2
\end{aligned}
\tag{7.385}
$$

where

F_j ($j = 1,2$) are the forces

J_j are the coupled fluxes

α_{ij} are the phenomenological coefficients

According to the Onsager reciprocal relations, α_{12} must be equal to α_{21}, i.e., the following relationships must be satisfied (see Equation 7.385):

$$
\left(\frac{J_1}{F_2}\right)_{F_1=0} = \left(\frac{J_2}{F_1}\right)_{F_2=0}
\tag{7.386}
$$

Other relations, which directly follow from the assumption $\alpha_{12} = \alpha_{21}$ are

$$
\left(\frac{J_1}{F_2}\right)_{J_2=0} = \left(\frac{J_2}{F_1}\right)_{J_1=0}; \quad \left(\frac{J_1}{J_2}\right)_{F_1=0} = -\left(\frac{F_2}{F_1}\right)_{J_2=0}; \quad \left(\frac{J_1}{J_2}\right)_{F_2=0} = -\left(\frac{F_2}{F_1}\right)_{J_1=0}
\tag{7.387}
$$

In the cases of the immobile solid phase (electroosmosis and streaming potential; see Figures 7.76a and b), one can identify [909,910]:

$$
\begin{aligned}
J_1 &\equiv J_w; \quad F_1 \equiv \Delta P \\
J_2 &\equiv I; \quad\;\; F_2 \equiv E
\end{aligned}
\tag{7.388}
$$

where

J_w is the water flux

I is the current

Then, the counterpart of Equation 7.386 reads

$$
\left(\frac{J_w}{E}\right)_{\Delta P=0} = \left(\frac{I}{\Delta P}\right)_{E=0}
\tag{7.389}
$$

Equation 7.389 connects the phenomenological coefficients appearing in electroosmosis (the left-hand side) with those in streaming potential experiments (the right-hand side). One must note that Equation 7.389 is valid even if the surface conductivity is important or when the double layers are not thin with respect to the capillary diameter. Furthermore, this

type of relationship is valid even for electrokinetic experiments with porous plugs and membranes having pores of nonuniform size and shape. The respective counterparts of the other relations (Equation 7.387) are

$$\left(\frac{I}{\Delta P}\right)_{J_w=0} = \left(\frac{J_w}{E}\right)_{I=0}; \quad \left(\frac{I}{J_w}\right)_{E=0} = -\left(\frac{\Delta P}{E}\right)_{J_w=0}; \quad \left(\frac{I}{J_w}\right)_{\Delta P=0} = -\left(\frac{\Delta P}{E}\right)_{I=0} \tag{7.390}$$

In the case of mobile charged particles (electrophoresis and sedimentation potential; Figures 7.76c and d), one should identify J_1 as the flux of particles, J_p, and F_1 as the gravity force, F_g. Then, the Onsager relations read

$$\left(\frac{J_p}{E}\right)_{F_g=0} = \left(\frac{I}{F_g}\right)_{E=0}; \qquad \left(\frac{I}{F_g}\right)_{J_p=0} = \left(\frac{J_p}{E}\right)_{I=0} \tag{7.391a}$$

$$\left(\frac{I}{J_p}\right)_{E=0} = -\left(\frac{F_g}{E}\right)_{J_p=0}; \quad \left(\frac{I}{J_p}\right)_{F_g=0} = -\left(\frac{F_g}{E}\right)_{I=0} \tag{7.391b}$$

Again, Equations 7.390 and 7.391 are valid even for concentrated dispersions when strong electrostatic and hydrodynamic interactions between the particles may take place.

One can verify that all explicit expressions given in Sections 7.8.2 through 7.8.5 satisfy the Onsager relations.

7.8.7 ELECTRIC CONDUCTIVITY AND DIELECTRIC RESPONSE OF DISPERSIONS

7.8.7.1 Electric Conductivity

Here we will consider briefly the conductivity, χ, of dispersions subjected to a constant electric field of intensity, E. The behavior of dispersions in alternating fields is considered in Section 7.8.7.2.

Charged particles influence the net conductivity in several ways: (1) the presence of particles having dielectric constant and conductivity different from those of the medium affects the local electrical field and the conditions for ion transport (e.g., nonconducting particles act as obstacles to the electromigrating ions and polarize the incident electric field); (2) the increased ionic concentration in the diffuse ion cloud, surrounding the particles, leads to higher local conductivity; and (3) the migrating charged particles may also contribute to the total electric current.

Effect (1) was analyzed by Maxwell [911], who derived the following expression for the conductivity of diluted suspension of uncharged particles:

$$\chi = \chi_b \left(\frac{1 - 2\Omega\phi}{1 + \Omega\phi}\right), \quad \Omega = \frac{\chi_b - \chi_p}{2\chi_b + \chi_p} \tag{7.392}$$

where
χ_p is the conductivity of the particles
χ_b is the conductivity of the medium
ϕ is the particle volume fraction

As shown by Maxwell, this result includes an important contribution from the polarization of the field by the particles. Fricke [912] modified the Maxwell approach to consider particles of oblate or prolate spheroidal shape and obtained the formula:

$$\chi = \chi_b \left(\frac{1 - X\Omega\phi}{1 + \Omega\phi}\right), \quad \Omega = \frac{\chi_b - \chi_p}{X\chi_b + \chi_p} \tag{7.393}$$

where the X factor depends on the particle conductivity and shape. Since the theory of Fricke [912] assumes random orientation of the particles, it is strictly valid only for diluted suspensions of noninteracting particles and a not-too-high intensity of the electrical field. These expressions were used by Zukoski and Saville [887] to interpret the conductivity data from human erythrocyte suspensions at high ionic strength and relatively low surface potential where the effect of the surface conductivity is negligible (see Equation 7.373).

The contribution of the particle surface conductivity (effect (2)) for a thin electrical double layer can be accounted for phenomenologically in a similar way, and the final result for nonconducting particles reads [827,913]:

$$\chi = \chi_b \left[1 - \frac{3}{2}\phi\left(1 - \frac{3\chi_s}{\chi_b R + \chi_s}\right)\right], \quad \kappa R \gg 1 \tag{7.394}$$

Numerical procedures for calculating the conductivity of dispersions without restriction to double layer thickness were developed by O'Brien [914,915]. A formula for thin electrical double layers, explicitly accounting for the ion mobility, is given by Ohshima et al. [916].

As discussed by Dukhin and Derjaguin [827], the electrophoretic migration of the particles (effect (3)) is negligible if the measurements are performed under conditions such that the particles cannot release their charges on the electrodes.

7.8.7.2 Dispersions in Alternating Electrical Field

As mentioned in Section 7.8.4, the electrical field, in general, polarizes the electrical double layer (EDL) around a charged particle. This means that the spherical symmetry of the ion cloud brakes down, and the additional force appearing between the charged particle and the distorted ion atmosphere must be taken into account for proper description of the particle dynamics. If the external field is suddenly switched off, some finite period of time is needed for restoration of the spherically symmetrical configuration. This time can be estimated [368,835,917] from the ion diffusivity and from the characteristic path length, l, the ions should travel:

$$\tau_{REL} \sim \frac{l^2}{D_{SI}} \approx \frac{(R + \kappa^{-1})^2}{D_{SI}} = \frac{(1 + \kappa R)^2}{\kappa^2 D_{SI}} \tag{7.395}$$

where $D_{SI} \approx 10^{-9}$ m^2 s^{-1} is the ion diffusion coefficient. If the particles are subjected to an oscillatory field of frequency, ω, much higher than τ_{REL}^{-1}, the ion clouds will have no time to respond, and the system will behave as though containing particles with nonpolarizable double layers. On the other hand, at a low frequency, $\omega \ll \tau_{REL}^{-1}$, the ion clouds will polarize, exactly following the temporal changes of the applied field. At intermediate frequencies, $\omega \sim \tau_{REL}^{-1}$, the EDL will follow the field variations with some delay, and the dielectric constant of the colloidal dispersion, ε, will show a strong dependence on ω. The numerical estimate (see Equation 7.395) shows that τ_{REL} is typically of the order of 10^{-3} s and the characteristic frequency, ω_{REL}, falls in the kilohertz range. For thin electrical double layers, there is an additional relaxation time, τ_κ, connected with the ion transport across the double layer [835,917,918] (i.e., in a radial direction with respect to the particle surface). Since the diffusion path in this case is $l \sim \kappa^{-1}$, the relaxation time is [918]

$$\tau_\kappa \sim \frac{\kappa^{-2}}{D_{SI}} \tag{7.396}$$

Therefore, τ_κ is inversely proportional to the electrolyte concentration, and the corresponding characteristic frequency, ω_κ, is typically in the megahertz range.

The polarizability of the individual molecules is also frequency dependent, but the characteristic values are of the order of 10^{11} s^{-1} and 10^{15} s^{-1} for the rotational and electronic polarization, respectively [34]. Therefore, in the typical frequency domain for investigation of dispersions (1 s$^{-1} \le \omega \le 10^8$ s^{-1}) the polarizability, ε_p, of the material building up the particles is frequency independent. On the other hand, the disperse medium (which is usually an electrolyte solution) has a dielectric permittivity, ε_b, for which the frequency dependence can be described by the Debye–Falkenhagen theory [919]. Besides, the characteristic relaxation time of the bulk electrolyte solutions is also given by Equation 7.396 [919].

The typical experiment for determination of the dielectric response of a suspension consists [368,835,917] of measuring the magnitude and phase-lag of the current, $I_c(t)$, passing through the suspension under an applied, oscillating electrical field, $E(t) = E_0 \cos(\omega t)$. The current, in turn, contains two components: one connected with the free charges and another connected with the polarization. It is widely accepted [368,835] to use the complex presentation of the applied field

$$E(t) = Re\{E_0 \exp(i\omega t)\} \tag{7.397}$$

where $Re\{f\}$ means that the real part of the complex function, f, is considered. Very often the $Re\{x\}$ sign is not explicitly stated, but is understood. This formalism, using complex functions, is rather convenient because the magnitude and the phase-lag of the current both can be described by one quantity—the complex conductivity, χ^*:

$$I_c(t) = Re\{\chi^* E_0 \exp(i\omega t)\} \tag{7.398}$$

The physical meaning of the real and of the imaginary parts of χ^* is the following [835]. $Re\{\chi^*\}$ is proportional to the dissipated energy in the system—the heat produced per one period of the field oscillation is equal to $1/2 E_0^2 Re\{\chi^*\}$. On the other hand, the phase-lag of the current (with respect to the applied field) is characterized by the phase angle, $\varphi = \arctan[Im\{\chi^*\}/Re\{\chi^*\}]$.

The complex conductivity, χ^*, of a dispersion is usually defined as [368]:

$$\chi^*(\omega,\phi) = \chi(\omega,\phi) - i\omega\varepsilon_0\varepsilon'(\omega,\phi) \tag{7.399}$$

where
χ is the real part of χ^*
ε' is the loss-free part of the dielectric response

Alternatively, one can define [368]:

$$\chi^*(\omega,\phi) = \chi(0,\phi) + \omega\varepsilon_0\varepsilon''(\omega,\phi) - i\omega\varepsilon_0\varepsilon'(\omega,\phi) \tag{7.400}$$

where the frequency dependence of the real part of χ^* was totally assigned to the imaginary part of the dielectric constant. Both conventions are used in the literature [368], and one should note that in the first case the dielectric constant of the suspension is a real number ($\varepsilon = \varepsilon'$, $\varepsilon'' = 0$), while in the second case ε is considered a complex number ($\varepsilon = \varepsilon' + i\varepsilon''$). Also, since the effect of the particles is of primary interest, one considers the changes of these quantities with respect to the properties of the disperse medium [368]:

$$\Delta\chi(\omega,\phi) \equiv \frac{\chi(\omega,\phi) - \chi(\omega,0)}{\chi(\omega,0)\phi}; \quad \Delta\varepsilon'(\omega,\phi) \equiv \frac{\varepsilon'(\omega,\phi) - \varepsilon'(\omega,0)}{\phi}$$

$$\Delta\varepsilon'' \equiv \frac{\chi(\omega,\phi) - \chi(0,\phi)}{\omega\varepsilon_0\phi} \tag{7.401}$$

In Figure 7.79 the typical frequency dependencies of $\Delta\chi$, $\Delta\varepsilon'$, and $\Delta\varepsilon''$ in the kilohertz range are schematically represented (a number of real experimental plots are given in the books by Dukhin and Shilov [835] and Russel et al. [368]). As shown in the figure, the value of ε'' goes through a maximum, which corresponds to a maximal dissipation of energy in the suspension. The values of χ and ε' are, respectively, monotonously decreasing and increasing with the frequency. In general, the experiments show that the magnitude of $\Delta\varepsilon'$ increases with the values of κR and the ζ potential. The magnitude of $\Delta\chi$ also increases with the ζ potential but decreases with κR. The magnitude of $\Delta\varepsilon''$ increases with the ζ potential. In dilute dispersions, none of the three quantities depend on the particle concentration in the framework of the experimental accuracy, as would be expected. The theory of the dielectric response in this low-frequency range was mostly developed by Dukhin and his colleagues [835], and analytical formulas are available for thin electrical double layers [835] or low surface potential [830].

During the last decade the dielectric response of dispersions in the megahertz range was extensively studied. O'Brien [918] presented the complex conductivity of a dilute dispersion in the form (see Equation 7.392):

$$\chi^* = (\chi_b + i\omega\varepsilon_0\varepsilon_b)\frac{(1 - 2\Omega\phi)}{(1 + \Omega\phi)} \tag{7.402}$$
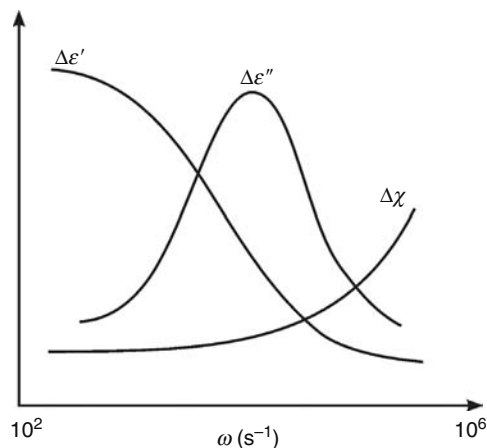

FIGURE 7.79 Schematic presentation of the electric conductivity, $\Delta\chi$, the real part, $\Delta\varepsilon'$, and the imaginary part, $\Delta\varepsilon''$, of the dielectric permittivity increments of dispersion as functions of the frequency of the electric field, ω. For definitions of $\Delta\chi$, $\Delta\varepsilon'$, and $\Delta\varepsilon''$, see Equation 7.401.

where the complex function $\Omega(\chi_b, \chi_s, \varepsilon_b, \varepsilon_p, \omega)$ is given by the expression:

$$\Omega \equiv \frac{\chi_b - 2\chi_s/R + i\omega\varepsilon_0(\varepsilon_b - \varepsilon_p)}{2(\chi_b + \chi_s/R) + i\omega\varepsilon_0(2\varepsilon_b + \varepsilon_p)} \tag{7.403}$$

Here, ε_p is the relative dielectric permittivity of the particle substance. As shown by O'Brien [918], at high frequency ($\omega \gg D\kappa^2 \sim \chi_b/\varepsilon_0\varepsilon_b$), Equation 7.403 reduces to the result for uncharged particles, $\Omega = (\varepsilon_b - \varepsilon_p)/(2\varepsilon_b + \varepsilon_p)$. At low frequency ($\omega \ll \chi_b/\varepsilon_0\varepsilon_b$), Equation 7.403 coincides with the high-frequency limit of the formula derived by Hinch et al. [920]:

$$\Omega = \frac{1}{2} - \frac{3}{2}\beta/[2 + \beta(1 + \delta)] \tag{7.404}$$

where

$$\beta = \frac{2}{\kappa R}\left(1 + 3\frac{m}{Z^2}\right)\exp\left(\frac{eZ\zeta}{2kT}\right) \tag{7.405}$$

$$\delta = \left[1 + \left(i\omega R^2/D_{SI}\right)^{1/2}\right] \Big/ \left[1 + \left(i\omega R^2/D_{SI}\right)^{1/2} + \frac{1}{2}i\omega R^2/D_{SI}\right] \tag{7.406}$$

The high-frequency limit of Equation 7.404 is $\Omega = (1 - \beta)/(2 + \beta)$ which, as stated above, is identical to the low-frequency limit of Equation 7.403 because $\chi_s/\chi_b R = \beta/2$ [918]. One can conclude that the combination of Equations 7.402 through 7.404 covers the whole range of frequencies that are of interest [918].

This approach was further extended by O'Brien [918] to include the cases of concentrated dispersion of randomly packed spheres and porous plugs. A comparison with experimental data on Pyrex plugs revealed very good agreement in the frequency range from 10^3 to 10^7 s^{-1}. Midmore et al. [921] measured the dielectric response of concentrated latex suspensions (ϕ was varied between 0.1 and 0.5) in the range between 1 and 10 MHz and also found that the data can be well reproduced by the cell type of theoretical model. However, the estimated ζ potential from the conductivity measurements was considerably larger than the value determined by electrophoretic measurement (this issue will be discussed in the following section). Equipment and procedures for performing calibration and measurement of the dielectric response of dispersions are described in Refs. [921–923]. A large set of numerical results for various values of the particle ζ potential and the ionic strength of the disperse medium were presented by Grosse et al. [924].

We will now briefly describe the technique of colloid vibration potential (CVP) for determination of the particle ζ potential. In this type of experiment, an ultrasonic wave is introduced into the suspension, thus leading to oscillatory motion of the particles. Due to the difference in the mass densities of the particles and the surrounding fluid, the ion cloud does not follow the particle motion (similar to the case of particle sedimentation), and spatial separation of the positive and negative charges appears. The corresponding electrical potential is called the CVP and can be measured by two probe electrodes separated by distance $\lambda/2$ in the direction of the ultrasound propagation (λ is the sound wavelength). The theory for diluted suspensions was developed by Enderby [925] and Booth [926] and further extended to concentrated systems by Marlow et al. [927]. The connection between the CVP, E_{CVP}, and the particle ζ potential is [927,928]

$$E_{CVP} = \frac{2P_0\phi}{\chi_b}\frac{(d_p - d_b)}{d_b}\frac{\varepsilon_b\varepsilon_0}{\eta}\zeta f_2(\kappa R, \phi) \tag{7.407}$$

where
  P_0 is the amplitude of the sound pressure
  d_p and d_b are the mass densities of the particles and medium, respectively

The function $f_2(\kappa R, \phi)$ accounts for the particle–particle interactions; for diluted systems, $f_2(\kappa R, \phi \to 0) = 1$, and for thin EDL $f_2(\kappa R \gg 1, \phi) = (1 - \phi)$.

The experiments performed by several research groups [927–929] showed good agreement of theoretical predictions with the experimental data. This is rather encouraging and a little surprising result, keeping in mind that the experiments with simple electrolytes (where a similar effect called "ionic vibration potential" is existing [930]) produced data which are often not well explained [929] by the corresponding theory [930]. The CVP technique can be applied to concentrated dispersions.

O'Brien [931] showed that the CVP is related through the Onzager relations to the so-called electrokinetic sonic amplitude (ESA). The latter appears when an alternating electric field is applied to a suspension of charged particles. The ensuing oscillatory motion of the particles creates a macroscopic acoustic wave, whose amplitude and phase lag can be experimentally

measured and used for characterization of the dispersed particles. The method allows one to determine the size and ζ potential of the particles in a concentrated dispersion without need of dilution [932–938]. In general, the problem consists of two stages: first, the dynamic electrophoretic mobility is determined from the CVP or ESA data, and second, the particle ζ potential is calculated from the dynamic mobility by using various theoretical models. The effect of surface conductivity on the analysis of the ESA and CVP data was recently considered by Dukhin et al. [937] and Löbbus et al. [938]. The CVP and ESA are often termed electroacoustic phenomena in the literature.

7.8.8 ANOMALOUS SURFACE CONDUCTANCE AND DATA INTERPRETATION

Theoretical interpretation of the measured electrokinetic quantities is always based on a number of explicit and implicit assumptions. Since the meaning of the obtained data depends on the adequacy of the theory used for their interpretation, the underlying assumptions are often questioned and discussed in the literature [825,827,836,939]. In this section, we briefly discuss the current evaluation of the importance of some effects that are not taken into account in the conventional theory.

All the consideration up to now implies that the dielectric permittivity and the viscosity in the electrical double layer (at least for $x \geq x_s$; see Figure 7.77) are equal to those of the bulk disperse medium. A more refined approach [913,939] shows that for thin double layers the formulas, stemming from the Smoluchowski theory, may remain unaltered if the real ζ potential ($\zeta = \psi(x_s)$) is replaced by the quantity [913]:

$$\zeta_{obs} = \frac{\eta_b}{\varepsilon_b} \int\limits_0^\infty \frac{\varepsilon(x)}{\eta(x)} \frac{d\psi}{dx} dx = \frac{\eta_b}{\varepsilon_b} \int\limits_0^\zeta \frac{\varepsilon(\psi)}{\eta(\psi)} d\psi \tag{7.408}$$

where

$\varepsilon(x)$ and $\eta(x)$ account for the local variations of the dielectric constant and viscosity in the double layer
ε_b and η_b are the respective values in the bulk medium

Hunter [939] analyzed a number of theoretical and experimental results and concluded that this effect is small under most conditions. Recently, Chan and Horn [940] and Israelachvili [941] performed dynamic experiments using the surface force apparatus and showed that the water viscosity is practically constant down to distances one to two molecular diameters from a smooth mica surface. Their experiments also demonstrated that the shear plane at a smooth surface is shifted no more than 1–2 molecular layers apart from the surface. Therefore, one may expect that for smooth surfaces the ζ potential should be very close to the surface potential, ψ_s, at least for not-too-high electrolyte concentrations and surface potentials.

The case of a rough solid surface is much more complicated [827,913], because the surface roughness affects not only the position of the shear plane, but also the surface charge density distribution and the surface conductivity. Therefore, a general approach to rough surfaces is missing and one should choose between several simple models (see below) to mimic as close as possible the real surface.

Another very important issue in this respect is the way to account for the surface conductivity. The formula of Bickerman [847] (Equation 7.370), the correction factor to the electrophoretic mobility of Henry [858] (Equation 7.379), and the formula of O'Brien and Hunter [864] (Equation 7.382) quoted above are derived under the assumption that only the ions in the movable part ($x \geq x_s$; Figure 7.77) of the EDL contribute to the surface conductivity, χ_s. Moreover, the ions in the EDL are taken to have the same mobility as that in the bulk electrolyte solution. A variety of experimental data [827,835,913,942–947] suggests, however, that the ions behind the shear plane ($x < x_s$) and even those adsorbed in the Stern layer may contribute to χ_s. The term "anomalous surface conductance" was coined for this phenomenon. Such an effect can be taken into account theoretically, but new parameters (such as the ion mobility in the Stern layer) must be included in the consideration. Hence, the interpretation of data by these more complex models usually requires the application of two or more electrokinetic techniques which provide complementary information [923,948]. Dukhin and van de Ven [948] specify three major (and relatively simple) types of models as being most suitable for data interpretation. These models differ in the way they consider the surface conductivity and the connection between ψ_s and ζ:

- Model 1 ($\zeta = \psi_s$ and $\chi_s = \chi_s^{EDL}$): This is the simplest possible model accounting for the surface conductivity, because it assumes that an immobile part of the diffuse layer is absent. As a result, $x_s = 0$, $\zeta = \psi_s$, and χ_s is due only to ions in the diffuse layer.
- Model 2 ($\zeta \neq \psi_s$, $\chi_s = \chi_s^{EDL}$): In this model two parts of the diffuse layer (hydrodynamically mobile and immobile, respectively) are distinguished. The surface conductivity is taken to include contributions from the ions in the whole diffuse layer, including the hydrodynamically immobile part. The mobility of the ions in the diffuse layer is considered to be the same as that in the bulk, while the mobility of the ions in the Stern layer is set equal to zero. The Gouy–Chapman theory (Equation 7.354) is used to connect the values of ζ and ψ_s. Therefore, the value of x_s is an important

parameter in this model. According to Dukhin and van de Ven [948], this model is most suitable for particles with a rough surface or for a surface covered with a layer of nonionic surfactants or polymers [942,943,945].

- Model 3 ($\zeta = \psi_s, \chi_s = \chi_s^{EDL} + \chi_s^{Stern}$): As in model 1, it is assumed that the whole diffuse part of the EDL is hydrodynamically mobile. In addition, the ions in the Stern layer are allowed to move in external electrical field and to contribute to χ_s. This model seems to be appropriate for the description of electrophoresis of biological cells (if glycocalix on the cell surface is not present) and particles covered by ionic surfactants [944].

Theoretical descriptions of the electrokinetic phenomena in the framework of these three models were developed in the literature and reviewed by Dukhin and van de Ven [948]. The effect of particle polydispersity on the data interpretation by the different models was analyzed in the same study [948].

The interest in anomalous surface conductance has been high during the last several years [915,937,938,942–953] due to the finding that most of the studied latex samples have showed electrokinetic properties that cannot be described by conventional theory. In particular, the electric potential determined by electrophoresis was substantially lower than that measured in dielectric studies [915,921,943–946]. Also, the electrophoretic ζ potential, calculated from the conventional theory, showed a maximum as a function of the electrolyte concentration, while one should expect a gradual decrease [923,949]. Several hypotheses [945,946] were discussed in the literature to explain this discrepancy, most of them being connected with the anomalous surface conductance of the latex particles. According to the hairy model [946,947], the particle surface is covered by a layer of flexible polymer chains, which are extended into the solution at a distance, which depends on the electrolyte concentration. Since the position of the shear plane, x_s, is to be close to the outer boundary of this polymer layer, the thickness of the immobile hydrodynamic layer (and the corresponding anomalous surface conductance created by the ions in the immobile layer) appears to be strongly dependent on the ionic strength. This hypothesis found some experimental confirmation in experiments [947] with latex particles, preheated for a certain period of time at a temperature above the glass transition temperature of the polymer. As shown by Rosen and Saville [947], the electrokinetic properties of the preheated latexes become much closer to those expected from the classical theory. On the other hand, Shubin et al. [923] made systematic measurements to distinguish which type of ions are responsible for the anomalous conductance of the latex particles, those in the diffuse part or those in the Stern layer. The authors [923] concluded that their data can be interpreted only by assuming ion transport in the Stern layer. Recent theoretical analysis of Saville [953] showed that the presence of a thin permeable (hairy) polymer layer on the surface of colloid particles indeed has an important effect on their electrophoretic mobility, while the suspension conductivity might be very slightly affected.

Experiments [950–952] made in different laboratories suggest that the importance of the discussed effect depends strongly on the type of used particles. Gittings and Saville [951] and Russell et al. [950] found out latex samples (commercial and laboratory-made ones) for which the electrokinetic properties can be well described by the classical theory, without need to invoke the anomalous surface conductance. These observations were complemented by the results of Bastos-Gonzalez et al. [952] who performed heat treatment of polystyrene latexes with different surface groups. The experiments by several methods showed [952] that the surface of the sulfate and aldehyde latexes changed upon heating, while the sulfonate and carboxyl latexes did not show a detectable change of their properties. Better understanding of the electrokinetic properties of latex particles is of significant importance, because the latexes are widely used [368,837] as model systems for quantitative investigation of a variety of colloidal phenomena, and their reliable characterization is needed for these tasks.

7.8.9 ELECTROKINETIC PROPERTIES OF AIR–WATER AND OIL–WATER INTERFACES

The experimental methods based on electrokinetic phenomena (and especially electrophoresis) have found very widespread application for routine characterization of electrical surface properties of solid particles, liquid droplets, porous media, synthetic membranes, etc. A systematic presentation of the main results obtained on different types of systems is given in Chapters 6 through 8 of Ref. [836], and in Chapters 8 through 33 of Ref. [838]. A glance at the books [368,835–838] and review articles [824–834] in the field, however, shows that the properties of air–water and oil–water interfaces are either not considered at all or only briefly mentioned. This fact is surprising, as a number of studies [954–963] (the first of them being performed more than 70 years ago) have convincingly demonstrated a substantial negative ζ potential at bare (without any surfactant) air–water and oil–water interfaces. This spontaneous charging cannot be explained in a trivial way—it requires the specific preferential adsorption of some kind of ion, because from a purely electrostatic viewpoint the approach of an ion to the interface of water and a nonpolar fluid is unfavorable because of the image forces [34]. Measurements of the electrophoretic mobility of air bubbles and oil droplets demonstrated a strong pH dependence of their ζ potential: it is almost zero at a pH of around 3 and goes down to -120 mV at a pH $\sim$11. Therefore, two main hypotheses, connected with the dissociation–association equilibrium of water ($H_2O = H^+ + OH^-$) were suggested in the literature to explain the phenomenon: (1) specific adsorption of HO^- ions in the boundary layer of water molecules, and (2) negative adsorption, i.e., depletion of H^+ ions in the boundary layer.

Marinova et al. [962] performed a series of systematic measurements of the electrophoretic mobility of O/W emulsion droplets to check these (and some other) possible hypotheses. Analyzis of the obtained results leads to the conclusion that the

charges originate from hydroxyl ions, which specifically adsorb at the oil–water interface. The pH dependence of the surface charge was interpreted by using Stern's adsorption isotherm, yielding the value of $\sim25\ kT$ for the specific adsorption energy per HO$^-$ ion. Although some speculations about the underlying mechanism were presented [961,962] the molecular picture behind this value is rather obscured. One may expect that the computer methods for studying the molecular structuring and dynamics at interfaces (including hydrogen-bond effects) will be very helpful in revealing the physical origin of the surface charge. Dunstan and Saville [961] suggested the idea that the specific adsorption of ions, responsible for the charging of hydrophobic surfaces, may be connected with the anomalous electrokinetic behavior of latex particles, as discussed in the previous Section 7.8.8.

The air–water and oil–water interfaces, covered with adsorption layers of nonionic surfactants, are also negatively charged at neutral pH, which has an important impact on the stability of foams and emulsions [579,955,962,964–966]. Again, a strong pH dependence of the ζ potential is established: the higher the pH, the larger in magnitude the ζ potential. The effect of the adsorbing nonionic surfactants on the magnitudes of the surface potential of air–water interfaces was analyzed in detail in Ref. [966]. The electrokinetic properties of fluid interfaces in the presence of cationic or anionic surfactants are more understandable (at least qualitatively): the interfaces are positively or negatively charged, respectively. In the presence of an adsorbed protein layer, the interfacial electric potential is usually close to that of the protein molecules at the pH of the disperse medium. In this way, the surface charge may change from negative to positive around the isoelectric point of the protein.

7.9 OPTICAL PROPERTIES OF DISPERSIONS AND MICELLAR SOLUTIONS

The light scattering methods for studying colloidal systems can be classified in two wide groups: SLS and DLS. The latter is often called quasi-elastic light scattering (QELS) or photon correlation spectroscopy (PCS). In SLS methods, the averaged-over-time intensity of the scattered light is measured as a function of the particle concentration and scattering angle. In DLS methods, the time fluctuations of the scattered light are measured. The light scattering methods possess a number of advantages, which make them particularly suitable for investigation of colloid systems. In general, these methods are noninvasive; applicable to very small and unstable (when dried) particles, such as surfactant micelles and lipid vesicles; suitable for characterization of particle size and shape, as well as of interparticle interactions; and relatively fast, and not requiring very expensive equipment. The theoretical basis of light scattering methods is outlined in Sections 7.9.1 and 7.9.2. The main applications of the methods to surfactant solutions and colloidal dispersions are summarized in Section 7.9.3.

7.9.1 STATIC LIGHT SCATTERING

A comprehensive presentation of the SLS theory can be found in the monographs by Van de Hulst [967] and Kerker [968]. The basic concepts are discussed in the textbooks by Hiemenz and Rajagopalan [969], and Lyklema [970]; a collection of the classical papers on this topic is reprinted in Ref. [971].

7.9.1.1 Rayleigh Scattering

The scattering of light from colloidal particles of dimensions much smaller than the light wavelength (e.g., surfactant micelles) can be analyzed in the framework of the Rayleigh theory [972], which was originally developed for light scattering from gases. A beam of monochromatic, polarized light can be described by the amplitude of its electrical vector (see Figure 7.80).

$$E = E_0 \cos 2\pi \left(\nu t - \frac{x}{\lambda} \right) \tag{7.409}$$

where

    x is the coordinate in direction of the incident beam
    t is the time
    ν and λ are the frequency and the wavelength of the light, respectively

The light induces a variable dipole in the particle:

$$p = \alpha E = \alpha E_0 \cos 2\pi \left(\nu t - \frac{x}{\lambda} \right) \tag{7.410}$$

where α is the excess particle polarizability (i.e., the difference between the polarizability of the particle and the polarizability of the same volume of the medium). The induced dipole creates an electromagnetic field of the same frequency (scattered light) with an intensity (energy flux per unit area perpendicular to the scattered beam) averaged over time of [969]:
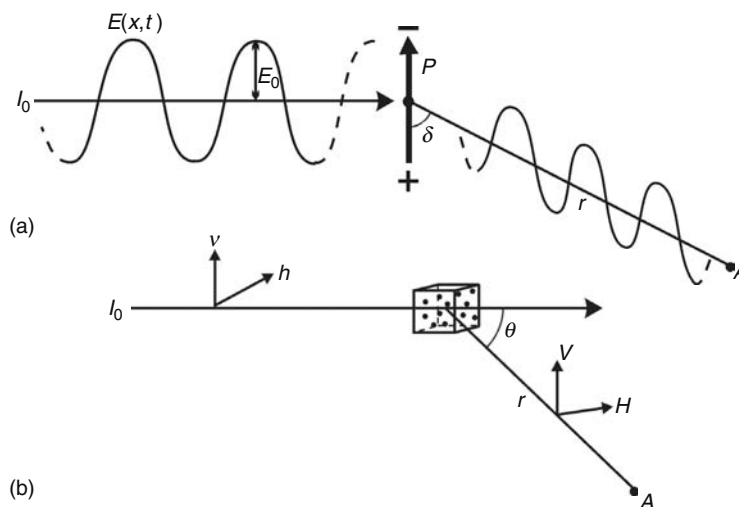
FIGURE 7.80 Geometry of the light scattering experiment. (a) Plane polarized monochromatic beam of intensity I_0 induces the variable dipole, p, which emits an electromagnetic wave (scattered light); the detector is at point A. (b) The incident beam can be vertically polarized, horizontally polarized or nonpolarized with respect to the scattering plane. Angle δ is formed between the directions of the dipole and the scattered beam, while the angle θ is between the directions of the incident and scattered beams. The axes (v,h) and (V,H) denote the vertical and horizontal directions for the incident and scattered beam, respectively.

$$\langle I_s \rangle_t = \frac{16\pi^4}{\lambda_0^4 r^2} \left(\frac{\alpha}{4\pi\varepsilon_0} \right)^2 \langle I_0 \rangle_t \sin^2 \delta, \quad \langle I_0 \rangle_t = \frac{c\varepsilon_0}{2} E_0^2 \approx 1.328 \times 10^{-3} E_0^2 \text{ W/m}^2 \tag{7.411}$$

where

Brackets $\langle\ \rangle$ denote time averaging
δ is the angle between the direction of the induced dipole and the direction of the scattered beam
$\langle I_0 \rangle_t$ is the intensity of the incident beam
λ_0 is the light wavelength in vacuo
r is the distance between the scattering dipole and the detector
c is the speed of light
ε_0 is the dielectric permittivity of the vacuo

For vertically polarized light, $\delta = \pi/2$, while for horizontally polarized light $\delta = (\pi/2 - \theta)$; θ is the scattering angle (see Figure 7.80). Nonpolarized light can be formally considered as the superposition of one vertically polarized and one horizontally polarized beam of equal intensity. In the Rayleigh theory [972], the scatterers are considered to be independent from each other, and the total intensity of the scattered light from a suspension of number concentration ρ is proportional to the number of particles observed by the detector, N ($N = \rho V_S$; V_S is the scattering volume). To characterize the light scattering with a quantity independent of the geometry of the equipment, one usually considers the reduced intensity of the scattered light called Rayleigh ratio:

$$R(\theta) \equiv \frac{\langle I_s \rangle_t}{\langle I_0 \rangle_t} \frac{r^2}{V_S} = \frac{16\pi^4}{\lambda_0^4} \left(\frac{\alpha}{4\pi\varepsilon_0} \right)^2 \rho P(\theta) \tag{7.412}$$

where the factor $P(\theta)$ depends on the polarization of the incident beam. In the case of small particles (of dimensions much smaller than λ):

$$P_v(\theta) = 1, \quad P_h(\theta) = \cos^2 \theta, \quad P_u(\theta) = \frac{1}{2}(1 + \cos^2 \theta) \tag{7.413}$$

where the subscripts v, h, and u denote vertically polarized, horizontally polarized, or nonpolarized incident beam, respectively. In the more general case, $P(\theta)$ also depends on the size and shape of the scattering particles (see below); hence, it is sometimes called scattering form factor of the particles. By using the continuum theory of dielectric polarization, one can express the excess polarizability of a spherical particle of radius R and refractive index n_p which is immersed in a medium of refractive index, n_m, by means of the Lorenz–Lorentz equation [34]:

$$\frac{\alpha}{4\pi\varepsilon_0} = n_m^2 \left(\frac{n_p^2 - n_m^2}{n_p^2 + 2n_m^2}\right) R^3 \tag{7.414}$$

Since in many cases n_p and R are not known and the particles may have a nonspherical shape, another way for deducing the excess particle polarizability is used: α is expressed through the change of the refractive index of the suspension, n, with the particle concentration [973]:

$$\alpha = \frac{\varepsilon_0(n^2 - n_m^2)}{\rho} \approx 2\varepsilon_0 n_m \left(\frac{dn}{d\rho}\right) = 2\varepsilon_0 n_m \frac{M}{N_A} \left(\frac{dn}{dc}\right) \tag{7.415}$$

where
  M is the mass of a particle
  c is the particle mass concentration ($c = \rho M/N_A$ and N_A is the Avogadro number)
  (dn/dc) is a quantity that presents the refractive index gradient of the suspension and is measured by refractometer of high sensitivity

Combining Equations 7.412 and 7.415, one can derive the following expression for the Rayleigh ratio of a suspension of independent scatterers:

$$R_j(\theta) \equiv cKMP_j(\theta), \quad K \equiv \frac{4\pi^2 n_0^2}{\lambda_0^4 N_A}\left(\frac{dn}{dc}\right)^2 \quad \text{and} \quad j = v, h, u \tag{7.416}$$

which (in principle) allows one to determine the particle mass, M, from the intensity of the scattered light. Equation 7.416 has several important limitations: (1) the particle dimensions must be much smaller compared to the light wavelength, (2) the particle concentration must be very low to avoid the interparticle interactions and the interference of light beams scattered by different particles, and (3) the particles do not absorb light (the suspension is colorless).

7.9.1.2 Rayleigh–Debye–Gans (RDG) Theory

The radiation of a particle, comparable in size to the light wavelength, leads to induction of dipoles in different parts of the particle that are not in phase (Figure 7.81). The net scattered light, received by the detector, is a result of the interference of the beams scattered from the different points of the particle. In this case, the function $P(\theta)$ depends on the particle size and shape. If the particles have an anisodiametrical shape, $P(\theta)$ could depend on their orientation as well. Typical examples are rod-like particles that are preferentially oriented along a given direction by electric [974–976] or hydrodynamic field. In most systems, however, the particles are randomly oriented, and averaging over all possible orientations is performed to calculate $P(\theta)$.

A rather general approach for determination of the function $P(\theta)$ was proposed by Rayleigh [977] and further developed by Debye [978] and Gans [979]. The main assumption in the RDG theory is that the incident beam that excites the electrical dipoles in the particle is not influenced (in neither magnitude nor phase) by the presence of the particle. This requirement is
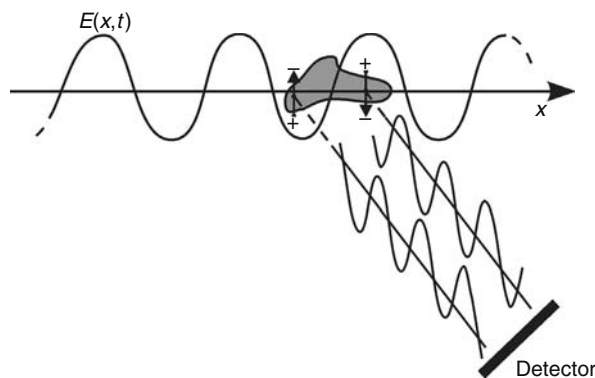
FIGURE 7.81 The RDG [977–979] theory is based on the assumptions that: (1) the incident beam propagates without being affected by the particles, and (2) the scattered light, received by the detector, is a superposition of the beams emitted from the induced dipoles in the different parts of the particle.

better satisfied by smaller particles having a refractive index close to that of the disperse medium. The respective quantitative criterion reads:

$$\frac{4\pi l}{\lambda}|n_p - n_m| \ll 1 \qquad (7.417)$$

where l is a length of the order of the size of the particle (l coincides with the radius for spheres). For such soft scatterers, the phase difference of the waves created by the induced dipoles in different parts of the particle (considered to be independent in the RDG theory) can be calculated by geometrical consideration.

Since the scattered waves propagating in a forward direction, $\theta = 0°$, are all in phase (positive interference), the intensity of the scattered light is maximal in this direction and $P(0) = 1$. Comparison with Equation 7.416 shows that $R(0) = cKM$; hence, one can define:

$$P_j(\theta) \equiv R_j(\theta)/R(0), \quad j = \mathrm{v}, \mathrm{h}, \mathrm{u} \qquad (7.418)$$

The general expression for the scattering form factor of randomly oriented particles and vertically polarized light reads [978]:

$$P_\mathrm{v}(\theta) = \frac{1}{N^2} \sum_{i=1}^{N} \sum_{j=1}^{N} \frac{\sin(q\, r_{ij})}{q\, r_{ij}} \qquad (7.419)$$

where
$q = \frac{4\pi n}{\lambda_0} \sin(\theta/2)$ is the magnitude of the scattering vector
r_{ij} is the distance between the ith and jth scattering subunit

The double sum is taken over all subunits of total number N. The particle scattering factor was calculated for typical particle shapes (see Table 7.10 on p. 334, as well as Table 8.5 in Ref. [968]).

Once $P_\mathrm{v}(\theta)$ is known, one can calculate $P_\mathrm{h}(\theta)$ and $P_\mathrm{u}(\theta)$ through the relationships (see Equation 7.413):

$$P_\mathrm{h}(\theta) = P_\mathrm{v}(\theta)\cos^2\theta, \quad P_\mathrm{u}(\theta) = \frac{1}{2}P_\mathrm{v}(\theta)(1 + \cos^2\theta) \qquad (7.420)$$

The expansion in series of $\sin(q r_{ij})$ in the right-hand side of Equation 7.419 leads to a fairly simple and general result [980]:

$$\lim_{\theta\to 0} P_\mathrm{v}(\theta) \approx 1 - \left[\frac{q^2}{3!N^2}\right] \sum_{i=1}^{N} \sum_{j=1}^{N} r_{ij}^2 = 1 - \frac{q^2\langle R_\mathrm{g}^2\rangle}{3} \qquad (7.421)$$

where $\langle R_\mathrm{g}^2\rangle^{1/2}$ is the radius of gyration for a particle that is arbitrary in shape and size. This result shows that the initial part of the function $P(\theta)$, corresponding to small scattering angles, enables one to determine the radius of gyration, no matter what the particle shape is. For that purpose, the experimentally measured intensity of the scattered light is represented in the form (see Equation 7.416):

$$\frac{Kc}{R_\mathrm{v}(\theta)} = [MP_\mathrm{v}(\theta)]^{-1} = \frac{1}{M}\left[1 + \frac{16}{3}\frac{\pi^2}{\lambda^2}\langle R_\mathrm{g}^2\rangle \sin^2(\theta/2) + O(q^4)\right] \qquad (7.422)$$

and $Kc/R_\mathrm{v}(\theta)$ is plotted versus $\sin^2(\theta/2)$. For a nonpolarized or horizontally polarized primary beam, $R_\mathrm{v}(\theta)$ in the left-hand side of Equation 7.422 is to be replaced by $2R_\mathrm{u}(\theta)/(1 + \cos^2\theta)$ or $R_\mathrm{h}(\theta)/\cos^2\theta$, respectively.

The radii of gyration for a sphere of radius R_s, for a thin rod-like particle of length L, for a Gaussian coil containing N segments of length l, and for a thin disk of radius R_d are given by [967,969,981]:

$$\langle R_\mathrm{g}^2\rangle = \frac{3}{5}R_\mathrm{s}^2 \quad \text{(sphere)} \qquad (7.423a)$$

$$\langle R_\mathrm{g}^2\rangle = \frac{1}{12}L^2 \quad \text{(rod like particle)} \qquad (7.423b)$$

$$\langle R_\mathrm{g}^2\rangle = \frac{1}{6}Nl^2 \quad \text{(Gaussian coil)} \qquad (7.423c)$$

$$\langle R_\mathrm{g}^2\rangle = \frac{1}{2}R_\mathrm{d}^2 \quad \text{(thin disk)} \qquad (7.423d)$$

TABLE 7.10

Scattering Function, $P_v(Q)$, Single Particle Translational Diffusion Coefficient, D_0, and Single Particle Rotational Diffusion Coefficient, Θ, for Particles of Different Shapes

Shape of particle	$P_v(q)$, D_0, Θ	References
Homogeneous sphere of radius R	$P_v(q) = \left[\dfrac{3}{\tilde{R}^3}(\sin\tilde{R} - \tilde{R}\cos\tilde{R})\right]$ $D_0 = \dfrac{kT}{6\pi\eta R}; \;\; \Theta = \dfrac{kT}{8\pi\eta R^3}$	[977]
Ellipsoid with semi-axes (R, R, pR)	$P_v(q) = \displaystyle\int_0^{\pi/2}\left[\dfrac{3}{\tilde{R}^3}(\sin\tilde{R} - \tilde{R}\cos\tilde{R})\right]^2 \left(\tilde{R}\sqrt{\cos^2\theta + p^2\sin^2\theta}\right)\cos\theta\,d\theta$ $D_0 = \dfrac{kT}{6\pi\eta R}\left[\dfrac{3}{4}p\beta + \dfrac{1}{8}p\alpha_{\mathrm{II}} + \dfrac{1}{4}\dfrac{\alpha_{\mathrm{I}}}{p}\right]$ $\Theta = \dfrac{3kT}{16\pi p R^3\eta}\dfrac{(p^2\alpha_{\mathrm{II}} + \alpha_{\mathrm{I}})}{(p^2 + 1)}$ $\alpha_{\mathrm{II}} = \dfrac{2(p^2\beta - 1)}{p^2 - 1}; \;\; \alpha_{\mathrm{I}} = \dfrac{p^2(1 - \beta)}{p^2 - 1}$ $\beta = \dfrac{\cosh^{-1}p}{p(p^2 - 1)^{1/2}}$ For $p > 1$ (prolate ellipsoid) $\beta = \dfrac{\cos^{-1}p}{p(1 - p^2)^{1/2}}$ For $p < 1$ (oblate ellipsoid)	[980] [982] [983] see also [984]
Thin rod-like particle of length L and diameter d	$P_v(q) = \dfrac{2}{qL}\displaystyle\int_0^{qL}\dfrac{\sin u}{u}du - \left[\dfrac{2\sin(qL/2)}{qL}\right]^2$ $D_0 = \dfrac{kT}{3\pi\eta L}\ln(L/d);$ $\Theta = \dfrac{3kT}{\pi\eta L^3}[\ln(2L/d) - 0.5]$	[985] see also [986,987] [983] see also [984,988,989]
Thin disc of radius R	$P_v(q) = \dfrac{2}{\tilde{R}^2}\left[1 - \dfrac{J_1(2\tilde{R})}{\tilde{R}}\right]$ $D_0 = \dfrac{kT}{12\eta R}; \;\; \Theta = \dfrac{3kT}{32\eta R^3}$	[990,991] [983]
Gaussian coil of contour length L and persistent length, l_p. If the coil is considered to contain N segments of length l, then $L = Nl$ and $l = 2l_p$	$P_v(q) = \dfrac{2}{z^2}[\exp(-z) + z - 1]; \;\; z = q^2\langle R_g^2\rangle$ $\langle R_g^2\rangle = \dfrac{1}{3}Ll_p = \dfrac{1}{6}Nl^2$ $D = \dfrac{kT}{3\pi\eta L}[1.303(L/l_p)^{1/2}], \;\; \Theta = \dfrac{kT}{1.013\eta L^3}(L/l_p)^{3/2}$	[992] [993]

Note: $\tilde{R} \equiv qR$

where

$q = 4\pi n\lambda_0^{-1}\sin(\theta/2)$ is the magnitude of the scattering vector

η is the shear viscosity of the medium and kT is thermal energy

$J_1(x)$ is the Bessel function of the first kind

The radius of gyration for a wormlike chain of length L, persistent length l_p, and diameter d was found to be [981]

$$\langle R_g^2\rangle = L^2\left\{\frac{1}{3}\tilde{l}_p - \tilde{l}_p^2 + 2\tilde{l}_p^4\left[\tilde{l}_p^{-1} - 1 + \exp\left(-\tilde{l}_p^{-1}\right)\right]\right\} + \frac{d^2}{8} \text{ (wormlike chain)} \tag{7.424}$$

where $\tilde{l}_p = l_p/L$. For a random coil ($\tilde{l}_p \ll 1$, $l_p = l/2$, $L = Nl$, and $d \ll L$), Equation 7.424 reduces to Equation 7.423c. In the other limiting case of $\tilde{l}_p \gg 1$, Equation 7.424 reduces to the result for a cylinder of length L and diameter d:

$$\langle R_g^2\rangle = \frac{1}{12}L^2 + \frac{1}{8}d^2 \quad \text{(cylinder)} \tag{7.425}$$

This consideration can be further generalized to account for the interaction between the particles (see Section 7.9.1.4).

7.9.1.3 Theory of Mie

If the condition in Equation 7.417 is violated, the RDG theory is not valid. A solution of the scattering problem for particles arbitrary in size has been found only for several particular shapes. Mie [994] succeeded in finding a complete general solution of the Maxwell equations for a sphere in a periodic electromagnetic field. The refractive indexes of the sphere, n_p, and of the medium, n_m, are considered to be complex numbers (i.e., the theory is applicable to light-absorbing substances, including metals):

$$n_j^2(\omega) = \varepsilon_j(\omega) - i\frac{4\pi\chi_j(\omega)}{\omega} \quad \text{or} \quad n_j(\omega) = \widetilde{n}_j(\omega) - ik_j(\omega); \quad j = \text{p or m} \tag{7.426}$$

Here, $\varepsilon_j(\omega)$ and $\chi_j(\omega)$ are the dielectric permittivity and the electrical conductivity, respectively, for a given circular frequency, ω, of the field, while $\widetilde{n}_j$ and k_j are the real and the imaginary parts, respectively, of the refractive index.

As shown by Mie [994] and Debye [995], the electromagnetic field of the light scattered by a sphere can be presented as an infinite series over associated Legendre polynomials, $P_n^1(\cos\theta)$, multiplied by spherical Bessel functions, $h_n^{(2)}(2\pi r/\lambda)$. The coefficients in this series must be determined from the boundary conditions and afterward can be used to calculate the angular dependence of the amplitude and polarization of the scattered field. Different boundary conditions were imposed in the case of conducting or dielectric materials of the sphere and of the medium.

The numerical calculation of the complete problem presents a formidable task, and a number of practical recommendations for appropriate simplifications are given in the specialized literature [967–969]. Typically, the final result of such calculations is presented in terms of the efficiency factors for absorption and scattering, Q_{abs} and Q_{sca}. The magnitudes of Q_{abs} and Q_{sca} depend on λ, $\tilde{n}$, k, θ, and the particle size. For nonabsorbing particles ($k_p = 0$), $Q_{abs} = 0$; for nonscattering particles ($\widetilde{n}_p = \widetilde{n}_m$), $Q_{sca} = 0$. The efficiency factors can be directly related to the absorbance and turbidity of the suspension (see Section 7.9.1.7). A similar approach was used to investigate the scattering from coated spheres; long circular, elliptic, and parabolic cylinders; flat disks; spheroids; and others [967,968,996].

The theory of Mie [994] is used also in the laser diffraction method for particle size analysis [997]. In this method, the light scattered by the particles is collected over a range of angles (usually between 1° and 20°) in the forward direction. The corresponding experimental setup is usually referred to as Fourier optics. The method is applied to relatively large particles (typically between 0.3 and 600 μm) when the scattered light in a forward direction (projected on a screen) presents a combination of concentric fringes. The angular intensity distribution of the scattered light is analyzed to deduce the particle size distribution. For particles of diameter above several micrometers, the diffraction pattern is usually interpreted by simpler approximate theories, like that of the Fraunhofer diffraction [997].

7.9.1.4 Interacting Particles

7.9.1.4.1 Fluctuation Theory of SLS

All discussion up to here has been based on the assumption that the scatterers are independent; however, in most of cases this assumption is not justified. A general approach for calculating $R(\theta)$ for a suspension of small interacting particles was proposed by Einstein [998]. He related the fluctuations in the polarizability of suspension with the fluctuations of the particle concentration. The final result reads:

$$R_j(\theta) = \frac{4\pi^2 n_m^2 \left(\dfrac{dn}{dc}\right)^2}{\lambda_0^4 N_A} cP_j(\theta)\left[\frac{\partial(\Pi/N_A kT)}{\partial c}\right]^{-1} \quad j = \text{v, u, h} \tag{7.427}$$

where $\Pi(c)$ is the osmotic pressure of the suspension. For a low particle concentration, the osmotic pressure is expanded in series with respect to the particle concentration:

$$\frac{\Pi}{N_A kT} = A_1 c + A_2 c^2 + A_3 c^3 + \cdots \quad j = \text{v, u, h} \tag{7.428}$$

where A_i are virial coefficients ($A_1 = 1/M$). Then, the relationship between c and $R(\theta)$ can be rewritten in the form [999]:

$$\frac{Kc}{R_j(\theta)}P_j(\theta) = \frac{1}{M} + 2A_2 c + \cdots \quad j = \text{v, u, h} \tag{7.429}$$

where $P_j(\theta)$ is given by Equation 7.413, depending on the polarization of the incident light. As seen from this expression, the particle mass can be determined by measuring $R(\theta)$ at several concentrations and extrapolating the result toward $c = 0$.

The intercept of the obtained straight line (at small concentrations) is equal to $1/M$, while the slope provides the second osmotic virial coefficient, A_2, which is a measure of the interparticle interactions.

The system of large interacting particles requires a modification of the Einstein approach, because one should account for correlations in the position of the scattering subunits within a given particle, along with correlations in the positions of different particles. If the condition in Equation 7.417 is satisfied, one can decompose these correlations into two different terms to obtain [1000]

$$R_j(\theta) = K_1 \rho P_j(\theta) S(\rho,q); \quad K_1 = \frac{4\pi^2 n_m^2 \left(\dfrac{dn}{d\rho}\right)^2}{\lambda_0^4 N_A} \quad j = v, u, h \tag{7.430}$$

where the particle form factor $P_j(\theta)$ is the same as for noninteracting particles, while the structure factor $S(\rho,q)$, accounts for the interactions. By definition, the static structure factor is

$$S(\rho,q) = 1 + \rho \int_0^\infty 4\pi r^2 [g(r) - 1] \frac{\sin qr}{qr} dr \tag{7.431}$$

where $g(r)$ is the pair radial distribution function.

For small particles, $g(r)$ is substantially different from unity only at interparticle distances $r \ll q^{-1}$. Then, the structure factor is equal to the inverse osmotic compressibility of the suspension [1000]:

$$S(\rho,q) \approx 1 + \rho \int_0^\infty 4\pi r^2 [g(r) - 1] dr \equiv \left[\frac{\partial(\Pi/kT)}{\partial \rho}\right]_T^{-1} \tag{7.432}$$

and Equation 7.430 reduces to the Einstein expression, Equation 7.427, with ρ (instead of c) being used as a measure of the particle concentration—note that Equation 7.427 does not depend on the particular choice of the concentration definition.

7.9.1.4.2 Zimm-Plot (Method of Double Extrapolation)

The substitution of Equation 7.421 in Equation 7.429 suggests a graphical procedure for interpretation of light scattering data from suspensions of large interacting particles of arbitrary shape. Keeping the leading terms we obtain:

$$\frac{Kc}{R_v(\theta)} = \frac{1}{M}\left[1 + \frac{16}{3}\left(\frac{\pi n}{\lambda_0}\right)^2 \sin^2(\theta/2)\langle R_g^2\rangle\right] + 2A_2 c + \cdots \tag{7.433}$$

Based on this formula, Zimm [1001] suggested plotting $Kc/R_v(\theta)$ against $[\sin^2(\theta/2) + bc]$, where b is an arbitrary constant usually chosen to satisfy the condition $bc_{max} \sim 1$. This method requires measurements at different concentrations and scattering angles. The data are presented as a grid of points (Figure 7.82) which allows extrapolation (1) to zero angle for each used concentration, and (2) to zero concentration for each scattering angle. Finally, the extrapolated points for zero concentration (at different angles) are extrapolated to zero angle, and the points for zero angle (at different concentrations) are extrapolated to zero concentration. In the ideal case, the two extrapolated curves must cut the ordinate $Kc/R_v(\theta)$ at the same point, which is the inverse mass of the particle. Respectively, the initial slope of the curve $c = 0$ provides the square radius of gyration, $\langle R_g^2\rangle$, while the initial slope of the curve $\theta = 0$ gives the second osmotic virial coefficient, A_2.

For nonpolarized or horizontally polarized incident beams, $R_v(\theta)$ in Equation 7.433 is to be replaced by $2R_u(\theta)/(1 + \cos^2\theta)$ or $R_h(\theta)/\cos^2\theta$, respectively.

7.9.1.4.3 Interpretation of the Second Osmotic Virial Coefficient

Generally speaking, positive values of A_2 mean net repulsion between the particles, while negative values of A_2 correspond to attraction. For more detailed analysis of the values of the second osmotic virial coefficient, the use of other definitions of the particle concentration is more convenient. The common virial expansion [11]:

$$\frac{\Pi}{kT} = \rho + \frac{1}{2}\beta_2 \rho^2 + \cdots \tag{7.434}$$
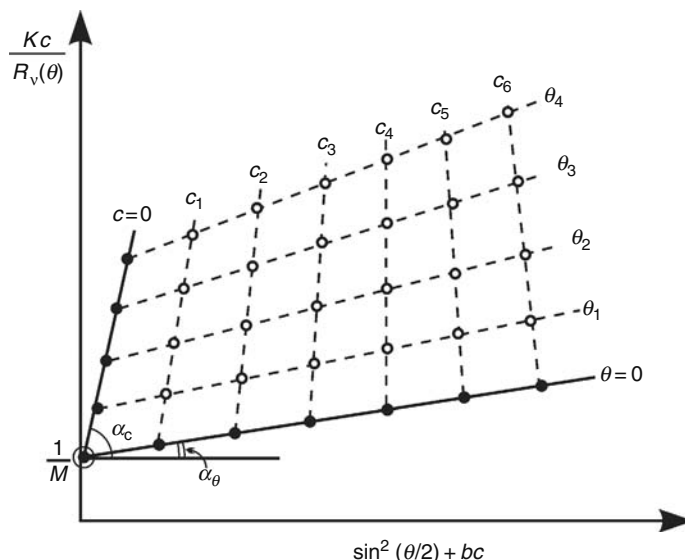
FIGURE 7.82 Schematic presentation of the Zimm plot [1001] (method of double extrapolation). The data from measurements at several concentrations (c_1–c_6) and scattering angles (θ_1–θ_4) are presented by empty circles. Then, extrapolation to $c=0$ for each angle and to $\theta=0$ for each concentration is numerically performed (see the black dots). Both lines, $c=0$ and $\theta=0$, should meet the ordinate at the point M^{-1}, where M is the particle mass. The slope angle of the line $c=0$ is equal to $\alpha_c = \tan^{-1}[(4\pi n/\lambda_0)^2\langle R_g^2\rangle/3M]$, while the slope angle of the line $\theta=0$ is equal to $\alpha_\theta = \tan^{-1}(2A_2)$.

defines another second virial coefficient, β_2, which has the dimensions of volume and is widely used in statistical thermodynamics. The coefficients, A_2 and β_2, are interconnected through the relationship:

$$\beta_2 = 2\frac{M^2}{N_A}A_2 \tag{7.435}$$

For the central interaction between the particles, one can rigorously show that [11,1000]:

$$\beta_2 = \int_0^\infty [1 - g(r)]4\pi r^2 \mathrm{d}r = \int_0^\infty \left[1 - \exp\left(-\frac{W(r)}{kT}\right)\right]4\pi r^2 \mathrm{d}r \tag{7.436}$$

where
  r is the distance between the centers of mass of the particles
  $W(r)$ is the pair interaction energy

More general expressions for β_2 in the case of anisodiametrical particles are also available [11,1000]. The usage of β_2 is convenient when the experimental results about the particle interactions must be compared to theoretical calculations. For hard spheres, β_2 is equal to $8V_p$, where V_p is the particle volume. This fact was used by some authors to define the so-called effective volume of the particle through the measured second virial coefficient [404,422]:

$$V_{EFF} = \frac{1}{8}\beta_2 = \frac{1}{4}\frac{A_2M^2}{N_A}; \quad A_2, \beta_2 > 0 \tag{7.437}$$

Note that V_{EFF} could be substantially different from the actual particle volume, V_p, if long-range interactions between the particles are present. The counterpart of Equation 7.433 in terms of ρ and β_2 reads:

$$\frac{K_1\rho}{R_v(\theta)} = \left[1 + \frac{16}{3}\left(\frac{\pi n}{\lambda_0}\right)^2\sin^2(\theta/2)\langle R_g^2\rangle\right] + \beta_2\rho + \cdots; \quad K_1 = \frac{4\pi^2 n_m^2}{\lambda_0^4}\left(\frac{\mathrm{d}n}{\mathrm{d}\rho}\right)^2 \tag{7.438}$$

In the case of microemulsions and suspensions of spherical particles, it is usually more convenient to use the volume fraction, ϕ, of the dispersed particles as a measure of their concentration [1002–1007]. By using the fact that $\phi = \rho V_p$, one can obtain the virial expansion:

$$\frac{\Pi}{kT} = B_1\phi + B_2\phi^2 + \cdots; \quad B_1 = \frac{1}{V_p} \quad \text{and} \quad B_2 = \frac{\beta_2}{2V_p^2} \tag{7.439}$$

The light scattering data can be interpreted by using the equation:

$$\frac{K_2\phi}{R_v(\theta)} = \frac{1}{V_p}\left[1 + \frac{16}{3}\left(\frac{\pi n}{\lambda_0}\right)^2 \sin^2(\theta/2)\langle R_g^2\rangle\right] + 2B_2V_p\phi; \quad K_2 = \frac{4\pi^2 n_m^2}{\lambda_0^4}\left(\frac{dn}{d\phi}\right)^2 \tag{7.440}$$

Therefore, the double extrapolation procedure in these variables provides the real volume of the particles, V_p. The quantity $2B_2V_p$ is dimensionless and often denoted in the literature as λ_V (see Section 7.9.2.4). For hard spheres, $\lambda_V = 8$.

7.9.1.5 Depolarization of Scattered Light

The polarization of the incident beam is denoted by subscripts v, h, or u for vertically polarized, horizontally polarized, or nonpolarized light, respectively. Generally, the Rayleigh constant can be considered as consisting of two components, R^V and R^H, corresponding to the vertical and horizontal directions of the electrical field of the scattered light (Figure 7.80). Therefore, one can define six quantities: $R_v^V, R_h^V, R_u^V, R_v^H, R_h^H,$ and R_u^H, the values of which provide information about the size, shape, and anisotropy of the scattering particles [1008–1010]. Depending on the polarization of the incident light, it is accepted to define three depolarization coefficients:

$$\Delta_v = \frac{R_v^H}{R_v^V}, \quad \Delta_h = \frac{R_h^H}{R_h^V}$$
$$\Delta_u = \frac{R_u^H}{R_u^V} = \frac{R_v^H + R_h^H}{R_v^V + R_h^V} = \frac{1 + \Delta_h}{1 + \Delta_v^{-1}} \tag{7.441}$$

Usually, Δ_v, Δ_h, and Δ_u refer to a scattering angle $\theta = 90°$ and small concentrations, $c \to 0$ (the scattering from the solvent is subtracted). The values of Δ_v, Δ_h, and Δ_u can be used to determine the type of the suspended particles (see Table 7.11). Note that the inherent particle anisotropy is reflected in the value of Δ_v, while Δ_u contains a contribution from the particle size as well.

One can define the so-called optical anisotropy of the particles

$$\delta^2 = \frac{(\alpha_1 - \alpha_2)^2 + (\alpha_2 - \alpha_3)^2 + (\alpha_3 - \alpha_1)^2}{(\alpha_1 + \alpha_2 + \alpha_3)^2} \tag{7.442}$$

where α_1, α_2, and α_3 are the polarizabilities of the particle along its three main axes. As shown by Cabannes [1008] for particles arbitrary in size:

$$\delta^2 = \frac{10\Delta_u}{6 - 7\Delta_u} \tag{7.443}$$

TABLE 7.11
Depolarization Coefficients of Different Types of Particles

Particles	Δ_v	Δ_h	Δ_u
Small, isotropic	0	Not defined	0
Small, anisotropic	$(0-1)$	1	$(0-1)$
Large, isotropic	0	∞	$(0-1)$
Large, anisotropic	$(0-1)$	1	$(0-1)$

Sources: Cabannes, P., *La Diffusion Moleculaire de la Lumiere*, Presses Universitaires de France, Paris, 1929.; Utiyama, H., in *Light Scattering from Polymer Solutions*, Huglin, M.B., Ed., Academic Press, New York, 1972, Chapter 4.

In the particular case of small particles and $\theta = 90°$, one has:

$$P_v(90°) = \frac{3 + 3\Delta_v}{3 - 4\Delta_v}; \quad R_v(90°) = cKM\frac{3 + 3\Delta_v}{3 - 4\Delta_v} \tag{7.444a}$$

$$P_u(90°) = \frac{6 + 6\Delta_u}{6 - 7\Delta_u}; \quad R_u(90°) = \frac{1}{2}cKM\frac{6 + 6\Delta_u}{6 - 7\Delta_u} \tag{7.444b}$$

Comparison of Equations 7.413, 7.416, and 7.444b shows that in the case of small anisotropic molecules, one has an additional multiplier $\left(\frac{6+6\Delta_u}{6-7\Delta_u}\right)$ called the Cabannes' factor. Therefore, the correct determination of the particle mass in such systems requires measurements of both, $R(90°)$ and $\Delta(90°)$.

7.9.1.6 Polydisperse Samples

The light scattering methods provide statistically averaged quantities when applied to polydisperse samples (e.g., micellar or polymer solutions). The case of independent scatterers can be rigorously treated [982,1001] by using the mass distribution function of the particles, $f(M)$. By definition, $dm = f(M)dM$ is the mass of particles in the range between M and $(M + dM)$, scaled by the total particle mass. As shown by Zimm [1001], the scattering law in such a system can be presented similar to the case of monodisperse particles (see Equation 7.416):

$$\left[\frac{Kc}{R_j(\theta)}\right]^{-1} = \int_0^\infty f(M)MP_j(\theta,M)dM = \langle M\rangle_m \langle P_j(\theta)\rangle_m \quad j = u, v, h \tag{7.445}$$

where c is the total particle concentration, while the averaged molecular mass, $\langle M\rangle_m$, and form factor, $\langle P(\theta)\rangle_m$, are defined as

$$\langle M\rangle_m = \int_0^\infty Mf(M)dM, \quad \langle P_j(\theta)\rangle_m = \frac{1}{\langle M\rangle_m}\int_0^\infty f(M)MP_j(\theta,M)dM \tag{7.446}$$

For small scattering angles, $P_v(\theta,M) \to 1 - \frac{1}{3}q^2\langle R_g^2(M)\rangle$, where $\langle R_g^2(M)\rangle$ is the squared radius of gyration of particles having mass M. Substituting this expression in Equation 7.445, one obtains [1001]:

$$\left[\frac{Kc}{R_V(\theta)}\right]^{-1}_{\theta\to 0} = \langle M\rangle_m\left(1 - \frac{1}{3}q^2\int_0^\infty f(M)\langle R_g^2(M)\rangle MdM\right) \tag{7.447}$$

This expression can be used as a starting point for analysis of the scattered light intensity by polydisperse samples. If the shape of the particles is known (that is, $\langle R_g^2(M)\rangle$ is a known function; see Equation 7.423), one can determine two parameters characterizing the distribution $f(M)$ (e.g., its mean value and standard deviation) from the experimentally measured intercept and slope of the line, $[cK/R_v(\theta)]^{-1}$ versus q^2. For small particles, $P(\theta \to 0, M) \approx 1$ and:

$$\left[\frac{Kc}{R(\theta)}\right] \approx 1/\langle M\rangle_m \tag{7.448}$$

Therefore, in this case, one can determine the mass averaged particle mass (Equation 7.446).

7.9.1.7 Turbidimetry

Instead of measuring the intensity of the scattered light at a given angle, θ, one can measure the extinction of the incident beam propagating through the suspension [973,999]. The method is called turbidimetry and was widely used in the past, because the necessary equipment was essentially the same as that for measuring the absorption of light by colored solutions. Usually, nonpolarized light is used in these experiments; hence, the following consideration corresponds to nonpolarized incident beams.

The turbidity, $\tau(m^{-1})$, of a suspension is defined through a counterpart of Beer–Lambert's equation [968,969]:

$$I(x) = I_0 \exp(-\tau x) \tag{7.449}$$

On the other hand, turbidity can be calculated by integrating scattered light in all directions and dividing by the intensity of the incident beam:

$$\tau = \int_{\theta=0}^{\pi} \int_{\varphi=0}^{2\pi} \frac{\langle I_s(\theta)\rangle_t}{\langle I_0\rangle_t} r^2 \sin\theta \, d\theta \, d\varphi = 2\pi \int_0^{\pi} R_u(\theta) \sin\theta d\theta \tag{7.450}$$

For suspension of noninteracting scatterers, it is convenient to introduce the so-called dissipation factor, Q:

$$Q = \frac{3}{8} \int_0^{\pi} P_v(\theta)(1 + \cos^2\theta) \sin\theta \, d\theta \tag{7.451}$$

Also, for noninteracting particles we have (see Equations 7.413 and 7.418):

$$R_u(\theta) \equiv R_u(0)P_u(\theta) = R_u(0)P_v(\theta)\left(\frac{1 + \cos^2\theta}{2}\right) \tag{7.452}$$

Therefore, τ can be expressed as (see Equations 7.416 and 7.418)

$$\tau = \frac{8\pi}{3} Q \, R_u(0) = \frac{16\pi}{3} Q \frac{R_u(90°)}{P_v(90°)} = \frac{8\pi}{3} QcKM \tag{7.453}$$

Note that for small particles $P_v(\theta) = 1$, $Q = 1$, and $\tau = (8\pi/3) \, cKM$. This simpler case can be generalized to suspensions of interacting particles and the final result reads [999]:

$$\tau = \frac{(8/3)\pi Kc}{(1/M) + 2A_2 c} \tag{7.454}$$

Therefore, for small particles, Kc/τ is a linear function of c in the low concentration range, and the intercept and slope of the straight line allow us to calculate M and A_2, respectively.

The above consideration was for particles not absorbing light. If the particles do absorb light, one must use the Mie theory (Section 7.9.1.3). Equation 7.449 is modified to read [967–969]:

$$I(x) = I_0 \exp\left[-(\xi + \tau)x\right] \tag{7.455}$$

and the absorbance, ξ, and the turbidity, τ, of a suspension containing spherical particles of radius R are determined from

$$\xi = \pi R^2 \rho Q_{abs} \quad \text{and} \quad \tau = \pi R^2 \rho Q_{sca} \tag{7.456}$$

where Q_{abs} and Q_{sca} must be numerically calculated as mentioned in Section 7.9.1.3.

7.9.2 DLS

We represent here only the basic methods and equations used for DLS data analysis. Detailed description of the subject can be found in the available monographs [1011,1017].

7.9.2.1 DLS by Monodisperse, Noninteracting Spherical Particles

In the DLS methods, the time fluctuations of the intensity of the scattered light, $I_s(t)$, are analyzed. These fluctuations are caused by the translational and rotational Brownian motion of the particles, which leads to perpetual variation of the particle configuration with the resulting change in the interference pattern of the scattered light. The time course of the detector signal (which is proportional to $I_s(t)$) can be analyzed by two different devices.

7.9.2.1.1 Spectrum Analyzer

This equipment is used when the intensity of the scattered light is high and an analog output from the photomultiplier tube (the detector) is available. The power spectrum, $P(q,\omega)$, of the output signal is extracted. For instance, in the case of translational diffusion of monodisperse spherical particles:

$$P^{(2)}(q,\omega) = \frac{2q^2D/\pi}{\omega^2 + (2q^2D)^2} + \delta(\omega) \tag{7.457}$$

where
   D is the translational diffusion coefficient of the particles
   $\delta(x)$ is the Dirac-delta function

According to Equation 7.457, the power spectrum is Lorentzian, centered at $\omega = 0$ with a half-width equal to $2q^2D$. From the value of D, one can calculate the hydrodynamic radius of the particle, R_h, by means of the Stokes–Einstein formula:

$$R_h = \frac{kT}{6\pi\eta D} \tag{7.458}$$

where η is the shear viscosity of the disperse medium.

7.9.2.1.2 Correlator

This type of instrument is aimed at calculating the autocorrelation function of the intensity of the scattered light, defined as

$$g^{(2)}(q,\tau) \equiv \frac{1}{\langle I_s \rangle_t^2} \lim_{T\to\infty} \frac{1}{2T} \int_{-T}^{T} I_s(t)I_s(t+\tau)dt = \langle I_s(t)I_s(t+\tau) \rangle_t / \langle I_s \rangle_t^2 \tag{7.459}$$

An important advantage of the correlators is that they are capable of working even with very low intensities of the scattered light, when each photon is separately counted by the detector. From a theoretical viewpoint, $P^{(2)}(q,\omega)$ and $g^{(2)}(q,\tau)$ provide essentially the same information, because for a stationary random process (as in the case with diffusion) these two quantities are Fourier transforms of each other (Wiener–Khintchine theorem) [1000]:

$$g^{(2)}(q,\tau) = \int_{-\infty}^{+\infty} P^{(2)}(\omega) \cos(\omega\tau)d\omega \tag{7.460a}$$

$$P^{(2)}(q,\omega) = \frac{1}{2\pi} \int_{-\infty}^{+\infty} g^{(2)}(\tau) \cos(\omega\tau)d\tau \tag{7.460b}$$

Therefore, $g^{(2)}(q,\tau)$ can be calculated if $P^{(2)}(q,\omega)$ is experimentally determined and vice versa. In the particular case of translational diffusion of monodisperse spherical particles (see Equation 7.457):

$$g^{(2)}(q,\tau) = \int_{-\infty}^{+\infty} \left[\delta(\omega) + \frac{2q^2D/\pi}{\omega^2 + (2q^2D)^2} \right] \cos(\omega\tau)d\omega = 1 + \exp(-2q^2D\tau) \tag{7.461}$$

In reality, the experiment provides the function:

$$G^{(2)}(q,\tau) = 1 + F\exp(-2q^2D\tau) \tag{7.462}$$

where the factor F accounts for the spatial coherence of the scattering volume and depends on the aperture of the detector. If the detector radius is $\sim\lambda r/b$ (r is the distance between the scattering volume and the detector, b is the radius of the scattering volume, and $\lambda^2 r^2/\pi b^2$ is the coherence area) [1018], F is close to unity. For a larger radius of the detector, F would be orders of magnitude smaller, and signal/noise ratio will be also small.

Equations 7.457 and 7.461 are applicable in the so-called homodyne method (or self-beating method), where only scattered light is received by the detector [1011–1016]. In some cases, it is also desirable to capture by the detector a part of the incident beam which has not undergone the scattering process. This method is called heterodyne (or method of the local oscillator) and sometimes provides information that is not accessible by the homodyne method [1012]. It can be shown that if the intensity of the scattered beam is much lower than that of the detected nonscattered (incident) beam, the detector measures the autocorrelation function of the electrical field of the scattered light defined as

$$g^{(1)}(q,\tau) \equiv \langle E_s^*(t) E_s(t+\tau) \rangle / \langle I_s \rangle_t \tag{7.463}$$

where
   $E_s(t)$ is the intensity of the electrical field of the light
   (*) indicates complex conjugation

The counterparts of Equations 7.457 and 7.461 in the heterodyne method read:

$$P^{(1)}(q,\omega) = \frac{q^2 D/\pi}{\omega^2 + (q^2 D)^2} \tag{7.464a}$$

$$g^{(1)}(q,\tau) = \exp(-q^2 D\tau) \tag{7.464b}$$

In this case, the Wiener–Khintchine theorem, Equation 7.460, is also valid if $g^{(2)}(q,\tau)$ is replaced by $g^{(1)}(q,\tau)$ and $P^{(2)}(q,\omega)$ by $P^{(1)}(q,\omega)$. In addition, for the diffusion process, $g^{(1)}(q,\tau)$ and $g^{(2)}(q,\tau)$ are interrelated by the Siegert equation:

$$g^{(2)}(q,\tau) = 1 + \left| g^{(1)}(q,\tau) \right|^2 \tag{7.465}$$

If charged particles are placed in an external, constant electrical field (e.g., in electrophoretic equipment), they acquire a drift velocity, $\mathbf{V}_{EL}$, which is superimposed upon the diffusion. The respective power spectrum in the heterodyne method is [1019]

$$P^{(1)}(q,\omega) = \frac{1}{2} \left[\frac{q^2 D/\pi}{(\omega + \mathbf{q} \cdot \mathbf{V}_{EL})^2 + (q^2 D)^2} + \frac{q^2 D/\pi}{(\omega - \mathbf{q} \cdot \mathbf{V}_{EL})^2 + (q^2 D)^2} \right] \tag{7.466a}$$

where $\mathbf{q}$ is the scattering vector equal to the difference between the scattered and incident wavevectors ($|\mathbf{q}| = (4\pi n/\lambda_0) \sin(\theta/2)$). Therefore, the power spectrum is a sum of two Lorentzians which are shifted in frequency, but their half-width remains determined by the translational diffusion coefficient. The autocorrelation function in this case is

$$g^{(1)}(q,\tau) = \exp(-q^2 D\tau) \cos[(\mathbf{q} \cdot \mathbf{V}_{EL})\tau] \tag{7.466b}$$

Equations 7.466a and b show that, in principle, from one experiment one can simultaneously determine D and V_{EL}. In practice, a series of experiments at different intensities of the external field, E, is performed, and the linear function V_{EL} versus E is plotted. The slope of the resulting line gives the electrophoretic mobility, $\mu \equiv V_{EL}/E$. In a similar way the velocity of aerodynamic fluxes can be studied by using tracer particles (laser Doppler anemometry) [1020].

The scattering geometry used in most of the commercial equipment for measuring the electrophoretic mobility of particles [1021] is shown schematically in Figure 7.83. The incident laser beam is split into two parts of equal intensity, which are afterward crossed in the scattering volume. At the crossing point a pattern of consecutive dark and bright interference planes is formed, due to the mutual coherence of the beams. Therefore, when the particle (driven by the external electrical field) crosses the bright planes, it scatters light which is received by the detector as a sequence of pulses. The time interval between the two pulses of light, scattered by one and the same particle, depends on the distance between the interference planes (determined by the geometry of the crossing beams) and on the particle velocity. The corresponding autocorrelation function of the intensity of the scattered light is a damped cosine function, the period of which allows one to calculate the particle drift velocity and electrophoretic mobility. A modification [1021] of the equipment allows one to measure relatively low mobilities with high precision, which is particularly important for nonaqueous dispersions.

7.9.2.2 DLS by Polydisperse, Noninteracting Spherical Particles

For polydisperse samples of noninteracting particles, the autocorrelation function (or the power spectrum) presents a superposition of the respective functions of the individual species, weighted by the intensities of light scattered by them. Several
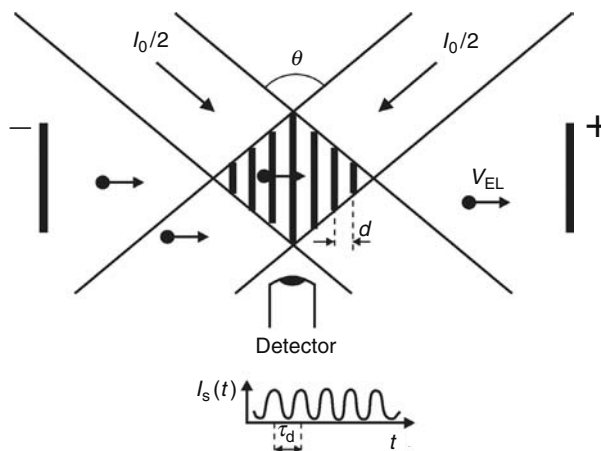
FIGURE 7.83 Method of crossed beams for measurement of particle drift velocity, V_{EL}. The incident laser beam of intensity I_0 is split into two coherent beams by using an optical prism (not shown in the figure). Then, the two beams meet each other in the scattering volume and form an interference pattern. The distance between the bright planes of this pattern is $d = \lambda_0/[2n\sin(\theta/2)]$. The particles, moving under the action of applied electrical potential, give rise to pulses of scattered light when passing through the bright planes. The time interval, τ_d, between two consecutive pulses, created by a given particle, is $\tau_d = d/V_{EL}$. Since d is known and τ_d is measured from the autocorrelation function of the scattered light, one can calculate the drift velocity, V_{EL}.

procedures have been employed to analyze the signal from polydisperse samples. The most straightforward procedure [1022] is the method of cumulants, in which the log of the measured correlation function is expanded in series:

$$\ln\left[g^{(1)}(q,\tau)\right] = \sum_{n=1}^{\infty} K_n(q) \frac{(-\tau)^n}{n!} \tag{7.467}$$

The first cumulant, $K_1(q) = \lim_{\tau \to 0} (\mathrm{d}\ln g^{(1)}(q,\tau)/\mathrm{d}\tau)$, defines an effective diffusion coefficient:

$$D_{EFF} = \frac{K_1(q)}{q^2} \tag{7.468}$$

For noninteracting particles, D_{EFF} presents the so-called z-average diffusion coefficient, $\langle D \rangle_z$:

$$D_{EFF} = \langle D \rangle_z \equiv \frac{\int\limits_0^{\infty} f(M)\, MP(q,M)D(M)\, \mathrm{d}M}{\int\limits_0^{\infty} f(M)\, MP(q,M)\, \mathrm{d}M} \tag{7.469}$$

The second cumulant, $K_2(q) = \lim_{\tau \to 0} \mathrm{d}^2 \ln g^{(1)}(q,\tau)/\mathrm{d}\tau^2$, provides information about the polydispersity of the sample:

$$\frac{K_2(q)}{q^4} = \langle D^2 \rangle_z - \langle D \rangle_z^2 \tag{7.470}$$

The higher order cumulants, K_3 and K_4, are measures of the distribution asymmetry and flatness, respectively. It is usually difficult to determine reliably K_3 and K_4.

The mean hydrodynamic radius, calculated from D_{EFF}, is given by

$$\langle R_h \rangle = \frac{kT}{6\pi\eta\langle D \rangle_z} = \frac{\int\limits_0^{\infty} f(M)\, MP(q,M)\, \mathrm{d}M}{\int\limits_0^{\infty} f(M)\, MP(q,M)\, R_h^{-1}(M)\, \mathrm{d}M} \tag{7.471}$$

The main advantage of the cumulant method is that it does not require any assumption about the particular shape of the size distribution. While the main disadvantage is that a variety of rather different distributions may have similar values of K_1 and K_2.

Therefore, one cannot obtain reliable information about the size distribution only from DLS data. The cumulant method is the most suitable when the size distribution is known to be monomodal and relatively narrow.

For polymodal or wide distributions the histogram method [1023–1031] (or the exponential sampling method) is more representative. In this method, the particle size distribution is presented by a finite number of discrete sizes, each of them being an adjustable fraction of the total concentration. Then, the correlation function is calculated and compared with the measured one. The relative amplitude of each size class is varied to give the best agreement between the calculated and the experimental functions. Although conceptually simple, the histogram method is not straightforward, because a given correlation function can be described by an infinite variety of particle distributions (ill-posed mathematical problem). To overcome this difficulty, one must invoke independent criteria to restrict the population of possible solutions and to choose the most reasonable one. Several procedures were proposed and realized as computer programs, the most widely used of them being CONTIN [1014,1024], nonnegative least squares (NNLS) [1025], singular value analysis [1027], maximum entropy [1030], regularization technique [1031], and several others [1026,1028,1029]. For more thorough and reliable results, multi angle measurements and combined analysis of the data from SLS and DLS on the basis of Mie theory are recommended.

7.9.2.3 DLS by Nonspherical Particles

In diluted suspensions, translation and rotation of the particles can be considered as statistically independent. Then, the correlation function of the scattered light can be presented as being composed of two parts: phase autocorrelation function, $C_\Phi(q,\tau)$, accounting for the translational diffusion, and amplitude autocorrelation function, $C_B(\tau)$, determined by the particle rotation [1032]:

$$g^{(1)}(q,\tau) = C_B(\tau)\, C_\Phi(q,\tau) \tag{7.472}$$

where, by definition

$$C_B(\tau) \equiv \langle B^*(0)B(\tau)\rangle_t / \langle B(0)^2\rangle_t \tag{7.473}$$

$B(t)$ is the scattering amplitude of a particle, which depends on the particle polarizability at given orientation. $B(t)$ changes with time due to reorientation of the particle. If the scatterers are spherical, $B(t)$ is constant and $C_B(\tau) = 1$. Note that $C_B(\tau)$ does not depend on the scattering angle and can be calculated if the polarizability tensor and the rotational diffusion tensor of the particles are known. The calculation of $C_\Phi(q,\tau)$ requires averaging of the translational diffusion tensor of the particle over all possible orientations in order to obtain the averaged translational diffusion coefficient.

The polarizability of cylindrically symmetrical particles (rod-shaped or ellipsoidal particles) can be characterized by isotropic (α) and anisotropic (β) parts of the polarizability tensors [1012]:

$$\alpha \equiv \frac{1}{3}(\alpha_{II} + 2\alpha_I), \quad \beta \equiv (\alpha_{II} - \alpha_I) \tag{7.474}$$

where α_{II} and α_I are the polarizabilities in directions parallel and perpendicular, respectively, to the symmetry axis. The autocorrelation function for small, monodisperse, cylindrically symmetrical particles has the form [1012]:

$$g_v^{(1)V}(q,\tau) = \alpha^2 \exp(-q^2 D\tau) + \frac{4}{45}\beta^2 \exp[-(q^2 D + 6\Theta)\tau] \tag{7.475}$$

where Θ is the rotational diffusion coefficient; the subscript v and the superscript V denote vertically polarized incident and scattered beams, respectively. Since $g_v^{(1)V}$ consists of two exponents (the second one being difficult for precise determination, because it is weaker in magnitude and decays more rapidly compared to the first one), it is preferable to perform measurements also in depolarized light [1012,1032]:

$$g_v^{(1)H}(q,\tau) = \frac{\beta^2}{15} \exp[-(q^2 D + 6\Theta)\tau] \tag{7.476}$$

which presents one exponent depending on both, D and Θ.

For long rod-like particles, the autocorrelation function is a sum of exponentials [1013]

$$g_v^{(1)V}(\tau) = \sum_{l=0,l\,even}^{\infty} B_l \exp\{-[q^2 D + l(l+1)\Theta]\tau\} \tag{7.477}$$

The amplitude coefficients B_l are defined through spherical Bessel functions and can be calculated if the particle length is specified. The extraction of the value of Θ from the experimentally obtained correlation function obeying Equation 7.477 is a formidable task, which makes it very difficult to deduce reliably results for large particles from only DLS. In such systems, the electro-optical methods [974–976] are more accurate for measurement of Θ.

If a homodyne method is used, the measured autocorrelation function $g^{(2)}(q,\tau)$ can be interpreted by using the Siegert relation (Equation 7.465). The translational and rotational diffusion coefficients for several specific shapes of the particles are given in Table 7.10. The respective power spectrum functions can be calculated by using the Fourier transform, Equation 7.460b.

7.9.2.4 Effect of the Particle Interactions

The diffusion coefficient of the particles in suspension depends on concentration of particles due to the interparticle interactions [1033–1040]. Furthermore, one should distinguish the self-diffusion (or tracer diffusion) coefficient, D_S, from the collective diffusion (or mutual diffusion) coefficient, D_C. The self-diffusion coefficient accounts for the motion of a given particle and can be formally defined as an autocorrelation function of the particle velocity [1000,1033]:

$$D_S = \frac{1}{3} \int_0^\infty \langle \mathbf{V}(0).\mathbf{V}(\tau) \rangle \mathrm{d}\tau \qquad (7.478)$$

where the brackets denote the averaging over the stochastic particle motion. The mean-square displacement, $\langle \Delta r^2(t) \rangle$, of a given particle is given by [1033]:

$$\langle \Delta r^2(t) \rangle = 6D_S t; \quad \text{for} \quad t \gg \tau_{\mathrm{Br}} \equiv M/6\pi\eta R_h \qquad (7.479)$$

where τ_{Br} is the characteristic time of the Brownian motion of a particle of mass M and hydrodynamic radius, R_h. The collective diffusion coefficient is a collective property of the suspension and characterizes the evolution of small concentration gradients in the linear approximation (Fick's low) [1033]:

$$\frac{\partial \rho}{\partial t} = -D_C \Delta \rho \qquad (7.480)$$

Hence, D_C is the quantity determined in conventional, gradient diffusion measurements. For noninteracting particles (very diluted suspension) $D_S = D_C$.

As discussed above, DLS experiment provides the autocorrelation function $g^{(1)}(q,\tau)$ or some other quantity which contains equivalent information ($g^{(2)}(q,\tau)$ or $P(q,\omega)$). Similar to the case of noninteracting particles, one can define an effective diffusion coefficient:

$$D_{\mathrm{EFF}}(q,\rho) \equiv K_1/q^2 \qquad (7.481)$$

where $K_1(q,\rho)$ is the first cumulant of the autocorrelation function. It was shown [1033,1037] that the low-q limit of D_{EFF} coincides with D_C:

$$D_C(\rho) = \lim_{q \to 0} [D_{\mathrm{EFF}}(q,\rho)]; \quad qR_h < 1 \qquad (7.482)$$

while the high-q limit of $D_{\mathrm{EFF}}(q,\rho)$ provides the so-called short-time self-diffusion coefficient [1033]:

$$D_S^S(\rho) = D_{\mathrm{EFF}}(q,\rho); \quad \text{for } qR_h \gg 1 \qquad (7.483)$$

More general expressions for $D_{\mathrm{EFF}}(q,\rho)$ at intermediate values of q are also available [1014,1017,1037–1042], in terms of the static structure factor, $S(q,\rho)$, and the so-called dynamic structure factor, $F(q,\rho,\tau)$ [1033]:

$$D_{\mathrm{EFF}}(q,\rho) = -\frac{1}{S(q,\rho)} \lim_{\tau \to 0} \left[\frac{\partial F(q,\rho,\tau)/q^2}{\partial \tau} \right]_{q,\rho} \equiv \frac{H(q,\rho)}{S(q,\rho)} \qquad (7.484)$$

By definition, the dynamic structure factor accounts for the correlations between the positions of the particles at different moments of time [1033]:

$$F(q,\rho,\tau) \equiv \frac{1}{N} \sum_{k=1}^{N} \sum_{j=1}^{N} \langle \exp\{i\mathbf{q} \cdot [\mathbf{r}_k(0) - \mathbf{r}_j(\tau)]\} \rangle \tag{7.485}$$

where
$\mathbf{q}$ is the scattering vector
$\mathbf{r}_k(t)$ is the position of particle k in the moment t

Both functions, $F(q,\rho,\tau)$ and $H(q,\rho)$, include contributions from hydrodynamic interactions between the particles. Note that $F(q, \rho,\tau=0) \equiv S(q,\rho)$, while for noninteracting Brownian particles [1012,1033]:

$$F(q,\tau) = \langle \exp[-i\mathbf{q} \cdot \Delta\mathbf{r}(\tau)] \rangle = \exp(-q^2 D_0 \tau) \tag{7.486}$$

where D_0 is the diffusion coefficient at negligible interparticle interactions.

An important consequence of Equations 7.482, 7.484, 7.485, and 7.432 can be derived at the low-q limit [1033]:

$$D_C(\rho) = \frac{(\partial \Pi/\partial \rho)}{f(\rho)} \tag{7.487}$$

where
$(\partial \Pi/\partial \rho)$ is the osmotic compressibility
$f(\rho) = H^{-1}(q=0,\rho)$ is the friction (drag) coefficient of the particles in the suspension

Equation 7.487 represents the generalized Stokes–Einstein relation. Equations 7.482 and 7.483 show that one can determine (at least in principle) $D_C(\rho)$ and $D_S^S(\rho)$ by measuring the first cumulant, $K_1(q,\rho)$, at different scattering angles. On the other hand, D_S and D_C can be calculated in numerical experiments performed by Monte Carlo or Brownian dynamics methods [1043,1044].

As shown by Batchelor [1034] and Felderhof [1036], to the first order in the volume fraction, ϕ, the diffusion coefficients, D_C and D_S^S, can be presented as:

$$D_C = D_0[1 + \lambda_C \Phi] \tag{7.488}$$

$$D_S^S = D_0[1 + \lambda_A \Phi] \tag{7.489}$$

where D_0 is the diffusion coefficient at infinite dilution, while λ_C and λ_A are coefficients which depend on the interparticle interactions (including the hydrodynamic ones). Felderhof [1036] succeeded in presenting λ_C as a sum of several terms, each of them being an explicit integral over the pair distribution function, $g(r)$ [1041,1045]:

$$\lambda_C = \lambda_V + \lambda_O + \lambda_A + \lambda_S + \lambda_D \tag{7.490}$$

$$\lambda_V = 3 \int_0^\infty dx[1 - g(x)]x^2 \tag{7.491a}$$

$$\lambda_O = -3 \int_0^\infty dx[1 - g(x)]x \tag{7.491b}$$

$$\lambda_A = \frac{3}{2} \int_0^\infty dx \big[-2.5x^{-4} + 2.25x^{-6} + 5.3334x^{-8} - 61.42x^{-10} - 94.24x^{-12} + 134.58x^{-14}$$
$$-248.46x^{-16} - 1587.4x^{-18} + 727.2x^{-20} + O(x^{-22}) \big] g(x)x^2 \tag{7.491c}$$

$$\lambda_S = \int_0^\infty dx \left[18.75x^{-7} - 7.5x^{-9} - 89.39x^{-11} + 215.5x^{-13} + 843.8x^{-15} \right.$$
$$\left. +435.9x^{-17} + 4164x^{-19} + O(x^{-21})\right]g(x)x^2 \tag{7.491d}$$

$$\lambda_D = 1 \tag{7.491e}$$

where $x = r/R$, and R is the particle radius. Comparison of Equation 7.491a with Equation 7.436 shows that λ_V presents another definition of the second osmotic virial coefficient:

$$\lambda_V = \frac{\beta_2}{V_p} = 2B_2 V_p = \frac{2M^2}{N_A V_p} A_2, \tag{7.492}$$

λ_O stems from the far-field (Oseen) hydrodynamic interaction, while λ_A, λ_S, and λ_D account for the near-field hydrodynamics [1036].

Note that Equations 7.491a, 7.491b, and 7.491e are exact, while in Equations 7.491c and 7.491d the terms up to x^{-20} in a series expansion are taken into account. For hard spheres, one can calculate [1046] $\lambda_V^{HS} = 8, \lambda_O^{HS} = -6, \lambda_A^{HS} = -1.831, \lambda_S^{HS} = 0.285$, and $\lambda_C^{HS} = 1.454$. DLS experiments [1047] with suspension of sterically stabilized silica particles in organic solvents (used as a model of hard sphere dispersion) gave $\lambda_C^{HS} = 1.4 \pm 0.2$, which is in a good agreement with the theoretical value. A numerical algorithm for calculation of the next terms in the expansions in Equations 7.491c and 7.491d was developed [1045], but usually the first several terms (up to x^{-7}) are enough to calculate precisely λ_A and λ_C. λ_k ($k = V, O, A, S, C$) were calculated for simple functions modeling the pair interaction energy (sticky potential, square-well potential, etc.), and some of the results are shown in Table 7.12.

The important case of charged particles, interacting through electrostatic and van der Waals forces was analyzed by several authors [1042,1049–1053]. It was shown [1041,1049] that the contribution of the near-field terms (λ_A, λ_S, and λ_D) is negligible for electrostatically repelling particles when the collective diffusivity is concerned. For weakly charged particles (low surface potential and small size), explicit formulae for the coefficients were obtained [1049] (see Table 7.12). For strongly charged particles and in the cases when the van der Waals attraction is operative, one needs numerical procedures to calculate λ_k [1041,1049]. This approach allows one to determine the particle charge (or electrical potential) from the measured values of λ_V (by SLS) or λ_C (by DLS) if the particle size and the ionic strength are known [1049,1050].

At low ionic strength ($\kappa R \sim 1$), other effects connected with the finite diffusivity of the small ions in the electrical double layer surrounding the particle are present [1049,1054,1055]. The noninstantaneous diffusion of the small ions (with respect to the Brownian motion of the colloid particle) could lead to detectable reduction of the single particle diffusion coefficient, D_0, from the value predicted by the Stokes–Einstein relation, Equation 7.458. For spherical particles, the relative decrease in the value of D_0 is largest at $\kappa R \approx 1$ and could be around 10%–15%. As shown in the normal mode theory [1039], the finite diffusivity of the small ions also affects the concentration dependence of the collective diffusion coefficient of the particles. Belloni et al. [1051] obtained an explicit expression for the contribution of the small ions in λ_C:

$$\Delta\lambda_{SI} = \frac{Z^2 L_B}{R} \frac{1}{(1 + \kappa R)^2} \frac{3}{(\kappa R)^2} \frac{D_0}{D_{SI}} \tag{7.493}$$

where
   Z is the number of charges per particle
   $L_B = e^2/(4\pi\varepsilon_0\varepsilon kT)$ is the Bjerrum length
   D_{SI} is the diffusion coefficient of the small ions

The ratio of $\Delta\lambda_{SI}$ and the electrostatic part in λ (see Table 7.12):

$$\frac{\Delta\lambda_{SI}}{\lambda_C^{EL}} = \frac{1}{(1 + \kappa R)} \frac{D_0}{D_{SI}} \approx \frac{1}{(1 + \kappa R)} \frac{R_{SI}}{R} \tag{7.494}$$

Shows [1049] that the relative contribution of the small ions is above 10% only when the particles are small ($R \leq 4$ nm) and at a not very high ionic strength ($\kappa R \sim 1$). This could be the case with protein molecules and charged spherical micelles. Otherwise, the effect of the finite diffusivity of the small ions is negligible in comparison with the effect of the direct particle–particle electrostatic interaction.

TABLE 7.12

Expressions for the Correction Factors, λ_V, λ_O, λ_C, and λ_A, for Different Types of Interaction between Spherical Particles

Type of Interaction	λ_V	λ_O	λ_C	λ_A	Ref.
Hard spheres $$W(r) = \begin{cases} 0; & r \geq 2R \\ +\infty; & r < 2R \end{cases}$$					
Nonslip boundary condition	$+8.00$	-6.00	$+1.454$	-1.8315	[1046]
Perfect slip boundary condition	$+8.00$	-4.00	$+3.511$	-0.562	
Sticky hard spheres $$g(r) = \begin{cases} 1; & r > 2R \\ 1+\frac{R}{6\tau}; & r = 2R \\ 0; & r < 2R \end{cases}$$	$+8 - (2/\tau)$	$-6 + (1/\tau)$	$1.454 - (1.125/\tau)$	$1.8315 - (0.295/\tau)$	[1048]
τ-stickiness parameter Weakly charged particles	$8 + \dfrac{Z^2 L_B}{R} \dfrac{(1+2\kappa R)}{(1+\kappa R)^2} \dfrac{3}{(\kappa R)^2}$	$-6 - \dfrac{Z^2 L_B}{R} \dfrac{1}{(1+\kappa R)^2} \dfrac{3}{\kappa R}$	$1.45 + \dfrac{Z^2 L_B}{R} \dfrac{1}{(1+\kappa R)} \dfrac{3}{(\kappa R)^2};$	$-1.83 + \dfrac{Z^2 L_B}{R} \dfrac{\exp(2\kappa R)}{(1+\kappa R)^2}$ $\times [\dfrac{15}{6} E_3(2\kappa R) - \dfrac{27}{18} E_5(2\kappa R)]$	[1049]

$$W(r) = \begin{cases} \dfrac{(Ze)^2}{4\pi\varepsilon_0\varepsilon} \dfrac{\exp[\kappa(2R-r)]}{r(1+\kappa R)^2}; & r \geq 2R \\ +\infty; & r < 2R \end{cases}$$

Notes: Z is the number of charges per particle; $L_B = e^2/(4\pi\varepsilon_0\varepsilon kT)$ is the Bjerrum length; $E_n(x) \equiv \int_0^\infty \frac{e^{-xt}}{t^n} dt$ $(n = 1, 2, 3, \dots)$ is the integral exponent function.

7.9.2.5 Concentrated Dispersions: Photon Cross-Correlation Techniques, Fiber Optics DLS, and Diffusing Wave Spectroscopy (DWS)

A major drawback of the conventional DLS experiment is that the dispersion must be transparent for the light beam. For micrometer-sized particles, this requires concentrations below 10^{-5} vol%. Often the concentration of the samples is higher and their dilution for investigation is not desirable. The autocorrelation function of multiply scattered light is difficult to interpret and to extract subsequent information about the particle size. Several powerful techniques have been proposed aimed at overcoming this problem and extending the application of DLS to more concentrated suspensions.

One obvious way to reduce the contribution of the multiple light scattering is to use a very thin sample cell of an optical path length below 100 μm [1056,1057]. Alternatively, Phillies [1058,1059] suggested using a more complex optical system comprising two laser beams and two detectors focussed in the same sample volume and having exactly the same scattering vector (in direction and magnitude). The signals from the two detectors are cross-correlated by using a photon correlator. It has been shown [1058,1061] that the signals from the two detectors are correlated only for the light that is scattered once (single scattering), whereas the contributions from double and higher-order multiple scattering are uncorrelated. Therefore, when the signals from the two detectors (single and multiple scattering) are cross-correlated, only the signal corresponding to single scattering from the particles gives a contribution into the time dependence of the cross-correlation function. As a result, one obtains a time correlation function from turbid samples, which is similar to those obtained from transparent samples and can be interpreted in the same way. Several other cross-correlation schemes were suggested by Schätzel [1061] and some of them have found realization in practice [1061–1065]. In the two-color dynamic light scattering (TCDLS) [1061–1064], two laser beams of different colors are used and the angles between the incident beams and the detectors (all in the same plane) are chosen in such a way as to define equal scattering vectors. In the three-dimensional light scattering (3DDLS) [1061,1065] two incident beams of the same wavelength enter the sample from slightly above and slightly below the average scattering plane. The two detectors are also placed above and below the average scattering plane, respectively, so that the third dimension is used to achieve equal scattering vectors in the 3DDLS method. Both techniques have proven to suppress efficiently the multiple scattering in concentrated latex dispersions (see, e.g., the recent review by Pusey [1062]). Furthermore, it was shown [1065] that the same cross-correlation techniques can be used to eliminate the multiple scattering in SLS experiments. These techniques can be applied to turbid samples, for which the contribution of the single light scattering is a detectable fraction ($>1\%$) of the total intensity of the scattered light.

Two different techniques have been developed for studying even more concentrated (opaque) colloidal dispersions. The fiberoptic DLS or fiberoptical quasielastic light scattering (FOQELS) was proposed by Tanaka and Benedek [1066] and has undergone substantial development during the last years [1067–1071]. In this method, an optical fiber is applied to guide the incident beam toward the suspension and to collect the scattered light. Since the same fiber is used for particle illumination and for collecting the scattered light, the optical path is the shortest possible, and the contribution of the multiple scattering is enormously reduced. The main problem with the first versions of FOQELS equipment was that the detected signal presented a superposition of homodyne and heterodyne components, the second being created by the light reflected from the front face of the optical fiber [1072]. The relative contribution of the homodyne component increased with the particle concentration and this lead to ambiguity in data interpretation. Several improvements were proposed [1073–1075] to avoid the detection of this backward reflected light. A schematic of the version developed by Wiese and Horn [1074] is shown in Figure 7.84. The laser beam 1 enters the fiber optic Y-coupler and illuminates the particles through fiber 2, which is submerged in the dispersion. The backscattered light reenters optical fiber 2 and through fiber 3 reaches the detector. The front face of the optical fiber is inclined at an angle of 10° with respect to the optical axis, in order to reduce the intensity of the back-reflected beam, which otherwise would act as a local oscillator. With this equipment, very concentrated dispersions (up to 40%) can be studied [1074]. Another type of miniaturized fiber probe, comprising two optical fibers (one for illumination, and the other one for receiving the scattered light), was proposed for in situ process control by Dhadwal et al. [1075] The use of single-mode fibers (whose core diameter is of the order of the light wavelength) is another innovation which facilitates the data interpretation in FOQELS experiments [1074,1075]. In the last years, the fiber optic DLS transformed into a useful tool for studying concentrated particle dispersions.

The diffusing wave spectroscopy (DWS) [1076–1079] is another useful technique for studying the dynamics of opaque dispersions. The key feature of the DWS experiment is the measurement of the autocorrelation function $g^{(2)}(\tau)$ of a light that has undergone multiple scattering. Both configurations, forward scattering and backward scattering, were studied (see Figure 7.85). To derive a theoretical expression for $g^{(2)}(\tau)$, the transport of light in the concentrated dispersion is considered [1078,1079] as a diffusion process (this explains the term "diffusion wave spectroscopy"). The path of each photon in the dispersion is modeled by random, multiple scattering from a sequence of particles. The attenuation of the temporal light correlation due to the Brownian motion of the particles is calculated for each light path. The contributions of all paths are then summed up (by using appropriate averaging procedure) to calculate the autocorrelation function. Therefore, it is essential to have many scattering events for each photon before its detection by the photomultiplier. In this multiple scattering regime, the characteristic time is determined by the cumulative effect of many particles and is much shorter, compared to the single scattering regime [1079].
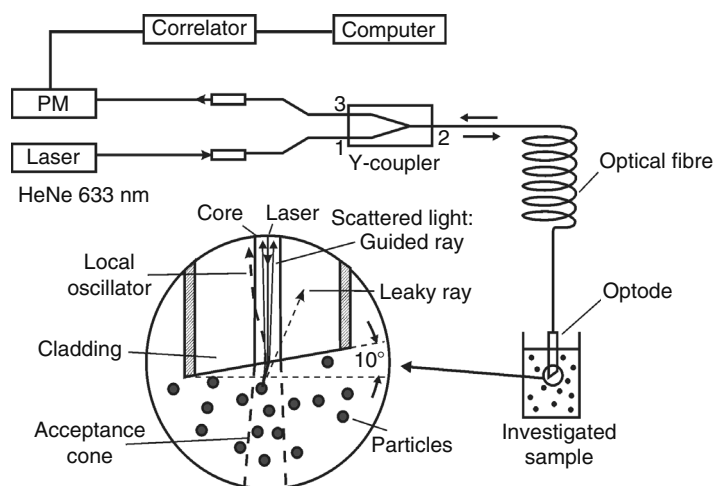
FIGURE 7.84 Schematics of experimental setup for fiber-optic DLS. Laser beam 1 illuminates the particles through the *Y*-coupler and fiber 2, which is submerged in the dispersion. The backscattered light reenters fiber 2, and through fiber 3 it reaches the detector. The front face of fiber 2 is cut at 10° with respect to the optical axis (the inset) to reduce the intensity of the back-reflected beam, which otherwise would act as a local oscillator reaching the detector. (Modified from Wiese, H. and Horn, D., *J. Chem. Phys.*, 94, 6429, 1991. With permission.)

Thus, the time scale in this experiment is much faster, and the particle motion is studied over length scales much smaller than λ. The experimental equipment for DWS is practically the same as that for conventional DLS. The main difficulties with the method arise when the autocorrelation function must be interpreted to extract information about the particle dynamics. The method was applied [1079–1090] to several complex colloidal systems (liquid-like concentrated dispersions, colloidal crystals, foams, emulsions, particles in porous media and under shear) and many nontrivial results have been obtained.

7.9.3 APPLICATION OF LIGHT SCATTERING METHODS TO COLLOIDAL SYSTEMS

The aim of this section is to illustrate the most typical applications of LS methods to dispersions and micellar surfactant solutions.

7.9.3.1 Surfactant Solutions

7.9.3.1.1 Critical Micellization Concentration, Aggregation Number, Second Virial Coefficient

The application of LS methods for investigating micellar solutions started with the studies of Debye [1091]. He showed that from measurements of the turbidity as a function of the surfactant concentration one can determine the critical micellization concentration (CMC), the micellar mass (and the corresponding aggregation number, ν_a), and the second osmotic virial coefficient, A_2. For larger micelles, additional information about the micellar size and shape was obtained [1092]. Later numerous studies have provided valuable information about CMC, ν_a and A_2 for a variety of nonionic and ionic surfactants [1093–1098]. Currently SLS is a routine method for determination of these quantities. Nevertheless, the information obtained by SLS from micellar solutions must be handled with some care [1099–1101], because one of the main assumptions of the SLS
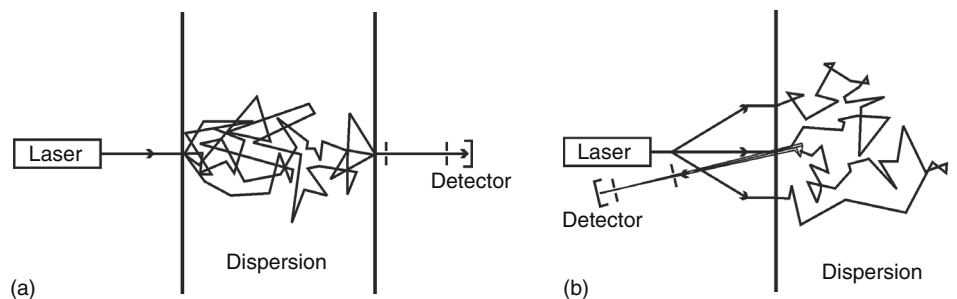
FIGURE 7.85 Diffusion wave spectroscopy (DWS). The light reaches the detector after multiple acts of scattering from dispersed particles. The optical path of the light in the dispersion is modeled as a result of random diffusion motion. Forward (a) or backward (b) scattered light can be analyzed.

theory (i.e., that the properties of the micelles, ν_a and A_2, remain constant with the micellar concentration) was shown to be not entirely fulfilled for these systems. This is particularly important for more concentrated surfactant solutions, where transitions in micellar size and shape may take place.

7.9.3.1.2 Diffusion Coefficient, Size, Shape, and Polydispersity of Micelles

DLS has the advantage that valuable information about the micellar diffusion coefficient [1102], D, and hydrodynamic radius, R_h, could be obtained at fixed surfactant concentration. Moreover, the effect of intermicellar interactions is less pronounced for the values of D and R_h, than the values measured by SLS. The combination of SLS and DLS allows one to determine the size, shape and polydispersity of micelles. Such systematic studies [1050,1102,1103] were performed for SDS micelles at large ionic strength (0.15–0.6 M NaCl) and variable temperature (10°C–85°C) to reveal the transition from small spherical to large rod-shaped micelles. A comparison of $\langle R_g \rangle$ (determined by SLS) with R_h (determined by DLS) was used to verify the rod-like shape of micelles. More refined analyzes [1104–1106] included the effects of the micellar polydispersity and flexibility of the rod-like micelles. The persistent length of the SDS rods was determined [1102] to be $\sim$70 nm; of cetylpyridinum bromide rods [1107,1108], $\sim$25–40 nm; of hexadecyltrimethylammonium salicylate [1109], $\sim$100–150 nm; of sodium dodecyl dioxyethylenesulfate [1110], $\sim$165–190 nm. Such studies provide data which are used as a test of the thermodynamic theories of the growth of rod-like micelles [1111].

7.9.3.1.3 Intermicellar Interactions

The concentration dependencies of $R(\theta)$ and D_{EFF} were used [1050,1112–1114] to investigate the interactions between SDS micelles at different electrolyte concentrations. Corti an Degiorgio [1050] interpreted the measured values of A_2 and λ_C by using a model accounting for the electrostatic repulsion and van der Waals attraction between the micelles. In this way, the Hamaker constant and the micellar charge were determined. The assumption that the micelles do not change in size and shape in the studied range of electrolyte concentrations was questioned later by Mazer [1102]. Indeed, Corti and Degiorgio [1050] and Dorshow et al. [1112] needed a rather large value of the Hamaker constant to describe the attraction between the micelles. Several other studies [1052,1113,1114] were directed to determine the micellar charge and its variation with the electrolyte concentration; however; some of them were based on approximated formulae for the electrostatic interaction energy between the micelles, assuming low electrical surface potential. The typical surface potential of SDS micelles is [1115] $\sim$60 to 70 mV, and more complex and rigorous approaches [1041,1116] must be used to describe correctly the electrostatic interaction. The accumulated LS data suggests that very often the observed concentration dependencies present a result of the combined action of intermicellar interactions and changes of the micellar size and shape. Mazer [1102] concludes that for SDS micelles the intermicellar interactions prevail only at low and moderate electrolyte concentrations ($\leq$0.2 M NaCl).

A combination of SLS and DLS methods was used [1117] to investigate the behavior of nonionic micellar solutions in the vicinity of their cloud point. It had been known for many years that at a high temperature the micellar solutions of polyoxyethylene-alkyl ether surfactants (C_nEO_m) separate into two isotropic phases. The solutions become opalescent with the approach of the cloud point, and several different explanations of this phenomenon were proposed. Corti and Degiorgio [1117] measured the temperature dependence of D_{EFF} and $\langle I_S \rangle_t$ and found that they can be described as a result of critical phase separation, connected with intermicellar attraction and long-range fluctuations in the local micellar concentration. Far from the cloud point, the micelles of nonionic surfactants with a large number of ethoxy-groups ($m \sim 30$) may behave as hard spheres [422].

7.9.3.1.4 Microemulsions

Microemulsions are another type of system which has been intensively studied by LS methods [1002–1007,1118–1121]. Vrij and coworkers [1002,1118] used SLS to determine the volume of water-in-oil microemulsion droplets and the second osmotic virial coefficient. Two interesting conclusions from their studies were drawn [1118]: (1) the van der Waals forces between the water cores of the droplets (if considered to be nondeformable spheres) are too weak to explain the observed strong attraction, and (2) the minimal distance between the centers of mass of two droplets upon collision is smaller than the droplet diameter. Similar observations were made by other authors and were explained by using several different models. Calje et al. [1118] and Lemaire et al. [1119] assumed that the aforementioned effects were due to mutual overlap of the surfactant monolayers covering the droplets. Denkov et al. [1006] argued that the droplets may deform upon collision and showed that the attraction between deformable droplets is stronger compared to that between hard spheres of the same Hamaker constant. Auvrey [1122] and Fletcher et al. [1123,1124] attributed the observed effects to the coalescence (fusion) of some fraction of the droplets. The droplet fusion also could be connected to the observed [1125,1126] sharp increase of the electric conductivity of water-in-oil microemulsions at a given threshold value of the droplet volume fraction (percolation model) and to the observed [1127] exchange of water-soluble fluorescent probes between droplets. The presence of droplet aggregates was demonstrated [1128,1129] by electro-optic birefringence, and their lifetime was estimated in some cases. Although a number of other experimental methods were invoked to analyze the structure and dynamics of microemulsions, the nature of the interdroplet interactions is by no means well understood [1007]. A critical behavior of microemulsions was observed [1130] at certain conditions.

LS methods (often in combination with other experimental methods) are widely used for the investigation of complex surfactant systems such as mixed micelles [1131,1132], block copolymer micelles [1133,1134], iridescent lamellar phases [1135,1136], complexes between micelles and polymers [1137–1140], aggregates of biosurfactants [1141–1143] (micelles and vesicles), and many others.

The scattering of light from interfaces [1144,1145] and thin liquid films [1146,1147] provides other possibilities for studying surfactant systems. LS from interfaces covered with surfactant monolayers allowed investigation of the interfacial tension and of the rheological properties of the monolayers. Such measurements were successfully applied [1144] for measurement of ultralow interfacial tension, as well as the bending constant of surfactant monolayers in microemulsion systems. SLS and DLS from liquid films were used [1146,1147] for measurement of the interaction forces between the film surfaces as a function of the film thickness.

7.9.3.2   Dispersions

7.9.3.2.1   Size, Shape, and Polydispersity of Particles

The classical application of SLS to dispersions is for determination of the particle size, shape and polydispersity [967,968]. Earlier studies were restricted to diluted samples of noninteracting particles with size comparable to the light wavelength. Substantial progress has been achieved during the last decades in the application of LS methods to more difficult samples. The invention of DLS allowed the precise determination of particle size in the nanometer range. On the other side, the application of the laser diffraction method [997,1148] extended the upper limit of measurable particle size up to several hundred micrometers. A variety of theoretical procedures has been proposed [1023–1031] to solve the inverse scattering problem and to determine more reliably the particle size distribution from LS data. Several theoretical approaches were developed to handle data from SLS [1149–1151] and DLS [1076–1081,1152] experiments on concentrated samples, where the multiple scattering is substantial. Alternatively, the cross-correlation techniques [1058–1065] and fiber optic probes were applied [1068–1075] to avoid the multiple scattering in concentrated suspensions. A new types of theories, based on extensive computer calculations, emerged in 1970s for description of the light scattering from large arbitrary shaped particles—the extended boundary condition method [1153,1154] (EBCM) and the coupled dipole method (CDM) [1155,1156]. All these new directions are rapidly developing and they substantially enlarge the area of application of LS methods.

7.9.3.2.2   Static and Dynamic Structure Factors

Static and dynamics LS experiments have played a very important role for a deeper understanding of the structure and dynamics of suspensions containing strongly interacting particles [1033,1157–1171]. A number of theoretical approaches, based on modern statistical theories, were proposed for calculation of the static and dynamic structure factors of monodisperse [1033,1042,1037–1039] and polydisperse suspensions [1172–1174]. The hydrodynamic and electrostatic interactions between charged particles have been subjects of particular interest. The experimentally attainable quantities, such as pair distribution function and effective diffusion coefficients, were used as test probes for the rapidly developing theories. The importance of different factors (particle and electrolyte concentrations, particle charge, etc.) for the phase transitions in suspensions have been systematically investigated. The liquid-like and colloidal crystal states were found to have distinct features, which can be quantitatively studied by LS experiments. An excellent review of this topic is given by Pusey and Tough [1033].

The kinetics of crystallization of colloidal suspensions at high particle concentration and/or low ionic strength is another phenomenon which has been the subject of intensive experimental studies [1165–1171,1175,1176]. The time scale of the crystallization process in suspensions is much slower (compared to that in atomic liquids), which makes it available for direct measurement by LS methods. The induction time, the crystallization rate, and the structure and size distribution of the growing crystallites have been studied as functions of different factors. The structure of the colloid crystals is conventionally studied by Bragg-diffraction [159,1165] or Kossel lines analysis [1167–1169].

Substantial interest has been raised the problem of the structure and dynamics of suspensions in shear hydrodynamic fields [1177–1185]. The experiments showed that both shear-induced melting and shear-induced ordering can be observed at different particle volume fractions and shear rates. The nonequilibrium microstructure of the suspension under shear can be investigated in these experiments and compared with the predictions from analytical theories and computer simulations.

7.9.3.2.3   Kinetics of Coagulation and Structure of the Formed Aggregates

During the last decade, a substantial progress has been achieved in our understanding of coagulation phenomenon (see also Section 7.6). Light scattering, electron microscopy, and other experimental methods [1186,1187], in combination with extensive numerical experiments and theoretical work [1188–1190], revealed that the aggregates formed upon the coagulation of colloidal particles have a fractal-type structure [1191], i.e., they exhibit size-scale invariance. The fractal dimension of the aggregates (which is a measure of their compactness) depends on the specific regime of aggregation. Two limiting regimes of colloid aggregation can be distinguished: diffusion-limited aggregation (DLA), which corresponds to barrierless (rapid) coagulation, and reaction-limited aggregation (RLA), in which the repulsive barrier in the pair interaction energy is around several kT (slow coagulation). In DLA, the coagulation rate is limited solely by the time between the collisions of the particles

due to the diffusion. In RLA, a large number of collisions is required before two particles can stick together, which leads to much slower aggregation rate. Computer simulations and analytical theories [1192] predict that for DLA the clusters formed have a fractal dimension $d_f \approx 1.8$ and the average mass of the aggregates must be a linear function of time [1193], $\langle M \rangle \propto t$ (see, e.g., Equation 7.339). In contrast, for RLA [1194,1195] $d_f \approx 2.1$ and $\langle M \rangle \propto \exp(k_a t)$ [1196], where the aggregation constant k_a depends on the sticking probability and the time between collisions. The size distribution of the formed aggregates is also different in the two regimes [1197]. All these theoretical predictions were verified [1198–1200] by SLS and DLS methods on colloid particles of different material (silica, polystyrene, gold, hematite). The results about the size distribution of the aggregates were scaled [1198] on a single master curve, whose shape was found to be independent of the regime of aggregation and the material of the particles. The fractal approach and the light scattering techniques have found also a wide application for analysis of the protein aggregation and the early stages of protein crystallization [1201–1205].

7.9.4 Recent Developments in Light Scattering Techniques

The aim of this section is to make a short overview of several, relatively new light scattering techniques, which have been rapidly developing during the last years. The recent progress in this area is driven mostly by (1) introduction of array detectors, which collect simultaneously information at large number of scattering angles, (2) significant development of the instrumentation for small scattering angles, and (3) application of new light sources, such as the light emitting diodes (LED) and superluminscent diodes (SLD) [1206]. The new methods widened the range of systems amenable to light scattering studies, with noticeable progress in the analysis of systems with high opacity, large characteristic structural scales (large particles and colloidal aggregates, polymer blends, biological cells), or exhibiting sudden dynamic events, such as the structural rearrangements in emulsions, foams, and granular media.

7.9.4.1 Opaque Systems

The opaque colloidal systems are widely spread and the LS techniques for studying such systems have been continuously evolving during the last decades.

The DWS, described in Section 7.9.2.5, has been steadily gaining popularity among the researchers, due to its relatively simple hardware and its unique ability to provide accurate information for highly turbid systems. Another important advantage of this technique is the possibility to study very small displacements of the scatterers (of the order of nanometers or even less), which makes the DWS particularly suitable for viscoelastic solids, such as glasses and gels.

The cross-correlation techniques are also developing, due to the possibility they provide for efficient filtering out of the multiply scattered light and analyzing only the remaining signal from the single-scattering events. The methods described in Section 7.9.2.5 were complemented with the ''single-beam two-detector'' technique [1232,1233], which is simpler for realization. This technique uses the fact that the single scattering events and the multiple scattering generate correlated areas (speckles) of different size—the single scattering generates larger speckles, whereas the multiple scattering generates smaller speckles. This circumstance allows one to position the two detectors, used in this method, at carefully chosen distance from the sample, for which the cross-correlation supresses significantly the multiple scattering.

The DWS is most suitable for very opaque systems, for which the signal comes predominantly from photons that are multiply scattered within the sample. In contrast, the cross-correlation techniques are useful when the signal from the single scattering events is significant (at least several percent from the total signal) and can be extracted by cross-correlation filtering. There are intermediate in opacity systems, for which neither of these extreme cases is realized, and other techniques should be applied. One class of such techniques is based on the use of low-coherence light source, such as the LEDs and superluminiscent diodes (SLDs). The interest to such light sources (giving intensive light with relatively wide wavelength peak) stems in the fact that interference fringes would appear only, if the path length difference between the scattered beams is smaller than the coherence length of the light, $l_C \approx \lambda^2 / \Delta\lambda$ (where $\Delta\lambda$ is the width of the spectrum of emitted light). Diodes with coherence length of 20–30 μm are commercially available and are particularly suitable for Low Coherence Interferometry (LCI), which has several variations [1239]. From these variations, one can use for structural studies the optical coherence tomography (OCT), which allows depth-resolved scattering experiments, with penetration into opaque samples up to 2 cm [1240]. The OCT is particularly appropriate for studying biological tissues and is used in medicine. For dynamic studies, the optical path length Spectroscopy (OPS) was developed [1239], which allows one to determine the probability distribution of photon path lengths within the sample, with a resolution $\approx l_C$. This method fills the gap of intermediate particle concentrations between the DWS and the classical single-scattering DLS.

7.9.4.2 Small Angle Light Scattering

The small angle light scattering (SALS) techniques have undergone rapid development during the last years, mostly due to the incorporation of charge-coupled devices (CCD) in the optical scheme of the detectors [1208–1212]. By using appropriate lens

behind the sample, one can focus the scattered light and the transmitted collimated beam in the focal plane of the lens (the so-called Fourier optics), which allows precise suppression of the collimated beam by placing circular obstacle (beam stop) in the focal plane. The resulting image is a 2D projection of the scattered intensity onto the focal plane, which can be collected by CCD detector. With this method, accurate SLS and DLS experiments can be performed, with scattering vectors in the range between 2×10^2 and 2×10^4 cm^{-1}.

An interesting new technique of this type, called near-field scattering (NFS), was recently developed by Giglio et al. [1213–1215,1222]. In this method, the scattered light is directly collected by CCD sensor, located at very small distance after the sample. The obtained image has a typical speckle appearance, with the speckle size corresponding to the size of the scatterers. The distribution of the light intensity $\langle I_S \rangle$ as a function of the scattering vector q is determined by Fourier analysis of this speckle image. The technique can be realized in homodyne or heterodyne mode. In the homodyne mode, the transmitted beam is removed by a beam stop, whereas in the heterodyne method, the interference between the transmitted beam and the scattered light is used to study the range of very small scattering angles. The heterodyne method has several important advantages and is preferred in practice [1216].

Typically, scattering angles of 0.01° to 10° can be covered with the SALS techniques, which correspond to probing relatively large lengthscales $2\pi q^{-1} \approx 1$–300 μm. Because of this specific advantage, SALS has found a wide application for particle sizing in pollution monitoring (for both aerosols and hydrosols), as well as in the studies of colloidal aggregates and gels, polymer blends, critical systems, emulsions, vesicles, and biological cells.

7.9.4.3 Multispeckle DLS

Several new methods were developed recently for studying solid-like systems, exhibiting dynamic relaxation (i.e., gradually evolving with time, such as aging gels), or systems undergoing sudden structural changes, such as slowly sheared emulsions, foams, and granular media [1248,1251,1253,1256,1258–1260]. A major problem for studying such systems is that the measured time-averaged quantities (such as the scattered intensity or the autocorrelation functions) differ from the ensemble-averaged ones, and the classical description assuming stationary or quasi-stationary processes is not always applicable.

One approach for analysis of such systems is based on using CCD detector, located at appropriate distance from the sample, so that the size of the projected speckle spots is matched with the size of the detector pixels [1209]. In this way, the CCD sensor becomes equivalent to a very large array of parallel light-intensity autocorrelators. The main limitation of such CCD-based detectors is the relatively long characteristic times that can be studied (>1 ms), which is rather restrictive as compared to the current fast autocorrelators (>10 ns). The sensitivity of the CCD sensors is also lower with respect to the intensity of the scattered light (as compared to the photon counters), so that stronger illumination is needed. These two drawbacks are usually not problematic in the SALS measurements, but create problems at large scattering angles.

In the speckle visibility spectroscopy (SVS), the contrast of a single CCD image of the speckle is investigated, as a function of the exposure time used to collect this image [1253]. All fluctuations in the sample with characteristic time shorter than the exposure time, blur the image and decrease the speckle contrast. Therefore, by varying the exposure time, the researcher could obtain information about the characteristic times of the system dynamics. Exposure times as short as 50 μs are achievable with relatively simple instrumentation, which makes the method convenient for various applications.

Echo-techniques (echo-DLS or echo-DWS) are based on different approach [1256,1258,1259]. In these techniques, usually a cylindrical sample is rotated rapidly. The shape of the correlation functions, determined after each revolution of the sample, brings information about the ensemble-averaged correlation function of the sample (and its change with time). A major advantage of the method is that the data can be recorded by using conventional LS instruments with simple modification. Another version of the echo-methods is based on using a two-cell geometry, with the advantage of recording the ensemble-averaged correlation function without rotating the sample, thus covering a very wide range of correlation times (down to 10 ns) with single experimental setup and almost in real time [1260].

For analysis of systems, whose evolution involves sudden intermittent changes (e.g., sheared foams, emulsions, pastes, and granular materials), the time resolved correlation (TRC) method was developed [1263–1265]. In this method, the correlation coefficient $c(t,\tau)$ is determined by multiplying two speckle images, recorded by area detector in the moments t and $(t+\tau)$. This coefficient brings quantitative information about the ensemble-averaged correlation in the system, as function of t and τ. For stationary processes, $c(t,\tau)$ does not depend on t, however, for intermittent processes $c(t,\tau)$ fluctuates. For example, the rearrangement of bubbles in foams leads to sudden jumps in the correlation coefficient $c(t,\tau)$, thus bringing information about the bubble dynamics. In an alternative method, the intermittent events are studied by determining the time-averaged four-order correlation function, $g^{(4)}(\tau)$ [1261,1262].

ACKNOWLEDGMENT

REFERENCES

1. Jungermann, E., *Cationic Surfactants*, Marcel Dekker, New York, 1970.
2. Lucassen-Reynders, E.H., *Anionic Surfactants—Physical Chemistry of Surfactant Action*, Marcel Dekker, New York, 1981.
3. Schick, M.J., *Nonionic Surfactants: Physical Chemistry*, Marcel Dekker, New York, 1986.
4. Gibbs, J.W., *The Scientific Papers of J.W. Gibbs*, Vol. 1, Dover, New York, 1961.
5. Ono, S. and Kondo, S., Molecular theory of surface tension in liquids, in *Handbuch der Physik*, Vol. 10, Flügge, S., Ed., Springer, Berlin, 1960.
6. Adamson, A.W. and Gast, A.P., *Physical Chemistry of Surfaces*, 6th edn., Wiley, New York, 1997.
7. Freundlich, H., *Colloid and Capillary Chemistry*, Methuen, London, 1926.
8. Langmuir, I., *J. Amer. Chem. Soc.*, 40, 1361, 1918.
9. Volmer, M., *Z. Physikal. Chem.*, 115, 253, 1925.
10. Frumkin, A., *Z. Physikal. Chem.*, 116, 466, 1925.
11. Hill, T.L., *An Introduction to Statistical Thermodynamics*, Addison-Wesley, Reading, MA, 1962.
12. Lucassen-Reynders, E.H., *J. Phys. Chem.*, 70, 1777, 1966.
13. Borwankar, R.P. and Wasan, D.T., *Chem. Eng. Sci.*, 43, 1323, 1988.
14. Derjaguin, B.V., *Theory of Stability of Colloids and Thin Liquid Films*, Plenum Press, Consultants Bureau, New York, 1989.
15. Shchukin, E.D., Pertsov, A.V., and Amelina, E.A., *Colloid Chemistry*, Moscow University Press, Moscow, 1982 (Russian); Elsevier, 2001 (English).
16. Zeldowitch, J., *Acta Physicochim. (USSR)*, 1, 961, 1934.
17. Halsey, G. and Taylor, H.S., *J. Chem. Phys.*, 15, 624, 1947.
18. Gurkov, T.G., Kralchevsky, P.A., and Nagayama, K., *Colloid Polym. Sci.*, 274, 227, 1996.
19. Butler, J.A.V., *Proc. Roy. Soc. Ser. A*, 135, 348, 1932.
20. Fainerman, V.B. and Miller, R., *Langmuir*, 12, 6011, 1996.
21. Vaughn, M.W. and Slattery, J.C., *J. Colloid Interface Sci.*, 195, 1, 1997.
22. Makievski, A.V., Fainerman, V.B., Bree, M., Wüstneck, R., Krägel, J., and Miller, R., *J. Phys. Chem. B*, 102, 417, 1998.
23. Landau, L.D. and Lifshitz, E.M., *Statistical Physics*, Part 1, Pergamon, Oxford, 1980.
24. Hachisu, S., *J. Colloid Interface Sci.*, 33, 445, 1970.
25. Kalinin, V.V. and Radke, C.J., *Colloids Surf. A*, 114, 337, 1996.
26. Warszyñski, P., Barzyk, W., Lunkenheimer, K., and Fruhner, H., *J. Chys Chem., B*, 102, 10948, 1998.
27. Kralchevsky, P.A., Danov, K.D., Broze, G., and Mehreteab, A., *Langmuir*, 15, 2351, 1999.
28. Prosser, A.J. and Frances, E.I., *Colloids Surf. A*, 178, 1, 2001.
29. Kirkwood, J.G. and Oppenheim, I., *Chemical Thermodynamics*, McGraw-Hill, New York, 1961.
30. Robinson, R.A. and Stokes, R.H., *Electrolyte Solutions*, Butterworths, London, 1959.
31. Gouy, G., *J. Phys. Radium*, 9, 457, 1910.
32. Davies, J. and Rideal, E., *Interfacial Phenomena*, Academic Press, New York, 1963.
33. Grahame, D.C., *Chem. Rev.*, 41, 441, 1947.
34. Israelachvili, J.N., *Intermolecular and Surface Forces*, Academic Press, London, 1992.
35. Kralchevsky, P.A. and Nagayama, K., *Particles at Fluid Interfaces and Membranes*, Elsevier, Amsterdam, The Netherlands, 2001.
36. Matijević, E. and Pethica, B.A., *Trans. Faraday Soc.*, 54, 1382, 1958.
37. van Voorst Vader, F., *Trans. Faraday Soc.*, 56, 1067, 1960.
38. Tajima, K., *Bul. Chem. Soc. Jpn*, 44, 1767, 1971.
39. Stern, O., *Ztschr. Elektrochem.*, 30, 508, 1924.
40. Tajima, K., Muramatsu, M., and Sasaki, T., *Bul. Chem. Soc. Jpn*, 43, 1991, 1970.
41. Tajima, K., *Bul. Chem. Soc. Jpn*, 43, 3063, 1970.
42. Kolev, V.L., Danov, K.D., Kralchevsky, P.A., Broze, G., and Mehreteab, A., *Langmuir*, 18, 9106, 2002.
43. Cross, A.W. and Jayson, G.G., *J. Colloid Interface Sci.*, 162, 45, 1994.
44. Johnson, S.B., Drummond, C.J., Scales, P.J., and Nishimura, S., *Langmuir*, 11, 2367, 1995.
45. Alargova, R.G., Danov, K.D., Petkov, J.T., Kralchevsky, P.A., Broze, G., and Mehreteab, A., *Langmuir*, 13, 5544, 1997.
46. Rathman, J.F. and Scamehorn, J.F., *J. Phys. Chem.*, 88, 5807, 1984.
47. Berr, S.S., Coleman, M.J., Marriot, J., and Johnson Jr., J.S., *J. Phys. Chem.*, 90, 6492, 1986.
48. Rosen, M.J., *Surfactants and Interfacial Phenomena*, Wiley, New York, 1989.
49. Clint, J., *Surfactant Aggregation*, Chapman & Hall, London, 1992.
50. Alargova, R.G., Danov, K.D., Kralchevsky, P.A., Broze, G., and Mehreteab, A., *Langmuir*, 14, 4036, 1998.
51. Dimov, N.K., Kolev, V.L., Kralchevsky, P.A., Lyutov, L.G., Brose, G., and Mehreteab, A., *J. Colloid Interface Sci.*, 256, 23, 2002.
52. Kralchevsky, P.A., Danov, K.D., Kolev, V.L., Broze, G., and Mehreteab, A., *Langmuir*, 19, 5004, 2003.
53. Danov, K.D., Kralchevsky, P.A., Ananthapadmanabhan, K.P., and Lips, A., *J. Colloid Interface Sci.*, 300, 809, 2006.
54. Lunkenheimer, K., Barzyk, W., Hirte, R., and Rudert, R., *Langmuir*, 19, 6140, 2003.
55. Christov, N.C., Danov, K.D., Kralchevsky, P.A., Ananthapadmanabhan, K.P., and Lips, A., *Langmuir*, 22, 7528, 2006.
56. Danov, K.D., Kralchevska, S.D., Kralchevsky, P.A., Broze, G., and Mehreteab, A., *Langmuir*, 19, 5019, 2003.
57. Danov, K.D., Kralchevska, S.D., Kralchevsky, P.A., Ananthapadmanabhan, K.P., and Lips, A., *Langmuir*, 20, 5445, 2004.
58. Valkovska, D.S., Shearman, G.C., Bain, C.D., Darton, R.C., and Eastoe, J., *Langmuir*, 20, 4436, 2004.

59. Day, J.P.R., Campbell, R.A., Russell, O.P., and Bain, C.D., *J. Phys. Chem. C*, 111, 8757, 2007.
60. Valkovska, D.S., Danov, K.D., and Ivanov, I.B., *Colloids Surf. A*, 175, 179, 2000.
61. Danov, K.D., Kralchevsky, P.A., and Ivanov, I.B., in *Encyclopedic Handbook of Emulsion Technology*, Sjöblom, J., Ed., Marcel Dekker, New York, 2001, Chapter 26.
62. Dukhin, S.S., Kretzschmar, G., and Miller, R., *Dynamics of Adsorption at Liquid Interfaces*, Elsevier, Amsterdam, The Netherlands, 1995.
63. Eastoe, J. and Dalton, J.S., *Adv. Colloid Interface Sci.*, 85, 103, 2000.
64. Lord, R., *Proc. Roy. Soc. (Lond.)*, 29, 71, 1879.
65. Bohr, N., *Phil. Trans. Roy. Soc. (Lond.)*, A, 209, 281, 1909.
66. Defay, R. and Pétré, G., Dynamic surface tension, in *Surface and Colloid Science*, Vol. 3, Matijević, E., Ed., Wiley, New York, 1971. p. 27.
67. Miller, R. and Kretzschmar, G., *Adv. Colloid Interface Sci.*, 37, 97, 1991.
68. Wantke, K.-D., Lunkenheimer, K., and Hempt, C., *J. Colloid Interface Sci.*, 159, 28, 1993.
69. Chang, C.-H. and Franses, E.I., *J. Colloid Interface Sci.*, 164, 107, 1994.
70. Johnson, D.O. and Stebe, K.J., *J. Colloid Interface Sci.*, 182, 525, 1996.
71. Horozov, T. and Arnaudov, L., *J. Colloid Interface Sci.*, 219, 99, 1999.
72. Horozov, T. and Arnaudov, L., *J. Colloid Interface Sci.*, 222, 146, 2000.
73. van den Tempel, M. and Lucassen-Reynders, E.H., *Adv. Colloid Interface Sci.*, 18, 281, 1983.
74. Langevin, D., *Colloids Surf.*, 43, 121, 1990.
75. Lemaire, C. and Langevin, D., *Colloids Surf.*, 65, 101, 1992.
76. Grigorev, D.O., Krotov, V.V., and Noskov, B.A., *Colloid J.*, 56, 562, 1994.
77. Mysels, K.J., *Colloids Surf.*, 43, 241, 1990.
78. Kralchevsky, P.A., Radkov, Y.S., and Denkov, N.D., *J. Colloid Interface Sci.*, 161, 361, 1993.
79. Fainerman, V.B., Miller, R., and Joos, P., *Colloid Polym. Sci.*, 272, 731, 1994.
80. Fainerman, V.B. and Miller, R., *J. Colloid Interface Sci.*, 176, 118, 1995.
81. Horozov, T.S., Dushkin, C.D., Danov, K.D., Arnaudov, L.N., Velev, O.D., Mehreteab, A., and Broze, G., *Colloids Surf. A*, 113, 117, 1996.
82. Mishchuk, N.A., Dukhin, S.S., Fainerman, V.B., Kovalchuk, V.I., and Miller, R., *Colloids Surf. A*, 192, 157, 2001.
83. van den Bogaert, R. and Joos, P., *J. Phys. Chem.*, 83, 17, 1979.
84. Möbius, D. and Miller, R., Eds., *Drops and Bubbles in Interfacial Research*, Elsevier, Amsterdam, The Netherlands, 1998.
85. Jho, C. and Burke, R., *J. Colloid Interface Sci.*, 95, 61, 1983.
86. Joos, P. and van Hunsel, J., *Colloid Polym. Sci.*, 267, 1026, 1989.
87. Fainerman, V.B. and Miller, R., *Colloids Surf. A*, 97, 255, 1995.
88. Miller, R., Bree, M., and Fainerman, V.B., *Colloids Surf. A*, 142, 237, 1998.
89. Senkel, O., Miller, R., and Fainerman, V.B., *Colloids Surf. A*, 143, 517, 1998.
90. Bain, C.D., Manning-Benson, S., and Darton, R.C., *J. Colloid Interface Sci.*, 229, 247, 2000.
91. Rotenberg, Y., Boruvka, L., and Neumann, A.W., *J. Colloid Interface Sci.*, 37, 169, 1983.
92. Makievski, A.V., Loglio, G., Krägel, J., Miller, R., Fainerman, V.B., and Neumann, A.W., *J. Phys. Chem.*, 103, 9557, 1999.
93. Joos, P., *Dynamic Surface Phenomena*, VSP BV, AH Zeist, The Netherlands, 1999.
94. Ward, A.F.H. and Tordai, L., *J. Chem. Phys.*, 14, 453, 1946.
95. Miller, R., *Colloid Polym. Sci.*, 259, 375, 1981.
96. McCoy, B.J., *Colloid Polym. Sci.*, 261, 535, 1983.
97. Hansen, R.S., *J. Chem. Phys.*, 64, 637, 1960.
98. Filippov, L.K., *J. Colloid Interface Sci.*, 164, 471, 1994.
99. Daniel, R. and Berg, J.C., *J. Colloid Interface Sci.*, 237, 294, 2001.
100. Sutherland, K.L., *Austr. J. Sci. Res.*, A5, 683, 1952.
101. Abramowitz, M. and Stegun, I.A., *Handbook of Mathematical Functions*, Dover, New York, 1965.
102. Korn, G.A. and Korn, T.M., *Mathematical Handbook*, McGraw-Hill, New York, 1968.
103. Danov, K.D., Kolev, V.L., Kralchevsky, P.A., Broze, G., and Mehreteab, A., *Langmuir*, 16, 2942, 2000.
104. Dukhin, S.S., Miller, R., and Kretzschmar, G., *Colloid Polym. Sci.*, 261, 335, 1983.
105. Dukhin, S.S. and Miller, R., *Colloid Polym. Sci.*, 272, 548, 1994.
106. MacLeod, C. and Radke, C.J., *Langmuir*, 10, 3555, 1994.
107. Vlahovska, P.M., Danov, K.D., Mehreteab, A., and Broze, G., *J. Colloid Interface Sci.*, 192, 194, 1997.
108. Danov, K.D., Vlahovska, P.M., Kralchevsky, P.A., Broze, G., and Mehreteab, A., *Colloids Surf. A*, 156, 389, 1999.
109. Diamant, H. and Andelman, D., *J. Phys. Chem.*, 100, 13732, 1996.
110. Diamant, H., Ariel, G., and Andelman, D., *Colloids Surf. A*, 259, 183–185, 2001.
111. Dattwani, S.S., and Stebe, K.J., *J. Colloid Interface Sci.*, 219, 282, 1999.
112. Danov, K.D., Kralchevsky, P.A., Ananthapadmanabhan, K.P., and Lips, A., *J. Colloid Interface Sci.*, 303, 56, 2006.
113. Nayfeh, A.H., *Perturbation Methods*, Wiley, New York, 1973.
114. Rillaerts, E., Joos, P., *J. Colloid Interface Sci.*, 88, 1, 1982.
115. Durbut, P., Surface activity, in *Handbook of Detergents*, Part A, Broze, G., Ed., Marcel Dekker, New York, 1999, Chapter 3.
116. Bond, W.N. and Puls, H.O., *Phil. Mag.*, 24, 864, 1937.

117. Doss, K.S.G., *Koll. Z.*, 84, 138, 1938.
118. Blair, C.M., *J. Chem. Phys.*, 16, 113, 1948.
119. Ward, A.F.H. and Tordai, L., *Surface Chemistry*, Butterworths Scientific Publications, London, 1949.
120. Dervichian, D.G., *Koll. Z.*, 146, 96, 1956.
121. Hansen, R.S. and Wallace, T., *J. Phys. Chem.*, 63, 1085, 1959.
122. Baret, J.F., *J. Phys. Chem.*, 72, 2755, 1968.
123. Baret, J.F., *J. Chem. Phys.*, 65, 895, 1968.
124. Baret, J.F., *J. Colloid Interface Sci.*, 30, 1, 1969.
125. Borwankar, R.P. and Wasan, D.T., *Chem. Eng. Sci.*, 38, 1637, 1983.
126. Danov, K.D., Valkovska, D.S., and Kralchevsky, P.A., *J. Colloid Interface Sci.*, 251, 18, 2002.
127. Dong, C., Hsu, C.-T., Chin, C.-Y., and Lin, S.-Y., *Langmuir*, 16, 4573, 2000.
128. Kresheck, G.C., Hamory, E., Davenport, G., and Scheraga, H.A., *J. Am. Chem. Soc.*, 88, 246, 1966.
129. Aniansson, E.A.G. and Wall, S.N., *J. Phys. Chem.*, 78, 1024, 1974.
130. Lucassen, J., *Faraday Discuss. Chem. Soc*, 59, 76, 1975.
131. Noskov, B.A., *Kolloidn. Zh.*, 52, 509, 1990.
132. Johner, A. and Joanny, J.F., *Macromolecules*, 23, 5299, 1990.
133. Dushkin, C.D., Ivanov, I.B., and Kralchevsky, P.A., *Colloids Surf.*, 60, 235, 1991.
134. Joos, P. and van Hunsel, J., *Colloids Surf.*, 33, 99, 1988.
135. Li, B., Joos, P., and van Uffelen, M., *J. Colloid Interface Sci.*, 171, 270, 1995.
136. Geeraerts, G. and Joos, P., *Colloids Surf. A*, 90, 149, 1994.
137. Danov, K.D., Kralchevsky, P.A., Denkov, N.D., Ananthapadmanabhan, K.P., and Lips, A., *Adv. Colloid Interface Sci.*, 119, 1, 2006.
138. Danov, K.D., Kralchevsky, P.A., Denkov, N.D., Ananthapadmanabhan, K.P., and Lips, A., *Adv. Colloid Interface Sci.*, 119, 17, 2006.
139. Danov, K.D., Kralchevsky, P.A., Ananthapadmanabhan, K.P., and Lips, A., *Colloids Surf. A*, 143, 282–283, 2006.
140. McBain, J.W., *Colloidal Science*, D.C. Heat, Lexington, MA, 1950.
141. Christian, S.D. and Scamehorn, J.F., *Solubilization in Surfactant Aggregates*, Marcel Dekker, New York, 1995.
142. Miller, C.A., in *Handbook of Surface and Colloid Chemistry*, 1st edn., Birdi, K.S., Ed., CRC Press, Boca Raton, FL, 1997, p. 157.
143. Vasilescu, M., Caragheorgheopol, A., and Caldararu, H., *Adv. Colloid Interface Sci.*, 169, 89–90, 2001.
144. Carroll, B.J., *J. Colloid Interface Sci.*, 79, 126, 1981.
145. Kabalnov, A. and Weers, J., *Langmuir*, 12, 3442, 1996.
146. Weiss, J., Coupland, J.N., Brathwaite, D., and McClements, D.J., *Colloids Surf. A*, 121, 53, 1997.
147. Todorov, P.D., Kralchevsky, P.A., Denkov, N.D., Broze, G., and Mehreteab, A., *J. Colloid Interface Sci.*, 245, 371, 2002.
148. Kralchevsky, P.A. and Denkov, N.D., in *Molecular Interfacial Phenomena of Polymers and Biopolymers*, Chen, P., Ed., Woodhead, Cambridge, UK, 2005, Chapter 15, p. 538.
149. Sailaja, D., Suhasini, K.L., Kumar, S., and Gandhi, K.S., *Langmuir*, 19, 4014, 2003.
150. Chan, A.F., Evans, D.F., and Cussler, E.L., *AIChE J.*, 22, 1006, 1976.
151. Huang, C., Evans, D.F., and Cussler, E.L., *J. Colloid Interface Sci.*, 82, 499, 1981.
152. Shaeiwitz, J.A., Chan, A.F.-C., Cussler, E.L. and Evans, D.F., *J. Colloid Interface Sci.*, 84, 47, 1981.
153. Plucinski, P. and Nitsch, W., *J. Phys. Chem.*, 97, 8983, 1993.
154. Chen, B.-H., Miller, C.A., and Garrett, P.R., *Colloids Surf. A*, 128, 129, 1997.
155. Chen, B.-H., Miller, C.A., and Garrett, P.R., *Langmuir*, 14, 31, 1998.
156. Christov, N.C., Denkov, N.D., Kralchevsky, P.A., Broze, G., and Mehreteab, A., *Langmuir*, 18, 7880, 2002.
157. Kralchevsky, P.A., Denkov, N.D., Todorov, P.D., Marinov, G.S., Broze, G., and Mehreteab, A., *Langmuir*, 18, 7887, 2002.
158. Todorov, P.D., Marinov, G.S., Kralchevsky, P.A., Denkov, N.D., Durbut, P., Broze, G., and Mehreteab, A., *Langmuir*, 18, 7896, 2002.
159. Granek, R., *Langmuir*, 12, 5022, 1996.
160. Lawrence, A.S.C., *Discuss. Faraday Soc.*, 25, 51, 1958.
161. Lawrence, A.S.C., Bingham, A., Capper, C.B., and Hume, K., *J. Phys. Chem.*, 68, 3470, 1964.
162. Stowe, L.R. and Shaeiwitz, J.A., *J. Colloid Interface Sci.*, 90, 495, 1982.
163. Raterman, K.T. and Shaeiwitz, J.A., *J. Colloid Interface Sci.*, 98, 394, 1984.
164. Lim, J.-C. and Miller, C.A., *Langmuir*, 7, 2021, 1991.
165. Somasundaran, P. and Krishnakumar, S., *Colloids Surf. A*, 491, 123–124, 1997.
166. Ward, A.J., in *Solubilization in Surfactant Aggregates*, Christian, S.D. and Scamehorn, J.F., Eds., Marcel Dekker, New York, 1995, Chapter 7.
167. Nagarajan, R. and Ganesh, K., *J. Colloid Interface Sci.*, 184, 489, 1996.
168. Lebens, P.J.M. and Keurentjes, J.T.F., *Ind. Eng. Chem. Res.*, 35, 3415, 1996.
169. Xing, L. and Mattice, W.L., *Macromolecules*, 30, 1711, 1997.
170. Křiž, J., Masař, B., and Doskočilová, D., *Macromolecules*, 30, 4391, 1997.
171. Marinov, G., Michels, B., and Zana, R., *Langmuir*, 14, 2639, 1998.
172. Kositza, M.J., Bohne, C., Alexandridis, P.T., Hatton, T.A., and Holzwarth, J.F., *Langmuir*, 15, 322, 1999.
173. Walderhaug, H., *J. Phys. Chem. B*, 103, 3352, 1999.
174. Paterson, I.F., Chowdhry, B.Z., and Leharne, S.A., *Langmuir*, 15, 6178, 1999.
175. Bromberg, L. and Temchenko, M., *Langmuir*, 15, 8627, 1999.

176. Laplace, P.S., *Traité de mécanique céleste*, Suppléments au Livre X, 1805, 1806.
177. Bakker, G., Kapillatytät und oberflächenspannung, in *Handbuch der Experimentalphysik*, Band 6, Akademische Verlagsgesellschaft, Leipzig, 1928.
178. Princen, H.M., The equilibrium shape of interfaces, drops, and bubbles, in *Surface and Colloid Science*, Vol. 2, Matijevic, E., Ed., Wiley, New York, 1969, p. 1.
179. Finn, R., *Equilibrium Capillary Surfaces*, Springer-Verlag, New York, 1986.
180. Weatherburn, C.E., *Differential Geometry in Three Dimensions*, Cambridge University Press, Cambridge, 1930.
181. McConnell, A.J., *Application of Tensor Analysis*, Dover, New York, 1957.
182. Young, T., *Philos. Trans. Roy. Soc. Lond.*, 95, 55, 1805.
183. Jonson, R.E. and Dettre, R.H., Wettability and contact angles, in *Surface and Colloid Science*, Vol. 2, Matijevic, E., Ed., Wiley, New York, 1969, p. 85.
184. Starov, V.M., *Adv. Colloid Interface Sci.*, 39, 147, 1992.
185. Neumann, F., *Vorlesungen über die Theorie der Capillarität*, B.G. Teubner, Leipzig, 1894.
186. Ivanov, I.B., Kralchevsky, P.A., and Nikolov, A.D., *J. Colloid Interface Sci.*, 112, 97, 1986.
187. Hartland, S. and Hartley, R.W., *Axisymmetric Fluid–Liquid Interfaces*, Elsevier, Amsterdam, The Netherlands, 1976.
188. Kralchevsky, P.A., Eriksson, J.C., and Ljunggren, S., *Adv. Colloid Interface Sci.*, 48, 19, 1994.
189. Tachev, K.D., Angarska, J.K., Danov, K.D., and Kralchevsky, P.A., *Colloids Surf. B*, 19, 61, 2000.
190. Meunier, J. and Lee, L.T., *Langmuir*, 7, 1855, 1991.
191. Dan, N., Pincus, P., and Safran, S.A., *Langmuir*, 9, 2768, 1993.
192. Kralchevsky, P.A., Paunov, V.N., Denkov, N.D., and Nagayama, K., *J. Chem. Soc. Faraday Trans.*, 91, 3415, 1995.
193. Petsev, D.N., Denkov, N.D., and Kralchevsky, P.A., *J. Colloid Interface Sci.*, 176, 201, 1995.
194. De Gennes, P.G. and Taupin, C., *J. Phys. Chem.*, 86, 2294, 1982.
195. Concus, P., *J. Fluid Mech.*, 34, 481, 1968.
196. Kralchevsky, P.A., Ivanov, I.B., and Nikolov, A.D., *J. Colloid Interface Sci.*, 112, 108, 1986.
197. Abramowitz, M. and Stegun, I.A., *Handbook of Mathematical Functions*, Dover, New York, 1965.
198. Jahnke, E., Emde, F., and Lösch, F., *Tables of Higher Functions*, McGraw-Hill, New York, 1960.
199. Lo, L.L., *J. Fluid Mech.*, 132, 65, 1983.
200. Derjaguin, B.V., *Dokl. Akad. Nauk USSR*, 51, 517, 1946.
201. Scheludko, A., *Colloid Polymer Sci.*, 155, 39, 1957.
202. Sheludko, A., *Adv. Colloid Interface Sci.*, 1, 391, 1967.
203. Dimitrov, A.S., Kralchevsky, P.A., Nikolov, A.D., and Wasan, D.T., *Colloids Surf.*, 47, 299, 1990.
204. J. Plateau, Experimental and theoretical researches on the figures of equilibrium of a liquid mass withdrawn from the action of gravity, in *The Annual Report of the Smithsonian Institution*, Washington, DC, 1863, pp. 207–285.
205. J. Plateau, The figures of equilibrium of a liquid mass, in *The Annual Report of the Smithsonian Institution*, Washington, DC, 1864. pp. 338–369.
206. J. Plateau, *Statique Expérimentale et Théoretique des Liquides Soumis aux Seules Forces Moléculaires*, Gauthier-Villars, Paris, 1873.
207. Zettlemoyer, A.C., *Nucleation*, Marcel Dekker, New York, 1969.
208. Abraham, E.F., *Homogeneous Nucleation Theory*, Academic Press, New York, 1974.
209. Thomson, W. (Lord Kelvin), *Proc. Roy. Soc.*, 9, 225, 1858; *Phil. Mag.*, 17, 61, 1859.
210. Lupis, C.H.P., *Chemical Thermodynamics of Materials*, North Holland, New York, 1983.
211. Lifshitz, I.M. and Slyozov, V.V., *Zh. Exp. Theor. Fiz.*, 35, 479, 1958 (in Russian).
212. Wagner, C., *Z. Electrochem.*, 35, 581, 1961.
213. Kalhweit, M., *Faraday Discuss. Chem. Soc.*, 61, 48, 1976.
214. Parbhakar, K., Lewandowski, J., and Dao, L.H., *J. Colloid Interface Sci.*, 174, 142, 1995.
215. Kabalnov, A.S., Pertzov, A.V., and Shchukin, E.D., *Colloids Surf.*, 24, 19, 1987.
216. Kabalnov, A.S. and Shchukin, E.D., *Adv. Colloid Interface Sci.*, 38, 69, 1992.
217. McClements, D.J., Dungan, S.R., German, J.B., and Kinsela, J.E., *Food Hydrocolloids*, 6, 415, 1992.
218. Weiss, J., Coupland, J.N., and McClements, D.J., *J. Phys. Chem.*, 100, 1066, 1996.
219. Weiss, J., Canceliere, C., and McClements, D.J., *Langmuir*, 16, 6833, 2000.
220. Kabalnov, A.S., *Langmuir*, 10, 680, 1994.
221. Ivanov, I.B. and Kralchevsky, P.A., Mechanics and thermodynamics of curved thin liquid films, in *Thin Liquid Films*, Ivanov, I.B., Ed., Marcel Dekker, New York, 1988, p. 49.
222. Kralchevsky, P.A. and Ivanov, I.B., *J. Colloid Interface Sci.*, 137, 234, 1990.
223. Kralchevsky, P.A., Danov, K.D., and Ivanov, I.B., Thin liquid film physics, in *Foams: Theory, Measurements and Applications*, Prud'homme, R.K., Ed., Marcel Dekker, New York, 1995, p. 1.
224. Rusanov, A.I., *Phase Equilibria and Surface Phenomena*, Khimia, Leningrad, 1967 (Russian); *Phasengleichgewichte und Grenzflächenerscheinungen*, Akademie Verlag, Berlin, 1978 (German).
225. Derjaguin, B.V. and Kussakov, M.M., *Acta Physicochem. USSR*, 10, 153, 1939.
226. Exerowa, D. and Scheludko, A., *Bull. Inst. Chim. Phys. Bulg. Acad. Sci.*, 4, 175, 1964.
227. Mysels, K.J., *J. Phys. Chem.*, 68, 3441, 1964.
228. Exerowa, D., *Commun. Dept. Chem. Bulg. Acad. Sci.*, 11, 739, 1978.

229. Kruglyakov, P.M., Equilibrium properties of free films and stability of foams and emulsions, in *Thin Liquid Films*, Ivanov, I.B., Ed., Marcel Dekker, New York, 1988, p. 767.
230. Martynov, G.A. and Derjaguin, B.V., *Kolloidn. Zh.*, 24, 480, 1962.
231. Toshev, B.V. and Ivanov, I.B., *Colloid Polym. Sci.*, 253, 558, 1975.
232. Ivanov, I.B. and Toshev, B.V., *Colloid Polym. Sci.*, 253, 593, 1975.
233. Frumkin, A., *Zh. Phys. Khim. USSR*, 12, 337, 1938.
234. de Feijter, J.A., Thermodynamics of thin liquid films, in *Thin Liquid Films*, Ivanov, I.B., Ed., Marcel Dekker, New York, 1988, p. 1.
235. Kralchevsky, P.A. and Ivanov, I.B., *Chem. Phys. Lett.*, 121, 111, 1985.
236. Nikolov, A.D., Kralchevsky, P.A., Ivanov, I.B., and Dimitrov, A.S., *AIChE Symposium Ser.*, 252, 82, 82, 1986.
237. de Feijter, J.A. and Vrij, A., *J. Electroanal. Chem.*, 47, 9, 1972.
238. Kralchevsky, P.A. and Ivanov, I.B., *Chem. Phys. Lett.*, 121, 116, 1985.
239. Denkov, N.D., Petsev, D.N., and Danov, K.D., *J. Colloid Interface Sci.*, 176, 189, 1995.
240. Derjaguin, B.V., *Acta Physicochim. USSR*, 12, 181, 1940.
241. Princen, H.M. and Mason, S.G., *J. Colloid Sci.*, 20, 156, 1965.
242. Prins, A., *J. Colloid Interface Sci.*, 29, 177, 1969.
243. Clint, J.H., Clunie, J.S., Goodman, J.F., and Tate, J.R., *Nature (Lond.)*, 223, 291, 1969.
244. Yamanaka, T., *Bull. Chem. Soc. Jap.*, 48, 1755, 1975.
245. Princen, H.M., *J. Phys. Chem.*, 72, 3342, 1968.
246. Princen, H.M. and Frankel, S., *J. Colloid Interface Sci.*, 35, 186, 1971.
247. Scheludko, A., Radoev, B., and Kolarov, T., *Trans. Faraday Soc.*, 64, 2213, 1968.
248. Haydon, D.A. and Taylor, J.L., *Nature (Lond.)*, 217, 739, 1968.
249. Kolarov, T. and Zorin, Z.M., *Kolloidn. Zh.*, 42, 899, 1980.
250. Kruglyakov, P.M. and Rovin, Y.G., *Physical Chemistry of Black Hydrocarbon Films*, Nauka, Moskow, 1978 (in Russian).
251. Marinova, K.G., Gurkov, T.D., Dimitrova, T.D., Alargova, R.G., and Smith, D., *Langmuir*, 14, 2011, 1998.
252. Françon, M., *Progress in Microscopy*, Pergamon Press, London, 1961.
253. Beyer, H., *Theorie und Praxis der Interferenzmicroscopie*, Academische Verlagesellschaft, Leipzig, 1974.
254. Zorin, Z.M., *Kolloidn. Zh.*, 39, 1158, 1977.
255. Zorin, Z., Platikanov, D., Rangelova, N., and Scheludko, A., in *Surface Forces and Liquid Interfaces*, Derjaguin, B.V., Ed., Nauka, Moscow, 1983, p. 200 (in Russian).
256. Nikolov, A.D., Kralchevsky, P.A., and Ivanov, I.B., *J. Colloid Interface Sci.*, 112, 122, 1986.
257. Lobo, L.A., Nikolov, A.D., Dimitrov, A.S., Kralchevsky, P.A., and Wasan, D.T., *Langmuir*, 6, 995, 1990.
258. Dimitrov, A.S., Nikolov, A.D., Kralchevsky, P.A., and Ivanov, I.B., *J. Colloid Interface Sci.*, 151, 462, 1992.
259. Picard, G., Schneider, J.E., and Fendler, J.H., *J. Phys. Chem.*, 94, 510, 1990.
260. Picard, G., Denicourt, N., and Fendler, J.H., *J. Phys. Chem.*, 95, 3705, 1991.
261. Skinner, F.K., Rotenberg, Y., and Neumann, A.W., *J. Colloid Interface Sci.*, 130, 25, 1989.
262. Dimitrov, A.S., Kralchevsky, P.A., Nikolov, A.D., Noshi, H., and Matsumoto, M., *J. Colloid Interface Sci.*, 145, 279, 1991.
263. Hadjiiski, A., Dimova, R., Denkov, N.D., Ivanov, I.B., and Borwankar, R., *Langmuir*, 12, 6665, 1996.
264. Ivanov, I.B., Hadjiiski, A., Denkov, N.D., Gurkov, T.D., Kralchevsky, P.A., and Koyasu, S., *Biophys. J.*, 75, 545, 1998.
265. Nicolson, M.M., *Proc. Camb. Phil. Soc.*, 45, 288, 1949.
266. Chan, D.Y.C., Henry, J.D., and White, L.R., *J. Colloid Interface Sci.*, 79, 410, 1981.
267. Paunov, V.N., Kralchevsky, P.A., Denkov, N.D., Ivanov, I.B., and Nagayama, K., *J. Colloid Interface Sci.*, 157, 100, 1993.
268. Kralchevsky, P.A., Paunov, V.N., Ivanov, I.B., and Nagayama, K., *J. Colloid Interface Sci.*, 151, 79, 1992.
269. Kralchevsky, P.A., Paunov, V.N., Denkov, N.D., Ivanov, I.B., and Nagayama, K., *J. Colloid Interface Sci.*, 155, 420, 1993.
270. Kralchevsky, P.A. and Nagayama, K., *Langmuir*, 10, 23, 1994.
271. Kralchevsky, P.A. and Nagayama, K., *Adv. Colloid Interface Sci.*, 85, 145, 2000.
272. Denkov, N.D., Velev, O.D., Kralchevsky, P.A., Ivanov, I.B., Nagayama, K., and Yoshimura, H., *Langmuir*, 8, 3183, 1992.
273. Dimitrov, A.S., Dushkin, C.D., Yoshimura, H., and Nagayama, K., *Langmuir*, 10, 432, 1994.
274. Sasaki, M. and Hane, K., *J. Appl. Phys.*, 80, 5427, 1996.
275. Du, H., Chen, P., Liu, F., Meng, F.-D., Li, T.-J., and Tang, X.-Y., *Materials Chem. Phys.*, 51, 277, 1977.
276. Price, W.C., Williams, R.C., and Wyckoff, R.W.G., *Science*, 102, 277, 1945.
277. Cosslett, V.E. and Markham, R., *Nature*, 161, 250, 1948.
278. Horne, R.W. and Pasquali-Ronchetti, I., *J. Ultrastruct. Res.*, 47, 361, 1974.
279. Harris, J.R., *Micron Microscopica Acta*, 22, 341, 1991.
280. Yoshimura, H., Matsumoto, M., Endo, S., and Nagayama, K., *Ultramicroscopy*, 32, 265, 1990.
281. Yamaki, M., Higo, J., and Nagayama, K., *Langmuir*, 11, 2975, 1995.
282. Nagayama, K., *Colloids Surf. A*, 109, 363, 1996.
283. Burmeister, F., Schäfle, C., Keilhofer, B., Bechinger, C., Boneberg, J., and Leiderer, P., *Adv. Mater.*, 10, 495, 1998.
284. Xia, Y., Tien, J., Qin, D., and Whitesides, G.M., *Langmuir*, 12, 4033, 1996.
285. Lindström, H., Rensmo, H., Sodergren, S., Solbrand, A., and Lindquist, S.E., *J. Phys. Chem.*, 100, 3084, 1996.
286. Matsushita, S., Miwa, T., and Fujishima, A., *Langmuir*, 13, 2582, 1997.
287. Murray, C.B., Kagan, C.R., and Bawendi, M.G., *Science*, 270, 1335, 1995.

288. Jap, B.K., Zulauf, M., Scheybani, T., Hefti, A., Baumeister, W., Aebi, U., and Engel, A., *Ultramicroscopy*, 46, 45, 1992.
289. De Rossi, D., Ahluwalia, A., and Mulè, M., *IEEE Eng. Med. Biol.*, 13, 103, 1994.
290. Kralchevsky, P.A. and Denkov, N.D., *Cur. Opin. Colloid Interface Sci.*, 6, 383, 2001.
291. Gil, T., Ipsen, J.H., Mouritsen, O.G., Sabra, M.C., Sperotto, M.M., and Zuckermann, M.J., *Biochim. Biophys. Acta*, 1376, 245, 1998.
292. Mansfield, S.L., Gotch, A.J., and Harms, G.S., *J. Phys. Chem.*, *B*, 103, 2262, 1999.
293. Fisher, L.R. and Malloy, A.R., *Annu. Rep. Prog. Chem.*, Sect. C, 95, 373, 1999.
294. Kralchevsky, P.A., Paunov, V.N., and Nagayama, K., *J. Fluid Mech.*, 299, 105, 1995.
295. Camoin, C., Roussel, J.F., Faure, R., and Blanc, R., *Europhys. Lett.*, 3, 449, 1987.
296. Velev, O.D., Denkov, N.D., Paunov, V.N., Kralchevsky, P.A., and Nagayama, K., *Langmuir*, 9, 3702, 1993.
297. Dushkin, C.D., Kralchevsky, P.A., Yoshimura, H., and Nagayama, K., *Phys. Rev. Lett.*, 75, 3454, 1995.
298. Lucassen, J., *Colloids Surf.*, 65, 131, 1992.
299. Stamou, D., Duschl, C., and Johannsmann, D., *Phys. Rev.*, *E*, 62, 5263, 2000.
300. Kralchevsky, P.A., Denkov, N.D., and Danov, K.D., *Langmuir*, 17, 2001, 7694.
301. Danov, K.D., Kralchevsky, P.A., Naydenov, B.N., and Brenn, G., *J. Colloid Interface Sci.*, 287, 121, 2005.
302. Bowden, N., Terfort, A., Carbeck, J., and Whitesides, G.M., *Science*, 276, 233, 1997.
303. Bowden, N., Choi, I.S., Grzybowski, B.A., and Whitesides, G.M., *J. Am. Chem. Soc.*, 121, 5373, 1999.
304. Brown, A.B.D., Smith, C.G., and Rennie, A.R., *Phys. Rev. E*, 62, 951, 2000.
305. Loudet, J.C., Alsayed, A.M., Zhang, J., and Yodh, A.G., *Phys. Rev. Lett.*, 94, 018301, 2005.
306. Velikov, K.P., Durst, F., and Velev, O.D., *Langmuir*, 14, 1148, 1998.
307. Sur, J. and Pak, H.K., *J. Korean Phys. Soc.*, 38, 582, 2001.
308. Danov, K.D., Pouligny, B., Angelova, M.I., and Kralchevsky, P.A., in *Studies in Surface Science and Catalysis*, Vol. 132, Iwasawa, Y., Oyama, N., and Kunieda, H., Eds., Elsevier, Amsterdam, The Netherlands, 2001. p. 519.
309. Danov, K.D., Pouligny, B., and Kralchevsky, P.A., *Langmuir*, 17, 2001, 6599.
310. Kralchevsky, P.A., Paunov, V.N., Denkov, N.D., and Nagayama, K., *J. Colloid Interface Sci.*, 167, 47, 1994.
311. Velev, O.D., Denkov, N.D., Paunov, V.N., Kralchevsky, P.A., and Nagayama, K., *J. Colloid Interface Sci.*, 167, 66, 1994.
312. Petkov, J.T., Denkov, N.D., Danov, K.D., Velev, O.D., Aust, R., and Durst, F., *J. Colloid Interface Sci.*, 172, 147, 1995.
313. Danov, K.D., Aust, R., Durst, F., and Lange, U., *J. Colloid Interface Sci.*, 175, 36, 1995.
314. Petkov, J.T., Danov, K.D., Denkov, N.D., Aust, R., and Durst, F., *Langmuir*, 12, 2650, 1996.
315. Petkov, J.T., Gurkov, T.D., and Campbell, B.E., *Langmuir*, 17, 4556, 2001.
316. Danov, K.D., Kralchevsky, P.A., Ananthapadmanabhan, K.P., and Lips, A., *Langmuir*, 22, 106, 2006.
317. Danov, K.D., Kralchevsky, P.A., and Boneva, M.P., *Langmuir*, 20, 6139, 2004.
318. Aveyard, R., Clint, J.H., Nees, D., and Paunov, V.N., *Langmuir*, 16, 1969, 2000.
319. Nikolaides, M.G., Bausch, A.R., Hsu, M.F., Dinsmore, A.D., Brenner, M.P., Gay, C., and Weitz, D.A., *Nature*, 420, 299, 2002.
320. Danov, K.D., Kralchevsky, P.A., and Boneva, M.P., *Langmuir*, 22, 2653, 2006.
321. Danov, K.D. and Kralchevsky, P.A., *J. Colloid Interface Sci.*, 298, 213, 2006.
322. Aveyard, R., Binks, B.P., Clint, J.H., Fletcher, P.D.I., Horozov, T.S., Neumann, B., Paunov, V.N., Annesley, J., Botchway, S.W., Nees, D., Parker, A.W., Ward, A.D., and Burgess, A., *Phys. Rev. Lett.*, 88, 246102, 2002.
323. Horozov, T.S., Aveyard, R., Clint, J.H., and Binks, B.P., *Langmuir*, 19, 2822, 2003.
324. Horozov, T.S., Aveyard, R., Binks, B.P., and Clint, J.H., *Langmuir*, 21, 7407, 2005.
325. Horozov, T.S. and Binks, B.P., *Colloids Surf. A*, 267, 64, 2005.
326. Ray, M.A. and Li, J., *Advanced Materials*, 19, 2020, 2007.
327. Stancik, E.J., Kouhkan, M., and Fuller, G.G., *Langmuir*, 20, 90, 2004.
328. Labib, M.E. and Williams, R., *J. Colloid Interface Sci.*, 115, 330, 1987.
329. Philipse, A.P. and Vrij, A., *J. Colloid Interface Sci.*, 128, 121, 1989.
330. Langevin, D., *Chem. Phys. Chem.*, 4, 1057, 2003.
331. Foret, L. and Würger, A., *Phys. Rev. Lett.*, 92, 058302, 2004.
332. Oettel, M., Domínguez, A., and Dietrich, S., *Phys. Rev. E*, 71, 051401, 2005.
333. Oettel, M., Domínguez, A., and Dietrich, S., *Langmuir*, 22, 846, 2006.
334. Danov, K.D. and Kralchevsky, P.A., *Langmuir*, 22, 848, 2006.
335. Oettel, M., Domínguez, A., and Dietrich, S., *J. Phys. Condensed Matter*, 17, L337, 2005.
336. Würger, A. and Foret, L., *J. Phys. Chem. B*, 109, 16435, 2005.
337. Würger, A., *Europhys. Lett.*, 75, 978, 2006.
338. Gómez-Guzmán, O. and Ruiz-Garcia, J., *J. Colloid Interface Sci.*, 291, 1, 2005.
339. Chen, W., Tan, S., Ng, T.-K., Ford, W.T., and Tong, P., *Phys. Rev. Lett.*, 95, 218301, 2005.
340. Chen, W., Tan, S., Huang, Z., Ng, T.-K., Ford, W.T., and Tong, P., *Phys. Rev. E*, 74, 021406, 2006.
341. Ngai, T., Auweter, H., and Behrens, S.H., *Macromolecules*, 39, 8171, 2006.
342. Megens, M. and Aizenberg, J., *Nature*, 424, 1014, 2003.
343. Boneva, M.P., Christov, N.C., Danov, K.D., and Kralchevsky, P.A., *Phys. Chem. Chem. Phys.*, 9, 6371, 2007.
344. Derjaguin, B.V., Churaev, N.V., and Muller, V.M., *Surface Forces*, Plenum Press, Consultants Bureau, New York, 1987.
345. Derjaguin, B.V., *Kolloid Zeits.*, 69, 155, 1934.
346. Attard, P. and Parker, J.L., *J. Phys. Chem.*, 96, 5086, 1992.
347. Tabor, D. and Winterton, R.H.S., *Nature*, 219, 1120, 1968.

348. Keesom, W.H., *Proc. Amst.*, 15, 850, 1913.
349. Debye, P., *Physik*, 2, 178, 1920.
350. London, F., *Z. Physics*, 63, 245, 1930.
351. Hamaker, H.C., *Physics*, 4, 1058, 1937.
352. Usui, S., Sasaki, H., and Hasegawa, F., *Colloids Surf.*, 18, 53, 1986.
353. Lifshitz, E.M., *Soviet Phys. JETP (Engl. Transl.)*, 2, 73, 1956.
354. Dzyaloshinskii, I.E., Lifshitz, E.M., and Pitaevskii, L.P., *Adv. Phys.*, 10, 165, 1961.
355. Nir, S. and Vassilieff, C.S., Van der Waals interactions in thin films, in *Thin Liquid Films*, Ivanov, I.B., Ed., Marcel Dekker, New York, 1988, p. 207.
356. Danov, K.D., Petsev, D.N., Denkov, N.D., and Borwankar, R., *J. Chem. Phys.*, 99, 7179, 1993.
357. Casimir, H.R. and Polder, D., *Phys. Rev.*, 73, 360, 1948.
358. Mahanty, J. and Ninham, B.W., *Dispersion Forces*, Academic Press, New York, 1976.
359. Moelwyn-Hughes, E.A., *Physical Chemistry*, Pergamon Press, London, 1961, Chapter 21.
360. Langmuir, I., *J. Chem. Phys.*, 6, 873, 1938.
361. Tenchov, B.G. and Brankov, J.G., *J. Colloid Interface Sci.*, 109, 172, 1986.
362. Vassilieff, C.S., Tenchov, B.G., Grigorov, L.S., and Richmond, P., *J. Colloid Interface Sci.*, 93, 8, 1983.
363. Verwey, E.J.W. and Overbeek, J.T.G., *The Theory of Stability of Liophobic Colloids*, Elsevier, Amsterdam, The Netherlands, 1948.
364. Muller, V.M., *Kolloidn. Zh.*, 38, 704, 1976.
365. McCormack, D., Carnie, S.L., and Chan, D.Y.C., *J. Colloid Interface Sci.*, 169, 177, 1995.
366. Hogg, R., Healy, T.W., and Fuerstenau, D.W., *Trans. Faraday Soc.*, 62, 1638, 1966.
367. Usui, S., *J. Colloid Interface Sci.*, 44, 107, 1973.
368. Russel, W.B., Saville, D.A., and Schowalter, W.R., *Colloidal Dispersions*, University Press, Cambridge, 1989.
369. Debye, P. and Hückel, E., *Z. Phys.*, 24, 185, 1923.
370. McCartney, L.N. and Levine, S., *J. Colloid Interface Sci.*, 30, 345, 1969.
371. Derjaguin, B.V. and Landau, L.D., *Acta Physicochim. USSR*, 14, 633, 1941.
372. Efremov, I.F., Periodic colloidal structures, in *Colloid and Surface Science*, Vol. 8, Matijevic, E., Ed., Wiley, New York, 1976, p. 85.
373. Schulze, H., *J. Prakt. Chem.*, 25, 431, 1882.
374. Hardy, W.B., *Proc. Roy. Soc. (Lond.)*, 66, 110, 1900.
375. Guldbrand, L., Jönsson, B., Wennerström, H., and Linse, P., *J. Chem. Phys.*, 80, 2221, 1984.
376. Kjellander, R. and Marčelja, S., *J. Phys. Chem.*, 90, 1230, 1986.
377. Attard, P., Mitchell, D.J., and Ninham, B.W., *J. Chem. Phys.*, 89, 4358, 1988.
378. Attard, P., Mitchell, D.J., and Ninham, B.W., *J. Chem. Phys.*, 88, 4987, 1988.
379. Kralchevsky, P.A. and Paunov, V.N., *Colloids Surf.*, 64, 245, 1992.
380. Marra, J., *J. Phys. Chem.*, 90, 2145, 1986.
381. Marra, J., *Biophys. J.*, 50, 815, 1986.
382. Kjellander, R., Marčelja, S., Pashley, R.M., and Quirk, J.P., *J. Phys. Chem.*, 92, 6489, 1988.
383. Kjellander, R., Marčelja, S., Pashley, R.M., and Quirk, J.P., *J. Chem. Phys.*, 92, 4399, 1990.
384. Khan, A., Jönsson, B., and Wennerström, H., *J. Phys. Chem.*, 89, 5180, 1985.
385. Kohonen, M.M., Karaman, M.E., and Pashley, R.M., *Langmuir*, 16, 5749, 2000.
386. Paunov, V.N. and Kralchevsky, P.A., *Colloids Surf.*, 64, 265, 1992.
387. Tadros, T.F., Steric interactions in thin liquid films, in *Thin Liquid Films*, Ivanov, I.B., Ed., Marcel Dekker, New York, 1988, p. 331.
388. Patel, S.S. and Tirel, M., *Ann. Rev. Phys. Chem.*, 40, 597, 1989.
389. Ploehn, H.J. and Russel, W.B., *Adv. Chem. Eng.*, 15, 137, 1990.
390. de Gennes, P.G., *Scaling Concepts in Polymer Physics*, Cornell University Press, Ithaca, NY, 1979, Chapter 3.
391. Dolan, A.K. and Edwards, S.F., *Proc. Roy. Soc. (Lond.) A*, 337, 509, 1974.
392. Dolan, A.K. and Edwards, S.F., *Proc. Roy. Soc. (Lond.) A*, 343, 427, 1975.
393. de Gennes, P.G., *C.R. Acad. Sci. (Paris)*, 300, 839, 1985.
394. de Gennes, P.G., *Adv. Colloid Intrface Sci.*, 27, 189, 1987.
395. Alexander, S.J., *Physique*, 38, 983, 1977.
396. Taunton, H.J., Toprakcioglu, C., Fetters, L.J., and Klein, J., *Macromolecules*, 23, 571, 1990.
397. Klein, J. and Luckham, P., *Nature*, 300, 429, 1982. *Macromolecules*, 17, 1041, 1984.
398. Luckham, P.F. and Klein, J., *J. Chem. Soc. Faraday Trans.*, 86, 1363, 1990.
399. Sonntag, H., Ehmka, B., Miller, R., and Knapschinski, L., *Adv. Colloid Interface Sci.*, 16, 381, 1982.
400. Horn, R.G. and Israelachvili, J.N., *Chem. Phys. Lett.*, 71, 192, 1980.
401. Nikolov, A.D., Wasan, D.T., Kralchevsky, P.A., and Ivanov, I.B., Ordered structures in thinning micellar foam and latex films, in *Ordering and Organisation in Ionic Solutions*, Ise, N. and Sogami, I., Eds., World Scientific, Singapore, 1988.
402. Nikolov, A.D. and Wasan, D.T., *J. Colloid Interface Sci.*, 133, 1, 1989.
403. Nikolov, A.D., Kralchevsky, P.A., Ivanov, I.B., and Wasan, D.T., *J. Colloid Interface Sci.*, 133, 13, 1989.
404. Nikolov, A.D., Wasan, D.T., Denkov, N.D., Kralchevsky, P.A., and Ivanov, I.B., *Prog. Colloid Polym. Sci.*, 82, 87, 1990.
405. Wasan, D.T., Nikolov, A.D., Kralchevsky, P.A., and Ivanov, I.B., *Colloids Surf.*, 67, 139, 1992.
406. Asakura, S. and Oosawa, F., *J. Chem. Phys.*, 22, 1255, 1954. *J. Polym. Sci.*, 33, 183, 1958.
407. de Hek, H. and Vrij, A., *J. Colloid Interface Sci.*, 84, 409, 1981.

408. Snook, I.K. and van Megen, W., *J. Chem. Phys.*, 72, 2907, 1980.
409. Kjellander, R. and Marčelja, S., *Chem. Phys. Lett.*, 120, 393, 1985.
410. Tarazona, P. and Vicente, L., *Mol. Phys.*, 56, 557, 1985.
411. Evans, R. and Parry, A.O., *J. Phys. Condens. Matter*, 2, SA15, 1990.
412. Henderson, J.R., *Mol. Phys.*, 59, 89, 1986.
413. Henderson, D. and Lozada-Cassou, M., *J. Colloid Interface Sci.*, 114, 180, 1986.
414. Henderson, D., *J. Colloid Interface Sci.*, 121, 486, 1988.
415. Kjellander, R. and Sarman, S., *Chem. Phys. Lett.*, 149, 102, 1988.
416. Attard, P. and Parker, J.L., *J. Phys. Chem.*, 96, 5086, 1992.
417. Pollard, M.L. and Radke, C.J., *J. Chem. Phys.*, 101, 6979, 1994.
418. Chu, X.L., Nikolov, A.D., and Wasan, D.T., *Langmuir*, 10, 4403, 1994.
419. Chu, X.L., Nikolov, A.D., and Wasan, D.T., *J. Chem. Phys.*, 103, 6653, 1995.
420. Trokhymchuk, A., Henderson, D., Nikolov, A., and Wasan, D.T., *J. Phys. Chem. B*, 107, 3927, 2003.
421. Blawzdziewicz, J. and Wajnryb, E., *Europhysics Letters*, 71, 269, 2005.
422. Kralchevsky, P.A. and Denkov, N.D., *Chem. Phys. Lett.*, 240, 385, 1995. *Prog. Colloid Polymer Sci.*, 98, 18, 1995.
423. Trokhymchuk, A., Henderson, D., Nikolov, A., and Wasan, D.T., *Langmuir*, 17, 4940, 2001.
424. Carnahan, N.F. and Starling, K.E., *J. Chem. Phys.*, 51, 635, 1969.
425. Basheva, E.S., Kralchevsky, P.A., Danov, K.D., Ananthapadmanabhan, K.P., and Lips, A., *Phys. Chem. Chem. Phys.*, 9, 5183, 2007.
426. Mysels, K.J. and Jones, M.N., *Discuss. Faraday Soc.*, 42, 42, 1966.
427. Beresford-Smith, B. and Chan, D.Y.C., *Chem. Phys. Lett.*, 92, 474, 1982.
428. Richetti, P. and Kékicheff, P., *Phys. Rev. Lett.*, 68, 1951, 1992.
429. Bondy, C., *Trans. Faraday Soc.*, 35, 1093, 1939.
430. Patel, P.D. and Russel, W.B., *J. Colloid Interface Sci.*, 131, 192, 1989.
431. Aronson, M.P., *Langmuir*, 5, 494, 1989.
432. van Lent, B., Israels, R., Scheutjens, J.M.H.M., and Fleer, G.J., *J. Colloid Interface Sci.*, 137, 380, 1990.
433. Joanny, J.F., Leibler, L., and de Gennes, P.G., *J. Polym. Sci.*, 17, 1073, 1979.
434. Evans, E. and Needham, D., *Macromolecules*, 21, 1822, 1988.
435. Johnnott, E.S., *Phil. Mag.*, 70, 1339, 1906.
436. Perrin, R.E., *Ann. Phys.*, 10, 160, 1918.
437. Bruil, H.G. and Lyklema, J., *Nature*, 233, 19, 1971.
438. Friberg, S., Linden, S.E., and Saito, H., *Nature*, 251, 494, 1974.
439. Keuskamp, J.W. and Lyklema, J., *ACS Symp. Ser.*, 8, 191, 1975.
440. Kruglyakov, P.M., *Kolloidn. Zh.*, 36, 160, 1974.
441. Kruglyakov, P.M. and Rovin, Y.G., *Physical Chemistry of Black Hydrocarbon Films*, Nauka, Moscow, 1978 (in Russian).
442. Denkov, N.D., Yoshimura, H., Nagayama, K., and Kouyama, T., *Phys. Rev. Lett.*, 76, 2354, 1996.
443. Denkov, N.D., Yoshimura, H., and Nagayama, K., *Ultramicroscopy*, 65, 147, 1996.
444. Kralchevsky, P.A., Nikolov, A.D., Wasan, D.T., and Ivanov, I.B., *Langmuir*, 6, 1180, 1990.
445. Bergeron, V. and Radke, C.J., *Langmuir*, 8, 3020, 1992.
446. Bergeron, V., Jimenez-Laguna, A.I., and Radke, C.J., *Langmuir*, 8, 3027, 1992.
447. Parker, J.L., Richetti, P., and Kékicheff, P., *Phys. Rev. Lett.*, 68, 1955, 1992.
448. McNamee, C.E., Tsujii, Y., Ohshima, H., and Matsumoto, M., *Langmuir*, 20, 1953, 2004.
449. Krichevsky, O. and Stavans, J., *Phys. Rev. Lett.*, 74, 2752, 1995.
450. Bergeron, V. and Radke, C.J., *Colloid Polym. Sci.*, 273, 165, 1995.
451. Marinova, K.G., Gurkov, T.D., Dimitrova, T.D., Alargova, R.G., and Smith, D., *Langmuir*, 14, 2011, 1998.
452. Basheva, E.S., Nikolov, A.D., Kralchevsky, P.A., Ivanov, I.B., and Wasan, D.T., in *Surfactants in Solution*, Vol. 12, Mittal, K.L., and Shah, D.O., Eds., Plenum Press, New York, 1991. p. 467.
453. Basheva, E.S., Danov, K.D., and Kralchevsky, P.A., *Langmuir*, 13, 4342, 1997.
454. Dushkin, C.D., Nagayama, K., Miwa, T., and Kralchevsky, P.A., *Langmuir*, 9, 3695, 1993.
455. Sethumadhavan, G.N., Nikolov, A.D., and Wasan, D.T., *J. Colloid Interface Sci.*, 240, 105, 2001.
456. Koczo, K., Nikolov, A.D., Wasan, D.T., Borwankar, R.P., and Gonsalves, A., *J. Colloid Interface Sci.*, 178, 694, 1996.
457. Asnacios, A., Espert, A., Colin, A., and Langevin, D., *Phys. Rev. Lett.*, 78, 4974, 1997.
458. Bergeron, V. and Claesson, P.M., *Adv. Colloid Interface Sci.*, 96, 1, 2002.
459. Kolaric, B., Förster, S., and von Klitzing, R., *Progr. Colloid Polym. Sci.*, 117, 195, 2001.
460. von Klitzing, R. and Kolaric, B., *Tenside Surfactants Detergents*, 39, 247, 2002.
461. Stubenrauch, C. and von Klitzing, R., *J. Phys. Condens. Matter*, 15, R1197, 2003.
462. Beltran, C.M., Guillot, S., and Langevin, D., *Macromolecules*, 36, 8506, 2003.
463. Beltran, C.M. and Langevin, D., *Phys. Rev. Lett.*, 94, 217803, 2005.
464. Heinig, P., Beltran, C.M., and Langevin, D., *Phys. Rev. E*, 73, 051607, 2006.
465. Stanley, H.E. and Teixeira, J., *J. Chem. Phys.*, 73, 3404, 1980.
466. Israelachvili, J.N. and Adams, G.E., *J. Chem. Soc. Faraday Trans. 1*, 74, 975, 1978.
467. Israelachvili, J.N. and Pashley, R.M., *Nature*, 300, 341, 1982.
468. Pashley, R.M., *J. Colloid Interface Sci.*, 80, 153, 1981.

469. Pashley, R.M., *J. Colloid Interface Sci.*, 83, 531, 1981.
470. Healy, T.W., Homola, A., James, R.O., and Hunter, R.J., *Faraday Discuss. Chem Soc.*, 65, 156, 1978.
471. Marčelja, S. and Radič, N., *Chem. Phys Lett.*, 42, 129, 1976.
472. Schibi, D. and Ruckenstein, E., *Chem. Phys Lett.*, 95, 435, 1983.
473. Attard, P. and Batchelor, M.T., *Chem. Phys. Lett.*, 149, 206, 1988.
474. Jönsson, B. and Wennerström, H., *J. Chem. Soc. Faraday Trans. 2*, 79, 19, 1983.
475. Leikin, S. and Kornyshev, A.A., *J. Chem. Phys.*, 92, 6890, 1990.
476. Israelachvili, J.N. and Wennerström, H., *J. Phys. Chem.*, 96, 520, 1992.
477. Henderson, D. and Lozada-Cassou, M., *J. Colloid Interface Sci.*, 162, 508, 1994.
478. Basu, S. and Sharma, M.M., *J. Colloid Interface Sci.*, 165, 355, 1994.
479. Paunov, V.N., Dimova, R.I., Kralchevsky, P.A., Broze, G., and Mehreteab, A., *J. Colloid Interface Sci.*, 182, 239, 1996.
480. Booth, F., *J. Chem. Phys.*, 19, 391, 1951.
481. Bikerman, J.J., *Philos. Mag.*, 33, 384, 1942.
482. Rowlinson, J.S., Development of theories of inhomogeneous fluids, in *Fundamentals of Inhomogeneous Fluids*, Henderson, D., Ed., Marcel Dekker, New York, 1992.
483. Claesson, P., Carmona-Ribeiro, A.M., and Kurihara, K., *J. Phys. Chem.*, 93, 917, 1989.
484. Horn, R.G., Smith, D.T., and Haller, W., *Chem. Phys. Lett.*, 162, 404, 1989.
485. Tchaliovska, S., Herder, P., Pugh, R., Stenius, P., and Eriksson, J.C., *Langmuir*, 6, 1535, 1990.
486. Pashley, R.M., McGuiggan, P.M., Ninham, B.W., and Evans, D.F., *Science*, 229, 1088, 1985.
487. Rabinovich, Y.I. and Derjaguin, B.V., *Colloids Surf.*, 30, 243, 1988.
488. Parker, J.L., Cho, D.L., and Claesson, P.M., *J. Phys. Chem.*, 93, 6121, 1989.
489. Christenson, H.K., Claesson, P.M., Berg, J., and Herder, P.C., *J. Phys. Chem.*, 93, 1472, 1989.
490. Christenson, H.K., Fang, J., Ninham, B.W., and Parker, J.L., *J. Phys. Chem.*, 94, 8004, 1990.
491. Ducker, W.A., Xu, Z., and Israelachvili, J.N., *Langmuir*, 10, 3279, 1994.
492. Eriksson, J.C., Ljunggren, S., and Claesson, P.M., *J. Chem. Soc. Faraday Trans. 2*, 85, 163, 1989.
493. Joesten, M.D. and Schaad, L.J., *Hydrogen Bonding*, Marcel Dekker, New York, 1974.
494. Stillinger, F.H. and Ben-Naim, A., *J. Chem. Phys.*, 47, 4431, 1967.
495. Conway, B.E., *Adv. Colloid Interface Sci.*, 8, 91, 1977.
496. Kuzmin, V.L. and Rusanov, A.I., *Kolloidn. Z.*, 39, 455, 1977.
497. Dubrovich, N.A., *Kolloidn. Z.*, 57, 275, 1995.
498. Eriksson, J.C., Henriksson, U., and Kumpulainen, A., *Colloids Surf. A*, 79, 282–283, 2006.
499. Paunov, V.N., Sandler, S.I., and Kaler, E.W., *Langmuir*, 17, 4126, 2001.
500. Angarska, J.K., Dimitrova, B.S., Danov, K.D., Kralchevsky, P.A., Ananthapadmanabhan, K.P., and Lips, A., *Langmuir*, 20, 1799, 2004.
501. Christenson, H.K. and Claesson, P.M., *Science*, 239, 390, 1988.
502. Parker, J.L., Claesson, P.M., and Attard, P., *J. Phys. Chem.*, 98, 8468, 1994.
503. Carambassis, A., Jonker, L.C., Attard, P., and Rutland, M.W., *Phys. Rev. Lett.*, 80, 5357, 1998.
504. Mahnke, J., Stearnes, J., Hayes, R.A., Fornasiero, D., and Ralston, J., *Phys. Chem. Chem. Phys.*, 1, 2793, 1999.
505. Considine, R.F., Hayes, R.A., and Horn, R.G., *Langmuir*, 15, 1657, 1999.
506. Considine, R.F. and Drummond, C., *Langmuir*, 16, 631, 2000.
507. Attard, P., *Langmuir*, 16, 4455, 2000.
508. Yakubov, G.E., Butt, H.-J., and Vinogradova, O., *J. Phys. Chem. B*, 104, 3407, 2000.
509. Ederth, T., *J. Phys Chem. B*, 104, 9704, 2000.
510. Ishida, N., Sakamoto, M., Miyahara, M., and Higashitani, K., *Langmuir*, 16, 5681, 2000.
511. Ishida, N., Inoue, T., Miyahara, M., and Higashitani, K., *Langmuir*, 16, 6377, 2000.
512. Tanford, C., *The Hydrophobic Effect*, Wiley, New York, 1980.
513. Leckband, D.E., Israelachvili, J.N., Schmitt, F.-J., and Knoll, W., *Science*, 255, 1419, 1992.
514. Helfrich, W., *Z. Naturforsch.*, 33a, 305, 1978.
515. Servuss, R.M. and Helfrich, W., *J. Phys.* (*France*), 50, 809, 1989.
516. Fernandez-Puente, L., Bivas, I., Mitov, M.D., and Méléard, P., *Europhys. Lett.*, 28, 181, 1994.
517. Safinya, C.R., Roux, D., Smith, G.S., Sinha, S.K., Dimon, P., Clark, N.A., and Bellocq, A.M., *Phys. Rev. Lett.*, 57, 2718, 1986.
518. McIntosh, T.J., Magid, A.D., and Simon, S.A., *Biochemistry*, 28, 7904, 1989.
519. Abillon, O. and Perez, E., *J. Phys.* (*France*), 51, 2543, 1990.
520. Evans, E.A. and Skalak, R., *Mechanics and Thermodynamics of Biomembranes*, CRC Press, Boca Raton, FL, 1980.
521. Aniansson, G.A.E., Wall, S.N., Almgren, M., Hoffman, H., Kielmann, I., Ulbricht, W., Zana, R., Lang, J., and Tondre, C., *J. Phys. Chem.*, 80, 905, 1976.
522. Aniansson, G.A.E., *J. Phys. Chem.*, 82, 2805, 1978.
523. Dimitrova, T.D., Leal-Calderon, F., Gurkov, T.D., and Campbell, B., *Langmuir*, 17, 8069, 2001.
524. Danov, K.D., Ivanov, I.B., Ananthapadmanabhan, K.P., and Lips, A., *Adv. Colloid Interface Sci.*, 185, 128–130, 2006.
525. Bird, R.B., Stewart, W.E., and Lightfoot, E.N., *Transport Phenomena*, Wiley, New York, 1960.
526. Germain, P., *Mécanique des Milieux Continus*, Masson et Cie, Paris, 1962.
527. Batchelor, G.K., *An Introduction of Fluid Mechanics*, Cambridge University Press, London, 1967.

528. Slattery, J.C., *Momentum, Energy, and Mass Transfer in Continua*, R.E. Krieger, Huntington, New York, 1978.
529. Landau, L.D. and Lifshitz, E.M., *Fluid Mechanics*, Pergamon Press, Oxford, 1984.
530. Barnes, H.A., Hutton, J.F., and Walters, K., *An Introduction to Rheology*, Elsevier, Amsterdam, The Netherlands, 1989.
531. Walters, K., Overview of macroscopic viscoelastic flow, in *Viscoelasticity and Rheology*, Lodge, A.S., Renardy, M., and Nohel, J.A., Eds., Academic Press, London, 1985. p. 47.
532. Boger, D.V., *Ann. Rev. Fluid Mech.*, 19, 157, 1987.
533. Barnes, H.A., *J. Rheol.*, 33, 329, 1989.
534. Navier, M., *Mém. de l'Acad. d. Sci.*, 6, 389, 1827.
535. Stokes, G.G., *Trans. Cambr. Phil. Soc.*, 8, 287, 1845.
536. Happel, J. and Brenner, H., *Low Reynolds Number Hydrodynamics with Special Applications to Particulate Media*, Prentice-Hall, Englewood Cliffs, New York, 1965.
537. Kim, S. and Karrila, S.J., *Microhydrodynamics: Principles and Selected Applications*, Butterworth-Heinemann, Boston, 1991.
538. Reynolds, O., *Phil. Trans. Roy. Soc. (Lond.)*, A177, 157, 1886.
539. Lamb, H., *Hydrodynamics*, Cambridge University Press, London, 1963.
540. Felderhof, B.U., *J. Chem. Phys.*, 49, 44, 1968.
541. Sche, S. and Fijnaut, H.M., *Surface Sci.*, 76, 186, 1976.
542. Maldarelli, C. and Jain, R.K., The hydrodynamic stability of thin films, in *Thin Liquid Films*, Ivanov, I.B., Ed., Marcel Dekker, New York, 1988, p. 497.
543. Valkovska, D.S. and Danov, K.D., *J. Colloid Interface Sci.*, 241, 400, 2001.
544. Hardy, W. and Bircumshaw, I., *Proc. Roy. Soc. (Lond.)*, A108, 1, 1925.
545. Horn, R.G., Vinogradova, O.I., Mackay, M.E., and Phan-Thien, N., *J. Chem. Phys.*, 112, 6424, 2000.
546. Dimitrov, D.S. and Ivanov, I.B., *J. Colloid Interface Sci.*, 64, 97, 1978.
547. Ivanov, I.B., Dimitrov, D.S., Somasundaran, P., and Jain, R.K., *Chem. Eng. Sci.*, 40, 137, 1985.
548. Ivanov, I.B. and Dimitrov, D.S., Thin film drainage, in *Thin Liquid Films*, Ivanov, I.B., Ed., Marcel Dekker, New York, 1988, p. 379.
549. Danov, K.D., Kralchevsky, P.A., and Ivanov, I.B., in *Handbook of Detergents, Part A: Properties*, Broze, G., Ed., Marcel Dekker, New York, 1999, p. 303.
550. O'Neill, M.E. and Stewartson, K., *J. Fluid Mech.*, 27, 705, 1967.
551. Goldman, A.J., Cox, R.G., and Brenner, H., *Chem. Eng. Sci.*, 22, 637, 1967.
552. Goldman, A.J., Cox, R.G., and Brenner, H., *Chem. Eng. Sci.*, 22, 653, 1967.
553. Levich, V.G., *Physicochemical Hydrodynamics*, Prentice-Hall, Englewood Cliffs, NJ, 1962.
554. Edwards, D.A., Brenner, H., and Wasan, D.T., *Interfacial Transport Processes and Rheology*, Butterworth-Heinemann, Boston, 1991.
555. Charles, G.E. and Mason, S.G., *J. Colloid Sci.*, 15, 236, 1960.
556. Danov, K.D., Denkov, N.D., Petsev, D.N., Ivanov, I.B., and Borwankar, R., *Langmuir*, 9, 1731, 1993.
557. Danov, K.D., Valkovska, D.S., and Ivanov, I.B., *J. Colloid Interface Sci.*, 211, 291, 1999.
558. Hartland, S., Coalescence in dense-packed dispersions, in *Thin Liquid Films*, Ivanov, I.B., Ed., Marcel Dekker, New York, 1988. p. 663.
559. Hetsroni, G., Ed., *Handbook of Multiphase System*, Hemisphere, New York, 1982, pp. 1–96.
560. Davis, A.M.J., Kezirian, M.T., and Brenner, H., *J. Colloid Interface Sci.*, 165, 129, 1994.
561. Brenner, H., *Chem. Eng. Sci.*, 18, 1, 1963.
562. Brenner, H., *Chem. Eng. Sci.*, 19, 599, 1964. *Chem. Eng. Sci.*, 19, 631, 1964.
563. Brenner, H. and O'Neill, M.E., *Chem. Eng. Sci.*, 27, 1421, 1972.
564. Van de Ven, T.G.M., *Colloidal Hydrodynamics*, Academic Press, London, 1988.
565. Jeffery, G.B., *Proc. Lond. Math. Soc.*, 14, 327, 1915.
566. Stimson, M. and Jeffery, G.B., *Proc. R. Soc. (Lond.)*, A111, 110, 1926.
567. Cooley, M.D.A. and O'Neill, M.E., *Mathematika*, 16, 37, 1969.
568. Cooley, M.D.A. and O'Neill, M.E., *Proc. Cambridge Philos. Soc.*, 66, 407, 1969.
569. Davis, M.H., *Chem. Eng. Sci.*, 24, 1769, 1969.
570. O'Neill, M.E. and Majumdar, S.R., *Z. Angew. Math. Phys.*, 21, 164, 1970. *Z. Angew. Math. Phys.*, 21, 180, 1970.
571. Davis, M.H., *Two Unequal Spheres in a Slow Linear Shear Flow*, Rept. NCAR-TN/STR-64, National Center for Atmospheric Research, Bolder, CO, 1971.
572. Batchelor, G.K., *J. Fluid Mech.*, 74, 1, 1976.
573. Davis, R.H. and Hill, N.A., *J. Fluid Mech.*, 236, 513, 1992.
574. Batchelor, G.K., *J. Fluid Mech.*, 119, 379, 1982.
575. Batchelor, G.K. and Wen, C.-S., *J. Fluid Mech.*, 124, 495, 1982.
576. Jeffrey, D.J. and Onishi, Y., *J. Fluid Mech.*, 139, 261, 1984.
577. Fuentes, Y.O., Kim, S., and Jeffrey, D.J., *Phys. Fluids*, 31, 2445, 1988. *Phys. Fluids*, A1, 61, 1989.
578. Stokes, G.G., *Trans. Cambridge Phil. Soc.*, 1, 104, 1851.
579. Exerowa, D. and Kruglyakov, P.M., *Foam and Foam Films: Theory, Experiment, Application*, Elsevier, New York, 1998.
580. Ivanov, I.B., Radoev, B.P., Traykov, T.T., Dimitrov, D.S., Manev, E.D., and Vassilieff, C.S., *Proceedings of the International Conference on Colloid Surface Science*, Wolfram, E., Ed., Akademia Kiado, Budapest, 1975. p. 583.
581. Denkov, N.D., Petsev, D.N., and Danov, K.D., *Phys. Rev. Let.*, 71, 3226, 1993.
582. Valkovska, D.S., Danov, K.D., and Ivanov, I.B., *Colloid Surf. A*, 156, 547, 1999.

583. Davis, R.H., Schonberg, J.A., and Rallison, J.M., *Phys. Fluids*, A1, 77, 1989.
584. Chi, B.K. and Leal, L.G., *J. Fluid Mech.*, 201, 123, 1989.
585. Ascoli, E.P., Dandy, D.S., and Leal, L.G., *J. Fluid Mech.*, 213, 287, 1990.
586. Yiantsios, S.G. and Davis, R.H., *J. Fluid Mech.*, 217, 547, 1990.
587. Zhang, X. and Davis, R.H., *J. Fluid Mech.*, 230, 479, 1991.
588. Chesters, A.K., *Trans. Inst. Chem. Engrs. A*, 69, 259, 1991.
589. Yiantsios, S.G. and Davis, R.H., *J. Colloid Interface Sci.*, 144, 412, 1991.
590. Yiantsios, S.G. and Higgins, B.G., *J. Colloid Interface Sci.*, 147, 341, 1991.
591. Joye, J.-L., Hirasaki, G.J., and Miller, C.A., *Langmuir*, 8, 3083, 1992.
592. Joye, J.-L., Hirasaki, G.J., and Miller, C.A., *Langmuir*, 10, 3174, 1994.
593. Abid, S. and Chestrers, A.K., *Int. J. Multiphase Flow*, 20, 613, 1994.
594. Li, D., *J. Colloid Interface Sci.*, 163, 108, 1994.
595. Saboni, A., Gourdon, C., and Chesters, A.K., *J. Colloid Interface Sci.*, 175, 27, 1995.
596. Rother, M.A., Zinchenko, A.Z., and Davis, R.H., *J. Fluid Mech.*, 346, 117, 1997.
597. Singh, G., Miller, C.A., and Hirasaki, G.J., *J. Colloid Interface Sci.*, 187, 334, 1997.
598. Cristini, V., Blawzdziewicz, J., and Loewenberg, M., *J. Fluid Mech.*, 366, 259, 1998.
599. Bazhlekov, I.B., Chesters, A.K., and van de Vosse, F.N., *Int. J. Multiphase Flow*, 26, 445, 2000.
600. Bazhlekov, I.B., van de Vosse, F.N., and Chesters, A.K., *J. Non-Newtonian Fluid Mech.*, 93, 181, 2000.
601. Chesters, A.K. and Bazhlekov, I.B., *J. Colloid Interface Sci.*, 230, 229–243, 2000.
602. Boulton-Stone, J.M. and Blake, J.R., *J. Fluid Mech.*, 254, 437, 1993.
603. Frankel, S. and Mysels, K., *J. Phys. Chem.*, 66, 190, 1962.
604. Velev, O.D., Constantinides, G.N., Avraam, D.G., Payatakes, A.C., and Borwankar, R.P., *J. Colloid Interface Sci.*, 175, 68, 1995.
605. Exerowa, D., Nikolov, A., and Zacharieva, M., *J. Colloid Interface Sci.*, 81, 419, 1981.
606. de Vries, A.J., *Rec. Trav. Chim. Pays-Bas.*, 77, 441, 1958.
607. Vrij, A., *Discuss. Faraday Soc.*, 42, 23, 1966.
608. Ivanov, I.B., Radoev, B.P., Manev, E.D., and Sheludko, A.D., *Trans. Faraday Soc.*, 66, 1262, 1970.
609. Gumerman, R.J. and Homsy, G.M., *Chem. Engng. Commun.*, 2, 27, 1975.
610. Malhotra, A.K. and Wasan, D.T., *Chem. Engng. Commun.*, 48, 35, 1986.
611. Valkovska, D.S., Danov, K.D., and Ivanov, I.B., *Adv. Colloid Interface Sci.*, 96, 101, 2002.
612. Manev, E.D., Sazdanova, S.V., and Wasan, D.T., *J. Colloid Interface Sci.*, 97, 591, 1984.
613. Ivanov, I.B., *Pure Appl. Chem.*, 52, 1241, 1980.
614. Aveyard, R., Binks, B.P., Fletcher, P.D.I., and Ye, X., *Prog. Colloid Polymer Sci.*, 89, 114, 1992.
615. Velev, O.D., Gurkov, T.D., Chakarova, Sv.K., Dimitrova, B.I., and Ivanov, I.B., *Colloids Surf. A*, 83, 43, 1994.
616. Dickinson, E., Murray, B.S., and Stainsby, G., *J. Chem. Soc. Faraday Trans.*, 84, 871, 1988.
617. Ivanov, I.B., Lectures at INTEVEP, Petroleos de Venezuela, Caracas, June 1995.
618. Ivanov, I.B. and Kralchevsky, P.A., *Colloid Surf. A*, 128, 155, 1997.
619. Basheva, E.S., Gurkov, T.D., Ivanov, I.B., Bantchev, G.B., Campbell, B., and Borwankar, R.P., *Langmuir*, 15, 6764, 1999.
620. Gurkov, T.D. and Basheva, E.S., in *Encyclopedia of Surface and Colloid Science*, Hubbard, A.T., Ed., Marcel Dekker, New York, 2002.
621. Danov, K.D. in *Fluid Dynamic of Surfactant and Polymer Solutions*, Starov, V. and Ivanov I., Eds., Springer-Verlag, New Your, 2004.
622. Boussinesq, M.J., *Ann. Chim. Phys.*, 29, 349, 1913. *Ann. Chim. Phys.*, 29, 357, 1913.
623. Aris, R., *Vectors, Tensors, and the Basic Equations of Fluid Mechanics*, Prentice Hall, Englewood Cliffs, NJ, 1962.
624. Brenner, H. and Leal, L.G., *J. Colloid Interface Sci.*, 62, 238, 1977.
625. Brenner, H. and Leal, L.G., *J. Colloid Interface Sci.*, 65, 191, 1978.
626. Brenner, H. and Leal, L.G., *AIChE J.*, 24, 246, 1978.
627. Brenner, H. and Leal, L.G., *J. Colloid Interface Sci.*, 88, 136, 1982.
628. Stone, H.A., *Phys. Fluids*, A2, 111, 1990.
629. Valkovska, D.S. and Danov, K.D., *J. Colloid Interface Sci.*, 223, 314, 2000.
630. Stoyanov, S.D. and Denkov, N.D., *Langmuir*, 17, 1150, 2001.
631. Feng, S.-S., *J. Colloid Interface Sci.*, 160, 449, 1993.
632. Stebe, K.J. and Maldarelli, Ch., *Phys. Fluids*, A3, 3, 1991.
633. Stebe, K.J. and Maldarelli, Ch., *J. Colloid Interface Sci.*, 163, 177, 1994.
634. Scriven, L.E., *Chem. Eng. Sci.*, 12, 98, 1960.
635. Scriven, L.E. and Sternling, C.V., *J. Fluid Mech.*, 19, 321, 1964.
636. Slattery, J.C., *Chem. Eng. Sci.*, 19, 379, 1964. *Chem. Eng. Sci.*, 19, 453, 1964.
637. Slattery, J.C., *I&EC Fundam.*, 6, 108, 1967.
638. Slattery, J.C., *Interfacial Transport Phenomena*, Springer-Verlag, New York, 1990.
639. Barton, K.D. and Subramanian, R.S., *J. Colloid Interface Sci.*, 133, 214, 1989.
640. Feuillebois, F., *J. Colloid Interface Sci.*, 131, 267, 1989.
641. Merritt, R.M. and Subramanian, R.S., *J. Colloid Interface Sci.*, 131, 514, 1989.
642. Mannheimer, R.J. and Schechter, R.S., *J. Colloid Interface Sci.*, 12, 98, 1969.
643. Pintar, A.J., Israel, A.B., and Wasan, D.T., *J. Colloid Interface Sci.*, 37, 52, 1971.

644. Gardner, J.W. and Schechter, R.S., *Colloid Interface Sci.*, 4, 98, 1976.
645. Li, D. and Slattery, J.C., *J. Colloid Interface Sci.*, 125, 190, 1988.
646. Tambe, D.E. and Sharma, M.M., *J. Colloid Interface Sci.*, 147, 137, 1991.
647. Tambe, D.E. and Sharma, M.M., *J. Colloid Interface Sci.*, 157, 244, 1993.
648. Tambe, D.E. and Sharma, M.M., *J. Colloid Interface Sci.*, 162, 1, 1994.
649. Horozov, T., Danov, K., Kralchevsky, P., Ivanov, I., and Borwankar, R., A local approach in interfacial rheology: Theory and experiment, in *First World Congress on Emulsion*, Paris, 137, 3–20, 1993.
650. Danov, K.D., Ivanov, I.B., and Kralchevsky, P.A., Interfacial rheology and emulsion stability, in *Second World Congress on Emulsion*, Paris, 152, 2–2, 1997.
651. Ivanov, I.B., Danov, K.D., Ananthapadmanabhan, K.P., and Lips, A., *Adv. Colloid Interface Sci.*, 61, 114–115, 2005.
652. de Groot, S.R. and Mazur, P., *Non-equilibrium Thermodynamics*, Interscience, New York, 1962.
653. Moeckel, G.P., *Arch. Rat. Mech. Anal.*, 57, 255, 1975.
654. Rushton, E. and Davies, G.A., *Appl. Sci. Res.*, 28, 37, 1973.
655. Haber, S., Hetsroni, G., and Solan, A., *Int. J. Multiphase Flow*, 1, 57, 1973.
656. Reed, L.D. and Morrison, F.A., *Int. J. Multiphase Flow*, 1, 573, 1974.
657. Hetsroni, G. and Haber, S., *Int. J. Multiphase Flow*, 4, 1, 1978.
658. Morrison, F.A. and Reed, L.D., *Int. J. Multiphase Flow*, 4, 433, 1978.
659. Beshkov, V.N., Radoev, B.P., and Ivanov, I.B., *Int. J. Multiphase Flow*, 4, 563, 1978.
660. Murdoch, P.G. and Leng, D.E., *Chem. Eng. Sci.*, 26, 1881, 1971.
661. Reed, X.B., Riolo, E., and Hartland, S., *Int. J. Multiphase Flow*, 1, 411, 1974. *Int. J. Multiphase Flow*, 1, 437, 1974.
662. Ivanov, I.B. and Traykov, T.T., *Int. J. Multiphase Flow*, 2, 397, 1976.
663. Traykov, T.T. and Ivanov, I.B., *Int. J. Multiphase Flow*, 3, 471, 1977.
664. Lu, C.-Y.D. and Cates, M.E., *Langmuir*, 11, 4225, 1995.
665. Jeelany, S.A.K. and Hartland, S., *J. Colloid Interface Sci.*, 164, 296, 1994.
666. Zapryanov, Z., Malhotra, A.K., Aderangi, N., and Wasan, D.T., *Int. J. Multiphase Flow*, 9, 105, 1983.
667. Malhotra, A.K. and Wasan, D.T., *Chem. Eng. Commun.*, 55, 95, 1987.
668. Malhotra, A.K. and Wasan, D.T., Interfacial rheological properties of adsorbed surfactant films with applications to emulsion and foam stability, in *Thin Liquid Films*, Ivanov, I.B., Ed., Marcel Dekker, New York, 1988, p. 829.
669. Singh, G., Hirasaki, G.J., and Miller, C.A., *J. Colloid Interface Sci.*, 184, 92, 1996.
670. Traykov, T.T., Manev, E.D., and Ivanov, I.B., *Int. J. Multiphase Flow*, 3, 485, 1977.
671. Bancroft, W.D., *J. Phys. Chem.*, 17, 514, 1913.
672. Griffin, J., *Soc. Cosmet. Chem.*, 5, 4, 1954.
673. Davies, J.T., in *Proceedings of the 2nd International Congress on Surface Activity*, Vol. 1, Butterworths, London, 1957. p. 426.
674. Shinoda, K. and Friberg, S., *Emulsion and Solubilization*, Wiley, New York, 1986.
675. Davis, H.T., Factors determining emulsion type: HLB and beyond, in *Proc. First World Congress on Emulsion 19–22 Oct. 1993*, Paris, 1993, p. 69.
676. Israelachvili, J., The history, applications and science of emulsion, in *Proc. First World Congress on Emulsion 19–22 Oct. 1993*, Paris, 1993, p. 53.
677. Kralchevsky, P.A., *J. Colloid Interface Sci.*, 137, 217, 1990.
678. Gompper, G. and Schick, M., *Phys. Rev.*, B41, 9148, 1990.
679. Lerczak, J., Schick, M., and Gompper, G., *Phys. Rev.*, 46, 985, 1992.
680. Andelman, D., Cates, M.E., Roux, D., and Safran, S., *J. Chem. Phys.*, 87, 7229, 1987.
681. Chandra, P. and Safran, S., *Europhys. Lett.*, 17, 691, 1992.
682. Danov, K.D., Velev, O.D., Ivanov, I.B., and Borwankar, R.P., Bancroft rule and hydrodynamic stability of thin films and emulsions, in *First World Congress on Emulsion 19–22 Oct. 1993*, Paris, 1993, p. 125.
683. Kunieda, H., Evans, D.F., Solans, C., and Yoshida, *Colloids Surf.*, 47, 35, 1990.
684. Koper, G.J.M., Sager, W.F.C., Smeets, J., and Bedeaux, D., *J. Phys. Chem.*, 99, 13291, 1995.
685. Ivanov, I.B., Danov, K.D., and Kralchevsky, P.A., *Colloids Surf. A*, 152, 161, 1999.
686. Velev, O.D., Gurkov, T.D., and Borwankar, R.P., *J. Colloid Interface Sci.*, 159, 497, 1993.
687. Velev, O.D., Gurkov, T.D., Ivanov, I.B., and Borwankar, R.P., *Phys. Rev. Lett.*, 75, 264, 1995.
688. Danov, K., Ivanov, I., Zapryanov, Z., Nakache, E., and Raharimalala, S., Marginal stability of emulsion thin film, in *Proceedings of the Conference of Synergetics, Order and Chaos*, Velarde, M., Ed., World Scientific, Singapore, 1988, p. 178.
689. Valkovska, D.S., Kralchevsky, P.A., Danov, K.D., Broze, G., and Mehreteab, A., *Langmuir*, 16, 8892, 2000.
690. Danov, K.D., Gurkov, T.D., Dimitrova, T.D., and Smith, D., *J. Colloid Interface Sci.*, 188, 313, 1997.
691. Ivanov, I.B., Chakarova, S.K., and Dimitrova, B.I., *Colloids Surf.*, 22, 311, 1987.
692. Dimitrova, B.I., Ivanov, I.B., and Nakache, E., *J. Dispersion Sci. Technol.*, 9, 321, 1988.
693. Sternling, C.V. and Scriven, L.E., *AIChE J.*, 5, 514, 1959.
694. Lin, S.P. and Brenner, H.J., *J. Colloid Interface Sci.*, 85, 59, 1982.
695. Holly, F.J., in *Wetting, Spreading and Adhesion*, Padday, J.F., Ed., Academic Press, New York, 1978, p. 439.
696. Castillo, J.L. and Velarde, M.G., *J. Colloid Interface Sci.*, 108, 264, 1985.
697. Davis, R.H., *Adv. Colloid Interface Sci.*, 43, 17, 1993.
698. Uijttewaal, W.S.J., Nijhof, E.-J., and Heethaar, R.M., *Phys. Fluids*, A5, 819, 1993.

699. Zapryanov, Z. and Tabakova, S., *Dynamics of Bubbles, Drops and Rigid Particles*, Kluwer Academic, London, 1999.
700. Lorentz, H.A., *Abhandl. Theoret. Phys.*, 1, 23, 1906.
701. Faxen, H., *Arkiv. Mat. Astron. Fys.*, 17, 27, 1923.
702. Wakiya, S., *J. Phys. Soc. Jpn*, 12, 1130, 1957.
703. Dean, W.R. and O'Neill, M.E., *Mathematika*, 10, 13, 1963.
704. O'Neill, M.E., *Mathematika*, 11, 67, 1964.
705. Cooley, M.D.A. and O'Neill, M.E., *J. Inst. Math. Appl.*, 4, 163, 1968.
706. Keh, H.J. and Tseng, C.H., *Int. J. Multiphase Flow*, 1, 185, 1994.
707. Schonberg, J. and Hinch, E.J., *J. Fluid Mech.*, 203, 517, 1989.
708. Ryskin, G. and Leal, L.G., *J. Fluid Mech.*, 148, 1, 1984. *J. Fluid Mech.*, 148, 19, 1984. *J. Fluid Mech.*, 148, 37, 1984.
709. Liron, N. and Barta, E., *J. Fluid Mech.*, 238, 579, 1992.
710. Shapira, M. and Haber, S., *Int. J. Multiphase Flow*, 14, 483, 1988.
711. Shapira, M. and Haber, S., *Int. J. Multiphase Flow*, 16, 305, 1990.
712. Yang, S.-M. and Leal, L.G., *J. Fluid Mech.*, 149, 275, 1984.
713. Yang, S.-M. and Leal, L.G., *Int. J. Multiphase Flow*, 16, 597, 1990.
714. Lebedev, A.A., *Zhur. Russ. Fiz. Khim.*, 48, 1916.
715. Silvey, A., *Phys. Rev.*, 7, 106, 1916.
716. Hadamar, J.S., *Comp. Rend. Acad. Sci. (Paris)*, 152, 1735, 1911.
717. Rybczynski, W., *Bull. Intern. Acad. Sci. (Cracovie)*, A, 1911.
718. He, Z., Dagan, Z., and Maldarelli, Ch., *J. Fluid Mech.*, 222, 1, 1991.
719. Danov, K.D., Aust, R., Durst, F., and Lange, U., *Chem. Eng. Sci.*, 50, 263, 1995.
720. Danov, K.D., Aust, R., Durst, F., and Lange, U., *Chem. Eng. Sci.*, 50, 2943, 1995.
721. Danov, K.D., Aust, R., Durst, F., and Lange, U., *Int. J. Multiphase Flow*, 21, 1169, 1995.
722. Danov, K.D., Gurkov, T.D., Raszillier, H., and Durst, F., *Chem. Eng. Sci.*, 53, 3413, 1998.
723. Stoos, J.A. and Leal, L.G., *J. Fluid Mech.*, 217, 263, 1990.
724. Danov, K.D., Dimova, R.I., and Pouligny, B., *Phys. Fluids*, 12, 2711, 2000.
725. Dimova, R.I., Danov, K.D., Pouligny, B., and Ivanov, I.B., *J. Colloid Interface Sci.*, 226, 35, 2000.
726. Angelova, M.I. and Pouligny, B., *Pure Appl. Optics*, 2, 261, 1993.
727. Pouligny, B., Martinot-Lagarde, G., and Angelova, M.I., *Progr. Colloid Polym. Sci.*, 98, 280, 1995.
728. Dietrich, C., Angelova, M., and Pouligny, B., *J. Phys. II France*, 7, 1651, 1997.
729. Velikov, K., Dietrich, C., Hadjiski, A., Danov, K., and Pouligny, B., *Europhys. Lett.*, 40(4), 405, 1997.
730. Velikov, K., Danov, K., Angelova, M., Dietrich, C., and Pouligny, B., *Colloids Surf. A*, 149, 245, 1999.
731. Dimova, R., Dietrich, C., Hadjiisky, A., Danov, K., and Pouligny, B., *Eur. Phys. J. B*, 12, 589, 1999.
732. Danov, K.D., Pouligny, B., Angelova, M.I., and Kralchevsky, P.A., in *Studies in Surface Science and Catalysis*, Vol. 132, Elsevier, Amsterdam, The Netherlands, 2001.
733. Hunter, R.J., *Foundation of Colloid Science*, Vol. 1, Clarendon Press, Oxford, 1987.
734. Hunter, R.J., *Foundation of Colloid Science*, Vol. 2, Clarendon Press, Oxford, 1989.
735. Einstein, A., *Ann. Phys.*, 19, 289, 1906.
736. Kubo, R., *Rep. Prog. Phys.*, 29, 255, 1966.
737. Einstein, A., *Ann. Phys.*, 34, 591, 1911.
738. Taylor, G.I., *Proc. Roy. Soc. A*, 138, 41, 1932.
739. Oldroyd, J.G., *Proc. Roy. Soc. A*, 232, 567, 1955.
740. Taylor, G.I., *Proc. Roy. Soc. A*, 146, 501, 1934.
741. Fröhlich, H. and Sack, R., *Proc. Roy. Soc. A*, 185, 415, 1946.
742. Oldroyd, J.G., *Proc. Roy. Soc. A*, 218, 122, 1953.
743. Batchelor, G.K., *J. Fluid Mech.*, 83, 97, 1977.
744. De Kruif, C.G., Van Iersel, E.M.F., Vrij, A., and Russel, W.B., *J. Chem. Phys.*, 83, 4717, 1985.
745. Loewenberg, M. and Hinch, E.J., *J. Fluid Mech.*, 321, 395, 1996.
746. Da Cunha, F.R. and Hinch, E.J., *J. Fluid Mech.*, 309, 211, 1996.
747. Li, X. and Pozrikidis, C., *J. Fluid Mech.*, 341, 165, 1997.
748. Loewenberg, M., *J. Fluids Eng.*, 120, 824, 1998.
749. Blawzdziewicz, J., Vajnryb, E., and Loewenberg, M., *J. Fluid Mech.*, 395, 29, 1999.
750. Ramirez, J.A., Zinchenko, A., Loewenberg, M., and Davis, R.H., *Chem. Eng. Sci.*, 54, 149, 1999.
751. Blawzdziewicz, J., Vlahovska, P., and Loewenberg, M., *Physica A*, 276, 50, 2000.
752. Breyannis, G. and Pozrikidis, C., *Theor. Comp. Fluid Dynam.*, 13, 327, 2000.
753. Li, X. and Pozrikidis, C., *Int. J. Multiphase Flow*, 26, 1247, 2000.
754. Rednikov, A.Y., Ryazantsev, Y.S., and Velarde, M.G., *Phys. Fluids*, 6, 451, 1994.
755. Velarde, M.G., *Phil. Trans. Roy. Soc., Math. Phys. Eng. Sci.*, 356, 829, 1998.
756. Danov, K.D., *J. Colloid Interface Sci.*, 235, 144, 2001.
757. Barnes, H.A., Rheology of emulsions—a review, in *Proc. First World Congress on Emulsion 19–22 Oct. 1993*, Paris, 1993. p. 267.
758. Krieger, L.M. and Dougherty, T.J., *Trans. Soc. Rheol.*, 3, 137, 1959.
759. Wakeman, R., *Powder Tech.*, 11, 297, 1975.

760. Prud'home, R.K. and Khan, S.A., Experimental results on foam rheology, in *Foams: Theory, Measurements, and Applications*, Prud'home, R.K. and Khan, S.A., Eds., Marcel Dekker, New York, 1996. p. 217.
761. Tadros, T.F., Fundamental principles of emulsion rheology and their applications, in *Proc. First World Congress on Emulsion 19–22 Oct. 1993*, Paris, 1993. p. 237.
762. Pal, R., Bhattacharya, S.N., and Rhodes, E., *Can. J. Chem. Eng.*, 64, 3, 1986.
763. Edwards, D.A. and Wasan, D.T., Foam rheology: the theory and role of interfacial rheological properties, in *Foams: Theory, Measurements, and Applications*, Prud'home, R.K. and Khan, S.A., Eds., Marcel Dekker, New York, 1996. p. 189.
764. Wessel, R. and Ball, R.C., *Phys. Rev.*, A46, 3009, 1992.
765. Kanai, H., Navarrete, R.C., Macosko, C.W., and Scriven, L.E., *Rheol. Acta*, 31, 333, 1992.
766. Pal, R., *Chem. Eng. Comm.*, 98, 211, 1990.
767. Pal, R., *Colloids Surf. A*, 71, 173, 1993.
768. Prins, A., Liqiud flow in foams as affected by rheological surface properties: A contribution to a better understanding of the foaming behaviour of liquids, in *Hydrodynamics of Dispersed Media*, Hulin, J.P., Cazabat, A.M., Guyon, E., and Carmona, F., Eds., Elsevier/North-Holland, Amsterdam, The Netherlands, 1990. p. 5.
769. Babak, V.G., *Colloids Surf. A*, 85, 279, 1994.
770. Yuhua, Y., Pal, R., and Masliyah, J., *Chem Eng. Sci.*, 46, 985, 1991.
771. Giesekus, H., Disperse systems: dependence of rheological properties on the type of flow with implications for food rheology, in *Physical Properties of Foods*, Jowitt, R. et al., Eds., Applied Science Publishers, 1983, Chapter 13.
772. Turian, R. and Yuan, T.-F., *AIChE J.*, 23, 232, 1977.
773. Clarke, B., *Trans. Inst. Chem. Eng.*, 45, 251, 1967.
774. von Smoluchowsky, M., *Phys. Z.*, 17, 557, 1916.
775. von Smoluchowsky, M., *Z. Phys. Chem.*, 92, 129, 1917.
776. Wang, H. and Davis, R.H., *J. Colloid Interface Sci.*, 159, 108, 1993.
777. Rogers, J.R. and Davis, R.H., *Metal. Trans.*, A21, 59, 1990.
778. Young, N.O., Goldstein, J.S., and Block, M.J., *J. Fluid Mech.*, 6, 350, 1959.
779. Fuchs, N.A., *Z. Phys.*, 89, 736, 1934.
780. Friedlander, S.K., *Smoke, Dust and Haze: Fundamentals of Aerosol Behaviour*, Wiley-Interscience, New York, 1977.
781. Singer, J.M., Vekemans, F.C.A., Lichtenbelt, J.W.Th., Hesselink, F.Th., and Wiersema, P.H., *J. Colloid Interface Sci.*, 45, 608, 1973.
782. Leckband, D.E., Schmitt, F.-J., Israelachvili, J.N., and Knoll, W., *Biochemistry*, 33, 4611, 1994.
783. Bak, T.A. and Heilmann, O., *J. Phys. A: Math. Gen.*, 24, 4889, 1991.
784. Martinov, G.A. and Muller, V.M., in *Research in Surface Forces*, Vol. 4, Plenum Press, Consultants Bureau, New York, 1975. p. 3.
785. Elminyawi, I.M., Gangopadhyay, S., and Sorensen, C.M., *J. Colloid Interface Sci.*, 144, 315, 1991.
786. Hartland, S. and Gakis, N., *Proc. Roy. Soc. (Lond.)*, A369, 137, 1979.
787. Hartland, S. and Vohra, D.K., *J. Colloid Interface Sci.*, 77, 295, 1980.
788. Lobo, L., Ivanov, I.B., and Wasan, D.T., *AIChE J.*, 39, 322, 1993.
789. Danov, K.D., Ivanov, I.B., Gurkov, T.D., and Borwankar, R.P., *J. Colloid Interface Sci.*, 167, 8, 1994.
790. van den Tempel, M., *Recueil*, 72, 433, 1953.
791. Borwankar, R.P., Lobo, L.A., and Wasan, D.T., *Colloid Surf.*, 69, 135, 1992.
792. Dukhin, S., Sæther, Ø., and Sjöblom, J., Coupling of coalescence and flocculation in dilute O/W emulsions, in *Encycloped Handbook of Emulsion Technology*, Sjöblom, J., Ed., Marcel Dekker, New York, 2001, p. 71.
793. Garrett, P.R., Ed., *Defoaming: Theory and Industrial Applications*, Marcel Dekker, New York, 1993.
794. Garrett, P.R., The Mode of Action of Antifoams, in *Defoaming: Theory and Industrial Applications*, Marcel Dekker: New York, 1993, Chapter 1.
795. Exerowa, D. and Kruglyakov, P.M., *Foams and Foam Films*, Elsevier, Amsterdam, The Netherlands, 1998, Chapter 9.
796. Wasan, D.T. and Christiano, S.P., in *Handbook of Surface and Colloid Chemistry*, Birdi, K.S., Ed., CRC Press, Boca Raton, FL, 1997. p. 179.
797. Kralchevsky, P.A. and Nagayama, K., *Particles at Fluid Interfaces and Membranes*, Studies in Interface Science, Vol. 10; Elsevier, Amsterdam, The Netherlands, 2001, Chapter 14.
798. Basheva, E.S., Ganchev, D., Denkov, N.D., Kasuga, K., Satoh, N., and Tsujii, K., *Langmuir*, 16, 1000, 2000.
799. Basheva, E.S., Stoyanov, S., Denkov, N.D., Kasuga, K., Satoh, N., and Tsujii, K., *Langmuir*, 17, 969, 2001.
800. Denkov, N.D., *Langmuir*, 20, 9463, 2004.
801. Koczo, K., Koczone, J.K., and Wasan, D.T., *J. Colloid Interface Sci.*, 166, 225, 1994.
802. Denkov, N.D. and Marinova, K., Antifoaming action of oils, *Proceedings of the 3rd EuroConference on Foams, Emulsions and Applications*, Zitha, P., Banhart, J., and Verbist, G., Eds., MIT, Bremen, 2000. p. 199.
803. Marinova, K. and Denkov, N.D., *Langmuir*, 17, 2426, 2001.
804. Denkov, N.D., Tcholakova, S., Marinova, K., and Hadjiiski, A., Role of oil spreading for the efficiency of mixed oil-solid antifoams, *Langmuir*, 18, 5810, 2002.
805. Marinova, K.M., Denkov, N.D., Branlard, P., Giraud, Y., and Deruelle, M., Optimal hydrophobicity of silica in mixed oil-silica antifoams, *Langmuir*, 18, 3399, 2002.
806. Arnaudov, L., Denkov, N.D., Surcheva, I., Durbut, P., Broze, G., and Mehreteab, A., *Langmuir*, 17, 6999, 2001.
807. Hadjiiski, A., Tcholakova, S., Denkov, N.D., Durbut, P., Broze, G., and Mehreteab, A., *Langmuir*, 17, 7011, 2001.
808. Denkov, N.D., *Langmuir*, 15, 8530, 1999.

809. Garrett, P.R., *J. Colloid Interface Sci.*, 76, 587, 1980.
810. Kulkarni, R.D., Goddard, E.D., and Kanner, B., *J. Colloid Interface Sci.*, 59, 468, 1977.
811. Kruglyakov, P.M., in *Thin Liquid Films: Fundamentals and Applications*, Ivanov, I.B., Ed., Surfactant Science Series, Vol. 29, Marcel Dekker: New York, 1988, Chapter 11.
812. Bergeron, V., Fagan, M.E., and Radke, C., *Langmuir*, 9, 1704, 1993.
813. Bergeron, V., Cooper, P., Fischer, C., Giermanska-Kahn, J., Langevin, D., and Pouchelon, A., *Colloids Surf. A: Physicochem. Eng. Aspects*, 122, 103, 1997.
814. Koczo, K., Lloyd, L., and Wasan, D.T., *J. Colloid Interface Sci.*, 150, 492, 1992.
815. Kulkarni, R.D., Goddard, E.D., and Chandar, P., in *Foams: Theory, Measurements, and Applications*, Prud'homme, R.K. and Khan, S.A., Eds., Surfactant Science Series, Vol. 57; Marcel Dekker, New York, 1996, Chapter 14.
816. Aveyard, R., Binks, B.P., Fletcher, P.D.I., Peck, T-G., and Garrett, P., *J. Chem. Soc. Faraday Trans.*, 89, 4313, 1993.
817. Hadjiiski, A., Tcholakova, S., Ivanov, I.B., Gurkov, T.D., and Leonard, E., *Langmuir*, 18, 127, 2002.
818. Hadjiiski, A., Denkov, N.D., Tcholakova, S., and Ivanov, I.B., Role of entry barriers in the foam destruction by oil drops, *Proceedings of the 13th Symposium on Surfactants in Solution*, Mittal, K.L., Moudgil, B., and Shah, D., Eds., Marcel Dekker, New York, 2002.
819. Lichtman, I.A., Sinka, J.V., and Evans, D.W., *Assoc. Mex. Tec. Ind. Celul. Pap. (Bol.)*, 15, 2632, 1975.
820. Ross, S., *J. Phys. Colloid Chem.*, 54, 429, 1950.
821. Jha, B.K., Christiano, S.P., and Shah, D.O., *Langmuir*, 16, 9947, 2000.
822. Garrett, P.R., Davis, J., and Rendall, H.M., *Colloids Surf. A: Physicochem. Eng. Aspects*, 85, 159, 1994.
823. Denkov, N.D., Marinova, K., Christova, C., Hadjiiski, A., and Cooper, P., *Langmuir*, 16, 2515, 2000.
824. Overbeek, J.Th.G., *Adv. Colloid Sci.*, 3, 97, 1950.
825. Overbeek, J.Th.G., in *Colloid Science*, Vol. 1, Kruyt, H.R., Ed., Elsevier, Amsterdam, The Netherlands, 1952, p. 197.
826. Overbeek, J.Th.G. and Wiersema, P.H., in *Electrophoresis*, Bier, M., Ed., Vol. 2, Academic Press, New York, 1967, Chapter 1.
827. Dukhin, S.S. and Derjaguin, B.V., in *Surface and Colloid Science*, Vol. 7, Matijevic, E., Ed., Wiley, New York, 1974, Chapter 3.
828. Derjaguin, B.V., Dukhin, S.S., and Shilov, V.N., *Adv. Colloid Interface Sci.*, 13, 141 and 153, 1980.
829. Uzgiris, E., *Adv. Colloid Interface Sci.*, 14, 75, 1981.
830. Saville, D.A., *Adv. Colloid Interface Sci.*, 16, 267, 1982.
831. O'Brien, R.W., *Adv. Colloid Interface Sci.*, 16, 281, 1982.
832. Mandel, M. and Odjik, T., *Ann. Rev. Phys. Chem.*, 35, 75, 1984.
833. Dukhin, S.S., *Adv. Colloid Interface Sci.*, 44, 1, 1993.
834. Dukhin, A.S. and Goetz, P.J., *Adv. Colloid Interface Sci.*, 92, 73, 2001.
835. Dukhin, S.S. and Shilov, V.N., *Dielectric Phenomena and the Double Layer in Disperse Systems and Polyelectrolytes*, Wiley, New York, 1974.
836. Hunter, R.J., *Zeta Potential in Colloid Science*, Academic Press, New York, 1981.
837. Hunter, R.J., *Foundations of Colloid Science*, Vol. 2, Clarendon Press, Oxford, 1989, Chapters 6 and 13.
838. Ohshima, H. and Furusawa, K., Eds., *Electrical Phenomena at Interfaces: Fundamentals, Measurements, and Applications*, 2nd Ed., Marcel Dekker, New York, 1998.
839. Chew, W.C. and Sen, P.N., *J. Chem. Phys.*, 77, 2042, 1982.
840. Loeb, A.L., Wiersema, P.H., and Overbeek, J.Th.G., *The Electric Double Layer Around a Spherical Colloidal Particle*, MIT Press, Cambridge (Mass.), 1961.
841. Dukhin, S.S., Semenikhin, N.M., and Shapinskaia, L.M., *Dokl. Akad. Nauk SSSR*, 193, 385, 1970.
842. Stokes, A.N., *J. Chem. Phys.*, 65, 261, 1976.
843. Ohshima, H., Healy, T.W., and White, L.R., *J. Colloid Interface Sci.*, 90, 17, 1982.
844. Ohshima, H., Electrical double layer, in *Electrical Phenomena at Interfaces: Fundamentals, Measurements, and Applications*, 2nd Ed., Ohshima, H. and Furusawa, K., Eds., Marcel Dekker, New York, 1998, Chapter 1.
845. Ohshima, H., *J. Colloid Interface Sci.*, 171, 525, 1995.
846. von Smoluchowski, M., in *Handbuch der Electrizität und des Magnetismus*, Vol. 2, Barth, Leipzig, 1921. p. 366.
847. Bikerman, J.J., *Trans. Faraday Soc.*, 36, 154, 1940.
848. O'Brien, R.W., *J. Colloid Interface Sci.*, 110, 477, 1986.
849. Bowen, W.R. and Jacobs, P.M., *J. Colloid Interface Sci.*, 111, 223, 1986.
850. Sasaki, H., Muramatsu, A., Arakatsu, H., and Usui, S., *J. Colloid Interface Sci.*, 142, 266, 1991.
851. Nishimura, S., Tateyama, H., Tsunematsu, K., and Jinnai, K., *J. Colloid Interface Sci.*, 152, 359, 1992.
852. Furusawa, K., Sasaki, H., and Nashima, T., Electro-osmosis and streaming potential measurements, in *Electrical Phenomena at Interfaces: Fundamentals, Measurements, and Applications*, 2nd Ed., Ohshima, H. and Furusawa, K., Eds., Marcel Dekker, New York, 1998, Chapter 9.
853. Usui, S., Imamura, Y., and Sasaki, H., *J. Colloid Interface Sci.*, 118, 335, 1987.
854. Scales, P.J., Healy, T.W., and Evans, D.F., *J. Colloid Interface Sci.*, 124, 391, 1988. Scales, P.J., Grieser, F., and Healy, T.W., *Langmuir*, 6, 582, 1989.
855. Van den Hoven, T.J.J. and Bijsterbosch, B.H., *Colloids Surf.*, 22, 187, 1987.
856. von Smoluchowksi, M., *Z. Phys. Chem.*, 92, 129, 1918.
857. Hückel, E., *Phys. Z.*, 25, 204, 1924.
858. Henry, D.C., *Proc. R. Soc. London*, A133, 106, 1931.
859. Henry, D.C., *Trans. Faraday Soc.*, 44, 1021, 1948.

860. Overbeek, J.Th.G., *Kolloid Beih.*, 54, 287 and 364, 1943.
861. Booth, F., *Proc R. Soc. London*, A203, 514, 1950.
862. Wiersema, P.H., Loeb, A.L., and Overbeek, J.Th.G., *J. Colloid Interface Sci.*, 22, 78, 1966.
863. O'Brien, R.W. and White, L.R., *J. Chem. Soc. Faraday Trans. 2*, 74, 1607, 1978.
864. O'Brien, R.W. and Hunter, R.J., *Canad. J. Chem.*, 59, 1878, 1981.
865. Ohshima, H., Healy, T.W., White, L.R., and O'Brien, R.W., *J. Chem. Soc. Faraday Trans. 2*, 79, 1613, 1983; 80, 1299 and 1643, 1984.
866. Ohshima, H., *J. Colloid Interface Sci.*, 168, 269, 1994.
867. Ohshima, H., *J. Colloid Interface Sci.*, 239, 587, 2001.
868. Stigter, D., *J. Phys. Chem.*, 82, 1417 and 1424, 1978.
869. Van der Drift, W.P.J.T., de Keizer, A., and Overbeek, J.Th.G., *J. Colloid Interface Sci.*, 71, 67 and 79, 1979.
870. Ohshima, H., *J. Colloid Interface Sci.*, 180, 299, 1996.
871. Hermans, J.J., *J. Polym. Sci.*, 18, 527, 1955.
872. Overbeek, J.T.G. and Stigter, D., *Rec. Trav. Chim.*, 75, 543, 1956.
873. Imai, N. and Iwasa, K., *Israel J. Chem.*, 11, 223, 1973.
874. Koopal, L.K. and Lyklema, J., *Disc. Faraday Soc.*, 59, 230, 1975. *J. Electroanal. Chem.*, 100, 895, 1979.
875. Brooks, D.E. and Seaman, G.V.F., *J. Colloid Interface Sci.*, 43, 670, 1973. *J. Colloid Interface Sci.*, 43, 687, 1973. *J. Colloid Interface Sci.*, 43, 700, 1973. *J. Colloid Interface Sci.*, 43, 714, 1973.
876. Ohshima, H. and Kondo, T., *J. Colloid Interface Sci.*, 116, 305, 1987. *J. Colloid Interface Sci.*, 135, 443, 1990. 163, 474, 1994.
877. Ohshima, H., Interfacial electrokinetic phenomena, in *Electrical Phenomena at Interfaces: Fundamentals, Measurements, and Applications*, 2nd Ed., Ohshima, H. and Furusawa, K., Eds., Marcel Dekker, New York, 1998, Chapter 2.
878. Ohshima, H., *J. Colloid Interface Sci.*, 233, 142, 2001.
879. Churaev, N.V. and Nikologorskaja, *Colloids Surf.*, 59, 71, 1991.
880. Furusawa, K., Chen, Q., and Tobori, N., *J. Colloid Interface Sci.*, 137, 456, 1990.
881. Levine, S. and Neale, G.H., *J. Colloid Interface Sci.*, 47, 520, 1974. *J. Colloid Interface Sci.*, 49, 332, 1974.
882. Happel, J., *Amer. Inst. Chem. Eng. J.*, 4, 197, 1958.
883. Kuwabara, S., *J. Phys. Soc. Jpn*, 14, 527, 1959.
884. Deggelmann, M., Palberg, T., Hagenbüchle, M., Maier, E.E., Krause, R., Graf, C., and Weber, R., *J. Colloid Interface Sci.*, 143, 318, 1991.
885. Kozak, M.W. and Davis, E.J., *J. Colloid Interface Sci.*, 127, 497, 1989. *J. Colloid Interface Sci.*, 129, 166, 1989.
886. Ohshima, H., *J. Colloid Interface Sci.*, 188, 481, 1997.
887. Zukoski, C.F. and Saville, D.A., *J. Colloid Interface Sci.*, 115, 422, 1987.
888. Mangelsdorf, C.S. and White, L.R., *J. Chem. Soc. Faraday Trans.*, 88, 3567, 1992. *J. Colloid Interface Sci.*, 160, 275, 1993.
889. Gaigalas, A.K., Woo, S., and Hubbard, J.B., *J. Colloid Interface Sci.*, 136, 213, 1990.
890. Ohshima, H., *J. Colloid Interface Sci.*, 179, 431, 1996.
891. Ohshima, H., *J. Colloid Interface Sci.*, 185, 131, 1997.
892. Schätzel, K., Weise, W., Sobotta, A., and Drewel, M., *J. Colloid Interface Sci.*, 143, 287, 1991.
893. Abramson, H.A., Moyer, L.S., and Gorin, M.H., *Electrophoresis of Proteins*, Reinhold, New York, 1942.
894. Tiselius, A., *Trans. Faraday Soc.*, 33, 524, 1937.
895. Imai, T., Otani, W., and Oka, K., *J. Phys. Chem.*, 94, 853, 1990.
896. Kameyama, K. and Takagi, T., *J. Colloid Interface Sci.*, 140, 517, 1990.
897. Imai, T., *J. Phys. Chem.*, 94, 5953, 1990.
898. Imai, T. and Kohsaka, T., *J. Phys. Chem.*, 96, 10030, 1992.
899. Imai, T. and Hayashi, N., *Langmuir*, 9, 3385, 1993.
900. Imae, T., Electrostatic and electrokinetic properties of micelles, in *Electrical Phenomena at Interfaces: Fundamentals, Measurements, and Applications*, 2nd edn., Ohshima, H. and Furusawa, K., Eds., Marcel Dekker, New York, 1998, Chapter 28.
901. Anderson, J.L., *J. Colloid Interface Sci.*, 105, 45, 1985.
902. Fair, M.C. and Anderson, J.L., *J. Colloid Interface Sci.*, 127, 388, 1989.
903. Yoon, B.J. and Kim, S., *J. Colloid Interface Sci.*, 128, 275, 1989.
904. Yoon, B.J., *J. Colloid Interface Sci.*, 142, 575, 1991.
905. von Smoluchowski, M., *Bull. Akad. Sci. Cracovie, Sci. Math. Natur.*, 1, 182, 1903.
906. Booth, F., *J. Chem. Phys.*, 22, 1956, 1954.
907. Ohshima, H., Healy, T.W., White, L.R., and O'Brien, R.W., *J. Chem. Soc. Faraday Trans. 2*, 80, 1299, 1984.
908. Levine, S., Neale, G., and Epstein, N., *J. Colloid Interface Sci.*, 57, 424, 1976.
909. Mazur, P. and Overbeek, J.Th.G., *Rec. Trav. Chim.*, 70, 83, 1951.
910. De Groot, S.R., Mazur, P., and Overbeek, J.Th.G., *J. Chem. Phys.*, 20, 1825, 1952.
911. Maxwell, J.C., *Electricity and Magnetism*, Oxford University Press (Clarendon), London, 1873.
912. Fricke, H., *Phys. Rev.*, 24, 575, 1924. 26, 682, 1925.
913. Dukhin, S.S., *Electroconductivity and Electrokinetic Properties of Disperse Systems*, Naukova Dumka, Kiev, 1975, Chapter 2 (in Russian).
914. O'Brien, R.W., *J. Colloid Interface Sci.*, 81, 234, 1981.
915. O'Brien, R.W. and Perrins, W.T., *J. Colloid Interface Sci.*, 99, 20, 1984. *J. Colloid Interface Sci.*, 110, 447, 1986.

916. Ohshima, H., Healy, T.W., and White, L.R., *J. Chem. Soc. Faraday Trans. 2*, 79, 1613, 1983.
917. De Lacey, E.H.B. and White, L.R., *J. Chem. Soc. Faraday Trans. 2*, 77, 2007, 1981.
918. O'Brien, R.W., *J. Colloid Interface Sci.*, 113, 81, 1986.
919. Debye, P. and Falkenhagen, H., *Phys. Ztschr.*, 29, 121 and 401, 1928.
920. Hinch, E.J., *J. Chem. Soc. Faraday Trans 2*, 80, 535, 1984.
921. Midmore, B.R., Hunter, R.J., and O'Brien, R.W., *J. Colloid Interface Sci.*, 120, 210, 1987. *J. Colloid Interface Sci.*, 123, 486, 1988.
922. Myers, D.F. and Saville, D.A., *J. Colloid Interface Sci.*, 131, 448, 1989.
923. Shubin, V.E., Hunter, R.J., and O'Brien, R.W., *J. Colloid Interface Sci.*, 159, 174, 1993.
924. Grosse, C., Arroyo, F.J., Shilov, V.N., and Delgado, A.V., *J. Colloid Interface Sci.*, 242, 75, 2001.
925. Enderby, J.A., *Proc. Phys. Soc.*, A207, 321, 1951.
926. Booth, F. and Enderby, J.A., *Proc. Phys. Soc.*, A208, 351, 1952.
927. Marlow, B.J., Fairhurst, D., and Pendse, H.P., *Langmuir*, 4, 611, 1988.
928. Hozumi, Y. and Furusawa, K., *Colloid Polym. Sci.*, 268, 469, 1990.
929. Durand Vidal, S., Simonin, J.P., Turq, P., and Bernard, Q., *Progress Colloid Polym. Sci.*, 98, 184, 1995.
930. Debye, P., *J. Chem. Phys.*, 1, 13, 1933.
931. O'Brien, R.W., *J. Fluid Mech.*, 190, 71, 1988.
932. Rider, P.F. and O'Brien, R.W., *J. Fluid Mech.*, 257, 607, 1993.
933. Takeda, S., Tobori, N., Sugawara, H., and Furusawa, K., Dynamic electrophoresis, in *Electrical Phenomena at Interfaces: Fundamentals, Measurements, and Applications*, 2nd edn., Ohshima, H. and Furusawa, K., Eds., Marcel Dekker, New York, 1998, Chapter 13.
934. Gibb, S.E. and Hunter, R.J., *J. Colloid Interface Sci.*, 224, 99, 2000.
935. Kong, L., Beattie, J.K., and Hunter, R.J., *J. Colloid Interface Sci.*, 238, 70, 2001.
936. Rasmusson, M., *J. Colloid Interface Sci.*, 240, 432, 2001.
937. Dukhin, A.S., Shilov, V.N., Ohshima, H., and Goetz, P.J., *Langmuir*, 16, 2615, 2000.
938. Löbbus, M., Sonnefeld, J., van Leeuwen, H.P., Vogelsberger, W., and Lyklema, J, *J. Colloid Interface Sci.*, 229, 174, 2000.
939. Hunter, R.J., *J. Colloid Interface Sci.*, 22, 231, 1966.
940. Chan, D.Y.C. and Horn, R.G., *J. Chem. Phys.*, 83, 5311, 1985.
941. Israelachvili, J.N., *J. Colloid Interface Sci.*, 110, 263, 1986.
942. Dukhin, S.S. and Semenikhin, M.M., *Kolloidn. Zh.*, 32, 360, 1978.
943. Fridrikhsberg, D.A., Sidorova, M.P., Shubin, V.E., and Ermakova, L.E., *Kolloidn. Zh.*, 48, 967, 1986.
944. Zukoski, C.F. and Saville, D.A., *J. Colloid Interface Sci.*, 114, 32, 1986.
945. Midmore, B.R. and Hunter, R.J., *J. Colloid Interface Sci.*, 122, 521, 1988. Midmore, B.R., Diggins, D., Hunter, R.J., *J. Colloid Interface Sci.*, 129, 153, 1989.
946. Van der Put, A.G. and Bijsterbosch, B.H., *J. Colloid Interface Sci.*, 75, 512, 1980. 92, 499, 1983.
947. Rosen, L.A. and Saville, D.A., *J. Colloid Interface Sci.*, 144, 82, 1990. *J. Colloid Interface Sci.*, 149, 2, 1992.
948. Dukhin, A.S. and van de Ven, T.G.M., *J. Colloid Interface Sci.*, 165, 9, 1994.
949. Meijer, A.E.J., van Megen, W.J., and Lyklema, J., *J. Colloid Interface Sci.*, 66, 99, 1978.
950. Russel, A.S., Scales, P.J., Mangelsdorf, C.S., and White, L.R., *Langmuir*, 11, 1553, 1995.
951. Gittings, M.R. and Saville, D.A., *Langmuir*, 11, 798, 1995.
952. Bastos-Gonzalez, D., Hidalgo-Alvarez, R., and de las Nieves, F.J., *J. Colloid Interface Sci.*, 177, 372, 1996.
953. Saville, D.A., *J. Colloid Interface Sci.*, 222, 137, 2000.
954. Alty, T., *Proc. Royal Soc.*, A106, 315, 1924.
955. Usui, S., Sasaki, H., and Matsukawa, H., *J. Colloid Interface Sci.*, 65, 36, 1978. *J. Colloid Interface Sci.*, 81, 80, 1981.
956. McShea, J.A. and Callaghan, I.C., *Colloid Polymer Sci.*, 261, 757, 1983.
957. Yoon, R.-H. and Yordan, J.L., *J. Colloid Interface Sci.*, 113, 430, 1986.
958. Graciaa, A., Morel, G., Saulnier, R., Lachaise, J., and Schechter, R.S., *J. Colloid Interface Sci.*, 172, 131, 1995.
959. Dickinson, W., *Trans. Faraday Soc.*, 37, 140, 1941.
960. Taylor, A.J. and Wood, F.W., *Trans. Faraday Soc.*, 53, 523, 1957.
961. Dunstan, D.E. and Saville, D.A., *J. Chem. Soc. Faraday Trans.*, 88, 2031, 1992. *J. Chem. Soc. Faraday Trans.*, 89, 527, 1993. *J. Colloid Interface Sci.*, 166, 472, 1994.
962. Marinova, K.G., Alargova, R.G., Denkov, N.D., Velev, O.D., Petsev, D.N., Ivanov, I.B., and Borwankar, R., *Langmuir*, 12, 2045, 1996.
963. Graciaa, A., Morel, G., Saulner, P., Lachaise, J., and Schechter, R.S., *J. Colloid Interface Sci.*, 172, 131, 1995.
964. Exerowa, D., Zachariewa, M., Cohen, R., and Platikanov, D., *Colloid & Polymer Sci.*, 257, 1089, 1979.
965. Waltermo, A., Manev, E., Pugh, R., and Claesson, P., *J. Dispersion Sci. Technology*, 15, 273, 1994.
966. Karraker, K.A. and Radke, C.J., *Adv. Colloid Interface Sci.*, 96, 231, 2002.
967. Van de Hulst, H.C., *Light Scattering by Small Particles*, Wiley, New York, 1957. 2nd edn., Dover, New York, 1981.
968. Kerker, M., *The Scattering of Light and other Electromagnetic Radiation*, Academic Press, New York, 1969.
969. Hiemenz, P.C. and Rajagopalan, R., *Principles of Colloid and Surface Chemistry*, 3rd edn., Marcel Dekker, New York, 1997, Chapter 5.
970. Lyklema, J., *Fundamentals of Interface and Colloid Science*, Vol. 1, Academic Press, New York, 1991, Chapter 7.
971. McIntyre, D. and Gornick, F., Eds., *Light Scattering from Dilute Polymer Solutions*, Gordon and Breach, New York, 1964.

972. Rayleigh, L., *Phil. Mag.*, 41, 107, 1871. *Phil. Mag.*, 41, 274, 1871. *Phil. Mag.*, 41, 447, 1871.
973. Debye, P., *J. Appl. Phys.*, 15, 338, 1944.
974. O'Konski, C.T., Ed., *Molecular Electrooptics*, Marcel Dekker, New York, 1976.
975. Jennings, B.R., Ed., *Electro-optics and Dielectrics of Macromolecules and Colloids*, Plenum Press, New York, 1979.
976. Stoilov, S.P., *Colloid Electroptics: Theory, Techniques and Applications*, Academic Press, New York, 1991.
977. Rayleigh, L., *Proc. Royal Soc.*, A84, 25, 1910. *Proc. Royal Soc.*, A90, 219, 1914. *Proc. Royal Soc.*, A94, 296, 1918.
978. Debye, P., *Ann. Phys.*, 46, 809, 1915.
979. Gans, R., *Ann. Phys.*, 65, 97, 1921. *Ann. Phys.*, 67, 353, 1923. *Ann. Phys.*, 76, 29, 1925.
980. Guinier, A., *Ann. Phys.* (France), 12, 161, 1939.
981. Yamakawa, H., *Modern Theory of Polymer Solutions*, Harper & Row, New York, 1971.
982. Shull, C.C. and Roess, L.C., *J. Appl. Phys.*, 18, 295, 1947.
983. Brenner, H., *Int. J. Multiphase Flow*, 1, 195, 1974.
984. Zero, K. and Pecora, R., in *Dynamic Light Scattering*, Pecora, R., Ed., Plenum Press, New York, 1985, Chapter 3.
985. Neugebauer, T., *Ann. Phys.*, 42, 509, 1942.
986. Saito, N. and Ikeda, Y., *J. Phys. Soc. Jpn*, 6, 305, 1951.
987. Fournet, G. and Guinier, A., *J. Phys. Radium*, 11, 516, 1950.
988. Riseman, J. and Kirkwood, J.G., *J. Chem. Phys.*, 18, 512, 1950.
989. Broersma, S., *J. Chem. Phys.*, 32, 1626, 1960. *J. Chem. Phys.*, 32, 1632, 1960.
990. Kratky, O. and Porod, G., *J. Colloid Sci.*, 4, 35, 1949.
991. Becher, P., *J. Phys. Chem.*, 63, 1213, 1959.
992. Debye, P., Technical Report No 637 to Rubber Reserve Company, Washington, DC, April 9, 1945.
993. Hearst, J.E., *J. Chem. Phys.*, 38, 1062, 1963.
994. Mie, G., *Ann. Phys.*, 25, 377, 1908.
995. Debye, P., *Ann. Phys.*, 30, 755, 1909.
996. Asano, S. and Yamamoto, G., *Appl. Opt.*, 14, 29, 1975. *Appl. Opt.*, 18, 712, 1979.
997. Glatter, O., Sieberer, J., and Schnablegger, H., *Part. Part. Syst. Charact.*, 8, 274, 1991.
998. Einstein, A., *Ann. Phys.*, 33, 1275, 1910.
999. Debye, P., *J. Phys. Colloid Chem.*, 51, 18, 1947.
1000. McQuarrie, D.A., *Statistical Mechanics*, Harper & Row, New York, 1976.
1001. Zimm, B.H., *J. Chem. Phys.*, 16, 1093, 1948; *J. Chem. Phys.*, 16, 1099, 1948.
1002. Agterof, W.G.M., van Zomeren, J.A.J., and Vrij, A., *Chem. Phys. Lett.*, 43, 363, 1976.
1003. Cazabat, A.M. and Langevin, D., *J. Chem. Phys.*, 74, 3148, 1981.
1004. Brunetti, S., Roux, D., Bellocq, A.M., Fourche, G., and Bothorel, P., *J. Phys. Chem.*, 87, 1028, 1983.
1005. Baker, R.C., Florence, A.T., Ottewill, R.H., and Tadros, T.F., *J. Colloid Interface Sci.*, 100, 332, 1984.
1006. Denkov, N.D., Kralchevsky, P.A., Ivanov, I.B., and Vassilieff, C.S., *J. Colloid Interface Sci.*, 143, 157, 1991.
1007. Koper, G.J.M., Sager, W.F.C., Smeets, J., and Bedeaux, D., *J. Phys. Chem.*, 99, 13 291, 1995.
1008. Cabannes, P., *La Diffusion Moleculaire de la Lumiere*, Presses Universitaires de France, Paris, 1929.
1009. Utiyama, H., in *Light Scattering from Polymer Solutions*, Huglin, M.B., Ed., Academic Press, New York, 1972, Chapter 4.
1010. Eskin, B.E., *Light Scattering from Polymer Solutions*, Nauka, Leningrad, 1986, Chapter 1 (in Russian).
1011. Chu, B., *Laser Light Scattering: Basic Principles and Practice*, Academic Press, New York, 1974 (2nd ed., 1991).
1012. Berne, B.J. and Pecora, R., *Dynamic Light Scattering with Applications to Chemistry, Biology and Physics*, Wiley, New York, 1976.
1013. Pecora, R., Ed., *Dynamic Light Scattering: Applications of Photon Correlation Spectroscopy*, Plenum Press, New York, 1985.
1014. Schmitz, K.S., *An Introduction to Dynamic Light Scattering by Molecules*, Academic Press, New York, 1990.
1015. Brown, W., Ed., *Dynamic Light Scattering: The Method and Some Applications*, Clarendon Press, Oxford, 1993.
1016. Brown, W., Ed., *Light Scattering: Principles and Development*, Clarendon Press, Oxford, 1996.
1017. Dhont, J.K.G., *An Introduction to Dynamics of Colloids*, Elsevier, Amsterdam, The Netherlands, 1996.
1018. Jakeman, E., Oliver, C.J., and Pike, E.R., *J. Phys. A*, 3, L 45, 1970.
1019. Ware, B.R., *Adv. Colloid Interface Sci.*, 4, 1, 1974.
1020. Durst, F., Melling, A., and Whitelaw, J.H., *Principles and Practice of Laser Doppler Anemometry*, 2nd edn., Academic Press, New York, 1981.
1021. Miller, J.F., Schatzel, K., and Vincent, B., *J. Colloid Interface Sci.*, 143, 532, 1991.
1022. Koppel, D.E., *J. Chem. Phys.*, 57, 4814, 1972.
1023. Gulari, E., Gulari, E., Tsunashima, Y., and Chu, B., *J. Chem. Phys.*, 70, 3965, 1979.
1024. Provencher, S.W., *Comput. Phys. Commun.*, 27, 213, 1982.
1025. Morrison, I.D., Grabowski, E.F., and Herb, C.A., *Langmuir*, 4, 496, 1985.
1026. Bertero, M., Boccacci, P., De Mol, C., and Pike, E.R., *Optical Particle Sizing, Theory and Practice*, Gousbet, G. and Greban, G., Eds., Plenum Press, New York, 1988.
1027. Finsy, R., de Groen, P., Deriemaeker, L., and Van Laethem, M., *J. Chem. Phys.*, 91, 7374, 1989.
1028. Nicolai, T., Brown, W., Johnsen, R.M., and Stepanek, P., *Macromolecules*, 23, 1165, 1990.
1029. Nicolai, T., Brown, W., Hvidt, S., and Heller, K., *Macromolecules*, 23, 5088, 1990.
1030. Bryan, R.K., *Eur. Biophys. J.*, 18, 165, 1990; Landowski, J. and Bryan, R.K., *Macromolecules*, 24, 6364, 1991.
1031. Schnablegger, H. and Glatter, O., *Appl. Opt.*, 30, 4889, 1991.

1032. Pecora, R., *J. Chem. Phys.*, 49, 1036, 1968.
1033. Pusey, P.N. and Tough, R.J.A., in *Dynamic Light Scattering*, Pecora, R., Ed., Plenum Press, New York, 1985, Chapter 4.
1034. Batchelor, G.K., *J. Fluid Mech.*, 52, 245, 1972; *J. Fluid Mech.*, 74, 1, 1976.
1035. Felderhof, B.U., *Physica*, 89A, 373, 1977.
1036. Felderhof, B.U., *J. Phys. A: Math. Gen.*, 11, 929, 1978.
1037. Ackerson, B.J., *J. Chem. Phys.*, 64, 242, 1976; *J. Chem. Phys.*, 69, 684, 1978.
1038. Hess, W. and Klein, R., *Adv. Physics*, 32, 173, 1983.
1039. Schurr, J.M., *Chem. Phys.*, 111, 55, 1987.
1040. Russel, W.B. and Glendinning, A.B., *J. Chem. Phys.*, 74, 948, 1981.
1041. Denkov, N.D. and Petsev, D.N., *Physica A*, 183, 462, 1992.
1042. Nägele, G., *Phys. Reports*, 272, 215, 1996.
1043. Hirtzel, C.S. and Rajagopalan, R., in *Micellar Solutions and Microemulsions: Structure, Dynamics and Statistical Thermodynamics*, Springer-Verlag, New York, 1990, Chapter 7.
1044. Gaylor, K.J., Snook, I.K., van Megen, W.J., and Watts, R.O., in *Light Scattering in Liquids and Macromolecular Solutions*, Degiorgio, V., Corti, M., and Giglio, M., Eds., Plenum Press, New York, 1980.
1045. Jones, R.B. and Schimtz, R., *Physica A*, 149, 373, 1988.
1046. Cichocki, B. and Felderhof, B.U., *J. Chem. Phys.*, 89, 1049 and 3705, 1988.
1047. Kops-Werkhoven, M.M. and Fijnaut, H.M., *J. Chem. Phys.*, 74, 1618, 1981.
1048. Cichocki, B. and Felderhof, B.U., *J. Chem. Phys.*, 93, 4427, 1990; *J. Chem. Phys.*, 94, 563, 1991.
1049. Petsev, D.N. and Denkov, N.D., *J. Colloid Interface Sci.*, 149, 329, 1992; Petsev, D.N., Denkov, N.D., and Nagayama, K., *Chem. Phys.*, 175, 265, 1993.
1050. Corti, M. and Degiorgio, V., *J. Phys. Chem.*, 85, 711, 1981.
1051. Belloni, L., Drifford, M., and Turq, P., *J. Phys. Lett.*, 46, L207, 1985. *J. Phys. Lett.*, 46, L1183, 1985.
1052. Drifford, M., Belloni, L., Dalbiez, J.P., and Chattopadhyay, A.K., *J. Colloid Interface Sci.*, 105, 587, 1985.
1053. Nagele, G., Mandl, B., and Klein, R., *Prog. Colloid Polym. Sci.*, 98, 117, 1995.
1054. Ohshima, H., Healy, T.W., White, L.R., and O'Brien, R.W., *J. Chem. Soc. Faraday Trans. 2*, 80, 1299, 1984.
1055. Schumacher, G.A. and van de Ven, T.G.M., *Faraday Discussions Chem. Soc.*, 83, 75, 1987; *J. Chem. Soc., Faraday Trans.*, 87, 971, 1991.
1056. Bauer, D.R., *J. Phys. Chem.*, 84, 1592, 1980.
1057. Cummins, P.G. and Staples, E.J., *J. Phys. E*, 14, 1171, 1981.
1058. Phillies, G.D.J., *J. Chem. Phys.*, 74, 260, 1981.
1059. Phillies, G.D.J., *Phys. Rev. A*, 24, 1939, 1981.
1060. Dhont, J.K.G. and de Kruif, C.G., *J. Chem. Phys.*, 79, 1658, 1983.
1061. Schätzel, K., *J. Modern Opt.*, 38, 1849, 1991.
1062. Pusey, P.N., *Curr. Opinion Colloid Interface Sci.*, 4, 177, 1999.
1063. Drewel, M., Ahrens, J., and Schatzel, K., in *Proceedings of the 2nd International Congress on Particle Sizing*, Arizona University Press, Tempe, Arizona, 1990.
1064. Segré, P.N., van Megen, W., Pusey, P.N., Schätzel, K., and Peters, W., *J. Modern Opt.*, 42, 1929, 1995.
1065. Aberle, L.B., Hulstede, P., Wiegand, S., Schroer, W., and Staude, W., *Appl. Optics*, 37, 6511, 1998.
1066. Tanaka, T. and Benedek, G.B., *Appl. Opt.*, 14, 189, 1975.
1067. Sorensen, C.M., Mockler, R.C., and O'Sullivan, W.J., *Phys. Rev. A*, 14, 1520, 1976; *Phys. Rev. A*, 17, 2030, 1978.
1068. Dhadwal, H.S. and Ross, D.A., *J. Colloid Interface Sci.*, 76, 478, 1980.
1069. Auweter, H. and Horn, D., *J. Colloid Interface Sci.*, 105, 399, 1985; *J. Phys. D*, 22, 1257, 1989.
1070. Thomas, J.C. and Tjin, S.C., *J. Colloid Interface Sci.*, 129, 15, 1989.
1071. MacFayden, A.J. and Jennings, B.R., *Opt. Laser Technol.*, 22, 715, 1990.
1072. Thomas, J.C., *Langmuir*, 5, 1350, 1989.
1073. Meeren, P.V., Bogaert, H., Stastny, M., Vanderdeelen, J., and Baert, L., *J. Colloid Interface Sci.*, 160, 117, 1993.
1074. Wiese, H. and Horn, D., *J. Chem. Phys.*, 94, 6429, 1991.
1075. Dhadwal, H.S., Ansari, R.R., and Meyer, W.V., *Rev. Sci. Instrum.*, 62, 2963, 1991.
1076. Maret, G. and Wolf, P.E., *Z. Phys. B*, 65, 409, 1987.
1077. Rosenbluch, M., Hoshen, M., Freund, I., and Kaveh, M., *Phys. Rev. Lett.*, 58, 2754, 1987; *Phys. Rev. Lett.*, 60, 1130, 1988.
1078. Pine, D.J., Weitz, D.A., Chaikin, P.M., and Herbolzheimer, E., *Phys. Rev. Lett.*, 60, 1134, 1988.
1079. Pine, D.J., Weitz, D.A., Maret, G., Wolf, P.E., Herbolzheimer, E., and Chaikin, P.M., in *Scattering and Localization of Classical Waves in Random Media*, Sheng, P., Ed., World Scientific, Singapore, 1989.
1080. Golubentsev, A.A., *Sov. Phys. JETP*, 59, 26, 1984.
1081. Stephen, M.J., *Phys. Rev. B*, 37, 1, 1988.
1082. Durian, D.J., Weitz, D.A., and Pine, D.J., *Science*, 252, 686, 1991.
1083. Sanyal, S., Sood, A.K., Ramkumar, S., Ramaswamy, S., and Kumar, N., *Phys. Rev. Lett.*, 72, 2963, 1994.
1084. Liu, A.J., Ramaswamy, S., Mason, T.G., Gang, H., and Weitz, D.A., *Phys. Rev. Lett.*, 76, 3017, 1996.
1085. Mason, T.G., Hu, G., and Weitz, D.A., *J. Opt. Soc. Am. A*, 14, 139, 1997.
1086. Durian, D.J., *Phys. Rev. E*, 55, 1739, 1997.
1087. Durian, D.J., *Curr. Opinion Colloid Interface Sci.*, 2, 615, 1997.

1088. Hebraud, P., Lequeux, F., Munch, J.P., and Pine, D.J., *Phys. Rev. Lett.*, 78, 4657, 1997.
1089. Maret, G., *Curr. Opinion Colloid Interface Sci.*, 2, 251, 1997.
1090. Gisler, T. and Weitz, D.A., *Curr. Opinion Colloid Interface Sci.*, 3, 586, 1998.
1091. Debye, P., *Ann. N.Y. Acad. Sci.*, 51, 575, 1949.
1092. Debye, P. and Anacker, E.W., *J. Phys. Colloid Chem.*, 55, 644, 1959.
1093. Mysels, K.J. and Princen, L.H., *J. Phys. Chem.*, 63, 1696, 1959.
1094. Huisman, H.F., *Proc. Kon. Ned. Akad. Wet.*, B67, 367, 1964; *Proc. Kon. Ned. Akad. Wet.*, B67, 376, 1964; *Proc. Kon. Ned. Akad. Wet.*, B67, 388, 1964; *Proc. Kon. Ned. Akad. Wet.*, B67, 407, 1964.
1095. Vrij, A. and Overbeek, J.T.G., *J. Colloid Sci.*, 17, 570, 1962.
1096. Becher, P., in *Nonionic Surfactants*, Schick, M.J., Ed., Marcel Dekker, New York, 1967, Chapter 15.
1097. Hall, D.J. and Tiddy, G.J.T., in *Anionic Surfactants: Physical Chemistry of Surfactant Action*, Lucassen-Reynders, E.H., Ed., Marcel Dekker, New York, 1981, Chapter 2.
1098. Eicke, H.-F., *Topics Current Chem.*, 87, 85, 1980.
1099. Mukerjee, P., *J. Phys. Chem.*, 76, 565, 1972.
1100. Israelachvili, J.N., Mitchell, D.J., and Ninham, B.W., *J. Chem. Soc. Faraday Trans. 2*, 72, 1525, 1976.
1101. Ruckenstain, E. and Nagarajan, R., *J. Colloid Interface Sci.*, 57, 388, 1976; *J. Colloid Interface Sci.*, 91, 500, 1983.
1102. Mazer, N.A., in *Dynamic Light Scattering*, Pecora, R., Ed., Plenum Press, 1985, Chapter 8.
1103. Mazer, N.A., Benedek, G.B., and Carey, M.C., *J. Phys. Chem.*, 80, 1075, 1976.
1104. Briggs, J., Nicoli, D.F., and Ciccolello, R., *Chem. Phys. Lett.*, 73, 149, 1980.
1105. Mishic, J.R. and Fisch, M.R., *J. Chem. Phys.*, 92, 3222, 1990.
1106. Schillen, K., Brown, W., and Johnsen, R.M., *Macromolecules*, 27, 4825, 1994.
1107. Porte, G., Appell, J., and Poggi, Y., *J. Phys. Chem.*, 84, 3105, 1980.
1108. Appell, J. and Porte, G., *J. Colloid Interface Sci.*, 81, 85, 1981.
1109. Imae, T., *J. Phys. Chem.*, 94, 5953, 1990.
1110. Alargova, R., Petkov, J., Petsev, D., Ivanov, I.B., Broze, G., and Mehreteab, A., *Langmuir*, 11, 1530, 1995.
1111. Alargova, R.G., Danov, K.D., Kralchevsky, P.A., Broze, G., and Mehreteab, A., *Langmuir*, 14, 4036, 1998.
1112. Dorshow, R., Briggs, J., Bunton, C.A., and Nicoli, D.F., *J. Phys. Chem.*, 86, 2388, 1982. *J. Phys. Chem.*, 87, 1409, 1983.
1113. Missel, P.J., Mazer, N.A., Benedek, G.B., Young, C.Y., and Carey, M.C., *J. Phys. Chem.*, 84, 1044, 1980.
1114. Rohde, A. and Sackman, E., *J. Colloid Interface Sci.*, 78, 330, 1980.
1115. Hartland, G.V., Grieser, F., and White, L.R., *J. Chem. Soc. Faraday Trans. 1*, 83, 591, 1987; Dunstan, D.E. and White, L.R., *J. Colloid Interface Sci.*, 134, 147, 1990.
1116. Ortega, F., Bacaloglu, R., McKenzie, D.C., Bunton, C.A., and Nicoli, D.F., *J. Phys. Chem.*, 94, 501, 1990.
1117. Corti, M. and Degiorgio, V., *Phys. Rev. Lett.*, 45, 1045, 1980; *J. Phys. Chem.*, 85, 1442, 1981.
1118. Calje, A., Agterof, W., and Vrij, A., in *Micellization, Solubilization and Microemulsions*, Mittal, K., Ed., Plenum Press, New York, 1977.
1119. Lemaire, B., Bothorel, P., and Roux, D., *J. Phys. Chem.*, 87, 1023, 1983.
1120. Cazabat, A.M., Langevin, D., and Pouchelon, A., *J. Colloid Interface Sci.*, 73, 1, 1980.
1121. Hou, M.J., Kim, M., and Shah, D.O., *J. Colloid Interface Sci.*, 123, 398, 1988.
1122. Auvrey, L., *J. Phys. Chem. (Paris)*, 46, 163, 1985.
1123. Fletcher, P.D.I., Howe, A.M., and Robinson, B.H., *J. Chem. Soc. Faraday Trans. 1*, 83, 985, 1987.
1124. Fletcher, P.D.I. and Holzwarth, J.F., *J. Phys. Chem.*, 95, 2550, 1991.
1125. Lagues, M., Ober, R., and Taupin, C., *J. Phys. Lett.*, 39, 487, 1978.
1126. Lagourette, B., Peyrelasse, J., Boned, C., and Clausse, M., *Nature*, 281, 60, 1979.
1127. Eicke, H.-F., Shepherd, J.C.W., and Steineman, A., *J. Colloid Interface Sci.*, 56, 168, 1976.
1128. Guering, P. and Cazabat, A.M., *J. Phys. Lett.*, 44, 601, 1983.
1129. Guering, P., Cazabat, A.M., and Paillette, M., *Europhys. Lett.*, 2, 953, 1986.
1130. Dorshow, R.B. and Nicoli, D.F., in *Measurement of Suspended Particles by QELS*, Dahneke, B.E., Ed., Wiley, New York, 1983. p. 529.
1131. Guering, P., Nilsson, P.-G., and Lindman, B., *J. Colloid Interface Sci.*, 105, 41, 1985.
1132. Kato, T., Takeuchi, H., and Seimiya, T., *J. Colloid Interface Sci.*, 140, 253, 1990.
1133. Tuzar, Z. and Kratohvil, P., in *Surface and Colloid Science*, Vol. 15, Matijevi, E., Ed., Plenum Press, New York, 1993, Chapter 1.
1134. Cogan, K.A. and Gast, A.P., *Macromolecules*, 23, 745, 1990; Chu, B., *Langmuir*, 11, 414, 1995.
1135. Satoh, N. and Tsujii, K., *J. Phys. Chem.*, 91, 6629, 1987.
1136. Thunig, C., Hoffmann, H., and Platz, G., *Prog. Colloid Polymer Sci.*, 79, 297, 1989; *Prog. Colloid Polym. Sci.*, 83, 167, 1990.
1137. McDonald, J.A. and Rennie, A.R., *Progress Colloid Polym. Sci.*, 98, 75, 1995.
1138. Goddard, E.D. and Ananthapadmanabhan, K.P., Eds., *The Interactions of Surfactants with Polymers and Proteins*, CRC Press, Boca Raton, FL, 1993.
1139. Bahadur, P., Dubin, P., and Rao, Y.K., *Langmuir*, 11, 1951, 1995; Li, Y., Dubin, P.L., Havel, H.A., Edwards, S.L., and Dautzenberg, H., *Macromolecules*, 28, 3098, 1995.
1140. Hayakawa, K. and Kwak, J.C.T., in *Cationic Surfactants: Physical Chemistry*, Rubingh, D.N. and Holland, P.M., Eds., Marcel Dekker, New York, 1991, Chapter 5.

1141. Corti, M. and Canti, L., *Adv. Colloid Interface Sci.*, 32, 151, 1990.
1142. Bloomfield, V.A., in *Dynamic Light Scattering*, Pecora, R., Ed., Plenum Press, New York, 1985, Chapter 10.
1143. Egelhaaf, S.U., Pedersen, J.S., and Schurtenberger, P., *Progress Colloid Polymer Sci.*, 98, 224, 1995.
1144. Langevin, D., Ed., *Light Scattering by Liquid Surfaces and Complementary Techniques*, Marcel Dekker, New York, 1992.
1145. Earnshaw, J.C. and McCoo, E., *Langmuir*, 11, 1087, 1995.
1146. Vrij, A., Joosten, J.G.H., and Fijnaut, H.M., *Adv. Chem. Phys.*, 48, 329, 1981.
1147. Joosten, J.G.H., in *Thin Liquid Films*, Ivanov, I.B., Ed., Marcel Dekker, New York, 1988, Chapter 9.
1148. Hirleman, E.D., *Part. Part. Syst. Charact.*, 4, 128, 1987.
1149. van de Hulst, H.C., *Multiple Light Scattering*, Academic Press, New York, 1980.
1150. Penders, M.G.H.M. and Vrij, A., *J. Chem. Phys.*, 93, 3704, 1990.
1151. Apfel, U., Hörner, K.D., and Ballauff, M., *Langmuir*, 11, 3401, 1995.
1152. Bryant, G. and Thomas, J.C., *Langmuir*, 11, 2480, 1995.
1153. Barber, P.W., Yeh, C., and Wang, D.-S., *Appl. Opt.*, 14, 2864, 1975; *Appl. Opt.*, 17, 797, 1978; *Appl. Opt.*, 18, 1190, 1979.
1154. Quirantes, A. and Delgado, A.V., *Progress Colloid Polym. Sci.*, 98, 145, 1995.
1155. Purcell, E.M. and Pennypacker, C.R., *Astrophys. J.*, 186, 705, 1973.
1156. Buitenhuis, J., Dhont, J.K.G., and Lekkerkerker, H.N.W., *J. Colloid Interface Sci.*, 162, 19, 1994.
1157. Schaefer, D.W., *J. Chem. Phys.*, 66, 3980, 1977.
1158. Finsy, R., Moreels, E., Bottger, A., and Lekkerkerker, H., *J. Chem. Phys.*, 82, 3812, 1985.
1159. Clark, N.A., Hurd, A.J., and Ackerson, B.J., *Nature*, 281, 57, 1979.
1160. Pieranski, P., *Contemp. Phys.*, 24, 25, 1983.
1161. Pusey, P.N., *Phil. Trans. R. Soc. London*, A293, 429, 1979.
1162. van Megen, W., Pusey, P.N., and Bartlett, P., *Phase Transitions*, 21, 207, 1990.
1163. Piazza, R. and Degiorgio, V., *Physica A*, 182, 576, 1982.
1164. Degiorgio, V., Piazza, R., Corti, M., and Stavans, J., *J. Chem. Soc. Faraday Trans*, 87, 431, 1991.
1165. Dhont, J.K.G., Smits, K., and Lekkerkerker, H.N.M., *J. Colloid Interface Sci.*, 152, 386, 1992.
1166. Hiltner, P.A. and Krieger, I.M., *J. Phys. Chem.*, 73, 2386, 1969.
1167. Yoshiyama, T., Sogami, I., and Ise, N., *Phys. Rev. Lett.*, 53, 2153, 1984.
1168. Sogami, I. and Yoshiyama, T., *Phase Transitions*, 21, 171, 1990.
1169. Monovoukas, Y. and Gast, A.P., *Phase Transitions*, 21, 183, 1990.
1170. Bartsch, E., *Curr. Opinion Colloid Interface Sci.*, 3, 577, 1998.
1171. Van Megen, W., Mortenson, T.C., Müller, J., and Williams, S.R., *Phys. Rev. E*, 58, 6073, 1998.
1172. D'Aguanno, B. and Klein, R., *J. Chem. Soc. Faraday Trans.*, 87, 379, 1991.
1173. Krause, R., Arauz-Lara, J.L., Nagele, G., Ruiz-Estrada, H., Medina-Noyola, M., Weber, R., and Klein, R., *Physica A*, 178, 241, 1991.
1174. Wagner, N.J., Krause, R., Rennie, A.R., D'Aguanno, B., and Goodwin, J., *J. Chem. Phys.*, 95, 494, 1991.
1175. Pusey, P.N. and van Megen, W., *Nature*, 320, 340, 1986.
1176. Härtl, W., Klemp, R., and Versmold, H., *Phase Transitions*, 21, 229, 1990.
1177. Harland, J.L. and van Megen, W., *Phys. Rev. E*, 55, 3054, 1997.
1178. Russel, W.B., Chaikin, P.M., Zhu, J., Meyer, W.V., and Rogers, R., *Langmuir*, 13, 3871, 1997.
1179. Palberg, T., *Curr. Opinion Colloid Interface Sci.*, 2, 607, 1997.
1180. Hoffman, R.L., *J. Colloid Interface Sci.*, 46, 491, 1974.
1181. Bossis, G., Brady, J.F., and Mathis, C., *J. Colloid Interface Sci.*, 126, 1 and 16, 1988.
1182. Wagner, N.J. and Russel, W.B., *Phys. Fluids*, A2, 491, 1990.
1183. Ackerson, B.J. and Clark, N.A., *Physica A*, 118, 221, 1983; *Phys. Rev. A*, 30, 906, 1984.
1184. Ackerson, B.J. and Pusey, P.N., *Phys. Rev. Lett.*, 61, 1033, 1988.
1185. Ackerson, B.J., *Physica A*, 174, 15, 1991.
1186. Weitz, D.A. and Oliveria, M., *Phys. Rev. Lett.*, 52, 1433, 1984.
1187. Weitz, D.A., Huang, J.S., Lin, M.Y., and Sung, J., *Phys. Rev. Lett.*, 53, 1651, 1984; *Phys. Rev. Lett.*, 54, 1416, 1985; *Phys. Rev. Lett.*, 57, 2037, 1986.
1188. Meakin, P., in *Phase Transitions*, Vol. 12, Domb, C. and Lebowitz, J.L., Eds., Academic Press, New York, 1988.
1189. Weitz, D.A., Lin, M.Y., and Huang, J.S., in *Physics of Complex and Supermolecular Fluids*, Safran, S.A., and Clark, N.A., Eds., Wiley-Interscience, New York, 1987.
1190. Kolb, M., *Phys. Rev. Lett.*, 53, 1654, 1984.
1191. Mandelbrot, B.B., *The Fractal Geometry of Nature*, Freeman, New York, 1983.
1192. Meakin, P., *Phys. Rev. Lett.*, 51, 1119, 1983.
1193. Van Dongen, G.J. and Ernst, M.H., *Phys. Rev. Lett.*, 54, 1396, 1985.
1194. Brown, W.D. and Ball, R.C., *J. Phys. A*, 18, L517, 1985.
1195. Schaeffer, D.W., Martin, J.E., Wiltzius, P., and Cannell, D.S., *Phys. Rev. Lett.*, 52, 2371, 1984.
1196. Ball, R.C., Weitz, D.A., Witten, T.A., and Leyvraz, F., *Phys. Rev. Lett.*, 58, 274, 1987.
1197. Meakin, P., Vicsek, T., and Family, F., *Phys. Rev. B*, 31, 564, 1985.
1198. Lin, M.Y., Lindsay, H.M., Weitz, D.A., Ball, R.C., Klein, R., and Meakin, P., in *Fractals in the Natural Sciences*, Fleischmann, M., Tildesley, D.J., and Ball, R.C., Eds., Princeton University Press, Princeton, 1989.

1199. Amal, R., Raper, J.A., and Waite, T.D., *J. Colloid Interface Sci.*, 140, 158, 1990.
1200. Odriozola, G., Tirado-Miranda, M., Schmidt, A., Martinez Lopez, F., Callejas-Fernandez, J., Martinez-Garcia, R., and Hidalgo-Alvarez, R., *J. Colloid Interface Sci.*, 240, 90, 2001.
1201. Georgialis, Y. and Saenger, W., *Adv. Colloid Interface Sci.*, 46, 165, 1993.
1202. Georgialis, Y., Zouni, A., Eberstein, W., and Saenger, W., *J. Crystal Growth*, 126, 245, 1993.
1203. Eberstein, W., Georgialis, Y., and Saenger, W., *J. Crystal Growth*, 143, 71, 1994.
1204. Muschol, M. and Rosenberger, F., *J. Chem Phys.*, 103, 10424, 1995.
1205. Nikolai, T., Urban, C., and Schurtenberger, S., *J. Colloid Interface Sci.*, 240, 419, 2001.
1206. Scheffold, F. and Cerbino, R., *Curr. Opin. Colloid Interface Sci.*, 12, 5057, 2007.
1207. Tromp, R.H., Rennie, A.R., and Jones, R.A.L., *Macromolecules*, 284129, 38, 1995.
1208. Ferri, F., *Rev. Sci. Instrum.*, 68, 2265, 1997.
1209. Cipelletti, L. and Weitz, D.A., *Rev. Sci. Instrum.*, 70, 3214, 1999.
1210. Vogel, H.J., Baur, G., and Burchard, W., *Colloid Polym. Sci.*, 279, 166, 2001.
1211. Thill, A., Desert, S., and Delsanti, M., *Eur. Phys. J. Appl. Phys.*, 17, 201, 2002.
1212. Bhat, S., Tuinier, R., and Scurtenberger, P., *J. Phys. Condens Matter*, 18, 1339, 2006.
1213. Giglio, M., Carpineti, M., and Vailati, A., *Phys. Rev. Lett.*, 85, 1416, 2000.
1214. Brogioli, D., Vailati, A., and Giglio, M., *Appl. Phys.*, 81, 4109–2002.
1215. Brogioli, D., Vailati, A., and Giglio, M., *Europhys. Lett.*, 63, 220, 2003.
1216. Ferri, F., Magatti, D., Pescini, D., Potenza, M.A.C., and Giglio, M., *Phys. Rev. E*, 70, 041405, 2004.
1217. Trainoff, S.P. and Cannell, D.S., *Phys. Fluids*, 14, 1340, 2002.
1218. Cerbino, R., Mazzoni, S., Vailati, A., and Giglio, M., *Phys. Rev. Lett.*, 94, 064501, 2005.
1219. Vailati, A., Cerbino, R., Mazzoni, S., Giglio, M., Nikolaenko, G., Takacs, C.J., et al., *Appl. Opt.*, 45, 2155, 2006.
1220. Croccolo, F., Brogioli, D., Vailati, A., Giglio, M., and Cannell, D.S., *Appl. Opt.*, 45, 2166, 2006.
1221. Lehner, D., Kellner, G., Schnablegger, H., and Glatter, O., *J. Colloid Interface Sci.*, 201, 34, 1998.
1222. Thomas, J. and Tjin, S., *J. Colloid Interface Sci.*, 129, 15, 1989.
1223. Lilge, D. and Horn, D., *Colloid Polym. Sci.*, 269, 704, 1991.
1224. Horn, F.M., Richtering, W., Bergenholtz, J., Willenbacher, N., and Wagner, N.J., *J. Colloid Interface Sci.*, 225, 166, 2000.
1225. Schatzel, K., *J. Mod. Opt.*, 38, 1849, 1991.
1226. Pusey, P.N., *Curr. Opin. Colloid Interface Sci.*, 4, 177, 1999.
1227. Drewel, M., Ahrens, J., and Podschus, U., *J. Opt. Soc. Am. A*, 7, 206, 1990.
1228. Overbeck, E., Sinn, C., and Palberg, T., *Prog. Colloid Polym. Sci.*, 104, 117, 1997.
1229. Aberle, L.B., Wiegand, S., Scherr, W., and Staude, W., *Prog. Polym. Sci.*, 104, 121, 1997.
1230. Urban, C. and Schurtenberger, P., *J. Colloid Interface Sci.*, 207, 150, 1998.
1231. Meyer, W.V., Cnahhell, D.S., Smart, A.E., Taylor, T.W., and Tin, P., *Appl. Opt.*, 30, 7551, 1997.
1232. Schroder, J.M., Becker, A., and Wiegand, S., *J. Chem. Phys.*, 118, 11307, 2003.
1233. Zakharov, P., Bhat, S., Schurtenberger, P., and Scheffold, F., *Appl. Opt.*, 45, 1756, 2006.
1234. Kaplan, P.D., Dinsmore, A.D., Yodh, A.G., and Pine, D.J., *Phys. Rev. E*, 50, 4827, 1994.
1235. Bavarian, C., Caton, F., Dillet, J., and Mougel, J., *Phys. Rev. E*, 71, 066603, 2005.
1236. Richter, S.M. and Sevick-Muraca, E.M., *Colloids Surf. A*, *Physicochem. Eng. Asp.*, 172, 163, 2000.
1237. Maret, G. and Wolf, P.E., *Z. Phys. B*, 54, 409, 1987.
1238. Pine, D.J., Weitz, D.A., Chaikin, P.M., and Herbolzheinner, E., *Phys. Rev. Lett.*, 60, 1134, 1988.
1239. Popescu, G. and Dogariu, A., *Eur. Phys. J. Appl. Phys.*, 32, 73, 2005.
1240. Fercher, A.F., Drexter, W., Hiltzenberger, C.K., and Lasser, T., *Rep. Prog. Phys.*, 66, 239, 2003.
1241. Bizheva, K.K., Siegel, A.M., and Boas, D.A., *Phys. Rev. E*, 58, 7664, 1998.
1242. Popescu, G. and Dogariu, A., *Opt. Lett.*, 24, 442, 1999.
1243. Pusey, P.N. and van Megen, W., *Physica A*, 157, 705, 1989.
1244. Joosten, J.G.H., Geladé, E.T.F., and Pusey, P.N., *Phys. Rev. A*, 42, 2161, 1990.
1245. van Megen, W., Underwood, S.M., and Pusey, P.N., *Phys. Rev. Lett.*, 67, 1586, 1991.
1246. Xue, J.Z., Pine, D.J., Milner, S.T., Wu, X.I., and Chaikin, P.M., *Phys. Rev. A*, 46, 6550, 1992.
1247. Scheffold, F., Skipetrov, S.E., Romer, S., and Schurtenberger, P., *Phys. Rev. E*, 63, 061404, 2001,
1248. Kirsch, S., Frenz, V., Schartl, W., Bartsch, E., and Sillescu, H., *J. Chem. Phys.*, 104, 1758, 1996.
1249. Cipelletti, L., Manley, S., Ball, R.C., and Weitz, D.A., *Phys. Rev. Lett.*, 84, 2275, 2000.
1250. Viasnoff, V., Lequeux, F., and Pine, D.J., *Rev. Sci. Instrum.*, 73, 2336, 2002.
1251. Knaebel, A., Bellour, M., Munch, J.P., Viasnoff, V., Lequeux, F., and Harden, J.L., *Europhys. Lett.*, 52, 73, 2000.
1252. Cardinaux, F. and Cipelletti, F., *Europhys. Lett.*, 57, 738, 2002.
1253. Bandyopadhyay, R., Gittings, A.S., Suh, S.S., Dixon, P.K., and Durian, D.J., *Rev. Sci. Instrum.*, 76, 093110, 2005.
1254. Fercher, A.F. and Briers, J.D., *Opt. Commun.*, 37(5), 326, 1981.
1255. Briers, J.D., *Physiol. Meas.*, 22, R35, 2001.
1256. Pham, K.N., Egelhaaf, S.U., Moussaid, A., and Pusey, P.N., *Rev. Sci. Instrum.*, 75, 2419, 2004.
1257. Muller, J. and Palberg, T., *Prog. Colloid Polym. Sci.*, 100, 121, 1996.
1258. Hebraud, P., Lequeux, F., Munch, J.P., and Pine, D.J., *Phys. Rev. Lett.*, 78, 4657, 1997.

1259. Hoehler, R., Cohen-Addad, S., and Hoballah, H., *Phys. Rev. Lett.*, 79, 1154, 1997.
1260. Zakharov, P., Cardinaux, F., and Scheffold, F., *Phys. Rev. E*, 73, 011413, 2006.
1261. Lemieux, P.A. and Durian, D.J., *J. Opt. Soc. Am. A*, 16, 1651, 1999.
1262. Lemieux, P.A. and Durian, D.J., *Phys. Rev. Lett.*, 85, 4273, 2000.
1263. Cipelletti, L., Bissig, H., Trappe, V., Ballesta, P., Mazoyer, S., *J. Phys. Condens. Matter*, 15, 257, 2003.
1264. Duri, A., Bissig, H., Trappe, V., and Cipelletti, L., *Phys. Rev. E*, 72, 051401, 2005.
1265. Mayer, P., Bissig, H., Berthier, L., Cipelletti, L., Garraham, J.P., Sollich, P., et al., *Phys. Rev. Lett.*, 93, 115701, 2004.